I. R. IRAN

ISSN: 1728-1431
e-ISSN: 1735-9244

International Journal of Engineering

Journal Homepage: www.ije.ir

MERC

TRANSACTIONS A: BASICS

Volume 35, Number 10, October 2022

Materials and Energy Research Center

In the Name of God

INTERNATIONAL JOURNAL OF ENGINEERING
Transactions A: Basics

International **J**ournal of **E**ngineering *Transactions A: Basics* (ISSN 1728-1431) (EISSN 1735-9244)
International **J**ournal of **E**ngineering *Transactions B: Applications* (ISSN 1728-144X) (EISSN 1735-9244)
International **J**ournal of **E**ngineering *Transactions C: Aspects* (ISSN 2423-7167) (EISSN 1735-9244)
Web Sites: www.ije.ir & www.ijeir.info E-mails: ije.editor8@gmail.com, Tel: (+9821) 88771578, Fax: (+9821) 88773352
Materials and Energy Research Center (MERC)

ISSN: 1728-1431, e-ISSN: 1735-9244

International Journal of Engineering, Volume 35, Number 10, October 2022

CONTENTS

Transactions A: Basics

ISSN: 1728-1431, e-ISSN: 1735-9244

International Journal of Engineering, Volume 35, Number 10, October 2022

IJE TRANSACTIONS A: Basics Vol. 35 No. 10, (October 2022) 1803-1819

International Journal of Engineering

Journal Homepage: www.ije.ir

Bi-level Scenario-based Location-allocation-inventory Models for Post-crisis Conditions and Solving with Electromagnetic and Genetic Algorithms

Z. Sahraei, P. Samouei*

Department of Industrial Engineering, Faculty of Engineering, Bu-Ali Sina University, Hamedan, Iran

PAPER INFO

Paper history:
Received 16 December 2020
Received in revised form 02 May 2022
Accepted 14 May 2021

Keywords:
Crisis
Location
Allocation
Inventory
Mixed-integer Linear Programming
Meta-heuristic Algorithms

ABSTRACT

Incidents that occur suddenly due to natural and human functions and impose hardships on society are called crises. As the Earth's climate changes have increased the number of natural crises, including earthquakes, floods, hurricanes, etc., in recent years, human beings have felt the need for crisis management and the necessary planning in critical situations more than ever. This research aims to model and solve the problem of location, allocation, and inventory in post-crisis conditions. To meet this purpose, first, we have conducted a review of the previous papers. Then, we have identified the research gaps in management and planning in critical situations. In this study, uncertain budgets and demands and bi-level programming decision-making are the innovations. As a result, we have developed mixed-integer linear mathematical models to cover the research gaps. Finally, several problems have been solved in small dimensions by GAMS software and large-sized problems by genetic and electromagnetic meta-heuristic algorithms. Then, we analyzed the algorithms' performance which indicates the genetic algorithm is better than the electromagnetic algorithm in this issue.

***doi**: 10.5829/ije.2022.35.10a.01*

1. INTRODUCTION

A disaster or crisis is a set of events that disrupt human beings' environmental relations with their surroundings. Due to the accidental and unpredictable nature of natural crises, comprehensive plans are necessary to reduce and mitigate the risks and consequences of the crisis and deal with it. Demand for logistic items and services increases with the emergence of critical situations and the reduced capabilities due to the damage to infrastructures. In recent years, Earth's climate changes are increasing the number of natural disasters, including earthquakes, floods, hurricanes, etc., and their corresponding losses. According to the related latest statistics, approximately, 70000 people die, and 200 million people are annually injured due to natural disasters [1]. Despite the governmental and non-governmental organizations' efforts to respond promptly to disasters and use resources effectively, numerous studies indicate a relatively low level of crisis preparedness [2]. In addition, there was not any research that considered the problem as discussed in this paper. As a result, the above reasons motivated us to do this research.

The first step that we required to take in the case of a crisis is building local warehouses to transport medicine, food, and other necessities of the victims and allocate the warehouses to the disaster areas. In this research, the proposed mathematical model determines local warehouses' optimal location among the potential points intending to minimize construction costs and the optimal allocation of constructed warehouses to the damaged sites to minimize allocation costs. After constructing local warehouses and simultaneous with their optimal allocation, we need to take necessary measures to purchase emergency items such as food, medicine, clothing and blankets, and transfer them to the warehouses. Since there is a possibility of an aftershock, and it will be almost time-consuming to respond to a catastrophe, it is also essential to plan, manage, and inventory control in each period after preparing the items.

*Corresponding Author Institutional Email: p.samouei@basu.ac.ir
(P. Samouei)

Please cite this article as: Z. Sahraei, P. Samouei, Bi-level Scenario-based Location-allocation-inventory Models for Post-crisis Conditions and Solving with Electromagnetic and Genetic Algorithms, ***International Journal of Engineering, Transactions A: Basics***, Vol. 35 No. 10, (2022), 1803-1819

The mathematical model in this research considers this issue by using the periodic preparation and distribution of items to minimize inventory costs [3-6]. Ferreira et al. [7] have addressed the issue of the distribution of relief items with the assumption of the items' normalcy. Failure to pay attention to the expiration date of some items, such as medicine and food, can cause further damage to the victims because the slightest negligence can endanger the lives of the people who survived the disaster or prevent the timely supply and distribution of essential items. For instance, in Bam earthquake in Iran in 2007, about 30% of the antibiotics stored in the warehouses expired. The relief network faced the problem of preparing and responding quickly to the crisis [8]. Therefore, it is necessary to adopt the most appropriate policy to recover perishable products to preclude this problem. In this research, we assumed that in our periodic ordering policy, some necessary items are perishable, and we need to check the expiry date of the products and take out the obsolete items.

In the real world, we can state uncertainty in all factors. In critical situations, indeterminacy can also occur at the time and place of the accident, the severity of the incident, the likelihood of a strike, infrastructure disruption, the amount of damage, access to communication routes to the affected areas, supply and demand of relief items, and the specific budget allocated to cover the existing costs. Such uncertainties may happen because of insufficient information about the degree of personal injuries or financial damages, so they should be regarded when making more accurate and realistic planning decisions. Since few surveys have considered the assumption of uncertainty in demand (54%) and budget (0.02%) in their model, the present study covered the premise of demand and budget uncertainty by considering the scenarios on the magnitude of the earthquake.

Bi-level programming is a powerful tool for modeling and solving decentralized planning problems, but it has enormous computational complexity. In the real world, various systems have different subsystems that make it a hierarchical structure, and decision-making has its characteristics. In this type of planning, decisions are at different levels, and each identifies only some decision variables. Because of the computational complexity of planning, few articles in recent years have included this assumption in their research. In the present study, we turn the issue into bi-level programming, in which the leading decision-maker determines the variable of the optimal location of warehouses. Consequently, the decision-maker at the lower level determines the optimal amount of the items' allocation and inventory control according to the parameters and functional criteria.

The remaining structure of the paper is as follows:

Literature review of the related papers is presented in section 2. Problem description, assumptions, and mathematical model are given in section 3. Using solving methods consisting of the electromagnetic and genetic algorithms are in section 4. Section 5 is related to the computational results and discussions for different problems. Finally, in the last section, conclusion and future research directions are presented.

2. LITERATURE REVIEW

Cozzolino et al. [9] define disaster cycle management as the four main stages of mitigation, preparedness, response, and recovery. In our research, we have performed part of the measures related to the response phase. Naji Azimi et al. [10] proposed a location model. The points are selected from some potential points as satellite distribution centers, and people come to these locations to receive relief items. Their purpose was to minimize the distance that the vehicles traveled. Hu and Sheu [11] examined the reverse supply chain issue in waste management after a disaster. Their multi-objective linear programming model minimizes reverse logistic costs, the corresponding environmental and operational risks and the psychological harm to residents. Bozorgi Amiri et al. [12] proposed a mixed-integer linear programming model for natural disaster relief logistics under uncertain conditions. They used the particle swarm optimization approach to solve their proposed mathematical model. Finally, they presented computational results for several cases of this problem to demonstrate the feasibility and effectiveness of their proposed model and algorithm. A location-allocation model in uncertain crisis conditions for post-disaster debris management was presented by Habib and Sarkar [4]. It selected the temporary disaster debris management site and allocated waste from the affected areas to selected areas in two phases. Yu [13] proposed a multi-objective optimization model to maximize minimum access guarantee and minimize operating costs for pre-determining the location of emergency facilities. For this purpose, he used the concepts of the maximum flow and the shortest path in the network, respectively. He also showed the effect of the minimum access guarantee in the model by solving an example and comparing the number of inaccessible points in different random scenarios and proved that the proposed model could effectively determine the appropriate location of emergency facilities. Oksuz and Satoglu [14] presented a two-staged random model to determine the location and number of temporary medical centers in the event of a disaster, intending to minimize the total cost of construction and transportation. They tried to find an optimal solution for locating temporary medical centers by considering the location of the existing hospitals, the types of casualties, demand, the possibility of damage to roads and hospitals, and the distance between the disaster area and the medical center. Boonmee et al. [15] examined an integrated mathematical optimization model and the

fuzzy hierarchical analysis process for shelter location and evacuation planning. They tested their proposed model with a real case study in Banta Municipality, Chiang Rai Province, Thailand. Finally, they proposed a suitable and realistic plan as an alternative for the decision-maker, whether an organization or the government in Banta Municipality. One year later, Boonmee et al. [3] examined post-crisis waste management issue to optimize the location and allocate resources. Chakravarty [16] offered a stochastic two-stage mathematical model for determining response time and post-accident relief values to minimize order, maintenance, and transportation costs as well as the expected response time. Hong et al. [17] proffered a two-stage stochastic programming model that determined the number and location of facilities with a limited capacity and the number of relief supplies available at each center. They efficiently calculated the proposed model using a method based on hybrid patterns. Mohammadi et al. [18] proposed a multi-objective stochastic programming model to develop earthquake response planning that integrated pre-and post-disaster decisions. They aimed to locate distribution centers, determine their inventory levels, and the relief items' flow to distribute essential items immediately in affected areas. Tofighi et al. [19] developed a two-stage stochastic programming problem consisting of multiple central warehouses and local distribution centers. They have implemented their relief network in Tehran city in the probable pre-and post-earthquake stages. One year later, Hu et al. [20] proposed a two-stage stochastic programming model to integrate decisions in critical situations. The model determines the location and number of suppliers and the pre-disaster inventory level in the first phase. In the second phase, this model makes decisions about logistic quantifying, transportation fleet, and selection of post-disaster procurement quantities. Their purpose is to minimize transportation, logistics, and construction costs and set penalties for customer dissatisfaction. Some researchers have added inventory management to facility location, resource allocation, and other types of disaster management to improve their work in recent years. Shen et al. [21] proposed a modified economic manufacturing quantity model for perishable inventory with a minimum volume limit for drug management for the National Strategic Plan. They indicated in their article that minimizing such a system's maintenance cost can be formulated as an optimization issue without non-uniform convex constraints. They showed the performance of their proposed model by analyzing sensitivities for various parameters. Manopiniwes et al. [22] offered a mixed-integer programming model to locate distribution centers and their inventory level according to capacity and time constraints with minimum total logistic costs. Roni et al. [23] proffered a mixed-integer programming model, including regular and irregular demand modes. They solved their model using the forbidden search algorithm for a hypothetical example to minimize the total costs of ordering, maintenance, and scarcity, showing the proposed model's efficiency. Tavana et al. [24] scrutinized the location-inventory-routing problem in the humanitarian supply chain, assuming pre-and post-disaster management. Their model determines the location of central warehouses and the amount of purchase and transfer of items from suppliers to central warehouses based on the prediction of product demands before the disaster. In the second phase and after the disaster, it determines the location of local warehouses, allocation of demand points to the local warehouses, and the local warehouses inventory. To solve this Mixed-integer linear programming problem, they proposed an Epsilon-constraint method, a Nondominated Sorting Genetic Algorithm (NSGA-II), and the Reference-Point-Based Nondominated Sorting Genetic Algorithm-II. Ferreira et al. [7] presented a decision-making model for the inventory management of perishable items for long-term relief operations (continuous assistance) using the Markov decision-making process. They sought to determine the optimal quantity of perishable items to minimize inventory costs (maintenance and corruption). Resource allocation models allot resources or tasks without considering the flow of items in each direction. Researchers often model resource allocation in addition to facility location. Celik et al. [25] presented a two-stage stochastic location-allocation model to determine the number and the location of relief distribution centers in the pre-disaster phase and to allocate the demand points to the relief distribution centers in the post-disaster phase. Loree et al. [26] developed a mathematical model for determining the location of different distribution centers and allocating them to the demand points in post-crisis conditions. They modeled their problem to minimize the costs of construction, procurement, and deprivation (such as some points of demand's lack of access to vital resources). Cavdur et al. [27] provided a spreadsheet-based decision support tool for allocating temporary disaster relief facilities to distribute relief resources. Their tool allowed the user (i.e., decision-makers) to provide the necessary facilities for the transient response to various disasters by considering the possible uncertainties after the disaster (i.e., different rates of the affected population, planning periods, etc.). Baharmand et al. [28] offered a multi-objective multi-layered model to locate and allocate facilities for sudden disasters, assuming limitations in the facilities and fleets' number and capacity. They selected the 2015 Nepal earthquake as a case study to solve the model. Recently, Liu et al. [29] proposed an integrated model of location-inventory-routing for perishable products, considering the factors of carbon emissions and product freshness. They developed a multi-objective mathematical model to minimize cost and carbon emissions and maximize product freshness. They used the YALMIP toolbox to solve the model. Mahtab et al. [30] proposed a multi-objective robust-

stochastic humanitarian logistics model for relief goods distribution. They determined the location of temporary facilities, and the number of commodites to be pre-positioned and provided a detailed schedule for the distribution of commodities and the dispatch of vehicles.

Having reviewed the previous research (from 2008 until now), we realized that the increasing number of natural disasters had increased the papers on crisis and its management, demonstrating the importance of research in this field. More than 75% (30 out of 39) of the articles have dealt with determining the optimal location of emergency facilities. Table 1 clearly shows this information. As a result, we can state that the issue of locating emergency facilities like the optimal location of local warehouses is one of the essential topics in the research on crisis management. However, there were gaps in the reviewed articles we covered in this study. Table 1 shows the most related reviewed papers' comparison in terms of subject matter, planning horizon, solution method, proposed mathematical model and used algorithms, optimization levels, facility capacity, type of relief items, and definite or indefinite demand budget.

TABLE 1. Review of the latest studies in disaster

Literature	Subject			Planning horizon		Solution Method			Algorithm	Modeling Method	Level of optimization		Facility capacity		Kind of items		Demand		Budget	
	Inventory	Location	Allocation	Pre-Disaster	Post-Disaster	Heuristic	Meta-Heuristic	Exact			MILP model	Bi-level	Limited	Unlimite	Normal	perishab	Certain	uncertain	Certain	uncertai
[3]		●	●		●		●		PSO/DE	MILP	●		●		●		●			
[15]		●	●		●			●		MILP	●		●		●		●			
[31]		●	●		●			●		MINLP	●		●		●		●			
[4]		●	●		●			●		MILP	●		●		●			●	●	
[11]		●	●		●			●		LP	●		●		●		●			
[32]		●	●		●		●		Shortest path problem	LP	●			●	●		●			
[5]		●	●		●			●		MILP	●		●		●		●			
[33]		●	●		●		●		NSGA-ll	MILP	●			●	●		●			
[34]		●	●		●		●		Tabu Search	MILP	●		●		●		●			
[35]			●		●		●	●	Warshall Floyd	MILP	●		●		●		●			
[6]		●		●		●			Evolutionary Optimization Algorithm	LP	●		●		●			●	●	
[10]		●			●	●			Modified local search	MILP	●		●		●			●		
[36]	●	●		●	●			●		MILP	●		●		●			●	●	
[12]	●	●	●	●				●		MILP	●		●		●			●		
[16]	●			●	●			●		stochastic programming	●		●		●			●		●
[37]	●			●		●			Sample average approximation	MILP	●		●		●			●		
[17]	●	●		●				●		MILP		●	●		●			●		
[22]	●	●		●				●		MILP	●		●		●		●			

[18]	•	•		•	•			•			MOPSO	stochastic programming	•		•		•			•	•			
[38]	•	•		•	•				•			LP	•		•			•		•				
[39]	•	•	•	•					•			MILP	•		•		•		•					
[19]	•	•		•	•			•			Tailored Differential Evolution	LP		•	•		•			•				
[7]	•				•	•					VI	MDP	•			•		•		•				
[20]	•	•		•	•				•			MILP	•		•		•			•				
[40]	•	•	•		•				•			MILP		•	•		•			•				
[23]	•				•			•			Tabu Search	MILP	•			•	•			•				
[21]	•				•				•			EMQ	•			•	•		•					
[26]		•	•		•				•			MINLP	•		•		•		•					
[41]		•	•		•				•			MILP	•		•		•			•				
[12]		•	•	•	•			•			PSO	MILP	•			•	•			•				
[24]	•	•	•	•	•			•			An epsilon-constraint/ NSGA-II	MILP	•		•			•		•				
[25]		•	•	•	•			•			Genetic	MILP	•		•		•			•				
[1]	•	•	•	•	•	•						MILP	•		•			•		•				
[27]	•		•		•				•			IP	•		•		•		•					
[28]		•	•		•	•					Augmented epsilon-constraint method version 2 (AUGMECON2)	MILP	•		•		•		•					
[13]		•		•					•			MILP	•			•	•		•		•			
[14]		•			•				•			MILP	•		•									
This Study	•	•	•		•			•			Electromagnetic and Genetic Algorithms	MILP		•	•			•		•				•

In this research, an attempt has been made to examine recent articles in crisis management in terms of uncertainty in budget and demand parameters. Most papers do not address the budget in their research and often assume sufficient and available financial resources. But in reality, this may not be the case because the problem of examining budget deficits and surpluses is one of the most challenging issues facing organizations. According to Table 1, out of only six articles that have applied the budget in their model, one of them has considered the uncertain budget. Uncertainty in demand is also one of the gaps studied in this research that more than half of the articles have ignored. Humanitarian relief operations management involves many actors, who differ in culture, goals, interests, commitments, capacity, and, most importantly, expertise. Therefore, each actor has a different role and task in crisis management. In many of the articles reviewed in this study (about 87%), only one decision-maker makes decisions about facility location, inventory control, or resource allocation. But in the real world, there are different organizations involved in crisis management that have various tasks. It is necessary to establish the required coordination to exchange information and establish coordinated communication in decisions. In recent years, this issue has been considered a research gap and needs more research than we have covered in this study.

3. MODELING

Defining and expressing an issue necessitates the statement, analysis, and resolution of the problem. In this research, we developed two mixed-integer linear

programming models. These models determine the optimal location of local warehouses among the existing points, allocation of disaster-affected areas to the warehouses, purchase, inventory control, and the distribution of relief items. Figure 1 indicates an overview of the proposed supply chain network. In these models, we assume the unlimited supply capacity of perishable and ordinary relief items. Perishable items have an expiration date, before which we take them out of local warehouses at a cost to preclude the storage and distribution of spoiled items. Demand for items and the budget for the construction of local warehouses are considered uncertain. Decisions to determine the optimal location of warehouses, optimal allocation, and control of the inventory of items are modeled as mixed-integer and bi-level mathematical models. Then, they are compared with each other. A quadratic constraint has caused the model to deviate from the linear mode. For linearization and improvement of the model, we use a series of changes. At the first, we propose a nonlinear model, and then introduce its linear form.

The proposed mathematical model includes the following assumptions:

1) The problem is a three-level supply chain network with a central warehouse (supplier), several local warehouses (distributors), and several demand points (disaster-affected areas).

2) Relief items include two categories of ordinary and perishable items.

3) Crisis management is related to the post-disaster phase.

4) The central warehouse location and the demand points are known, and the location of the local warehouses is unknown.

5) The inventory policy is considered by the method of [1]. In this way, perishable items have an expiration date that we should pay attention to their date. Also, to reduce the risk of the items remaining in the warehouses and their decay, we should not purchase items with longer expiration dates. Moreover, since the deterioration items, such as canned food, can endanger human lives and even contaminate the warehouse environment, we will remove them from the warehouse at a cost before the expiration date.

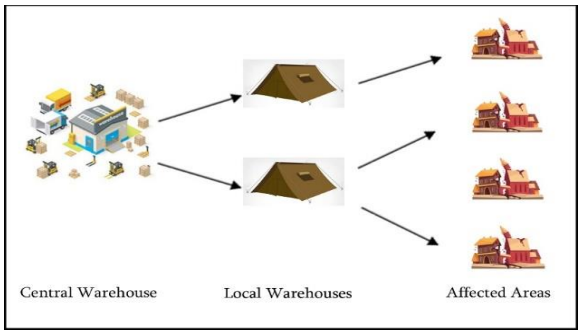

Figure 1. Overview of the relief supply chain

6) Demand and budget are considered uncertain. Therefore, the budget and demand will be different in various scenarios.

7) In this research, a bi-level decision-making process is considered. In this way, one organization is responsible for locating warehouses, and another makes decisions about inventory control and allocation. These two organizations make the optimal decision by contributing and swapping information. How one decision-maker makes all the decisions is also considered and compared to the multi-decision mode.

8) Some parameters are considered according to various scenarios.

Indices

i: index of local warehouse $i=1,\ldots, I$

j: index of demand point $j=1,\ldots, J$

k: index of relief items $k=1,\ldots, K$

s: index of possible scenarios $s=1,\ldots,S$

t: index of periods $t=1,\ldots,T$

h_k: index of the remaining lifetime of product k $h_k=1,\ldots, H_k$

Deterministic parameters

CH_k: additional unit holding penalty of item type k

SP_k: penalty cost of unit shortage of item type k

CP_k: purchase cost for each item type k

CM_{ki} : cost of unit item type k movement to warehouse i

α_k: allowable remaining lifetime (period) for item type k for purchasing

Δ_{pq}: acceptable difference of the equity level between two demand points p and q ($p\neq q$)

CE_k: removal cost for each item type k

U_{ik}: The capacity of warehouse i to store item k

β_k: allowable remaining lifetime (period) for item type k for removing from warehouses

$CT_{kijts h_k}$: The cost of transporting item k with the lifetime of h_k from warehouse i to point j in period t under scenario s

Uncertain parameters

f_{is}:The fixed cost of building warehouse i under scenario s

p_s: Probability of scenario s' occurrence

d_{jkst}: The amount of point j's demand for item k under scenario s in period t

τ_{jkst} : The cost of the shortage of item k at point j under scenario s in period t

ψ_{jks}: The ratio of item k's deficiency at point j under scenario s

B_s: The available budget for the construction of warehouses under scenario s

variables:

Scenario dependent

X_{ijksth_k}: The amount of the type-k item transferred from warehouse i to point j in period t under scenario s

W_{jkst}: The amount of the shortage of item k at point j under scenario s in period t

Q_{kitsh_k}: The quantity of the item k purchased for warehouse i in period t under scenario s with a lifetime ofh_k

I_{kitsh_k}: The Inventory level of item k with the lifetime of$h_k$in warehouse i kept in period t under scenario s

b_{kitsh_k}: The amount of item k with the lifespan of h_k taken out from warehouse i under scenario s in period t to prevent decay

Scenario independent

E_{kit}: The mathematical expectation of the shortage of item k in warehouse i in period t

φ_{jt}: The amount of deficiency at point j in period t

y_i: The binary variable whose value is one if warehouse i is constructed; otherwise, its value is zero

g_{ij}: The binary variable whose value is one if point j is allocated to warehouse i; otherwise, it is zero.

3. 1. Mixed Integer Linear Programming Model Mathematical Model

$$Min \quad z = \sum_{i=1}^{I}\sum_{1=1}^{S} f_{1s}y_i\ p_s\ + \sum_{k=1}^{K}\Big(\sum_{t=1}^{T}\Big(\sum_{j=1}^{J}\sum_{s=1}^{S}\tau_{jkst}W_{jkst}p_s + \sum_{i=1}^{I}\Big(SP_k\ E_{kit} + \sum_{s=1}^{S}\Big(\sum_{h_k=\alpha_k}^{H_k} Q_{kitsh_k}(\ CM_{ki} + CP_k)\ p_s + \sum_{h_k=1}^{\beta_k} CE_k\ b_{kitsh_k}\ p_s + \sum_{h_k=1}^{H_k}(\ CH_k\ I_{k1tsh_k}\ p_s + \sum_{j=1}^{J} CT_{kijtsh_k}X_{ijksth_k}\ p_s)\Big)\Big)\Big)\Big) \tag{1}$$

$$I_{kitsh_k} = 0 \qquad \forall k.i.s.\ h_k.t = 0 \tag{2}$$

$$X_{ijksth_k} = 0 \qquad \forall i.j.k.s.\ h_k.t = 0 \tag{3}$$

$$I_{kitsh_k} = I_{kit-1sh_k+1} + Q_{kitsh_k} - b_{kitsh_k} - \sum_{j=1}^{J} X_{ijksth_k} * p_s \qquad \forall k.i.s.h_k.t \in \{1.\dots.T\}. \tag{4}$$

$$b_{kitsh_k} = 0 \qquad \forall k.i.s.h_k \in \{\beta_k + 1.\dots.\ H_k\}.t \in \{1.\dots.T\} \tag{5}$$

$$Q_{kitsh_k} = 0 \quad \forall k.i.s.h_k.t. \in \{1.\dots.\alpha_k\} \tag{6}$$

$$b_{kitsh_k} \le I_{kitsh_k} \qquad \forall k.i.s.t \in \{1.\dots.T\}.\ h_k \in \{1.\dots.\ \beta_k\} \tag{7}$$

$$\sum_{h_k=\alpha_k}^{H_k} Q_{kitsh_k} \le U_{ik}\ y_i \qquad \forall k.s.i.t \tag{8}$$

$$X_{ijksth_k} \le g_{ij}\ I_{kitsh_k} \quad \forall i.j.k.h_k.s.t \in \{1.\dots.T\} \tag{9}$$

$$W_{jkst} + \sum_{i=1}^{I}\sum_{h_k}^{H_k} X_{ijksth_k} = d_{jkst} \quad \forall j.k.s.t \in \{1.\dots.T\} \tag{10}$$

$$W_{jkst} \le \psi_{jks}\ d_{jkst} \quad \forall j.k.s.t \in \{1.\dots.T\} \tag{11}$$

$$\sum_{i=1}^{I} f_{is}y_i \le B_s \qquad \forall s \tag{12}$$

$$g_{ij} \le y_i \qquad \forall i.j \tag{13}$$

$$-\Delta_{pq} \le \varphi_{pt} - \varphi_{qt} \le \Delta_{pq} \quad \forall p.q \in \{1.\dots.J\}.t \qquad p \ne q \tag{14}$$

$$\varphi_{jt} = \sum_{k=1}^{K}\sum_{s=1}^{S} W_{jkst} * p_s \quad \forall j.t \in \{1.\dots.T\} \tag{15}$$

$$E_{kit} = \sum_{j=1}^{J}\sum_{s=1}^{S} d_{jkst}\ g_{ij} * p_s - \sum_{s=1}^{S}\sum_{h_k=1}^{H_k} I_{kitsh_k} * p_s \qquad \forall k.i.t \in \{1.\dots.T\} \tag{16}$$

$$X_{ijksth_k}.W_{jkst}.E_{kit}\ .Q_{kitsh_k}\ .I_{kitsh_k}\ .b_{kitsh_k}\ .\varphi_{jt} \ge 0 \quad \forall i.j.k.s.t.\ h_k \tag{17}$$

$$y_i.\ g_{ij} \in \{0.1\} \qquad \forall i.j \tag{18}$$

Relation (1) represents the objective function of the problem which minimizes total cost. Its first part is the cost of the warehouse construction. Total shortage cost in demand points is in the second part of this relation. Total shortage cost in warehouses is shown in the third part, and the fourth part is the costs of purchasing and transporting items from the central warehouse to local warehouses. Part five to seven, respectively, demonstrate the costs of transporting items out of the warehouse to prevent decay and their maintenance and transportation from local warehouses to demand points. In this model, we assume the disaster occurred at t = 0. Constraints (2) to (4) show the number of items in the warehouses and their purchase and transfers at t = 0 are zero. The Constraint sets (5) and (6) show the inventory balance the constraint set's difference is between the lifetimes of the purchased and transferred items. The Constraint set (7) indicates the number of items transported out of the warehouse to prevent decay should be less than the inventory of items in that period. The Constraint set (8) guarantees that the total purchased items for that warehouse shall not exceed its capacity if a warehouse is constructed. The Constraint set (9) ensures that if a warehouse is allocated to a demand point, the quantity of the items sent from that warehouse to that point shall not exceed that warehouse's inventory. Constraints (10) and (11) prove that the shortage at one point is equal to the difference between the demand of that point and the quantity of the items transferred to the point, and it should not be more than the allowed limit. The Constraint set (12) ensures the construction of warehouses does not cost more than the available budget. The Constraint set (13) proves if there is no warehouse, no demand point will be allocated. The Constraint set (15) calculates the weight deficit of a point in various periods. The Constraint set (14) indicates the difference in the weight deficiency of two points in a period should not exceed a particular value. This limitation assures us that the weight deficiency of the points is close to each other. The Constraint set (16) shows deficiencies in each warehouse, and Constraints (17) and (18) indicate the types of

decision variables. The Constraint set (9) has taken the mathematical model out of the linear form. To solve this problem, we convert it to the following two constraints:

$$X_{ijksth_k} \leq g_{ij}\, U_{ik} \qquad \forall i.j.k.s.h_k.t \qquad (19)$$

$$X_{ijksth_k} \leq I_{kitsh_k} \qquad \forall i.j.k.s.h_k.t \qquad (20)$$

Which show that the number of transferred items will not exceed the warehouse's capacity and inventory.

3. 2. Scenarios According to Rezaei-Malek et al. [1], the magnitude of an earthquake is considered in three ranges: less than 6 Richter, between 6 and 8 Richter, and more than 8 Richter, which their probabilities are 0.3, 0.5, and 0.2, respectively. In this study, we divide the day's hours into two categories, rest and working hours. These categories occupy eight and sixteen hours of the day, respectively. Since planning is related to the post-crisis phase, we considered the scenarios for the aftershocks. The importance of this classification lies in considering the difference in human beings' reaction speed to earthquakes during sleep and wakefulness; different reaction speeds affect the extent of the possible damage. Accordingly, we regarded six different scenarios with different probabilities and calculated them. Table 2 summarized the calculation results. For example, statement 21 is the calculated probability of the first scenario related to an earthquake with less than 6 Richter during sleep or rest.

$$p_1 = \left(\frac{8}{24}\right) \times 0.3 = 0.1 \qquad (21)$$

Since the question is related to the post-crisis phase, we have considered the scenarios for the possible aftershocks.

3. 3. Bi-level Programming Bi-level programming is an effective tool for modeling and solving decentralized planning problems, but it has too many computational complexities. In the real world, numerous existing systems have different subsystems that make them a hierarchical structure, and decision-making in this structure has its characteristics. For instance, consider a company includes several factories. The board of directors is at the forefront of decision-making. Given its responsibilities and information, this board makes more critical decisions to develop and optimize the objective functions of the company. Managers of the subsidiary factories must make such decisions because they have higher ranks; however, factory managers can make decisions based on their authority to optimize their performance criteria. Different parts of factories have the same attitude towards managers.

TABLE 2. Probability of the occurrence of scenarios

Scenario	Magnitude≤6 (Richter)		6≤Magnitude≤8		Magnitude≥8 (Richter)	
	W	N	W	N	W	N
Scenario Number	1	2	3	4	5	6
Probability	0.1	0.2	0.17	0.33	0.07	0.13

Note: N, Non-Working; W, Working

On the other hand, these decisions can affect the company's goal and the decision-making space of the board and force them to change their decisions. These types of decisions are called bi-level programming. In this structure, decisions are at different levels, and each identifies only a few decision variables. In this study, we also turned the problem into bi-level programming, and while the leader determines the optimal location of warehouses, the follower determines the optimal amount of the items' allocation and inventory according to their parameters and criteria.

Relations 22 to 42 specify the bi-level programming model. In this model, at the first, the optimal location of warehouses is determined, then, the optimal allocation and control of the inventory of the items are planned.

$$Min \quad z = \sum_{i=1}^{I} \sum_{s=1}^{S} f_{is} y_i \qquad (22)$$

$$s.t: \sum_{i=1}^{I} f_{is} y_i \leq B_s \qquad \forall s \qquad (23)$$

$$g_{ij} \leq y_i \qquad \forall i.j \qquad (24)$$

$$y_i.\ g_{ij} \in \{0.1\} \qquad \forall i.j \qquad (25)$$

$$\begin{aligned} Min \quad zz = \\ &\sum_{k=1}^{K} \Big(\sum_{t=1}^{T} \Big(\sum_{j=1}^{J} \sum_{s=1}^{S} \tau_{jkst}\, W_{jkst}\, p_s + \\ &\sum_{i=1}^{I} \Big(SP_k\, E_{kit} + \sum_{s=1}^{S} \Big(\sum_{h_k=\alpha_k}^{H_k} Q_{kitsh_k} (CM_{ki} + \\ &CP_k) + \sum_{h_k=1}^{\beta_k} CE_k\, b_{kitsh_k} + \\ &\sum_{h_k=1}^{H_k} (CH_k\, I_{kitsh_k} + \\ &\sum_{j=1}^{J} CT_{kijtsh_k} X_{ijksth_k}\, p_s) \Big) \Big) \Big) \Big) \Big) \end{aligned} \qquad (26)$$

$$\begin{aligned} &s.t: \\ &I_{kitsh_k} = 0 \qquad \forall k.i.\ h_k.t = 0 \end{aligned} \qquad (27)$$

$$X_{ijksth_k} = 0 \qquad \forall i.j.k.s.\ h_k.t = 0 \qquad (28)$$

$$\begin{aligned} &I_{kitsh_k} = I_{kit-1sh_{k+1}} + Q_{kitsh_k} - b_{kith_k} - \\ &\sum_{j=1}^{J} \sum_{s=1}^{S} X_{ijksth_k} * p_s \qquad \forall k.i.s.h_k.t \notin \{0\} \end{aligned} \qquad (29)$$

$$\begin{aligned} &b_{kitsh_k} = 0 \qquad \forall k.i.s.h_k \in \{ \beta_k + 1. \ldots . H_k \}.t \in \\ &\{1. \ldots . T\} \end{aligned} \qquad (30)$$

$$Q_{kitsh_k} = 0 \qquad \forall k.i.s.h_k.t. \in \{1. \ldots . \alpha_k\} \qquad (31)$$

$$\begin{aligned} &b_{kitsh_k} \leq I_{kitsh_k} \qquad \forall k.i.s.t \in \{1. \ldots . T\}.\ h_k \in \\ &\{1. \ldots .\ \beta_k\} \end{aligned} \qquad (32)$$

$$\sum_{h_k=\alpha_k}^{H_k} Q_{kitsh_k} \leq U_{ik}\, y_i \qquad \forall k.s.i.t \tag{33}$$

$$X_{ijksth_k} \leq g_{ij}\, U_{ik} \qquad \forall i.j.k.s.h_k.t \in \{1.\ldots.T\} \tag{34}$$

$$X_{ijksth_k} \leq \sum_{h_k=1}^{H_k} I_{kith_k}\, \rho_{iks} \qquad \forall i.j.k.s.h_k.t \in \{1.\ldots.T\} \tag{35}$$

$$W_{jkst} + \sum_{i=1}^{I} X_{ijksth_k} = d_{jkst} \quad \forall j.k.s.h_k.t \in \{1.\ldots.T\} \tag{36}$$

$$W_{jkst} \leq \psi_{jks}\, d_{jkst} \qquad \forall j.k.s.t \in \{1.\ldots.T\} \tag{37}$$

$$-\Delta_{pq} \leq \varphi_{pt} - \varphi_{qt} \leq \Delta_{pq} \qquad \forall p.q \in \{1.\ldots.J\}.t \quad p \neq q \tag{38}$$

$$\varphi_{jt} = \sum_{k=1}^{K}\sum_{s=1}^{S} W_{jkst} * p_s \qquad \forall j.t \in \{1.\ldots.T\} \tag{39}$$

$$E_{kit} = \sum_{j=1}^{J}\sum_{s=1}^{S} d_{jks}\; g_{ij} * p_s - \sum_{s=1}^{S}\sum_{h_k=1}^{H_k} I_{kitsh_k} * p_s \qquad \forall k.i.t \in \{1.\ldots.T\} \tag{40}$$

$$X_{ijksth_k}.W_{jkst}.E_{kit}.Q_{kitsh_k}.I_{kitsh_k}.b_{kitsh_k}.\varphi_{jt} \geq 0 \qquad \forall i.j.k.s.t.\ h_k \tag{41}$$

$$g_{ij} \in \{0.1\} \qquad \forall i.j \tag{42}$$

4. SOLVING METHODS

4. 1. The Electromagnetic Algorithm Electromagnetism is a branch of physics that considers electrical and magnetic phenomena and their relationship. In electromagnetic theory, forces are described by an electromagnetic field. In fact, electromagnetism states that the force exerted on a point by other points is inversely related to the distance between the points and is directly related to these points' charge. This algorithm is a population-based method and like the genetic algorithm, we equate an answer with a chromosome. Each solution is announced as a charged particle. Each point is assumed to be a charged particle in space, and its amount of charge also changes based on the value of its objective function. As a result, the fitness function in this algorithm is the particle charge. In each iteration, after changing the charge of each point, we determine the result of the forces acting on the points and their movement. Like electromagnetic forces, the force exerted on each point is obtained by summing all the forces exerted on it. Hence, after getting the initial population, calculating the total forces on each particle and moving the particle using the resultant force exerted are necessary.

• **Steps of electromagnetic algorithm**

This algorithm consists of four main phases:

1. Setting up or producing an initial population
2. Local search (using local search in neighborhoods to find the optimal local)
3. Calculation of the force exerted on each particle (calculation of the total force exerted on each particle)
4. Moving in the direction of the exerted force

4. 2. Genetic Algorithm A genetic algorithm is a search technique in computer science to find approximate solutions to optimize models, mathematics, and search problems. It is a type of evolutionary algorithm that utilizes biological processes like inheritance, biology mutation, and Darwin's selection principles to find the optimal solution. Genetic algorithms are often item choices for regression-based prediction techniques. The problem to be solved has inputs converted into solutions during a modeled process of genetic evolution. Then, the solutions are investigated by the evaluation function, and if the stopping rule has been satisfied, the algorithm terminates. In general, it is an iteration-based algorithm whose parts are selected through random processes; these algorithms consist of parts of the fitness function, display, selection, and modification.

• **Steps of the genetic algorithm**

1. Creating an initial population and evaluating it,
2. Selecting parents and combining them to create a crossover population
3. Selecting population members to cause mutations and create mutation populations (mutation)
4. Integrating the initial population and crossover and mutation populations, as well as developing a new main population and evaluating it
5. Checking the termination condition (If the condition is met, the algorithm is terminated; otherwise, we go to step two).

In this algorithm, the way the problem's answer is displayed is called a chromosome. Since this algorithm is population-based, we first generate a set of chromosomes randomly or based on an innovative method as the initial population selection. After examining the fitness function's value, we select some of these chromosomes as parents for neighborhood production. Then we create neighborhoods using crossover and mutation concepts. The crossover operator directs the answers to the optimal solution, and the mutation operator prevents falling into the optimal local trap. We perform this procedure until the stop condition occurs.

4. 3. How To Display the Answers The first step in applying and implementing any metaheuristic algorithm is to display its coding.

4. 3. 1. How to Display the Answer in the Ga This section displays the answer or the chromosome associated with the problem using Figure 2. The answer is represented by a matrix in which the number of rows equals the number of items. The number of columns represents the sum of the number of local warehouses and

demand points. In each row, the cells have integer values between one and the sum of the number of local warehouses and the number of demand points. These values indicate the importance of the warehouses for distributing the desired items or the importance of receiving the items by the demand points; the larger the numbers, the higher the priority.

An example of solution representation is displayed in Figure 2 which the first row represents the product distribution priorities. In this row, considering the largest number, i.e., number 5, is located in the second cell, and this cell belongs to the second warehouse, the priority is distributing items from the second warehouse. According to the distribution cost, out of the four demand points, the point to which sending items from this warehouse costs the lowest obtains the license to receive the items, and the items have transferred to that point. Based on the warehouse's capacity, the quantity of the transferred items is equal to or less than the demand at that point. In this way, items are distributed based on the priority of each warehouse or point. In this problem, if there is no warehouse within the potential points, the cell value of that warehouse and the number of dispatched items from there will be zero, and the cost of delivering items will be infinite.

4. 3. 2. Operators Genetic operators imitate the process of inherited gene transfer to create new offspring in each generation. An essential part of the genetic algorithm is the creation of new chromosomes called parents. This critical process is carried out by mutation and crossover operators. But in practice, operators are defined by the type of problem and are utterly dependent on the analyst's ability, and are empirical. The efficiency of these operators in achieving optimal solutions varies in different problems. Some operators work on just one chromosome and others on a few chromosomes or even all the chromosomes in the previous population. The role of genetic operators in the performance algorithm is very significant. Genetic operators are divided into mutation operators and crossover operators.

• Crossover operators

Operators select one or more points from two or more answers and exchange their values. These operators consider a solution and swap their places with other solutions to generate new solutions. The fewer the responses that participate in this operation, the closer the responses will be to the previous population. These operators are themselves divided into one, two, or multiple cutting points.

In this study, the crossover operator is defined is as follows. First, a pair of current-generation chromosomes are selected. Since the chromosome in question is a matrix chromosome, we cut both selected chromosomes longitudinally and transversely. Thus, we divide each chromosome into four parts. These two parent chromosomes produce two children; the upper-left- and

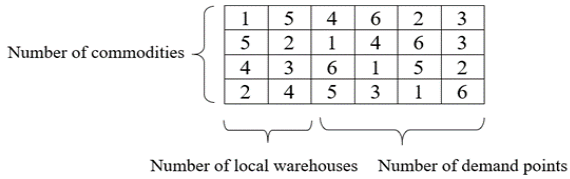

Figure 2. An example of a solution representation in the GA

lower-right-corner genes of the first parent make the values of the first child's upper-left and lower-right corner genes, and the second parent genes produce the second child. The remaining values of the genes are examined cell by cell from the other parent chromosome and if repeated, removed from the parent cell's same values. In this way, two children are produced with different amounts of genes. Figure 3 shows an example of producing offspring with this crossover method.

• Mutation operators

Mutation operators are operators with random change characteristics. One or more locations of a string of characters with a certain length are considered in them, and the values of the characters in those locations are varied. Important items in this type of operator are:

- The number of locations to be changed
- How to select locations
- How the change operation is performed

In this study, for mutation, we select two genes in each row randomly and exchange their values. Figure 4 indicates an example of producing a new chromosome by this method.

4. 3. 3. How to Display the Answer in the Electromagnetic Algorithm Figure 5 displays the answer for the electromagnetic algorithm in the present research. In this case, we computed the charged particle's length by multiplying the number of items by the total number of local warehouses and demand points.

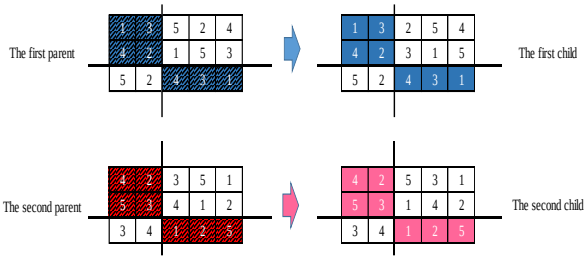

Figure 3. An example of child production employing the crossover method

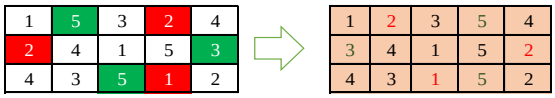

Figure 4. An example of producing a new chromosome using a mutation operator

There are also upper and lower limits for the cell values. Each cell, in the initial population takes a random value between -10 and 10. Subsequent generations are produced based on the structure of the algorithm. We consider the discrete problem-solving space and use the electromagnetic algorithm structurally for continuous problems. Therefore, to convert the discrete solution after creating the initial population, we reshape the charged particle to the number of items and the total number of warehouses and demand points and convert it to a matrix. Then, we arrange the numbers in each row to produce a matrix containing integers. At this stage, the display mode turns into the display mode in the genetic algorithm. Then we calculate the fitness function and continue the algorithm until the procedure stops.

Figure 5 shows an example of how the coding of the answer in the electromagnetic algorithm is prepared for a problem with three types of items, two demand points, and two local warehouses. Figure 6 indicates the conversion of an array to a matrix. Figure 5 transforms into Figure 6 because the array is converted to a matrix with the number of rows equal to the number of items and the number of columns equal to the total number of warehouses and demand points. MATLAB software uses the reshape function for this purpose. Figure 7 also shows the sorted mode of the matrix indicated in Figure 6.

4. 3. 4. Stop Condition of the Algorithm We continue repeating algorithms and producing a new generation until the stop condition is met. The stop condition in algorithms can be one way to reach an acceptable minimum of response (objective function), the number of iterations, time, convergence, and getting a certain number of responses in the solution space. In this research, both algorithms' stop condition is the number of repetitions of the new generation production.

5. COMPUTATIONAL RESULTS

5. 1. Small-Sized Problems To show the proposed model's efficiency and compare the solution methods, we have first solved several small-sized problems with GAMS software version 24.1.3 by a core i5 computer with 4GB of memory. Table 3 presents the information about the problem's size, the objective function's value, solution time, and the number of constructed warehouses. Table 4 shows the number of items allocated to the demand points from local warehouses for the first problem. The dash in the column corresponding to each demand point means that point is unassigned to the warehouse associated with its row. Since the problem is a Np-hard and cannot be solved in large-scale in polynomial time, we have solved several small-sized problems with GAMS which their results have shown the results in Tables 3 and 4.

We have considered two scenarios with probabilities of 0.25 and 0.75 to solve small-sized problems. Figure 8 shows the sensitivity of the objective function to these parameters by changing the cost parameters from 0.75% to 200%. As it is known, the total cost varies more with the change in purchase cost and shows the sensitivity of the total cost to this parameter. As a result, to reduce costs, managers should look for cheaper suppliers than trying to reduce other parameters. Also, Figure 9 shows increasing the number of warehouses reduces the total cost, even though it incurs construction costs because having several different warehouses with different shipping costs reduces the total costs. However, since we have a budget constraint for the construction of warehouses, it is impossible to build the desired number of local warehouses. If the relevant organizations can get more funding from the government, the total cost can be reduced.

5. 2. Problem-solving by the Bi-level Method In this study, we considered a bi-level programming approach for only small-sized problems. Out of the problems solved in Table 3, we selected three problems and solved them by Gams software with EPM solver. we turned the issue into a bi-level programming in which the leader decision-maker determines the optimal location of the warehouses, and the follower determines the optimal allocation and inventory planning.

0.25	2.15	5.24	-2.5	4.95	-7.59	-8.14	7.65	5.78	3.69	-4.87	3.78

Figure 5. An example of an answer displaying in the electromagnetic algorithm

0.25	2.15	5.24	2.5-
4.95	7.59-	8.14-	7.65
5.78	3.69	4.87-	3.78

Figure 6. Figure 5's converted array into a matrix

2	3	4	1
3	2	1	4
4	2	1	3

Figure 7. The sorted mode of Figure 6

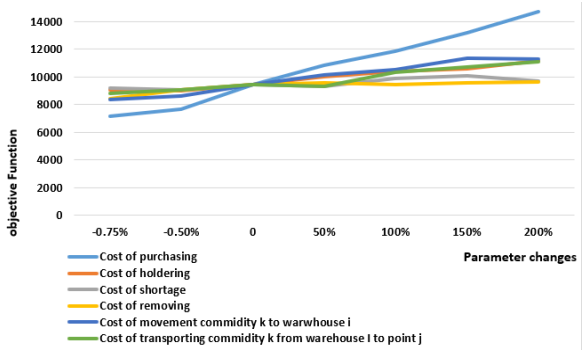

Figure 8. Impact of changing parameters on the objective function

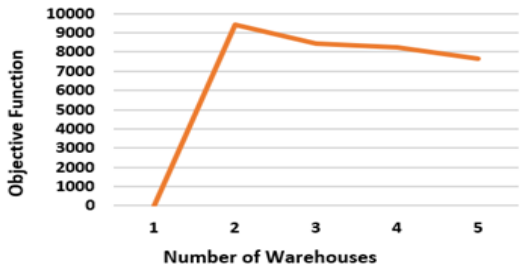

Figure 9. Impact of changing the number of warehouses on the value of the objective function

As indicated in Figure 10, the total cost of the bi-level programming increases compared to the mixed-integer linear programming. This type of planning has complexities that can be optimally addressed and answered at a cost. In critical situations, unsuitable planning, such as buying fewer items to reduce costs, can have irreparable consequences; thus, spending a little more if the budget is responsive will benefit the decisive bi-level programming decision-making.

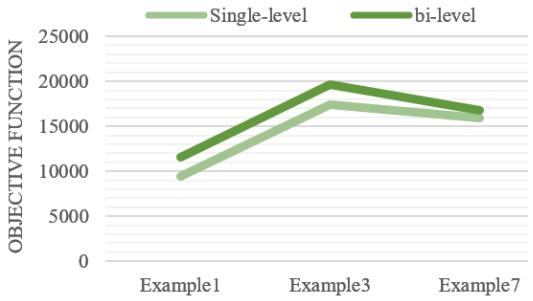

Figure 10. Comparing the mixed-integer linear programming model and bi-level programming

TABLE 3. Sample problems solved with a Mixed integer linear programming model method by GAMS software

Example	*I.J*	*T*	*S*	*K*	H_k	Objective Function (dollar)	Constructed Warehouse	Solving Time (s)
1	2.2	2	2	1	2	9434	1,2	1
2	2.3	2	2	1	2	8419	1,2	1000
3	3.3	2	2	1	2	17387	1,2,3	428
4	3.2	2	2	1	2	13640	1,2	30
5	4.2	2	2	1	3	19481	1,2	1995
6	4.3	2	2	1	3	15550	1,3	1872
7	2.2	5	2	1	2	15952	1,2	3
8	2.2	2	2	1	5	12272	1,2	13

TABLE 4. Distribution of items from warehouses to demand points

Example	Scenario	Period	Remainaing Lifetime	Warehouse	Demand Point	
					1	2
			1	1	19	3
				2	-	0
		1	2	1	30	63
	1			2	-	30
			1	1	28	35
		2		2	-	19
			2	1	19	4
1				2	-	0
			1	1	18	16
		1		2	-	0
			2	1	5	4
	2			2	-	30
			1	1	23	24
		2		2	-	7
			2	1	0	17
				2	-	0

5. 3. Large-Size Problems NP-hard class problems are the problems that no known definitive algorithm solves in polynomial time. In these cases, we use meta-heuristic algorithms to find solutions close to the optimal solution in a short time. This research solves and analyzes several relatively large problems in the mixed-integer programming model with genetic meta-heuristic and electromagnetic algorithms.

5. 3. 1. Parameter Setting The importance of any optimization algorithm parameters, especially meta-heuristic algorithms that have been designed to simplify the solution of optimization problems, is unquestionable. The optimal values of these parameters have a significant impact on the algorithms' performance and better searching of the answer space. Regarding this issue, we set the parameters of both algorithms to solve different problems by the Taguchi method in this research. The Taguchi method is a fractional factor scheme that selects the levels to be tested from orthogonal arrays. Each array is a specific set of parameter levels to be tested. An essential and critical factor in the Taguchi method is the reduction of variability. As indicated in Table 5, there are three different levels for setting the parameters. Because most articles graded them this way, we have considered an example of the experiment design answer in the same way. In Tables 5 and 6, Maxiter is the number of iterations, Npop is the number of the population, Pc and Pm are crossovers and mutation rates, respectively. Beta is the selection pressure by the roulette wheel method, and alpha is the movement radius. After designing the experiments and setting the parameter using the Taguchi method, we obtained the optimal levels of these parameters for each problem. Figures 11 and 12 show these results.

Higher rates of the SN demonstrate the algorithm's better performance. Table 7 shows the optimal value of both algorithms' parameters in this problem.

TABLE 5. Different levels of the genetic algorithm parameters

Level	Npop	Maxiter	Pc	Pm	Beta
1	50	100	0.7	0.1	5
2	100	150	0.8	0.2	10
3	150	200	0.9	0.3	15

TABLE 6. Different levels of ELA parameters

Level	Alpha	Npop	Maxiter
1	0.7	50	100
2	0.8	100	150
3	0.9	150	200

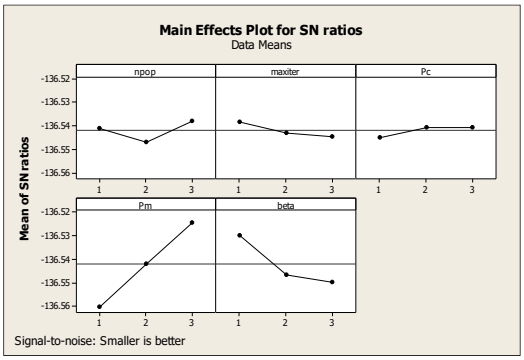

Figure 11. The SN rate in the genetic algorithm

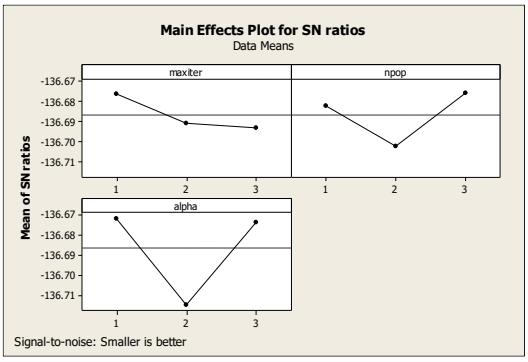

Figure 12. The SN rate in the electromagnetic algorithm

TABLE 7. The optimal value of the algorithms' parameters

Algorithm	Npop	Maxiter	Alpha	Beta	Pm	Pc
Genetic	150	100	-	5	0.3	0.9
Electromagnetic	150	100	0.7	-	-	-

After setting the algorithms' parameters, we solved ten problems in different sizes 25 times by GA and ELA which their results for maximum (the worth), minimum (the best), and the average objective function for each problem and their average solution time have presented in Table 8. Furthermore, for better comparison in terms of objective function and solution time have given in Table 8. According to this table, the genetic algorithm has better answers in most problems and less solution time than the electromagnetic algorithm. Also this table shows the standard deviation values for different problems for the both algorithms. Clearly, the standard deviation in the GA was less in most cases. In other words, the amount of variability is less, and this algorithm has achieved solutions closer to its mean than the electromagnetic algorithm.

To ensure the analysis and its generalization to the whole community, we initially test the normality of each index's data by Minitab software. After confirming the normality of the data, we perform the statistical

TABLE 8. Results of solving various problems with GA, ELA, and GAMS

Problem	Problem Size	The average objective functions in 25 run		The best objective functions in 25 run (the Minimum values)		The worst objective functions in 25 run (the maximum values)		The average solution time in 25 run		Standard deviation		GAMS	
	I,J,K,S,T,Hk	ELA	GA	ELA	GA	ELA	GA	ELA	GA	ELA	GA	Objective function	Time
1	3,2,3,2,3,3	1137430	1137430	1137430	1137430	1137430	1137430	49.88	36.114	0	0	Out of terminated time	2000
2	5,10,3,2,3,3	6826893.4	6708191.1	6771344	6701451	6864270	6721358	91.952	90.113	64.12	3.146	Out of terminated time	2000
3	10,10,3,2,3,3	7360067.4	7235276.3	7156690	7110647	7657959	7426157	117.831	113.889	34.52	15.17	Out of terminated time	2000
4	5,10,3,6,3,3	14490057.9	14194760.2	14331598	14181847	14572258	14257658	231.106	265.552	75.42	9.17	Out of terminated time	2000
5	10,10,3,6,3,3	22863938.4	21741634.5	21968322	20541369	23578461	23654123	328.024	318.311	85.45	52.37	Out of terminated time	2000
6	10,15,3,2,3,3	9362477.2	9326083.7	9351950	9321457	9369298	9331584	204.939	217.643	36.45	31.25	Out of terminated time	2000
7	15,15,3,2,3,3	12404516.8	23276003.1	12362354	12147362	12463952	122458763	229.376	223.776	47.98	3.71	Out of terminated time	2000
8	10,10,5,6,3,3	35103002.2	34226200.2	34125874	33457812	36312488	35124784	407.472	367.407	72.15	65.7	13640	30
9	2,3,1,2,2,2	13640	13640	13640	13640	13640	13640	2.384	2.16	0	0	15550	1872
10	3,4,1,2,2,2	15550	15550	15550	15550	15550	15550	26.023	24.756	0	0	Out of terminated time	2000

hypothesis test to prove our claim. Table 9 present the normality test results by the Kolmogorov-Smirnov method in Minitab software. Since the p-value is greater than 0.05 in all cases, all data have a normal distribution. Figure 13 shows an example of the normality test result performed on the electromagnetic algorithm's MID index data.

Having assured that the data are normal, we can now perform the t-test, a statistical hypothesis test, to compare the indicators more accurately. Table 10 indicates the test results conducted in the Minitab software with a 95% confidence level.

As indicated in Table 10, the p-values for both hypotheses are greater than 0.05, so there is no reason to reject the H0 hypothesis. Moreover, the genetic algorithm's convergence time to the answer is earlier than that of the electromagnetic algorithm. The genetic algorithm converges to its optimal solution in fewer iterations. We infer this result from Figure 14 obtained for Problem 2 in one iteration, and Table 11 presents the result. As observed from the table's values, the genetic algorithm gets to the answer in fewer iterations.

TABLE 9. The normality test result

Index	Algorithm	P-Value	Result
MID	GA	0.065	Normal
	ELA	0.118	Normal
MT	GA	0.15	Normal
	ELA	0. 32	Normal

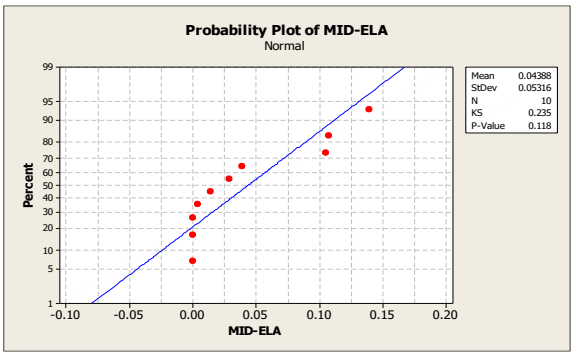

Figure 13. The result of the normality test on the MID index of the electromagnetic algorithm

TABLE 10. The results of the t-test

Null(H0) hypothesis	T-Test	P-Value	Result
The MID index in GA is lower than ELA.	2.25	0.35	H0 Hypothesis is not rejected
The MT index in GA is lower than ELA.	1.84	0.28	H0 Hypothesis is not rejected

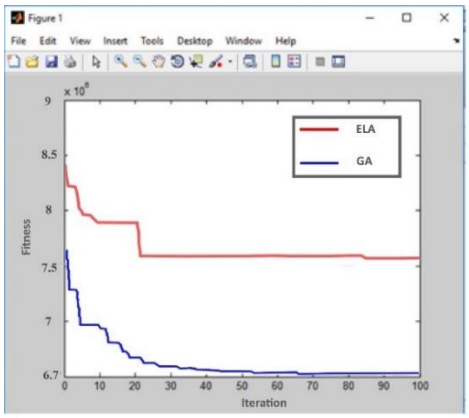

Figure 14. Comparing the convergence speed in genetic and electromagnetic algorithms

TABLE 11. The results of comparing the convergence in genetic and electromagnetic algorithms in problem 2

Algorithm	The iteration where convergence begins	Solution Time	Objective function
ELA	85	233.19	6809638
GA	66	210.65	6722158

Fallahpour et al. [42] developed an integrated model to consider the sustainability and Industry 4.0 criteria for the supplier selection management. They used the fuzzy best worst method and the two-stage fuzzy inference system to assess the selection of suppliers. Researchers can use their approach for extension of our paper. Fathollahi-Fard et al. [43] presented a bi-level programming for home health care supply chain considering outsourcing. Another direction for developing our paper is considering home health care with outsourcing in post-disaster phase. Another issue for developing our paper is related to Pasha et al. [44] research. They developed an integrated optimization model for liner shipping. Researchers can extend our paper with their approach.

6. CONCLUSION

Disaster or crisis is an event that occurs suddenly and sometimes increasingly and leads to a dangerous and unstable situation for an individual, a group, or society. A crisis creates a situation that needs fundamental and extraordinary action. The random and unpredictable nature of a crisis requires the presentation of comprehensive crisis plans to reduce and mitigate the crisis's risks and consequences. The improvement of the area of relief and support leads to significant results in such reductions. After reviewing the literature in recent years, we identified issues like the assumption of a budget for relief costs, the uncertainty of the budget and demand, bi-level programming in critical issues, and the negligence of assuming the items' decay in most reviewed articles as research gaps. The purpose of this study is to cover the identified research gaps. For this purpose, we developed an integer linear programming model that finds the optimal location of local warehouses from among the available points and determines the optimal allocation of demand points and the optimal number of items transferred to those points. Also, we designed the inventory policy to take the items out of the warehouse before the expiration date at a cost to prevent corruption. We solved several hypothetical problems in small sizes by GAMS software and in larger sizes by genetic and electromagnetic meta-heuristic algorithms to investigate the proposed model. After solving hypothetical problems with larger dimensions by electromagnetic and genetic algorithms and comparing the performance indices in these two algorithms, we found that genetics has a better performance than electromagnetism in this problem. This algorithm also converges to its optimal answer in fewer iterations than its competing algorithm, showing the high speed of genetics compared to electromagnetism. On the other hand, in most cases, the standard deviation of the objective function in genetics was less than electromagnetism, which indicates that genetic responses have fewer digressions, and they are close to the mean. As a result, genetics generally performed better than electromagnetism. This claim has also been substantiated in this study by a statistical hypothesis. Consequently, in the case of an earthquake, the relevant organizations can use this efficient model to decide on the optimal location of warehouses or field tents, the optimal number of purchased and stored items in local warehouses, and the optimal allocation of items to demand points in situations with uncertain budgets and demand.

Relief operations, like any other operations, need their costs. Moreover, the premise of demand uncertainty enhanced the issue's verisimilitude. In this study, we also covered the bi-level programming gap. After solving a problem in both mixed-integer linear programming model and bi-level programming models and recording the value of the problem's cost function, we found that this assumption increases the total cost to some extent. This increased cost is reasonable because we sometimes have to change the decision to make the necessary coordination for decision-making, and thus, the costs will increase. The organizations in charge are responsible for accepting the increased cost of the bi-level programming compared to the mode; it is up to them to pay the price to take advantage of the bi-level programming benefits. Unfortunately, one of the limitations of this study was the lack of access to real-world data, which we could not access despite our best efforts. Therefore, we had to use random data.

In this study, since the scenarios have been arranged based on the severity of the events, they can be

generalized to other crises like floods and storms. Moreover, because of the high probability of ruining the infrastructure for relief during a crisis, we suggest adding routing and transportation of items through various communication routes such as land and air to the model to develop it. Another issue that one can augment is temporary hospitals with different equipment and conditions to treat the injured. Additionally, other objective functions, such as the satisfaction level of the victims and, most importantly, the response time to demand in the critical situation, can be inserted into the model.

7. REFERENCES

1. Rezaei-Malek, M., Tavakkoli-Moghaddam, R., Zahiri, B. and Bozorgi-Amiri, A., "An interactive approach for designing a robust disaster relief logistics network with perishable commodities", ***Computers & Industrial Engineering***, Vol. 94, (2016), 201-215, doi: 10.1016/j.cie.2016.01.014.
2. Kohn, S., Eaton, J. L., Feroz, S. and Bainbridge, A. A., Hoolachan, J., Barnett, D. J., "Personal disaster preparedness: an integrative review of the literature", ***Disaster medicine and Public Health Preparedness***, Vol. 6, No. 3, (2012), 217-231, doi: 10.1001/dmp.2012.47.
3. Boonmee, C., Arimura, M. and Asada, T., "Location and allocation optimization for integrated decisions on post-disaster waste supply chain management: On-site and off-site separation for recyclable materials", ***International Journal of Disaster Risk Reduction***, Vo. l31, (2018), 902-917, https://doi.org/10.1016/j.ijdrr.2018.07.003.
4. Habib, M. S. and Sarkar, B., "An integrated location-allocation model for temporary disaster debris management under an uncertain environment", ***Sustainability***, Vol. 9, (2017), 716, https://doi.org/10.3390/su9050716.
5. Lorca, Á., Çelik, M., Ergun, Ö. and Keskinocak, P., "An optimization-based decision-support tool for post-disaster debris operations", ***Production and Operations Management***, Vol. 26, No. 6, (2017), 1076-1091, doi: 10.1111/poms.12643.
6. Paul, J. A. and MacDonald, L., "Location and capacity allocations decisions to mitigate the impacts of unexpected disasters", ***European Journal of Operational Research***, Vol. 251, No. 1, (2016), 252-263, https://doi.org/10.1016/j.ejor.2015.10.028.
7. Ferreira, G. O., Arruda, E. F. and Marujo, L. G., "Inventory management of perishable items in long-term humanitarian operations using Markov decision processes", ***International Journal of Disaster Risk Reduction***, Vol. 31, (2018), 460-469, https://doi.org/10.1016/j.ijdrr.2018.05.010.
8. JICA, C. "The study on seismic microzoning of the Greater Tehran Area in the Islamic Republic of Iran.", Pacific Consultants International Report, OYO Cooperation, Japan, (2000), 291-390.
9. Cozzolino, A., Rossi, S. and Conforti, A., "Agile and lean principles in the humanitarian supply chain: The case of the United Nations World Food Programme", ***Journal of Humanitarian Logistics and Supply Chain Managemen***t, Vol. 2, No. 1, (2012), 16-33, https://doi.org/10.1108/20426741211225984.
10. Naji-Azimi, Z., Renaud, J., Ruiz, A. and Salari, M., "A covering tour approach to the location of satellite distribution centers to supply humanitarian aid", ***European Journal of Operational Research***, Vol. 222, No. 3, (2012), 596-605, doi: 10.1016/j.ejor.2012.05.001.
11. Hu, Z. H. and Sheu, J. B., "Post-disaster debris reverse logistics management under psychological cost minimization", ***Transportation Research Part B: Methodological,*** Vol. 55, (2013), 118-141, https://doi.org/10.1016/j.trb.2013.05.010.
12. Bozorgi-Amiri, A., Jabalameli, M. S., Alinaghian, M. and Heydari, M., "A modified particle swarm optimization for disaster relief logistics under uncertain environment", ***The International Journal of Advanced Manufacturing Technology***, Vol. 60, No. 1-4, (2012), 357-371, doi: 10.1007/s00170-011-3596-8.
13. Yu, W., "Reachability guarantee-based model for pre-positioning of emergency facilities under uncertain disaster damages", ***International Journal of Disaster Risk Reduction***, Vol. 42, (2020), 101335, https://doi.org/10.1016/j.ijdrr.2019.101335.
14. Oksuz M. K. and Satoglu, S. I., "A two-stage stochastic model for location planning of temporary medical centers for disaster response", ***International Journal of Disaster Risk Reduction***, Vol. 44, (2020), 101426, https://doi.org/10.1016/j.ijdrr.2019.101426.
15. Boonmee, C., Naotaka, I., Takumi, A. and Mikiharu, A., "Multi-model optimization for shelter-site selection: A case study in Banta municipality, Thailand", The 53rd Japan Society of Civil Engineers Conference, Hokkaido University, Japan, (2017), 2175-2181.
16. Chakravarty, A. K., "Humanitarian relief chain: Rapid response under uncertainty", ***International Journal of Production Economics***, Vol. 151, (2014), 146-157, https://doi.org/10.1016/j.ijpe.2013.10.007.
17. Hong, X., Lejeune, M. A. and Noyan, N., "Stochastic network design for disaster preparedness", ***IIE Transaction***s, Vol. 47, No. 4, (2015), 329-357, https://doi.org/10.1080/0740817X.2014.919044.
18. Mohammadi, R., Ghomi, S. F. and Jolai, F., "Prepositioning emergency earthquake response supplies: A new multi-objective particle swarm optimization algorithm", ***Applied Mathematical Modelling***, Vol. 40, No. 9-10, (2016), 5183-5199, https://doi.org/10.1016/j.apm.2015.10.022.
19. Tofighi, S., Torabi, S. A. and Mansouri, S. A., "Humanitarian logistics network design under mixed uncertainty", ***European Journal of Operational Research***, Vol. 250, (2016), 239-250, https://doi.org/10.1016/j.ejor.2015.08.059.
20. Hu, S. L., Han, C. F. and Meng, L. P., "Stochastic optimization for joint decision making of inventory and procurement in humanitarian relief", ***Computers & Industrial Engineering***, Vol. 111, (2017), 39-49, https://doi.org/10.1016/j.cie.2017.06.029.
21. Shen, Z., Dessouky, M. and Ordóñez, F., "Perishable inventory management system with a minimum volume constraint", ***Journal of the Operational Research Society***, Vol. 62, No. 19, (2011), 2063-2082, https://doi.org/10.1057/jors.2010.181.
22. Manopiniwes, W., Nagasawa, K. and Irohara, T., "Humanitarian relief logistics with time restriction: Thai flooding case study", ***Industrial Engineering & Management Systems***, Vol. 13, No. 4, (2014), 398-407, https://doi.org/10.1057/jors.2010.181.
23. Roni, M. S., EksiogluJin, M. and Mamun, S., "A hybrid inventory policy with split delivery under regular and surge demand", ***International Journal of Production Economics***, Vol. 172, (2016), 126-136, doi: 10.1016/j.ijpe.2015.11.015.
24. Tavana, M., Abtahi, A. R., Di Caprio, D., Hashemi, R. and Yousefi-Zenouz, R., "An integrated location-inventory-routing humanitarian supply chain network with pre-and post-disaster management considerations", ***Socio-Economic Planning Sciences***, Vol. 64, (2018), 21-37.
25. Celik, E., Aydin, N. and Gumus, A. T., "A stochastic location and allocation model for critical items to response large-scale emergencies: A case of Turkey", ***An International Journal of Optimization and Control: Theories & Applications (IJOCTA)***, Vol. 7, No.1, (2016), 1-15, doi: 10.11121/ijocta.01.2017.00300.

26. Loree, N. and Aros-Vera, F., "Points of distribution location and inventory management model for Post-Disaster Humanitarian Logistics", ***Transportation Research Part E: Logistics and Transportation Review***, Vol. 116, (2018), 1-24, https://doi.org/10.1016/j.tre.2018.05.003.
27. Cavdur, F., Sebatli-Saglam, A. and Kose-Kucuk, M., "A spreadsheet-based decision support tool for temporary-disaster-response facilities allocation", ***Safety Science***, Vol. 124, (2020), 104581, doi: 10.1016/j.ssci.2019.104581.
28. Baharmand, H., Comes, T. and Lauras, M., "Bi-objective multi-layer location–allocation model for the immediate aftermath of sudden-onset disasters", ***Transportation Research Part E: Logistics and Transportation Review***, Vol. 127, (2019), 86-110, https://doi.org/10.1016/j.tre.2019.05.002.
29. Liu, A., Zhu, Q., Xu, L., Lu, Q. and Fan, Y., "Sustainable supply chain management for perishable products in emerging markets: An integrated location-inventory-routing model***", Transportation Research Part E: Logistics and Transportation Review***, Vol. 150, (2021), 102319, doi: 10.1016/j.tre.2021.102319.
30. Mahtab, Z., Azeem, A., Ali, S. M., Paul, S. K. and Fathollahi-Fard, A. M. "Multi-objective robust-stochastic optimisation of relief goods distribution under uncertainty: a real-life case study", ***International Journal of Systems Science: Operations & Logistics***, (2021), 1-22. https://doi.org/10.1080/23302674.2021.1879305.
31. Fetter, G. and Rakes, T., "Incorporating recycling into post-disaster debris disposal", ***Socio-Economic Planning Sciences***, Vol. 46, No. 1, (2012), 14-22, https://doi.org/10.1016/j.seps.2011.10.001.
32. Kim, J., Deshmukh, A. and Hastak, M., "Selecting a temporary debris management site for effective debris removal", 10th Annual Conference of the International Institute for Infrastructure Renewal and Reconstruction, (2014), 214-218, doi: 10.5703/1288284315362.
33. Onan, K., Ülengin, F. and Sennaroğlu, B., "An evolutionary multi-objective optimization approach to disaster waste management: A case study of Istanbul, Turkey", ***Expert Systems with Applications,*** Vol. 42, No. 22, (2015), 8850-8857, https://doi.org/10.1016/j.eswa.2015.07.039.
34. Pramudita, A., Taniguchi, E. and Qureshi, A. G., "Location and routing problems of debris collection operation after disasters with realistic case study", ***Procedia-Social and Behavioral Sciences***, Vol. 125, (2014), 445-458, https://doi.org/10.1016/j.sbspro.2014.01.1487.
35. Takeda, T., Mori, Y., Kubota, N. and Arai, Y., "A route planning for disaster waste disposal based on robot technology", In 2014 IEEE Symposium on Robotic Intelligence in Informationally Structured Space (RiiSS), (2014), 1-6.
36. Balcik, B. and Beamon, B. M., "Facility location in humanitarian relief", ***International Journal of Logistics***, Vol. 11, No. 2, (2008), 101-121, https://doi.org/10.1080/13675560701561789.
37. Garrido, R. A., Lamas, P. and Pino, F. J., "A stochastic programming approach for floods emergency logistics", ***Transportation Research Part E: Logistics and Transportation Review,*** Vol. 75, (2015), 18-31, doi: 10.1016/j.tre.2014.12.002.
38. Rabbani, M., Manavizadeh, N., Samavati, M. and Jalali, M., "Proactive and reactive inventory policies in humanitarian operations", ***Uncertain Supply Chain Management,*** Vol. 3, (2015), 253-272, doi: 10.5267/j.uscm.2015.3.004.
39. Renkli, Ç. and Duran, S., "Pre-positioning disaster response facilities and relief item", ***Human and Ecological Risk Assessment: An International Journal***, Vol. 21, No. 5, (2015), 1169-1185, https://doi.org/10.1080/10807039.2014.957940.
40. Noyan, N., Balcik, B. and Atakan, S., "A stochastic optimization model for designing last mile relief networks", ***Transportation Science,*** Vol. 50, (2015), 1092-1113, https://doi.org/10.1287/trsc.2015.0621.
41. Escudero, L. F., Garín, M. A., Monge J. F. and Unzueta, A., "On preparedness resource allocation planning for natural disaster relief under endogenous uncertainty with time-consistent risk-averse management", ***Computers & Operations Research***, Vol. 98, (2018), 84-102, doi: 10.1016/j.cor.2018.05.010.
42. Fallahpour, A., Wong, K. Y., Rajoo, S., Fathollahi-Fard, A. M., Antucheviciene, J. and Nayeri, S., "An integrated approach for a sustainable supplier selection based on Industry 4.0 concept", ***Environmental Science and Pollution Research***, (2021), 1-19. https://doi.org/10.1007/s11356-021-17445-y.
43. Fathollahi-Fard, A. M., Hajiaghaei-Keshteli, M., Tavakkoli-Moghaddam, R. and Smith, N. R. "Bi-level programming for home health care supply chain considering outsourcing***", Journal of Industrial Information Integration***, Vol. 25, (2022), 100246. https://doi.org/10.1016/j.jii.2021.100246
44. Pasha, J., Dulebenets, M. A., Fathollahi-Fard, A. M., Tian, G., Lau, Y. Y., Singh, P. and Liang, B. "An integrated optimization method for tactical-level planning in liner shipping with heterogeneous ship fleet and environmental considerations", ***Advanced Engineering Informatics***, Vol. 48, (2021), 101299. https://doi.org/10.1016/j.aei.2021.101299.

Persian Abstract

چکیده

حوادثی که بر اثر کارکردهای طبیعی و انسانی به طور ناگهانی رخ می دهد و سختی هایی را بر جامعه تحمیل می کند، بحران نامیده می شود. از آنجایی که تغییرات اقلیمی کره زمین در سال های اخیر بر تعداد بحران های طبیعی از جمله زلزله، سیل، طوفان و ... افزوده است، بشر نیاز به مدیریت بحران و برنامه ریزی های لازم را در شرایط بحرانی بیش از پیش احساس کرده است. هدف این تحقیق مدلسازی و حل مشکل مکان، تخصیص و موجودی در شرایط پس از بحران است. برای رسیدن به این هدف، ابتدا به بررسی مقالات قبلی پرداخته ایم. سپس خلأهای پژوهشی در مدیریت و برنامه ریزی در شرایط بحرانی را شناسایی کرده ایم. در این مطالعه، بودجه‌ها و خواسته‌های نامشخص و تصمیم‌گیری برنامه‌ریزی دوسطحی نوآوری‌ها هستند. در نتیجه، ما مدل‌های ریاضی خطی عدد صحیح مختلط را برای پوشش شکاف‌های تحقیق توسعه داده‌ایم. در نهایت چندین مسئله در ابعاد کوچک توسط نرم افزار GAMS و مسائل بزرگ توسط الگوریتم های فراابتکاری ژنتیک و الکترومغناطیسی حل شده است. سپس عملکرد الگوریتم‌ها را تحلیل کردیم که نشان می‌دهد الگوریتم ژنتیک در این شماره بهتر از الگوریتم الکترومغناطیسی است.

International Journal of Engineering

Journal Homepage: www.ije.ir

Optimum Bacteria Suspension Volume for Stabilizing Silty Sand Soils by *Sporosarcina pasteurii* Bacteria

A. Karami[a], I. Shooshpasha*[a], H. A. Alikhani[b]

[a] *Department of Geotechnical Engineering, Babol Noshirvani University of Technology, Babol, Iran*
[b] *Department of Soil Sciences and Engineering, University of Tehran, Tehran, Iran*

PAPER INFO

Paper history:
Received 01 March 2022
Received in revised form 18 May 2022
Accepted 25 May 2022

Keywords:
Bio-mediated Soil Improvement
Microbial Geo-Technology
Sporosarcina pasteurii Bacterium
Optimum Bacteria Suspension Volume
Triaxial Tests

ABSTRACT

Recently, the bio-mediated soil improvement techniques have gained an increasing attention. In this method, the bacteria was cultivated aerobically in the laboratory and added to the soil with reactant solutions such as urea and calcium chloride. Most of the existing studies are on sandy soils and a few researches have done on silty sandy soils. However, most soils in nature are compounds of fine-grained and coarse-grained soils. In fine-grained soils, silt does not have very good resistance due to the lack of adhesion between its particles. Hence, in this study *Sporosarcina pasteurii* bacterium was aerobically cultivated for stabilizing the sand with different percentages of silt to determine the optimum bacteria suspension volume. After some bacterial tests such as measuring bacterial growth, standard plate count, gram staining, pH determination, growth without urea, and urease test, geo-technical tests like soil sieve, compaction, and Atterberg limits were also done. Standard plate count was estimated $2.5*10^8$ through serial dilution plating and culture media pH was determined 8.64 from different samples. Moreover, to achieve the best results, different sampling methods were compared. As the calcium carbonate creates a network of calcified bridges of calcite between sand grains, an electron microscope was used for scanning the surface with a focused beam of electrons. Results of triaxial tests showed that by adding optimum bacteria suspension volume, the maximum strength for samples with 0, 10, 20, 30 and 40% of silt was improved from 700, 900, 750, 600 and550 to 1100, 1400, 1550, 1600, and 1500 kPa, respectively.

doi: *10.5829/ije.2022.35.10a.02*

1. INTRODUCTION

Microbial geo-technology is considered as a branch of geo-technical engineering. Surface soil may contain 109-1012 cells per gram several in situ conditions such as light, heat, pH, oxygen, toxic substances, organic matter, and pressure. The bio-geochemical byproducts change the engineering properties of soil; hence the bio-mediated soil improvement techniques have gained an especial attention [1]. Mitchell and Santamarina [2] introduced microbiological concepts and illustrated their potential roles in soils and rock. DeJong et al. [3] reported the outcomes of the workshop entitled "Geological and Geotechnical Engineering in the New Millennium: Opportunities for Research and Technological Innovation". Moreover, there are some reviews of the existing or potential applications of microorganisms in geo-technology to discuss their advantages and disadvantages [4-6].

There are two approaches in microbial geo-technology: bio-clogging and bio-cementation. Bio-clogging is the process of filling the soil voids with microbial biomass thus reducing porosity and hydraulic conductivity [7]. Bio-cementation is to enhance the shear strength and stiffness of soil through the production of particle-binding materials via microbial means. It is also diminishing the permeability of tropical residual soil and sand [8].

One of the bio-mediated soil improvement techniques is Microbially Induced Carbonate Precipitation (MICP) which is used for various geotechnical engineering applications such as improving foundation bearing

*Corresponding Author Institutional Email: shooshpasha@nit.ac.ir
(I. Shooshpasha)

Please cite this article as: A. Karami, I. Shooshpasha, H. A. Alikhani, Optimum Bacteria Suspension Volume for Stabilizing Silty Sand Soils by *Sporosarcina pasteurii* Bacteria, ***International Journal of Engineering, Transactions A: Basics***, Vol. 35 No. 10, (2022), 1820-1829

capacity, remediation of liquefaction potential during earthquakes, diminishing foundation settlements, and reducing excavation and tunnel support requirements. MICP can be achieved by various processes [9] and among these processes urea hydrolysis is more favorable which has come to prominence in the late nineteenth [10, 11]. The urease is cultivated aerobically in the laboratory and added to the soil with a solution of urea and calcium chloride. The microbial urease catalyzes the hydrolysis of urea to produce carbonate and ammonium (Equation (1)). That action may increases the pH which accelerates calcium carbonate production in the presence of calcium ion [12, 13].

$$CO(NH_2)_2 + 2H_2O \xrightarrow{urease} 2NH_4^+ + CO_3^{2-} \quad (1)$$

The produced carbonate ions precipitate in the presence of calcium ions as calcium carbonate crystals, which form cementing bonds between the existing sand grains (Equation (2))

$$Ca^{2+} + CO_3^{2-} \rightarrow CaCO_3(s) \quad (2)$$

The precipitated calcium carbonate will be durable under natural groundwater conditions and in the absence of acidifying processes in the pores. A sufficient quantity of calcium carbonate significantly increases soil stabilization [14, 15].

Certain bacterial species cause urease enzyme which catalyzes the hydrolysis of urea to ammonia and carbonic acid. Mwandira et al. [16] used the microbially induced calcium carbonate precipitation technique in conjunction with the bacterium *Pararhodobacter* sp. to bioremediate lead. DeJong et al. [17] used *Sporosarcina pasteurii* to engineer a cemented soil matrix within initially loose and collapsible sand. They demonstrated that the MICP-treated specimens exhibit a noncollapse strain-softening shear behavior, with a higher initial shear stiffness and ultimate shear capacity than untreated loose specimens. Chou et al. [18] carried out direct shear and California Bearing Ratio (CBR) tests on sand specimens subjected to treatment by growing, resting, and dead *S. pasteurii* cells. The peak strength and the friction angles were significantly increased for the loose sand with the growing-cell treatment. Martinez et al. [19] compared two injection methods and expressed that the injection of urea- and calcium-rich solution produces a more uniform calcite distribution as compared to a continuous injection method. AL Qabani et al. [20] assessed the optimum use of *S. pasteurii* to induce precipitation and determined the time required for the process. Tirkolaei and Bilsel [21] examined environmental factors on the microbial urea hydrolysis process for bio-cement production. Kim and Youn [22] employed five microbes (which urease activities of the four of them were higher than *S. pasteurii*) to precipitate calcite in cohesionless soils of two different relative densities (60% and 80%). They showed that the relative density of cohesionless soils significantly affects the amount of calcite precipitation and that there is a weak correlation between urease activity and calcite precipitation. Li et al. [23] studied the effects of microbial-induced carbonate precipitation on fine sand samples by adding some additives. They showed that the precipitated calcium carbonate in the core increased 1.6 times through this method. Jalili et al. [24] expressed that bio-cementation method compared with the conventional injection method has many features such as lower cost, less pressure, more radius of influence, in accordance with the environmental conditions that would justify the use of this method. They showed that bio-cementation method in addition to increasing uniaxial compressive strength causes to increase the Stiffness of the soil granular samples. Kahani et al. [25] used inexpensive nutrients and water resources in composition of the culture media and examined sanitized media instead of sterilized ones in order to reducing the cost of production of urease bacteria and achieving an ecofriendly process.

Given the above and the environmental benefits of soil biological improvement, this issue has received much attention in recent years. It is worth mentioning that the effect of this bacterium on sandy soil has been studied so far, but there are few studies about silty sand soils with different combinations and comparison between sand and silty sand soils. However, most soils in nature are compounds of fine-grained and coarse-grained soils. In fine-grained soils, silt does not have very good resistance due to the lack of adhesion between its particles. In addition, for biologically soil improvement, the volume and amount of bacterial suspension added to the soil is important both in terms of increasing resistance and in terms of economics. Therefore, for any type of soil composition, it is necessary first to determine the optimal volume of bacterial suspension for soil remediation. In this study, the samples were sand with different percentages of silt (0 to 60%) and for further accuracy the experiments were also done for pure silt samples. Moreover, the optimum bacteria suspension volume for different percentages of silt was determined by triaxial tests. For this purpose, bacterium *S. pasteurii* was used for soil improvement after basic bacterial tests such as measuring bacterial growth by conducting an optical density test, Standard Plate Count (by serial dilution experiments), gram staining, pH determination, growth without urea, and urease test. Geotechnical tests like soil sieve, compaction, and Atterberg limits were also done on samples. Moreover, several methods were tested for sampling construction to accomplish the homogenous distribution of bacterial culture and cementation solution within the soil grains. As the calcium carbonate creates a network of calcified bridges of calcite between sand grains, an electron microscope was used to produce images of a sample by scanning the surface with a focused beam of electrons. At last, the optimum bacteria

suspension volume for different percentages of silt was determined by triaxial tests.

2. MATERIALS AND METHODS

The most important things in microbial geo-technology are type of the bacteria and preparing suitable culture medium for it. After cultivation, some bacterial tests are needed to make sure the bacteria are healthy. At first, the optical density (OD) method was used for cell density measurement. Distilled water was used as a blank and the bacterium was tested some days after culturing. Then, the gram staining method and the pH was tested as well. Moreover, two samples from each solid and liquid medium were prepared for the urease test.

Then, the geotechnical tests were done for investigating the effect of different values of bacteria suspension values and determining the optimum amount for mixing with soil. For this purpose, the soil was seeded in two different manually and mathematical methods. Compaction tests were performed on all samples with different percentages of silt and optimum moisture percentage and maximum specific dry weight were obtained. In order to achieve the best sampling method due to the presence of bacteria, nutrients and silt in the soil, various methods were tested. After preparing the samples, they were kept at normal temperature for stabilization and one day before the test they were placed in an oven (60ºC) in order to dry. Then, since the surfaces of the samples were not perfectly flat, a thin layer of clay was drawn on them before testing. All experiments were performed at 200 kPa confining stress 7 days after sample preparation.

The experimental setups are described in the following sections.

2. 1. Culture Medium The most common growth media for microorganisms are nutrient broths (liquid medium) and agar plates (solid medium). The compositions of the culture medium are pepton, meat extract, agar, distilled water and urea (Table 1). Agar is not added or used while preparing the liquid medium. If agar is added to a nutrient broth, it becomes solid medium for petri-dish studies.

All materials except urea were mixed and then sterilized in an autoclave at 121°C for 20 minutes. For liquid medium, the lid was opened under the laminar hood and the urea was added by using sterilized filter. The bacteria are then spilled, and the resulting solution incubated at 30°C in a shaker at 200 revolutions/min for some days in accordance with the growth time of the strain.

For solid medium, after sterilizing and before reaching 50°C, the urea was added under the laminar hood. It stayed inside the hood until it became solid at normal temperature after about 24 hours. It was then ready for cultivation.

TABLE 1. Composition of media for *S. pasteurii* strain

Item	Unit	Amount
Pepton	g/l	5.0
Meat Extract	g/l	3.0
Agar	g/l	15.0
Distilled water	l	1.0
Urea	%	2

In addition, suitable pH is an important requirement for optimum microbial growth in culture media. The bacteria grow at pH higher than 6.5 and the optimum pH is in the range of 8.5 to 9 [26, 27]. The initial pH of nutrient broth is 7 and adding urea the pH increased. To ensure that pH reaches the desired level, it was measured from different samples at different stages of culture and bacterial growth. For testing, the apparatus was first calibrated by solutions with pH 4 and 7, and then a bacterial culture medium was tested. The pH obtained from this experiment was 8.64 which is good for the growth of specific strain of bacteria.

2. 2. Standard Plate Count by Serial Dilution Experiments (SPC) It is essential to determine the number of microorganisms in a given sample. Estimation of Standard Plate Counts (SPC) through serial dilution plating is the most common technique for monitoring cultivable bacteria. In our experiment, the sample was serially diluted and then plated out on an agar surface in such a manner that single isolated bacteria form visible isolated colonies. After two days, the SPC is determined by multiplying the number of colonies on a dilution plate by the corresponding dilution factor. It should be noted that for statistical reasons, only the data from plates that had between 30 and 300 colonies was used in this calculation. The SPC obtained from this experiment was $2.5*10^8$ which is suitable.

2. 3. Growth without Urea Since urea increases pH, a lack of bacterial growth in urea-free media indicates a proper cultivation process. Bacteria were cultured in urea-free medium and disappeared after 4 days.

2. 4. Sample Construction The samples were sand with different percentages of silt (0, 10, 20, 30 and 40%). As previously mentioned, the experiments were also done for samples with 50 and 60% of silt and pure silt in order to provide further accuracy. The following methods were tested for sampling construction:

1. Injection of bacteria and reactant solution: The soil sample was made inside the mold at a specified moisture content, which varied from the lowest moisture to optimum moisture, then the bacteria and after that, reactant solution were injected into the soil sample.

2. Injection of reactant solution: As the previous method, but the bacterial suspension was mixed with the soil instead of adding water as moisture, and then reactant solution was injected into the sample.
3. Mixing all materials while making samples: All materials, including bacterial suspension and reactant solution, were mixed with the soil and then the sample was made.
4. Put the sample in the aquarium containing nutrients and reactant solution: The bacterial suspension was mixed with the soil. The sample was placed into the aquarium containing nutrients and reactant solution [28]. This method was done in several ways, including the time of sample placement in the aquarium and the aeration in the aquarium solution while the sample was in it.
5. Injection of calcium chloride: In this method, the bacterial suspension was mixed with the soil with a portion of reactant solution and the sample was made. The calcium chloride was then injected into the sample by controlling pressure and discharge.

In the injection method, the silt particles in the sample were displaced by flow of bacteria suspension or reactant solution and caused heterogeneity. Naveed et al. [29] stated that when the bacteria are injected within the soil, they are likely to be filtered within the soil particles with a reduction of bacterial population along the path of injection. Hence, it is difficult to accomplish the homogenous distribution of bacterial culture and cementation solution within the soil grains. Mixing all material for making samples produces lower strength because of rapid reaction of the bacteria with the reactant solution. It causes loss of cementitious bonds between the soil particles. Finally, in the aquarium method, the exact amount of nutrients and reactant solution imported into the sample cannot be controlled. The samples made by this method achieve the same strength with the injection method; however, it is not practicable in field. Hence, injection calcium chloride was considered as the final sample preparation method. To prevent silt leaching in the samples, calcium chloride was injected 2 times (each time 6 hours) with 0.2 bar hydrostatic pressure [30].

3. RESULTS OF BACTERIAL TESTS

Results and discussions for the microcosm experiments are described in the following sections.

3. 1. OD Test The measurement of bacterial cell numbers is a critical process during bacterial cell culture. The OD method is widely used among the different methods which have been developed for cell density measurement. It measures the absorbance/scattering of the media containing bacterial cell particles. When a fresh medium is inoculated with a given number of cells, and the population growth is monitored over a while, plotting the data will yield a typical bacterial growth curve. The exponential phase of growth is a pattern of balanced growth wherein all the cells are growing. Exponential growth cannot be continued forever, and population growth is limited. After the population reaches the stationary phase, a death phase follows, in which the viable cell population declines. The best time for using bacteria is the end of the growth stage.

Since the experimental aim was to compare the population of bacteria with respect to time, distilled water was used as blank. The bacterium was tested the day after culturing. As shown in Figure 1, the population of the tested bacteria reaches to the maximum after four days so the best time to use the bacteria is four days after cultivation.

3. 2. Gram Staining Gram staining is one of the most important and widely used bacteriological laboratory methods used to distinguish and classify bacterial species into two categories based on the physical properties of their cell walls. Gram-positive bacteria have a thick mesh-like cell wall and as a result, are stained purple by crystal violet. Alternatively, gram-negative bacteria stain red and have a thinner layer [31]. The bacterium *S. pasteurii* is gram-positive, so it should naturally be purple after the staining. The result of the experiment is shown in Figure 2 with two different magnifications and purple rod bacteria are visible under the microscope.

3. 3. Urease Test The urease test is used to find out the ability of an organism to split urea, through the

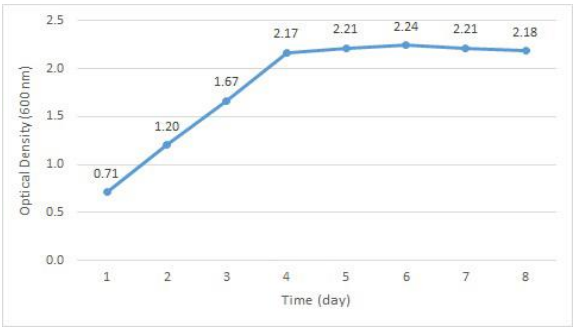

Figure 1. Measured average population variation with time duration from an optical density test Not Acceptable, y-axces

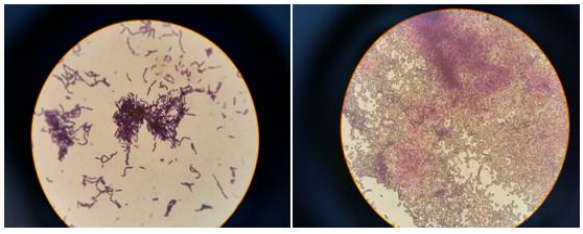

Figure 2. Gram staining result

production of the urease. When urea undergoes hydrolysis, it produces ammonia and carbon dioxide. Urea is acidic but the formation of ammonia turns the medium into alkaline. The change in pH is indicated by the changes in color from yellow to purple. Therefore, an organism that tests positive for urease makes the medium magenta-colored. The bacterium *S. pasteurii* is a positive urease bacterium.

The urease test compounds are urea, Na_2HPO_4, KH_2PO_4, yeast extract and phenol red (Table 2). Explain that these compounds belong to the liquid medium, 15 g/l agar is added to provide a solid medium.

Two samples from each solid and liquid medium were prepared, one for control and the other one for bacterial inoculation. Figure 3 shows the colors after four days. Figure 3(a) is a liquid culture medium, as it can be seen the left inoculated sample was changed to purple however the right one retains its natural color. Figure 3(b) is a solid culture medium; the color was changed where the bacteria were inoculated.

3. 4. Scanning Electron Microscope (SEM) Image

The calcium carbonate creates a network of calcified bridges of calcite between sand grains, while crystals can also get fixed on sand surfaces. A scanning electron microscope is a type of electron microscope that produces images of a sample by scanning the surface with a focused beam of electrons [32]. There are many ASTM standards that specify procedures in microscopy, and several of them are specific to electron microscopes. E 766 is a standard practice for calibrating the magnification of an SEM. It describes calibration in both the x- and y-directions as well as calibration of the scale marker [33]. E 986 is a standard practice for SEM beam size characterization. It describes an experiment for measuring the electron beam diameter with suitable precautions to achieve reproducible results [34].

Figure 4 demonstrates the SEM images showing calcite formation. As it can be seen in Figure 4, some of the pure sand particles form cement bonds with increasing the bacteria and the calcium carbonate deposition between the particles is evident. In the samples with 10, 20 and 30% silt, with increasing the silt, the pores between sands are filled with silt due to the particle size, which results in better and more cementitious bonds between the soil particles. By increasing the silt to 40%, the silt particles are found to lose the cohesion in part of calcium carbonate to the sand particles and to be seen as a non-bonded part in the soil, which reduces the strength in the soil containing 40% silt to that in the soil with 30% silt.

TABLE 2. Urease test compounds

Item	Amount (g/l)
Urea	20
Na_2HPO_4	9.5
KH_2PO_4	9.1
Yeast extract	0.1
Phenol Red	0.01

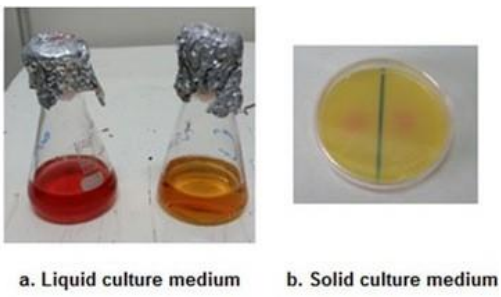

Figure 3. Urease test; the color was changed where the bacteria were inoculated

4. RESULTS OF GEOTECHNICAL TESTS

Results and discussions for the geotechnical tests are described in the following sections.

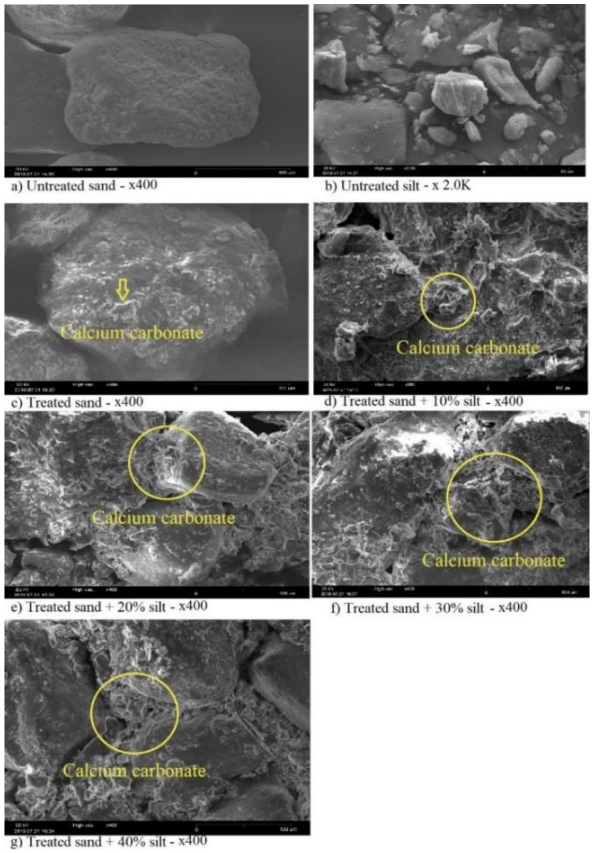

Figure 4. Photos of SEM analyse of untreated and treated soil

4. 1. Grading Curve The soil was seeded in two different ways. The tested soil is manually made by combining different percentages of silt with sand. Hence, sand and silt were graded separately and then the grading curve was plotted using mathematical methods. Also, each sample with a specified percentage of silt was made at first and then the new sample was seeded (Figure 5).

After grading tests, the specific gravity of the solid matter of the soil was determined (Gs=2.7).

4. 2. Compaction Test The compaction tests were performed on all samples with different percentages of silt (0, 10, 20, 30 and 40%). For further accuracy, the experiment was also done for samples with 50 and 60% of silt and pure silt. The specific dry weight of samples for different moisture percentages is shown in Figure 6. Optimum moisture percentage and maximum specific dry weight for different silt percentages are illustrated in Figure 7. Increasing fine grained size in sandy soil decreases the void ratio and arranges soil skeleton in more compacted form. This soil needs less moisture and achieves higher density in compared to poorly graded sand. Hence by adding silt particles in sandy soils, maximum dry weight increases and optimum moisture of content decreases. This trend continues up to the special percent of fine grained size particles. After that, by increasing the special surface of soils, the trend is reversed [35].

4. 3. Effect of Optimum Bacteria Suspension Volume on Stress-strain Variation According to the results of the compaction test, to determine the optimum bacterial for soil stabilization, the required fluid for optimum water content is determined first. The volume of the mold was calculated to be 188.44 cubic centimeters. Then, for determining the optimum bacteria suspension volume for different percentages of silt, 5 samples are made with higher and fewer bacteria in comparison to water content. In other words, one sample with 5 g higher and three samples with 5 to 15 g lower than the required fluid are also made. It should be noted that for samples with bacterial levels below the required fluid, distilled water is added to the bacterial suspension.

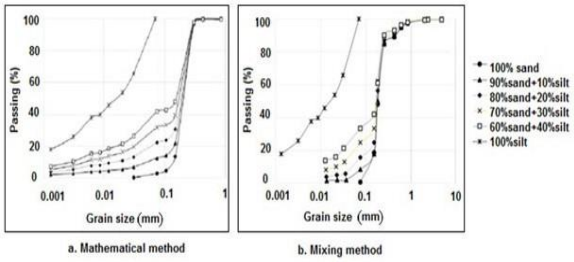

Figure 5. Grain size distribution curve

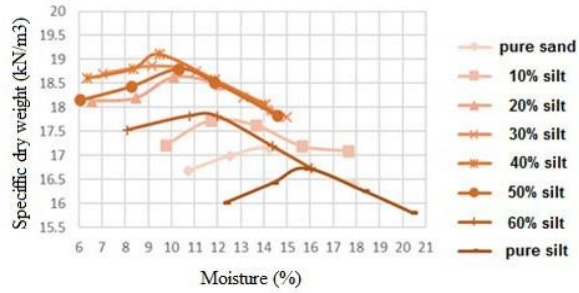

Figure 6. Dry unit weight variation with moisture content

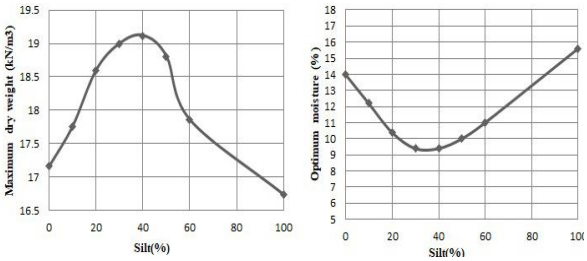

Figure 7. Maximum dry unit weight and optimum moisture content variation with silt percentages

The samples were kept at normal temperature for stabilization and one day before the test they were placed in an oven (60ºC) to dry. Then, since the surfaces of the samples were not perfectly flat, a thin layer of clay was drawn on them before testing. All experiments were performed at 200 kPa confining stress 7 days after sample preparation. As expected, untreated samples failed in barrel shape (Figure 8-a) but treated samples were first deformed into barrel shape and then broke at an angle of about 65 degrees (Figures 8-b and 8-c).

To determine the effect of bacteria on increasing resistance, triaxial experiments were performed on untreated soil samples initially. After that, triaxial tests were done with 5 different values of bacteria suspension to determine optimum volume for each soil (pure sand or sand with different silt percentages). Results are illustrated in Figures 9 to 13. The numbers written next to the graph are bacterial values (g). As can be seen from all samples, the optimum bacterial is equal to the optimum moisture at 95% of relative density. From figures, in each series with different content of silt, the strength of untreated samples is much less than the treated samples; and this is higher in samples with 0% and 40% of silt in comparison of others. For pure sand samples (0% silt), the maximum strength is improved from 700 kPa to 1100 kPa and it is improved from 900 to 1400 kPa, 750 to 1550, 600 to 1600, and 550 to 1500 kPa for samples with 10, 20, 30 and 40% of silt, respectively. As can be seen in the figures, the soil behavior more brittle when it is treated.

As it can be seen the maximum triaxial strength in stabilized soil increases from 1097 (0% silt) to 1671 kPa (30% silt) then, decreases again to 1488 kPa (40% silt).

Figure 8. Broken sample in triaxial test: (a) Ductility behavior (barell shape failure), (b) Brittle bihavior (barell shape and linier failure), (c) Failure angle

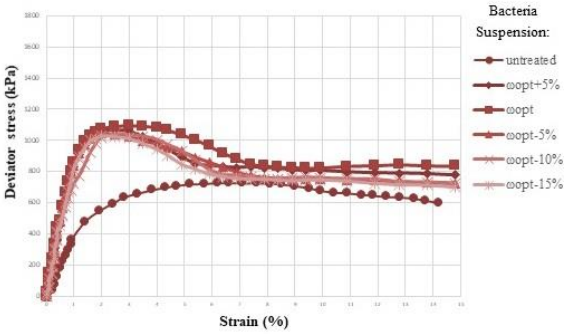

Figure 9. Deviator stress variation with strain for sand and different percent of bacteria suspension

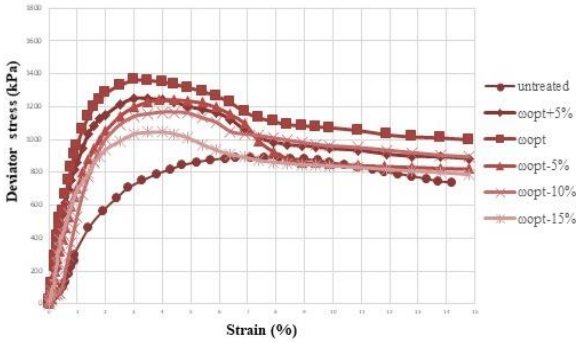

Figure 10. Deviator stress variation with strain for sand with 10% silt and different percent of bacteria suspension

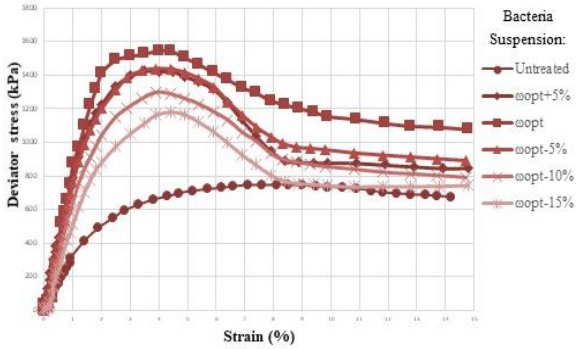

Figure 11. Deviator stress variation with strain for sand with 20% silt and different percent of bacteria suspension

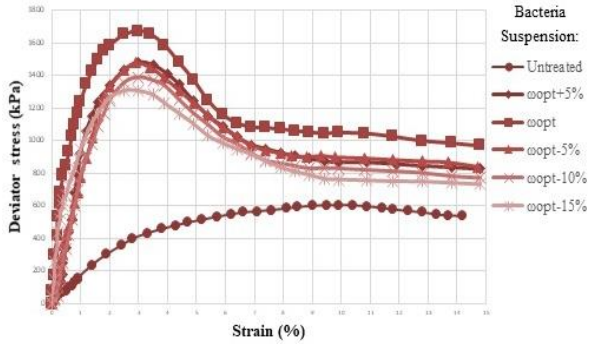

Figure 12. Deviator stress variation with strain for sand with 30% silt and different percent of bacteria suspension

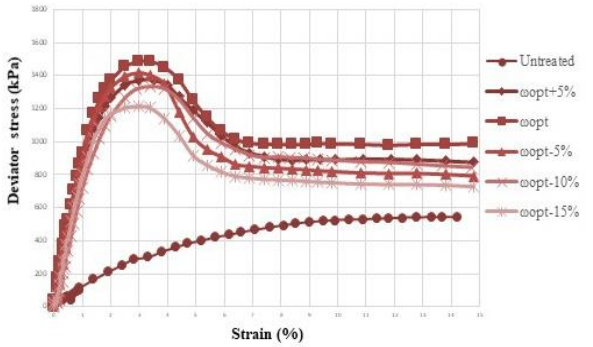

Figure 13. Deviator stress variation with strain for sand with 40% silt and different percent of bacteria suspension

The maximum strength is obtained 1671 kPa in stabilized soil while it is near 900 kPa in unstabilized soil. Hence, the strength is improved by almost 80% by stabilizing.

The variation of maximum Deviator stress for all stabilized samples with different bacteria suspension is shown in Figure 14. The figure illustrates that maximum major stress for all samples is obtained at bacteria suspension equal to optimum moisture and by increasing moisture (Wopt+5%), it decreases. As well as, the

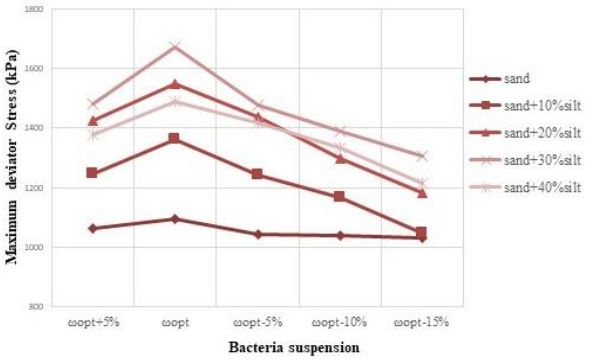

Figure 14. Maximum deviator stress variation with different bacteria suspension for all stabilized samples

strength reduces when the bacteria suspension in samples is less than optimum amount. It is worth noting that variation of maximum major stress in sandy samples with different bacteria suspension is neglectable. Moreover, the maximum major stresses are very close in samples with 20 and 40% silt.

5. CONCLUSION

In this study bacterium *Sporosarcina pasteurii* is used for soil improvement. The samples were sand with different percentages of silt (0, 10, 20, 30 and 40%). For further accuracy, the experiments were also done for samples with 50 and 60% of silt and pure silt. At first, the OD method was used for cell density measurement. Distilled water was used as a calibration liquid and the bacterium was tested some days after culturing. The cell density of the tested bacteria reached maximum after four days. Also, the SPC was obtained $2.5*10^8$ from serial dilution experiment. Then, the gram staining method was done, and purple rod bacteria were observed under the microscope. Moreover, two samples from each solid and liquid medium were prepared for the urease test. It was shown that the colors after four days were changed to purple. Results of triaxial tests can be summarized as follows:

- The samples were first deformed into barrel shape and then broke at an angle of about 65 degrees.
- The optimum bacteria suspension volume for different percentages of silt is determined by triaxial tests and results showed that this is equal to the optimum moisture.
- By adding silt into the soil, the maximum triaxial strength in stabilized soil increased from 1097 (0% silt) to 1671 kPa (30% silt). However, by adding more silt (40% silt), the resistance decreases again to 1488 kPa.
- The maximum strength was obtained 1671 kPa in stabilized soil while it was near 900 kPa in untreated soil.
- The strength was improved by almost 80% by stabilizing.

The main limitation in this study was the use of bacteria as living organisms and sensitive to environmental conditions. In biological methods the most important point is providing the necessary and required conditions for bacteria. Other limitation of this study was the method of combining bacterial suspension with soil and preparing suitable samples. The best method was selected by performing several experimental samples. It is worth mentioning that in future studies, the native bacteria in the soils of each region can be studied to investigate their effects on increasing soil resistance. This can reduce the environmental impacts and costs.

6. REFERENCES

1. Saricicek, Y. E., Gurbanov, R., Pekcan, O. and Gozen, A. G. "Comparison of microbially induced calcium carbonate precipitation eligibility using *sporosarcina pasteurii* and bacillus licheniformis on two different sands", ***Geomicrobiology Journal***, Vol. 36, No. 1, (2018), 42-52. doi: 10.1080/01490451.2018.1497732
2. Mitchell, J. K. and Santamarina J. C. "Biological considerations in geotechnical engineering", ***Journal of Geotechnical and Geoenvironmental Engineering***, Vol. 131, (2005), 1222-1233. doi: 10.1061/(ASCE)1090-0241(2005)131:10(1222)
3. Dejong, J., Mortensen, B. and Martinez, B. "Bio-soils interdisciplinary science & engineering initiative: meeting societal needs through international transformative research", NSF Final Report, (2007).
4. Ivanov, V. and Chu, J. "Applications of microorganisms to geotechnical engineering for bioclogging and biocementation of soil in situ", ***Environmental Science and Biotechnology***, Vol. 7, (2008), 139-153. doi: 10.1007/s11157-007-9126-3
5. Karatas, I. "Microbiological improvement of the physical properties of soils", Arizona State University, (2008).
6. Dejong, J. T., Soga, K., Kavazanjian, E., Burns, S., Van Paassen, L., AL Qabany, A., Aydilek, A., Bang, S., Burbank, M., Caslake, L., Chen, C., Cheng, X., Chu, J., Ciurli, S., Esnault, A., Fauriel, S., Hamdan, N., Hata, T., Inagaki, Y., Jefferis, S., Kuo, M., Laloui, L., Larrahondo, J., Manning, D., Martinez, B., Montoya, B., Nelson, D., Palomino, A., Renforth, P., Santamarina, J., Seagren, E., Tanyu, B., Tsesarsky, M. and Weaver, T., "Biogeochemical processes and geotechnical applications: progress, opportunities and challenges", ***Géotechnique***, Vol. 63, (2013), 287-301. doi: 10.1680/geot.SIP13.P.017
7. Alshiblawi, P. "Investigating of bioclogging in homogenous and heterogeneous uncontaminated and contaminated sands", Ph.D. Thesis, Cardiff University, (2016).
8. Umar, M., Kassim, K. A. and Ping Chiet, K. T. "Biological process of soil improvement in civil engineering: A review", ***Journal of Rock Mechanics and Geotechnical Engineering***, Vol. 8, (2016), 767-774. doi: 10.1016/j.jrmge.2016.02.004
9. DeJong, J. T., Mortensen, B. M., Martinez, B. C. and Nelson, D. C. "Bio-mediated soil improvement", ***Ecological Engineering***, Vol. 36, (2010), 197-210. doi: 10.1016/j.ecoleng.2008.12.029
10. Benini, S., Rypniewski, W. R., Wilson, K. S., Miletti, S., Ciurli, S. and Mangani, S., "A new proposal for urease mechanism based on the crystal structures of the native and inhibited enzyme from Bacillus pasteurii: Why urea hydrolysis costs two nickels", ***Structure***, Vol. 7, (1999), 205-216. doi: 10.1016/S0969-2126(99)80026-4
11. Hammes, F., "Ureolytic microbial calcium carbonate precipitation ureolytische microbiele calciumcarbonaat", Ph.D. diss, Ghent University, (2003), http://hdl.handle.net/1854/LU-539712.
12. Jain, S. and Arnepalli, D. N. " Biochemically induced carbonate precipitation in aerobic and anaerobic environments by Sporosarcina pasteurii", ***Geomicrobiology Journal***, Vol. 36, No. 5, (2019), 443-451. doi: 10.1080/01490451.2019.1569180
13. Karnati, V. R., Munaga, T., Gonavaram, K. K. and Amitava, B., "Study on Strength and Leaching Behavior of Biogeochemical Cemented Sand", ***Geomicrobiology Journal***, Vol. 6, (2020). doi: 10.1080/01490451.2020.1761912
14. Van Paassen, L. A. "Biogrout, ground improvement by microbial induced carbonate precipitation", (2009).
15. Zhao, Y., Xiao, Z., Lv, J., Shen, W. and Xu, R. "A Novel Approach to Enhance the Urease Activity of Sporosarcina pasteurii and its Application on Microbial-Induced Calcium

Carbonate Precipitation for Sand", ***Geomicrobiology Journal***, Vol. 36, No. 9, (2019), 819-825. doi: 10.1080/01490451.2019.1631911

16. Mwandira, W., Nakashima, K. and Kawasaki, S. "Bioremediation of lead-contaminated mine waste by Pararhodobacter sp. based on the microbially induced calcium carbonate precipitation technique and its effects on strength of coarse and fine grained sand", ***Ecological Engineering***, Vol. 109, (2017), 57-64. doi: 10.1016/j.ecoleng.2017.09.011
17. DeJong, J. T., Fritzges, M. B. and Nüsslein, K. "Microbially Induced Cementation to Control Sand Response to Undrained Shear" ***Journal of Geotechnical and Geoenvironmental Engineering***, Vol. 132, (2006), 1381-1392. doi: 10.1061/(ASCE)1090-0241(2006)132:11(1381)
18. Chou, C. W., Seagren, E. A., Aydilek, A. H. and Lai, M. "Biocalcification of Sand through Ureolysis", ***Journal of Geotechnical and Geoenvironmental Engineering***, Vol. 137, (2011), 1179-1189. doi: 10.1061/(ASCE)GT.1943-5606.0000532
19. Martinez, B. C., Barkouki, T. H., DeJong, J.D. and Ginn, T. R., "Upscaling Microbial Induced Calcite Precipitation in 0.5m Columns: Experimental and Modeling Results", ***Geo-Frontiers: Advances in Geotechnical Engineering***, (2011), 4049-4059. doi: 10.1061/41165(397)414
20. Al Qabany, A., Soga, K. and Santamarina, C., "Factors affecting efficiency of microbially induced calcite precipitation", ***Journal of Geotechnical and Geoenvironmental Engineering***, Vol. 138, (2012), 992-1001. doi: 10.1061/(ASCE)GT.1943-5606.0000666
21. Tirkolaei, H. K. and Bilsel, H., "Statistical modeling of environmental factors on microbial urea hydrolysis process for biocement production", ***Advances in Materials Science and Engineering***, (2015), doi: 10.1155/2015/340930
22. Kim, G. and Youn, H. "Microbially induced calcite precipitation employing environmental isolates", ***Materials***, Vol. 9, No. 6, (2016). doi: 10.3390/ma9060468
23. Li, H., Li, C., Zhou, T., Liu, S. and Li, L. "An Improved Rotating Soak Method for MICP-Treated Fine Sand in Specimen Preparation", ***Geotechnical Testing Journal***, Vol. 41, No. 4, (2018), 805-814. doi: 10.1520/GTJ20170109
24. Jalili, M., Ghasemi, M. R. , Pifloush, A. R., "Stiffness and strength of granular soils improved by biological treatment bacteria microbial cements", ***Emerging Science Journal***, Vol. 2, No. 4, (2018), 219-227. doi: 10.28991/esj-2018-01146
25. Kahani, M., Kalantary, F., Soudi, M. R., Pakdel, L. and Aghaalizadeh, S., "Optimization of cost effective culture medium for Sporosarcina pasteurii as biocementing agent using response surface methodology: Up cycling dairy waste and seawater", ***Journal of Cleaner Production***, Vol. 253, (2020). doi: 10.1016/j.jclepro.2020.120022
26. Mortensen, B. M., Haber, M. J., DeJong, J. T., Caslake, L. F. and Nelson, D. C., "Effects of environmental factors on microbial induced calcium carbonate precipitation", ***Journal of Applied Microbiology***, Vol. 111, No. 2, (2011). 338-349. doi: 10.1111/j.1365-2672.2011.05065.x
27. Wiley, W. R., Stokes, J. L., "Requirement of an alkaline pH and ammonia for substrate oxidation by Bacillus pasteurii", ***Journal of Bacteriology***, Vol. 84, No. 4, (1962), 730-734. doi: 10.1128/jb.84.4.730-734.1962
28. Zhao, Q., Li, L., Li, Ch., Li, M., Amini, F., Zhang, H., "Factors Affecting Improvement of Engineering Properties of MICP-Treated Soil Catalyzed by Bacteria and Urease", ***Journal of Materials in Civil Engineering***, Vol. 26, No. 12, (2014). doi: 10.1061/(ASCE)MT.1943-5533.0001013.
29. Naveed, M., Duan, J., Uddin, S., Suleman, M., Hui, Y. and Li, H., "Application of microbially induced calcium carbonate precipitation with urea hydrolysis to improve the mechanical properties of soil", ***Ecological Engineering***, Vol. 153, (2020), doi: 10.1016/j.ecoleng.2020.105885
30. Soon, N. W., Lee, L. M., Khun, T. C. and Ling, H. S., "Factors affecting improvement in engineering properties of residual soil through microbial-induced calcite precipitation", ***Journal of Geotechnical and Geoenvironmental Engineering***, Vol. 140, No. 5, (2014). doi: 10.1061/(ASCE)MT.1943-5533.0001013.
31. Claus, D., "A standardized Gram staining procedure", ***World Journal of Microbiology and Biotechnology***, Vol. 8, No. 4, (1992), 451-452. https://doi.org/10.1007/BF01198764
32. Choobbasti, A. J., Kutanaei, S. S. and Afrakoti, M. T. P., "Modeling of compressive strenght of cemented sandy soil", ***Journal of Adhesion Science and Technology***, Vol. 33, No. 8, (2019), 791-807. doi: 10.1080/01694243.2018.1548535
33. ASTM E766-14, "Standard Practice for Calibrating the Magnification of a Scanning Electron Microscope", (2019). doi: 10.1520/E0766-14R19
34. ASTM E986-04, Standard Practice for Scanning Electron Microscope Beam Size Characterization, (2017). doi: 10.1520/E0986-04R17
35. Azmi, N.W., "Effect of Fine Content on Compaction Characteristics of Sand", (Doctoral dissertation, Universiti Malaysia Sarawak). (2005).

Persian Abstract

چکیده

یکی از مسائل مهم در مهندسی ژئوتکنیک که اخیرا مطالعات زیادی در رابطه با آن انجام شده است، بهسازی بیولوژیکی خاک می‌باشد. در این روش باکتریهای اوره آز مثبت به همراه مواد مغذی نظیر اوره و کلسیم کلراید به خاک اضافه میشوند و باعث رسوب کربنات کلسیم و ایجاد چسبندگی بین ذرات خاک و در نتیجه بهبود خواص فیزیکی و مکانیکی خاک میشود. با توجه به اینکه اکثر مطالعات انجام شده بر روی خاک های ماسه ای می باشد و تحقیقات اندکی بر روی خاک های ماسه ای لای دار انجام شده است، در این مطالعه از نوعی باسیل به نام اسپورسارسینا پاستیوری که به صورت هوازی کشت داده می شود برای تثبیت خاک ماسه ای لای دار با درصدهای مختلف لای (۰ تا ٦٠) استفاده شده است تا حجم بهینه سوسپانسیون لازم برای بهسازی خاک برای درصدهای مختلف لای تعیین شود. برای این منظور، ابتدا آزمایشهای بیولوژیکی برای بررسی، صحت سنجی و اطمینان از سلامت باکتری انجام شد که این آزمایشها شامل آزمون تعیین جمعیت باکتری، آزمایش سری رقت، رنگ آمیزی باکتری، آزمایش pH، کشت باکتری بدون افزودن اوره و آزمون اوره آز می باشد. پس از انجام آزمایش های بیولوژیکی و کشت باکتری، آزمایش های فیزیکی و اندکس نظیر دانه بندی، تعیین حدود اتربرگ و تراکم به روش پروکتور بر روی خاک مورد استفاده انجام شد. همچنین، برای دستیابی به مناسب ترین روش نمونه سازی برای تثبیت خاک با درصد های مختلف لای با حضور سوسپانسیون باکتری و مواد مغذی، روش های مختلف نمونه سازی مورد آزمون قرار گرفت و روش مناسب انتخاب گردید. علاوه بر آن، جهت بررسی عملکرد قابل مشاهده باکتری در داخل خاک و به تصویر کشیدن شبکه منسجم حاصل از کربنات کلسیم، تصویر برداری از نمونه های تثبیت شده و تثبیت نشده خاک با استفاده از میکروسکوپ الکترونی انجام شد. نتایج حاصل از آزمایش های سه محوری نشان می دهد که با افزودن حجم بهینه سوسپانسیون باکتری و انجام آزمایش های سه محوری، حداکثر مقاومت برای نمونه های حاوی ۰، ۱۰، ۲۰، ۳۰ و ٤٠ درصد لای به ترتیب از ۷۰۰ به ۱۱۰۰، ۹۰۰ به ۱٤۰۰، ۷۵۰ به ۱۵۵۰، ٦۰۰ به ۱٦۰۰ و ۵۵۰ تا ۱۵۰۰ کیلو پاسکال افزایش یافته است. این موضوع بیانگر افزایش ۸۰ درصدی مقاومت خاک تثبیت شده با استفاده از باکتری نسبت به نمونه های تثبیت نشده می باشد.

International Journal of Engineering

Journal Homepage: www.ije.ir

A 65 nm CMOS Feedforward Transimpedance Amplifier for Optical Fibers Communications

M. S. H. Alsheikhjader, G. S. Aziz, A. I. Mustafa*, L. M. Al Taan

Department of Physics, College of Science, University of Mosul, Mosul, Iraq

PAPER INFO

Paper history:
Received 19 August 2021
Received in revised form 28 May 2022
Accepted 30 May 2022

Keywords:
Transimpedance Amplifier
Wideband Amplifier
Optical Fiber Circuit
Front-end Preamplifier

ABSTRACT

A series of inductor loads may not be the best design criterion for improvement in circuit performance. In this work, the best compromise so far for the trade-off in power consumption, input referred noise current spectral density, with wide bandwidth, high transimpedance gain and low DC supply voltage is reported. A simulated 65 nm CMOS feedforward transimpedance amplifier is introduced with a series of single PMOS loads instead of a series of inductor loads. A bandwidth of 20.16 GHz with a transimpedance gain of 51.16 dBΩ, an input referred noise current spectral density of 34.3 p A/√Hz, a power consumption of 1.052 mW and with a 1V DC supply voltage are presented. In addition, an active inductor load (instead of inductor load) is introduced within the 65 nm CMOS feedforward transimpedance amplifier. A bandwidth of 3.75 GHz with a transimpedance gain of 42.7 dBΩ, an input referred noise current spectral density of 21.4 p A/√Hz, a power consumption of 0.66 mW and with a 1V DC supply voltage are reported. This 65 nm CMOS feedforward design process provides enough voltage headrom for gate-to-source terminals in amplifying transistors due to less DC voltage drop across PMOS loads. As a result, this design process consumes the lowest possible power consumption especially with the single PMOS loads as well as with the active inductor load.

***doi**: 10.5829/ije.2022.35.10a.03*

1. INTRODUCTION

Demands have risen for Giga bit per second fiber optic receivers due to ever growing data transmission in various communication systems. Front-end optical preamplifiers in the form of transimpedance amplifers (TIA) have become a viable optical receiver option as a first stage integrated within a comprehensive optical communication system. The search for low-power transimpedance amplifiers with wide bandwidth lead to the common form of regulated cascode (RGC) used in optical receiver topologies [1-6]. However, modification of the RGC structure in terms of input impedance has been the subject for research to achieve wider bandwidths. Structures such as T-matching network [1], series inductor peaking [2], a capacitive degeneration technique [4], a common-gate feedforward TIA [7], a dual-mode feedforward TIA [8] and a feedforward current amplifier TIA [9] were considered. In terms of 65 nm CMOS process technology, various topologies were reported such as an modified RGC TIA using peaking inductors [10], an RGC block and a differential amplifier with active feedback TIA [11] and adjustable gain peaking TIA [12]. In terms of modulated-wavelength division radio signals over an optical fiber, hybrid optical sources were used for better performance of a fiber communication network [13]. Advanced technologies work in conjunction with fiber networks include Internet of Things (IOT) based 5G networks in which an algorithm based on physical key layer generation (PLKG) and Physical Layer Encryption were used as measures for protection [14]. Wideband inductive elements were utilized in order to design I/O impedance matching circuits given the capacitive nature of I/O impedances of millimeter wave amplifiers [15]. Millimeter wave low noise amplifiers were utilized in 65 nm common-gate inductive feedback by adopting a gate inductor within a cascode stage [16].

*Corresponding Author Institutional Email: abdullahidrees@uomosul.edu.iq (A. I. Mustafa)

Please cite this article as: M. S. H. Alsheikhjader, G. S. Aziz, A. I. Mustafa, L. M. Al Taan, A 65 nm CMOS Feedforward Transimpedance Amplifier for Optical Fibers Communications, ***International Journal of Engineering, Transactions A: Basics***, Vol. 35 No. 10, (2022), 1830-1840

1. 1. Common-Gate Feedforward Transimpedance Amplifier In Figure 1a, transistor M_2 operates as a common gate stage and also being in a feedback loop, it works as a source follower. Resistor R_2 is equivalent to the overall TIA gain at low frequencies. If the loop at M_2 gate is broken, provided that body effect and channel length modulation are neglected, the input resistance is represented by Razavi [17]:

$$R_{in} = \frac{1}{g_{m2}}\left(\frac{1}{1+g_{m1}R_1}\right) \quad (1)$$

Due to the feedback loop, the input resistance is lowered, hence, the bandwidth is extended. The circuit in Figure 1a can be redrawn as in Figure 1b which is basically a feedforward amplifier that drives the gate of transistor M_2 which is in a common source formation. Theoretically, an ideal current source I_B leads to make resistor R_2 as the only major noise contributor since there is no noise current that emerges from the drain of transistor M_2. In practice, the input referred current noise is as follows [17]:

$$\overline{I_{in}^2} = \frac{4kT}{R_2} + \overline{I_{n,B}^2} \quad (2)$$

Equation (2) is similar to the input referred noise current for the common gate stage which proves that the feedforward case does not contribute to the noise rise while it lowers input resistance.

One drawback arises from Figure 1a in which the bias voltage at node X approaches $V_{gs1} + V_{gs2}$ which imposes a voltage drop limitation across resistor R_1 and hence lowering gain $g_{m1}R_1$. However, an alternative is available which is in the addition of level shifter to the circuit in Figure 1(b) with an inclusion of a common gate as in Figure 2. The amount of voltage at node X can now be available to overcome V_{gs2} (only) and hence enables the current path for I_B. The input resistance can be summarized as follows [17]:

$$R_{in} = \frac{1}{g_{m3}+(1+g_{m3}R_3g_{m1}R_1)g_{m2}} \quad (3)$$

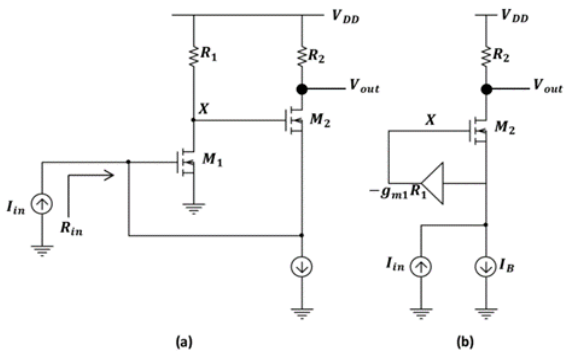

Figure 1. (a) TIA in feedback form, (b) Amplifier inserted in feedforward path [17]

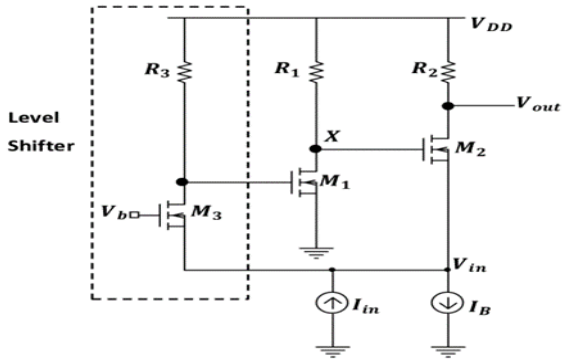

Figure 2. Feedforward path in TIA [12]

It is obvious from Equation (3) that the input resistance is lowered (by a factor of $1 + g_{m3}R_3g_{m1}R_1$).

The output resistance of the circuit in Figure 2 is stated below [17].

$$R_o = \frac{g_{m2}R_2(1+g_{m3}R_3g_{m1}R_1)}{g_{m3}+(1+g_{m3}R_3g_{m1}R_1)g_{m2}} \quad (4)$$

The output resistance R_o is nearly equal to R_2 given that $(1 + g_{m3}R_3g_{m1}R_1)g_{m2} \gg g_{m3}$. It shows that this circuit does have a transimpedance gain of a common gate stage, however, with a significant reduction of the input resistance.

1. 2. Main Contribution of this Work The main contribution of this work is to provide tangible evidence that Single PMOS Loads (SPL) TIA is a better alternative than inductor loads TIA in terms of circuit performance. In addition, to illustrate that an Active Inductor Load (AIL) TIA can have a much lower power consumption and input referred noise current in comparison with inductor loads TIA. The SPL TIA and the AIL TIA are aimed for 20 Gb/s and 3.5 Gb/s applications, respectively.

2. PROPOSED TIA TOPOLOGIES

2. 1. SPL TIA The proposed 65 nm CMOS Common-Gate feedforward SPL TIA configuration is shown in Figure 3 which is a development of a previous work [9]. In this work, no inductor based current sources were used and instead, low aspect ratio (W/L) PMOS transistors (M_5, M_6 and M_7) were connected. Down to 65 nm imposes short channel effects in which MOSFETs drain current roughly becomes [18]:

$$I_D = \frac{1}{2}\left(\frac{\mu_0 C_{ox}}{1+\theta(V_{gs}-V_{th})}\right)\frac{W}{L}\left(V_{gs}-V_{th}\right)^2 \quad (5)$$

where θ is the fitting parameter that is roughly equals to $(10^{-7}/t_{ox})$ V^{-1}. A 65 nm Predictive Technology Model (PTM) is utilized throughout LTspice XVII simulation

run of the envisaged TIA design. The presence of NMOS transistor M_2 (DC level shifting of NMOS transistor M_3) makes it easier to accommodate V_{gs3} and therefore enabling wider headroom for faster sinking of M_3 drain current. Serving as an amplifier in a local feedback form, NMOS transistor M_1 showed a finite voltage amplification from node Y to node O. The (W/L) aspect ratio for the PMOS and NMOS transistors used in this work is as follows:

The aspect ratios shown in Table 1 proved to be optimal for 1V DC supply voltage that contributed to the lowest noise and power consumption reported in this work for 65 nm CMOS process. However, these ratios can be applied for other processes, though, noise and power consumption can be a challenge. Compatibility with 65 nm CMOS process required 100 fF photodiode capacitance (C_{PD}) in which the total input capacitance is $C_{in,tot} = C_{PD} + C_{db4} + C_{sb1} + C_{sb2}$, while the load capacitance C_L was in the order of 200 fF. The node Y (the drain of transistor M_3) can now easily accommodate the gate-to-source voltage of transistor M_1 given the fact that DC voltage-level raising capability of transistor M_2 has the input source of transistor M_1 from the gate of transistor M_3. From another standpoint, low voltage drop on PMOS loads serves the same purpose.

The design process in Figure 3 overcomes many problems associated with classic regulated cascode (RGC) which has no M2 transistor presence. RGC drawbacks include the need to have two gate-to-source voltages at node Y and that may exceed the 1V budget supply. In addition, in RGC topology, there has to be enough voltage room at the output node for drain-to-source saturation with an additional gate-to-source voltage. The presence of M2 transistor in feedforward design enables biasing of transistors M1 and M3 at half of the budget DC voltage value. This design concept along with the discussion stated in section 4.1 relating to the advantages of SPL versus classic inductor loads clarify the reasons behind the selection of the design shown in Figure 3.

An exclusive small signal model for the proposed TIA design is envisaged in Figure 4. Values such as g_{mbx} were included implicitly, however, it is important to point out that values such as r_{dsx} , C_{dx} , C_{gx} were not possible to ignore. The effect of Miller parasitic capacitances involving C_{gd1} and C_{gd3} was minimal. Enough headroom was provided for the gate-source voltages for transistor M_1 and M_3 which enabled better transconductance parameters for these amplifying transistors as follows in

TABLE 1. W/L aspect ratio for NMOS and PMOS transistors used in this work

Ref. M_x	M_1	M_2	M_3	M_4	M_5	M_6	M_7
W/L	125	125	50	187.5	40	40	36.9

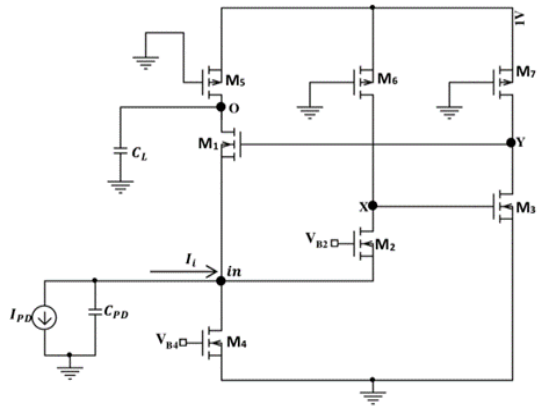

Figure 3. Proposed SPL TIA topology

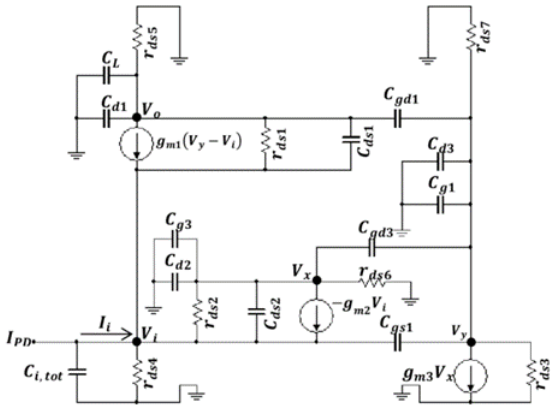

Figure 4. Small signal model of the proposed SPL TIA topology

Table 2. In this table, transconductance parameters for other transistors are also included.

2. 1. 1. Transimpedance Gain Formula

Following on the small signal model of Figure 4, the TIA gain formula can be established. To start with, the voltage gain from the input node to node X. Equations (6)-(8) are with symbolic transconductances parameters g_{mx}, body transconductance g_{mbx} drain-to-source conductances g_{dsx} and drain capacitance C_{dx} of transistor Mx and C_{gx} gate capacitance of transistor Mx (referenced to body ground) shown in Figure 3 is as follows:

$$A_2 = \frac{V_x}{V_i} \approx \frac{g_{m2}+g_{mb2}+g_{ds2}}{g_{ds6}+g_{ds2}+s(C_{d2}+C_{g3})} \quad (6)$$

TABLE 2. Transconductance parameters for transistors M_1 – M_7

Transistor No.	M_1	M_2	M_3	M_4	M_5	M_6	M_7
g_m/mS	5.49	5.80	2.70	9.28	3.20	3.54	1.58

Voltage gain from node X to node Y is represented as:

$$A_3 = \frac{V_y}{V_x} \approx -\frac{g_{m3}}{g_{ds7}+g_{ds3}+s(C_{d3}+C_{g1})} \quad (7)$$

The overall voltage gain of the proposed circuit is:

$$A = \frac{V_o}{V_i} = A_1\left[1 + |A_2A_3| + \frac{1}{g_{m1}}[g_{mb1} + g_{ds1}]\right] \quad (8)$$

In which the voltage gain of transistor M_1 is expressed as:

$$A_1 = \frac{g_{m1}}{g_{ds5}+g_{ds1}+s(C_{d1}+C_L)} \quad (9)$$

It is important to notice that from Equations (6-9), many terms were not possible to neglect. The voltage gain is increased by a factor of $((1 + |A_2A_3|) + (1/g_{m1})(g_{mb1} + g_{ds1}))$ compared to previous literature which was only by a factor of $(1 + |A_2A_3|)$ [9]. Similarly, a much more reduced input impedance is formulized in Equation (10):

$$Z_i = \frac{1}{\beta+sC_{eq}} \quad (10)$$

In which an exclusive formula of β which is the circuit input admittance is obtained as follows,

$$\beta = g_{m1}(1 + |A_2A_3|) + g_{ds2}(1 - A_2) + g_{ds1}(1 - A) + g_{mb1} + g_{m2} + g_{mb2} + g_{ds4} \quad (11)$$

As the equivalent capacitance C_{eq} is influenced by the total input capacitance $C_{i,tot}$ and the unitless magnitude of $|A_2A_3|$ multiplied by gate-to-source capacitance C_{gs1} of transistor M1 as:

$$C_{eq} = [C_{i,tot} + |A_2A_3|C_{gs1}] \quad (12)$$

The DC input resistance is therefore,

$$R_{in_{DC}} = \frac{1}{\beta} \quad (13)$$

Taking into account that the f_{-3dB} TIA bandwidth becomes:

$$f_{-3dB} = \frac{\beta}{2\pi C_{eq}} \quad (14)$$

Leading to the following exclusive TIA gain formula:

$$Z_{TIA} = \frac{A}{\beta+sC_{eq}} \quad (15)$$

A much reduced input impedance with high voltage gain contributing to high TIA gain as in Equation (15).

2. 2. AIL TIA In Figure 5, an active inductor load is presented within the TIA which consists of two PMOS transistors (M_5 and M_8) that have similar aspect ratios (W/L). As for the small signal model, it is similar to that of Figure 4 except for the replacement of r_{ds5} by the active inductor load impedance Z_{AIL} which is expressed as follows [19]:

$$Z_{AIL} = \frac{r_{o8}C_{gs5}s+1}{g_{m5}+C_{gs5}s} \quad (16)$$

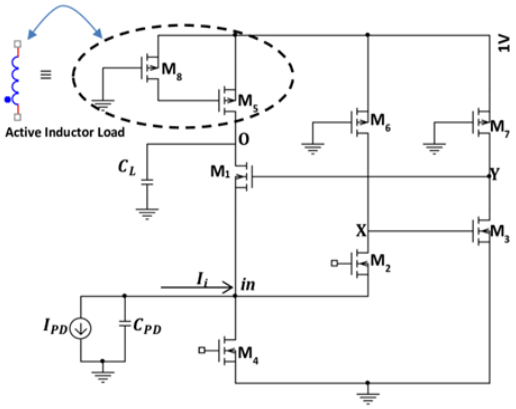

Figure 5. Proposed AIL TIA topology

The AIL admittance Y_{AIL} constitutes a part of the M_1 transistor voltage gain and given the fact that this admittance is of an extremely low value at high frequencies, it is valid to assume that the voltage gain of transistor M_1 has become more dominant within the overall voltage gain A, in contrast with the SPL TIA that had an expression for A_1 given in Equation (9). In the case of the AIL TIA, it is represented as:

$$A_1 = \frac{g_{m1}}{Y_{AIL}+g_{ds1}+s(C_{d1}+C_L)} \quad (17)$$

In fact, high frequency cases lead to situation where $g_{ds1} \gg Y_{AIL}$ as:

$$A_1 \approx \frac{g_{m1}}{g_{ds1}+s(C_{d1}+C_L)} \quad (18)$$

It is therefore important to point out that Equations (8-11) and (13-15) (from previous section) are implicitly influenced by Equation (18). According to extracted data from simulation, compared with SPL TIA, a lower g_{m1} is obtained for the AIL TIA with higher g_{ds1}. This reduction in A_1 leads to lower voltage gain A, eventually lowering TIA gain and bandwidth according to Equations (11), (14) and (15). However, a reduction in the input referred noise current and power consumption do occur. The much reduced drain current I_{D1} in the AIL TIA compared with the SPL TIA is due to having the AIL to be near an open circuit situation at high frequencies (i.e. near ideal current source).

Following on Equation (16) with regard to the active inductor impedance, and in an ideal situation, a pole zero is created to resonate with the output capacitance for the purpose of bandwidth extension. However, in the AIL TIA, the focus is on an input referred noise lowering mechanism through lowering the AIL admittance.

3. NOISE ANALYSIS

3. 1. Noise Analysis of SPL TIA The common formula for the mean square channel thermal noise

voltage (spectral density) at the drain of transistor M_1 is as follows [9]:

$$\overline{V_{no,d1}^2} = 4kT\alpha g_{m1}(Z_{TIA} - Z_o)^2 \quad (19)$$

Where $\alpha = \gamma(g_{d0}/g_m)$, as γ is the channel thermal noise coefficient, g_{d0} is the zero bias drain conductance. A unique formula for the output impedance in this work is as:

$$Z_o = \frac{1}{(g_{ds5}+g_{ds1})+s(C_{d1}+C_L+C_{ds1})} \quad (20)$$

The drain of transistor M_2 mean square channel thermal noise voltage is:

$$\overline{V_{no,d2}^2} = 4kT\alpha g_{m2}\left(Z_{TIA} - Z_x\frac{V_o}{V_x}\right)^2 \quad (21)$$

where the impedance at node X is worked out as:

$$Z_x = \frac{1}{(g_{ds2}+g_{ds6})+s(C_{d2}+C_{g3}+C_{ds2}+C_{gd3})} \quad (22)$$

And the voltage gain from node X to output node O is derived as:

$$\frac{V_o}{V_x} = \frac{A[(g_{ds6}+g_{ds2})+s(C_{d2}+C_{g3})]}{g_{m2}+g_{mb2}+g_{ds2}} \quad (23)$$

The drain of transistor M_3 mean square channel thermal noise voltage is:

$$\overline{V_{no,d3}^2} = 4kT\alpha g_{m3}\left(Z_{TIA} - Z_y\frac{V_o}{V_y}\right)^2 \quad (24)$$

where the impedance at node Y is worked out as:

$$Z_y = \frac{1}{(g_{ds3}+g_{ds7})+s(C_{gs1}+C_{gd3}+C_{g1}+C_{d3}+C_{gd1})} \quad (25)$$

while the voltage gain from node Y to output node O is:

$$\frac{V_o}{V_y} = \frac{Ag_{m1}}{(g_{m1}+g_{mb1}+g_{ds1}-A(g_{ds5}+g_{ds1}))-sA(C_{d1}+C_L)} \quad (26)$$

A modification to previous literature [9] is worked out based on short channel effects literature [15] regarding mean square induced gate noise voltage (spectral density) for transistor M_1 as follows:

$$\overline{V_{no,g1}^2} = 4kT\delta\frac{(\omega C_{gs1})^2}{5g_{d01}}\left(Z_{TIA} - Z_y\frac{V_o}{V_y}\right)^2 \quad (27)$$

In which the shunt conductance g_g is equal to $(\omega C_{gs1})^2/5g_{d01}$which was previously thought to be $(\omega C_O)^2/g_{d01}$, where C_O was given as the gate-oxide capacitance, while g_{d0} is the drain conductance at zero bias [9], given that γ is the channel thermal noise coefficient, while δ is the gate noise coefficient. Similarly, the mean square induced gate noise voltage for transistor M_2 and M_3 is:

$$\overline{V_{no,g2}^2} = 4kT\delta\frac{(\omega C_{gs2})^2}{5g_{d02}}(Z_{TIA})^2 \quad (28)$$

$$\overline{V_{no,g3}^2} = 4kT\delta\frac{(\omega C_{gs3})^2}{5g_{d03}}\left(Z_x\frac{V_o}{V_x}\right)^2 \quad (29)$$

The overall gate and drain noise contribution is defined in common form as [9]:

$$\overline{V_{no,Mx}^2} = \overline{V_{no,dx}^2} + \overline{V_{no,gx}^2} + 2|c|\sqrt{\overline{V_{no,dx}^2}\cdot\overline{V_{no,gx}^2}} \quad (30)$$

where c is the cross correlation coefficient (drain-to-gate noise). The noise voltage contribution of transistor M_4 is defined in this work as:

$$\overline{V_{no,M4}^2} = 4kT(Z_{TIA})^2 g_{ds4} \quad (31)$$

While noise voltage contribution of current sources M_5, M_6 and M_7 is defined in this work as:

$$\overline{V_{no,r}^2} = 4kT\left(Z_o^2 g_{ds5} + Z_x^2 g_{ds6}\left(\frac{V_o}{V_x}\right)^2 + Z_y^2 g_{ds7}\left(\frac{V_o}{V_y}\right)^2\right) \quad (32)$$

And the total integrated mean square noise voltage spectral density contribution is:

$$\overline{V_{no}^2} = \overline{V_{no,M1}^2} + \overline{V_{no,M2}^2} + \overline{V_{no,M3}^2} + \overline{V_{no,M4}^2} + \overline{V_{no,r}^2} \quad (33)$$

And the input referred noise current is given in the following common formula:

$$\overline{I_{in}^2} = \frac{\overline{V_{no}^2}}{(Z_{TIA})^2} \quad (34)$$

3. 2. Noise Analysis of AIL TIA The output impedance representation for the AIL TIA is manifested as:

$$Z_o = \frac{1}{(Y_{AIL}+g_{ds1})+s(C_{d1}+C_L+C_{ds1})} \quad (35)$$

The output impedance is characterized through which $g_{ds1} \gg Y_{AIL}$ and so as the voltage gain from node Y to output node O is:

$$\frac{V_o}{V_y} = \frac{Ag_{m1}}{(g_{m1}+g_{mb1}+g_{ds1}-A(Y_{AIL}+g_{ds1}))-sA(C_{d1}+C_L)} \quad (36)$$

Then having an exclusive formula as:

$$\frac{V_o}{V_y} = \frac{Ag_{m1}}{(g_{m1}+g_{mb1}+g_{ds1}(1-A))-sA(C_{d1}+C_L)} \quad (37)$$

While noise voltage contribution of current sources M_6 and M_7 and the active inductor load noise voltage contribution is defined uniquely in this work as:

$$\overline{V_{no,r}^2} = 4kT\left(Z_o^2 Y_{AIL} + Z_x^2 g_{ds6}\left(\frac{V_o}{V_x}\right)^2 + Z_y^2 g_{ds7}\left(\frac{V_o}{V_y}\right)^2\right) \quad (38)$$

It is noticed that the term $Z_o^2 Y_{AIL}$can be neglected given what was stated before regarding an extremely low active inductor admittance and this concept explains a significant reduction in the overall input referred noise

compared to the SPL TIA. Bearing in mind that the TIA gain has changed in nature compared with the SPL TIA, however, the rest of formulas remained unchanged. In Equation (36), the term $A(Y_{AIL}+g_{ds1})$ is also reduced, leading to reduction in the voltage gain from node Y to output node O (i.e V_o/V_y) , hence lowering the magnitude of the term $Z_y^2 g_{ds7}(V_o/V_y)^2$ in Equations (37-38).

4. COMBINED TIAs RESULTS AND DISCUSSION

In simulation, the SPL TIA has a transimpedance gain of 51.16 dBΩ at f_{-3dB} bandwidth of 20.16 GHz as in Figure 6. The point of f_{-3dB} bandwidth is in total agreement with Equation (14). From Equation (15), transimpedance gain is proportional to voltage gain through which signal gain A_1 is extended by a factor of $\left(1+|A_2A_3|+\frac{1}{g_{m1}}[g_{mb1}+g_{ds1}]\right)$ according to Equations (8-9) that had an important impact. However, a greater extension of β as in Equation (11) could not affect the total TIA gain, while it serves in input impedance lowering mechanism. A slight capacitive peaking appears around 10 GHz, while in comparative work literature [9], it shows clear capacitive peaking well beyond 10 GHz. In an AIL TIA, a transimpedance gain of 42.7 dBΩ is achieved with f_{-3dB} bandwidth of 3.75 GHz. A transimpedance phase shift of 58.4° at the point of f_{-3dB} bandwidth is illustrated in Figure 7 for the SPL TIA, while it was 132.1° for the AIL TIA.

The TIA gain in terms of ohmic resistance is manifested in Figure 8 with 362.3 Ω at the point of f_{-3dB} bandwidth. Very limited ohmic gain peaking appears below 10 GHz which is well below the dominant pole. In the AIL TIA, a 136.5 Ω of TIA gain at the point of bandwidth is obtained.

The DC optimal supply voltage was applied at 1V for the SPL and the AIL TIAs. A range of supply voltages (0.9V-1.1V) were applied in Figure 9 in relation to TIA gain. A much more reduced bandwidth occurred at 0.9V, while the supply voltage of 1.1V happened to slightly extend the bandwidth at the expense of power consumption with slight reduction in SPL TIA gain. In Figure 10, a big TIA gain gap appeared in the AIL TIA between the DC biasing of 1.1V and the rest of DC biasing (0.9V, 1V) in which there was a limited shift if any with regard to the bandwidth. In Figure 11, a temperature sweep from 20°C-60°C was run to examine how the SPL TIA gain is influenced, while the bandwidth is not dramatically shifted. However, from the input

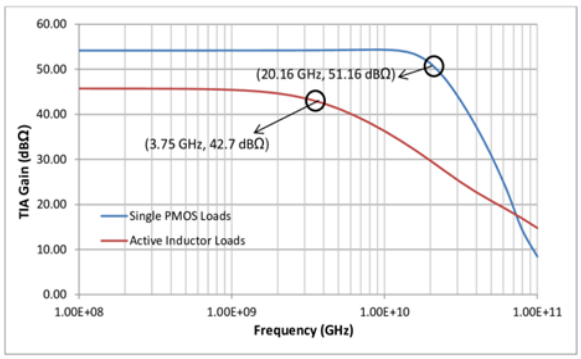

Figure 6. Simulated transimpedance gain in dBΩ unit

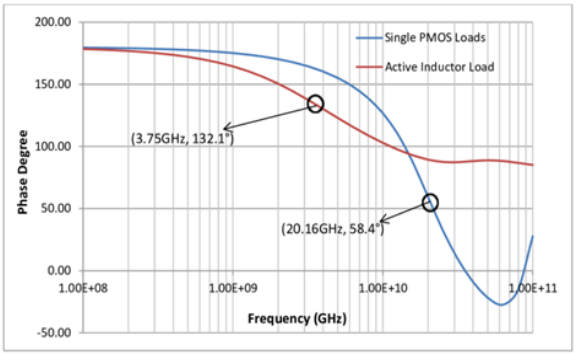

Figure 7. Transimpedance phase shift versus frequency relationship

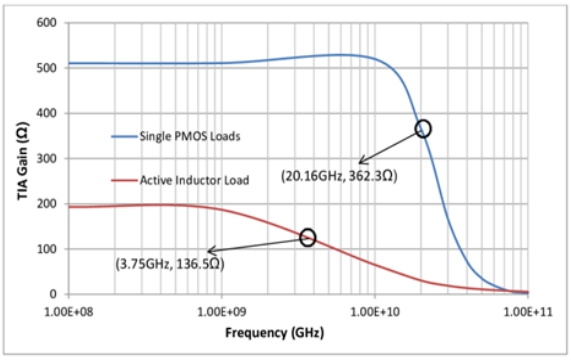

Figure 8. Simulated transimpedance gain in ohmic unit

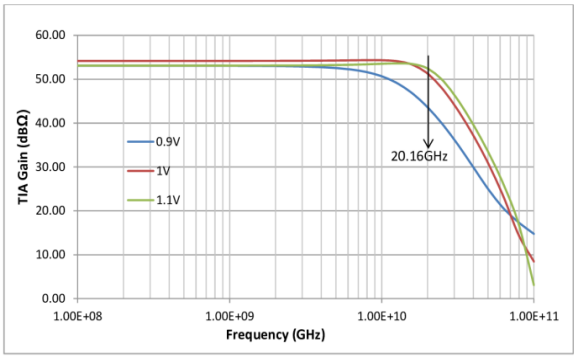

Figure 9. DC supply voltage sweep from 0.9 V–1.1 V with relationship to gain for SPL TIA

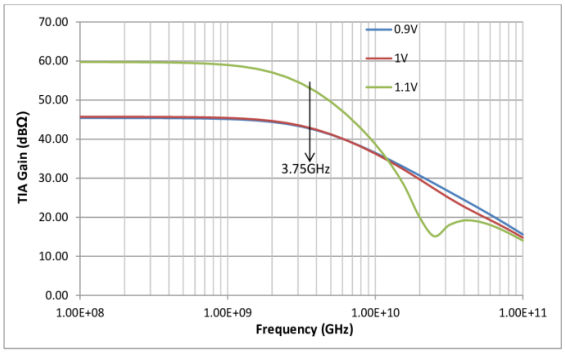

Figure 10. DC supply voltage sweep from 0.9 V–1.1 V with relationship to gain for AIL TIA

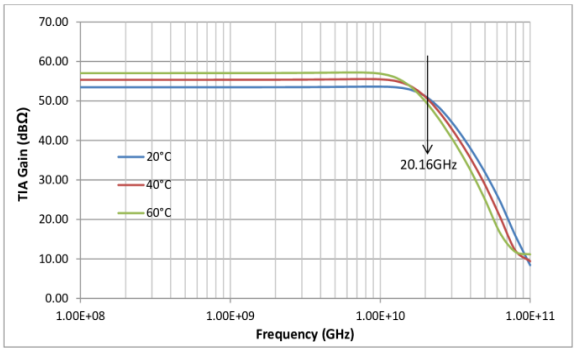

Figure 11. Temperature sweep from 20°C - 60°C in relation to gain for SPL TIA

referred noise current point of view, a rapid increase is expected at higher temperatures. A wider gap in TIA gain appeared in temperature sweep from 20°C-60°C for the AIL TIA as in Figure 12.

The input impedance of the SPL TIA shown in Figure 13 indicates low values in which at the point of f_{-3dB} bandwidth, a simulated value of 43.6 Ω was obtained. Capacitive peaking does appear beyond 10 GHz as it is possible in this case to have the dominant pole below the input impedance pole. The input impedance of the AIL TIA indicated a value of 128.2 Ω at the point of bandwidth.

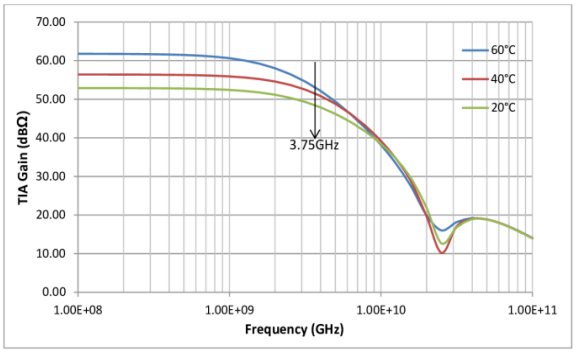

Figure 12. Temperature sweep from 20°C - 60°C in relation to gain for AIL TIA

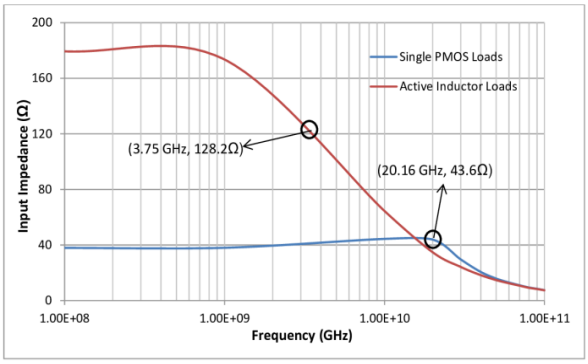

Figure 13. Input impedance of the proposed TIAs circuit based on simulated data

From an extracted data (from simulation) for the DC transfer function, I_{PD} input impedance as well as the output impedance at V_{out} are illustrated in Table 3. The DC transfer function for the AIL TIA is given in Table 4.

In Figure 14, a 20 Gb/s 2^{31}-1 NRZ PRBS eye diagram for the SPL TIA is simulated, in which for an input signal of 100 µA, with nonlinear simulation of 1 µs stop time and maximum time step of 13 ps. The amount of distortion (set by the signal-to-noise ratio) was about 8 mV, while the signal-to-noise ratio at the sampling point was 57 mV. Best time to sample (decision point) was at 43 ps which is the most open part of the eye (best signal-to-noise ratio) and the measure of jitter was 6.7 ps. In Figure 15, a 3.5 Gb/s 2^{31}-1 NRZ PRBS eye diagram for the AIL TIA is simulated. A nonlinear time-domain simulation with 7 µs stop time and a maximum time step of 5 ps was performed. An input signal of 100 µA was applied in which the amount of distortion in the eye diagram was around 1 mV and the signal-to-noise ratio at the sampling point was 18 mV. The decision point was at 283 ps and the measure of jitter was 4 ps.

In Table 5, a simulation extraction of total power consumption of 1.052 mW partitioned as per each transistor in the SPL TIA, while the total power consumption was 0.66 mW in the AIL TIA as in Table 6.

TABLE 3. Extracted data from simulation for the SPL TIA

DC Transfer Function	-510.743
I_{PD} Input Impedance	37.95 Ω
Output impedance at V_{out}	624.20 Ω

TABLE 4. Extracted data from simulation for the AIL TIA

DC Transfer Function	-193.304
I_{PD} Input Impedance	179.514
Output impedance at V_{out}	496.828

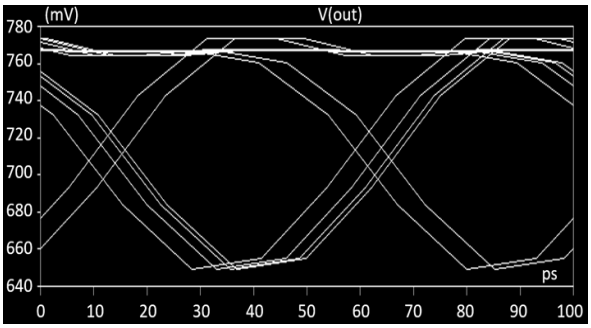

Figure 14. Screen shot of eye diagram for 20 Gbps bit sequencing for the SPL TIA

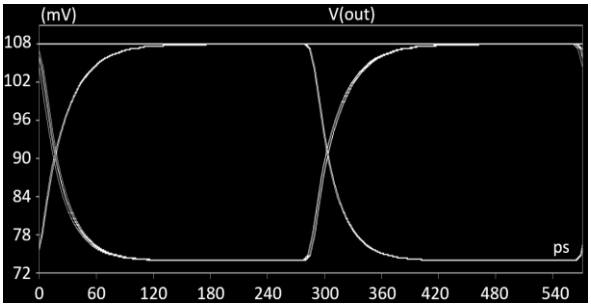

Figure 15. Screen shot of eye diagram for 3.5 Gbps bit sequencing for the AIL TIA

TABLE 5. A simulation extraction of total power consumption of 1.052 mW partitioned as per each transistor for the SPL TIA

Power Consumption mW	Transistor No.
0.259	$\mathbf{M_1}$
0.259	$\mathbf{M_2}$
0.190	$\mathbf{M_3}$
0.101	$\mathbf{M_4}$
0.093	$\mathbf{M_5}$
0.11	$\mathbf{M_6}$
0.028	$\mathbf{M_7}$

TABLE 6. A simulation extraction of total power consumption of 0.66 mW partitioned as per each transistor for the AIL TIA

Power Consumption mW	Transistor No.
9e-6	$\mathbf{M_1}$
0.273	$\mathbf{M_2}$
0.2	$\mathbf{M_3}$
0.045	$\mathbf{M_4}$
0.002	$\mathbf{M_5}$
0.105	$\mathbf{M_6}$
0.033	$\mathbf{M_7}$
1e-4	$\mathbf{M_8}$

The simulated input referred noise current spectral density for the SPL TIA is shown in Figure 16 in which 34.4 $pA/\sqrt{Hz}$ at the f_{-3dB} bandwidth (20.16 GHz) was reported. This result is quite important given the fact that the TIA gain was 51.16 dBΩ with a 362.3 Ω transimpedance in terms of ohmic resistance at 1V DC supply voltage with a power consumption of only 1.052 mW. The reported input referred noise current overcomes the drawbacks associated with the common gate amplifiers in which the thermal noise of the load resistor and the biasing network are basically referred back directly with unity gain [17-18]. As for the AIL TIA, an input referred noise of 21.4 $pA/\sqrt{Hz}$ at the point of bandwidth (3.75 GHz) was obtained.

4. 1. SPL Versus Inductor Loads The PMOS transistors loads M_5, M_6 and M_7 represent an extremely high small-signal resistance (ideally near infinite) having parallel r_{o5}, r_{o6} and r_{o7} resistances respectively in which for instance, the voltage gain of the common source transistor M_3 equals $(-g_{m3}r_{o3})$ as compared to the case where an inductive load Ls is present as in literature [9]. Despite the channel length modulation involved, a stable path for drain currents via transistors loads M_5, M_6 and M_7 is secured in which these drain currents are far less dependent on the voltages at nodes O, X and Y, in contrast with inductor loads voltage transients dependence on di/dt. The voltage gain of the mentioned common source stage represents the highest gain possible for a single transistor. Consequently, the trade-off between voltage gain and signal headroom can be eased when a PMOS load is introduced instead of an inductive load. Ultimately, PMOS transistor loads M_5, M_6 and M_7 will simply behave like a resistor, each resistor is exactly similar to the output resistance of the PMOS transistor given a constant gate-to-source voltage for each transistor. In addition to high voltage gain, the TIA gain with PMOS considerably depends on β, as in Equation (15), unlike the situation of inductor load where it depends mainly on the real part of the inductor load admittance.

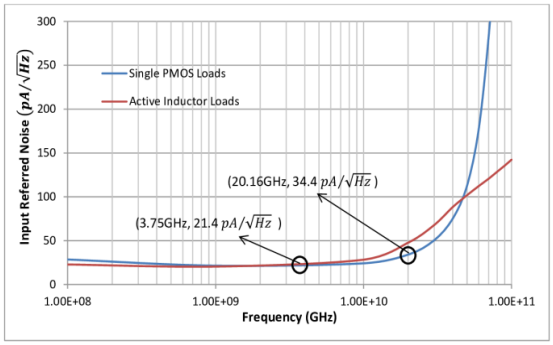

Figure 16. Input referred noise current spectral density based on simulated data

The PMOS current source load can improve SPL TIA performance since it enhances the TIA gain, while it does not suffer from the drawbacks of the inductor load especially when it comes to enabling NMOS transistors M_1, M_2 and M_3 to consume less power in contrast with actual inductor loads stated in previous literature [9]. Less thermal resistivity in NMOS transistors constitute less noise contribution. Conductances g_{ds5}, g_{ds6} and g_{ds7} in Equation (32) are optimized to have low enough values to reduce noise contribution through channel length modulation, while series resistances with inductor loads do not have this capability since the inductor loads are already a source of dissipating energy into the amplifier NMOS transistors in a form of thermal resistivity.

Comparative analysis between SPL TIA and inductor load TIA [9] in the feedforward structure show that the inductor load suffer from unclamped inductive switching which means that there is an absence of what is known as a "freewheeling'' diode for discharging energy especially when the input signal of NMOS transistors M_1 , M_2 and M_3 is in the lower state (from small signal point of view), essentially meaning that all the energy is dissipated into these transistors. Through inductance, current is rapidly turned off, while the magnetic field cannot respond and therefore, does not collapse instantaneously. As a result, an induced electromagnetic force (a counter one) can surprisingly accumulate high potential over the switching NMOS in which this potential is proportional to the speed through which the current is extremely low. Furthermore, inductor load may cause the NMOS transistors M_1, M_2 and M_3 to breakdown at low signal state due to stray capacitance (from drain to gate), while the ability of these NMOS transistors to withstand energy (thermal resistivity) is put into question. Signal switching from high to low state in the inductor load generate high voltage transients in which they can be coupled into the NMOS transistors gates through their stray capacitors C_{gd} causing damage.

4. 2. AIL Versus Inductor Load In Figure 5, parasitic capacitor C_{gs5} acts as an open circuit at low frequencies in which transistor M_5 effectively becomes diode-connected as the active inductor impedance given in Equation (16) becomes $Z_{AIL} = 1/g_{m5}$. At high frequencies however, the gate of M_5 is at ac ground in which $Z_{AIL} \approx r_{o8}$. Since r_{o8} only depends on channel length modulation and drain current, there is no possible current transients as in the case of inductor loads, hence there is no dissipation of energy into transistor M_1 (i.e less noise contribution). Apart from the fact that tuning the active inductor part is much more accurate (than an inductor load) by tuning the equivalent inductance for the purpose of realizing high frequency inductive impedance. In this work, since $r_{o8} \gg 1/g_{m5}$, the equivalent inductance is:

$$L_{eq} = \frac{r_{o8}C_{gs5}}{g_{m5}} \quad (39)$$

The power consumption reduction from 1.052 mW in SPL TIA to 0.66 mW in AIL TIA is due to the high frequency AIL impedance $Z_{AIL} = r_{o8}$ which enables higher voltage drop that approximates near ideal current source. From transistors M_6 and M_7 side view, the active inductor load deprives them from significant level of drain current and drives them into deep triode region. Consequently, it is just about enough voltage headroom for transistors M_2 and M_3 to operate.

4. 3. Comparative TIA Performance Analysis A comparative TIA performance analysis show that in this work, an extremely low power consumption and input referred noise with inductor less design, and wide bandwidth to considerable extent with reasonably good TIA gain using 1V DC supply voltage are illustrated in Table 7 which displays various performance analyses in relation to this work. The power consumption of the proposed TIA design is below half of that reported in

TABLE 7. A comparative performance analysis with other TIA topologies

No. of Inductors	Input Referred Noise $\left(\frac{pA}{\sqrt{Hz}}\right)$	Bandwidth (GHz)	TIA Gain dBΩ	DC Supply Voltage (V)	Power Consumption (mW)	CMOS Technology (nm)	Year	Ref.
2	30	26.1	46.7	1.2	8.2	65	2010	[10]
8	31	70	40	1.2	24	65	2014	[11]
7	2.5 μA_{rms}	40	55	1.6	107	65	2014	[12]
0	20.3	7	40.5	1	1.4	90	2018	[22]
3	**50**	**20**	**52**	**1**	**2.2**	**80**	**2004**	[9]
0	**34.3**	**20.16**	**51.16**	**1**	**1.052**	**65**	**2021**	**This Work SPL TIA**
0	**21.4**	**3.75**	**42.7**	**1**	**0.66**	**65**	**2021**	**This Work AIL TIA**

literature [9] in SPL TIA and is well below that in the AIL TIA. The input-referred noise current spectral density is considerably lower compared to same literature, while maintaining near levels in terms of TIA gain and bandwidth in the SPL TIA for 1V DC supply voltage. In the AIL TIA, despite of lower TIA gain and bandwidth, it registered a considerable reduction of input referred noise current and power consumption. Interestingly, budget DC supply voltage in literature within Table 7 ranged from 1.6V down to 1V (only 0.6V difference) and subsequently power consumption was reduced from 107 mW down to just 0.66 mW despite various design processes involved with moderate change in TIA gain. The rate of change in bandwidth is well below that of power consumption and that is expected. The common feature in various design topologies, device discrete dimensions and processes stated in literatures is that they all face short channel effects challenges as in Equation (5) in which mosfets depart from classic saturation condition square law and enter into $\theta(V_{gs} - V_{th}) \neq 0$. Nevertheless, the input referred noise current spectral density for instance maintained (in this work) its obvious comparable results. Ordinary spiral inductor presence in numbers deepens the trade-off gap especially in terms of gain and power consumption as reported in literature [12].

5. CONCLUSION

The major contribution of this work is that inductor loads may not be the best suitable solution for improving TIA circuit performance, while single PMOS current source loads in feed forward TIA topology proved to be the best compromise for the trade-off in power consumption, input referred noise current spectral density, with wide bandwidth, high transimpedance gain and low DC supply voltage. The AIL TIA have shown to have a challenging very low input referred noise and power consumption (instead of inductor loads), while maintaining relatively moderate TIA gain at a bandwidth suitable for many applications.

6. FUTURE SCOPE

The overcoming of classical inductor load peaking problems offers a new way of introducing active loads and active inductor loads in a manner that has not been possible before. In addition, an introduction of an active inductor which is embedded in a form of negative feedback loop (shunt-shunt feedback) is an interesting way to follow.

7. REFERENCES

1. Seifouri, M., Amiri, P. and Rakide, M., "Design of broadband transimpedance amplifier for optical communication systems", ***Microelectronics Journal***, Vol. 46, No. 8, (2015), 679-684, https://doi.org/10.1016/j.mejo.2015.05.007
2. Lee, J., Park, H.G., Kim, I.S., Pu, Y., Hwang, K.C., Yang, Y., Lee, K.-Y. and Seo, M., "A 6 gb/s low power transimpedance amplifier with inductor peaking and gain control for 4-channel passive optical network in 0.13 μm cmos", ***JSTS: Journal of Semiconductor Technology and Science***, Vol. 15, No. 1, (2015), 122-130, https://doi.org/10.5573/JSTS.2015.15.1.122
3. Taghavi, M.H., Naji, A., Belostotski, L. and Haslett, J.W., "On the use of multi-path inductorless tias for larger transimpedance limit", ***Analog Integrated Circuits and Signal Processing***, Vol. 77, No. 2, (2013), 221-233, https://doi.org/10.1007/s10470-013-0140-9
4. Zhenghao, L., Dandan, C. and Seng, Y.K., "An inductor-less broadband design technique for transimpedance amplifiers", in Proceedings of the 2009 12th international symposium on integrated circuits, IEEE., (2009), 232-235.
5. Atef, M., Aznar, F., Schidl, S., Polzer, A., Gaberl, W. and Zimmermann, H., "8 gbits/s inductorless transimpedance amplifier in 90 nm cmos technology", ***Analog Integrated Circuits and Signal Processing***, Vol. 79, No. 1, (2014), 27-36, https://doi.org/10.1007/s10470-013-0242-4
6. Atef, M. and Zimmermann, H., "Low-power 10 gb/s inductorless inverter based common-drain active feedback transimpedance amplifier in 40 nm cmos", ***Analog Integrated Circuits and Signal Processing***, Vol. 76, No. 3, (2013), 367-376, https://doi.org/10.1007/s10470-013-0117-8
7. Kim, S.H., Cho, S.B. and Park, S.M., "Dual-mode cmos feed-forward transimpedance amplifier for ladars", ***Electronics Letters***, Vol. 50, No. 23, (2014), 1678-1680, https://doi.org/10.1049/el.2014.2678
8. Chen, R.Y. and Yang, Z.-Y., "Cmos transimpedance amplifier for visible light communications", ***IEEE Transactions on Very Large Scale Integration (VLSI) Systems***, Vol. 23, No. 11, (2014), 2738-2742, doi: 10.1109/TVLSI.2014.2365462.
9. Kromer, C., Sialm, G., Morf, T., Schmatz, M.L., Ellinger, F., Erni, D. and Jackel, H., "A low-power 20-ghz 52-db/spl omega/transimpedance amplifier in 80-nm cmos", ***IEEE Journal of Solid-State Circuits***, Vol. 39, No. 6, (2004), 885-894, doi: 10.1109/JSSC.2004.827807.
10. Bashiri, S., Plett, C., Aguirre, J. and Schvan, P., "A 40 gb/s transimpedance amplifier in 65 nm cmos", in Proceedings of 2010 IEEE international symposium on circuits and systems, IEEE., (2010), 757-760.
11. Ahmed, M.N., Chong, J. and Ha, D.S., "A 100 gb/s transimpedance amplifier in 65 nm cmos technology for optical communications", in 2014 IEEE International Symposium on Circuits and Systems (ISCAS), IEEE., (2014), 1885-1888.
12. Ding, R., Xuan, Z., Baehr-Jones, T. and Hochberg, M., "A 40-ghz bandwidth transimpedance amplifier with adjustable gain-peaking in 65-nm cmos", in 2014 IEEE 57th International Midwest Symposium on Circuits and Systems (MWSCAS), IEEE., (2014), 965-968.
13. Alatwi, A.M., Rashed, A.N.Z. and Abd El Aziz, I.A., "High speed modulated wavelength division optical fiber transmission systems performance signature", ***Telkomnika (Telecommunication Computing Electronics and Control)***, Vol. 19, No. 2, (2021), 380-389, doi: 10.12928/TELKOMNIKA.v19i2.16871.

14. Dey, A., Nandi, S. and Sarkar, M., "Security measures in iot based 5g networks", in 2018 3rd International Conference on Inventive Computation Technologies (ICICT), IEEE. (2018), 561-566.
15. Ashrafian, A., Mohammad-Taheri, M., Naser-Moghaddasi, M., Khatir, M. and Ghalamkari, B., "Planar circuit analysis of ultra-wideband millimeter-wave inductor using transmission line sections", ***International Journal of Circuit Theory and Applications***, Vol. 49, No. 10, (2021), 3378-3393, https://doi.org/10.1002/cta.3070
16. Hsieh, H.-H., Wu, P.-Y., Jou, C.-P., Hsueh, F.-L. and Huang, G.-W., "60ghz high-gain low-noise amplifiers with a common-gate inductive feedback in 65nm cmos", in 2011 IEEE Radio Frequency Integrated Circuits Symposium, IEEE. (2011), 1-4.
17. Razavi, B., "Design of integrated circuits for optical communications, John Wiley & Sons, (2012).
18. Razavi, B., *Design of analog cmos integrated circuit tata mcgraw*. 2001, Hill.
19. Zohoori, S. and Dolatshahi, M., "A low-power cmos transimpedance amplifier in 90-nm technology for 5-gbps optical communication applications", ***International Journal of Circuit Theory and Applications***, Vol. 46, No. 12, (2018), 2217-2230, https://doi.org/10.1002/cta.2565

Persian Abstract

چکیده

مجموعه ای از بارهای سلف ممکن است بهترین معیار طراحی برای بهبود عملکرد مدار نباشد. در این کار، بهترین مصالحه تاکنون برای مبادله در مصرف برق، چگالی طیفی جریان نویز ارجاعی ورودی، با پهنای باند وسیع، بهره ترانس‌مپدانس بالا و ولتاژ منبع تغذیه DC پایین گزارش شده است. یک تقویت‌کننده ترانس‌مپدانس پیش‌خور CMOS 65 نانومتری شبیه‌سازی‌شده با یک سری بارهای PMOS منفرد به جای یک سری بارهای سلف معرفی شده است. پهنای باند ۲۰.۱۶ گیگاهرتز با بهره ترانسیمپدانس ۵۱.۱۶ dBΩ، تراکم طیفی جریان نویز ورودی ۳۴.۳ p A/√Hz، مصرف برق ۱.۰۵۲ مگاوات و با ولتاژ منبع تغذیه ۱ ولت DC ارائه شده است. علاوه بر این، یک بار سلف فعال (به‌جای بار سلف) در تقویت‌کننده ترانسیمپدانس پیش‌خور CMOS 65 نانومتری معرفی می‌شود. پهنای باند ۳.۷۵ گیگاهرتز با بهره ترانسیمپدانس ۴۲.۷ dBΩ، تراکم طیفی جریان نویز ورودی ۲۱.۴ p A/√Hz، مصرف برق ۰.۶۶ میلی‌وات و با ولتاژ منبع تغذیه ۱ ولت DC گزارش شده است. این فرآیند طراحی پیشخور CMOS 65 نانومتری به دلیل افت ولتاژ DC کمتر در بارهای PMOS، ولتاژ کافی را برای پایانه های گیت به منبع در ترانزیستورهای تقویت کننده فراهم می کند. در نتیجه، این فرآیند طراحی کمترین مصرف توان ممکن را به خصوص با بارهای تک PMOS و همچنین با بار سلف فعال مصرف می کند.

IJE TRANSACTIONS A: Basics Vol. 35 No. 10, (October 2022) 1841-1857

International Journal of Engineering

Journal Homepage: www.ije.ir

Evaluation and Prediction of Self-healing Assessments for AA2014 Based Hybrid Smart Composite Structures: A Novel Fuzzy Logic Approach

V. Srivastava*[a], M. Gupta[b]

[a] *Department of Mechanical Engineering, Anurag University, Hyderabad, India*
[b] *Department of Mechanical Engineering, Motilal Nehru National Institute of Technology Allahabad, Prayagraj, India*

PAPER INFO

Paper history:
Received 10 February 2022
Received in revised form 16 March 2022
Accepted 23 March 2022

Keywords:
Smart Structures
Fuzzy Logic Model
Regression Model
Taguchi Method
Self-healing Metallic Composites

ABSTRACT

An idea to heal the damaged surface through healing agents in metallic composite are at their developmental stage. Therefore, the selection of design parameters for a new generation smart composite is more complex and difficult. In the present study the two case studies on self healing smart strucures are included with different input design parameters to evaluate the healing properties. Taguchi based L-8 experiments were conducted to analyze the influencial parameters responsible for higher self healing assessments (i.e. recovery in crack width, recovery in crack depth and flexural strength recovery). To evaluate the self-healing assessments of the damaged structure, a soft computing technique based on S/N ratio from ANOVA analysis is obtained. The experimental results were further considered for constructing the fuzzy logic predictive model. Linear regression models i.e. a statistical tool is generated to judge the accuracy of the fuzzy based predicted model through various error analyses. Based on S/N ratio Fuzzy logic model, results show less error values of 6.33 and 4.94 % for case studies I and II, respectively in compared to the regression model adapted for all self-healing assessments. The model offers a close resemblance with the experimental observations even with less number of experimental runs. This concludes that the fuzzy logic model provides a powerful soft computing tool to perform large research work related to the design of input parameters for metallic based self-healing composites structures in near future.

doi: *10.5829/ije.2022.35.10a.04*

1. INTRODUCTION

Metals are always serving the development and advancement of civilization since the prehistoric ages. The diverse phase for the discovery of metals and their processes has been evolved according to the need and usage of mankind. A long journey of monolithic metals towards alloys to the different classes of composites has been globally accepted for their commercialized products and assets [1]. For centuries, nature is always an inspiration to mankind. Biomimetic is defined as applying the mechanism of biological species to employ in the engineering technology. The material which has an ability to self-sustain and recuperate itself with the resources available to it is called self-healing material [2]. The smart structure can be categorized depending upon the nature of healing i.e. intrinsic and extrinsic healing. The extrinsic healing approach has been adapted for higher melting point processed metals as a healing agent is stored in hollow fibre or tubes, microvascular networks etc. and reinforced in the matrix [3-6]. The damage control that occurs without the intervention of human effort comes under the category of passive modes. Whereas, the damage control that occurs with the intervention of human effort is termed as active mode. This emerges an interdisciplinary field both at macro and micro scale to explore the features of the mechanism in materials, electronic devices, structures etc. [7-8]. With the advancement in technologies and depletion of natural resources, researchers are bound to focus their research towards sustainable development. A global report shows that CO_2 emissions had been globally hit to a 2.7%

*Corresponding Author Institutional Email: vaibhavmech@anurag.edu.in (V. Srivastava)

Please cite this article as: V. Srivastava, M. Gupta, Evaluation and Prediction of Self-healing Assessments for AA2014 Based Hybrid Smart Composite Structures: A Novel Fuzzy Logic Approach, ***International Journal of Engineering, Transactions A: Basics,*** Vol. 35, No. 10, (2022) 1841-1857

increase in 2018 compared to 1.6% in the year 2017. United Nations environment programme reports that with expanding population, natural resources are expected to grow by 110 %, leading to reduced forest reduction by 10% and reduction in habitat to 20% by 2050. Implementing the self-healing phenomenon in metallic structures leads to the minimization of replacement of old components with new ones and serviceability of damaged components in remote conditions can be made more effective [9]. One of the successful cited examples of self-healing is the Nissan Company has successfully launched the clear coat hydrophobic paint "Scratch guard coat" that repairs the scratch depending upon the surrounding temperature and condition within 1 to 7 days of damage [10]. Similarly, Ionomers poly Ethylene-co-methacrylic acid has found its applications in self-repair windows and shooting targets under ballistics self-repair phenomenon [11]. Chromate based pigment (BaCrO4 or SrCrO4) introduced with epoxy polyamide matrix act as self-sealing coatings for corrosion protection. Bacteria based crack healing on degraded limestone; ornamental stone and concrete surface has been comprehensively reported during the research at Delft University [12]. Reinforcing agents are an essential source that provides the strength and healing nature of the composites [13-14]. Therefore before selecting the healing agent, it should fulfil certain criteria that are as follows:

1. The reinforcing agent should have sufficient high yield strength greater than that of the matrix.
2. The activation temperature of healing agents should fall within the conditions of the final healing temperature.
3. The healing agents should have high adhesive bonding (i.e. wetting property) with the parent matrix.
4. The healing agents should have high adhesive bonding (i.e. wetting property) with the parent matrix.
5. The healing agents should not lose their healing properties and dimensional stability even at high temperatures.
6. The reinforcing agents should respond to any external source (i.e. heat, light) to start the healing procedure.
7. The healing agents do not increase the overall weight of the composites' structure.

The right execution of smart material design may result in a viable solution for sustaining the structure's integrity and longevity even in difficult situations [15]. The design and fabrication of smart composites is a costly affair. Therefore there is a need of predictive model to evaluate the results more efficiently. Nowadays, a technique can be incorporated for optimal design selection process in order to identify new material selection approaches that cover more environmental considerations and time utilization and saving [16-17]. Fuzzy set theory was created to cope with these types of decision-making challenges and to arrive at a reasonable solutions for them in a timely manner [18]. An overall idea for successfully implementation for the design of smart materials is shown Figure 1.

To uncover the healing mechanism in metallic composites, parameters influencing the design of the self-healing composite structure for effective recovery in healing assessment are analyzed using orthogonal array L8 Taguchi techniques. A comparative analysis was done based on Taguchi analysis on all different smart structure fabricated namely AA2014-NiTi strip-solder based metallic composites and AA2014-NiTi wire-solder based metallic composites. The healing response is measured by considering maximum recovery in the healing assessment for all two different cases. The input parameter's individual contribution is also determined using S/N ratio of every healing assessment and for every experimental run during analysis. Further MATLAB based Fuzzy logic predictive model was developed to predict and compare the self-healing assessment for various fabricated self-healing composite structures.

This paper is organized as follows: Section 2 defines the material composition and a short description of fabricated composite, Section 3 comprises of testing setup for evaluating the self-healing assessments analysis. Section 4 includes design methodology, predictive models and error analysis involved in the present study. Section 5 includes the description and formulation of fuzzy model for both the case study i.e. (Self-healing assessments for AA2014-NiTi strip-solder alloy based hybrid metallic composites) and (Self-healing assessments for AA2014-NiTi strip-solder alloy based hybrid metallic composites) included in the study. The results obtained from the fuzzy based predictive rule and regression model is compared along with confirmatory test using different error analysis is discussed in section 6. Finally, the summarized results were described in conclusion section 7 followed by the references.

2. EXPERIMENTAL DETAILS FOR THE ANALYSIS OF SELF-HEALING COMPOSITES

The composites were fabricated via casting method. An ingot of AA2014 alloy was melted in an electric furnace at 750 ºC and poured directly into the customized die that already containing shape memory alloy (SMA) wire/strip inside it. Once casted and solidified the casted composite were filled with solder alloy and sealed with refractory cement to avoid draining of solder during heat treatment [19-22].

2. 1. Materials The functional biomimetic composite structure includes SMA's strip and low

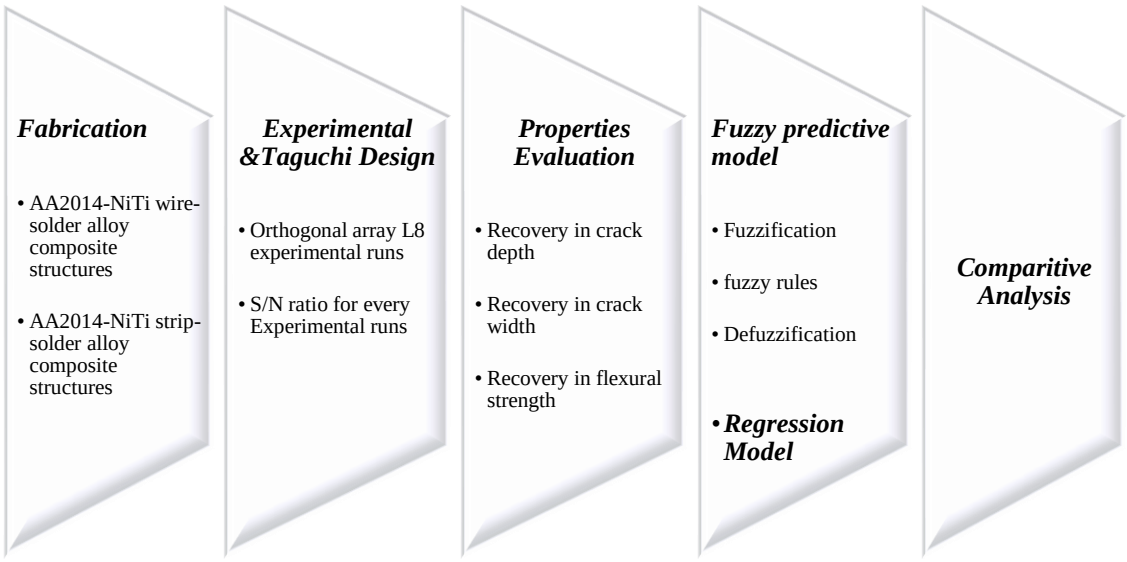

Figure 1. An overall procedure involved in conducting the analysis

melting alloy (Sn-Pb) as internal combination parameters reinforced in aluminium alloy-based matrix during fabrication. The purpose for introducing two healing agents was to revert the damage structure to its original state and simultaneously bind the micro crack interfaces.

2. 1. 1. Self-healing Composites Matrix Details An aluminium alloy AA2014 is used as a matrix which has been reinforced with different healing agent to form a hybrid MMC's. The transition temperature of the phase transformation (i.e. Martensite to Austenite phase) for SMA strip is 70 ºC, whereas, the melting point of solder alloy is 181 ºC. The chemical composition of AA2014 matrix confirmed through Energy Dispersion X-Ray (EDX) technique as summarized in Table 1 [19-22]

2. 1. 2. Healing Agents

2. 1. 2. 1. Ni-Ti alloy Owing to its advantages over other SMA groups, Ni45Ti55-based SMA was mostly employed as reinforcement, because of its transformation hysteresis, which aids in repeating actuation with a shorter time interval [22-23]. The nitinol wires with a diameter of 0.46 mm and nitinol strip of 0.98 mm having a final austenite temperature of 70°C was used as reinforced healing agents for case studies I and II, respectively. Nitinol is a frequently used and commercially accessible SMA and in the present study both forms (i.e. wire and strip) were acquired from SMA wires India Ltd. It offers great corrosion resistance, biocompatibility, high damping capability, and performs in low cycle fatique [20].

TABLE 1. Chemical composition of AA2014 used as a matrix [19-22]

Element	Al	Cu	Si	Mg	Mn
Wt. (%)	93.7	4.4	0.8	0.4	0.7

2. 1. 2. 2. Solder Alloy The most popular and commercially available is Sn60Pb40 based solder alloy with applications in electronics industries for the joining of copper wires and circuit boards. With an increase in Sn%, the solder alloy (i.e. Sn63Pb37) with a eutectic composition has more resistant to oxide formation with large shear and tensile strength. Although the commercialized solder alloy Sn60Pb40 has a low melting point of 180 ºC having a high wetting property, low oxide content, large flow ability that bonds the damaged crack through the phenomenon of capillary action and surface tension. The properties of solder alloy using in the analysis are stated in Table 2 [19-20].

TABLE 2. Chemical composition of solder alloy used as a healing agent [19-20]

Solder alloy	Melting Point (ºC)	Density (g/cm^3)	Electrical Resistivity (μΩ-m)	Thermal Conductivity (W/m-K)	Tensile strength (MPa)	Tensile Elongation (%)	Brinell Hardness (HB)
Sn60Pb40	183/191	8.51	0.155	50	52.46	41	17

2. 2. Composites Structures

2. 2. 1. AA2014-Niti Strip Solder Based Hybrid Metallic Composite Structure A hybrid metallic smart composite consists of nitinol strip at the center that extends longitudinally placed throughout the sample. The solder alloy is located at the middle of the strip both top and bottom throughout the length of the sample. AA2014-NiTi strip-solder alloy based hybrid metallic composites is shown in Figure 2.

2. 2. 2. AA2014-Ni-Ti Wire-solder Based Hybrid Metallic Composite Structure The structure consists of AA2014 as a matrix that contains solder alloy and Ni-Ti wires as a healing materials. The Ni-Ti wire extends longitudinally throughout the length of the composites, whereas solder alloy is located at the center of the composite material. After initial damage in the structure the healing agents activates by heating the damaged specimen and heals the crack developed in the structure. The fabricated composite is shown in Figure 3. A detailed fabrication setup for the self-healing composite is discussed in the literature [19].

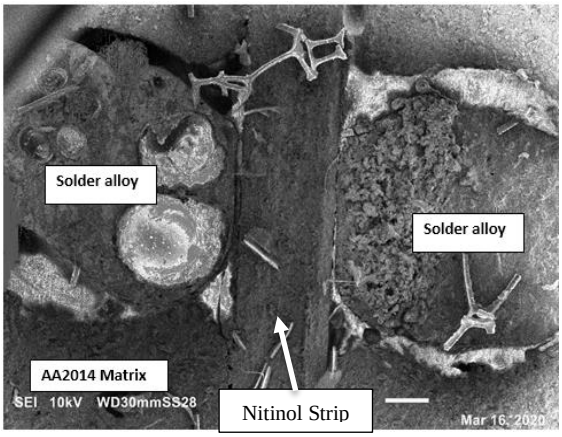

Figure 2. SEM micrograph of the fabricated hybrid composite

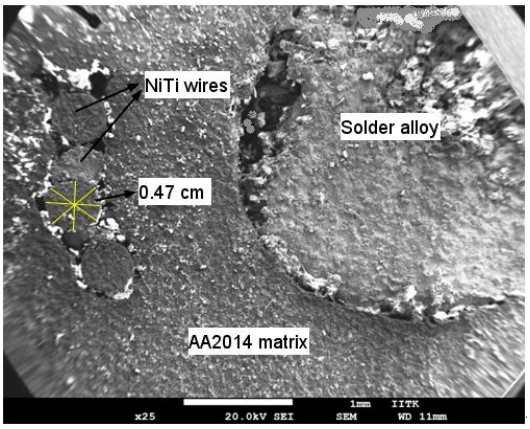

Figure 3. SEM micrograph of fabricated hybrid composite

3. TESTING SETUP

3. 1. 1. Crack Width Analysis The crack width were examined using optical microscope before and after healing. The analysis of crack width measurement were considered at the same and exact position before and after healing to maintain the uniformity in measurement [19-22]. Therefore, the recovery in crack width was evaluated. The crack width recovery %. is calculated using expression given in Equation (1) [13].

$$\eta_{reduction\ in\ crack\ width/crack\ depth} = \frac{\alpha_{before\ healing} - \beta_{after\ healing}}{\alpha_{before\ healing}} \quad (1)$$

where, **"α"** is the property of interest i.e. crack width or crack depth

3. 1. 2. Crack Depth Analysis The surface crack depth is difficult to quantify as surface crack is ranged in micrometer. Therefore, highly sensitive Nondestructive testing i.e. eddy current test was conducted at different frequencies [24]. A calibrated approach was opted to obtain the regression equation at different frequencies by calibrating the slots (created by EDM) of different depth of same nonferrous material to find the crack depth of actual samples. The electromagnetic signal received after calibration at different frequencies helps to formulate the regression equation using Equations (2) and (3) below [19, 21-22].

$$d = av + b\phi + c$$

where, d= Crack depth,

v = electromagnetic voltage, (2)

$\emptyset$ = Phase angle,

a, b, c= arbitrary constant

$$For\ Frequency\ 25\ kHz: d_{25} = 2.3255v + 0.00232\phi - 0.3790$$

$$For\ Frequency\ 50\ kHz: d_{50} = 3.9285v - 0.03571\phi + 6.5285$$

$$For\ Frequency\ 100kHz: d_{100} = 3.2456v - 0.01403\phi + 2.4763 \quad (3)$$

$$For\ Frequency\ 200kHz: d_{200} = 4.0566v - 0.0169\phi + 2.9564$$

3. 2. 3. Flexural Test Initially the samples were bend tested at yield point to produce a damage to the composite structure. Thereby after healing the samples at 600ºC the samples were undergone re-bending test to evaluate their recovery in flexural strength. The three point bend was performed on Universal Testing Machine (Tenius Olsen load capacity 10 KN) at constant strain rate of 0.0166/s [19-22]. The expression for calculating

the flexural stress and strain is given in Equation (4). The strength recovery % is obtained using expression in Equation (5) [14].

$$\sigma_{flexural\ stress} = \frac{3Fl}{2bt^2} \quad (4)$$

where, F = Flexural Load; l = Specimen length; b = Specimen breadth; t = Specimen thickness

$$\eta_{healing\ efficiency} = \frac{\alpha_{healed\ sample}}{\alpha_{damaged\ sample}} * 100 \quad (5)$$

where, **"α"** is the property of interest i.e. Flexural strength

4. DESIGN METHODOLOGY

4. 1. Taguchi Design of Experiment Taguchi's orthogonal array employs a significant portion of these choices, taking use of the features of fractional factorial design to choose the optimum process parameter combination. The design of experiments performed using L8 orthogonal array Taguchi technique was analyzed using Analysis of variance (ANOVA) based S/N ratios to observe the most influential parameters affecting the design and performance of self-healing assessments [14, 16]. The relation to find the S/N ratio for larger is better is calculated using Equation (6). Using Taguchi orthogonal columns of L8 (4^1 2^3) array technique different experimental run for different fabricated smart structures was carried out.

$$\frac{S}{N} = -10log\left(\sum\left(\frac{1}{Y^2}\right)/n\right) \quad (6)$$

where, Y = responses for the given factor level combination and

n = number of responses in the factor level combination.

The normalized S/N ratio is evaluated using the relation given below in Equation (7)

$$N_i = \frac{x_i}{\sum_{i=1}^{i=n} x_i} \quad (7)$$

The proposed methodology provides a regression correlations based on the linear fit obtained using the following experimental data as stated in Equation (8) [25].

$$U = a_0 + P1a_1 + P2a_2 + P3a_3 + P4a_4 \quad (8)$$

where, $U = Output\ response$,

$a_0 = Constant\ intercept\ at\ y\ axis$,

$a_1, a_2, a_3, a_4 = Coefficient\ of\ Regression\ equation$,

$P1, P2, P3, P4$ *are the input parameter for the design of composites*

Linear regression models i.e. a statistical tool is generated to judge the accuracy of the predicted model. The model is generated using Minitab 19. The quality measures are adopted to compare and measure the model using error analysis [18]. To compare anticipated and measured results of self-healing evaluations, statistical measures such as the root mean square error (RMSE) and the determination coefficient (R^2) are employed. The RSME is defined using expression in Equations (9) and (10) [26].

$$RSME = \sqrt{\frac{1}{n}\sum_{i=1}^{n}(y_{pred\ i} - y_{obsev}i)^2} \quad (9)$$

whereas, R^2 can be found using an expression below

$$R^2 = 1 - \frac{\sum_{i=1}^{n}(y_{pred\ i} - y_{observ\ i})^2}{\sum_{i=1}^{n} y_{observ\ i}{}^2} \quad (10)$$

The mean of the squares of the errors is assessed by the mean absolute percentage error (MAPE). MAPE values that are lower ensure that the suggested models perform better. The MAPE is computed using Equation (11) [27].

$$MAPE = \frac{1}{n}\sum_{i=1}^{n}\frac{|y_{pred\ i} - y_{observ\ i}|}{y_{pred\ i}} * 100\% \quad (11)$$

Furthermore, the suggested models' effectiveness and efficiency are also evaluated using mean absolute error (MAE) that is determined by Equation (12) [28-30].

$$MAE = \frac{1}{n}\sum_{i=1}^{n}|y_{pred\ i} - y_{obser\ i}| \quad (12)$$

where n is the number of data patterns in the data set, $y_{pred\ i}$ indicates the predicted value of one data point i and $y_{observ\ i}$ is the observed value of one data point i.

4. 2. Fuzzy Predictive Model According to this theory, it states, "If in an environment of discourse A, where $\hat{F}$ being a fuzzy subset of say X, can be specified by a membership function $f_f(a)$, which drafts each and every element "a" in A to a real number N within the interval [0, 1]. The function value $f_{\hat{F}}$(a) represents the grade of membership of "a" in $\hat{F}$. Larger the value of $f_{\hat{F}}$(a) stronger will be the grade of membership for "a" in $\hat{F}$ ". Fuzzy Logic is a multi-valued logic that provides the assessment of a collection of variables by establishing intermediate values between traditional evaluation schemes such as true/false, yes/no, high/low, and so on. In this approach, assessment concepts such as fairly tall or extremely quick may be mathematically expressed and analyzed by computers, allowing the software to use a more human-like style of thinking [31-32]. The event and kind of membership function are mostly determined by the relevant event when selecting membership functions for fuzzyfication [33-34]. The relationships between input parameters and output response were referred to construct the rules between them. On the basis of Mamdani fuzzy logic, the experimental data findings were simulated in the MATLAB programme. Parameters

{a b c} define the triangular shaped membership function for input is shown in Equation (13) [34].

$$triangle\ (x; a, b, c) = \begin{cases} 0, & x \le a \\ \frac{x-a}{b-a}, & a \le x \ge b \\ \frac{c-x}{c-b}, & b \le x \ge c \\ 0, & c \le x \end{cases} \quad (13)$$

where a, b, c defines the x coordinates of the three corners of the underlying triangle membership function, generated by the triangular fuzzy triplet. De-fuzzification is the process of converting a fuzzy quantity to a precise value, whereas fuzzyfication is the process of converting a precise value to a fuzzy number. The model selection is critical since it determines the model's accuracy [35-36]. The centroid of area (COA) De-fuzzification approach is employed in this model because it provides extremely accurate prediction and analysis, as shown in Equation (14) [37]. An overall fuzzy inference system is shown in Figure 4.

$$COA = \frac{\int_{x_{min}}^{x_{max}} f(x)xdx}{\int_{x_{min}}^{x_{max}} f(x)dx} \quad (14)$$

where, $COA = Center\ of\ Area, x = value\ of\ linguistic\ variable$
$x_{max}\ and\ x_{min}\ is\ the\ range\ of\ the\ linguistic\ variable.$

The knowledge base is generally referred as a combination of rule base and database. In most cases, a fuzzy IF THEN rule has two aspects. The first portion, IF, and the second, THEN, are referred to as the premise and consequence, respectively [38-40]. A fuzzy rule base is comprised of a series of if-then control rules that have been created to illustrate the inference link between the input parametric design and the output self-healing evaluations. It is represented as shown below.

Rule 1: If $x_1 = a_1, x_2 = b_1, x_3 = c_1\ and\ x_4 = d_1$ then healing assessment is e_1
Rule 2: If $x_1 = a_2, x_2 = b_2, x_3 = c_2\ and\ x_4 = d_2$ then healing assessment is e_2
Rule 3: If $x_1 = a_3, x_2 = b_3, x_3 = c_3\ and\ x_4 = d_3$ then healing assessment is e_3
Rule n: If $x_1 = a_n, x_2 = b_n, x_3 = c_n\ and\ x_4 = d_n$ then healing assessment is e_n

Where, a_i, b_i, c_i and d_i are the fuzzy subsets which are being defined by a membership functions and e_i healing assessment output.

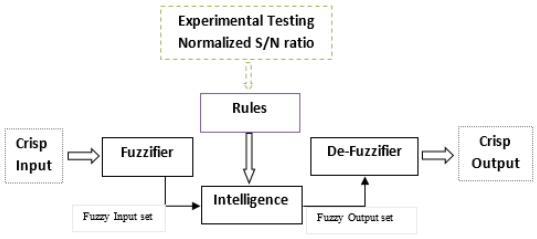

Figure 4. A flowchart rule based fuzzy inference system

5. VERIFICATION OF THE PROPOSED FUZZY MODEL FOR PREDICTION OF SELF-HEALING ASSESSMENTS

The proposed fuzzy model is designed with a view to accurately predict the self-healing assessment (i.e. Crack width recovery %, Crack depth recovery % and flexural strength %), respectively. The design consideration for the fabrication of smart composites is to achieve higher self-healing assessments. Therefore, based on knowledge and expertise of designer this predictive rule based model provides a tool for choosing an optimal input parameters for achieving the higher healing assessments. For evaluating the performance three cases were studied: (i) to predict Self-healing assessments for AA2014-NiTi strip-solder alloy based hybrid metallic composites. (ii) to predict Self-healing assessments for AA2014-NiTi wire-solder alloy based hybrid metallic composites.

5. 1. Case Study-I: To Predict Self-healing Assessments For AA2014-Niti Strip-Solder Alloy Based Hybrid Metallic Composites

The concept of the smart composites was made such that the reinforced SMA strip recovers the deflected damaged shape caused due to loading which ultimately heals the macro crack. Solder alloy heals the micro cracks by bonding the damaged site. A parametric study of AA2014 matrix considering different levels of input parameters (healing duration, SMA vol.%, solder alloy %, Reheat treatment) as reinforcement were studied using Taguchi L8 (Mixed level design) orthogonal array technique to determine the influential parameter affecting the self-healing assessments. The parameters and their levels considered for fabrication with different experimental runs is shown below in Table 3.

Initially, based on L8 mixed orthogonal array and based on the different combination of parameters, the experiments were carried out to evaluate the self-healing properties. The evaluated S/N ratio from Equation (6) for each experimental runs is utilized for deciding the range of output membership functions as shown in Table 4. Since the value for S/N ratio for each experimental run is unsystematic (i.e. negative); therefore, the values were normalized between 0 and 1. This will assists in deciding the range of output membership functions. In the later

TABLE 3. Input parameters selection with their considered levels

Parameters	Level 1	Level 2	Level 3	Level 4
Healing Duration (In min.)	30	60	90	120
Solder alloy vol. %	9	16	-	-
SMA strip vol. %.	10	13	-	-
Reheat treatment	Done (1)	Not Done (0)	-	-

TABLE 4. A summarized Table show the L8 orthogonal array experimental runs along with obtained healing assessments

Healing Duration.	Solder alloy vol. %	SMA strip vol. %.	Reheat Treatment.	Crack width Recovery %	S/N ratio	Normalized S/N ratio	Crack depth recover %	S/N ratio	Strength recover %	S/N ratio	Normalized S/N ratio
30	9	10	1	78.26	-2.12	0.114	37.89	31.57	35.94	-8.88	0.15
30	16	13	0	64.28	-3.83	0.207	22.21	26.93	15.76	-16.04	0.27
60	9	10	0	68.23	-3.32	0.179	50.89	34.13	36.2	-8.82	0.15
60	16	13	1	74.22	-2.58	0.139	53.95	34.63	45.4	-6.85	0.12
90	9	13	1	80.62	-1.87	0.100	54.87	34.78	55.96	-5.04	0.08
90	16	10	0	78.98	-2.05	0.110	78.45	37.89	64.08	-3.86	0.06
120	9	13	0	73.01	-2.73	0.147	60.06	35.57	56	-5.03	0.08
120	16	10	1	100	0	0	87.85	38.87	75.4	-3.01	0.05

stage during evolution for the recovery in healing properties, the normalized S/N ratio is converted into actual S/N ratio to acquire actual healing assessments for each experimental run.

An overall formulation of Mamdani based fuzzy interference system for predicting the self-healing assessment is shown in Figure 5. The next step includes the assessment and configuration of input membership design properties function to present in the linguistic variables. The crisp values of design parameters namely Healing duration, solder alloy vol. %, SMA vol. %, and reheat treatment factor are fuzzified as shown in Figure 6. For instance, the fuzzy set value for healing duration as input design parameters are classified as "Low", "Medium", "high", "Very high".

The S/N ratio of the heling assessment is considered as the actual response of output membership functions. The crisp values output response is fuzzified into linguistic domain. For instance, crack width recovery % is classified as "Very High", "High", "Medium", "Low" and "Very Low" respectively as shown in Figure 7. The formulation of knowledge based rule between input and output membership function provides an inference relationship between parametric combinations of experimental trails. This provides a wider scope and range of application in compared to other statistical methods. By studying the data set as shown in Table 4 fuzzy set data classified in the linguistics variable is used by the expert to create the set of rule between input and output membership functions as shown in Table 5.

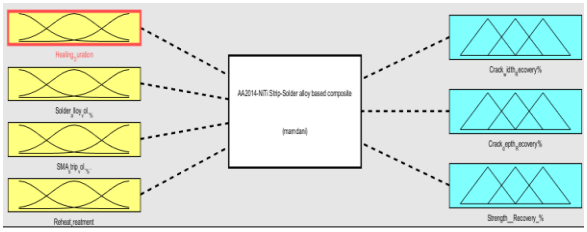

Figure 5. An overall Mamdani based fuzzy interference system for case study I

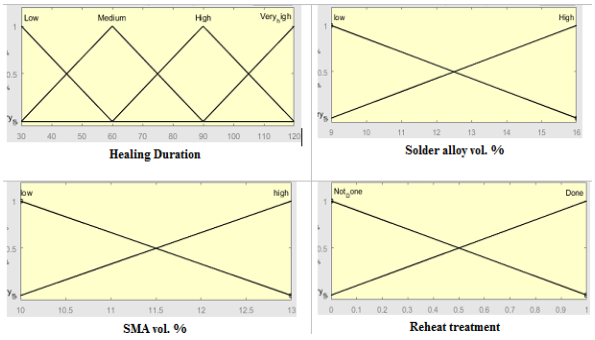

Figure 6. Linguistics variable for input membership functions

5. 2. Case Study-II: To Predict Self-Healing Assessments For AA2014-Niti Wires-Solder Alloy Based Hybrid Metallic Composites

Flexural testing has been used to evaluate the healing evaluation of the AA2014 matrix reinforced with Ni-Ti wires and solder alloy as healing agents. The concept behind a

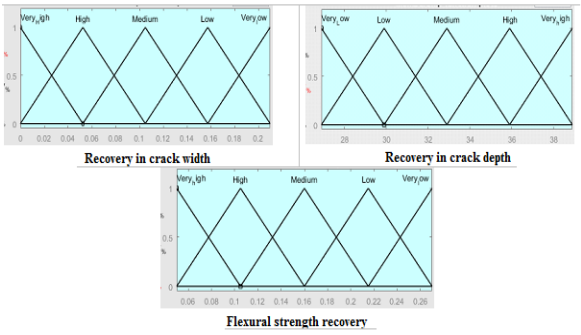

Figure 7. Linguistics variable for output membership functions

TABLE 5. Knowledge based rule formation based between input and output membership function

	Healing Duration		Solder alloy vol. %		SMA strip vol. %.		Reheat treatment		Normalized Crack width Recover %	Normalized Crack depth Recover %	Normalized Flexural strength Recover %
IF	L	&	L	&	L	&	D	**THEN**	M	L	M
IF	L	&	H	&	H	&	ND	**THEN**	VL	VL	VL
IF	M	&	L	&	L	&	ND	**THEN**	L	M	M
IF	M	&	H	&	H	&	D	**THEN**	L	M	H
IF	H	&	L	&	H	&	D	**THEN**	M	H	H
IF	H	&	H	&	L	&	ND	**THEN**	M	VH	VH
IF	VH	&	L	&	H	&	ND	**THEN**	L	H	H
IF	VH	&	H	&	L	&	D	**THEN**	VH	VH	VH

VL: VERY LOW; L: LOW; M: MEDIUM; H: HIGH; VH: VERY HIGH; D: DONE; ND: NOT DONE

smart composite was to keep its structural stability by reinforcing it with Ni-Ti wires, which mend macro cracks while the solder alloy binds micro-cracks by filling them with solder alloy. The focus of this research is to identify the factors that influence self-healing assessments. Furthermore, the principle of NDT utilizing ECT has been used to more effectively determine the crack depth [19, 21-22].

These experiments were initially done to test the self-healing properties of L8 mixed orthogonal array. The parameters and their levels considered for fabrication with different experimental runs is shown below in Table 6. For each experimental run, the resulting S/N ratio is utilized to determine the output membership functions' range as indicated in Table 7. Here the calculated S/N ratio is symmetric therefore normalizing for calculated S/N ratio was not considered. For deciding the range of output membership function, directly from S /N values the range was considered.

Figure 8 depicts an overall formulation of a Mamdani-based fuzzy interference system for forecasting the self-healing assessment. The following stage entails evaluating and configuring the input membership design properties function so that it may be displayed in the linguistic variables. In Figure 9, the crisp values of design parameters such as "Healing duration," "specimen size," "SMA vol. %," and "Diameter of wire" are fuzzified, whilst the fuzozy values. For example, the fuzzy set value for healing length as input design parameters is grouped into four categories: "Low," "Medium," "High," and "Very High."

TABLE 6. Input parameters selection with their considered levels

Parameters	Level 1	Level 2	Level 3	Level 4
Healing Duration (in min.)	30	60	90	120
Specimen size (mm) (Notations)	1 as (85X 11 X 10)	2 as (137 X 21 X 10)	-	-
SMA vol. (in %)	0.50	1.30	-	-
Diameter of SMA wires (in mm)	0.47	0.96	-	-

TABLE 7. A summarized table show the L8 orthogonal array experimental runs along with obtained healing assessments [19]

Healing Duration	Specimen size	SMA Vol.%	Dia. of SMA wires	Crack width Recovery %	S/N ratio	Crack depth Recovery %	S/N ratio	Strength Recovery %	S/N ratio
30	1	0.5	0.47	59.15	35.43	4.2	12.46	3.46	10.78
30	2	1.3	0.96	60.88	35.68	4.8	13.62	6.85	16.71
60	1	0.5	0.96	65.38	36.30	7.8	17.84	6.93	16.81
60	2	1.3	0.47	58.06	35.27	10.1	20.08	9.3	19.36
90	1	1.3	0.47	81.81	38.25	27.8	28.88	22.33	26.97
90	2`	0.5	0.96	76.55	37.67	11.9	21.51	35.73	31.06
120	1	1.3	0.96	100	40	96.9	39.72	73.76	37.35
120	2	0.5	0.47	77.1	37.74	43.1	32.68	44.89	33.04

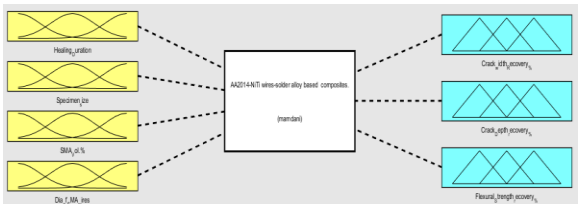

Figure 8. An overall Mamdani based fuzzy interference system for case study II

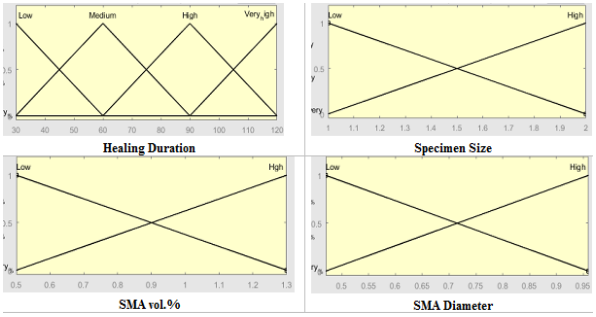

Figure 9. Linguistics variable for input membership functions

For healing assessments, the S/N ratio was regarded as a measurement performance of the output membership functions. An inference link is established between parametric combinations of experimental trails, as illustrated in Figure 10. Crack width recovery is categorized into linguistic terms such as crack width recovery is classified as "Very High", "High", "Medium", "Low", and "Very Low". A specific linguistics variable, called fuzzy set data, is employed by the expert to build a rule editor which describes how input and output membership functions relate to one another as shown in Table 8.

6. RESULTS AND DISCUSSION

The results obtained using regression correlations (based on the linear fit obtained using the following experimental data) for both case study is compared with developed fuzzy logic predictive rule based model. The model based on soft computing technique assists the designer to select optimal parameters for a design of higher self-healing assessments.

6. 1 Case Study-I To Predict Self-healing Assessments for AA2014-Niti Strip-solder Alloy Based Hybrid Structure

After decision making unit through rule based database and de-fuzzification interface the crisp value of output membership function is evaluated. A summarized results for all predictive models used in the analysis is shown in Table 9. The evaluated results depicts an overall satisfactory performance of predictive fuzzy model in minimum experimental runs. An average of error obtained for crack width recovery % is 2.62 %, for crack depth recovery 0.09 % and for flexural strength recovery 2.37 %, respectively. The range selected by considering S/N ratio

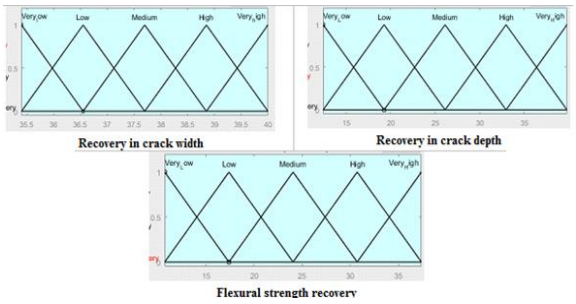

Figure 10. Linguistics variable for output membership functions

TABLE 8. Knowledge based rule formation based between input and output membership function

	Healing Duration		Specimen Size		SMA strip vol. %.		Dia. of SMA wire		Normalized Crack width Recover %	Normalized Crack depth Recover %	Normalized Flexural strength Recover %
IF	L	&	L	&	L	&	L	**THEN**	VL	VL	VL
IF	L	&	H	&	H	&	H	**THEN**	VL	VL	L
IF	M	&	L	&	L	&	H	**THEN**	L	L	L
IF	M	&	H	&	H	&	L	**THEN**	VL	L	L
IF	H	&	L	&	H	&	L	**THEN**	H	M	M
IF	H	&	H	&	L	&	H	**THEN**	M	L	H
IF	VH	&	L	&	H	&	H	**THEN**	VH	VH	VH
IF	VH	&	H	&	L	&	L	**THEN**	M	H	H

VL: VERY LOW; L: LOW; M: MEDIUM; H: HIGH; VH: VERY HIGH

minimizes the range of fuzzy data set that facilitates the design expert to create more precise and accurate rule based model. The Negative S/N ratio for each experimental runs is further normalized to positive values for considering the range of the output membership functions. The Positive S/N ratio is directly considered for choosing the range of output membership function. The linear regression analysis done using Minitab 19 helped in formulation of regression equation for predicting the self-healing assessments. The dependent variable i.e. crack width recovery, crack depth recovery % and recovery in flexural strength is formulated with independent variables (i.e. healing duration, solder alloy vol. %, SMA strip vol. % and reheat treatment) using linear fit regression equation as described in Equations (15), (16) and (17), respectively.

$$Crack\ width\ recovery = 81.8 + (0.819 * H) + (0.620 * S_a) - (2.778 * S_s) + (12.15 * R) \quad (15)$$

$$Crack\ depth\ recovery = 60.4 + (0.4865 * H) + (1.384 * S_a) - (5.33 * S_s) + (5.74 * R) \quad (16)$$

$$Flexural\ strength\ recovery = 37.8 + (0.4626 * H) + (0.591 * S_a) - (3.21 * S_s) + (10.17 * R)$$

$$H = Healing\ duration$$

$$S_a = Solder\ alloy\ vol.\%,$$

$$S_S = SMA\ strip\ vol.\%,$$

$$R = Reheat\ treatment \quad (17)$$

TABLE 9. Summarized result for all experimental runs with predictive models

Healing Assessment	Experiment No	Experimental Normalized S/N Ratio	Fuzzy Normalized Predicted S/N Ratio	Experimental Observation	Fuzzy Predicted Model	Regression Analysis
Crack Width Recovery %	1	0.114	0.105	78.26	70.05	77.17
	2	0.207	0.193	64.28	58.84	61.03
	3	0.179	0.157	68.23	58.08	70.45
	4	0.139	0.157	74.22	81.95	78.61
	5	0.100	0.105	80.62	82.96	79.69
	6	0.110	0.104	78.98	73.96	80.22
	7	0.147	0.157	73.01	77.01	72.97
	8	0	0	100	100	97.80
Crack Depth Recovery %	1	31.57	29.9	37.89	39.45	39.90
	2	26.93	27.9	22.21	22.83	27.85
	3	34.13	32.9	50.89	49.02	48.75
	4	34.63	32.9	53.95	55.91	48.18
	5	34.78	35.9	54.87	56.64	53.09
	6	37.89	37.9	78.45	78.39	73.03
	7	35.57	35.9	60.06	60.68	61.95
	8	38.87	37.9	87.85	85.51	93.36
Flexural strength Recovery %	1	0.15	0.162	35.94	37.63	35.06
	2	0.27	0.262	15.76	14.75	19.40
	3	0.15	0.162	36.2	38.14	38.77
	4	0.12	0.105	45.4	37.77	43.45
	5	0.08	0.102	55.96	63.87	53.19
	6	0.06	0.061	64.08	57.63	56.80
	7	0.08	0.102	56	63.97	56.90
	8	0.05	0.061	75.4	86.12	80.83

An effectiveness in fuzzy logic approach compared with experimental data shows significant improved results as shown in Table 9. Recovery in flexural strength % has shown the highest error due to more variation and non-linearity in the data sets. Although with only 8 experimental runs and less number of data sets an average of 3.48 % shows that proves that fuzzy logic approach is capable of predicting the self-healing assessments that assists in estimating the best possible combination of input parametrical design. The rule editor of the formulated fuzzy model for experiment no. 3 conditions is shown in Figure 11.

The residual plot for self-healing assessment is shown in Figure 12 whereas error analyis is shown in Figure 13. Further, in order to validate the predictive model with the statistical model error analysis is done using MAPE, MSE and RSME. The analysis shown that for each error analysis recovery in crack depth has shown less error in compared to linear regression model. Hence, formulated fuzzy model is feasible and able to predict the healing assessment results more accurately and precisely as shown in Figure 14.

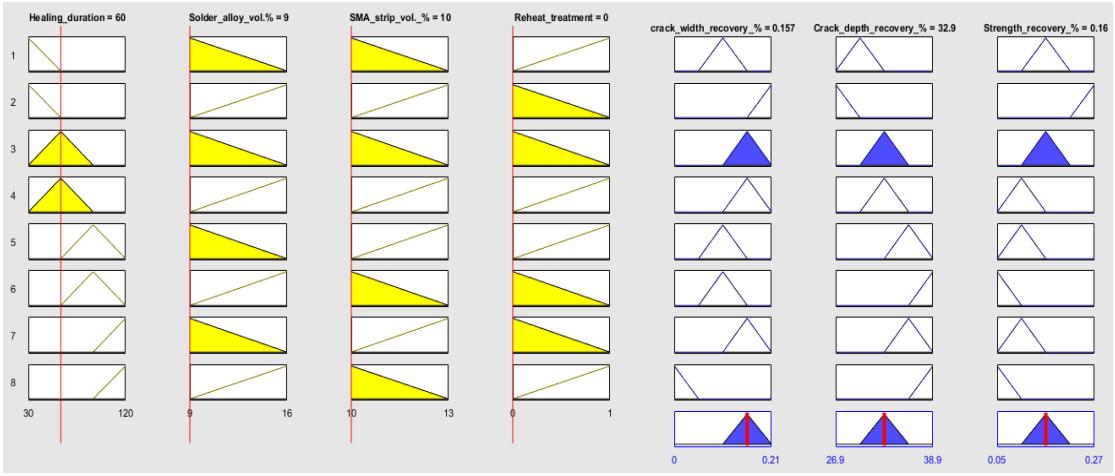

Figure 11. The fuzzy based rule editor dialog box result for experimental no. 3

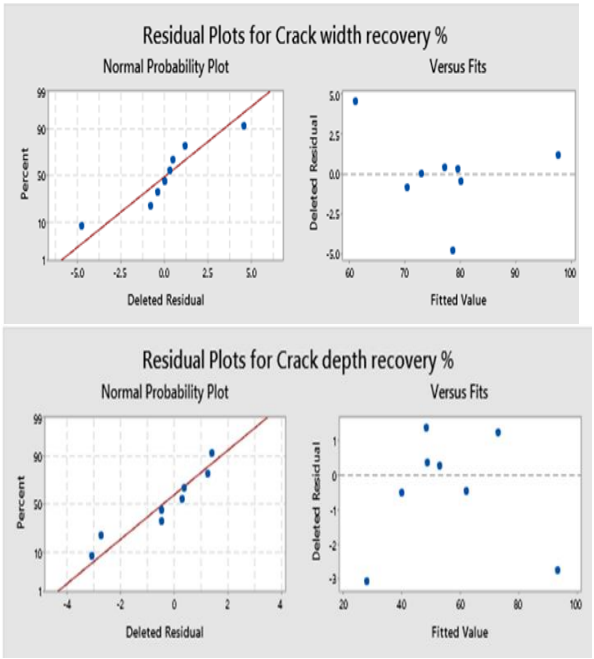

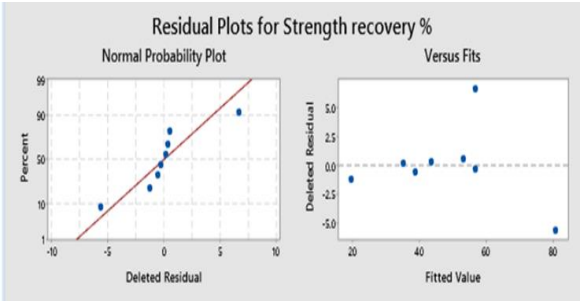

Figure 12. Linear fit and Residual plot of different experimental runs for all the healing assessments

6. 2. Case Study-II: To Predict Self-Healing Assessments for AA2014-Niti Wire-Solder Alloy Based Hybrid Composites After primary investigation of the parameters controlling the self-healing assessments, the formulated fuzzy predictive model (based on the rules) assists in determining the healing assessments. The soft computing technique helps to establish the relation between input and output

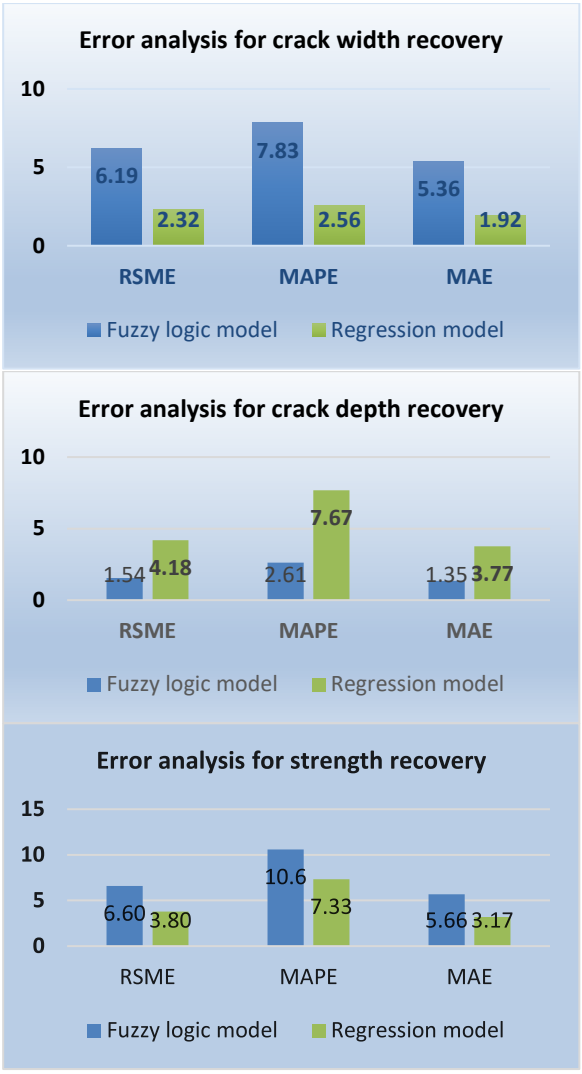

Figure 13. A comparative error analysis for different predictive model for different healing assessments

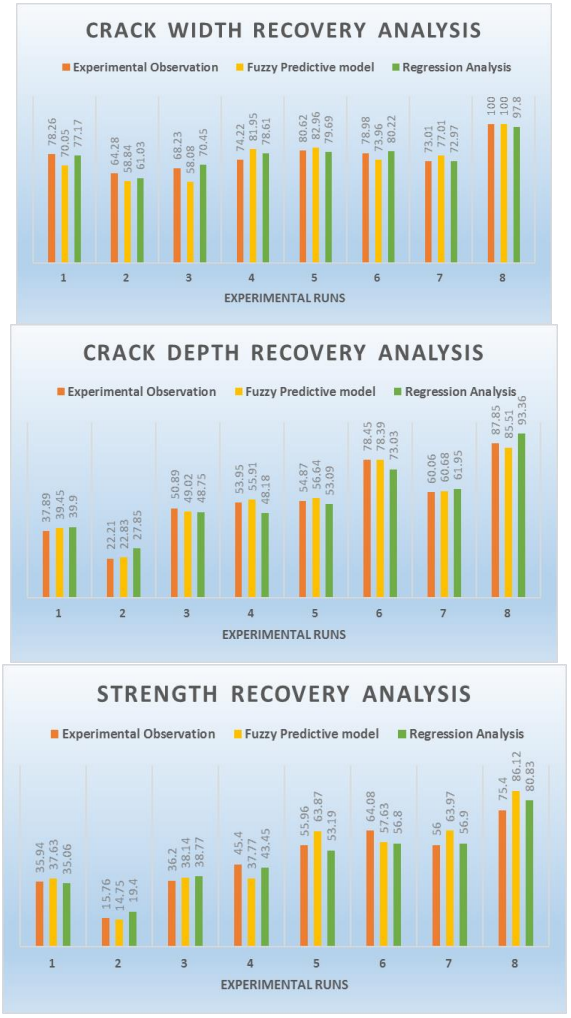

Figure 14. A summarized comparison of healing assessments for different predictive model with actual experimental observations

responses. The input membership functions i.e. healing durations, specimen size, SMA vol. % and Diameter of SMA wires has a large control over healing of the damaged structure. An average error is obtained for crack width recovery % is 0.10%, for crack depth recovery 2.80% and for flexural strength recovery 1.75%, respectively. The results obtained using predictive model is shown in Table 10. It is observed that with more variation in experimental observation the error is estimated to be more. Using S/N ratio for each experimental runs the variation in the data sets is lowered due to which predicted results is estimated to be closer to the experimental observations. The rule editor of the formulated fuzzy model for experiment no. 8 conditions is shown in Figure 15.

The dependent variable i.e. crack width recovery, crack depth recovery % and recovery in flexural strength is formulated with independent variables (i.e. healing duration, Specimen size, SMA vol. % and Dia. of SMA wire) using linear fit regression equation as described in Equations (18), (19) and (20), respectively.

$$Crack\ width\ recovery = 43.2 + (0.3435 * H_d) - (8.44 * S_s) + (7.05 * SMA_{vol\%}) + (13.62 * SMA_{dia}) \quad (18)$$

$$Crack\ depth\ recovery = -45.6 + (0.731 * H_d) - (10.7 * S_s) + (15.2 * SMA_{vol\%}) + (30.7 * SMA_{dia}) \quad (19)$$

$$Flexural\ strength\ recovery = -38.6 + (0.611 * H_d) - (2.433 * S_s) + (6.6 * SMA_{vol\%}) + (22.1 * SMA_{dia}) \quad (20)$$

$H_d = Healing\ Duration$

$SMA_{vol.\%} = SMA\ vol\ \%$

$SMA_{dia} = Diameter\ of\ SMA\ wire$

$S_s = Specimen\ Size$

TABLE 10. Summarized result for all experimental runs with predictive models

Healing Assessment	Experiment No	Experimental S/N Ratio	Fuzzy Predicted S/N Ratio	Experimental Observation	Fuzzy Predicted Model	Regression analysis
Crack Width Recovery %	1	35.43	35.6	59.15	59.43	55.00
	2	35.68	35.6	60.88	60.74	58.86
	3	36.30	35.6	65.38	64.09	71.97
	4	35.27	35.6	58.06	58.59	62.49
	5	38.25	38.8	81.81	82.96	81.24
	6	37.67	37.6	76.55	76.40	73.83
	7	40	39.6	100	98.98	98.22
	8	37.74	37.6	77.1	76.81	77.46
Crack Depth Recovery %	1	12.46	11.6	4.2	3.88	-10.52
	2	13.62	14.7	4.8	5.15	0
	3	17.84	19.3	7.8	8.39	19.27
	4	20.08	19.3	10.1	9.69	11.66
	5	28.88	26.1	27.8	24.83	49.09
	6	21.51	19.3	11.9	10.53	23.30
	7	39.72	37.5	96.9	91.16	78.89
	8	32.68	32.9	43.1	43.38	34.96
Flexural strength Recovery %	1	10.78	12.9	3.46	4.02	-9.01
	2	16.71	17.4	6.85	7.12	4.66
	3	16.81	17.4	6.93	7.16	20.14
	4	19.36	17.4	9.3	8.25	12.16
	5	26.97	24.1	22.33	19.67	32.92
	6	31.06	30.7	35.73	35.31	36.04
	7	37.35	35.2	73.76	69.25	62.08
	8	33.04	30.7	44.89	41.46	43.54

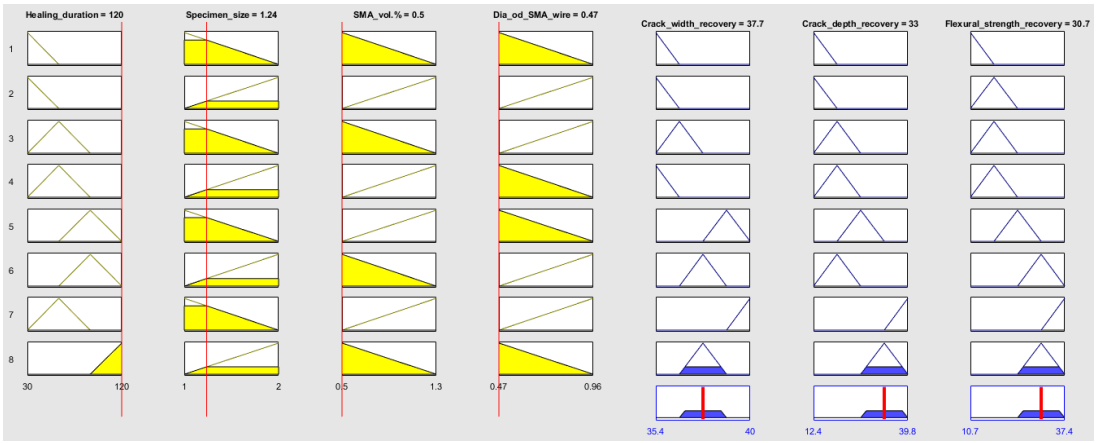

Figure 15. The fuzzy based rule editor dialog box result for experimental no. 8

The obtained results after implementing fuzzy logic model and regression analysis is compared using error analysis. The results observed from Fuzzy logic model shown a tremendous forecasting in predicting the

experimental observation built on knowledge based rule in compared to regression analysis. The errors analyses (i.e. RSME, MAPE, MAE) show more error in regression analysis for all self-healing assessments. The residual plot for self-healing assessment is shown in Figure 16. The summarized error analysis is shown in Figure 17. The analysis concludes the fuzzy predictive knowledge based model to be versatile and precise that can be seen in Figure 18.

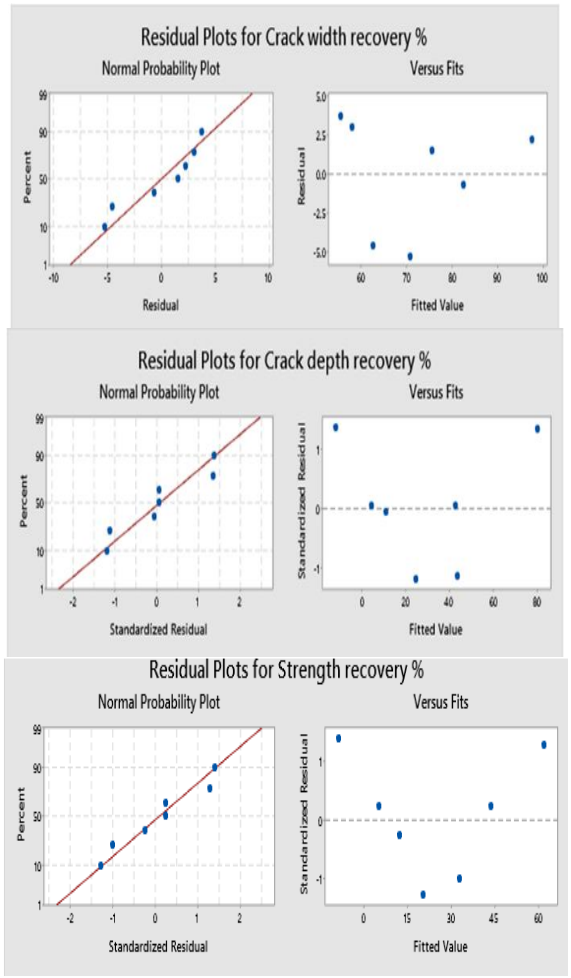

Figure 16. Linear fit and Residual plot of different experimental runs for all the healing assessments

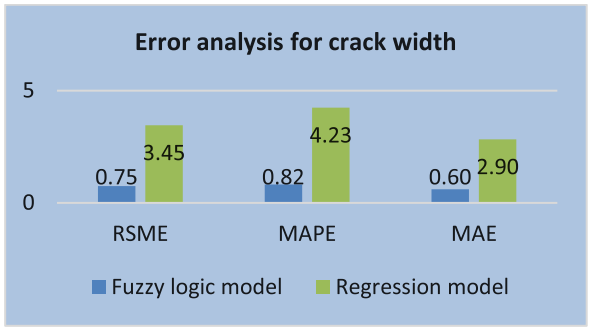

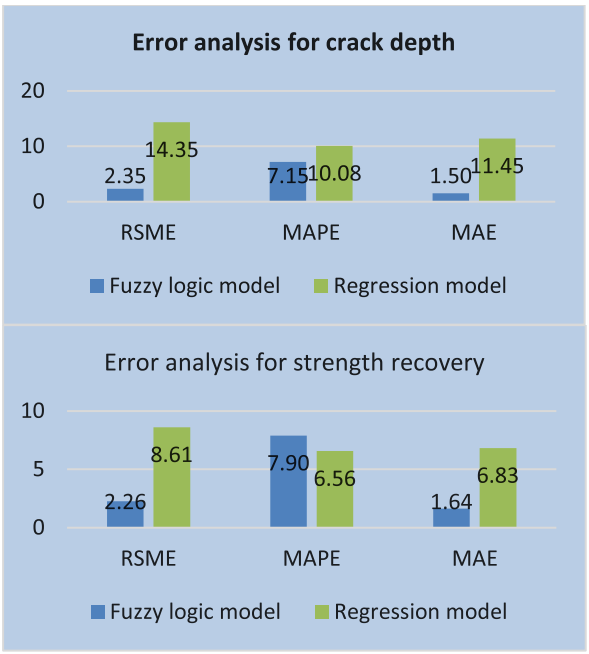

Figure 17. A comparative error analysis for different predictive model for different healing assessments

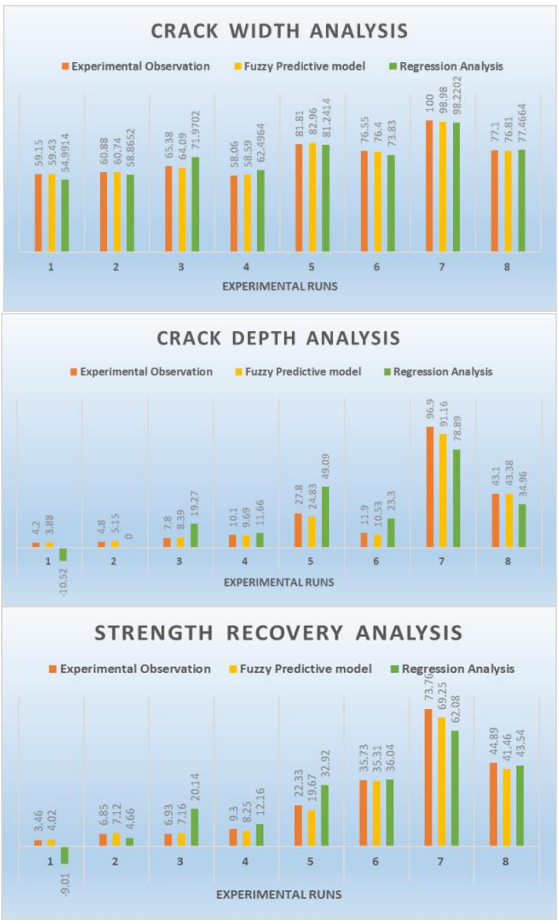

Figure 18. A summarized comparison of healing assessments for different predictive model with actual experimental observations

7. CONCLUSIONS

The study involves the design of a hybrid self-healing composite metallic structure through Fuzzy logic model for predicting the self-healing assessments. The predictive fuzzy model rules were formed between input and output membership function by utilizing S/N ratio using ANOVA analysis for every experimental runs. Further, the error analysis were performed using statistical tool (i.e. RSME, MAPE and MAE) to compare the error associated with fuzzy logic model and linear regression model. The observations drawn from the research are as follows:

1. The fuzzy logic model developed with the formulated S/N ratio has led to an accurate self-healing assessment predictions even with less number of experimental runs. The predictive fuzzy model results may further be improved by increasing the experimental runs for the analysis.
2. Fuzzy logic model has closely predicted the self-healing assessment of various structures with their respective experimental observations. For case study I, an average of about 6.33 % error in prediction of recovery in healing assessments was obtained by implementing fuzzy logic model.
3. For case study I, the comparative error analysis has shown good results for predicting recovery in crack depth compared to linear fit regression model. Based on S/N ratio obtained using ANOVA analysis, rules were formed that limit the large variations output responses range. This helps the domain expert in formulating the precise rules between input and output membership functions and evaluating the healing assessments more accurately.
4. For case study II for all healing assessments, fuzzy rule-based model has proved to be the best predictive model compared with linear regression model. An average error of about 4.94 % for recovery in healing assessments was observed after implementing fuzzy logic model. The error analysis resulted in lower error values for fuzzy model on contrary to higher error using linear regression model.
5. The analysis for case studies were performed for the fixed range of various input parametric design for designing the self-healing composite structure. However, other input parameters influencing the higher self-healing assessments can also be studied experimentally to overcome the limitations in healing of the structure and new predictive fuzzy based model can be formulated. As a future scope, other machine learning based predictive models like Artificial Neural Fuzzy interference system (ANFIS) and artificial neural network (ANN) can be compared simultaneous to analyze the effective design of self-healing composites. Large number of experimental runs generally L27 orthogonal array Taguchi design shall improve the predictability of machine learning based models with less variation in errors.

8. REFERENCES

1. Lancaster J.F. “Non-Ferrous Metals,” in Metallurgy of welding, 3rd ed., J. F. Lancaster, Ed. London: George Allen & Unwin, (1980), 197-222.
2. Grabowski B, Tasan C.C. “Self-Healing Metals,” in Springer International Publishing, (2016), 387-407.
3. Eslami-farsani R., Ebrahimnezhad-khaljiri H. “Smart Epoxy Composites 12. 2 Shape Memory Epoxy Polymers and their,” Wiley-VCH, No. 7, (2021), 349-394.
4. Shlyannikov V. “Nonlinear stress intensity factors in fracture mechanics and their applications,” ***Procedia Structural Integrity***, Vol. 2, (2016), 744-752, doi: 10.1016/j.prostr.2016.06.096.
5. Ghorbani M., Ebrahimnezhad-Khaljiri H., Eslami-Farsani R, et al. “The synergic effect of microcapsules and titanium nanoparticles on the self-healing and self-lubricating epoxy coatings: A dual smart application,” ***Surfaces and Interfaces***, Vol. 23, (2021), 100998, doi: 10.1016/j.surfin.2021.100998.
6. Ebrahimnezhad-Khaljiri H., Eslami-Farsani R. “Experimental investigation of flexural properties of glass fiber–epoxy self-healable composite structures containing capsulated epoxy healing agent and NiCl2(imidazole)4 catalyst,” ***Journal of Industrial Textiles***, Vol. 51, No. 5, (2021), 788-805, doi: 10.1177/1528083719892923.
7. Ghosh S. kumar, "Self-Healing Materials". In: *Wiley VCH*. Epub ahead of print, (2007). doi: 10.1007/978-1-4020-6250-6.
8. Das R., Melchior C., Karumbaiah K.M. “Self-healing composites for aerospace applications,” ***Advanced Composite Materials for Aerospace Engineering***, (2016), 333-364, doi: 10.1016/b978-0-08-100037-3.00011-0.
9. Nosonovsky M. and Rohatgi P.K. "Development of metallic and metal matrix composite self-healing materials.", Biomimetics in Material Science. New York, USA: Springer, (2012), 87-122.
10. Ghosh, S. K. (Ed.)., "Self-healing materials: fundamentals, design strategies, and applications" Vol. 18. Weinheim: Wiley-vch, (2009).
11. Kalista Jr, Stephen J., Thomas C. Ward, and Zainab Oyetunji. "Self-healing of poly (ethylene-co-methacrylic acid) copolymers following projectile puncture." ***Mechanics of Advanced Materials and Structures***, Vol. 14, No. 5, (2007), 391-397, doi: 10.1080/15376490701298819.
12. Scholes F.H., Furman S.A., Hughes A.E., Hughes, T. Nikpour, N. Wright, P. R. Curtis, C. M. Macrae, S. Intem, and A. J. Hill., “Chromate leaching from inhibited primers: Part 1. Characterisation of leaching,” ***Progress in Organic Coatings,*** Vol. 56, No. 1, (2006), 23-32.
13. Rohatgi P.K. “Materials Science & Engineering Al-shape memory alloy self-healing metal matrix composite,” ***Materials Science Engineering: A***, Vol. 619, (2014), 73-76, doi: dx.doi.org/10.1016/j.msea.2014.09.050.
14. Poormir M.A., Mohammad S., Khalili R., "Investigation of the Self-Healing Behavior of Sn-Bi Metal Matrix Composite Reinforced with NiTi Shape Memory Alloy Strips Under Flexural Loading", ***Metal and Polymer Matrix Composites***, Vol. 70, (2018), 806-810.
15. Srivastava V. and Gupta M., “Approach to self healing in Metal matrix Composites: A review,” in Materials Today: Proceedings, Vol. 5, No. 9, (2018), doi: 10.1016/j.matpr.2018.06.332.

16. Poormir M.A., Mohammad S., Khalili R. “Optimal design of a bio-inspired self-healing metal matrix composite reinforced with NiTi shape memory alloy strips,” ***Journal of Intelligent Material Systems and Structures***, Vol. 29, No. 20, (2018), 3972-3982, doi: 10.1177/1045389X18803448.
17. Fisher, Charles R., Hunter B. Henderson, Michael S. Kesler, Pingping Zhu, Glenn E. Bean, M. Clara Wright, John A. Newman, L. Catherine Brinson, Oscar Figueroa III, and Michele V. Manuel. "Repairing large cracks and reversing fatigue damage in structural metals", ***Applied Materials Today***, Vol. 13, (2018), 64-68. doi: 10.1016/j.apmt.2018.07.003.
18. Roy K., Mukherjee A., Jana D.K. “Prediction of maximum oil-yield from almond seed in a chemical industry: A novel type-2 fuzzy logic approach” ***South African Journal of Chemical Engineering,*** Vol. 29, (2019), 1-9, doi: 10.1016/j.sajce.2019.03.001.
19. Srivastava V. and Gupta M. “Experimental assessment of self-healing nature in aluminum-based smart composites with NiTi wires and solder alloy as healing agents through Taguchi approach” ***Journal of Intelligent Material Systems and Structures***, Vol. 31, No. 18, (2020), 2101-2116, doi: 10.1177/1045389X20942846.
20. Srivastava V. and Gupta M. "Experimental assessment of self-healing characteristics in AA2014 matrix with nitinol wire and solder alloy as healing agents", ***Materials Research Express***, Vol. 6, No. 8, (2019) 085704, https://doi.org/10.1088/2053-1591/ab1ee7
21. Srivastava V., Gupta M. "Impact of Post Hardening Mechanism on Self-Healing Assessment of AA2014 Nitinol-Based Smart Composites", ***Metals and Materials International,*** Vol. 27, No. 8, (2021), 2666-2681. doi: 10.1007/s12540-020-00630-y.
22. Srivastava V. and Gupta M. "Parametric Assessments of Self-Healing Characteristics in AA2014–NiTi-Based Metallic Composites through Destructive and Nondestructive Evaluation", ***Russian Journal of Non-destructive Testing,*** (2020), Vol. 56, No. 12, 1064-1082. https://doi.org/10.1134/S1061830920120104
23. Salowitz, N., Correa, A., Santebennur, T., Dorri Moghadam, A., Yan, X., & Rohatgi, P. “Mechanics of nickel–titanium shape memory alloys undergoing partially constrained recovery for self-healing materials,” ***Journal of Intelligent Material Systems and Structures***, Vol. 29, No. 15, (2018), 3025-3036, doi: 10.1177/1045389X18781260.
24. Burke SK. Crack depth measurement using Eddy current NDE. ***Non-destructive Testing Australia,*** Vol. 39, No. 1, (2002), 18-22.
25. Ferguson J.B., Schultz B.F., Rohatgi P.K. “Zinc alloy ZA-8/shape memory alloy self-healing metal matrix composite,” ***Materials Science and Engineering: A***, Vol. 620, (2014), 85-88, doi: 10.1016/j.msea.2014.10.002.
26. Chai T. “Root mean square error (RMSE) or mean absolute error (MAE)?,” ***Geoscientific Model Development Discussions,*** Vol. 7, No. 1, (2014), 1525-1534, doi: 10.5194/gmdd-7-1525-2014.
27. Kurt M., Bagci E., Kaynak Y. “Application of Taguchi methods in the optimization of cutting parameters for surface finish and hole diameter accuracy in dry drilling processes,” ***The International Journal of Advanced Manufacturing Technology,*** Vol. 40, No. 5, (2009), 458-469, doi: 10.1007/s00170-007-1368-2.
28. Zadeh, Lotfi A. "Fuzzy logic—a personal perspective." ***Fuzzy Sets and Systems,*** Vol. 281 (2015), 4-20. https://doi.org/10.1016/j.fss.2015.05.009
29. De Myttenaere, A., Golden, B., Le Grand, B. and Rossi, F., "Mean absolute percentage error for regression models", ***Neurocomputing***, Vol. 192, (2016), 38-48, doi: 10.1016/j.neucom.2015.12.114.
30. Wang W, Lu Y. “Analysis of the Mean Absolute Error (MAE) and the Root Mean Square Error (RMSE) in Assessing Rounding Model,” In IOP Conference Series: Materials Science and Engineering. IOP Publishing. Vol. 324, No. 1, (2018), 012049, doi: 10.1088/1757-899X/324/1/012049.
31. Rouvray DH. "Fuzzy sets and fuzzy logic: Theory and applications", ***Control Engineering Practice***, Vol. 9, No. 4, (1996), 1332-1333. doi: 10.1016/s0160-9327(96)90083-6.
32. Latha B, Senthilkumar VS. “Modeling and analysis of surface roughness parameters in drilling GFRP composites using fuzzy logic,” ***Materials and Manufacturing Processes***, Vol. 25, No. 8, (2010), 817-827, doi: 10.1080/10426910903447261.
33. Das, P.P., Diyaley, S., Chakraborty, S. and Ghadai, R.K. “Multi-objective optimization of wire electro discharge machining (WEDM) process parameters using grey-fuzzy approach,” ***Periodica Polytechnica Mechanical Engineering***, Vol. 63, No. 1, (2019), 16-25, doi: 10.3311/PPme.12167.
34. Khabbaz, R.S., Manshadi, B.D., Abedian, A. and Mahmudi, R. “A simplified fuzzy logic approach for materials selection in mechanical engineering design,” ***Materials & Design***, Vol. 30, No. 3, (2009), 687-697, doi: 10.1016/j.matdes.2008.05.026.
35. Mendel, J.M. "Fuzzy logic systems for engineering: a tutorial." ***Proceedings of the IEEE***, Vol. 83, No. 3, (1995), 345-377.
36. Topçu I.B., Saridemir M. “Prediction of mechanical properties of recycled aggregate concretes containing silica fume using artificial neural networks and fuzzy logic,” ***Computational Materials Science***, Vol. 42, No. 1, 74-82, (2008), doi: 10.1016/j.commatsci.2007.06.011.
37. Sivanandam SN, Sumathi S, Deepa SN. “Introduction to fuzzy logic using MATLAB,” Introd. to Fuzzy Log. using MATLAB Berlin: Springer, Vol. 1, (2007), 1-430, doi: 10.1007/978-3-540-35781-0.
38. Maghzi, P., M. Mohammadi, S. HR Pasandideh, and B. Naderi, “Operating room scheduling optimization based on a fuzzy uncertainty approach and metaheuristic algorithms,” ***International Journal of Engineering, Transactions B: Applications***, Vol. 35, No. 2, (2022), 258-275, doi: 10.5829/IJE.2022.35.02B.01.
39. Nozari H, Tavakkoli-Moghaddam R, Gharemani-Nahr J. “A Neutrosophic Fuzzy Programming Method to Solve a Multi-depot Vehicle Routing Model under Uncertainty during the COVID-19 Pandemic,” I ***International Journal of Engineering, Transactions B: Applications,*** Vol. 35, No. 2, (2022), 360-371, doi: 10.5829/ije.2022.35.02b.12.
40. Azami G, Gholizade Narm H. “Bandwidth management with congestion control approach and fuzzy logic,” ***International Journal of Engineering, Transactions A: Basics,*** Vol. 34, No. 4, (2021), 891-900, doi: 10.5829/ije.2021.34.04a.15.

Persian Abstract

چکیده

ایده ای برای ترمیم سطح آسیب دیده از طریق عوامل ترمیم کننده در کامپوزیت فلزی در مرحله توسعه است. بنابراین، انتخاب پارامترهای طراحی برای نسل جدید کامپوزیت هوشمند پیچیده تر و دشوارتر است. در مطالعه حاضر، دو مطالعه موردی در مورد سازه های هوشمند خود ترمیم شونده با پارامترهای طراحی ورودی مختلف برای ارزیابی خواص درمانی گنجانده شده است. آزمایش‌های L-8 مبتنی بر تاگوچی برای تجزیه و تحلیل پارامترهای تأثیرگذار مسئول ارزیابی‌های خود ترمیمی بالاتر (یعنی بازیابی در عرض ترک، بازیابی در عمق ترک و بازیابی مقاومت خمشی) انجام شد. برای ارزیابی ارزیابی های خود ترمیمی سازه آسیب دیده، یک تکنیک محاسباتی نرم افزار بر اساس نسبت S/N از تجزیه و تحلیل ANOVA به دست می آید. نتایج تجربی بیشتر برای ساخت مدل پیش‌بینی منطق فازی در نظر گرفته شد. مدل‌های رگرسیون خطی، یعنی یک ابزار آماری برای قضاوت در مورد دقت مدل پیش‌بینی‌شده مبتنی بر فازی از طریق تحلیل‌های خطای مختلف، تولید می‌شود. بر اساس مدل منطق فازی نسبت S/N، نتایج مقادیر خطای کمتری ٦.٣٣ و ٤.٩٤ درصد را برای مطالعات موردی I و II در مقایسه با مدل رگرسیون اقتباس شده برای همه ارزیابی‌های خود درمانی نشان می‌دهند. این مدل شباهت نزدیکی با مشاهدات تجربی حتی با تعداد کمتری از اجراهای آزمایشی ارائه می دهد. این نتیجه می‌گیرد که مدل منطق فازی یک ابزار محاسباتی نرم افزار قدرتمند برای انجام کارهای تحقیقاتی بزرگ مربوط به طراحی پارامترهای ورودی برای سازه‌های کامپوزیت خود ترمیم شونده مبتنی بر فلز در آینده نزدیک فراهم می‌کند.

International Journal of Engineering

Journal Homepage: www.ije.ir

Empowering Face Recognition Methods using a GAN-based Single Image Super-Resolution Network

M. B. Shahbakhsh, H. Hassanpour*

Computer Engineering and IT Department, Shahrood University of Technology, Shahrood, Iran

PAPER INFO

Paper history:
Received 30 April 2022
Received in revised form 06 June 2022
Accepted 07 June 2022

Keywords:
Face Recognition
Super-Resolution
Face Hallucination
Residual Self-attention
Generative Adversarial Network
Identity Preserving

ABSTRACT

Face recognition is one of the most common authentication techniques widely used due to its easy access. In many face recognition applications, captured images are often of low resolution. Face recognition methods perform poorly on low resolution images because they are trained on high resolution face images. Although existing face hallucination methods may generate visually pleasing images, they cannot improve the performance of face recognition methods at low resolution as the structure of the face image and high-frequency details are not sufficiently preserved. Recent advances in deep learning have been used in this paper to propose a new face super-resolution approach to empower face recognition methods. In this paper, a Generative Adversarial Network is used to empower face recognition in low-resolution images. This network considers image edges and reconstructs high-frequency details to preserve the face structure. The proposed technique to generate super-resolved features is usable in any face recognition method. We have used some state-of-the-art face recognition methods to evaluate the proposed method. The results showed a significant impact of the proposed method on the accuracy of face recognition of low resolution images.

doi: *10.5829/ije.2022.35.10a.05*

1. INTRODUCTION

Among the biometric techniques available for authentication, face recognition is widely used due to its simplicity of use, easy access, and the possibility of using it at long distances and secretly [1]. Face recognition is one of the primary research fields in computer vision and plays an essential role in machine learning. Video surveillance, access control of buildings, criminal identification, and self-driving cars are just a few applications of face recognition systems.

Despite recent advances, face recognition still has challenges such as obstruction, angle and brightness changes, resolution, and other factors. For example, in areas where Closed-Circuit Television (CCTV) cameras are used for surveillance, cropped face images usually have breakdowns such as blur and noise [2]. Also, the extracted face images may not have a suitable resolution due to the person's distance from the camera. In this problem, we encounter the challenge of recognizing faces in uncontrolled conditions and using low-resolution (LR) images.

Face recognition techniques based on deep neural networks have recently attained accuracy nearby human performance. Some are even more accurate than humans [3-5]. Advanced convolutional neural networks (CNNs) such as FaceNet [5], DeepFace [4], ArcFace [6], and VGGFace [7] have achieved extraordinary recognition performance in the Wild (LFW) database on Labeled Faces [8]. Alexnet-based Deep-Face [4] achieved 97.35% accuracy for labeled face images in the Wild (LFW) database. After that, VGGFace, based on VGG-16 [7], achieved 98.95% accuracy, and in 2018, Arc Face [6] reached the highest accuracy, 99.83%. Recently, state-of-the-art methods have used ResNet instead of visual geometry (VGG) because of its better performance and lower memory consumption [9]. These neural networks are trained on large datasets containing high-resolution (HR) images [10-14], including facial expressions and pose changes. Several factors affect the accuracy of face recognition methods, such as poses,

*Corresponding Author Institutional Email: h.hassanpour@shahroodut.ac.ir (H. Hassanpour)

Please cite this article as: M. B. Shahbakhsh, H. Hassanpour, Empowering Face Recognition Methods using a GAN-based Single Image Super-Resolution Network, ***International Journal of Engineering, Transactions A: Basics***, Vol. 35 No. 10, (2022), 1858-1866

brightness, and image resolution. It has been shown that one of the factors influencing the performance of face recognition is image resolution. [15, 16]. Face recognition accuracy decreases rapidly with reducing image resolution [17, 18]. Hence, face recognition with LR images remains a demanding problem [19].

Smaller images with lower resolution have less information than higher resolution images. Image super-resolution (SR) methods have been presented to increase image resolution and details [20, 21]. The LR image is mapped to an HR space for training the recognition model. For example, a deep SR method C-SRIP (cascaded SR and identity priors) was proposed by Grm et al. [20], with three cascading SR networks by a 2x SR factor including identity priorities in learning. Cascading SR networks are based on CNNs. Banerjee and Das [22] introduced a deep neural network based on generative adversarial networks (GANs) [23] to reconstruct more realistic face images from LR face inputs. Likewise, Zangeneh et al. [24] proposed a two-section deep convolutional model, Feature extraction convolutional neural network (FECNN) and SR-FECNN, for mapping HR and LR images into joint space for recognition. The SR network contains a five-layer CNN to enhance the LR input image, and FECNN is a VGG-16 pre-trained without the last two fully connected layers. These two pre-trained networks are connected and jointly trained again to minimize the loss function and reduce the distance between LR and HR paired in the common space. The LR image needs to have a fixed input size in this method. Another type of SR method is feature super-resolution (FSR) [25]. This kind of SR method increases the image resolution on the feature level. In 2018, Tan et al. [25] proposed an FSR-GAN neural network to enhance recognition accuracy and reduce training costs. They designed a GAN network to generate HR features from the LR features. This module has a simple structure with low training costs.

Face recognition accuracy will be severely reduced if the input image is distorted and noisy or the target is far from the camera. Especially in a large database, the face recognition model errs in distinguishing features. Previous works have used various methods like clustering [26] and hashing [27] to increase face recognition accuracy in uncontrolled conditions. These methods work well on a large dataset problem and the angularity of faces. Nevertheless, the remaining challenge in these methods is the LR input image as the features and facial components will not be distinguishable [28, 29].

In this paper, we proposed a GAN-based network to increase the resolution at the feature level. The face recognition methods can distinguish facial components more accurately using the proposed method. Many face hallucination methods generate visually desirable face images, but the accuracy of face recognition is lower than anticipated with the generated images. Because the face structure and its high-frequency details are not well preserved [30]. This paper proposes a new generative adversarial network with self-attention to reconstruct the high-frequency details. The proposed method to generate SR features is applicable in any face recognition method.

The main contributions of this paper include:

- A GAN structure is proposed to empower face recognition at LR images. This network considers image edges and restores high-frequency details to preserve the face structure.
- A self-attention mechanism is used residually to employ both global and local features. Super-resolving global and local features improve the accuracy of face recognition methods.

2. RELATED WORKS

After Dong et al. introduced the Super-Resolution Convolutional Neural Network (SRCNN) [31], the use of deep learning techniques for single image SR became widely considered. Further advances in network architectures [32] and upsampling techniques [33] help others improve quantitative and qualitative results. Wang et al. [34] expressed a deeper study of the developments in this area.

Deeper models with more layers have been shown to perform sufficiently in several tasks, including super-resolving [35]. The first extremely deep model for SR tasks is the VDSR model [36]. This model employs VGG architecture with 20 layers. This network also uses multi-scale and SR in a residual way. LR images are super-resolved in several scales by reconstructing the high-frequency details and adding them to the output of bicubic interpolation. In order to decrease the VDSR parameters, the DRCN model was introduced [37]. A recursive convolutional layer has been used 16 times in the DRCN model. A multi-supervised learning strategy has been deployed to devastate the tribulation of training this network. Since ResNet has surpassed the VGG model in several tasks, it was a good choice for the SR task [9]. SRResNet has been proposed for SR as the first ResNet model [32]. This network uses 16 residual blocks with batch normalization for stabilizing the training process. Lee et al. proposed EDSR, one of the most advanced models for general SR [38]. EDSR and SRResNet have several primary differences. In the EDSR, the batch normalization layers are deleted, the weights are initialized for a very large-scale SR, and the number of output features is increased.

Although general SR methods can be used on face images, there are techniques to take advantage of the unique features of face images [39]. The face

components distortion is the main obstacle in a face SR process. Several methods utilized facial landmarks or used facial priors to address this problem. For example, a network has been proposed in FSRNet [39] to extract the facial landmark heatmaps and estimate the priors. In the FSRNet method, the prior details are extracted using an Hour Glass (HG) [40] model to produce roughly super-resolved face images. Then, in the encoder network, the prior heatmaps are joined with feature maps. Eventually, a decoder network uses these feature maps to produce a super-resolved face image. Kim et al. [41], proposed a face alignment model to compare the super-resolved and ground-truth images' facial heatmaps. A pre-trained HG network is used with an MSE (Mean Squared Error) loss function. However, landmarks must be labeled in the HG network, which has a high computational cost.

3. PROPOSED METHOD

One of the shortcomings in most SR methods is their inability to preserve the overall structure of the face image as they focus on the local features using interconnected convolutional layers. In this paper, we intend to use both global and local features to properly reconstruct high-frequency details and essential features of the face image. Extracting the edges of the face image using the Local Binary Pattern (LBP) [42] and Unsharp Masking (UM) [43] techniques and then adding them to the input image as a preprocessing can help the proposed model to accurately extract the high-frequency information of the LR image. In addition, we use the Self-Attention mechanism residually to retrieve face components correctly. We also use an edge extraction network and its associated loss function to preserve the structure of the face image. Finally, the super-resolved features generated by the proposed model are transferred to the face recognition method to perform the recognition operation.

3. 1. Preprocessing Edge information plays an essential role in preserving the structure of the face image and retrieving high-frequency information. To better retrieve the high-frequency details of the face image, we must properly use the edges from the LR image. In addition, the use of LR image texture and its delicate edges are essential in preserving the structure. In this paper, we use some widely used methods such as UM and LBP to enhance the edges of LR images in preprocessing. In this section, the delicate edges and texture of the image are extracted by the LBP method and then added to the input image. Finally, all the edges of the LR image are sharpened using UM. Figure 1 shows an example of adding LBP output to an input image. The effect of λ, the gain factor of the filter in UM, is shown in Figure 2. The extracted high-frequency details are scaled with λ. Then, these details are added to the input face image.

Following the results shown in Figure 2, λ = 20 is chosen because the image details are more enhanced.

3. 2. Network Structure In this paper, we used a GAN model for super-resolving face images. GAN is a deep learning network that includes two networks called generator and discriminator. These two networks are in a zero-sum game [44].

3. 2. 1. Generator Network The overall structure used for training the generator network is shown in Figure 3. The proposed generator structure supper-resolves the input image up to 8x. Two convolutional

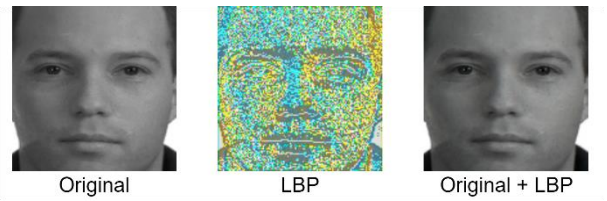

Figure 1. Adding LBP output to an input image

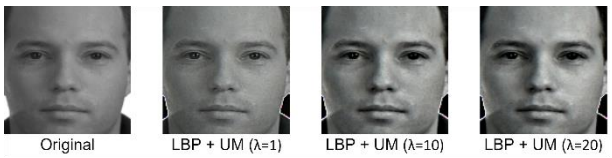

Figure 2. The effects of applying LBP and UM with different values of λ

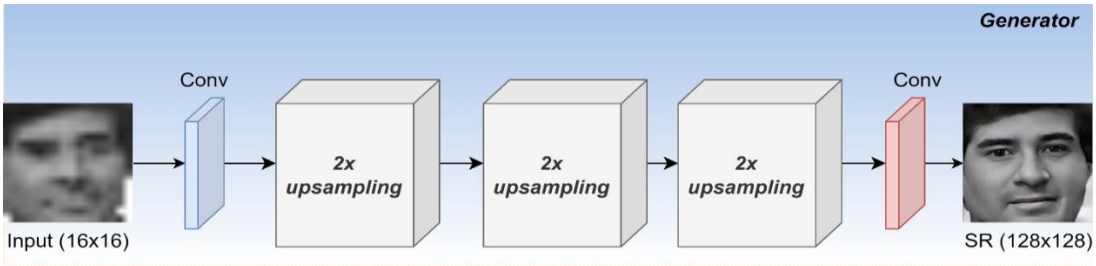

Figure 3. The overall structure used for training the proposed generator network

layers are placed at the end and beginning of the proposed generator structure. The first convolution layer has a 3×3 filter with stride one, and 512 output channels. The final 3×3 convolutional layer generates the output image.

Since this research aims not to generate an RGB super-resolved face image, the last 3×3 convolutional layer is only in the training section. This layer is removed from the network when combining the proposed method with the face recognition classifier. The combination of the face recognition classifiers with the proposed method is shown in Figure 4. The structure of the "2x upsampling" section is shown in Figure 5.

As shown in Figure 5, the 2x upsampling structure consists of a residual self-attention block, a residual block, an edge block, and a transposed convolutional block. The convolution kernel and original features are used in convolutional layers to compute the output features. The output feature map is usually local and limited. Therefore, we have used a residual self-attention mechanism to extract global and context information. Self-attention mechanism enhances the valuable features and learns each feature channel's weights by data-driven learning.

In summary, in the proposed 2x upsampling structure in Figure 5, the residual self-attention block extracts global features, and simultaneously, local features are extracted in the residual block. Finally, all global and local features are combined. The residual block has two convolution layers followed by two Rectifier Linear Unit (ReLU) activation functions. The convolutional kernel in all residual blocks is 3×3, and in the first 2x upsampling block, the number of filters is set to 512, in the second one 256, and 64 for the third one.

In the residual self-attention block, the combined feature map received from previous layers is first converted into two new feature spaces called *f* and *g*. Then the attention map is calculated by a softmax operation. The *h* channel normalizes the correlation between each pixel and all other position pixels in the feature maps. Finally, a 1×1 convolution layer is used. The output feature maps from the residual self-attention block and residual block are combined cascade-wise, and the transposed convolution layer is used for the 2x upsampling operation. We also used a ReLU activation function in transposed convolution layer.

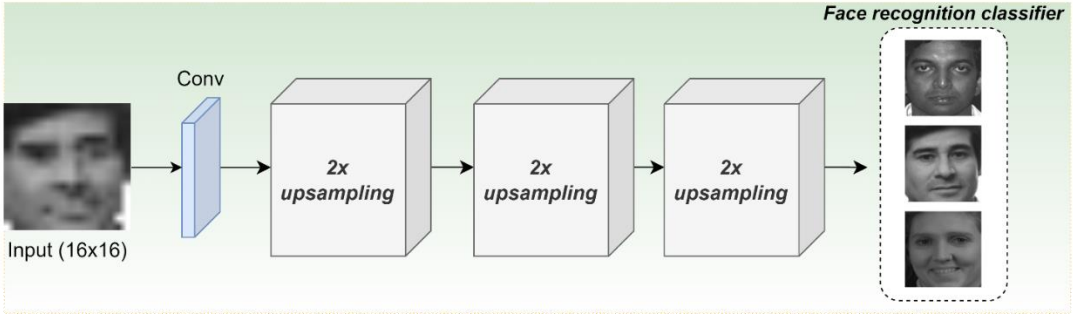

Figure 4. The combination of the face recognition classifier with the proposed method

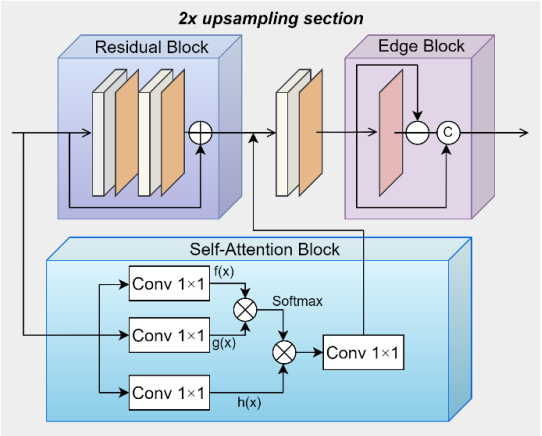

Figure 5. The proposed structure for the generator 2x upsampling in Figure 4

After upsampling feature maps using the transposed convolutional layer, to preserve the structure of the face image, the edge block is used to extract high-frequency details and sharpen edge information. We have used an average pooling layer in the edge block, followed by a 1×1 convolution layer. The smooth features extracted by the average pooling layer are subtracted from the main feature map to extract high-frequency details. Then, the extracted high-frequency information are concatenated with the original feature map to enhance the result and preserve the structure. As shown in Figure 3, the 2x upsampling operation is performed three times on an LR input image.

3. 2. 2. Discriminator Network In the proposed discriminator network, we used seven convolution

layers with Leaky Relu followed by a fully connected layer. The kernel size for convolution layers is 3×3, and filters are set to 128, 256, and 512.

3. 3. Loss Functions In this research, we have used several loss functions to train the proposed generator network. Each loss function compares the generated face image with the ground-truth face image from different aspects, and finally, the sum of these functions is applied to the gradient as a total loss.

3. 3. 1. Context Loss We have used the pixel-wise MSE function to decrease the distance between the ground truth and generated image. The MSE loss function is defined as:

$$L_{context} = \frac{1}{wh}\sum_{c=1}^{RGB}\sum_{x=1}^{w}\sum_{y=1}^{h}\|I_{GT}(x,y) - G(I_{LR})(x,y)\|^2 \quad (1)$$

where I_{GT} is the ground truth image, I_{LR} is the LR image, and c is RGB channels.

3. 3. 2. Edge Loss As mentioned in the previous sections, edge information is essential in preserving image structure. We have dealt with this issue both in preprocessing and the generator network. To train the model, preserve the structure, and optimal use of edges and high-frequency information, in this section, we define a loss function that compares the edges obtained from the edge block with the edges extracted by the Canny method. The edge block loss function is defined as:

$$L_{edge} = \frac{1}{r^2wh}\sum_{x=1}^{rw}\sum_{y=1}^{rh}\|C(I_{GT})(x,y) - E(I_{LR})(x,y)\|^2 \quad (2)$$

where r is the scaling factor, set to be 1, 2, and 4, C is the Canny edge detector method, and E is our edge extraction block.

3. 3. 3. GAN Loss As mentioned before, we utilize a GAN structure to generate more realistic super-resolved images. The GAN loss is defined as:

$$L_{GAN} = \mathbb{E}[\log D(I_{GT})] - \mathbb{E}[\log(1 - D(G(I_{LR})))] \quad (3)$$

where $\mathbb{E}$ is the probability distribution expectation, and D is the discriminator network.

3. 3. 4. Luminance Loss RGB domain is the most common image representation format used in image application researches. In face hallucination, several state-of-the-art methods have used RGB format with MSE loss function to compare the distance between output image and ground truth. However, the YUV domain is another popular representation format widely used in image processing; and following the results reported in literature [45], the YUV color space is better than the RGB format in terms of perceptually quality. In addition, the RGB format has details that combine chrominance and luminance components, which yields redundancy to color shift, color distortion, and channel information. We used the Luminance distance to reduce the above effects and generate enhanced SR images, which converted RGB format to YUV format to independently distribute illumination and color components.

3. 3. 5. Identity Loss Pixel distance is unreliable for comparing images on fidelity and diversity. For example, suppose a pixel is moved in the generated image. The difference is not evident in an HR image with millions of pixels. However, the absolute difference will be huge based on the pixel distance. One alternative is to compare images at the higher-level features instead of the pixels. Higher-level semantic information is less sensitive to small changes.

In this paper, to compare the high-level features of generated and ground truth images, we used the pre-trained Inception V3 network to extract class-encoded vectors. We used the last pooling layer of the Inception V3 network prior to the output classification to extract features. The covariance and mean of the images are calculated, and activations are summarized as multivariate Gaussian. Then the statistics are computed for activations across generated and ground truth images. Finally, the distance between two obtained distributions is calculated using the Frechet distance. The identity loss is defined as:

$$Identity\ loss = \|\mu_x - \mu_y\|^2 + Tr(\sum x + \sum y - 2\sqrt{\sum x \sum y}) \quad (4)$$

where μ_x and μ_y are the feature-wise mean of the ground truth and generated images, respectively. Including 512 element vectors where each element is the mean feature perceived across the images, $\sum x$ and $\sum y$ are the covariance matrices for the generated and ground truth feature vectors. $Tr()$ represents the trace linear algebra operation.

3. 3. 6. Total Loss Eventually, all loss functions are aggregated. Therefore, the total loss is as follows:

$$L_T = L_{Context} + \alpha L_{Edge} + \beta L_{GAN} + L_{Luminance} + \gamma L_{Identity} \quad (5)$$

where α, β, and γ are weight coefficients.

4. EXPERIMENTS AND DISCUSSION

In this section, we first introduce the datasets used to train the proposed SR network. The implementation details of the proposed method are then explained. Finally, we will discuss the effect of the proposed approach on face recognition accuracy.

4. 1. Datasets In this paper, for the training section, 990 face images from the FERET [46] Frontal (fa) collection are employed, along with images from several standard datasets such as MUCT [47], FEI [48], Face94, Psychological Image Collection at Stirling (PICS), and in total there are 1684 images in this part of training data. The CelebA [49] is a celebrities' face dataset with more than 0.2 million face images. We used 174,400 face images in the training set and 21,230 images in the test set.

To evaluate the impact of the proposed method on face recognition accuracy, we used 990 images from the frontal set (Fa) of the FERET dataset for the training section, and their related Fb images were used for testing.

4. 2. Implementation Details As mentioned in the preprocessing section, first, LBP features are extracted from the LR image and added to the input image. Since we intend to extract high-frequency details, texture, and delicate edges of the input image, the LBP technique is used in "uniform" mode with 8 points and a radius of 1. After extracting these details and adding them to the input image, we used the UM technique to sharpen all the edges of the input image. To improve the network performance and make the high-frequency details clearer, based on the results presented in Figure 2, we employed λ=20 in the UM method.

As shown in Figure 3, the input of the proposed generator network is a 16×16 LR image, which is super-resolved to 128 × 128. For training the network, we used Adam optimizer with a learning rate of 0.0001, epsilon = 1e-07, $\beta_1 = 0.5$, and $\beta_2 = 0.999$ in both generator and discriminator networks. All codes were written in Python 3.7, and we used Tensorflow 2. We have used a GeForce GTX 3060 GPU for network training and evaluation. As mentioned before, we do not intend to generate the final RGB super-resolved image to recognize the face. Therefore, the final layer is removed in combining the proposed method with a face recognition method, and the super-resolved features are given to the face recognition method.

4. 3. Super-resolution Results This research aims not to generate HR images at the output but to demonstrate the performance of the proposed method in super-resolving facial images. We compared the proposed method with several state-of-the-art face SR methods such as EIPNet [50] and GFP-GAN [51]. Qualitative comparison results are shown in Figure 6.
As shown in Figure 6, the structure of the generated images with the proposed method is well preserved due to the use of high-frequency details in different stages.

4. 4. Face recognition Results The purpose of face hallucination is to improve facial recognition accuracy. Many face SR methods generate eye-catching face images. However, when they are used in a face recognition method, the accuracy is not as expected. Because they produce new details instead of preserving the original structure of the LR image. In this section, we intend to examine the effect of LR face images on some of the newest face recognition methods, such as Nikan [52], Face Net [53], VGG Face [54], and Arc Face [6]. Then we showed the effect of using the proposed method compared to several state-of-the-art super-resolution methods on increasing face recognition accuracy. Therefore, we perform our experiments on several state-of-the-art SR methods, such as DFDNet [55], EIPNet [50], and GFP-GAN [51]. Table 1 compares the accuracy of some face recognition methods using the proposed method versus other SR methods. As shown in Table 1, the proposed method performs better than other SR methods in face recognition.

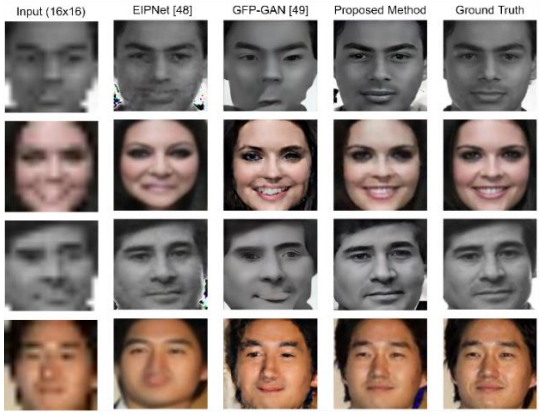

Figure 6. Qualitative comparison of SR images obtained using several state-of-the-art methods

TABLE 1. Face recognition accuracy comparison of the proposed method with state-of-the-art methods on LR images

		Super-resolution (%)						
		Original (128×128)	**LR (16×16)**	**Bicubic**	**DFDNet** [55]	**EIPNet** [50]	**GFPGAN** [51]	**Proposed method**
Face Recognition	**Nikan** [52]	92.7	3.1	9.32	41.8	49.04	26.32	**71.84**
	Face Net [53]	98.93	0.11	0.05	42.40	56.92	28.18	**75.09**
	VGG Face [54]	99.10	8.31	10.15	64.41	66.13	34.07	**79.51**
	Arc Face [6]	98.82	2.85	3.02	52.96	63.22	27.28	**76.89**

5. CONCLUSION

In this paper, we proposed a GAN-based network to increase the image resolution at the feature level and improve the accuracy of face recognition methods. The results provided in this paper indicate that a face recognition method can distinguish facial components more accurately using the proposed method. Many face super-resolution methods generate visually pleasant face images, but face recognition accuracy is lower than expected with their generated images. Because the structure of the face image and its high-frequency details are not well preserved. The proposed network considers the image's edges and restores high-frequency details to preserve the face's structure. The generated super-resolved features can be used in any face recognition method to improve the accuracy of recognition.

6. REFERENCES

1. Kortli, Y., Jridi, M., Al Falou, A. and Atri, M., "Face recognition systems: A survey", ***Sensors***, Vol. 20, No. 2, (2020), 342. doi: 10.3390/s20020342.
2. Annalakshmi, M., Roomi, S. and Naveedh, A.S., "A hybrid technique for gender classification with slbp and hog features", ***Cluster Computing***, Vol. 22, No. 1, (2019), 11-20. doi: 10.1007/s10586-017-1585-x.
3. Yang, W., Gao, H., Jiang, Y., Yu, J., Sun, J., Liu, J. and Ju, Z., "A cascaded feature pyramid network with non-backward propagation for facial expression recognition", ***IEEE Sensors Journal***, Vol. 21, No. 10, (2020), 11382-11392. doi: 10.1109/JSEN.2020.2997182.
4. Taigman, Y., Yang, M., Ranzato, M.A. and Wolf, L., "Deepface: Closing the gap to human-level performance in face verification", in Proceedings of the IEEE conference on computer vision and pattern recognition. (2014), 1701-1708.
5. Schroff, F., Kalenichenko, D. and Philbin, J., "Facenet: A unified embedding for face recognition and clustering", in Proceedings of the IEEE conference on computer vision and pattern recognition, (2015), 815-823.
6. Deng, J., Guo, J., Xue, N. and Zafeiriou, S., "Arcface: Additive angular margin loss for deep face recognition", in Proceedings of the IEEE/CVF conference on computer vision and pattern recognition, (2019), 4690-4699.
7. Parkhi, O.M., Vedaldi, A. and Zisserman, A., "Deep face recognition", (2015).
8. Huang, G.B., Mattar, M., Berg, T. and Learned-Miller, E., "Labeled faces in the wild: A database forstudying face recognition in unconstrained environments", in Workshop on faces in'Real-Life'Images: detection, alignment, and recognition, (2008).
9. He, K., Zhang, X., Ren, S. and Sun, J., "Deep residual learning for image recognition", in Proceedings of the IEEE conference on computer vision and pattern recognition, (2016), 770-778.
10. Taigman, Y., Yang, M., Ranzato, M.A. and Wolf, L., "Web-scale training for face identification", in Proceedings of the IEEE conference on computer vision and pattern recognition, (2015), 2746-2754.
11. Cao, Q., Shen, L., Xie, W., Parkhi, O.M. and Zisserman, A., "Vggface2: A dataset for recognising faces across pose and age", in 2018 13th IEEE international conference on automatic face & gesture recognition (FG 2018), IEEE. (2018), 67-74. doi: 10.1109/FG.2018.00020.
12. Guo, Y., Zhang, L., Hu, Y., He, X. and Gao, J., "Ms-celeb-1m: A dataset and benchmark for large-scale face recognition", in European conference on computer vision, Springer. (2016), 87-102. doi: 10.1007/978-3-319-46487-9_6.
13. Yi, D., Lei, Z., Liao, S. and Li, S.Z., "Learning face representation from scratch", arXiv preprint arXiv:1411.7923, (2014). doi: 10.48550/arXiv.1411.7923.
14. Lui, Y.M., Bolme, D., Draper, B.A., Beveridge, J.R., Givens, G. and Phillips, P.J., "A meta-analysis of face recognition covariates", in 2009 IEEE 3rd International Conference on Biometrics: Theory, Applications, and Systems, IEEE. (2009), 1-8. doi: 10.1109/BTAS.2009.5339025.
15. Zou, W.W. and Yuen, P.C., "Very low resolution face recognition problem", ***IEEE Transactions on Image Processing***, Vol. 21, No. 1, (2011), 327-340. doi: 10.1109/TIP.2011.2162423.
16. Van Ouwerkerk, J., "Image super-resolution survey", ***Image and Vision Computing***, Vol. 24, No. 10, (2006), 1039-1052. doi: 10.1016/j.imavis.2006.02.026.
17. Wu, J., Ding, S., Xu, W. and Chao, H., "Deep joint face hallucination and recognition", arXiv preprint arXiv:1611.08091, (2016). doi: 10.48550/arXiv.1611.08091.
18. Lu, Z., Jiang, X. and Kot, A., "Deep coupled resnet for low-resolution face recognition", ***IEEE Signal Processing Letters***, Vol. 25, No. 4, (2018), 526-530. doi: 10.1109/LSP.2018.2810121.
19. Luevano, L.S., Chang, L., Méndez-Vázquez, H., Martínez-Díaz, Y. and González-Mendoza, M., "A study on the performance of unconstrained very low resolution face recognition: Analyzing current trends and new research directions", ***IEEE Access***, Vol. 9, \ (2021), 75470-75493. doi: 10.1109/ACCESS.2021.3080712.
20. Grm, K., Scheirer, W.J. and Štruc, V., "Face hallucination using cascaded super-resolution and identity priors", ***IEEE Transactions on Image Processing***, Vol. 29, (2019), 2150-2165. doi: 10.1109/TIP.2019.2945835.
21. Seyyedyazdi, S. and Hassanpour, H., "Super-resolution of defocus blurred images", ***International Journal of Engineering, Transactions A: Basics***, Vol. 33, No. 4, (2020), 539-545. doi: 10.5829/ije.2020.33.04a.04.
22. Banerjee, S. and Das, S., "Lr-gan for degraded face recognition", ***Pattern Recognition Letters***, Vol. 116, (2018), 246-253. doi: 10.1016/j.patrec.2018.10.034.
23. Creswell, A., White, T., Dumoulin, V., Arulkumaran, K., Sengupta, B. and Bharath, A.A., "Generative adversarial networks: An overview", ***IEEE Signal Processing Magazine***, Vol. 35, No. 1, (2018), 53-65. doi: 10.1109/MSP.2017.2765202.
24. Zangeneh, E., Rahmati, M. and Mohsenzadeh, Y., "Low resolution face recognition using a two-branch deep convolutional neural network architecture", ***Expert Systems with Applications***, Vol. 139, (2020), 112854. doi: 10.1016/j.eswa.2019.112854.
25. Tan, W., Yan, B. and Bare, B., "Feature super-resolution: Make machine see more clearly", in Proceedings of the IEEE Conference on Computer Vision and Pattern Recognition. (2018), 3994-4002.
26. Abbaspoor, N. and Hassanpour, H., "Face recognition in a large dataset using a hierarchical classifier", ***Multimedia Tools and Applications***, (2022), 1-19. doi: 10.1007/s11042-022-12382-5

27. Hassanpour, H. and Ghasemi, M., "A three-stage filtering approach for face recognition", ***International Journal of Engineering*, *Transactions B: Applications*** Vol. 34, No. 8, (2021). doi: 10.5829/ije.2021.34.08b.06.
28. Dey, A. and Dasgupta, K., "Emotion recognition using deep learning in pandemic with real-time email alert", in Proceedings of Third International Conference on Communication, Computing and Electronics Systems, Springer. (2022), 175-190. doi: 10.1007/978-981-16-8862-1_13.
29. Chaabane, S.B., Hijji, M., Harrabi, R. and Seddik, H., "Face recognition based on statistical features and svm classifier", ***Multimedia Tools and Applications***, Vol. 81, No. 6, (2022), 8767-8784. doi: 10.1007/s11042-021-11816-w.
30. Shahbakhsh, M.B. and Hassanpour, H., "Enhancing face super-resolution via improving the edge and identity preserving network", in 2021 7th International Conference on Signal Processing and Intelligent Systems (ICSPIS), IEEE, (2021), 1-4. doi: 10.1109/ICSPIS54653.2021.9729372.
31. Dong, C., Loy, C.C., He, K. and Tang, X., "Learning a deep convolutional network for image super-resolution", in European conference on computer vision, Springer, (2014), 184-199. doi: 10.1007/978-3-319-10593-2_13.
32. Ledig, C., Theis, L., Huszár, F., Caballero, J., Cunningham, A., Acosta, A., Aitken, A., Tejani, A., Totz, J. and Wang, Z., "Photo-realistic single image super-resolution using a generative adversarial network", in Proceedings of the IEEE conference on computer vision and pattern recognition, (2017), 4681-4690.
33. Shi, W., Caballero, J., Huszár, F., Totz, J., Aitken, A.P., Bishop, R., Rueckert, D. and Wang, Z., "Real-time single image and video super-resolution using an efficient sub-pixel convolutional neural network", in Proceedings of the IEEE conference on computer vision and pattern recognition, (2016), 1874-1883.
34. Wang, Z., Chen, J. and Hoi, S.C., "Deep learning for image super-resolution: A survey", ***IEEE Transactions on Pattern Analysis and Machine Intelligence***, Vol. 43, No. 10, (2020), 3365-3387. doi: 10.1109/TPAMI.2020.2982166.
35. Montufar, G.F., Pascanu, R., Cho, K. and Bengio, Y., "On the number of linear regions of deep neural networks", ***Advances in Neural Information Processing Systems***, Vol. 27, (2014).
36. Kim, J., Lee, J.K. and Lee, K.M., "Accurate image super-resolution using very deep convolutional networks", in Proceedings of the IEEE conference on computer vision and pattern recognition, (2016), 1646-1654.
37. Kim, J., Lee, J.K. and Lee, K.M., "Deeply-recursive convolutional network for image super-resolution", in Proceedings of the IEEE conference on computer vision and pattern recognition, (2016), 1637-1645.
38. Lim, B., Son, S., Kim, H., Nah, S. and Mu Lee, K., "Enhanced deep residual networks for single image super-resolution", in Proceedings of the IEEE conference on computer vision and pattern recognition workshops, (2017), 136-144.
39. Chen, Y., Tai, Y., Liu, X., Shen, C. and Yang, J., "Fsrnet: End-to-end learning face super-resolution with facial priors", in Proceedings of the IEEE Conference on Computer Vision and Pattern Recognition, (2018), 2492-2501.
40. Newell, A., Yang, K. and Deng, J., "Stacked hourglass networks for human pose estimation", in European conference on computer vision, Springer, (2016), 483-499. doi: 10.1007/978-3-319-46484-8_29.
41. Kim, D., Kim, M., Kwon, G. and Kim, D.-S., "Progressive face super-resolution via attention to facial landmark", arXiv preprint arXiv:1908.08239, (2019). doi: 10.48550/arXiv.1908.08239.
42. Pavithra, L. and Sharmila, T.S., "An efficient framework for image retrieval using color, texture and edge features", ***Computers & Electrical Engineering***, Vol. 70, (2018), 580-593. doi: 10.1016/j.compeleceng.2017.08.030
43. Mortezaie, Z., Hassanpour, H. and Asadi Amiri, S., "An adaptive block based un-sharp masking for image quality enhancement", ***Multimedia Tools and Applications***, Vol. 78, No. 16, (2019), 23521-23534. doi: 10.1007/s11042-019-7594-4
44. Liu, H., Zheng, X., Han, J., Chu, Y. and Tao, T., "Survey on gan-based face hallucination with its model development", ***IET Image Processing***, Vol. 13, No. 14, (2019), 2662-2672. doi: 10.1049/iet-ipr.2018.6545.
45. Podpora, M., Korbas, G.P. and Kawala-Janik, A., "Yuv vs rgb-choosing a color space for human-machine interaction", in FedCSIS (Position Papers), (2014), 29-34. doi: 10.15439/2014F206.
46. Phillips, P.J., Moon, H., Rizvi, S.A. and Rauss, P.J., "The feret evaluation methodology for face-recognition algorithms", ***IEEE Transactions on Pattern Analysis and Machine Intelligence***, Vol. 22, No. 10, (2000), 1090-1104. doi: 10.1109/34.879790.
47. Milborrow, S., Morkel, J. and Nicolls, F., "The muct landmarked face database", ***Pattern Recognition Association of South Africa***, Vol. 201, (2010).
48. Thomaz, C.E. and Giraldi, G.A., "A new ranking method for principal components analysis and its application to face image analysis", ***Image and Vision Computing***, Vol. 28, No. 6, (2010), 902-913. doi: 10.1016/j.imavis.2009.11.005
49. Liu, Z., Luo, P., Wang, X. and Tang, X., "Large-scale celebfaces attributes (celeba) dataset", ***Retrieved August***, Vol. 15, No. 2018, (2018), 11.
50. Kim, J., Li, G., Yun, I., Jung, C. and Kim, J., "Edge and identity preserving network for face super-resolution", ***Neurocomputing***, Vol. 446, (2021), 11-22. doi: 10.1016/j.neucom.2021.03.048
51. Wang, X., Li, Y., Zhang, H. and Shan, Y., "Towards real-world blind face restoration with generative facial prior", in Proceedings of the IEEE/CVF Conference on Computer Vision and Pattern Recognition, (2021), 9168-9178.
52. Nikan, F. and Hassanpour, H., "Face recognition using non-negative matrix factorization with a single sample per person in a large database", ***Multimedia Tools and Applications***, Vol. 79, No. 37, (2020), 28265-28276. doi: 10.1007/s11042-020-09394-4.
53. Jose, E., Greeshma, M., Haridas, M.T. and Supriya, M., "Face recognition based surveillance system using facenet and mtcnn on jetson tx2", in 2019 5th International Conference on Advanced Computing & Communication Systems (ICACCS), IEEE, (2019), 608-613. doi: 10.1109/ICACCS.2019.8728466.
54. Prasad, P.S., Pathak, R., Gunjan, V.K. and Ramana Rao, H., Deep learning based representation for face recognition, in Iccce 2019. 2020, Springer.419-424. doi: 10.1007/978-981-13-8715-9_50.
55. Li, X., Chen, C., Zhou, S., Lin, X., Zuo, W. and Zhang, L., "Blind face restoration via deep multi-scale component dictionaries", in European Conference on Computer Vision, Springer, (2020), 399-415. doi: 10.1007/978-3-030-58545-7_23.

Persian Abstract

چکیده

شناسایی چهره یکی از رایج‌ترین تکنیک‌های احراز هویت است که به دلیل دسترسی آسان آن به طور گسترده مورد استفاده قرار می‌گیرد. در بسیاری از کاربردهای تشخیص چهره، تصاویر ضبط شده وضوح پایینی دارند. روش‌های شناسایی چهره روی تصاویر وضوح پایین عملکرد ضعیفی دارند زیرا این روش‌ها عموماً با استفاده از تصاویر چهره وضوح بالا آموزش داده می‌شوند. اگرچه روش‌های بزرگنمایی چهره موجود ممکن است تصاویر بصری چشم‌نوازی تولید کنند، اما نمی‌توانند عملکرد روش‌های تشخیص چهره را در وضوح پایین بهبود بخشند زیرا ساختار تصویر و جزئیات فرکانس بالا به خوبی حفظ نمی‌شوند. در این مقاله، پیشرفت‌های اخیر در حوزه یادگیری عمیق با هدف ساخت یک روش بزرگنمایی چهره جدید جهت توانمندسازی روش‌های شناسایی چهره استفاده شده‌اند. در این مقاله، یک شبکه متخاصم مولد جهت توانمندسازی شناسایی چهره با تصاویر چهره وضوح پایین پیشنهاد شده است. این شبکه با تمرکز بر لبه‌ها و بازسازی جزئیات فرکانس بالا، ساختار تصویر چهره وضوح پایین را به خوبی حفظ می‌کند. روش پیشنهادی جهت بزرگنمایی ویژگی‌ها، قابل استفاده در هر روش شناسایی چهره است. ما از برخی از جدیدترین روش‌های شناسایی چهره جهت ارزیابی روش پیشنهادی استفاده کرده‌ایم. نتایج حاکی از تأثیر قابل توجه روش پیشنهادی بر دقت شناسایی چهره با تصاویر وضوح پایین است.

International Journal of Engineering

Journal Homepage: www.ije.ir

Effect of Graphite Addition on the Microstructure, Mechanical Properties and Oxidation Resistance of HfB_2-SiC Composites Prepared by the SPS Method

M. Sakvand[a], M. Shojaie-Bahaabad*[a], L. Nikzad[b]

[a] *Faculty of Chemical and Materials Engineering, Shahrood University of Technology, Shahrood, Iran*
[b] *Department of Ceramics, Materials and Energy Research Center, Karaj, Iran*

PAPER INFO

Paper history:
Received 09 March 2022
Received in revised form 06 May 2022
Accepted 20 May 2022

Keywords:
HfB_2-SiC Composite
Spark Plasma Sintering
Ultra-high Temperature Ceramic
Oxidation
Graphite

ABSTRACT

In this study, HfB_2-SiC-graphite composites were fabricated using spark plasma sintering at 1900 ℃ for 10 min. The effect of graphite content on the microstructure and mechanical properties was studied; also, oxidation resistance of the prepared composites was investigated at 1400 ℃ for 32 h. Weight changes and thickness of the formed oxide layer were measured. The relative density, toughness and strength of the SPSed composites increased with raising graphite up 2.5 wt% and then decraesed. On the other hand, the hardness of the composites was decreased when graphite was added. Oxidation resistance of the composites was, thus, improved following graphite addition up 2.5 wt%, while the ecessive quantity of graphite caused poor oxidation resistance of the composites.

doi: *10.5829/ije.2022.35.10a.06*

1. INTRODUCTION

Compounds such as borides, carbides and nitrides of the IV-V group intermediate metals, which have melting temperatures above 3000 °C [1], are known as ultra high temperature ceramics (UHTCs) [2]. Good oxidation resistance [3] and high thermal and electrical conductivity [4] of diboride refractory compounds, as compared to other intermetallic compounds (carbides, nitrides), have led to extensive research on diborides such as (Ta, Nb, Hf, Zr, Ti)B_2 [5]. Among intermediate metal diborides, HfB_2 and ZrB_2 are the most suitable options for high temperature applications such as turbine blade coatings, furnace elements, high temperature electrodes, rocket motors, sharp noses and heat resistant systems [6]. HfB_2, compared to other compounds at high temperature ceramics family, has received more attention by researchers due to its higher thermal conductivity and chemical stability [7]. However, like many refractory ceramics, strong covalent bonds and low self-diffusion coefficient in HfB_2, as well as the presence of oxide contaminants, can limit the complete densification of these ceramics. Numerous studies have been reported on the synthesis and sinterability of HfB_2 ceramics using mechanical alloying, borothermal or carbothermal solid state reduction, Self-propagating high-temperature synthesis (SHS), non-pressure sintering, reactive hot press, hot isostatic press and spark plasma sintering (SPS) [8-12]. In the recent years, several researchers have used the SPS method for the compaction of HfB_2 ceramics. This method simultaneously employs a direct pulse current and an external axial force on a compacted powder in graphite die to accelerate sintering. High heating rate (100 °C/min) and lower sintering temperature, compared to other methods, can lead to a finer microstructure. In addition, in this method, due to the spark between the powder particles and the use of direct pulse flow, materials with poor sinterability can be successfully compacted [13]. Also, up to now, metal additives (Fe, Ni, Co, W), nitrides (AlN, HfN, Si_3N_4), carbides (SiC, HfC, WC, VC) and desilicides ($MoSi_2$, $HfSi_2$, $TiSi_2$, $TaSi_2$) have been used to improve the sintering and mechanical properties of HfB_2 ceramics [14-22]. The addition of SiC as the most common carbide

*Corresponding Author Institutional Email: mshojaieb@shahroodut.ac.ir (M. Shojaie-Bahaabad)

Please cite this article as: M. Sakvand, M. Shojaie-Bahaabad, L. Nikzad, Effect of Graphite Addition on the Microstructure, Mechanical Properties and Oxidation Resistance of HfB_2-SiC Composites Prepared by the SPS Method, ***International Journal of Engineering, Transactions A: Basics***, Vol. 35 No. 10, (2022), 1867-1876

additive to HfB_2 not only improves its sinterability, but also enhances its mechanical properties and oxidation resistance. Oxidation of HfB_2 occurs at low temperatures (<1000 °C). Reports indicate that the presence of 10-30 vol% SiC is required to obtain the oxidation resistance of HfB_2 ceramics. The presence of SiC improves the oxidation resistance of these composites by forming a borosilicate glass layer and also protects the HfB_2 - SiC composites up to 2000 °C in an oxidized atmosphere without air flow. One model suggests that active oxidation of SiC below the borosilicate glass layer leads to the formation of a Si-depleted layer [23, 24]. As the SiO_2 glass layer acts as a protective barrier, the oxygen activity under the glass layer is much lower than that in its surface in the presence of air. Under the reducing conditions, SiO (g) and CO (g) have higher vapor pressures in comparison to SiC below the SiO_2 layer, which can lead to the active oxidation of SiC. It has been reported that the addition of graphite to the ZrB_2-SiC composite could affect the formation of the Si-depleted layer below the SiO_2 layer [25, 26]. In addition, the increase in the siterability, toughness and microstructure of ZrB_2-SiC composites has been observed due to the presence of carbon [27-30]. So far, the effects of different sintering methods, sintering temperatures and different values of SiC on HfB_2-SiC composites have been extensively investigated [8-13]. The present study , thus, focused on the fabrication and estimation of the mechanical and oxidation properties of HfB_2-SiC-C composites by the SPS method. The aim of the present study was, therefore, to study the effect of different amounts of graphite on the microstructure and mechanical and oxidation properties of the HfB_2-SiC composite.

2. MATERIALS AND METHOD

Commercial HfB2 (< 2 µm, purity 99%, Beijing Cerametek Materials Co., China) as the matrix, and SiC (< 10 µm, purity 99%, Xuzhou Co., China) and graphite flakes (< 50 nm, purity 99.9%, Qingdao Tiansheng Graphite Co.,China) as additives were used to synthesize HfB_2-20 vol%SiC-C. Figure 1 shows the morphological characteristics of the starting powders. As can be seen, the morphology of HfB_2 and SiC particles was spherical and angular, respectively. Some oxide impurities (HfO_2 and B_2O_3) might exist on the surface of HfB_2 particles. Also, graphite was morophologically nano-sized flakes. Graphite flakes were introduced at two content levels (2.5 and 5 wt%) to the HfB_2 powders. At first, HfB_2 and SiC powder mixtures were milled by high-energy planetary milling using balls and a WC-Co cup at 300 rpm for 3 h in ethanol medium, with the weight ratio of balls to powders being 10: 1. The graphite nano-flakes were ultrasonically stirred in diluted ethanol for 1 h; then, the mixtures of HfB_2 and SiC powder was added to the

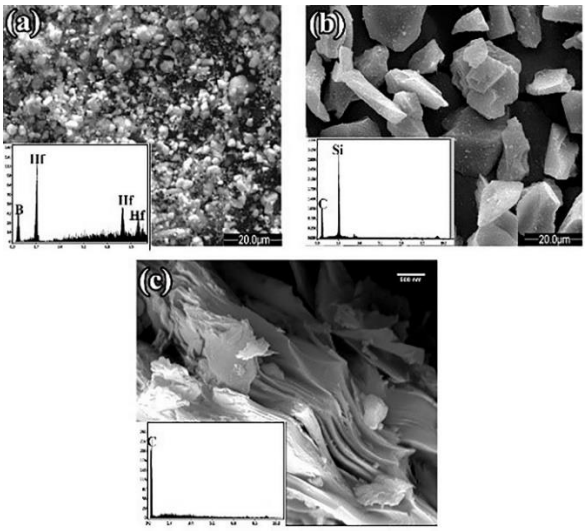

Figure 1. SEM image of starting powders (a) HfB_2, (b) SiC and (C) graphite

slurry. The slurry was dried at 60 °C for 2 h and then sieved using the mesh number 100. HfB_2-20SiC composites were fabricated by the SPS method at 1900 °C for 10 min in the vacuum of 0.05 mbar and under 40 MPa pressure. The obtained composites with different amounts of graphite, including 0, 2.5 and 5 wt%, were named as G0, G2.5 and G5, respectively. The microstructure of the composites was investigated without thermal or chemical etching. Relative density values and porosity percent of the composites were then calculated by the Archimedes method in distilled water. Theoretical density was calculated according to the law of mixtures. Phase analysis of the composites was then performed using X-ray diffraction pattern (XRD, Philips, Model: X'Pert MPD, Tube: Co, and l: 1.78897 Å); their surface and microstructure were examined using field emission scanning electron Microscope (FESEM, TESCAN, Model: MIRA) equipped with energy dispersive spectroscopy (EDS). The average grain size of the composites was measured using the MIP Cloud software. The hardness of the composites was measured using a Vickers hardness tester under 1 kg with a loading time of 10 s. The flexural strength of the composites was evaluated using a three-point flexural machine (Zwick Roell SP600, Germany) with a loading rate of 0.05 mm/min. Oxidation tests were performed in an electric furnace at 1400 °C for 32 h. The oxidation resistance of the composites was evaluated according to the weight changes and thickness of the oxide layer after oxidation.

3. RESULTS AND DISCUSSION

The displacement-temperature-time (DTT) curve of the composites is shown in Figure 2. In the displacement-time curve of the samples, three regions could be seen. In

the first region, the displacement was due to the rearrangement of the particles, the increase of the contact surface of the particles, the creation of more sparks, and the improved thermal efficiency due to the rise of pressure and temperature. With the improvment of thermal efficiency, the local temperature at the particle contact surface was increased rapidly, causing a change in the temperature-time curve. This phenomenon has also been reported by other researchers [31-33]. In the second region, there was a sharp change in the displacement curve. This sharp change was due to the increase in pressure on the powder particles up to a final pressure of 40 MPa. Bulk deformation occurred in this area due to high temperature, neck growth between particles, full contact of the particles and noticeable contraction. In samples G2.5 and G5, in the second region, the displacement was first decreased and then increased. The initial decrease indicated the expansion caused by the gases created by the evaporation of impurities and surface oxide contaminants due to the presence of the graphite additive. In the third region of the displacement-time curve, the increase in the slope of the curve was very slow, thus indicating that the sintering process of the composites was complete. In the third region, the displacement-timecurve was almost smooth, thus showing the complete compaction of these composites [32]. Oxide contaminants on the surface of the HfB_2 powder could increase the vapor phase transfer velocity and particles coagulation, and reduce the direct contact of the particles and the sintering driving force. It seems, therefore, that the contact surface of HfB_2 particles was increased through the reaction of oxygen impurities (HfO_2 and B_2O_3) with SiC [34].The result of this chemical reaction is gaseous products such as SiO, CO and BxOy;these, before the production of gaseous products, cause the formation of the liquid phase, finally increasing the sinterability of the HfB_2 powder [36]. Comparison of the displacement-time curve, as can be seen in Figure 2, showed that the sinterability was improved by adding 2.5 wt% graphite. This was due to the lubricating properties of the layered graphite and the increased particle slip as a result of improving the sinterability of the composites [27]. It seems, therefore, that with increasing the amount of the graphite additive up to 5 wt% in the composite, due to more reaction with surface oxide contaminants and removal of them, the

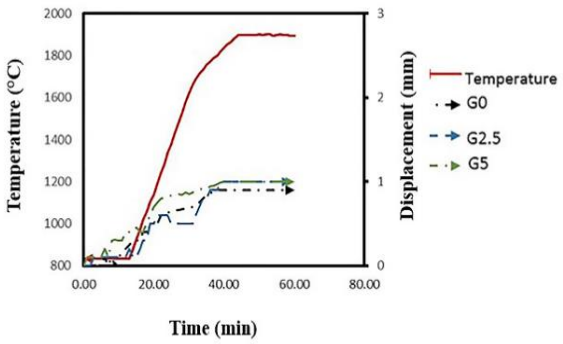

Figure 2. The displacement-temperature-time (DTT) curves of the sintered composites, (a) G0, (b) G2.5 and (c) G5

amount of liquid phase was reduced; as a result, the rate of compaction and shrinkage was decreased. The density and apparent porosity of the composites are given in Table 1. By increasing the amount of graphite to 2.5 wt%, due to the effect of graphite on removing surface impurities on SiC and HfB_2 particles and helping to improve the densification of the composite, density was increased, while the percentage of porosity in the composite was decreased. As the amount of graphite was increased to 5 wt%, density was decreased, while porosity was raised. With increasing graphite up to 5 wt%, due to graphite agglomeration and the space between graphite layers, as a result of the lack of the proper compaction of graphite layers, there was a decrease in density and an increase in the porosity of the composites [35]. The XRD patterns of the composites after the SPS process are shown in Figure 3. As shown, HfB_2 and SiC phases were observed in the samples and there were no unwanted phases in the composites. Figure 4 shows the SEM images along with the elemental analysis (EDS) of the composites surface after the SPS process. SEM image (Figure 4a) showed the HfB_2-SiC composite (G0) surface areas with severe agglomeration. EDS analysis of the G0 sample surface also revealed that the existing agglomerates contained HfB_2 particles. The presence of this agglomerate could be due to the high density difference of HfB_2 (10.5-11.2 g/cm^3) and SiC (3.2 g/cm^3), and graphite (2.25 g/cm^3). According to the SEM images in the G2 and G5 samples, the phases forming the composite were uniformly distributed on the

TABLE 1. Physical properties of the sintered composites

Sample	True density (gr/cm^3)	Apparent density (gr/cm^3)	Relative density (%)	Total porosity (%)	Open porosity (%)	Closed porosity (%)
G0	8.75	8.62	98.5	1.5	0.98	0.52
G2.5	8.07	8.02	99.39	0.6	0.28	0.32
G5	7.08	6.87	97.1	2.9	0.96	1.94

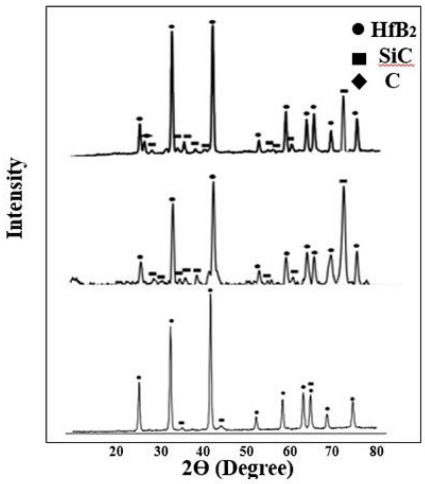

Figure 3. XRD patterns of (a) G0, (b) G2.5 and (c) G5

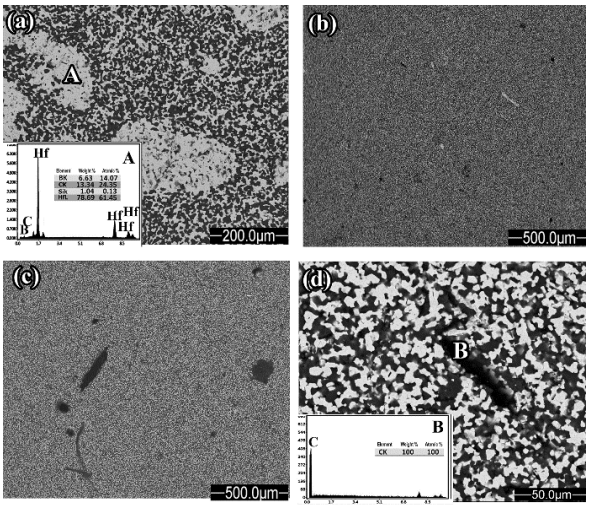

Figure 4. FESEM images and EDS analysis of the sintered composites: (a) G0, (b) G2.5 and (c,d) G5

surface; with increasing the amount of graphite up to 5 wt%, the formation of graphite agglomerates was observed. SEM images along with the EDS analysis of the HfB_2-SiC composites at higher magnifications are shown in Figure 5. As can be seen, the structure was homogeneous and the particles were evenly distributed. Two areas were clearly observed on the surface of the composites. According to the EDS analysis, the dark areas were related to the SiC phase and the light ones were associated to the HfB_2 phase. According to the SEM images, except for some cavities due to surface polishing after the sintering process, no traces of porosity were visible, thus confirming the results obtained for the density of the composites. In addition, microcracks were observed in HfB_2 (white arrow) particles. Differences in the thermal expansion coefficients of these two phases could lead to compressive or tensile residual stresses in

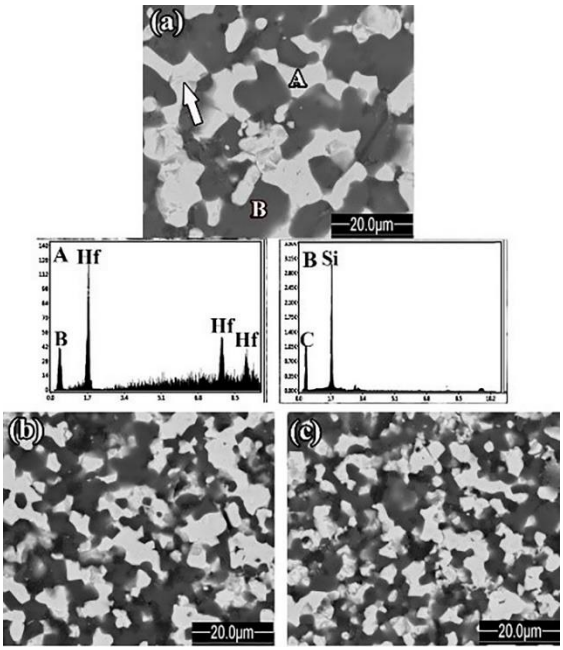

Figure 5. High magnification of FESEM images and EDS analysis of the sintered composites: (a) G0, (b) G2.5 and (c) G5

the deboride matrix, eventually creating micro-cracks [36, 37]. The mean grain size curve of HfB_2-SiC composites after the sintering process is shown in Figure 6. The grain size was reduced by adding graphite to the HfB_2-SiC composites. The grain size of prepared G0, G2.5 and G5 composites were 5.3, 3.3 and 2.4 µm, respectively. Researchers have shown that the presence of oxide impurities on the surfaces of boride particles causes HfB_2 grains to coagulate. It seems, therefore, that adding more graphite, by removing oxide impurities, could prevent the growth of HfB_2 grains, thus causing the structure to become fine. Figure 7 shows the scanning electron images of the fracture ross-section of the composites after the SPS process. According to the images, the composites had a good density and the formation of a neck between the particles, which accelerated the compaction process (thin arrow), was evident. Although neck formation is the characteristic of the controlled sintering process, it seems that applying pressures up to 40 MPa at high temperatures during the SPS process could deform the plastic at the HfB_2 grains.

The deformed HfB_2 grains in the form of a uniform polygonal surface could be distinguished from the other grains in Figure7 (thick arrow). Adding SiC particles to the HfB_2-based composites could cause the formation of an intergranular liquid phase during the SPS process. The presence of an oxide layer on the surface of non-oxide particles (such as HfO_2, SiO_2 and B_2O_3) caused the formation of borosilicate glass phases. . Sabree et al. [38] in their research work on the ZrB_2-SiC composite

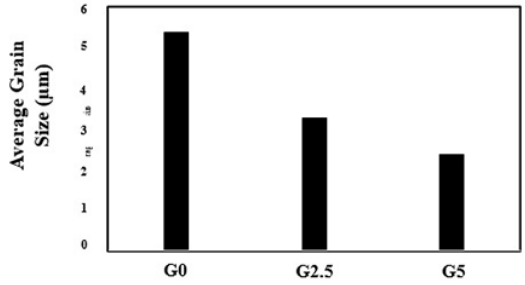

Figure 6. HfB_2 grain size of the sintered composites

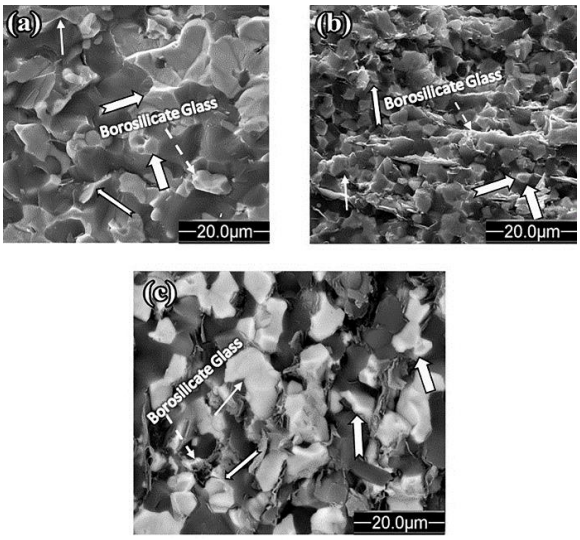

Figure 7. FESEM images of the fracture surface of the sintered composites, (a) G0, (b) G2.5 and (c) G5

sintered by the hot pressing method, also stated that the glass phase in SEM images was visible in the form of a coating, a uniform and brittle fracture surface or a low thickness layer. Such a glass phase was clearly visible in the SEM images of the cross-sections of the composites prepared in the present research work (dashed flash).

In the HfB_2-SiC composites cross-section images with different amounts of graphite, graphite layers were observed in the cross section. This indicated that graphite was not converted to new phases. Thus, it could be concluded that the sintering and compressibility in the HfB_2-SiC-C systems was non-reactive. According to the images, the graphite layers distributed between the grains showed that they were placed between the grains by applying pressure during the SPS process with a specific orientation. Shahedi et al. [35] also reported the orientation of graphite when applying pressure to the microstructure with a micron grain size. The fracture surface of the sintered composites showed a combination of intragranular and intergranular fractures. Particles pull out and sharp edges could be seen in the images, which could be related to the intergranular fracture that had occurred in grain boundaries (thin arrows) [39]. In some areas, especially when comparing surfaces with the abnormal grain growth to other grains, wide and smooth surfaces could be seen, thus indicating the intragranular fracture (thick arrows). The results of the mechanical analysis for the HfB_2-SiC composites after the SPS process are given in Table 2. According to the results obtained from the hardness test, with increasing the amount of graphite in the composites, hardness was decreased from 19.04 to 10.16 GPa and then to 6.11 GPa.

Although the composite containing 2.5 wt% had a high density, due to the inherent softness of graphite, hardness was decreased. With increasing the amount of graphite, hardness was further decreased in the G5 sample. Among the effective factors in the flexural strength of materials, grain size and density or porosity can be noted; so, the smaller the grain size and the higher the density, the higher the flexural strength of the composite. In the samples, flexural strength was enhanced with increasing graphite up to 2.5 wt% due to decreasing the matrix grain size and increasing the density,; meanwhile, with further increasing the graphite content to 5 wt%, flexural strength was decreased due to the decrease in the density of the composite. Figure 8 shows the effect of the Vickers hardness test on the HfB_2-SiC composites. As can be seen, in the G2/5 sample, due to the high density of this sample, as compared to others, the effect of hardness was regular and no deformation was observed around it. In other samples, the hardness effect was more irregular due to porosity.The HfB_2-SiC-C X-ray diffraction pattern after oxidation at 1400 °C for 32 h is shown in Figure 9. According to the XRD results, $HfSiO_4$ and HfO_2 phases were observed in these composites after oxidation at 1400 °C for 32 h. The main phase was $HfSiO_4$, although some HfO_2 phase was also formed during the oxidation test. The formation of the $HfSiO_4$ silicate phase due to the locking effect of this phase and finally, the non-defective and crack-free oxide coating on the composite surfaces could cause the resistance to the oxidation of HfB_2 base composites [42]. HfO_2 and $HfSiO_2$ formation and oxidation of graphite were formed according to the equation of the following reactions [40-42]:

$$2SiC(s) + 3O_2(g) = 2SiO_2(l) + 2CO(g) \quad (1)$$

$$2HfB_2(s) + 5O_2(g) = 2HfO_2(s) + 2B_2O_3(l) \quad (2)$$

$$SiO_2(l) + HfO_2(s) = HfSiO_4(s) \quad (3)$$

TABLE. 2. Mechanical properties of the sintered composites

Sample	Hardness (GPa)	Strength (MPa)
G0	8.75	8.62
G2.5	8.07	8.02
G5	7.08	6.87

$$2\,C\,(s) + O_2\,(g) = 2CO\,(g) \quad (4)$$

$$B_2O_3\,(l) = B_2O_3\,(g) \quad (5)$$

It has been reported in the literature that molten B_2O_3 evaporates at temperatures above 1100 °C; its evaporation rate is faster than the formation rate of the molten B_2O_3 at the 1100-1400 °C range, according to the reaction (5) [42]. Thus, B_2O_3 phase was not observed in the X-ray pattern of the composites after oxidation. The SEM image of the surface of the composites after oxidation at 1400 °C for 32 h is shown in Figure 10. As can be seen, the surfaces of the composites were coated with a glass layer of SiO_2.

Oxidation of SiC particles, at temperatures above 1100 °C resulted in the formation of a glass layer of SiO_2 on the surface of the composites. Except for the G0 specimen, the glass layer was evenly distributed on the HfB_2-SiC composite surface. Two types of bubbles were observed on the surface of this oxide layer. Some of these bubbles had grown to the surface (Figure 10a), but some had not been opened to the surface (Figure 10b). Researchers believe that due to the high viscosity of the glass layer, this layer could not flow near these bubbles and cover the open bubbles. These bubbles could be attributed to the accumulation of gaseous products due to the active oxidation of SiC at the high temperature of 1400 °C (reaction (6)), as well as the evaporation of B_2O_3 [43].

$$SiC\,(s) + O2(g) = SiO\,(g) + CO\,(g) \quad (6)$$

As reported in the previous sections, HfB_2 agglomerates were observed in the G0 sample of the composite. Thus, due to the inhomogeneous and random distribution of SiC particles in the composite, the glass layer was formed locally on the composite surfaces; as a result, it was expected that the oxidation resistance of this composite would be decreased [5]. The white crystals with different sizes and shapes were observed on the surface of the composites after oxidation. According to the XRD results, these crystals were HfO_2 and $HfSiO_4$. According to results related to the ZrB_2-SiC oxidation resistance by De-We, the formation of crystalline phases in the present study could be described as follows. After forming HfO_2 and SiO_2, according to reactions (1) and (2), HfO_2 was first dissolved in the SiO_2–B_2O_3 melt, forming SiO_2-B_2O_3 (HSB) liquid in the glass layer. Then, as the oxidation process progressed, the HSB liquid flowed on the top of the glass layer. When B_2O_3 was evaporated, HfO_2 particles were precipated from the

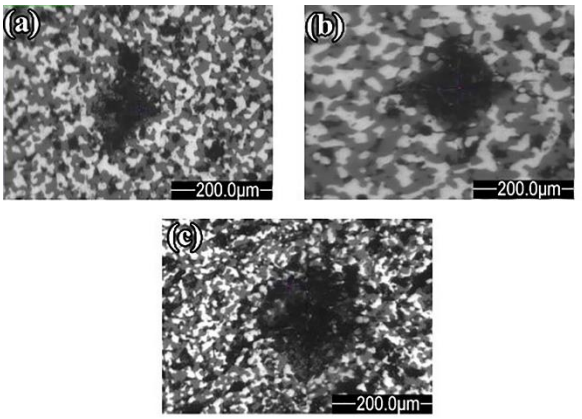

Figure 8. FESEM images of the Vickers indenter effect of the sintered composites: (a) G0, (b) G2.5 and (c) G5

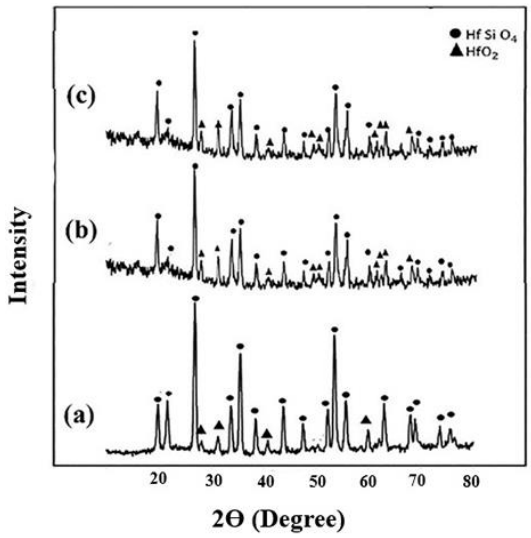

Figure 9. XRD patterns of the samples after the oxidation test at 1400 °C for 32 h: (a) G0, (b) G2.5 and (c) G5

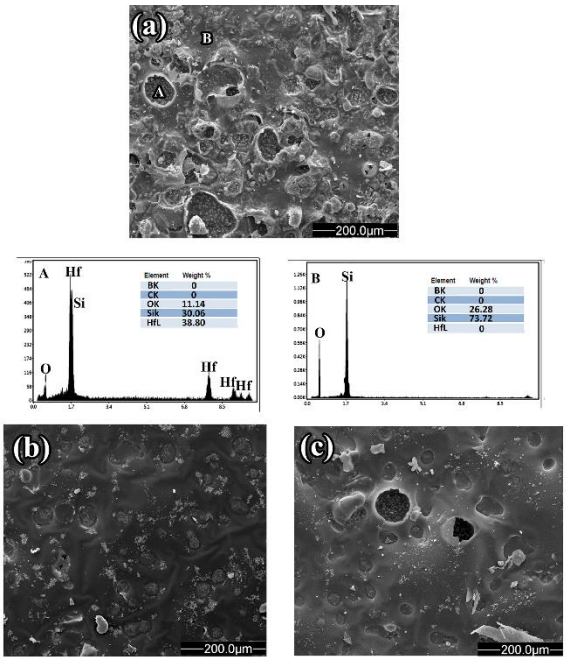

Figure 10. FESEM image and EDS analysis of the surface of the sintered samples after the oxidation test at 1400 °C for 32 h: (a) G0, (b) G2.5 and (c) G5

HSB liquid. In addition, HfO_2 could react with SiO_2 according to reaction (3) and $HfSiO_4$ particles might also be formed. Due to the higher melting points of HfO_2 and $HfSiO_4$ (>2500 °C), as compared to the glass layer (1650°C), the presence and homogeneous distribution of these crystals in the glass layer improved the stability of the glass layer [43]. Also, according to Figure 10, microcracks were observed on the surface of the oxide layer of the sample G0. These cracks could be due to the high porosity of this composite and its higher oxidation rate, leading to the formation of gaseous products (CO_2, CO, SiO, B_2O_3). In addition, as previously mentioned, given the encouragement of the active oxidation of SiC in this composite, due to its high porosity and release of more gaseous SiO, less $HfSiO_4$ was formed on the surfaces of the oxide layer. As a result, the locking effect of $HfSiO_4$ was reduced, ultimately leading to a decrease in the mechanical strength of the oxide layer and cracking of the surfaces. Figure 11 shows the cross-section of the composite samples after the oxidation test. As shown, two layers were formed on the surface of the composites. According to the EDX analysis, the first layer (outer layer) was rich in Si, while the second one had moderate amounts of Si and Hf. The thickness of each layer formed and the weight gain of the HfB_2-based composites after the oxidation test are shown in Figure 12. Comparison of HfB_2-SiC composites containing different amounts of graphite also showed that with increasing the amount of graphite and burning graphite during the oxidation

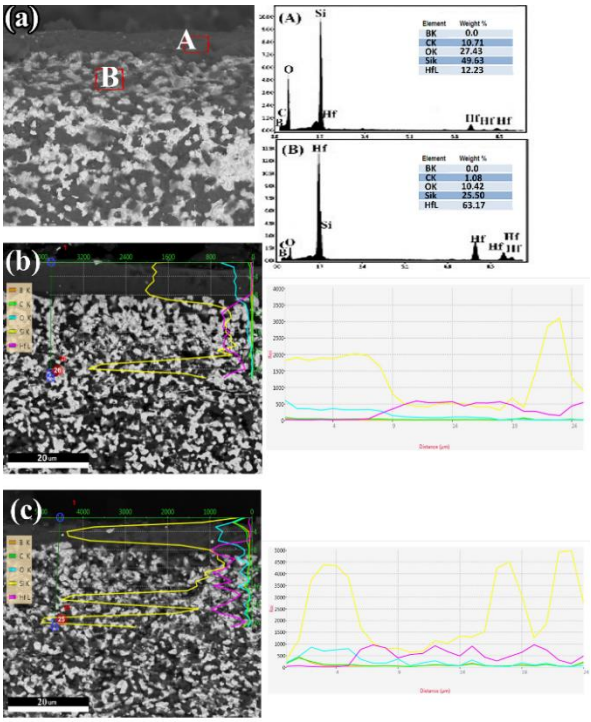

Figure 11. FESEM image of the cross section of the sintered samples after the oxidation test at 1400 °C for 32 h: (a) G0, (b) G2.5 and (c) G5

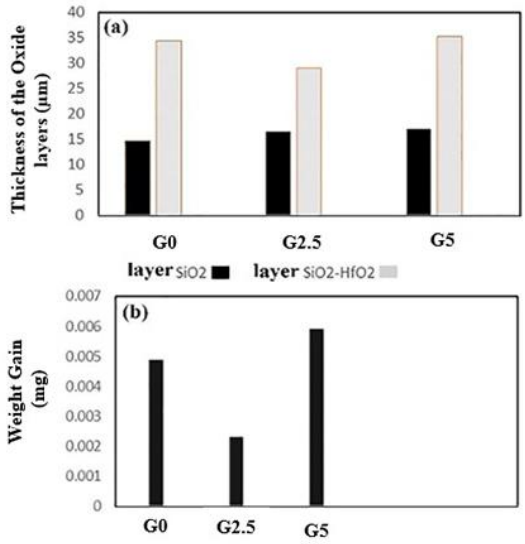

Figure 12. (a) Thickness of oxide layers and (b) weight gain of the sintered samples after the oxidation test at 1400 °C for 32 h

process at 500 °C, along with the formation of new channels for more oxygen to penetrate the composite, the oxidation rate and thickness of the SiO_2 rich layer were increased. However, with increasing the amount of graphite up to 2.5 wt%, due to the formation of a thicker glass layer and the reduced rate of oxygen penetration into the composite, the thickness of the second layer and the increase in the weight of the composite were decreased. Meanwhile, with increasing the amount of graphite up to 5 wt%, due to the lower density of this composite, the thickness of the second layer and weight were raised again. The results of the thermodynamic calculations showed that, due to the high negative free energy in the HfB_2 base composite, reaction (2) occurred at 1400 °C, resulting in HfO_2 and B_2O_3. Oxidation of SiC particles occurred with a lower negative free energy; therefore, SiC particles were then oxidized in two steps. In the first one, the SiC oxidation reaction (1) occurred at the temperature of 1400 °C. On the other hand, the results reported by Mashaykh et al. [46] showed that this reaction could occur at a temperature above 1200 °C. In the second stage of the SiC oxidation process, reaction (6) was performed; as a result, SiO and gaseous CO were formed. Comparing the free energy of reactions (1) and (6) also showed that reaction (1) had occurred; then the SiC particles were oxidized according to the reaction (6). Performing reactions (1) and (6) consistently could lead to the formation of a Si-depleted layer. This layer was not, however, observed in the composites prepared in the present study. It seems, therefore, that the glass phase formed by reaction (1) filled the remaining pores in the composite structure and prevented reaction (6). According to the literature [26, 40], there are three theories to justify the the non-formation of a Si-depleted

layer. According to the first theory, SiO_2 formed during reaction (1) prevented reaction (6) by creating a coating on the composite surface as a diffusion barrier layer. Thus, gaseous SiO and consequently, Si-depleted layer were not formed. The second theory states that even if gaseous SiO is formed during reaction (6), the Si-rich glass layer fills the pores and prevents the gaseous SiO from escaping. Therefore, no Si-depleted layer was observed in the oxidation test. The third theory holds that graphite could increasethe activity of carbon, as compared to sic, thus affecting the CO pressure below the SiO_2 layer. Therefore, the addition of carbon prevented the evaporation of SiC due to drop of the CO pressure and the formation of the Si-depleted layer.

4. CONCLUSION

In the present work, HfB_2-20 SiC composite reinforced with 2.5 and 5% by weight of graphite, as prepared by Spark Plasma Synthesis, and its effects on the microstructure, mechanical properties and oxidation resistance for 32 hours at 1400 ° C were investigated. The addition of graphite improved compressibility due to lubrication and the slip between particles. On the other hand, the hardness of the composite was decreased significantly with the increase of graphite, which could be referred to as inherent softness. Addition of 2.5 %wt graphite increased flexural strength. The HfB_2-20 SiC composite containing 5 %wt graphite had poor oxidation resistance.The reason for encouraging the active oxidation of SiC in this composite was the high porosity and emission of SiO gas, which contained less $HfSiO_4$ at the oxide layer surfaces. As a result, the locking effect of $HfSiO_4$ was reduced, ultimately leading to a reduction in the mechanical strength of the oxide layer and cracking of surfaces.

5. REFERENCES

1. Balak, Z. and Zakeri, M., "Effect of HfB_2 on microstructure and mechanical properties of ZrB_2-SiC-based composites", ***International Journal of Refractory Metals and Hard Materials***, Vol. 54, (2016), 127-137. doi: 10.1016/j.ijrmhm.2015.07.011
2. Shojaie-Bahaabad, M. and Hasani-Arefi, A., "Ablation properties of ZrC-SiC-HfB_2 ceramic with different amount of carbon fiber under an oxyacetylene flame", ***Materials Research Express***, Vol. 7, (2020), doi: 10.1088/2053-1591/ab70db
3. Binner, J., Porter, M., Baker, B., Zou, J. and Venkatachalam, V., "Selection, processing, properties and applications of ultra-high temperature ceramic matrix composites, UHTCMCs – a review", ***International Materials Reviews***, (2019), doi: 10.1080/09506608.2019.1652006
4. Balak, Z. and Azizieh, M., "Oxidation of ZrB_2 -SiC composites at 1600°C : effect of carbides, borides, silicides and chopped carbon fiber", ***Advanced Ceramics Progress***, Vol. 4, (2018), 18-23. doi: 10.30501/ACP.2018.90829
5. Ghadami, S., Taheri-Nassaj, E., Baharvandi, H. R. and Ghadami, F., "Improvement of mechanical properties of HfB_2-based composites by incorporating in situ SiC reinforcement", ***Scientific Reports***, (2021). doi: 10.1038/s41598-021-88566-0
6. Hassan, R., Kundu, R. and Balani, K., "Oxidation behaviour of coarse and fine SiC reinforced ZrB_2 at re-entry and atmospheric oxygen pressures", ***Ceramics International Journal***, Vol. 46, (2020), 11056-11065. doi: 10.1016/j.ceramint.2020.01.125
7. Ghelich, R., Jahannama, M. R., Abdizadeh, H., Torknik, F. S. and Vaezi, M. R., "Hafnium diboride nonwoven mats with porosity/morphology tuned via different heat treatments", ***Materials Chemistry and Physics***, Vol. 248, (2020), doi: 10.1016/j.matchemphys.2020.122876
8. Tian, Y. H., and Dong, L. H., "Effect of mechanical alloying on sinterability and phase evolution in pressure-less sintered TiB_2–TiC ceramics", ***Journal of Materiomics***, Vol. 5, No. 4, (2019), 670-678. doi: 10.1016/j.jmat.2019.05.001
9. Ghadami, S., Taheri-Nassaj, E. and Baharvandi, H. R., "Novel HfB_2-SiC-$MoSi_2$ composites by reactive spark plasma sintering", ***Journal of Alloys and Compounds***, Vol. 809, (2019), doi: 10.1016/j.jallcom.2019.151705
10. Sakkaki, M., Sadegh Moghanlou, F., Vajdi, M. and Shahedi Asl, M., "Numerical simulation of heat transfer during spark plasma sintering of zirconium diboride", ***Ceramics International***, Vol. 46, (2020), 4998-5007. doi: 10.1016/j.ceramint.2019.10.240
11. Liang, X., Wei-Ming, G., Yan, Z., Yang, Y. and Hua-Tay, L., "Pressureless densification of HfB_2-based ceramics using HfB_2 powders by borothermal reduction", ***Ceramics International***, Vol. 47, No. 23, (2021), 33922-33925. doi: 10.1016/j.ceramint.2021.08.245
12. Simonenkoa, E. P., Simonenkoa, N. P. and Lysenkovb, A. S., "Reactive hot pressing of HfB_2–SiC–Ta_4HfC_5 ultra-high temperature ceramics", ***Journal of Inorganic Chemistry***, Vol. 65, No. 3, (2020), 446-457. doi: 10.1134/S0036023620030146
13. EL-Wazery, M. S., "Fabrication and characteristics of 8YSZ/Ni functionally graded materials by applying spark plasma sintering procedure", ***International Journal of Engineering, Transactions C: Aspects***, Vol. 27, No. 12, (2014), 1907-1912. doi: 10.5829/idosi.ije.2014.27.12c.14
14. Mashayekh, S. and Baharvandi, H. R., "Effects of SiC or $MoSi_2$ second phase on the oxide layers structure of HfB_2-based composites", ***Ceramics International Journal***, Vol. 43, (2017), 15053-15059. doi: 10.1016/j.ceramint.2017.08.031
15. Ren, X., Shang, T. and Wang, W., "Dynamic oxidation protective behaviours and mechanisms of HfB_2-20wt%SiC composite coating for carbon materials", ***Journal of the European Ceramic Society***, Vol. 39, (2019), 1955-1964. doi: 10.1016/j.jeurceramsoc.2019.01.033
16. Guerineau, V., Vilmart, G. and Dorval, N., "Comparison of ZrB_2-SiC, HfB_2-SiC and HfB_2-SiC-Y_2O_3 oxidation mechanisms in air using LIF of BO_2 (g)", ***Corrosion Science***, (2019), doi: 10.1016/j.corsci.2019.108278
17. Ghadami, S., Taheri-Nassaj, E., Baharvandi, H. R. and Ghadami, F., "Effect of in situ VSi_2 and SiC phases on the sintering behaviour and the mechanical properties of HfB_2-based composites", ***Scientific Reports***, (2020), doi: 10.1038/s41598-020-73295-7
18. Simonenkoa, E. P., Simonenkoa, N. P., Nagornova, I. A. and Sevastyanova, V. G., "Production and oxidation resistance of HfB_2–30 vol % SiC composite powders modified with $Y_3Al_5O_{12}$", ***Russian Journal of Inorganic Chemistry***, Vol. 65, No. 9, (2020), 1416-1423. doi: 10.1134/S003602362009020X
19. Wang, P., Li, H., Sun, J.,Yuan, R., Zhang, L., Zhang, Y. and Li, T., "The effect of HfB_2 content on the oxidation and thermal shock resistance of SiC coating", ***Surface and Coatings Technology***, Vol. 339, (2018), 124-131. doi:

10.1016/j.surfcoat.2018.02.029

20. Elizaveta, P., Simonenkoa, N. P., Nikolay, P. Simonenkoa, E. P. and Anatoly, F., "Oxidation of HfB_2-SiC-Ta_4HfC_5 ceramic material by a supersonic flow of dissociated air", ***Journal of the European Ceramic Society***, (2020), doi: 10.1016/j.jeurceramsoc.2020.10.001
21. Gurcan, K. and Derin, B., "Effect of SiC particle size on the microstructural, mechanical and oxidation properties of In-situ synthesized HfB_2-SiC composites", ***Politeknik Dergisi***, Vol. 24, No. 2, (2021), 503-551. doi: 10.2339/politeknik.682256
22. Ren, X., Mo, H., Wang, W., Feng, P., Guo, L. T. and Li, Z., "Ultra high temperature ceramic HfB_2-SiC coating by liquid phase sintering method to protect carbon materials from oxidation", ***Materials Chemistry and Physics***, Vol. 217, (2018), 504-512. doi: 10.1016/j.matchemphys.2018.07.018
23. Guo, S., "Oxidation and strength retention of HfB_2−SiC composite with La_2O_3 additives", ***Advances in Applied Ceramics***, (2020), doi: 10.1080/17436753.2020.1755510
24. Opila, E., Levine, S., and Lorincz, J., "Oxidation of ZrB_2- And HfB_2-based ultra-high temperature ceramics: Effect of Ta additions", ***Journal of Materials Science***, Vol. 39, (2004), 5969-5977. doi: 10.1023/B:JMSC.0000041693.32531.d1
25. Rezaie, A., Fanrenholtz, W. G. and Hilmas, G. E., "Oxidation of zirconium diboride-silicon carbide at 1500°C at a low partial pressure of oxygen", ***Journal of the American Ceramic Society***, Vol. 89, (2006), 3240-3245. doi: 10.1111/j.1551-2916.2006.01229.x
26. Rezaie, A., Fahrenholtz, W. G. and Hilmas, G. E., "The effect of a graphite addition on oxidation of ZrB_2-SiC in air at 1500°C", ***Journal of the European Ceramic Society***, Vol. 33, (2013), 413. doi: 10.1016/j.jeurceramsoc.2012.09.016
27. Zamora, V., Nygren, M., Guiberteau, F. and Ortiz, A. L., "Effect of graphite addition on the spark-plasma sinterability of ZrB_2 and ZrB_2–SiC ultra-high-temperature ceramics", ***Ceramics International***, Vol. 40, (2014), 11457-11464. doi: 10.1016/j.ceramint.2014.03.130
28. Shahedi Asl , M., Zamharir, M. J., Ahmadi, Z. and Parvizi, S., "Effects of nano-graphite content on the characteristics of spark plasma sintered ZrB_2–SiC composites", ***Materials Science and Engineering A***, Vol. 716, (2018), 99-106. doi: 10.1016/j.msea.2018.01.038
29. Azizian-Kalandaragh, Y., Namini, A. S., Ahmadi, Z. and Shahedi Asl, M., "Reinforcing effects of SiC whiskers and carbon nanoparticles in spark plasma sintered ZrB_2 matrix composites", ***Ceramics Internationa,*** Vol. 44, (2018), 19932-19938. doi: 10.1016/j.ceramint.2018.07.258
30. Nasiri, Z. and Mashhadi , M., "Microstructure and mechanical behavior of ternary phase ZrB_2-SiC-AlN nanocomposite", ***International Journal of Refractory Metals and Hard Materials***, Vol. 78, (2019), 186-192. doi: 10.1016/j.ijrmhm.2018.09.009
31. Sergey, N., "Processing and characterization of spark plasma sintered SiC-TiB_2-TiC powders", ***Materials***, Vol. 15, No. 5, (2022), 1946. doi: 10.3390/ma15051946
32. Shahriari, M., Zakeri. M., Razavi, M. and Rahimipour, M. R., "Investigation on microstructure and mechanical properties of HfB_2.SiC-HfC ternary system with different HfC content prepared by spark plasma sintering", ***International Journal of Refractory Metals and Hard Materials***, Vol. 93, (2020), 105350. doi: 10.1016/j.ijrmhm.2020.105350
33. Emami, S. M., Salahi, E., Zakeri, M. and Tayebifard, S. A., "Effect of composition on spark plasma sintering of ZrB_2–SiC–ZrC nanocomposite synthesized by MASPSyn", ***Ceramics International***, Vol. 43, (2017), 111-115. dot: 10.1016/j.ceramint.2016.09.118
34. Shahedi Asl, M., "Microstructure, hardness and fracture toughness of spark plasma sintered ZrB_2–SiC–Cf composites", ***Ceramics International***, Vol. 43, (2017), 15047-15052. doi: 10.1016/j.ceramint.2017.08.030
35. Shahedi Asl, M., Pazhouhanfar, Y., Sabahi Namini, A., Shaddel , S., Fattahi, M. and Mohammadi, M., "Role of graphite nano-flakes on the characteristics of ZrB_2-based composites reinforced with SiC whiskers", ***Diamond and Related Materials***, Vol. 105, (2020), 107786. doi: 10.1016/j.diamond.2020.107786
36. Yuan, Y., Liu, J. X. and Zhang, G. J., "Effect of HfC and SiC on microstructure and mechanical properties of HfB_2-based ceramics", ***Ceramics International***, Vol.42, (2016), 7861-7867. doi: 10.1016/j.ceramint.2016.01.067
37. Hosseinia, Z., Mollazadeh Beidokhti, S., Vahdati Khakib, J. and Pourabdoli, M., "Preparation of porous alumina/nano-nickel composite by gel casting and carbothermic reduction", ***International Journal of Engineering, Transaction A: Basics***, Vol. 35, No. 01, (2022), 220-227. doi: 10.5829/IJE.2022.35.01A.21
38. Sabree, I. K., Aswad, M. A. and Abd Ali, H. S., "Effect of additional zirconia on fracture mechanics of bioactive glass-ceramics using digital image correlation", ***International Journal of Engineering, Transactions C: Aspects***, Vol. 34, No. 9, (2021), 2053-2059. doi: 10.5829/IJE.2021.34.09C.02
39. Taghian Dehaghani, M. and Ahmadian, M., "Fracture mechanism of CoCrMo porous nano-composite prepared by powder metallurgy route", ***International Journal of Engineering, Transaction A: Basics***, Vol. 31, No. 1, (2018), 19-24. doi: 10.5829/ije.2018.31.01a.03
40. Ghadami, S., Taheri-nassaj, E., Baharvandi, H. R. and Ghadami, F., "Effect of in situ SiC and $MoSi_2$ phases on the oxidation behavior of HfB_2 - based composites", ***Ceramics International Journal***, Vol. 46, (2020), 20299-20305. doi: 10.1016/j.ceramint.2020.05.116
41. Wang, P., Li, H., Sun, J., Yuan, R., Zhang, L., Zhang, Y. and Li, T., "The effect of HfB_2 content on the oxidation and thermal shock resistance of SiC coating", ***Surface & Coatings Technology***, Vol. 339, (2018), 124-131. doi: 10.1016/j.surfcoat.2018.02.029
42. Jin, H., Meng, S., Zhang, X., Zeng, Q. and Niu, J., "Effects of oxidation temperature, time and ambient pressure on the oxidation of ZrB_2 – SiC-graphite composites in atomic oxygen", ***Journal of the European Ceramic Society***, Vol. 36, (2016), 1855-1861. doi: 10.1016/j.jeurceramsoc.2016.02.040
43. Ren, X., Mo, H., Wang, W., Feng, P., Guo, L. and Li, Z., "Ultra high temperature ceramic HfB_2-SiC coating by liquid phase sintering method to protect carbon materials from oxidation", ***Materials Chemistry and Physics***, (2018), doi: 10.1016/j.matchemphys.2018.07.018

Persian Abstra

چکیده

در مطالعه حاضر، کامپوزیت‌های HfB_2-SiC-graphite به روش سنترینگ پلاسمای جرقه‌ای در دمای ℃ ۱۹۰۰ به مدت ۱۰ دقیقه تهیه شدند. تاثیر مقدار گرافیت بر ریزساختار، خواص مکانیکی مطالعه شد. همچنین مقاومت به اکسیداسیون کامپوزیت‌های اماده شده در دمای ℃ ۱٤۰۰ به مدت ۳۲ ساعت بررسی شد. تغییرات وزن و ضخامت لایه اکسیدی تشکیل شده بر روی سطح کامپوزیت اندازه‌گیری شد. دانسیته نسبی، چقرمگی و استحام کامپوزیت‌های سینتر شده با افزایش مقدار گرافیت تا ۲/۵ درصد وزنی افزایش یافت و سپس کاهش یافت. سختی کامپوزیت‌ها وقتی گرافیت افزوده شد، کاهش یافت. مقاومت به اکسیداسیون کامپوزیت بعد از افزودن گرافیت تا ۲/۵ درصد وزنی بهبود یافت در حالیکه مقدار اضافی گرافیت سبب افت مقاومت به اکسیداسیون کامپوزیت شد.

IJE TRANSACTIONS A: Basics Vol. 35 No. 10, (October 2022) 1877-1886

International Journal of Engineering

Journal Homepage: www.ije.ir

Distance Measures of Pythagorean Fuzzy TOPSIS Approach for Online Food Delivery Apps

H. D. Arora*, A. Naithani, S. Gupta

Department of Applied Mathematics, Amity Institute of Applied Sciences, Amity University Uttar Pradesh, Noida, India

P A P E R I N F O

Paper history:
Received 15 May 2022
Received in revised form 27 May 2022
Accepted 29 May 2022

Keywords:
Decision Making
Fuzzy Sets
TOPSIS
Distance Measures

A B S T R A C T

The expansion of the online food delivery apps (OFDAs) around the globe has accelerated because of the sudden growing cases of the COVID-19 pandemic. OFDAs are quickly expanding in India, providing a huge number of chances for different OFDA platforms and creating a competitive market. There are several criteria and dimensions for OFDAs businesses to explore to keep with the frequently changing competitive market and achieve long-term success. A Pythagorean fuzzy set (PFS) is a powerful tool for dealing with uncertainty. Distance measure of PFS is a hot research topic and has real-life applications in many areas, such as decision making, medical diagnosis, patterns analysis, clustering, etc. The article aims to examine the results of the novel Pythagorean fuzzy distance measure strategy to select the best online app using TOPSIS method to select the best OFDAs. Firstly, all the axioms related to distance measures are proved for the proposed measures. The proposed work uses five distinct alternatives/options and four attributes/criteria in a fuzzy environment to deal with imprecise and conflicting information. The findings indicate that the proposed methodology is a more realistic way to choose the best OFDAs among others. Finally, a sensitivity analysis is used to determine whether the chosen alternative was the best option among the other components and to ensure that the TOPSIS technique results were accurate.

***doi**: 10.5829/ije.2022.35.10a.07*

NOMENCLATURE

OFDA	Online food delivery apps	FS	Fuzzy sets
MCDM	Multi-criteria decision making	IFS	Intuitionistic fuzzyzy sets
TOPSIS	Technique for order of preference by similarity to ideal solution	PFS	Pythagorean fuzzy sets
MD	Membership degree	NMD	Non-membership degree
PIS	Positive ideal solution	NIS	Negative ideal solution

1. INTRODUCTION

Making decision is undoubtedly one of the most fundamental activities of human beings. Decision making is the study of how decisions are made and how they can be made better. It is broadly defined to include any choice of alternatives and is of importance in many fields. It refers to identifying the optimum alternative or determining the ranking of alternatives.

MCDM is a complex decision-making method that incorporates both quantitative and qualitative elements. Several MCDM strategies and approaches have been suggested to to choose the most likely optimal options. As an augmentation to the fuzzy MCDM approach is suggested in this work, where the rankings of options versus attributes, and the weights of all criteria, are assessed in linguistic values represented by fuzzy numbers. MCDM models under fuzzy environment have been proposed by several researchers [1-5].

Zadeh [6] introduced the fuzzy concept for handling ambiguity in a better way. By assigning the MD to elements with respect to a set, a fuzzy set describes the state between "exist" and "does not exist." Atanassov [7, 8] suggested IFS which also included NMD $'\varrho(x)'$ along

*Corresponding Author Institutional Email: hdarora@amity.edu
(H. D. Arora)

Please cite this article as: H. D. Arora, A. Naithani, S. Gupta, Distance Measures of Pythagorean Fuzzy TOPSIS Approach for Online Food Delivery Apps, ***International Journal of Engineering, Transactions A: Basics***, Vol. 35 No. 10, (2022), 1877-1886

with $'\kappa(x)'$ satisfying $0 \leq \kappa(x) + \varrho(x) \leq 1$ and $\kappa(x) + \varrho(x) + \lambda(x) = 1$, where $\lambda(x)$ is the hesitancy function. As a result, it has been discovered that IFSs are better at representing human expressions such as perception, knowledge, and behaviour than FS. PFS was proposed by Yager [9, 10], in which the square sum of the MD and NMD is less than one. The main advantages of such extended FSs are that they use MD, NMD, and the degree of reluctance to represent ambiguous information. Later it was found that there were sets which were not satisfying the above condition hence a need to revise the sets were felt.

Several similarity and distance measures have been designed and analysed in the previous studies to quantify the similarity or difference between PFS. These measures have been effectively used to a variety of applications. Chen [11] established a distance for PFS based on the Minkowski distance measure and applied it to many real life problems such as Internet stock and reseaech and development project investment and various other practical situations. Lai et al. [12] presented and demonstrated the utility of numerous distance measures for PFS and Pythagorean fuzzy numbers. Wei and Wei [13] proposed ten different forms of PFS similarity measurements based on covariance. Ejegwa [14] applied distance measures for IFS, such as Hamming, Euclidean, normalized Hamming, and normalized Euclidean distances, as well as similarities to PFSs, multi-criteria and multi-attribute decision-making situations. Xiao and Ding [15] proposed a new measure using Jenson-Shannon divergence measure. Peng [16] and Adabitabar et al. [17] devised new Pythagorean distance and similarity measures with real life illustrations. Ejegwa [18] normalized the distance function introduced by Zhang and Xu [19] and validated the axiomatic definition of a metric for the updated version, which was missing in Zadeh's work. Zhou and Chen [20] proposed new distance measure and applied it to real-life problems [21].

Boran and Akay [22] developed a biparametric similarity measure and applied to the approach to pattern recognition. Iqbal and Rizwan [23] considered the importance of intuitionistic fuzzy sets using similarity measure and its applications to decision making. Ejegwa and Agbetayo [24] introduced a new similarity-distance measure and applied it to decision making problem. A comparative analysis was also presented to validate the measure proposed. A modified PF correlation measure with application to decision making was suggested by Ejegwa et al. [25]. Lin et al. [26] gave some practical examples to highlight how the proposed directional correlation coefficient can be used in virus detection and in what way the suggested weighted directional coefficient of correlation can be used in cluster analysis.

In today's economy, due to the importance of quality and quantity of the product, supplier selection plays a significant role in procurement planning of each factory. A growing trend towards computerization and competition in supply chains results in uncertainty and quick variability that make the decisions difficult for both levels of retailers and manufacturers. Kaviyani-Charati et al. [27] novel approach to determine the optimal production and order quantities and prices with and without agile abilities. Cheraghalipour et al. [28] considered supplier selection framework for this industry and employed the best worst method (BWM) along with a well-known MCDM technique with the name of VIKOR. Shahsavar et al. [29] propsoed an efficient and robust decision-making framework for the concept of a green city and sustainable development goals to manage municipal plastic wastes. Sardi et al. [30] introduced a new approach in the field of port performance evaluation based on the components of greenness and intelligence. Ghoushchi et al. [31] proposed a novel approach to selecting the optimal landfill for medical waste using Multi-Criteria Decision-Making (MCDM) methods. For better considerations of the uncertainty in choosing the optimal landfill, the MCDM methods are extended by spherical fuzzy sets (SFS). Cheraghalipour et al. [32] developed a hybrid MCDM method and mixed integer linear programming (MILP) approach in order to evaluation of the returned products' collectors along with their ordered quantities. Fasihi et al. [33] proposed a novel mathematical model to maximize responsiveness to customer demand and minimize the cost of the fish closed-loop supply chain. A new three-phase model is presented by Valinejad et al. [34] to supply chain sustainability risks management. This model includes the failure mode and effects analysis phase for identifying and assessing all risks and classification them, fuzzy VIKOR phase for ranking critical risks, and management phase to deal with critical risks. The categorization of risks was conducted according to a new five-dimensional approach to sustainable progress, including environmental, economic, social, technical, and organizational aspects on various sectors of the supply chain. Afshar et al. [35]investigated dimensions of the cost of quality in a cold supply chain design such as the cost of quality related to suppliers and the cost of distribution service quality to close the problem to real-world conditions. Moreover, the quality of suppliers, manufacturers, and distributors was simultaneously considered throughout a supply chain with a new approach. Nozari et al. [36] suggested a model to locate warehouses and production centers and route vehicles for the distribution of medical goods to hospitals. The robust fuzzy method controled uncertain parameters, such as demand, transmission, and distribution costs. The effect of uncertainty using a neutrosophic fuzzy programming method showed that by increasing demand, the volume of medical goods exchanges and the number of vehicles used to distribute goods increase. Zahedi-Anaraki et al. [37] propsoed a modified benders decomposition

algorithm for a last-mile network with flexible delivery options.

An ideal solution comprises of the optimal values of all criteria whereas a negative-ideal solution comprises of worst values of all criteria and the selection criteria for alternatives are based on Euclidean distance. The TOPSIS method is easy in implementation and has been applicable in the problems of selection and ranking of alternatives. MCDM methods are popular among the researchers in handling with decision- making problems to get the most reliable alternative. The TOPSIS method was developed by Hwang and Yoon [38] to solve decision-making problems. Using TOPSIS, we can conveniently determine the minimum distance between a positive ideal and a negative ideal solution, which supports choosing the best alternative. Several researchers used the TOPSIS method after its development for decision making and extended it to FSs, IFSs and PF environments [39-48].

According to statistics, India has 749 million mobile internet users till 2020. There's no doubt that mobile apps have become our live partners for anything and everything. Mobile apps have made our lives so much easier, from paying bills to ordering groceries over the phone. Food delivery apps on demand are handy and simple to use, and they offer tempting savings and faster delivery. The best food is delivered at the most affordable prices. Bangalore, Pune, Delhi, Gurgaon, Hyderabad, Chennai, and Mumbai are all hotspots for this trend of Indian cities. Therefore, goal of this article is to find a best online food delivering app based on certain criteria selected.

Research Gap

The study of PFS is recently gaining importance due to its wide application in situations involving ambiguity. It can easily be merged with MCDM techniques to solve real life problems. Many distance measures approaches have been suggested and applied to solve decision-making problems. Though the existing distance measures are somewhat significant, they possess some shortcomings in terms of accuracy and their alignments with the concept of IPFS, which needed to be strengthened to enhance reliable outputs. The study focusses on

- re-examines certain existing distance measures between PFS,
- offers an improved distance technique between PFSs,
- validate the proposed distance measures using axiomatic definition of distance measures,
- presents comparison analyses of the new distance technique in Pythagorean fuzzy environment,
- applies the new distance technique to determine some decision-making situations, and
- sensitivity analysis for assigning different weights by changing the criteria weights to those obtained by PF-distance measures to observe how much it would influence the final rankings of alternatives.

The rest of this article is organized as follows: The second section delivers many terminologies which will help evaluate performance of various app. The next section proposes a novel distance measure and its axioms are proved. In section 4, TOPSIS algorithm and the procedure to find the ranking of these apps are discussed. Section 5 presents the results and discussion. Finally, section 6 concludes the article.

2. PRELIMINARIES

Definition 2.1 [49]. Let $\mathcal{H}$ be defined as a Fuzzy set in non-empty set X then it is represented as:

$$\mathcal{H} = \{<x, \kappa_{\mathcal{H}}(x) \mid x \in X\} \quad (1)$$

where $\kappa_{\mathcal{H}}(\mathbb{x})$: X → [0, 1] is the MD of an element x in set X.

Definition 2.2 [7]. Let $\mathcal{H}$ be an IFS in X we can define:

$$\mathcal{H} = \{<x, \kappa_{\mathcal{H}}(x), \varrho_{\mathcal{H}}(x) \mid \forall\, x \in X\} \quad (2)$$

where $\kappa_{\mathcal{H}}(x)$: X → [0,1] and $\varrho_{\mathcal{H}}(x)$: X → [0,1]
$\kappa_{\mathcal{H}}(x)$ is the MD and $\varrho_{\mathcal{H}}(x)$ is the NMD such that $0 \leq \kappa_{\mathcal{H}}(x) + \varrho_{\mathcal{H}}(x) \leq 1$.

Definition 2.3 [9] A PFS is given as:

$$\mathcal{H} = \{<x, \kappa_{\mathcal{H}}(x), \varrho_{\mathcal{H}}(x) \mid \forall\, x \in X\} \quad (3)$$

and $\kappa_{\mathcal{H}}(x)$: X → [0, 1] and $\varrho_{\mathcal{H}}(x)$: X → [0, 1]
where, $\kappa_{\mathcal{H}}(x)$ is MD and $\varrho_{\mathcal{H}}(x)$ is the NMD such that:

$$0 \leq \kappa^2_{\mathcal{H}}(x) + \varrho^2_{\mathcal{H}}(x) \leq 1 \quad (4)$$

and

$$\lambda^2_{\mathcal{H}}(x) = 1 - \kappa^2_{\mathcal{H}}(x) - \varrho^2_{\mathcal{H}}(x) \quad (5)$$

where $\lambda_{\mathcal{H}}(\mathbb{x})$ called hesitancy or indeterminacy of PFS $\mathcal{H}$.

Definition 2.4 [50]. Assume $\Delta_n = \{P = (p_1, p_2, \dots, p_n): p_i \geq 0, \sum_{i=1}^{n} p_i = 0\}$ be a collection of $n-$complete probability distributions. For any probability distribution:

$$E(P) = -E_0 \sum P_{ij}\, In(P_{ij}) \quad (6)$$

where, $i = 1,2 \dots n$; $j = 1,2, \dots m$ and E_0 is the entropy constant calculated by $\frac{1}{In\, m}$.

3. DISTANCE MEASURES FOR PFS

3. 1. Existing Distance Measures

Definition 3.1 [19]. Distance between PFSs $\wp$ and $\mathbb{Q}$, is defined as:

$$D_{ZX}(\wp, \mathbb{Q}) = \frac{1}{2}\sum_{i=1}^{n}\left\{\left|\kappa^2_{\wp}(x_i) - \kappa^2_{\mathbb{Q}}(x_i)\right| + \left|\varrho^2_{\wp}(x_i) - \varrho^2_{\mathbb{Q}}(x_i)\right| + \left|\lambda^2_{\wp}(x_i) - \lambda^2_{\mathbb{Q}}(x_i)\right|\right\} \quad (7)$$

Definition 3.2 [51]. Normalized Hausdorff distance between PFSs $\wp$ and $\mathbb{Q}$, is defined as:

$$D_{HY}(\wp,\mathbb{Q})=\frac{1}{n}\left\{\sum_{i=1}^{n}\max\left\{\begin{matrix}\left|\kappa_{\wp}^{2}(\mathrm{x_i})-\kappa_{\mathbb{Q}}^{2}(\mathrm{x_i})\right|,\\ \left|\varrho_{\wp}^{2}(\mathrm{x_i})-\varrho_{\mathbb{Q}}^{2}(\mathrm{x_i})\right|\end{matrix}\right\}\right\} \quad (8)$$

Definition 3.3 [18]. Modified Zhang and Xu distance between PFSs $\wp$ and $\mathbb{Q}$ is defined as:

$$D_{MZX}(\wp,\mathbb{Q})=\frac{1}{n}D_{ZX}(\wp,\mathbb{Q}) \quad (9)$$

where $D_{ZX}(\wp,\mathbb{Q})$ denotes Zhang and Xu [19] distance measure demonstrated in Equation (7).

Definition 3.4 [11]. Chen's distance measure between PFSs $\wp$ and $\mathbb{Q}$, is defined as:

$$D_{C}(\wp,\mathbb{Q})=\frac{1}{2n}\sum_{i=1}^{n}\left\{\left|\kappa_{\wp}^{2}(x_i)-\kappa_{\mathbb{Q}}^{2}(x_i)\right|^{\beta}+\left|\varrho_{\wp}^{2}(x_i)-\varrho_{\mathbb{Q}}^{2}(x_i)\right|^{\beta}+\left|\lambda_{\wp}^{2}(x_i)-\lambda_{\mathbb{Q}}^{2}(x_i)\right|^{\beta}\right\}^{\frac{1}{\beta}} \quad (10)$$

where β is a distance parameter, satisfying $\beta\geq 1$. If $\beta=1$, it reduces to the Hamming distance. If $\beta=2$, it reduces to Euclidean distance.

Definition 3.5 [52]. Given a finite universe $\mho$, distance measure between PFSs $\wp$ and $\mathbb{Q}$ is defined as:

$$D_{MP}(\wp,Q)=\frac{1}{n}\sum_{i=1}^{n}\frac{\left|\kappa_{\wp}^{2}(x_i)-\kappa_{\mathbb{Q}}^{2}(x_i)\right|+\left|\varrho_{\wp}^{2}(x_i)-\varrho_{\mathbb{Q}}^{2}(x_i)\right|}{\kappa_{\wp}^{2}(x_i)+\kappa_{\mathbb{Q}}^{2}(x_i)+\varrho_{\wp}^{2}(x_i)+\varrho_{\mathbb{Q}}^{2}(x_i)} \quad (11)$$

where $\wp=\left\{\langle \mathrm{x_i},\kappa_{\wp}(\mathrm{x_i}),\varrho_{\wp}(\mathrm{x_i})\rangle|\mathrm{x_i}\in\mho\right\}$ and $\mathbb{Q}=\left\{\langle \mathrm{x_i},\kappa_{\mathbb{Q}}(\mathrm{x_i}),\varrho_{\mathrm{Q}}(\mathrm{x_i})\rangle|\mathrm{x_i}\in\mho\right\}$

3. 2. Proposed Distance Measure for PFSs

Firstly, we recall the axiomatic preposition of divergence for Pythagorean fuzzy sets.

Proposition 1. Let $\wp, \mathbb{Q}, \mathcal{R}\in$ PFS (X) where X is a non-empty set. The distance measure between $\wp$ and $\mathbb{Q}$ is a function that satisfies

(D1) $0\leq Div(\wp,\mathbb{Q})\leq 1$

(D2) $Div(\wp,\mathbb{Q})=0\Leftrightarrow\wp=\mathbb{Q}$.

(D3) $Div(\wp,\mathbb{Q})=Div(\mathbb{Q},\wp)$

(D4) If $\mathcal{R}$ is a PFS in X and $\wp\subseteq\mathbb{Q}\subseteq\mathcal{R}$, then $Div(\wp,\mathbb{Q})\leq Div(\wp,\mathcal{R})$ and $Div(\mathbb{Q},\mathcal{R})\leq Div(\wp,\mathcal{R})$.

It is important to consider the weight of each elements as in decision making process, factors typically have distinctive importance, so they should be given different weights. Taking weights into considerations, we proposed two novel distance measures between $\wp$ and $\mathbb{Q}$ as follows:

Assume $\wp,\mathbb{Q}\in$ PFS (X) where $X=\{x_1,x_2\ldots,x_n\}$ then:

$$D_{PFS}(\wp,\mathbb{Q})=1-\frac{3}{n}\left[\sum_{i=1}^{n}\left\{\frac{2^{1-\frac{1}{3}\left|\kappa_{\wp}^{2}(x_i)-\kappa_{\mathbb{Q}}^{2}(x_i)\right|+\left|\varrho_{\wp}^{2}(x_i)-\varrho_{\mathbb{Q}}^{2}(x_i)\right|+\left|\lambda_{\wp}^{2}(x_i)-\lambda_{\mathbb{Q}}^{2}(x_i)\right|}_{-1}}{2^{1-\frac{1}{3}\left|\kappa_{\wp}^{2}(x_i)-\kappa_{\mathbb{Q}}^{2}(x_i)\right|+\left|\varrho_{\wp}^{2}(x_i)-\varrho_{\mathbb{Q}}^{2}(x_i)\right|+\left|\lambda_{\wp}^{2}(x_i)-\lambda_{\mathbb{Q}}^{2}(x_i)\right|}_{+1}}\right\}\right] \quad (12)$$

$$D_{WPFS}(\wp,\mathbb{Q})=1-\frac{3}{n}\left[\sum_{i=1}^{n}\omega_i\left\{\frac{2^{1-\frac{1}{3}\left|\kappa_{\wp}^{2}(x_i)-\kappa_{\mathbb{Q}}^{2}(x_i)\right|+\left|\varrho_{\wp}^{2}(x_i)-\varrho_{\mathbb{Q}}^{2}(x_i)\right|+\left|\lambda_{\wp}^{2}(x_i)-\lambda_{\mathbb{Q}}^{2}(x_i)\right|}_{-1}}{2^{1-\frac{1}{3}\left|\kappa_{\wp}^{2}(x_i)-\kappa_{\mathbb{Q}}^{2}(x_i)\right|+\left|\varrho_{\wp}^{2}(x_i)-\varrho_{\mathbb{Q}}^{2}(x_i)\right|+\left|\lambda_{\wp}^{2}(x_i)-\lambda_{\mathbb{Q}}^{2}(x_i)\right|}_{+1}}\right\}\right] \quad (13)$$

where, $\lambda_{\wp}(x_i)=\sqrt{1-\kappa_{\wp}^{2}(x_i)-\varrho_{\wp}^{2}(x_i)}$ and $\lambda_{\mathbb{Q}}(x_i)=\sqrt{1-\kappa_{\mathbb{Q}}^{2}(x_i)-\varrho_{\mathbb{Q}}^{2}(x_i)}$; ω is the weight vector of $x_i(i=1,2,\ldots,n)$, with $\omega_i\in[0,1]$, $i=1,2,\ldots,n$, $\sum_{i=1}^{n}\omega_i=1$. If we take $\omega_i=1$, then then $D_{WPFS}(\wp,\mathbb{Q})=D_{PFS}(\wp,\mathbb{Q})$.

Theorem 3.1. The proposed measures specified in Equations (12) and (13) are valid measures of PFS.

Proof. All four criteria for a distance measure are satisfied by the proposed distance measures listed below:

(D1) $0\leq D_{PFS}(\wp,\mathbb{Q}),D_{WPFS}(\wp,\mathbb{Q})\leq 1$

Proof. For $\mathrm{D_{PFS}}(\wp,\mathbb{Q})$: As all the values of MD and NMD lies between 0 and 1, hence we can say that:

$$0\leq\left|\kappa_{\wp}^{2}(x_i)-\kappa_{\mathbb{Q}}^{2}(x_i)\right|\leq 1,$$

$$0\leq\left|\varrho_{\wp}^{2}(x_i)-\varrho_{\mathbb{Q}}^{2}(x_i)\right|\leq 1,$$

$$0\leq\left|\lambda_{\wp}^{2}(x_i)-\lambda_{\mathbb{Q}}^{2}(x_i)\right|\leq 1.\ \text{Hence,}$$

$$0\leq\left|\kappa_{\wp}^{2}(x_i)-\kappa_{\mathbb{Q}}^{2}(x_i)\right|+\left|\varrho_{\wp}^{2}(x_i)-\varrho_{\mathbb{Q}}^{2}(x_i)\right|+\left|\lambda_{\wp}^{2}(x_i)-\lambda_{\mathbb{Q}}^{2}(x_i)\right|\leq 3$$

$$\Rightarrow 0\leq\frac{1}{3}\left\{\left|\kappa_{\wp}^{2}(x_i)-\kappa_{\mathbb{Q}}^{2}(x_i)\right|+\left|\varrho_{\wp}^{2}(x_i)-\varrho_{\mathbb{Q}}^{2}(x_i)\right|+\left|\lambda_{\wp}^{2}(x_i)-\lambda_{\mathbb{Q}}^{2}(x_i)\right|\right\}\leq 1 \quad (14)$$

$$\Rightarrow 0\leq 1-\frac{1}{3}\left\{\left|\kappa_{\wp}^{2}(x_i)-\kappa_{\mathbb{Q}}^{2}(x_i)\right|+\left|\varrho_{\wp}^{2}(x_i)-\varrho_{\mathbb{Q}}^{2}(x_i)\right|+\left|\lambda_{\wp}^{2}(x_i)-\lambda_{\mathbb{Q}}^{2}(x_i)\right|\right\}\leq 1$$

$$\Rightarrow 2\leq 2^{1-\frac{1}{3}\left\{\left|\kappa_{\wp}^{2}(x_i)-\kappa_{\mathbb{Q}}^{2}(x_i)\right|+\left|\varrho_{\wp}^{2}(x_i)-\varrho_{\mathbb{Q}}^{2}(x_i)\right|+\left|\lambda_{\wp}^{2}(x_i)-\lambda_{\mathbb{Q}}^{2}(x_i)\right|\right\}}\leq 1$$

$$1\leq 2^{1-\frac{1}{3}\left\{\left|\kappa_{\wp}^{2}(x_i)-\kappa_{\mathbb{Q}}^{2}(x_i)\right|+\left|\varrho_{\wp}^{2}(x_i)-\varrho_{\mathbb{Q}}^{2}(x_i)\right|+\left|\lambda_{\wp}^{2}(x_i)-\lambda_{\mathbb{Q}}^{2}(x_i)\right|\right\}}-1\leq 0$$

Also,

$$\Rightarrow 3\leq 2^{1-\frac{1}{3}\left\{\left|\kappa_{\wp}^{2}(x_i)-\kappa_{\mathbb{Q}}^{2}(x_i)\right|+\left|\varrho_{\wp}^{2}(x_i)-\varrho_{\mathbb{Q}}^{2}(x_i)\right|+\left|\lambda_{\wp}^{2}(x_i)-\lambda_{\mathbb{Q}}^{2}(x_i)\right|\right\}}+1\leq 2 \quad (15)$$

From (14) and (15), we have:

$$\frac{1}{3}\leq\frac{2^{1-\frac{1}{3}\left\{\left|\kappa_{\wp}^{2}(x_i)-\kappa_{\mathbb{Q}}^{2}(x_i)\right|+\left|\varrho_{\wp}^{2}(x_i)-\varrho_{\mathbb{Q}}^{2}(x_i)\right|+\left|\lambda_{\wp}^{2}(x_i)-\lambda_{\mathbb{Q}}^{2}(x_i)\right|\right\}}-1}{2^{1-\frac{1}{3}\left\{\left|\kappa_{\wp}^{2}(x_i)-\kappa_{\mathbb{Q}}^{2}(x_i)\right|+\left|\varrho_{\wp}^{2}(x_i)-\varrho_{\mathbb{Q}}^{2}(x_i)\right|+\left|\lambda_{\wp}^{2}(x_i)-\lambda_{\mathbb{Q}}^{2}(x_i)\right|\right\}}+1}\leq 0$$

$$0\leq 1-\frac{3}{\mathrm{n}}\left[\sum_{\mathrm{i}=1}^{\mathrm{n}}\left\{\frac{2^{1-\frac{1}{3}\left\{\left|\kappa_{\wp}^{2}(x_i)-\kappa_{\mathbb{Q}}^{2}(x_i)\right|+\left|\varrho_{\wp}^{2}(x_i)-\varrho_{\mathbb{Q}}^{2}(x_i)\right|+\left|\lambda_{\wp}^{2}(x_i)-\lambda_{\mathbb{Q}}^{2}(x_i)\right|\right\}}_{-1}}{2^{1-\frac{1}{3}\left\{\left|\kappa_{\wp}^{2}(x_i)-\kappa_{\mathbb{Q}}^{2}(x_i)\right|+\left|\varrho_{\wp}^{2}(x_i)-\varrho_{\mathbb{Q}}^{2}(x_i)\right|+\left|\lambda_{\wp}^{2}(x_i)-\lambda_{\mathbb{Q}}^{2}(x_i)\right|\right\}}_{+1}}\right\}\right]\leq 1$$

$$0\leq 1-\frac{3}{\mathrm{n}}\left[\sum_{\mathrm{i}=1}^{\mathrm{n}}\left\{\frac{2^{1-\frac{1}{3}\left\{\left|\kappa_{\wp}^{2}(x_i)-\kappa_{\mathbb{Q}}^{2}(x_i)\right|+\left|\varrho_{\wp}^{2}(x_i)-\varrho_{\mathbb{Q}}^{2}(x_i)\right|+\left|\lambda_{\wp}^{2}(x_i)-\lambda_{\mathbb{Q}}^{2}(x_i)\right|\right\}}_{-1}}{2^{1-\frac{1}{3}\left\{\left|\kappa_{\wp}^{2}(x_i)-\kappa_{\mathbb{Q}}^{2}(x_i)\right|+\left|\varrho_{\wp}^{2}(x_i)-\varrho_{\mathbb{Q}}^{2}(x_i)\right|+\left|\lambda_{\wp}^{2}(x_i)-\lambda_{\mathbb{Q}}^{2}(x_i)\right|\right\}}_{+1}}\right\}\right]\leq 1$$

$$\Rightarrow 0\leq\mathrm{D_{PFS}}(\wp,\mathbb{Q})\leq 1.$$

Thus, $0\leq\mathrm{D_{PFS}}(\wp,\mathbb{Q})\leq 1$.

Measure $\mathrm{D_{WPFS}}(\wp,\mathbb{Q})$ can be proved similarly.

(D2) $D_{PFS}(\wp, \mathbb{Q}) = 0 \Leftrightarrow \wp = \mathbb{Q}$ and $D_{WPFS}(\wp, \mathbb{Q}) = 0 \Leftrightarrow \wp = \mathbb{Q}$.

Proof: For $D_{PFS}(\wp, \mathbb{Q})$: We consider two PFS $\wp$ and $\mathbb{Q}$ in $X = \{x_1, x_2 \dots, x_n\}$,
Let $\wp = Q$, then $\kappa_{\wp}^2(x_i) = \kappa_{\mathbb{Q}}^2(x_i)$, $\varrho_{\wp}^2(x_i) = \varrho_{\mathbb{Q}}^2(x_i)$ and $\lambda_{\wp}^2(\mathrm{x_i}) = \lambda_{\mathbb{Q}}^2(\mathrm{x_I})$ which implies, $\left|\kappa_{\wp}^2(x_i) - \kappa_{\mathbb{Q}}^2(x_i)\right| = 0$, $\left|\varrho_{\wp}^2(x_i) - \varrho_{\mathbb{Q}}^2(x_i)\right| = 0$ and $\left|\lambda_{\wp}^2(\mathrm{x_i}) - \lambda_{\mathbb{Q}}^2(\mathrm{x_i})\right| = 0$.
Therefore,

$2^{1-\frac{1}{3}\{|\kappa_{\wp}^2(x_i)-\kappa_{\mathbb{Q}}^2(x_i)|+\ |\varrho_{\wp}^2(x_i)-\varrho_{\mathbb{Q}}^2(x_i)|+|\lambda_{\wp}^2(x_i)-\lambda_{\mathbb{Q}}^2(x_i)|\}}$-1=1 and

$2^{1-\frac{1}{3}\{|\kappa_{\wp}^2(x_i)-\kappa_{\mathbb{Q}}^2(x_i)|+\ |\varrho_{\wp}^2(x_i)-\varrho_{\mathbb{Q}}^2(x_i)|+|\lambda_{\wp}^2(x_i)-\lambda_{\mathbb{Q}}^2(x_i)|\}}$+1 = 3

$$\Rightarrow \frac{2^{1-\frac{1}{3}\{|\kappa_{\wp}^2(x_i)-\kappa_{\mathbb{Q}}^2(x_i)|+\ |\varrho_{\wp}^2(x_i)-\varrho_{\mathbb{Q}}^2(x_i)|+|\lambda_{\wp}^2(x_i)-\lambda_{\mathbb{Q}}^2(x_i)|\}}-1}{2^{1-\frac{1}{3}\{|\kappa_{\wp}^2(x_i)-\kappa_{\mathbb{Q}}^2(x_i)|+\ |\varrho_{\wp}^2(x_i)-\varrho_{\mathbb{Q}}^2(x_i)|+|\lambda_{\wp}^2(x_i)-\lambda_{\mathbb{Q}}^2(x_i)|\}}+1} = \frac{1}{3}$$

$$\Rightarrow \frac{3}{\mathrm{n}}\left[\sum_{\mathrm{i}=1}^{\mathrm{n}}\left\{\frac{2^{1-\frac{1}{3}\{|\kappa_{\wp}^2(x_i)-\kappa_{\mathbb{Q}}^2(x_i)|+\ |\varrho_{\wp}^2(x_i)-\varrho_{\mathbb{Q}}^2(x_i)|+|\lambda_{\wp}^2(x_i)-\lambda_{\mathbb{Q}}^2(x_i)|\}}-1}{2^{1-\frac{1}{3}\{|\kappa_{\wp}^2(x_i)-\kappa_{\mathbb{Q}}^2(x_i)|+\ |\varrho_{\wp}^2(x_i)-\varrho_{\mathbb{Q}}^2(x_i)|+|\lambda_{\wp}^2(x_i)-\lambda_{\mathbb{Q}}^2(x_i)|\}}+1}\right\}\right] = 1$$

$$\Rightarrow 1 - \frac{3}{\mathrm{n}}\left[\sum_{\mathrm{i}=1}^{\mathrm{n}}\left\{\frac{2^{1-\frac{1}{3}\{|\kappa_{\wp}^2(x_i)-\kappa_{\mathbb{Q}}^2(x_i)|+\ |\varrho_{\wp}^2(x_i)-\varrho_{\mathbb{Q}}^2(x_i)|+|\lambda_{\wp}^2(x_i)-\lambda_{\mathbb{Q}}^2(x_i)|\}}-1}{2^{1-\frac{1}{3}\{|\kappa_{\wp}^2(x_i)-\kappa_{\mathbb{Q}}^2(x_i)|+\ |\varrho_{\wp}^2(x_i)-\varrho_{\mathbb{Q}}^2(x_i)|+|\lambda_{\wp}^2(x_i)-\lambda_{\mathbb{Q}}^2(x_i)|\}}+1}\right\}\right] = 0$$

$$\Rightarrow D_{PFS}(\wp, \mathbb{Q}) = 0.$$

If $D_{PFS}(\wp, \mathbb{Q}) = 0$, this implies

$$\frac{3}{\mathrm{n}}\left[\sum_{\mathrm{i}=1}^{\mathrm{n}}\left\{\frac{2^{1-\frac{1}{3}\{|\kappa_{\wp}^2(x_i)-\kappa_{\mathbb{Q}}^2(x_i)|+\ |\varrho_{\wp}^2(x_i)-\varrho_{\mathbb{Q}}^2(x_i)|+|\lambda_{\wp}^2(x_i)-\lambda_{\mathbb{Q}}^2(x_i)|\}}-1}{2^{1-\frac{1}{3}\{|\kappa_{\wp}^2(x_i)-\kappa_{\mathbb{Q}}^2(x_i)|+\ |\varrho_{\wp}^2(x_i)-\varrho_{\mathbb{Q}}^2(x_i)|+|\lambda_{\wp}^2(x_i)-\lambda_{\mathbb{Q}}^2(x_i)|\}}+1}\right\}\right] = 1$$

$$\frac{2^{1-\frac{1}{3}\{|\kappa_{\wp}^2(x_i)-\kappa_{\mathbb{Q}}^2(x_i)|+\ |\varrho_{\wp}^2(x_i)-\varrho_{\mathbb{Q}}^2(x_i)|+|\lambda_{\wp}^2(x_i)-\lambda_{\mathbb{Q}}^2(x_i)|\}}-1}{2^{1-\frac{1}{3}\{|\kappa_{\wp}^2(x_i)-\kappa_{\mathbb{Q}}^2(x_i)|+\ |\varrho_{\wp}^2(x_i)-\varrho_{\mathbb{Q}}^2(x_i)|+|\lambda_{\wp}^2(x_i)-\lambda_{\mathbb{Q}}^2(x_i)|\}}+1} = \frac{1}{3}$$

Let $2^{1-\frac{1}{3}\{|\kappa_{\wp}^2(x_i)-\kappa_{\mathbb{Q}}^2(x_i)|+\ |\varrho_{\wp}^2(x_i)-\varrho_{\mathbb{Q}}^2(x_i)|+|\lambda_{\wp}^2(x_i)-\lambda_{\mathbb{Q}}^2(x_i)|\}} = x$

$\frac{x-1}{x+1} = \frac{1}{3}$.

Therefore,

$3x - 3 = x + 1 \Rightarrow \mathrm{x} = 2.$

$\Rightarrow 2^{1-\frac{1}{3}\{|\kappa_{\wp}^2(x_i)-\kappa_{\mathbb{Q}}^2(x_i)|+\ |\varrho_{\wp}^2(x_i)-\varrho_{\mathbb{Q}}^2(x_i)|+|\lambda_{\wp}^2(x_i)-\lambda_{\mathbb{Q}}^2(x_i)|\}} = 2$
$\Rightarrow \left|\kappa_{\wp}^2(x_i) - \kappa_{\mathbb{Q}}^2(x_i)\right| = 0, \quad \left|\varrho_{\wp}^2(x_i) - \varrho_{\mathbb{Q}}^2(x_i)\right| = 0$ and $\left|\lambda_{\wp}^2(\mathrm{x_i}) - \lambda_{\mathbb{Q}}^2(\mathrm{x_i})\right| = 0$. Therefore $\kappa_{\wp}^2(x_i) = \kappa_{\mathbb{Q}}^2(x_i)$, $\varrho_{\wp}^2(x_i) = \varrho_{\mathbb{Q}}^2(x_i)$ and $\lambda_{\wp}^2(\mathrm{x_i}) = \lambda_{\mathbb{Q}}^2(\mathrm{x_i})$. Hence $\wp = \mathbb{Q}$.
Measure $D_{WPFS}(\wp, \mathbb{Q})$ can be proved similarly.
(D3) $D_{PFS}(\wp, \mathbb{Q}) = D_{PFS}(\mathbb{Q}, \wp)$ and $D_{WPFS}(\wp, \mathbb{Q}) = D_{WPFS}(\mathbb{Q}, \wp)$
Proof for the above property is self-evident and direct.
(D4) If $\mathcal{R}$ is a PFS in X and $\wp \subseteq \mathbb{Q} \subseteq \mathcal{R}$, then $D_{PFS}(\wp, \mathbb{Q}) \leq D_{PFS}(\wp, \mathcal{R})$ and $D_{PFS}(\mathbb{Q}, \mathcal{R}) \leq D_{PFS}(\wp, \mathcal{R})$.
Proof. If $\wp \subseteq \mathbb{Q} \subseteq \mathcal{R}$, therefore for $x_i \in$ X, we get

$0 \leq \kappa_{\wp}^2(x_i) \leq \kappa_{\mathbb{Q}}^2(x_i) \leq \kappa_{\mathcal{R}}^2(x_i) \leq 1,$

$1 \geq \varrho_{\wp}^2(x_i) \geq \varrho_{\mathbb{Q}}^2(x_i) \geq \varrho_{\mathcal{R}}^2(x_i) \geq 0,$

$0 \leq \lambda_{\wp}^2(x_i) \leq \lambda_{\mathbb{Q}}^2(x_i) \leq \lambda_{\mathcal{R}}^2(x_i) \leq 1$. That implies

$\left|\kappa_{\wp}^2(x_i) - \kappa_{\mathbb{Q}}^2(x_i)\right| \leq \left|\kappa_{\wp}^2(x_i) - \kappa_{\mathcal{R}}^2(x_i)\right|$;
$\left|\kappa_{\mathbb{Q}}^2(x_i) - \kappa_{\mathcal{R}}^2(x_i)\right| \leq \left|\kappa_{\wp}^2(x_i) - \kappa_{\mathcal{R}}^2(x_i)\right|$;
$\left|\varrho_{\wp}^2(x_i) - \varrho_{\mathbb{Q}}^2(x_i)\right| \leq \left|\varrho_{\wp}^2(x_i) - \varrho_{\mathcal{R}}^2(x_i)\right|$;
$\left|\varrho_{\mathbb{Q}}^2(x_i) - \varrho_{\mathcal{R}}^2(x_i)\right| \leq \left|\varrho_{\wp}^2(x_i) - \varrho_{\mathcal{R}}^2(x_i)\right|$;
$\left|\lambda_{\wp}^2(x_i) - \lambda_{\mathbb{Q}}^2(x_i)\right| \leq \left|\lambda_{\wp}^2(x_i) - \lambda_{\mathcal{R}}^2(x_i)\right|$;
$\left|\lambda_{\mathbb{Q}}^2(x_i) - \lambda_{\mathcal{R}}^2(x_i)\right| \leq \left|\varrho_{\wp}^2(x_i) - \varrho_{\mathcal{R}}^2(x_i)\right|$

From the above we can write,

$$\begin{aligned}&\left|\kappa_{\wp}^2(x_i) - \kappa_{\mathbb{Q}}^2(x_i)\right| + \left|\varrho_{\wp}^2(x_i) - \varrho_{\mathbb{Q}}^2(x_i)\right| + \left|\lambda_{\wp}^2(x_i) - \lambda_{\mathbb{Q}}^2(x_i)\right| \leq \left|\kappa_{\wp}^2(x_i) - \kappa_{\mathcal{R}}^2(x_i)\right| + |\zeta_P^2(x_i) - \zeta_R^2(x_i)| + |\eta_P^2(x_i) - \eta_R^2(x_i)| \Rightarrow \\ &2^{1-\frac{1}{3}[|\kappa_{\wp}^2(x_i)-\kappa_{\mathbb{Q}}^2(x_i)|+\ |\varrho_{\wp}^2(x_i)-\varrho_{\mathbb{Q}}^2(x_i)|+|\lambda_{\wp}^2(x_i)-\lambda_{\mathbb{Q}}^2(x_i)|]} - 1 \leq \\ &2^{1-\frac{1}{3}[|\kappa_{\wp}^2(x_i)-\kappa_{\mathcal{R}}^2(x_i)|+|\varrho_{\wp}^2(x_i)-\varrho_{\mathcal{R}}^2(x_i)|+|\lambda_{\wp}^2(x_i)-\lambda_{\mathcal{R}}^2(x_i)|]} - 1\end{aligned} \tag{16}$$

and

$$\begin{aligned}&\mathbf{2^{1-\frac{1}{3}[|\kappa_{\wp}^2(x_i)-\kappa_{\mathbb{Q}}^2(x_i)|+\ |\varrho_{\wp}^2(x_i)-\varrho_{\mathbb{Q}}^2(x_i)|+|\lambda_{\wp}^2(x_i)-\lambda_{\mathbb{Q}}^2(x_i)|]}} + \\ &\mathbf{1} \leq \\ &2^{1-\frac{1}{3}[|\kappa_{\wp}^2(x_i)-\kappa_{\mathcal{R}}^2(x_i)|+|\varrho_{\wp}^2(x_i)-\varrho_{\mathcal{R}}^2(x_i)|+|\lambda_{\wp}^2(x_i)-\lambda_{\mathcal{R}}^2(x_i)|]} + 1\end{aligned} \tag{17}$$

Dividing (16) by (17), we have:

$$\frac{2^{1-\frac{1}{3}\{|\kappa_{\wp}^2(x_i)-\kappa_{\mathbb{Q}}^2(x_i)|+\ |\varrho_{\wp}^2(x_i)-\varrho_{\mathbb{Q}}^2(x_i)|+|\lambda_{\wp}^2(x_i)-\lambda_{\mathbb{Q}}^2(x_i)|\}}-1}{2^{1-\frac{1}{3}\{|\kappa_{\wp}^2(x_i)-\kappa_{\mathbb{Q}}^2(x_i)|+\ |\varrho_{\wp}^2(x_i)-\varrho_{\mathbb{Q}}^2(x_i)|+|\lambda_{\wp}^2(x_i)-\lambda_{\mathbb{Q}}^2(x_i)|\}}+1} \leq \frac{2^{1-\frac{1}{3}[|\kappa_{\wp}^2(x_i)-\kappa_{\mathbb{Q}}^2(x_i)|+\ |\varrho_{\wp}^2(x_i)-\varrho_{\mathbb{Q}}^2(x_i)|+|\lambda_{\wp}^2(x_i)-\lambda_{\mathbb{Q}}^2(x_i)|]}-1}{2^{1-\frac{1}{3}[|\kappa_{\wp}^2(x_i)-\kappa_{\mathcal{R}}^2(x_i)|+|\varrho_{\wp}^2(x_i)-\varrho_{\mathcal{R}}^2(x_i)|+|\lambda_{\wp}^2(x_i)-\lambda_{\mathcal{R}}^2(x_i)|]}+1} \Rightarrow 1 - \frac{3}{\mathrm{n}}\left[\sum_{i=1}^{n}\left\{\frac{2^{1-\frac{1}{3}\{|\kappa_{\wp}^2(x_i)-\kappa_{\mathbb{Q}}^2(x_i)|+\ |\varrho_{\wp}^2(x_i)-\varrho_{\mathbb{Q}}^2(x_i)|+|\lambda_{\wp}^2(x_i)-\lambda_{\mathbb{Q}}^2(x_i)|\}}-1}{2^{1-\frac{1}{3}\{|\kappa_{\wp}^2(x_i)-\kappa_{\mathbb{Q}}^2(x_i)|+\ |\varrho_{\wp}^2(x_i)-\varrho_{\mathbb{Q}}^2(x_i)|+|\lambda_{\wp}^2(x_i)-\lambda_{\mathbb{Q}}^2(x_i)|\}}+1}\right\}\right] \geq 1 - \frac{3}{\mathrm{n}}\left[\sum_{\mathrm{i}=1}^{\mathrm{n}}\left\{\frac{2^{1-\frac{1}{3}[|\kappa_{\wp}^2(x_i)-\kappa_{\mathcal{R}}^2(x_i)|+|\varrho_{\wp}^2(x_i)-\varrho_{\mathcal{R}}^2(x_i)|+|\lambda_{\wp}^2(x_i)-\lambda_{\mathcal{R}}^2(x_i)|]}-1}{2^{1-\frac{1}{3}[|\kappa_{\wp}^2(x_i)-\kappa_{\mathcal{R}}^2(x_i)|+|\varrho_{\wp}^2(x_i)-\varrho_{\mathcal{R}}^2(x_i)|+|\lambda_{\wp}^2(x_i)-\lambda_{\mathcal{R}}^2(x_i)|]}+1}\right\}\right] \Rightarrow$$
$D_{PFS}(\wp, \mathcal{R}) \leq D_{PFS}(\wp, \mathbb{Q})$. Similarly, $D_{PFS}(\wp, \mathcal{R}) \leq D_{PFS}(\mathbb{Q}, \mathcal{R})$

Similar proofs can be made for $\mathrm{D_{WPFS}}(\wp, \mathcal{R}) \leq \mathrm{D_{WPFS}}(\wp, \mathbb{Q})$ and $\mathrm{D_{WPFS}}(\wp, \mathcal{R}) \leq \mathrm{D_{WPFS}}(\mathbb{Q}, \mathcal{R})$.

4. PRACTICAL APPLICATION OF PFS USING TOPSIS APPROACH

The following are the steps for proposed PFS TOPSIS approach [36]
Step 1. Construct decision matrix (DM) for PFS as follows:
Let there be n possibilities from the available options $\mathfrak{F} = \{\mathfrak{F}_1, \mathfrak{F}_2, \dots, \mathfrak{F}_n\}$. The possible criteria set can be written as $\mathfrak{C} = \{\mathfrak{C}_1, \mathfrak{C}_2, \dots, \mathfrak{C}_m\}$ with m options. Let us denote $D = \left[d_{ij}^k\right]_{m\times n}$ be a set of *k*-decision-makers or experts of PFSs value $d_{ij} = (\kappa_{ij}, \varrho_{ij})$ is structured. Here, κ_{ij} and ϱ_{ij} are the MD and NMD of the alternatives $\mathfrak{F}_i$ satisfying the criteria $\mathfrak{C}_j$. The PFSs index $\lambda_{\mathrm{ij}} = \sqrt{1 - \kappa_{\mathrm{ij}}^2 - \varrho_{\mathrm{ij}}^2}$ displays the hesitation index of the alternative $\mathfrak{F}_i$ with respect to the criteria $\mathfrak{C}_j$.

Step 2. Normalize DM for PFS as follows:
Normalize the fuzzy DM based on benefit and cost criteria by interchanging MD with NMD and vice versa. In case of cost criteria; however, benefit criteria remain unchanged.
Step 3*:* Determination of weights for the criteria:
Initially weights of the criteria is taken as 0.37, 0.3, 0.23, and 0.1 for calculations. Later, sensitivity analysis has been done to validate our results.
Step 4*:* Compute PIS and NIS:
Find PIS and NIS for each criteria. This method divides assessment criteria into benefit (B) and cost (C). PIS and NIS can be constructed using PFSs and the traditional TOPSIS approach as:

$$\tilde{A}^{+} = \{r_1^{+}, r_2^{+}, \dots, r_n^{+}\} = \left\{ \left(\max_i \left(r_{ij}\right)/j \in B\right), \left(\left(\min_i (r_{ij}) \,/\, j \in C\right)\right) \right\} \tag{18}$$

$$\tilde{A}^{-} = \{r_1^{-}, r_2^{-}, \dots, r_n^{-}\} = \left\{ \left(\min_i \left(r_{ij}\right)/j \in B\right), \left(\left(\max_i (r_{ij}) \,/\, j \in C\right)\right) \right\} \tag{19}$$

Step 5: Calculate the divergence measures from the positive ideal and negative ideal solutions using propsoed mesures suggested in (12) and (13)

$$S_{WPFS}^{+} = D(A_i, \tilde{A}^{+}) = 1 - \left[\sum_{i=1}^{n} \left\{ \frac{2^{1-\frac{1}{3}\left|\kappa_{\wp}^{2}(x_i)-\kappa_{\mathbb{Q}}^{2+}(x_i)\right|+\left|\varrho_{\wp}^{2}(x_i)-\varrho_{\mathbb{Q}}^{2+}(x_i)\right|+\left|\lambda_{\wp}^{2}(x_i)-\lambda_{\mathbb{Q}}^{2+}(x_i)\right|\}_{-1}}}{2^{1-\frac{1}{3}\left|\kappa_{\wp}^{2}(x_i)-\kappa_{\mathbb{Q}}^{2+}(x_i)\right|+\left|\varrho_{\wp}^{2}(x_i)-\varrho_{\mathbb{Q}}^{2+}(x_i)\right|+\left|\lambda_{\wp}^{2}(x_i)-\lambda_{\mathbb{Q}}^{2+}(x_i)\right|\}_{+1}}} \right\}\right] \tag{20}$$

And

$$S_{WPFS}^{-} = D(A_i, \tilde{A}^{-}) = 1 - \frac{3}{n}\left[\sum_{i=1}^{n} \left\{ \frac{2^{1-\frac{1}{3}\left|\kappa_{\wp}^{2}(x_i)-\kappa_{\mathbb{Q}}^{2-}(x_i)\right|+\left|\varrho_{\wp}^{2}(x_i)-\varrho_{\mathbb{Q}}^{2-}(x_i)\right|+\left|\lambda_{\wp}^{2}(x_i)-\lambda_{\mathbb{Q}}^{2-}(x_i)\right|\}_{-1}}}{2^{1-\frac{1}{3}\left|\kappa_{\wp}^{2}(x_i)-\kappa_{\mathbb{Q}}^{2-}(x_i)\right|+\left|\varrho_{\wp}^{2}(x_i)-\varrho_{\mathbb{Q}}^{2-}(x_i)\right|+\left|\lambda_{\wp}^{2}(x_i)-\lambda_{\mathbb{Q}}^{2-}(x_i)\right|\}_{+1}}} \right\}\right] \tag{21}$$

Step 6: Calculate the relative closeness to the positive ideal solution
For each decision-maker, the relative closeness coefficient of each alternative with respect to PFSs ideal solution is determined as:

$$\psi_i = \frac{D(A_i,\tilde{A}^{-})}{D(A_i,\tilde{A}^{+})+D(A_i,\tilde{A}^{-})} = \frac{S_i^{-}}{S_i^{+}+S_i^{-}} \tag{22}$$

where $\psi_i \in [0,1], i = 1,2,\dots,n$.
The highest value of ψ_i indicates the preferred better the estimation of the available options.

4. 1. A Case Study With the growing popularity of smartphones, we can now have anything we need with only a few touches. This holds true for food as well. Food can be ordered online and delivered to our homes in minutes or hours, depending on the quantity of order and location. Several large organizations and startups are working hard to improve meal delivery services. In India, there are many meal delivery services that are competing to provide excellent service and cuisine. Most of them are limited to a single city, but a few have grown in popularity and are now available in many cities, providing excellent food delivery service. These meal delivery smartphone applications are vying to provide better service. Some of these meal delivery applications also include live tracking of the food delivery person, allowing us to keep track of our food and ensure that we never miss it. In this competitive environment, our objective is to find the best online food delivery app based on few criteria with the help of distance measure for Pythagorean fuzzy sets using TOPSIS approach. For that matter, we have chosen five top rated online food delivery apps viz., $\mathfrak{F}_1$, $\mathfrak{F}_2$, $\mathfrak{F}_3$, $\mathfrak{F}_4$ and $\mathfrak{F}_5$ as alternatives and four criteria viz., Well designed app ($\mathfrak{C}_1$), offers ($\mathfrak{C}_2$), delivery time ($\mathfrak{C}_3$) and price ($\mathfrak{C}_4$), Five leading online food delivery apps are to be evaluated by the decision-maker under the above four criteria in the following steps:
Step 1: Construct a decision matrix for each alternative according to each decision maker in terms of PFSs which is presented in Table 1.
Step 2: Based on this data, these apps required to be ranked and the best app needs to be determined. In MADM, the second step is to classify the considered problem in benefit and cost criteria. Benefit criteria are those criteria for which higher values are desired and cost criteria are those for which lower values are desired. In the considered case study, $\mathfrak{C}_1$ and $\mathfrak{C}_2$ are benefit criteria whereas $\mathfrak{C}_3$, and $\mathfrak{C}_4$ are cost criteria. The normalized data is presented in Table 2.
Step 3: We identify the fuzzy PIS and fuzzy NIS.
The subsequent values are presented in Table 3
Step 4: We find the measures values from PIS and NIS using Equations (20) and (21) for the measure and depicted in Tables 4 and 5, respectively.
Step 5: Relative closeness coefficient using Equation (24) can be found and shown in Table 6.
Analysing the ranking of alternatives, we rank these food delivery apps based on how close they are to one another. From the above table it is evident that F1 is the best food delivery app, and they are categorized as $F1 \succ F5 \succ F4 \succ F3 \succ F2$. Figure 1 depicts the ranking of the alternatives.

4. 2. Sensitivity Assessment If decision-makers arrive at different rankings for the available options, the output of getting optimum alternative remain unsolved. To eliminate ambiguity regarding the best options in terms of

TABLE 1. Rating values of DM in terms of PFS

	$\mathfrak{C}_1$	$\mathfrak{C}_2$	$\mathfrak{C}_3$	$\mathfrak{C}_4$
$\mathfrak{F}_1$	(0.81, 0.57)	(0.36, 0.63)	(0.64, 0.31)	(0.75, 0.57)
$\mathfrak{F}_2$	(0.59, 0.72)	(0.25, 0.75)	(0.25, 0.92)	(0.52, 0.84)
$\mathfrak{F}_3$	(0.28, 0.63)	(0.29, 0.53)	(0.39, 0.56)	(0.37, 0.61)
$\mathfrak{F}_4$	(0.47, 0.60)	(0.33, 0.67)	(0.46, 0.35)	(0.47, 0.59)
$\mathfrak{F}_5$	(0.26, 0.42)	(0.82, 0.48)	(0.64, 0.72)	(0.79, 0.51)

TABLE 2. Rating values of DM in terms of PFS

	$\mathfrak{C}_1$	$\mathfrak{C}_2$	$\mathfrak{C}_3$	$\mathfrak{C}_4$
$\mathfrak{F}_1$	(0.81, 0.57)	(0.36, 0.63)	(0.31, 0.64)	(0.57, 0.75)
$\mathfrak{F}_2$	(0.59, 0.72)	(0.25, 0.75)	(0.92, 0.25)	(0.84, 0.52)
$\mathfrak{F}_3$	(0.28, 0.63)	(0.29, 0.53)	(0.56, 0.39)	(0.61, 0.37)
$\mathfrak{F}_4$	(0.47, 0.60)	(0.33, 0.67)	(0.35, 0.46)	(0.59, 0.47)
$\mathfrak{F}_5$	(0.26, 0.42)	(0.82, 0.48)	(0.72, 0.64)	(0.51, 0.79)

TABLE 3. PIS and NIS for each criterion

	$\mathfrak{C}_1$	$\mathfrak{C}_2$	$\mathfrak{C}_3$	$\mathfrak{C}_4$
FPIS	(0.81, 0.42)	(0.82, 0.48)	(0.31, 0.64)	(0.51, 0.79)
FNIS	(0.26, 0.72)	(0.25, 0.75)	(0.92, 0.25)	(0.84, 0.37)

TABLE 4. Separation measures for fuzzy PIS

		$\mathfrak{C}_1$	$\mathfrak{C}_2$	$\mathfrak{C}_3$	$\mathfrak{C}_4$
For FPIS	$\mathfrak{F}_1$	0.11192	0.06528	0.07666	0.031995
	$\mathfrak{F}_2$	0.09669	0.06084	0.03944	0.023893
	$\mathfrak{F}_3$	0.07767	0.06227	0.06427	0.022982
	$\mathfrak{F}_4$	0.08923	0.06391	0.06717	0.024812
	$\mathfrak{F}_5$	0.07679	0.10000	0.05611	0.03333

TABLE 5. Separation measures for fuzzy NIS

		$\mathfrak{C}_1$	$\mathfrak{C}_2$	$\mathfrak{C}_3$	$\mathfrak{C}_4$
For FNIS	$\mathfrak{F}_1$	0.07679	0.08967	0.039446	0.024326
	$\mathfrak{F}_2$	0.10157	0.10000	0.076666	0.030564
	$\mathfrak{F}_3$	0.11401	0.08229	0.050559	0.026317
	$\mathfrak{F}_4$	0.11115	0.09294	0.040806	0.025800
	$\mathfrak{F}_5$	0.09669	0.06084	0.059857	0.022982

TABLE 6. Ranking result obtained from TOPSIS approach

	S_i^+	S_i^-	R_i	Ranking
$\mathfrak{F}_1$	0.7855956	0.8273251	0.512936	1
$\mathfrak{F}_2$	0.83434	0.768393	0.4794267	5
$\mathfrak{F}_3$	0.8295969	0.7951123	0.4893874	4
$\mathfrak{F}_4$	0.8161437	0.7969739	0.4940582	3
$\mathfrak{F}_5$	0.8003206	0.8197145	0.5059857	2

decision-makers, distinct expert values are combined by allocating a priority value to each expert so that $\rho_i > 0$ and $\sum_{i=1}^{n} \rho_i = 1$. Using these weight vectors, the distance measure of each expert is consolidated, and the overall estimated values of the alternatives are derived, as shown in Table 6:

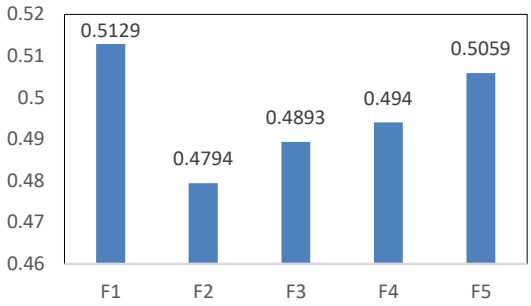

Figure 1. Ranking of alternative

$$\eta_i^+ = \sum_{k=1}^{s} \rho_k C_{ij}^+ \quad (23)$$

$$\eta_i^- = \sum_{k=1}^{s} \rho_k C_{ij}^- \quad (24)$$

Also,

$$\psi_i = \frac{\eta_i^-}{\eta_i^+ + \eta_i^-} \quad (25)$$

where $\psi_i \in [0,1], i = 1,2,\ldots,5$.

The relative closeness and ranking for each app is summarized in Table 7.

We opted to slightly adjust the original initial weights by examining four different situations to give accurate analysis in testing, the sensitivity of the results to changes in input parameters, especially decision makers weights. The suggested models provide the same output as (OFDA) is the best choice in all the cases. Therefore, it suggests that the proposed technique is accurate and reliable.

5. COMPARATIVE ANALYSIS

The proposed distance measures are compared with current measures based on the numerical scenarios presented to establish the supremacy. Table 8 shows a comparative analysis of the distance measures.

From the numerical results presented in Table 8, it was noticed that the findings achieved by projected distance measures are analogous with outcomes of prevailing measures.

TABLE 7. Relative closeness and ranking for each app

$Case\ I$: $\rho_1 = 0.42, \rho_2 = 0.28, \rho_3 = 0.1, \rho_4 = 0.2$

Alternatives	Distance Measures		ψ_i	Rank	Best App
	η_i^+	η_i^-			
$\mathfrak{F}_1$	0.786019	0.8225029	0.511340	1	$\mathfrak{F}_1$
$\mathfrak{F}_1$	0.826383	0.7726748	0.483206	5	
$\mathfrak{F}_1$	0.834847	0.7893657	0.485998	4	
$\mathfrak{F}_1$	0.820162	0.7883032	0.490096	3	

$\mathfrak{F}_1$	0.796325	0.8210934	0.507656	2	

Case II: $\rho_1 = 0.5, \rho_2 = 0.2, \rho_3 = 0.2, \rho_4 = 0.1$

Alternatives	Distance Measures		ψ_i	Rank	Best App
	η_i^+	η_i^-			
$\mathfrak{F}_1$	0.779924	0.833366	0.51656	1	
$\mathfrak{F}_1$	0.827927	0.774125	0.483208	5	
$\mathfrak{F}_1$	0.830985	0.790586	0.487543	4	$\mathfrak{F}_1$
$\mathfrak{F}_1$	0.815180	0.794910	0.493705	3	
$\mathfrak{F}_1$	0.810574	0.815299	0.501452	2	

Case III: $\rho_1 = 0.15, \rho_2 = 0.2, \rho_3 = 0.4, \rho_4 = 0.25$

Alternatives	Distance Measures		ψ_i	Rank	Best App
	η_i^+	η_i^-			
$\mathfrak{F}_1$	0.773333	0.83475	0.519097	1	
$\mathfrak{F}_1$	0.843926	0.761807	0.474429	5	
$\mathfrak{F}_1$	0.818319	0.808894	0.497104	4	$\mathfrak{F}_1$
$\mathfrak{F}_1$	0.806764	0.818130	0.503497	3	
$\mathfrak{F}_1$	0.790957	0.81901	0.508712	2	

Case IV: $\rho_1 = 0.15, \rho_2 = 0.2, \rho_3 = 0.25, \rho_4 = 0.40$

Alternatives	Distance Measures		ψ_i	Rank	$\mathfrak{F}_1$
	η_i^+	η_i^-			
$\mathfrak{F}_1$	0.774838	0.826680	0.516185	1	
$\mathfrak{F}_1$	0.836340	0.764922	0.477699	5	
$\mathfrak{F}_1$	0.823901	0.804017	0.493892	4	
$\mathfrak{F}_1$	0.811707	0.809064	0.499184	3	
$\mathfrak{F}_1$	0.780905	0.822432	0.512950	2	

TABLE 8. Comparative Analysis of the Distance Measures

Comparison	$\mathfrak{F}_1$	$\mathfrak{F}_2$	$\mathfrak{F}_3$	$\mathfrak{F}_4$	$\mathfrak{F}_5$
Distance Measure [19]	0.6827	0.1819	0.3641	0.4148	0.5818
Normalized Hausdorff distance [49]	0.6827	0.1819	0.3641	0.4148	0.5818
Chen's distance measure [11]	0.6740	0.1995	0.3733	0.4255	0.5654
Distance Measure [52]	0.7162	0.1257	0.3338	0.4429	0.6380
Proposed Distance	0.5129	0.4794	0.4893	0.4940	0.5059

6. CONCLUSIONS

Distance measures are an effective tool for measuring uncertainty using Pythagorean fuzzy sets. In this article, an innovative approach is used to measure the performance of online food delivery apps (OFDA), ensuring that the results are accurate every time. The salient feature of the proposed distance measures is their efficiency in distinguishing PFS with high hesitancy. The proposed distance measures satisfy the useful properties in the proven theorems. Comparison between alternatives or characteristics that uses fuzzy membership tackles the uncertainty and erroneous judgement. By using the TOPSIS approach, this paper presents an innovative study in MCDM in a fuzzy TOPSIS environment. Because of its capacity to accommodate decision makers' hazy opinions and perceptions, the TOPSIS method is the best way for tackling MCDM challenges. This novel model assists decision makers in thematically making error-free decisions, regardless of the multi-criteria field. The concept of TOPSIS can be applied to solve real life problems in fuzzy environments, which have uncertainty problems associated with them.

From the study, it is observed that the novel distance measures for PFS give reliable outputs compared to the existing ones and, hence, can suitably handle multi criteria decision making effectively.

TOPSIS approach is rational and understandable, and the computation process are straightforward. However, this method presents certain drawbacks. One of the problems attributable to TOPSIS is that it can cause the phenomenon known as rank reversal. Rank reversal occurs when a decision maker, in the process of selecting an option from a set of choices, is confronted with new alternatives that were not thought about when the selection process was initiated. It depends on the relationship between this new alternative and the old ones under each criterion. Therefore, modifications in the algorithm of TOPSIS approach will certainly resolve this issue.

We believe, the proposed distance measures will find its serviceability in new avenues of application. Future study in this direction includes

- Parametric generalizations of similarity measures for PFS
- Application of proposed distance measures fro interval valued PFS,
- Development of new MCDM approaches and comparing them with the suggested approach
- Utility of distance measures to intuitionistic fuzzy sets, Fermatean fuzzy sets, soft sets, rough sets etc.
- Applications to entropy-distance measures in decision making.

6. REFERENCES

1. Bordogna, G., Fedrizzi, M. and Pasi, G., "A linguistic modeling of consensus in group decision making based on owa operators", ***IEEE Transactions on Systems, Man, and Cybernetics-Part A: Systems and Humans***, Vol. 27, No. 1, (1997), 126-133.
2. Chen, S.-J. and Hwang, C.-L., Fuzzy multiple attribute decision making methods, in Fuzzy multiple attribute decision making. 1992, Springer.289-486.
3. Fodor, J.C. and Roubens, M., "Fuzzy preference modelling and multicriteria decision support, Springer Science & Business Media, Vol. 14, (1994).

4. Herrera, F., Herrera-Viedma, E. and Verdegay, J., "A linguistic decision process in group decision making", ***Group Decision and Negotiation***, Vol. 5, No. 2, (1996), 165-176.
5. Kacprzyk, J., Fedrizzi, M. and Nurmi, H., "Group decision making and consensus under fuzzy preferences and fuzzy majority", ***Fuzzy Sets and Systems***, Vol. 49, No. 1, (1992), 21-31. doi.
6. Zadeh, L.A., Fuzzy sets, in Fuzzy sets, fuzzy logic, and fuzzy systems: Selected papers by lotfi a zadeh. 1996, World Scientific.394-432.
7. Atanassov, K.T., Intuitionistic fuzzy sets, in Intuitionistic fuzzy sets. 1999, Springer.1-137.
8. Atanassov, K.T., "More on intuitionistic fuzzy sets", ***Fuzzy Sets and Systems***, Vol. 33, No. 1, (1989), 37-45.
9. Yager, R.R., "Pythagorean fuzzy subsets", in 2013 joint IFSA world congress and NAFIPS annual meeting (IFSA/NAFIPS), IEEE., (2013), 57-61.
10. Yager, R.R., "Pythagorean membership grades in multicriteria decision making", ***IEEE Transactions on Fuzzy Systems***, Vol. 22, No. 4, (2013), 958-965. doi: 10.1109/TFUZZ.2013.2278989.
11. Chen, T.-Y., "Remoteness index-based pythagorean fuzzy vikor methods with a generalized distance measure for multiple criteria decision analysis", ***Information Fusion***, Vol. 41, (2018), 129-150. https://doi.org/10.1016/j.inffus.2017.09.003
12. Lai, Y.-J., Liu, T.-Y. and Hwang, C.-L., "Topsis for modm", ***European Journal of Operational Research***, Vol. 76, No. 3, (1994), 486-500.
13. Wei, G. and Wei, Y., "Similarity measures of pythagorean fuzzy sets based on the cosine function and their applications", ***International Journal of Intelligent Systems***, Vol. 33, No. 3, (2018), 634-652. https://doi.org/10.1002/int.21965
14. Ejegwa, P.A., "Distance and similarity measures for pythagorean fuzzy sets", ***Granular Computing***, Vol. 5, No. 2, (2020), 225-238. https://doi.org/10.1007/s41066-018-00149-z
15. Xiao, F. and Ding, W., "Divergence measure of pythagorean fuzzy sets and its application in medical diagnosis", ***Applied Soft Computing***, Vol. 79, (2019), 254-267. https://doi.org/10.1016/j.asoc.2019.03.043
16. Peng, X., "New similarity measure and distance measure for pythagorean fuzzy set", ***Complex & Intelligent Systems***, Vol. 5, No. 2, (2019), 101-111. https://doi.org/10.1007/s40747-018-0084-x
17. Firozja, M.A., Agheli, B. and Jamkhaneh, E.B., "A new similarity measure for pythagorean fuzzy sets", ***Complex & Intelligent Systems***, Vol. 6, No. 1, (2020), 67-74. https://doi.org/10.1007/s40747-019-0114-3
18. Ejegwa, P.A., "Modified zhang and xu's distance measure for pythagorean fuzzy sets and its application to pattern recognition problems", ***Neural Computing and Applications***, Vol. 32, No. 14, (2020), 10199-10208. https://doi.org/10.1007/s00521-019-04554-6
19. Zhang, X. and Xu, Z., "Extension of topsis to multiple criteria decision making with pythagorean fuzzy sets", ***International Journal of Intelligent Systems***, Vol. 29, No. 12, (2014), 1061-1078. https://doi.org/10.1002/int.21676
20. Zhou, F. and Chen, T.-Y., "A novel distance measure for pythagorean fuzzy sets and its applications to the technique for order preference by similarity to ideal solutions", ***International Journal of Computational Intelligence Systems***, Vol. 12, No. 2, (2019), 955-969. https://doi.org/10.2991/ijcis.d.190820.001
21. Ullah, K., Mahmood, T., Ali, Z. and Jan, N., "On some distance measures of complex pythagorean fuzzy sets and their applications in pattern recognition", ***Complex & Intelligent Systems***, Vol. 6, No. 1, (2020), 15-27. doi. https://doi.org/10.1007/s40747-019-0103-6
22. Boran, F.E. and Akay, D., "A biparametric similarity measure on intuitionistic fuzzy sets with applications to pattern recognition", ***Information sciences***, Vol. 255, No., (2014), 45-57. doi. https:// doi.org/10.1016/ j.ins.2013.08. 013
23. Iqbal, M.N. and Rizwan, U., "Some applications of intuitionistic fuzzy sets using new similarity measure", ***Journal of Ambient Intelligence and Humanized Computing***, (2019), 1-5. https://doi.org/10.1007/s12652-019-01516-7
24. Ejegwa, P.A. and Agbetayo, J.M., "Similarity-distance decision-making technique and its applications via intuitionistic fuzzy pairs", ***Journal of Computational and Cognitive Engineering***, (2022). doi: 10.47852/bonviewJCCE512522514.
25. Ejegwa, P.A., Adah, V. and Onyeke, I.C., "Some modified pythagorean fuzzy correlation measures with application in determining some selected decision-making problems", ***Granular Computing***, Vol. 7, No. 2, (2022), 381-391. https://doi.org/10.1007/s41066-021-00272-4
26. Lin, M., Huang, C. and Xu, Z., "Topsis method based on correlation coefficient and entropy measure for linguistic pythagorean fuzzy sets and its application to multiple attribute decision making", ***Complexity***, Vol. 2019, (2019). https://doi.org/10.1155/2019/ 6967390
27. Kaviyani-Charati, M., Ghodsypour, S. and Hajiaghaei-Keshteli, M., "Impact of adopting quick response and agility on supply chain competition with strategic customer behavior", ***Scientia Iranica***, Vol. 29, No. 1, (2022), 387-411. doi: 10.24200/sci.2020.53691.3366.
28. Cheraghalipour, A., Paydar, M.M. and Hajiaghaei-Keshteli, M., "Applying a hybrid bwm-vikor approach to supplier selection: A case study in the iranian agricultural implements industry", ***International Journal of Applied Decision Sciences***, Vol. 11, No. 3, (2018), 274-301. doi: 10.1504/IJADS.2018.092796.
29. Shahsavar, M.M., Akrami, M., Kian, Z., Gheibi, M., Fathollahi-Fard, A.M., Hajiaghaei-Keshteli, M. and Behzadian, K., "Bio-recovery of municipal plastic waste management based on an integrated decision-making framework", ***Journal of Industrial and Engineering Chemistry***, Vol. 108, (2022), 215-234.
30. Sadri, E., Harsej, F., Hajiaghaei-Keshteli, M. and Siyahbalaii, J., "Evaluation of the components of intelligence and greenness in iranian ports based on network data envelopment analysis (dea) approach", ***Journal of Modelling in Management***, (2021). https://doi.org/10.1108/JM2-03-2021-0071
31. Ghoushchi, S.J., Bonab, S.R., Ghiaci, A.M., Haseli, G., Tomaskova, H. and Hajiaghaei-Keshteli, M., "Landfill site selection for medical waste using an integrated swara-waspas framework based on spherical fuzzy set", ***Sustainability***, Vol. 13, No. 24, (2021), 13950. doi: 10.3390/su132413950.
32. Cheraghalipour, A., Paydar, M. and Hajiaghaei-Keshteli, M., "An integrated approach for collection center selection in reverse logistics", ***International Journal of Engineering*, *Transactions A: Basics***, Vol. 30, No. 7, (2017), 1005-1016. doi: 10.5829/ije.2017.30.07a.10.
33. Fasihi, M., Tavakkoli-Moghaddam, R., Najafi, S.E. and Hajiaghaei-Keshteli, M., "Developing a bi-objective mathematical model to design the fish closed-loop supply chain", ***International Journal of Engineering*, *Transactions B: Applications***, Vol. 34, No. 5, (2021), 1257-1268. doi: 10.5829/ije.2021.34.05b.19.
34. Valinejad, F., Safaie, N., Rahmani, D. and Saadatmand, M.R., "A hybrid model for supply chain risk management based on five-dimensional sustainability approach in telecommunication industry", ***International Journal of Engineering*, *Transactions C: Aspects***, Vol. 35, No. 6, (2022), 1096-1110. doi: 10.5829/ije.2022.35.06c.01.
35. Aghaei Afshar, M., Hosseini, S. and Sahraeian, R., "A bi-objective cold supply chain for perishable products considering

quality aspects: A case study in iran dairy sector", ***International Journal of Engineering*, *Transactions B: Applications***, Vol. 35, No. 2, (2022), 458-470. doi: 10.5829/ije.2022.35.02b.22.

36. Nozari, H., Tavakkoli-Moghaddam, R. and Gharemani-Nahr, J., "A neutrosophic fuzzy programming method to solve a multi-depot vehicle routing model under uncertainty during the covid-19 pandemic", ***International Journal of Engineering*, *Transactions B: Applications,*** Vol. 35, No. 2, (2022), 360-371. doi: 10.5829/ije.2022.35.02b.12.
37. Zahedi-Anaraki, A., Tavakkoli-Moghaddam, R. and Sadeghian, R., "A modified benders decomposition algorithm for a last-mile network with flexible delivery options", ***International Journal of Engineering*, *Transactions B: Applications***, Vol. 35, No. 8, (2022), 1547-1557. doi: 10.5829/ije.2022.35.08B.11.
38. Hwang, C.-L. and Masud, A.S.M., "Multiple objective decision making—methods and applications: A state-of-the-art survey, Springer Science & Business Media, Vol. 164, (2012).
39. Adeel, A., Akram, M. and Koam, A.N., "Group decision-making based on m-polar fuzzy linguistic topsis method", ***Symmetry***, Vol. 11, No. 6, (2019), 735. https://doi.org/10.3390/sym11060735
40. Akram, M. and Adeel, A., "Topsis approach for magdm based on interval-valued hesitant fuzzy n-soft environment", ***International Journal of Fuzzy Systems***, Vol. 21, No. 3, (2019), 993-1009. https://doi.org/10.1007/s40815-018-0585-1
41. Askarifar, K., Motaffef, Z. and Aazaami, S., "An investment development framework in iran's seashores using topsis and best-worst multi-criteria decision making methods", ***Decision Science Letters***, Vol. 7, No. 1, (2018), 55-64. doi: 10.5267/j.dsl.2017.4.004.
42. Balioti, V., Tzimopoulos, C. and Evangelides, C., "Multi-criteria decision making using topsis method under fuzzy environment. Application in spillway selection", ***Multidisciplinary Digital Publishing Institute Proceedings***, Vol. 2, No. 11, (2018), 637. doi: 10.3390/proceedings211063.
43. Chen, C.-T., "Extensions of the topsis for group decision-making under fuzzy environment", ***Fuzzy Sets and Systems***, Vol. 114, No. 1, (2000), 1-9. https://doi.org/10.1016/S0165-0114(97)00377-1
44. Gao, P., Feng, J. and Yang, L., "Fuzzy topsis algorithm for multiple criteria decision making with an application in information systems project selection", in 2008 4th International Conference on Wireless Communications, Networking and Mobile Computing, IEEE., (2008), 1-4.
45. Gupta, P., Mehlawat, M.K., Grover, N. and Pedrycz, W., "Multi-attribute group decision making based on extended topsis method under interval-valued intuitionistic fuzzy environment", ***Applied Soft Computing***, Vol. 69, (2018), 554-567. https://doi.org/10.1016/j.asoc.2018.04.032
46. Kore, N.B., Ravi, K. and Patil, S., "A simplified description of fuzzy topsis method for multi criteria decision making", ***International Research Journal of Engineering and Technology***, Vol. 4, No. 5, (2017), 2047-2050.
47. Kumar, K. and Garg, H., "Topsis method based on the connection number of set pair analysis under interval-valued intuitionistic fuzzy set environment", ***Computational and Applied Mathematics***, Vol. 37, No. 2, (2018), 1319-1329. https://doi.org/10.1007/s40314-016-0402-0
48. Li, D.-F. and Nan, J.-X., "Extension of the topsis for multi-attribute group decision making under atanassov ifs environments", ***International Journal of Fuzzy System Applications***, Vol. 1, No. 4, (2011), 47-61. doi: 10.4018/ijfsa.2011100104.
49. Hussian, Z. and Yang, M.S., "Distance and similarity measures of pythagorean fuzzy sets based on the hausdorff metric with application to fuzzy topsis", ***International Journal of Intelligent Systems***, Vol. 34, No. 10, (2019), 2633-2654. https://doi.org/10.1002/int.22169
50. Shannon, C.E., "A mathematical theory of communication", ***The Bell System Technical Journal***, Vol. 27, No. 3, (1948), 379-423. doi.
51. Li, D. and Zeng, W., "Distance measure of pythagorean fuzzy sets", ***International Journal of Intelligent Systems***, Vol. 33, No. 2, (2018), 348-361. https://doi.org/10.1002/int.21934
52. Mahanta, J. and Panda, S., "Distance measure for pythagorean fuzzy sets with varied applications", ***Neural Computing and Applications***, Vol. 33, No. 24, (2021), 17161-17171. https://doi.org/10.1007/s00521-021-06308-9

Persian Abstract

چکیده

گسترش برنامه‌های ارسال غذای آنلاین (OFDA) در سراسر جهان به دلیل افزایش ناگهانی موارد همه‌گیری COVID-19 سرعت گرفته است. OFDA به سرعت در هند در حال گسترش است و فرصت های زیادی را برای پلتفرم های مختلف OFDA فراهم می کند و بازار رقابتی ایجاد می کند. معیارها و ابعاد مختلفی برای کسب‌وکارهای OFDA وجود دارد که باید آن‌ها را بررسی کنند تا با بازار رقابتی که اغلب در حال تغییر است و به موفقیت بلندمدت دست پیدا کنند. مجموعه فازی فیثاغورث (PFS)یک ابزار قدرتمند برای مقابله با عدم قطعیت است. اندازه گیری فاصله PFS یک موضوع تحقیقاتی داغ است و کاربردهای واقعی در بسیاری از زمینه ها مانند تصمیم گیری، تشخیص پزشکی، تجزیه و تحلیل الگوها، خوشه بندی و غیره دارد. هدف این مقاله بررسی نتایج استراتژی جدید اندازه گیری فاصله فازی فیثاغورث است. بهترین برنامه آنلاین را با استفاده از روش TOPSIS انتخاب کنید تا بهترین OFDA را انتخاب کنید. ابتدا، تمام بدیهیات مربوط به اندازه گیری های فاصله برای اقدامات پیشنهادی اثبات شده است. کار پیشنهادی از پنج گزینه / گزینه متمایز و چهار ویژگی / معیار در یک محیط فازی برای مقابله با اطلاعات نادقیق و متناقض استفاده می کند. یافته‌ها نشان می‌دهد که روش پیشنهادی روشی واقعی‌تر برای انتخاب بهترین OFDA در میان سایر روش‌ها است. در نهایت، از یک تحلیل حساسیت برای تعیین اینکه آیا جایگزین انتخاب شده بهترین گزینه در میان سایر مؤلفه‌ها بوده و برای اطمینان از دقیق بودن نتایج تکنیک TOPSIS استفاده می‌شود.

IJE TRANSACTIONS A: Basics Vol. 35 No. 10, (October 2022) 1887-1894

International Journal of Engineering

Journal Homepage: www.ije.ir

Study on Polycaprolactone Coated Hierarchical Meso/ Macroporous Titania Scaffolds for Bone Tissue Engineering

N. Hassanzadeh Nemati*[a], S. M. Mirhadi[b]

[a] *Department of Biomedical Engineering, Science and Research Branch, Islamic Azad University, Tehran, Iran*
[b] *Department of Materials Engineering, Shahreza Branch, Islamic Azad University, Shahreza, Isfahan, Iran*

PAPER INFO

Paper history:
Received 15 December 2021
Received in revised form 11 June 2022
Accepted 12 June 2022

Keywords:
Meso/Macrospore
Titania
Hierarchical
Elisa
Foamy Method
Polymer Coating

ABSTRACT

In this study, the effect of polycaprolactone (PCL) coating on the mechanical strength, cell behavior and cell attachment of the hierarchical meso/macroporous Titania scaffold were investigated. Titania scaffold as the substrate was fabricated through the evaporation-induced self-assembly coupled with the foamy method. Then prepared scaffolds were coated by polycaprolactone solution with three different weight percentages by the dip-coating method. SAXS, WAXRD, SEM, compressive strength, MTT and cell attachment test were applied to characterized the samples. Based on XRD results, as polycaprolactone concentration increased, the intensity of the crystalline polycaprolactone phase increased while the TiO_2 peak intensity decreased due to the covering of mesoporous titania by polycaprolactone. Compressive strength showed that by increasing polycaprolactone percent, the porosity decrease from 89.5 to 73.8 % which caused increasing strength from 0.2 to 0.79 MPa. The SEM results illustrated that by increasing polycaprolactone concentration from 1.2 to 1.5 wt%, the macrospores were filled by polycaprolactone. In this regard, The sample containing 1wt% polycaprolactone was choosen as the selective sample. Also, the MTT test reported a small trace of cytotoxicity in contact with the L929 mouse fibroblast cells. The cell attachment test that was performed by using MG63 cells, showed that the coated samples provided the suitable substrate for cells to attach and also showed cell viability on the surface of the coated substrate. Overall, according to the results, the hierarchical meso/macroporous Titania scaffold coated with 1 wt% polycaprolactone, could have good potential to be used in tissue engineering.

doi: *10.5829/ije.2022.35.10a.08*

1. INTRODUCTION

The natural bone is an alive complex structure made of organic/inorganic hierarchical porous composites that provide the metabolism and mechanical strength of the bone [1-3]. Bone injuries would be happened due to old age, accidents, and mechanical strikes altogether have made the researchers use bone grafts and artificial bone tissue engineering devices. In this way, bone tissue engineering scaffolds have good potential as a response to these challenges [4-8]. For this purpose, biomimetic ceramic-polymer composite which has controllable hierarchical porous could mimic the structure and function of natural bone and have positive interactions with cells of this tissue [9, 10]. Improvement of mechanical strength, increasing specific surface area, the possibility of collateral cell growth, and the potential of releasing biological agents and drugs are the positive point of this type of structure [11-13]. Recently, bio-glasses mesoporous structure, silica, and Titania that have bioactive features caused to showed a new approach in bone tissue engineering [13-17]. Titanium dioxide, with the ability to adsorb proteins and hydroxyapatite, can bone attachment. These results were considered in the in-vitro condition which showed a positive effect in the in-vivo condition [18-23]. The hierarchical porous titanium dioxide provides surface activity, nano roughness, and appropriate space for loading cellular and biological agents [24].

Polycaprolactone (PCL) is an organic component because of its adaptability and biodegradability has been considered much in tissue engineering applications [25].

*Corresponding Author Institutional Email: hasanzadeh@srbiau.ac.ir
(N. Hassanzadeh Nemati)

Please cite this article as: N. Hassanzadeh Nemati,S. M. Mirhadi, Study on Polycaprolactone Coated Hierarchical Meso/ Macroporous Titania Scaffolds for Bone Tissue Engineering, ***International Journal of Engineering, Transactions A: Basics***, Vol. 35 No. 10, (2022), 1887-1894

Hybrid structures containing PCL and titanium dioxide can increase the corrosion resistance of biodegradable alloys by coating them [26, 27] or to be used in drug release applications [28]. Some investigations also have focused on the use of PCL as an inorganic and titanium oxide with various designs as an inorganic component of the scaffolds for bone tissue repairing and regeneration. Some of them are mentioned in the following paragraph. Khoshroo et al. [29] designed and produced a scaffold for bone tissue engineering by exploiting the properties of PCL and combining it with titanium oxide nanotubes. De Santis et al. [30] investigated the cell compatibility and some features of the polycaprolactone/ hybrid titanium dioxide. Catauro et al. [31] studied the TiO_2/PCL hybrid layers through sol-gel on the surface of the titanium by deep coating. They investigated the characterization and biological features of this hybrid that shows it's in vitro bioactivity of it. Hierarchical meso/macroporous structure provides suitable bio-inspired geometry structure for scaffolds. Also by literature survey, it could be concluded that by polymer coating of mentioned scaffolds, the biocompatibility improved. Also, by improvement of biological behavior, it could be potentially suitable for the targeted control of biological agents, which could prevent the body's defensive response and reject of scaffold which provides a appropriate cell differentiation. In another word, using polycaprolactone in the composition of the scaffold provides a better possibility for the formation of calcium phosphates [32].

So far, no studies have been performed on a hierarchical porous titanium oxide (titania) coated with PCL, which has been considered in the present work. For this purpose, a hierarchical porous Titania scaffold fabricated by EISA along with the foamy method [33] were coated with polycaprolactone polymer to enhance the mechanical strength and make the structure susceptible to the support of bioactive agents for bone tissue engineering applications.

2. MATERIALS AND METHODS

2. 1. Sample Preparation The hierarchical meso/macroporous Titania scaffolds were synthesized as the substrate according to our previous studies [24, 30]. Briefly, Titanium (IV) butoxide ($C_{16}H_{36}O_4Ti$, 97%, Sigma Aldrich) is the precursor, the tri-block F127 copolymer (99.5%, Sigma Aldrich) as the template, and anhydrous ethanol (C_2H_6O, 99.5%, Sigma Aldrich), hydrochloric acid (HCl, 38 wt.%) and acetylacetone ($C_5H_8O_2$, 99.5%, Sigma Aldrich) were used as the solvent and restrain the speed of hydrolysis-condensation. The sol-gel process according to Catauro et al. [34] and Li et al. [35] was used. In this regard, the mass ratio of F127/TBT/HCl/EtOH/AcAc was kept to 3/100/8/5/2, respectively and then, aged for 48h at room temperature and 40% humidity, the pre-cut polyurethane foam blocks (60 ppi) in size of $1*1*1cm^3$ were soaked in colloid for 2 minutes. Then the samples were squeezed to remove the extra solution and dried at room temperature for 72h. Finally, the samples were calcined in 550 ^{0}C for 2h with a rate of 4^{0}C/min.

To prepare the coating solution 1, 1.2, and 1.5wt% polycaprolactone (Sigma-Aldrich 80000 Mn) and chloroform (99% purity) were made in a container and ceramic scaffolds were immersed in it for 3 minutes. After that scaffolds were dried for 72h at room temperature. Table 1 summarized the sample designations, where the number before PCL represents the percentage of PCL.

2. 2. Invitro Cell Viability To evaluate the in-vitro cell viability test, the fibroblast mouse cell (Mouse C34/connective tissue-L929) from the cell bank of Pasture Institue of Iran was provided. In this way, the massive cells were cultured in RPMI-1640 medium containing 50 unit penicillins, 50 μg/ mL streptomycin, and 10% fetal bovine serum in an incubation flask with 5% carbonic gas and 85% humidity at 37 °C. After 3 to 4 days (which cell layer formed), the cells were removed by trypsin enzyme (0.25%) from the flask surface. Then a suspension with 20000 cells/mL concentration was prepared.

The prepared specimens (5 ×5 mm) were sterilized by UV for 1 h. Then the samples were put in a 24-well (culture) plate, in which for each sample 3 separated wells were considered also 3 wells were considered for the control sample. In this way, 1 mL cellular suspension was added to each well and was put in the incubator. In each well, 20000 cells in a culture medium (RPMI-1640) containing 10% fetal bovine serum (FBS) were added. After 48 hours, 100 μL of MTT stain with 5 mg/mL concentration was added to the cell medium culture and incubated at 37 °C for 48 h. Then the medium culture on the cells was removed by phosphate-buffered saline (PBS), in the following, 0.5 mL of DMSO solution was added to each well. After dissolving the purple color in the samples, they were transferred to an ELISA plate and the absorbance of the samples was reported at 570 nm. Three wells were considered from each sample to determine the mean absorbance values.

TABLE 1. Titania scaffolds designations with PCL coating

Sample	Amount of pcl (wt%) in the coating solutions
0PCL	Without any coating
1PCL	1
1.2PCL	1.2
1.5PCL	1.5

2. 3. Cell Attachment Assay The cell attachment test was considered in sample 1PCL, in this regard; Human osteosarcoma bone cell (MG63) was obtained from Pasture Institue of Iran cell bank. The massive cells were initially cultured in a cultured media containing 50 units of penicillin and 50 µg/mL streptomycin supplemented with 10% fetal bovine serum in incubation flasks with 5% CO_2 and 85% humidity at 37 °C. After 3 to 4 days (which cell layer formed), the cells were removed by trypsin enzyme (0.25%) from the flask surface. Then a suspension with 40000 cells/mL concentration was used. Both sides of the prepared samples were sterilized by UV for 1 h. Then the samples were put in a 24-well (culture) plate (each sample individually in one well) and a non-sample well was considered as a control. Then 1 mL of cell suspension was added to samples and placed in an incubator, After 24 and 48h incubation, the sample (1PCL) was evaluated qualitatively by an inverted microscope (Nikon TE-100). In order to stabilize the cells, the samples were washed three times with PBS. Then the sample was placed in glutaraldehyde solution (2.5%) for 2h after 2h washed it again with PBS. In order to dehydrate the sample, different concentrations of alcohol and water were used (by the concentration of 50, 60, 70, 80, 90, and 100) for each concentration washed for 5 min. finally, the prepared sample was dried at room temperature and the cell attachment was examined by using an FEI- ESEM Quanta 200 scanning electron microscope.

2. 4. Characterization Coating of mesoporous with polycaprolactone was studied by small-angle X-ray diffraction (SAXS) by an Asenware AW-DX300 diffractometer with Cu Kα radiation (λ = 1.54184 Aº) in the 2θ range 0.5-10º) and Wide-angle X-ray diffraction (WAXRD) was also applied to evaluate the crystalline phase of scaffolds using the same machine in the 2θ range 10 -100º.SEM investigation was used to investigate the morphology and macroporous structure coated with polymer (Zeiss SEM, Germany, on gold-coated samples) also in order to investigate the morphology of the cell attachment of coated samples was examined at room temperature using an FEI- ESEM Quanta 200 scanning electron microscope. Compressive strength of Titania scaffolds and Titania scaffolds coated by polycaprolactone polymer were tested using (AG-400NL, SHIMADZU Co., JAPAN) with an overhead speed of 0.5 mm/min.

An ethanol immersion test also was performed for calculating of porosity percentages of the samples.

2. 5. Statistical Analysis All data were reported as mean values and standard deviation using SPSS software. Statistical analysis of the results was performed using ANOVA test. P-values less than 0.05 were considered statistically significant.

3. RESULTS AND DISCUSSIONS

3. 1. X-ray Diffraction Figure 1a. shows the low-angle X-ray diffraction pattern of samples. As can be seen in this figure, by increasing the weight percent of polycaprolactone, the peak intensity at about 2θ=0.7 which is representative of the mesoporous structure decreased sharply at small angles, which indicated that the mesoporous structure decreased due to filling the porosity by polycaprolactone .

Also, Wide-angle diffraction (WAXRD) approved the presence of crystalline and amorphous anatase phases and crystalline polycaprolactone. In this way Sownthari and Suthanthiraraj [36] reported that pure PCL has 3 strong diffraction peaks at 2θ=21.4, 22 and 23.7 that these peaks were related to (110) (111) and (200) orthorhombic plans, which the XRD results of our obtained data had a good agreement with the reports and had both 2θ=21.4 and 23.7. As the concentration of the polycaprolactone coating solution increased, the corresponding peak of polycaprolactone mentioned above was sharply increased and at the same time, the TiO_2 peak intensity decreased (see Figure 1b).

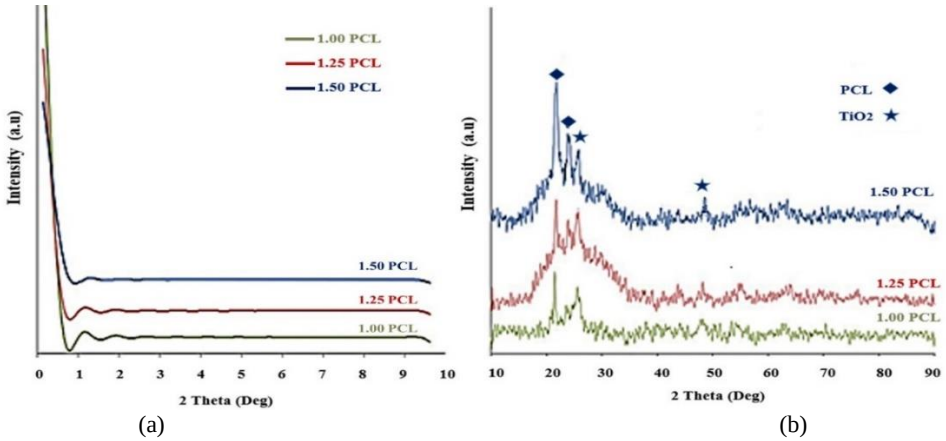

(a) (b)

Figure 1. XRD patterns of sample 1PCL, 1.2PCL, 1.5 PCL a) small-angle XRD (SAXS) and b) wide-angle XRD (WAXRD)

As porous ceramics have low mechanical strength, the coating of these materials by polymers could be an appropriate solution to solve this problem. Also at the same time decreasing the porosity could the other point which caused to increase in the mechanical strength of the titania scaffold in the presence of PCL coating [12].

3. 2. Scanning Electron Microscopy Figure 2 shows the SEM micrograph of samples 1.2 PCL and 1.5 PCL at 50 and 300 × magnifications. As could be seen in this figure by increasing the PCL concentration, the vesicular macroporous were filled by PCL and caused limited interconnections of the macroporous network for vascularization. In sum, although by increasing the concentration of PCL, the mechanical strength increased, but due to decreasing the interconnection of macroporous, the sample 1PCL was selected as an optimized sample, and additional investigation was considered in this sample.

In this regard, the microstructure of sample 0PCL was compared with sample 1PCL. Figure 3(a) shows the microstructure of sample 0PCL, by investigation of this micrograph it could be concluded that the 0PCL macroporous sample had an integrated structure without any cracks. Also, macroporous sizes of about 300 μm and vesicular porous made this macroporous structure a suitable scaffold for the cell growth. But despite all of these positive features and according to mechanical strength, the low strength of these scaffolds caused to protect them with PCL polymer (see Figure 3(a)).

Figure 3b shows the 1PCL sample, results showed the presence of PCL on the macroporous walls which had no negative effect on limiting macroporous interconnection and the integrated structure of this sample had been preserved. So we have a sample of the same positive features that have higher strength as it showed in Table 2. Also, a higher magnification of sample 1PCL is shown in Figures 3(c) and 3(d). Figure 3(c) shows a porous that is covered by the integrated PCL polymer coating and Figure 3d illustrates a polymer cover on the macroporous arm. It

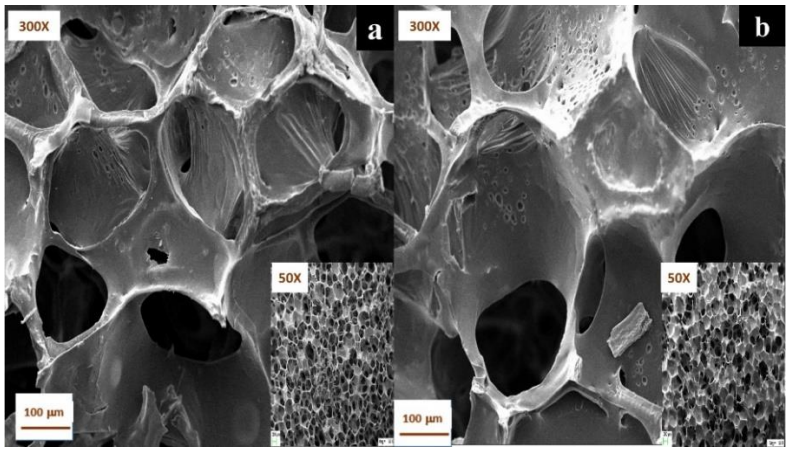

Figure 2. SEM micrograph of (a) sample 1.2 PCL (b) sample 1.5 PCL at 50 and 300× magnifications

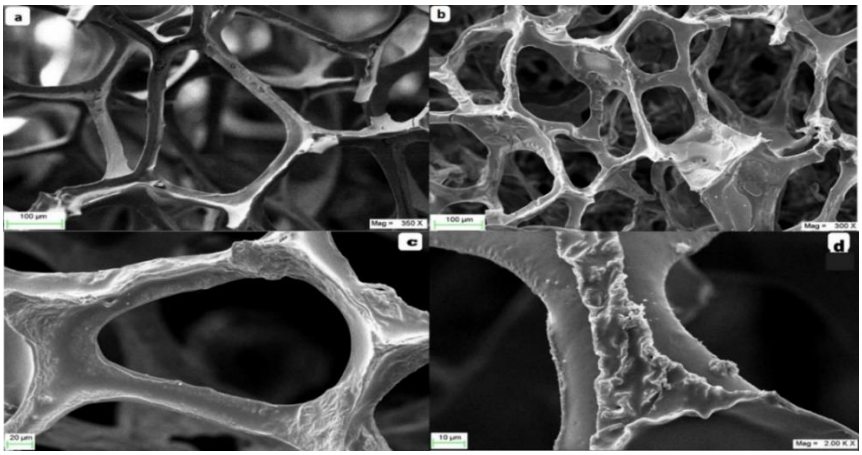

Figure 3. SEM micrograph of a) sample 0PCL b) sample 1PCL with the magnification of 300 c) sample 1PCL with the magnification 800 d) sample 1PCL with the magnification of 2000

relates to the appropriate concentration of the polymer solution and the dip-coating technique that was used to coat titania with PCL.

The technique had been used before in the formation of a thin polymer film on other macroporous ceramics such as alumina minimizing intrusion into the support pores [37].

3. 3. Mechanical Strength Test The compressive strength of uncoated Titania scaffolds which were measured and compared with coated samples (PCL 1, PCL 1.2, PCL 1.5) are summarized in Table 2.

Results showed that the uncoated sample had 89.5 % porosity by coating this scaffold with PCL the porosity decreased to 73.8 % with the addition of 1.5 % PCL. That the strength contrariwise effects with porosity and as porosity decreased, the strength increased from 0.29 MPa of uncoated sample to 0.79 MPa for the sample coated by 1.5% PCL.

Also, these results were approved by Kim et al. [38, 39] for the hydroxyapatite scaffold, he reported that a porous hydroxyapatite scaffold (with 8% porosity) synthesized through the inversion foam method showed 0.21 MPa compressive strength, as compositing with polycaprolactone the compressive strength increased to 0.45 MPa.

Taking everything into account, the macroporous titania which covered by 1 % PCL had suitable microstructure and mechanical strength in order to use it as a biomaterial.

3. 4. The Cytotoxicity Assay The cytotoxicity assay was performed using L929 fibroblast cells was used to compare samples 0PCL and 1PCL with a control sample. The results are shown in Figure 4. As could be seen in this figure the cell viability for the control sample was about 70.53% and this percentage decreased to 61.33% for sample 0PCL and 65.06% for sample 1PCL, that these results showed that all samples had good viability and no cytotoxicity was observed in these samples. In this way, the sample 1PCL which was coated by PCL showed better cell viability. The literature survey showed that The polymeric coating formed on the scaffold can enhance the mechanical strength and also can be considered as a carrier and a potential for sustained releasing of drugs and biological agents [34]. Khoshroo et al. [29] had pointed out that using PCL with TiO_2 could improve biological behavior for bone tissue engineering applications.

TABLE 2. Compressive strength and porosity of the samples

Sample	Mean Porosity %	Maximum compressive strength (MPa)
0PCL	89.5 ± 0.3	0.29 ± 0.04
1PCL	86.2 ± 0.2	0.69 ± 0.03
1.2PCL	79.3 ± 0.2	0.72 ± 0.02
1.5PCL	87.3± 0.3	0.79 ± 0.02

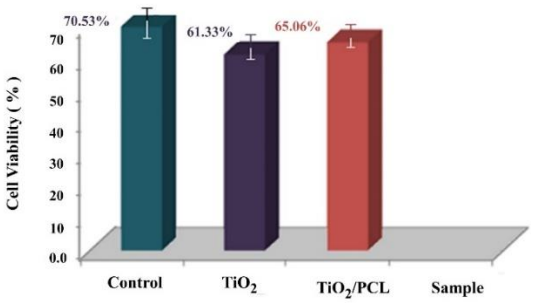

Figure 4. The bar chart of cell viability percentage (fibroblasts (L929) at 570 nm wavelength absorbance in control samples (without scaffold), of sample 0PCL and 1PCL during 48 h

In other words, the polymeric coating has improved the cell viability and a small trace of cytotoxicity was observed in these samples.

3. 5.The Cell Attachment Assay To the above results, it could be concluded that sample 1PCL had better potential to use as a biomaterial, so for the cell attachment assay, sample 1PCL was observed after 48 h immersion in a culture medium containing human osteosarcoma bone marrow (MG63) by using FEI ESEM Quanta 200 scanning electron microscope (see Figure 5). In this regard, Figures 5(a) and 5(b) show a cell that speared on the surface of the macroporous arm. Due to well cell attachment, 2 characteristics are important: cell spreading and cell adhesion, this sample shows both characteristics, so it showed a good cell attachment.

On the other hand, the cell had a spindle shape with pseudopodia of the osteosarcoma cell which caused better cell attachment in the arms of macroporous.

The higher magnification of sample 1PCL is shown in Figures 5(c) and 5(d). which Figure 5(c) shows the large number of cells attached to the macroporous arms. Also, Figure 5d illustrates the spindle shape of a cell attached by its pseudopodia of the osteosarcoma cell on the surface of macroporous which could provide cell proliferation.

Taking everything into account, sample 1PCL, simultaneously showed good strength and biological properties to use it as a scaffold in tissue engineering.

4. CONCLUSION

In this study, the effect of PCL coating on the mechanical strength, cell viability, and cell attachment of hierarchical meso/ macroporous titania scaffold for bone tissue engineering were reported. The mechanical strength of these samples showed that by coating hierarchical meso/ macroporous titania scaffold with PCL, the mechanical strength increased from 0.29 MPa to 0.79 MPa by coating 1.5% PCL. But in the same way, microstructure

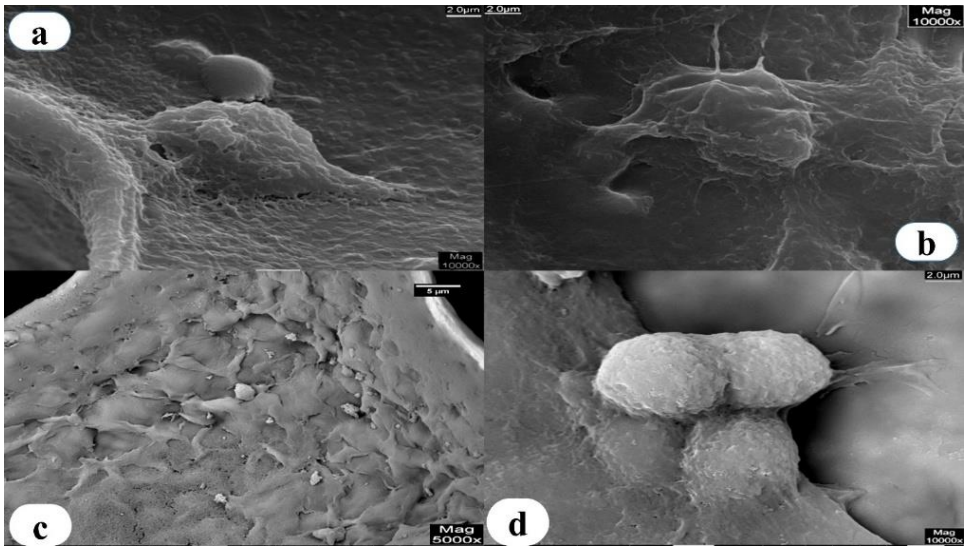

Figure 5. SEM micrograph of cell attachment of sample 1PCL at different magnification

investigation showed that by increasing polycaprolactone concentration from 1.2 to 1.5 wt%, the macrospores were filled with polycaprolactone and caused to decrease interconnection of pores. So the sample coated with 1% PCL was considered to evaluate the cytotoxicity and cell viability. Cell viability results showed that both hierarchical meso/ macroporous titania scaffold and hierarchical meso/ macroporous titania scaffold coated by 1% PCL had good cell viability, but the coated sample showed less cytotoxicity. So cell attachment of 1% PCL was evaluated and results showed cell spreading and cell adhesion on the surface of the macroporous arms which could provide cell proliferation.

5. REFERENCES

1. Ralston, S.H., "Bone structure and metabolism", ***Medicine***, Vol. 41, No. 10, (2013), 581-585. https://doi.org/10.1016/j.mpmed.2013.07.007
2. Seeman, E. and Delmas, P.D., "Bone quality—the material and structural basis of bone strength and fragility", ***New England Journal of Medicine***, Vol. 354, No. 21, (2006), 2250-2261. doi: 10.1056/NEJMra053077.
3. Müller, R., "Hierarchical microimaging of bone structure and function", ***Nature Reviews Rheumatology***, Vol. 5, No. 7, (2009), 373-381. https://www.nature.com/articles/nrrheum.2009.107
4. Kiuru, M.J., Pihlajamäki, H. and Ahovuo, J., "Bone stress injuries", ***Acta Radiologica***, Vol. 45, No. 3, (2004), 000-000. doi: 10.1080/02841850410004724.
5. Mistry, A.S. and Mikos, A.G., "Tissue engineering strategies for bone regeneration", ***Regenerative Medicine II***, (2005), 1-22. doi: 10.1007/b99997.
6. Porter, J.R., Ruckh, T.T. and Popat, K.C., "Bone tissue engineering: A review in bone biomimetics and drug delivery strategies", ***Biotechnology Progress***, Vol. 25, No. 6, (2009), 1539-1560. doi: 10.1002/btpr.246.
7. Jiang, S., Wang, M. and He, J., "A review of biomimetic scaffolds for bone regeneration: Toward a cell-free strategy", ***Bioengineering & Translational Medicine***, Vol. 6, No. 2, (2021), e10206. doi: 10.1002/btm2.10206.
8. Zimmermann, G. and Moghaddam, A., "Allograft bone matrix versus synthetic bone graft substitutes", ***Injury***, Vol. 42, (2011), S16-S21. doi: 10.1016/j.injury.2011.06.199.
9. Rezwan, K., Chen, Q., Blaker, J.J. and Boccaccini, A.R., "Biodegradable and bioactive porous polymer/inorganic composite scaffolds for bone tissue engineering", ***Biomaterials***, Vol. 27, No. 18, (2006), 3413-3431. https://doi.org/10.1016/j.biomaterials.2006.01.039
10. Bose, S., Roy, M. and Bandyopadhyay, A., "Recent advances in bone tissue engineering scaffolds", ***Trends in Biotechnology***, Vol. 30, No. 10, (2012), 546-554. doi. https://doi.org/10.1016/j.tibtech.2012.07.005
11. Chen, R.R. and Mooney, D.J., "Polymeric growth factor delivery strategies for tissue engineering", ***Pharmaceutical Research***, Vol. 20, No. 8, (2003), 1103-1112. doi: 10.1023/a:1025034925152.
12. Mohamad Yunos, D., Bretcanu, O. and Boccaccini, A.R., "Polymer-bioceramic composites for tissue engineering scaffolds", ***Journal of Materials Science***, Vol. 43, No. 13, (2008), 4433-4442. doi: 10.1517/17425247.2013.808183.
13. Peroglio, M., Gremillard, L., Chevalier, J., Chazeau, L., Gauthier, C. and Hamaide, T., "Toughening of bio-ceramics scaffolds by polymer coating", ***Journal of the European Ceramic Society***, Vol. 27, No. 7, (2007), 2679-2685. https://doi.org/10.1016/j.jeurceramsoc.2006.10.016
14. Gómez-Cerezo, M.N., Peña, J., Ivanovski, S., Arcos, D., Vallet-Regí, M. and Vaquette, C., "Multiscale porosity in mesoporous bioglass 3d-printed scaffolds for bone regeneration", ***Materials Science and Engineering: C***, Vol. 120, (2021), 111706. https://doi.org/10.1016/j.msec.2020.111706
15. Yan, X., Deng, H., Huang, X., Lu, G., Qiao, S., Zhao, D. and Yu, C., "Mesoporous bioactive glasses. I. Synthesis and structural characterization", ***Journal of non-crystalline Solids***, Vol. 351, No. 40-42, (2005), 3209-3217. https://doi.org/10.1016/j.jnoncrysol.2005.08.024
16. Tang, H., Guo, Y., Jia, D. and Zhou, Y., "High bone-like apatite-forming ability of mesoporous titania films", ***Microporous and***

Mesoporous Materials, Vol. 131, No. 1-3, (2010), 366-372. https://doi.org/10.1016/j.micromeso.2010.01.015

17. Li, Z., He, Y., Klausen, L.H., Yan, N., Liu, J., Chen, F., Song, W., Dong, M. and Zhang, Y., "Growing vertical aligned mesoporous silica thin film on nanoporous substrate for enhanced degradation, drug delivery and bioactivity", ***Bioactive Materials***, Vol. 6, No. 5, (2021), 1452-1463. https://doi.org/10.1016/j.bioactmat.2020.10.026
18. Kulkarni, M., Mazare, A., Gongadze, E., Perutkova, Š., Kralj-Iglič, V., Milošev, I., Schmuki, P., Iglič, A. and Mozetič, M., "Titanium nanostructures for biomedical applications", ***Nanotechnology***, Vol. 26, No. 6, (2015), 062002. doi: 10.1088/0957-4484/26/6/062002.
19. Haugen, H., Will, J., Köhler, A., Hopfner, U., Aigner, J. and Wintermantel, E., "Ceramic TiO_2-foams: Characterisation of a potential scaffold", ***Journal of the European Ceramic Society***, Vol. 24, No. 4, (2004), 661-668. https://doi.org/10.1016/S0955-2219(03)00255-3
20. Loca, D., Narkevica, I. and Ozolins, J., "The effect of TiO_2 nanopowder coating on in vitro bioactivity of porous TiO_2 scaffolds", ***Materials Letters***, Vol. 159, (2015), 309-312. https://doi.org/10.1016/j.matlet.2015.07.017
21. Zhang, P., Zhang, Z., Li, W. and Zhu, M., "Effect of ti-oh groups on microstructure and bioactivity of TiO_2 coating prepared by micro-arc oxidation", ***Applied Surface Science***, Vol. 268, (2013), 381-386. https://doi.org/10.1016/j.apsusc.2012.12.105
22. Tiainen, H., Wohlfahrt, J.C., Verket, A., Lyngstadaas, S.P. and Haugen, H.J., "Bone formation in TiO_2 bone scaffolds in extraction sockets of minipigs", ***Acta Biomaterialia***, Vol. 8, No. 6, (2012), 2384-2391. https://doi.org/10.1016/j.actbio.2012.02.020
23. Haugen, H.J., Monjo, M., Rubert, M., Verket, A., Lyngstadaas, S.P., Ellingsen, J.E., Rønold, H.J. and Wohlfahrt, J.C., "Porous ceramic titanium dioxide scaffolds promote bone formation in rabbit peri-implant cortical defect model", ***Acta Biomaterialia***, Vol. 9, No. 2, (2013), 5390-5399. https://doi.org/10.1016/j.actbio.2012.09.009
24. Mirhadi, S.M., Nemati, N.H., Tavangarian, F. and Joupari, M.D., "Fabrication of hierarchical meso/macroporous TiO_2 scaffolds by evaporation-induced self-assembly technique for bone tissue engineering applications", ***Materials Characterization***, Vol. 144, (2018), 35-41. https://doi.org/10.1016/j.matchar.2018.06.035
25. Liu, J., Hu, X., Dai, H., San, Z., Wang, F., Ren, L. and Li, G., "Polycaprolactone/calcium sulfate whisker/barium titanate piezoelectric ternary composites for tissue reconstruction", ***Advanced Composites Letters***, Vol. 29, (2020), 2633366X19897923. https://doi.org/10.1177/2633366X19897923
26. Alves, M.M., Santos, C. and Montemor, M., "Improved corrosion resistance on Mg-2Ca alloy with TiO_2 nanoparticles embedded in a polycaprolactone (pcl) coating", ***Applied Surface Science Advances***, Vol. 9, (2022), 100257. https://doi.org/10.1016/j.apsadv.2022.100257
27. Singh, N., Batra, U., Kumar, K. and Mahapatro, A., "Evaluation of corrosion resistance, mechanical integrity loss and biocompatibility of pcl/ha/TiO_2 hybrid coated biodegradable zm21 mg alloy", ***Journal of Magnesium and Alloys***, (2021). https://doi.org/10.1016/j.jma.2021.10.004
28. Jariya, S.I., Babu, A.A., Narayanan, T.S., Vellaichamy, E. and Ravichandran, K., "Development of a novel smart carrier for drug delivery: Ciprofloxacin loaded vaterite/reduced graphene oxide/pcl composite coating on TiO_2 nanotube coated titanium", ***Ceramics International***, Vol. 48, No. 7, (2022), 9579-9594. https://doi.org/10.1016/j.ceramint.2021.12.156
29. Khoshroo, K., Kashi, T.S.J., Moztarzadeh, F., Tahriri, M., Jazayeri, H.E. and Tayebi, L., "Development of 3d pcl microsphere/tio2 nanotube composite scaffolds for bone tissue engineering", ***Materials Science and Engineering: C***, Vol. 70, (2017), 586-598. https://doi.org/10.1016/j.msec.2016.08.081
30. De Santis, R., Catauro, M., Di Silvio, L., Manto, L., Raucci, M.G., Ambrosio, L. and Nicolais, L., "Effects of polymer amount and processing conditions on the in vitro behaviour of hybrid titanium dioxide/polycaprolactone composites", ***Biomaterials***, Vol. 28, No. 18, (2007), 2801-2809. https://doi.org/10.1016/j.biomaterials.2007.02.014
31. Catauro, M., Papale, F. and Bollino, F., "Characterization and biological properties of TiO_2/pcl hybrid layers prepared via sol–gel dip coating for surface modification of titanium implants", ***Journal of Non-crystalline Solids***, Vol. 415, (2015), 9-15. https://doi.org/10.1016/j.jnoncrysol.2014.12.008
32. Gupta, K.K., Kundan, A., Mishra, P.K., Srivastava, P., Mohanty, S., Singh, N.K., Mishra, A. and Maiti, P., "Retracted article: Polycaprolactone composites with TiO_2 for potential nanobiomaterials: Tunable properties using different phases", ***Physical Chemistry Chemical Physics***, Vol. 14, No. 37, (2012), 12844-12853. https://doi.org/10.1039/C2CP41789H
33. Hassanzadeh Nemati, N. and Mirhadi, S.M., "Synthesis and characterization of highly porous TiO_2 scaffolds for bone defects", ***International Journal of Engineering*, *Transactions A: Basics,*** Vol. 33, No. 1, (2020), 134-140. doi: 10.5829/ije.2020.33.01a.15.
34. Catauro, M., Bollino, F., Papale, F. and Lamanna, G., " TiO_2 /pcl hybrid layers prepared via sol-gel dip coating for the surface modification of titanium implants: Characterization and bioactivity evaluation", in Applied Mechanics and Materials, Trans Tech Publ. Vol. 760, (2015), 353-358.
35. Li, H., Wang, J., Li, H., Yin, S. and Sato, T., "High thermal stability thick wall mesoporous titania thin films", ***Materials Letters***, Vol. 63, No. 18-19, (2009), 1583-1585. https://doi.org/10.1016/j.matlet.2009.04.017
36. Sownthari, K. and Suthanthiraraj, S.A., "Synthesis and characterization of an electrolyte system based on a biodegradable polymer", ***Express Polymer Letters***, Vol. 7, No. 6, (2013). doi: 10.3144/expresspolymlett.2013.46.
37. Hamm, J.B., Ambrosi, A., Pollo, L.D., Marcilio, N.R. and Tessaro, I.C., "Thin polymer layer-covered porous alumina tubular membranes prepared via a dip-coating/phase-inversion process", ***Materials Chemistry and Physics***, Vol. 265, (2021), 124511. https://doi.org/10.1016/j.matchemphys.2021.124511
38. Kim, H.-W., Knowles, J.C. and Kim, H.-E., "Hydroxyapatite porous scaffold engineered with biological polymer hybrid coating for antibiotic vancomycin release", ***Journal of Materials science: Materials in Medicine***, Vol. 16, No. 3, (2005), 189-195. doi: 10.1007/s10856-005-6679-y.
39. Kim, H.-W., Knowles, J.C. and Kim, H.-E., "Hydroxyapatite/poly (ε-caprolactone) composite coatings on hydroxyapatite porous bone scaffold for drug delivery", ***Biomaterials***, Vol. 25, No. 7-8, (2004), 1279-1287. https://doi.org/10.1016/j.biomaterials.2003.07.003

Persian Abstract

چکیده

در این مطالعه، اثر پوشش PCL بر استحکام مکانیکی، رفتار سلولی و اتصال سلولی به داربست مزو/ ماکرو متخلخل تیتانیا با ساختار مرتبه ای مورد بررسی قرار گرفت. داربست تیتانیا به عنوان بستر از طریق خودآرایی ناشی از تبخیر همراه با روش فومی ساخته شد. سپس داربست های آماده شده با محلول پلی کاپرولاکتون با سه درصد وزنی مختلف به روش غوطه وری پوشش داده شدند. آزمون SAXS، WAXRD، SEM، مقاومت فشاری، MTT و چسبندگی سلولی برای مشخصه یابی نمونه‌ها اعمال شد. بر اساس نتایج XRD، با افزایش غلظت پلی‌کاپرولاکتون، شدت فاز پلی‌کاپرولاکتون کریستالی افزایش یافت در حالی که شدت پیک TiO_2 به دلیل پوشاندن تیتانیا مزوپور توسط پلی‌کاپرولاکتون کاهش یافت. مقاومت فشاری نشان داد که با افزایش درصد پلی‌کاپرولاکتون، تخلخل از ۸۹/۵ به ۷۳/۸ درصد کاهش می‌یابد که باعث افزایش مقاومت از ۰/۲ به ۰/۷۹ مگاپاسکال می‌شود. یکی از پارامترهای یک داربست ایده آل برای مهندسی بافت، شبکه ماکرو متخلخل به هم پیوسته برای رگزایی، نفوذ بافت و تحویل مواد مغذی است، به این ترتیب نتایج SEM نشان می دهد که با افزایش غلظت پلی کاپرولاکتون از ۱.۲ به ۱.۵ درصد وزنی، حفره های ماکرو با پلی کاپرولاکتون پر شدند و باعث کاهش اتصال منافذ می شود. در این راستا، اگرچه با افزایش درصد پلی‌کاپرولاکتون، استحکام افزایش یافت، اما کاهش شبکه ماکرو متخلخل به هم پیوسته باعث شد که نمونه‌ی حاوی ۱ درصد وزنی پلی‌کاپرولاکتون به عنوان نمونه انتخابی انتخاب شود. همچنین، آزمایش MTT سمیت سلولی کم را در تماس با سلول های فیبروبلاست موش L929 گزارش کرد. آزمایش اتصال سلولی که با استفاده از سلول‌های MG63 انجام شد، نشان داد که نمونه‌های پوشش‌داده‌شده بستر مناسبی را برای اتصال سلول‌ها فراهم می‌کنند و همچنین زنده‌مانی سلولی را در سطح بستر پوشش‌داده شده نشان می‌دهند. به طور کلی، طبق نتایج، داربست سلسله مراتبی مزو متخلخل تیتانیا با پوشش ۱ درصد وزنی پلی کاپرولاکتون، می تواند پتانسیل خوبی برای استفاده در مهندسی بافت داشته باشد.

IJE TRANSACTIONS A: Basics Vol. 35 No. 10, (October 2022) 1895-1905

International Journal of Engineering

Journal Homepage: www.ije.ir

Thermal Effects on the Bearing and Ductility of Tubular Reduced Beam Section Connection: Numerical Investigation

Y. Khalilpourazar[a], M. A. Lotfollahi Yaghin*[b], A. Maleki[a]

[a] *Department of Civil Engineering, Maragheh Branch, Islamic Azad University, Maragheh, Iran*
[b] *Faculty of Civil Engineering, University of Tabriz, Tabriz, Iran*

PAPER INFO

Paper history:
Received 15 March 2022
Received in revised form 06 June 2022
Accepted 10 June 2022

Keywords:
Sequentially Coupled Thermal-stress Analysis
Fire Damages
Hysteretic Curves
Ductility

ABSTRACT

In the present paper, an innovative fire-earthquake resistant joint called high-performance tube (HP-T) connection is presented and numerically validated. This HP-T connection improves the axial and rotational ductility as well as prevents brittle failure. Two series of models were simulated in ABAQUS software. In the first set of models, which was designed for heat simulation, a sequentially coupled thermal-stress analysis was performed to investigate the effects of different parameters such as web and flange tube thickness and the ratio of the applied load. To simulate the fire damage, two probable scenarios were considered: bottom flange tube damage and beam web damage when exposed to combined initial loading and fire. In the second set of models for seismic simulation, the failure mode, hysteretic curves, and strain distribution were analyzed. According to the results, HP-T robust connection not only provides appropriate ductility enhancement in force-variable fire conditions but also withstands at least 8% inter-story drift without considerable strength reduction.

doi: *10.5829/ije.2022.35.10a.09*

NOMENCLATURE

k	material conductivity in [W/m°C]	T_0	Initial temperature[°C]
T m, t	surface temperature in [°C]	**Greek Symbols**	
T g, t	gas temperature in [°C]	ε	Resultant emissivity
n	surface outward normal direction	σ	Stephan-Boltzmann constant [W/m^2 K^4]
T_z	Absolute zero temperature[°C]	α	Coefficient of convection [W/m^2 K]

1. INTRODUCTION

Annually, natural phenomena such as earthquakes, hurricanes, etc. and manmade ones such as fires and explosions inflict tremendous damage to structures, causing remarkable economic loss as well as jeopardizing lives. After the terrorist attacks on September 11th, 2001, the total collapse of the twin towers and the progressive failure of WTC in New York was a result of the thermal stress caused by the explosion, fire [1]. Cardington large-scale fire tests [2] in 1993 demonstrated that steel joints are particularly vulnerable in a fire scenario. Hence, the capability of the connection is critical for the overall stability and integrity of the structure and to alleviate the risk of progressive failure. On January 19, 2017, an unintentional fire resulted in the total collapse of the Plasco high-rise metal structure in Tehran [3]. As one of the causes, it should be noted that the structure was built in the years 1960s and modern fire engineering requirements were not met during its manufacturing, operation, or maintenance. The partial structural failure was initiated in the floor system and connections. Subsequently, the degradation of material properties simultaneous with intensifying load during the fire

*Corresponding Author Institutional Email: lotfollahi@tabrizu.ac.ir (M. A. Lotfollahi Yaghin)

Please cite this article as: Y. Khalilpourazar, M. A. Lotfollahi Yaghin, A. Maleki, Thermal Effects on the Bearing and Ductility of Tubular Reduced Beam Section Connection: Numerical Investigation, ***International Journal of Engineering, Transactions A: Basics***, Vol. 35 No. 10, (2022), 1895-1905

resulted in the buckling of external columns and an increase in the column slenderness. The collapse of external columns finally led to the abrupt destruction of the whole structure. These are just a few important examples which indicate that connections have the most crucial role in a structure. Since they supply strong links between the principal structural parts for transferring all the applied loads. Furthermore, the efficiency of the connection at normal temperature differs greatly from high temperatures. Hence, studying the connection behavior during different stages of a fire incident may help achieve the most optimum fire engineering design. In general, internal forces in a connection can be categorized into four phases during a fire scenario. In the initial stage, under normal temperatures, the connections are only considered to be subjected to simple load combinations such as vertical shear or shear and moment. In the early stages of heating, a considerable compressive force may be generated in the connection due to restrained thermal expansion of the connected beam. At elevated temperatures, as a result of a reduction in material strength and stiffness, and subsequently, rapid increase in the beam's vertical deflection, the connected beam's bending resistance will not be sufficient to carry out the imposed load and to keep equilibrium, catenary (tensile) forces will be generated in it. Therefore, connections undergo tension. In the cooling stage, with the thermal contraction of the beam, tensile forces may also develop in the beam and the connection. Extensive efforts have been made to assess the vulnerability of steel or steel-concrete composite connections during a fire event. Kruppa [4] was one of the pioneers of conducting fire tests on connections. This study did not focus on the global behavior of joints and aimed generally to determine the performance of high-strength bolts. Lawson [5] studied the global rotational behavior of conventional connections subjected to ISO834 standard fire. Leston-Jones [6] examined the moment rotation relationship of the steel beam-columns using flash endplate connections and presented that its stiffness and strength decreased as temperature increased. Al-Jabri [7] modeled flush endplate bolted connection at elevated temperatures using general commercial program ABAQUS and evaluated connection moment rotation characteristics under degradation of steel properties. He established that testing of isolated joints could not accurately reflect the behavior of connections due to the absence of concurrent axial force. Sarraj [8] successfully evaluated the application of the Component-based method and the fin plate connection tying resistance. Hu and Burgess [9] performed a quasi-static analysis using ABAQUS code to investigate the ductility and capacity of flexible endplate connections subjected to fire. Yu et al. [10] examined the robustness of web cleat connections under tying force at higher temperatures and also developed the component-based method for different types of connections. Han et al. [11] accomplished fire tests to assess the effect of the ISO834 standard fire on CFST column-RC beam joints. Wang and Ding [12] experimentally investigated the response of CFST column-steel beam connections under fire exposure conditions and the temperature variation effect on the joint was measured. A numerical simulation of a Constrained CFT columns-steel beam connected by a reverse channel was investigated by Elsawaf et al. [13].

After the occurrence of the Northridge (California,1994) and Kobe (Japan, 1995) earthquakes, brittle fractures of the weld-flexural joints to high ductility demands were widely observed. The most extensive study has been conducted by the SAC committee leading to useful results published in the set of FEMA350 (2000). Several studies were conducted to improve the seismic performance of moment connections [14]. The reduced beam section (RBS) moment resistance is one of the most economical and popular connections among the post-Northridge prequalified ones. In comparison to straight and tapered cuts, radius cut RBS connections have shown improved seismic behavior [15]. RBS connections were designed based on a novel technique named "weakening". By this technique, the plastic capacity of the beam section is deliberately reduced in the vicinity of the column face to act as a fuse for damage and seismic energy absorption in this weakened region. There have been numerous studies on the seismic efficiency of different RBS connections. Chen and Chao [16] have experimentally investigated the effects of the floor slabs on the performance of the RBS connections. Jones et al. [17] have examined the cyclic response of the RBS connection with concrete slabs and different panel zones. Roeder [18], Ricles et al. [19], and Lee et al. [20] have investigated the plastic rotation capacity of the connections with variable panel zone strength. According to their research, strong panel zones would centralize all inelastic loads on the shortened segment of the RBS connection; thereby, they would have harmful effects on the deformation capacity of the connections. Zhang and Ricles [21] have demonstrated that a composite floor slab can provide restraint to the top flange of the beam and increase the ultimate load in the plastic hinge. According to Han and Moon [22], reduced beam sections with web bolted connections are not suggested if the span-to-depth ratio is less than ten and the beam flanges provide less than 70% of the section's overall flexural strength. Despite the many advantages of RBS connections, these connections would experience local buckling of beam web and are vulnerable to lateral-torsional buckling [23]. Several RBS connections with rectangular hollow sections [24], hollow webs [25], and reduced beam web height [26]

have been proposed. Mirghaderi et al. [27] suggested an earthquake-resisting technique named AW-RBS connections with the provision of at least 8% story drift and efficient flange stability of the connected beam at larger rotational demands. Morrison et al. [28] experimentally studied HBS (heat-treated beam section connections) and presented that HBS connections experienced story drift as high as 6% without any weld or near weld fracture. Saleh et al. [29] attained approximate inter-story drifts of 6% without lateral-torsional buckling on newly developed tubular-web RBS connections. Zahrai et al. [30] utilized two pipes in TW-RBS for deep beams to increase plastic hinge length. A multitude of the literature review mentioned earlier has studied the performance of External, Through, and Internal diaphragm connections either subjected to fire or earthquake or fire after an earthquake event. These researches were investigated by Han et al. [31], Song et al. [32]. There is not enough research on the provision of fire-earthquake resistant connection with high ductility. The current study proposes an innovative connection to provide appropriate axial ductility enhancement in fire events simultaneous with favorable energy absorption in a seismic zone to prevent an abrupt failure and subsequent progressive collapse. Figure 1 depicts the configuration of the proposed connection, in this configuration, the beam web and flange are replaced with vertical and horizontal tubular sections in a restricted region near the column. Since the loss of material characteristics at high temperatures results in nonlinear behavior of structural components and given the limitations associated with costly fire tests, the construction of a numerical model is required. Therefore, the main objective of this paper is to develop robust numerical models to simulate the fire and seismic performance of innovative connections, separately. This study is divided into three parts. In the first part, discussed in section 2, relevant details about the numerical model of the proposed connection when exposed to fire are given including temperature field and stress analysis. When performing the model's thermal-mechanical analysis, two approaches may be proposed: performing either a sequentially or a completely coupled thermal-stress analysis. Since the completely coupled analysis requires long computational time and powerful computers, a sequentially coupled thermal-stress analysis is used in this investigation. The heat transfer model is first to run to obtain the temperature field of the connection during the ISO834 fire [33], and the temperature field findings are then imported as a predetermined field into the stress analysis model to execute the mechanical analysis. Based on the FEM model, the characteristics failure mode, midspan deflection of the beam, axial force variation of the beam, and plastic strain are the key aspects considered. In the second part, presented in section 3, due to the absence of experimental data, the mechanical subframe investigated by Liu et al. [34] is employed to verify the FE model. In the third part, detailed in section 4, finite element modeling of the proposed connection is conducted to assess the nonlinear cyclic response, the energy dissipated in the connection by plastic deformation and hysteresis curves.

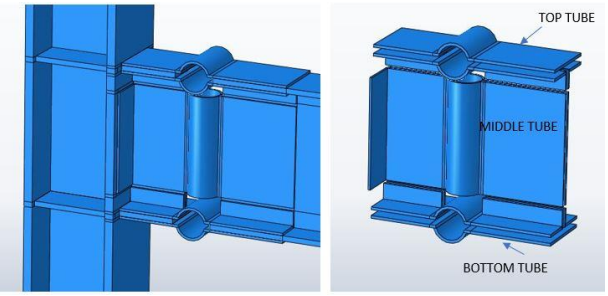

Figure 1. Assembly and related configuration of the proposed connection

2. NUMERICAL MODEL UNDER FIRE

2. 1. Heat Transfer Analysis To simulate the effect of fire loading on tubular connections, ABAQUS software was used to run a Nonlinear FE model. The proposed subassembly, geometry, material, boundary conditions, and heating were modeled precisely the same as those used in the reference test [34, 35] in order to explore the effects of dimensional parameters on the fire resistance and ductility of tube connections. To save computational expense, only half of the beam was modeled, and a symmetric boundary condition was implemented at the beam midspan. The specification of these sections with an appropriately designed tubular connection is presented in Table 1.

2. 1. 1. Thermal Properties and Element Divisions For structural steel, the temperature-dependent properties including thermal conductivity coefficient, specific heat, and density recommended in EN1993-1-2 (CEN 2005) were employed in the current

TABLE 1. Specification of Tubular RBS connection

Column section (mm)	UKC 305*305*198
Beam section (mm)	UKB 533*210*109
Inner radius of semi cylindrical Tubular RBS section (mm)	50
Connection depth (mm)	360
Beam span (m)	7.5

FE model. The model was meshed using 8-node brick elements (DC3D8). The results of the sensitivity of simulation presented that mesh sizes of 10 and 20mm are ideal for the finer and coarser areas of main structural elements. Nodal temperatures were saved as output data and then exerted to the mechanical model as the findings of temperature field analysis.

2. 1. 2. Thermal Boundary Condition and Loading

The heat is first transported to the outside surfaces subjected to fire via convection and radiation in the transient heat transfer analysis, followed by conduction into the internal surfaces of the members. The emissivity of a material is the ratio between the radiative heat absorbed by a surface made of this material and that of a black body surface. The temperature of the air as determined by the ISO834 standard fire curve, the fire temperature-time relationships and boundary conditions during the heating stages are presented by Equations (1), and (2), respectively.

$$T = T_0 + 345log_{10}(8t + 1) \quad (1)$$

$$-k\,\partial T/\partial n = \alpha\left(T_{m,t} - T_{g,t}\right) + \varepsilon\sigma\left[(T_{m,t} - T_z)^4 - (T_{g,t} - T_z)^4\right] \quad (2)$$

Table 2 lists the constants of the heat transfer run.

2. 2. Structural Analysis

2. 2. 1. Loading and Boundary Conditions

Two steps were considered in the second structural model. In the first step, three levels of loading (load ratios of 0.3, 0.4 and 0.5) were applied to the beam flange at ambient temperature and were kept constant throughout the whole analysis. The load ratio is designated as the ratio of the applied load under fire conditions to the design bearing capacity of the simply-supported beam at room temperature. In the second step, a transient time-temperature heat loading was applied as a predefined field. The * NLGEOM=ON was set to tackle such a geometric nonlinear analysis. Since the excessive deflections caused development of catenary action in the model, the simulated method proposed by Dai et al. [36] was used to achieve numerical stability with the static solver. The selection of a suitable damping factor (0.00001-0.00002) was tested by evaluating the applied loads in relation to the support reaction force and by restricting the ratio of damping dissipated energy to total strain energy (ratio of parameter ALLSD to ALLIE in ABAQUS) to roughly 10%. Figures 2a and 2b illustrate the thermal and mechanical boundary conditions of assembly for the proposed connection. Also, Beam to the column and tubes are bounded together with tie constraints to simulate the welded zones.

TABLE 2. Thermal constants and parameters used in heat transfer modeling

Parameter	Definition	Value
α	Coefficient of convection	25 W/m^2 K
ε	Resultant emissivity	0.5
σ	Stephan-Boltzmann constant	5.67*10^{-8} W/m^2 K^4
T_z	Absolute zero temperature	-273.15°C
T_0	Initial temperature	20°C

2. 2. 2. Material Mechanical Properties and Element Divisions

Material properties required in the stress analysis generally include elastic and plastic properties with thermal expansion coefficients. For steel, temperature-dependent values of stiffness (E) and thermal expansion coefficient (first derivative of thermal elongation) from EN1993-1-2 [37] were adopted, while the Poisson's ratio was considered to be temperature independent and a constant coefficient of 0.2 was selected. Note that the effect of thermal creep was not considered in this study. The stress-strain relationships at the ambient and heating stages are different for structural steel. A user-developed material subroutine UHARD was implemented to simulate the temperature-dependent mechanical properties recommended in EN1993-1-2 [37]. For the UHARD subroutine, the input parameters are, $\partial\sigma^0/\partial\bar{\varepsilon}^{pl}$, $\partial\sigma^0/\partial\dot{\bar{\varepsilon}}^{pl}$ and $\partial\sigma^0/\partial\theta$ in which $\bar{\varepsilon}$pl is equivalent plastic strain, $\dot{\bar{\varepsilon}}$pl is equivalent plastic strain rate, σ^0 is SYIELD and θ is the temperature. In the second structural model, the solid element with reduced integration (C3D8R) was employed to manage the hourglass modes. Moreover, at least two layers of elements in the thickness direction of the beam and tubes were used to prevent premature buckling. The same element meshing and node numbers used in the temperature analysis model were adopted in the structural analysis model.

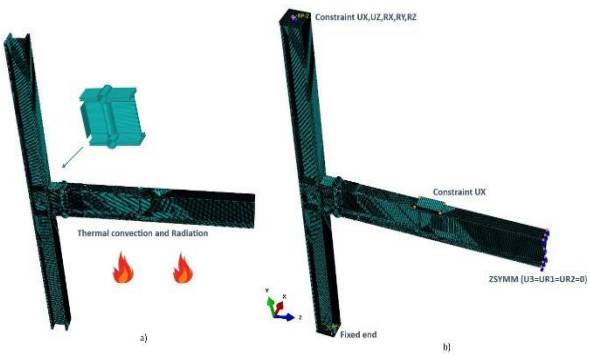

Figure 2. a) FE model for heat transfer analysis, b) FE model for mechanical analysis

3. NUMERICAL RESULTS

3. 1. Verification of the FE Model The experimental and numerical results of Wald et al. [38], Elsawaf et al. [13] and novel connection in the fire incident reported by Liu et al. [34, 35] were utilized to validate the FE model. In this paper, only the result of ductile connection in long-span beam [34, 35] and reverse channel connection in short-span beam [13] are presented. The steel sub-frame model [34, 35] consists of a beam connected to the column via a cylindrical connection. In the heat transfer model, the temperatures of connection and the lower column were about 50% of the temperature of the bottom flange of the beam. In the structural model the beam was initially exposed to an external load (load ratio 0.4) to generate the required moment. Then the temperature of the structure was gradually increased until the sub-frame failed to be convergent. Figures 3(a) and 3(b) demonstrate comparative results (mid-span deflection curves of the beam) between the frame [34, 35] or [13] predicted by the present research and the original studies. Based on Figures 3(a) and 3(b), the highest beam deflection was approximately 300 mm (15% of the beam span) and 1000 mm (13% of the beam span). The maximum deflection observed during the experiment [13] was 302 mm. The maximum deflection predicted by the present research was 285, a difference of only 5.6%. Furthermore, the difference between the maximum deflection of the original study [34, 35] and the present research was about 7%. These are very large deflections. According to these results, the FE model accurately captured the transition process from compression to tension in the beam during the fire and confirmed the model's capability to simulate large deflection behavior. However, using the different locations of measuring beam temperature may also lead to some minor differences in comparative results.

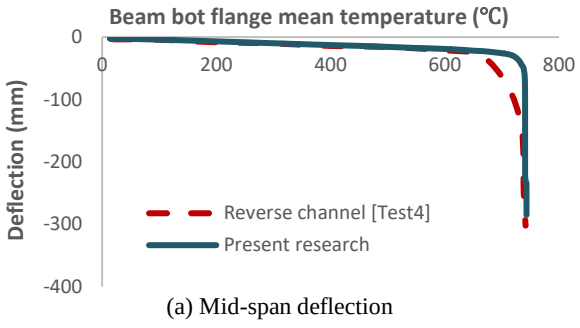

(a) Mid-span deflection

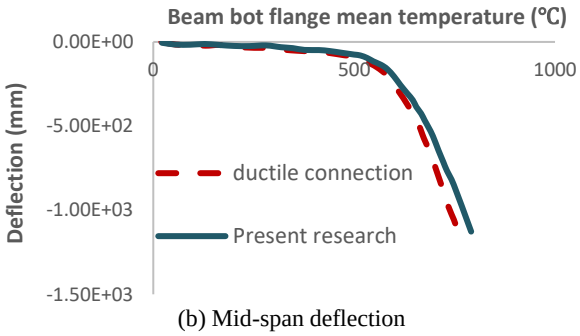

(b) Mid-span deflection

Figure 3. Mid-span deflection investigated by a) Elsawaf [13] and, (b) Liu [34, 35] and present research

3. 2. Numerical Results of HP-T Connection A parametric study was carried out to investigate the influence of tubular flange and web thickness of the proposed connection on its failure mode in the fire. The specifications of tubular connection with a constant height (360mm) are summarized in Table 3. In this table, the thickness of tubular flange and web vary for different models. TC1, TC2, TC3 and TC10 (series I) models, failed due to the formation of plastic hinges in the bottom flange tube in a specific location as shown in Figures 4 and 6. TC6 (series II) models failed due to bottom flange tube damage and minor-web local buckling (MI-WLB) as shown in Figure 5. For TC8 (series III), the damage mode of moderate-web local buckling (MO-WLB) was observed. Figures 7(a) and 7(b) show the relationship between mid-span deflection

TABLE 3. Summary of the thermal models

Model series	Model Number	Top-bot tube thickness (mm)	Mid tube thickness (mm)	Load ratio
	TC1	9	5	0.3
I	TC2	9	6	0.3
	TC3	9	7	0.3
	TC4	10	5	0.3
II	TC5	10	6	0.3
	TC6	10	7	0.3
	TC7	11	5	0.3
III	TC8	11	6	0.3
	TC9	11	7	0.3
II	TC10	9	7	0.5

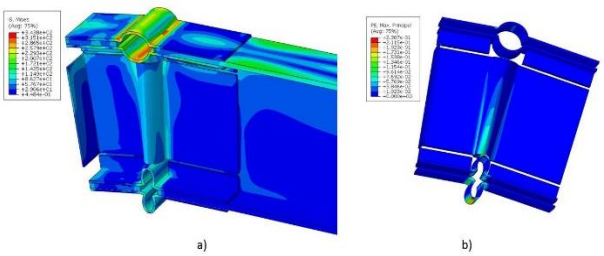

Figure 4. (a) Von mises stress, (b) strain counters at TC3 (plastic strain)

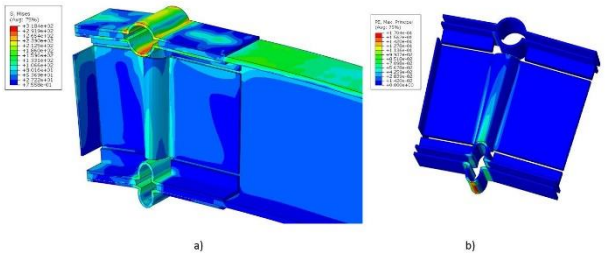

Figure 5. (a) Von mises stress, (b) strain counters at TC6 (plastic strain)

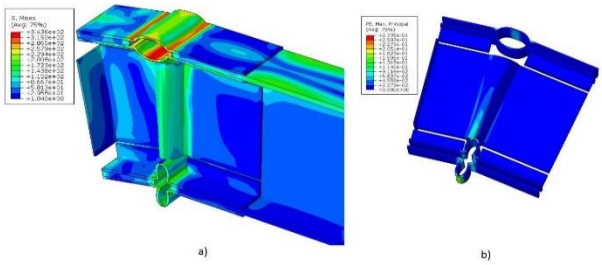

Figure 6. (a) Von mises stress, (b) strain counters at TC10 (plastic strain)

and beam axial force and temperature at the beam bottom flange. The results indicate that the proposed HP-T connection has the potential to develop more substantial catenary action and higher ductility through the deformation of the tubes.

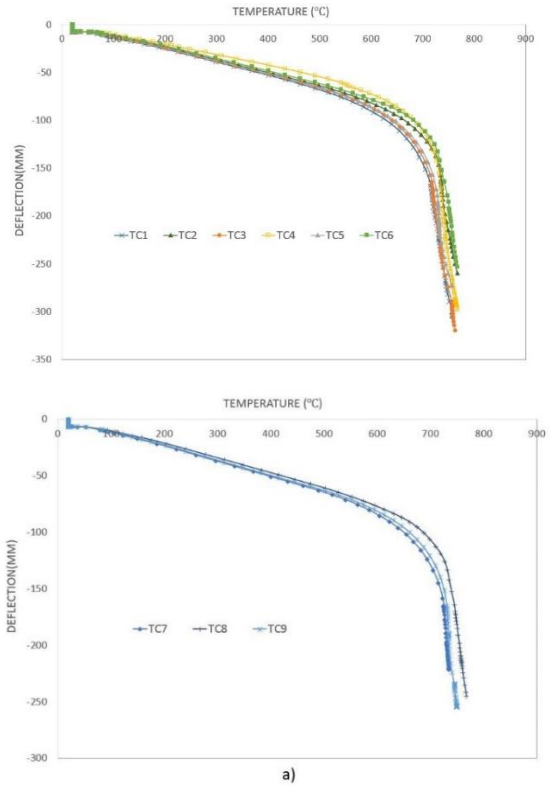

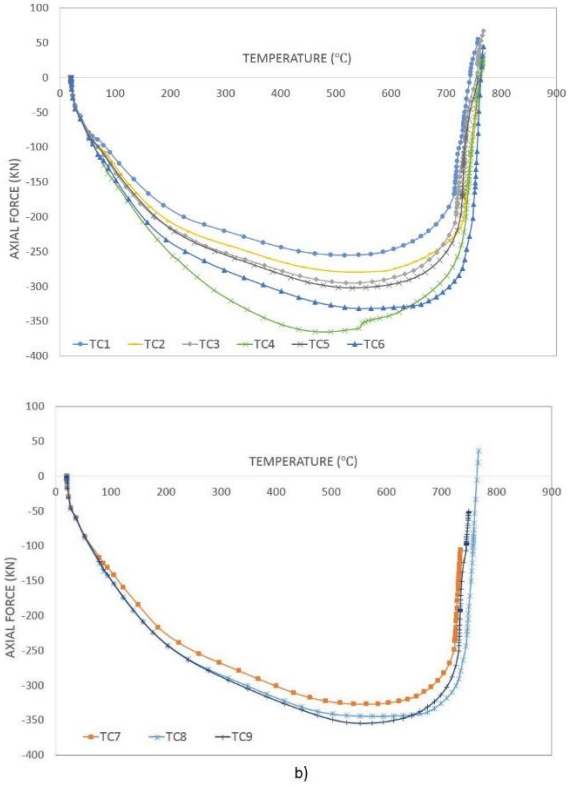

Figure 7. (a) Mid-span deflection, (b) Axial force of beam with HP-T connection

3. 3. Comparison of the Proposed Connection with Other Connection Types Figures 8(a) and 8(b) show the mid-span deflection and beam axial force versus beam bottom flange temperature curves of HP-T connection and conventional web cleat connection. Figure 8 indicates that the interactions between structural components trigger permanent changes in the internal forces of the connection during the fire. Not only was the thermally-induced force in the beam with new connection considerably reduced due to the high axial ductility capacity created, but also sufficient ductility was provided to accommodate the deformations generated by the attached beam exposure to fire.

4. SEISMIC PERFORMANCE OF HP-T CONNECTION

4. 1. Design Procedure of Tubular Connections The connection design approach is according to AISC seismic provisions [39] and according to the philosophy of AW-connection [27]. The foundation of the design of such seismic joints is the formation of a plastic joint in the reduced area of the beam and the uniform distribution of plastic strains in this area, in order to delay torsional buckling and avoid instability.

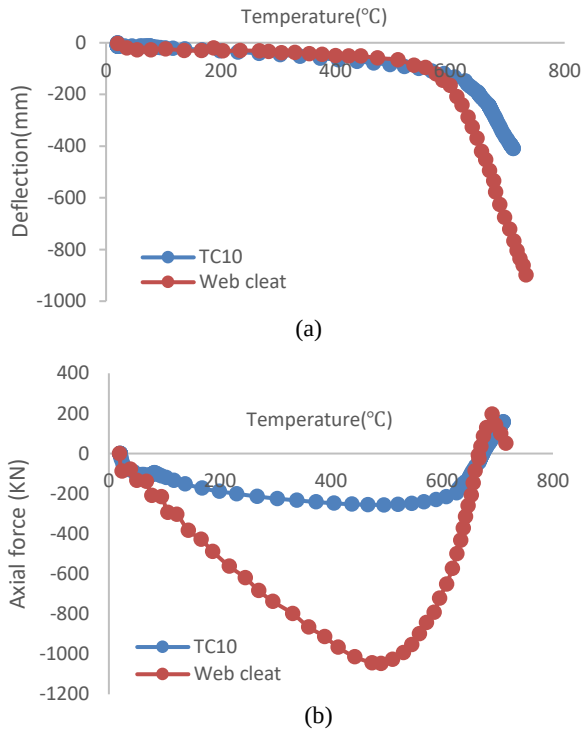

Figure 8. Results Comparing the new connection with Web cleat connections, (a) Deflection at beam mid-span (b) Axial force of beam

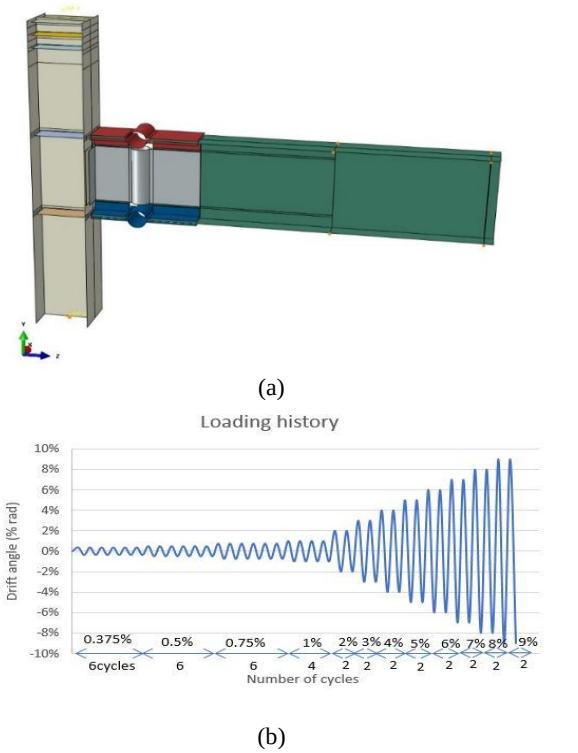

Figure 9. (a) 3D finite element modeling of HP-T connection, (b) Loading history

4. 2. Numerical Model Under Seismic Loading

The proposed sub-assembly utilized in laboratory studies investigated by Saleh et al. [29] was chosen to simulate seismic behavior. It consisted of an exterior joint with a 2.4m beam attached to a 2m column. The specification of the seismic models is presented in Table 4. It should be highlighted that appropriately designing continuity plates in seismic demands not only tolerate a couple of concentrated forces from the beam's flange but also conversely convert the axial force to shear force in the panel zone. The 3D FE model is illustrated in Figure 9(a).

4. 2. 1. Geometry and Finite Element Mesh

Two FE models were established to analyze the seismic performance of the HP-T connection. The geometries of the beam, column, and tubular connection were created separately, and were then assembled to form the model of beam-column connection and were bounded together with tie constraints. According to reference test [29], beam, column, connection, and continuity plates were modeled using 4-node shell elements with reduced integration (S4R). These elements include six degrees of freedom per node and three-section points to assess stress and strain variation through the thickness.

TABLE 4. Specification of the seismic models

Model number	TC11	TC12
Inner radius of Tubular RBS connection (mm)	50	50
Top-Bot tube thickness (mm)	9	10
Middle Tube thickness (mm)	7	6
Middle tube depth (mm)	360	360

4. 2. 2. Material Properties

The behavior of steel was modeled by a nonlinear kinematic hardening model with a von mises yield criterion. The mechanical characteristic, i.e. young's modulus and Poisson's ratio were set to be 206 GPA, and 0.3, respectively. The yield strength (F_y) and ultimate strength (F_u) and also elongation was the same as the reference test [29].

4. 2. 3. Boundary Condition and Loading

The standard solver of ABAQUS software was used to analyze the model. Based on the reference test [29] condition, the bottom of the column was modeled with a pinned end (the displacement of the centers of the column was constrained in the x, y, z directions $U_x = U_y = U_z = 0$). By fixing the degree of freedom in vertical direction ($U_y = 0$), roller support was defined at the beam end. Moreover, to define lateral support, out-of-plane displacement of beam web was fixed at x-direction from the side of the column ($U_x = 0$). The

displacement-controlled loading was imposed on the structure by defining boundary conditions on top of the column based on AISC seismic provisions [40]. Total story drift was calculated by dividing lateral displacement at the top of the column-by-column height. Figure 9b demonstrates the adopted loading protocol.

5. NUMERICAL RESULTS

5. 1. Hysteretic Graph The lateral force-total story drift cyclic curves are presented in Figure 10 for the proposed connection. The suggested connection meets AISC seismic [39] approval standards, confirming that the strength reduction of connection should not reduce flexural capacity at 0.04-radian to less than 80% of the nominal flexural capacity and special moment frame connection tolerates at least 0.03-radian story drift. As can be seen in Figure 10, the connection provides a stable and cyclic behavior without strength reduction up to 9% story drift.

5. 2. Investigation of the Plastic Hinge Behavior and Failure Modes The Von-Mises stress and strain contours of drift angles 0.04, 0.06, and 0.08-radian are illustrated in Figures 11 and 12. The extension of the plastic hinge in the predetermined zone (9cm from the column edge) is proved by greater values

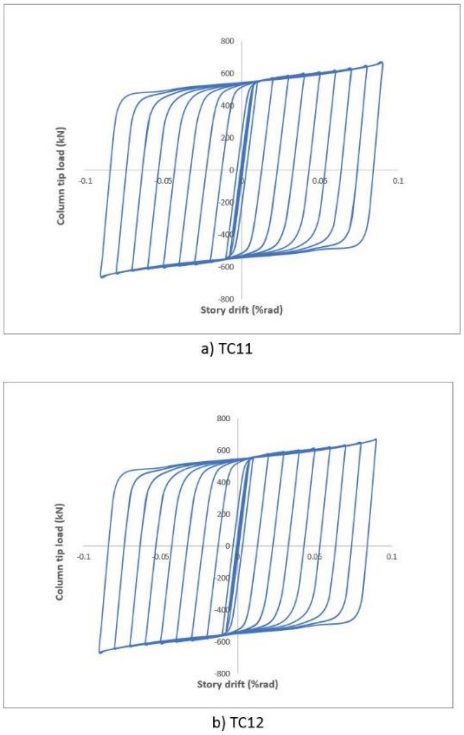

Figure 10. Column tip force versus story drift for HP-T connection a) TC11, b) TC12

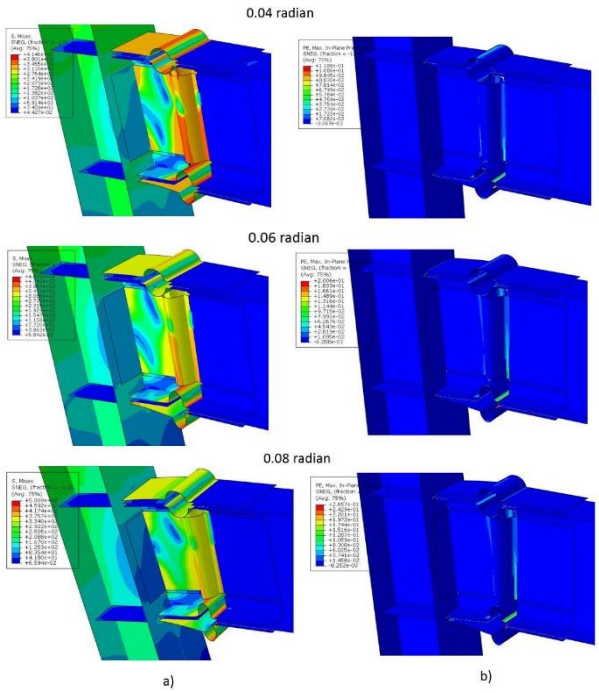

Figure 11. a) Von mises stress, b) strain counters at 0.04, 0.06 and 0.08 radian story drift (TC11)

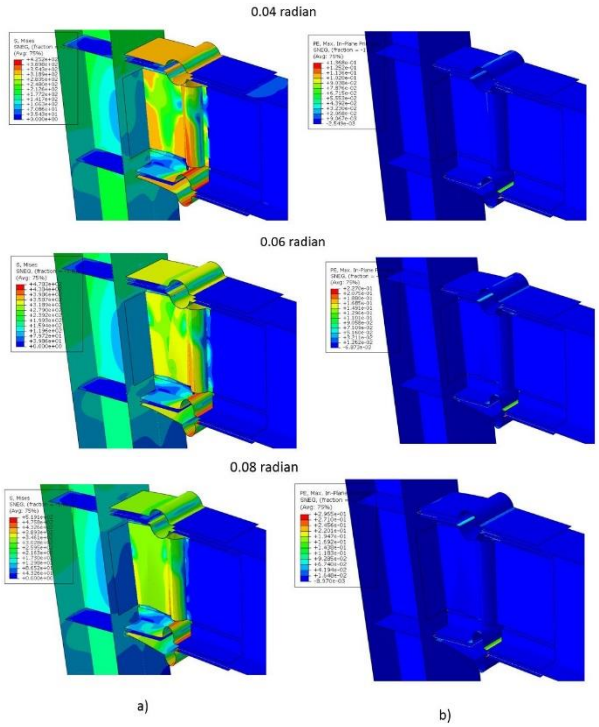

Figure 12. a) Von mises stress, b) strain counters at 0.04, 0.06 and 0.08 radian story drift (TC12)

of the plastic strain created in the beam flange, while the rest of the reduced area remains elastic. In other words, approaching the column face, the plastic strain diminishes and dramatically reduces the risk of failure at the welds in the beam-column connection. According to the results, local buckling of the middle tube at the reduced region occurred at 4% story drift.

6. CONCLUSION

The proposed connection is made through cutting continuous web and flange and replacing these parts with horizontal and vertical tubes at the designated position of the plastic hinge. The numerical validation of an innovative fire-earthquake resistant connection called HP-T connection is presented. To assess failure mechanism and plastic hinge formation models with variable tube thicknesses are simulated under fire and seismic loading separately. Based on the findings, the following can be concluded.

- The main exclusivity of using HP-T robust connection is satisfactory fire behavior with provision of appropriate axial ductility to reduce the compressive axial force which arises from thermal expansion of the connected beam and catenary tension forces generated by the beam exposed to fire.
- All of the numerical models, except for TC7, TC9, behaved in a ductile and robust manner in fire simulation. According to the results of the parametric study, under the tensile axial forces arising from the catenary action of the beam at elevated temperatures two damage scenarios were detected, namely bottom flange tube damage with minor beam web local buckling and bottom flange tube damage without beam web local buckling. Series I RBS connections exhibited much higher axial ductility through the development of more substantial catenary action as well as no beam web buckling being observed.
- The developed FE models can accurately predict the hysteretic behavior of the proposed connection. It is noteworthy that the HP-T connection displayed ductile seismic response and a large hysteretic enclosed area and more energy dissipation capacity. The HP-T connection can transfer the plastic strain zone away from the column edge and effectively concentrate the plastic strains zones within the flange tubes and as a result, prevent progressive failure.
- The HP-T connection can support 0.09 rad drift without any significant strength reduction which is higher than those stipulated by existing seismic codes for qualifying connections in a seismically active area. Besides, no lateral-torsional buckling (LTB) occurred at HP-T connection even in higher story drift.
- The discussed connection possesses a great potential to become one of the most practical ones. Nevertheless, experimental research is needed to assure the suitability of this innovative connection for eventual industry implementation.

7. REFERENCES

1. Shyam-Sunder, S., Gann, R.G., Grosshandler, W.L., Lew, H.S., Bukowski, R.W., Sadek, F., Gayle, F.W., Gross, J.L., McAllister, T.P. and Averill, J.D., "Federal building and fire safety investigation of the world trade center disaster: Final report of the national construction safety team on the collapses of the world trade center towers (nist ncstar 1)", (2005).
2. Bailey, C., Newman, G. and Robinson, J., "Fire safe design: A new approach to multi-storey steel-framed buildings, Steel Construction Institute, (2006).
3. Ahmadi, M., Aghakouchak, A., Mirghaderi, R., Tahouni, S., Garivani, S., Shahmari, A. and Epackachi, S., "Collapse of the 16-story plasco building in tehran due to fire", ***Fire Technology***, Vol. 56, No. 2, (2020), 769-799. https://doi.org/10.1007/s10694-019-00903-y
4. Kruppa, J., "Resistance au feu des assemblages par boulons haute resistance", ***CTICM, Puteaux***, (1976).
5. Lawson, R., "Behaviour of steel beam-to-column connections in fire", ***Structural Engineer***, Vol. 68, (1990), 263-271.
6. Leston-Jones, L.C., "The influence of semi-rigid connections on the performance of steel framed structures in fire", University of Sheffield, (1997),
7. Al-Jabri, K.S., "The behaviour of steel and composite beam-to-column connections in fire", University of Sheffield, (1999),
8. Sarraj, M., "The behaviour of steel fin plate connections in fire", University of Sheffield, (2007),
9. Hu, Y., Burgess, I., Davison, J. and Plank, R., "Modelling of flexible end plate connections in fire using cohesive elements", in Fifth International Conference of Structures in Fire, Singapore. (2008).
10. Yu, H., Burgess, I., Davison, J. and Plank, R., "Tying capacity of web cleat connections in fire, part 2: Development of component-based model", ***Engineering Structures***, Vol. 31, No. 3, (2009), 697-708. http:// doi.org/10.1016/j.engstruct.2008.11.006
11. Han, L.-H., Wang, W.-H. and Yu, H.-X., "Analytical behaviour of rc beam to cfst column frames subjected to fire", ***Engineering Structures***, Vol. 36, (2012), 394-410. https://doi.org/10.1016/j.engstruct.2011.12.030
12. Ding, J. and Wang, Y., "Experimental study of structural fire behaviour of steel beam to concrete filled tubular column assemblies with different types of joints", ***Engineering Structures***, Vol. 29, No. 12, (2007), 3485-3502. https://doi.org/10.1016/j.engstruct.2007.08.018
13. Elsawaf, S., Wang, Y. and Mandal, P., "Numerical modelling of restrained structural subassemblies of steel beam and cft columns connected using reverse channels in fire", ***Engineering Structures***, Vol. 33, No. 4, (2011), 1217-1231. https://doi.org/10.1016/j.engstruct.2010.12.043
14. Shahidi, F. and NATEGHI, A.F., "Non-linear behavior of new (fsfn) moment resisting connections in comparison to the existing kbb connections in steel frames", ***International Journal***

of Engineering, Transactions A: Basics, Vol. 26, No. 10, (2013). doi: 10.5829/idosi.ije.2013.26.10a.03.

15. SAC, J., "State of the art report on connection performance report no fema-355d", Federal Emergency Management Agency (FEMA), Washington, (2000).
16. Chen, S.-J. and Chao, Y., "Effect of composite action on seismic performance of steel moment connections with reduced beam sections", ***Journal of Constructional Steel Research***, Vol. 57, No. 4, (2001), 417-434. https://doi.org/10.1016/S0143-974X(00)00022-5
17. Jones, S.L., Fry, G.T. and Engelhardt, M.D., "Experimental evaluation of cyclically loaded reduced beam section moment connections", ***Journal of Structural Engineering***, Vol. 128, No. 4, (2002), 441-451. https://doi.org/10.1061/(ASCE)0733-9445(2002)128:4(441)
18. Roeder, C.W., "Connection performance for seismic design of steel moment frames", ***Journal of Structural Engineering***, Vol. 128, No. 4, (2002), 517-525. https://doi.org/10.1061/(ASCE)0733-9445(2002)128:4(517)
19. Zhang, X., Ricles, J.M., Lu, L.-W. and Fisher, J.W., "Development of seismic guidelines for deep-column steel moment connections", ***Development***, Vol. 6, (2004), 1-2004.
20. Lee, C.-H., Jeon, S.-W., Kim, J.-H. and Uang, C.-M., "Effects of panel zone strength and beam web connection method on seismic performance of reduced beam section steel moment connections", ***Journal of Structural Engineering***, Vol. 131, No. 12, (2005), 1854-1865. https://doi.org/10.1061/(ASCE)0733-9445(2005)131:12(1854)
21. Zhang, X. and Ricles, J.M., "Seismic behavior of reduced beam section moment connections to deep columns", ***Journal of Structural Engineering***, Vol. 132, No. 3, (2006), 358-367. https://doi.org/10.1061/(ASCE)0733-9445(2006)132:3(358)
22. Han, S.-W., Moon, K.-H. and Stojadinovic, B., "Design equations for moment strength of rbs-b connections", ***Journal of Constructional Steel Research***, Vol. 65, No. 5, (2009), 1087-1095. https://doi.org/10.1016/j.jcsr.2009.01.003
23. Mayes, R.L. and Naeim, F., "The seismic design handbook 2nd edition ch. 14 design of structures with seismic isolation", ***Kluwer Academic Publishers***, (2001).
24. Rao, D.P. and Kumar, S.S., "Rhs beam-to-column connection with web opening—parametric study and design guidelines", ***Journal of Constructional Steel Research***, Vol. 62, No. 8, (2006), 747-756. https://doi.org/10.1016/j.jcsr.2005.11.015
25. Yang, Q., Li, B. and Yang, N., "Aseismic behaviors of steel moment resisting frames with opening in beam web", ***Journal of Constructional Steel Research***, Vol. 65, No. 6, (2009), 1323-1336. https://doi.org/10.1016/j.jcsr.2009.01.007
26. Wilkinson, S., Hurdman, G. and Crowther, A., "A moment resisting connection for earthquake resistant structures", ***Journal of Constructional Steel Research***, Vol. 62, No. 3, (2006), 295-302. doi: 10.1016/j.jcsr.2005.07.011.
27. Mirghaderi, S.R., Torabian, S. and Imanpour, A., "Seismic performance of the accordion-web rbs connection", ***Journal of Constructional Steel Research***, Vol. 66, No. 2, (2010), 277-288. https://doi.org/10.1016/j.jcsr.2009.09.007
28. Morrison, M., Schweizer, D. and Hassan, T., "An innovative seismic performance enhancement technique for steel building moment resisting connections", ***Journal of Constructional Steel Research***, Vol. 109, (2015), 34-46. https://doi.org/10.1016/j.jcsr.2015.02.010
29. Saleh, A., Mirghaderi, S.R. and Zahrai, S.M., "Cyclic testing of tubular web rbs connections in deep beams", ***Journal of Constructional Steel Research***, Vol. 117, (2016), 214-226. https://doi.org/10.1016/j.jcsr.2015.10.020
30. Zahrai, S.M., Mirghaderi, S.R. and Saleh, A., "Tubular web reduced beam section (tw-rbs) connection, a numerical and experimental study and result comparison", ***Steel and Composite Structures***, Vol. 23, No. 5, (2017), 571-583. https://doi.org/10.12989/scs.2017.23.5.571
31. Han, L.-H., "Fire performance of concrete filled steel tubular beam-columns", ***Journal of Constructional Steel Research***, Vol. 57, No. 6, (2001), 697-711. https://doi.org/10.1016/S0143-974X(00)00030-4
32. Song, T.-Y. and Han, L.-H., "Post-fire behaviour of concrete-filled steel tubular column to axially and rotationally restrained steel beam joint", ***Fire Safety Journal***, Vol. 69, (2014), 147-163.
33. Standardization, I.O.F., *Iso 834: Fire-resistance tests: Elements of building construction-part 1.1: General requirements for fire resistance testing*. 1999, ISO834-1: 1999, Geneva.
34. Liu, Y., Huang, S. and Burgess, I., "Ductile connections to improve structural robustness in fire", in Proceedings of the 6th Applications of Structural Fire Engineering Conference (ASFE'19), Sheffield., (2019).
35. Liu, Y., Huang, S.-S. and Burgess, I., "Performance of a novel ductile connection in steel-framed structures under fire conditions", ***Journal of Constructional Steel Research***, Vol. 169, (2020), 106034. https://doi.org/10.1016/j.jcsr.2020.106034
36. Dai, X., Wang, Y. and Bailey, C., "Numerical modelling of structural fire behaviour of restrained steel beam–column assemblies using typical joint types", ***Engineering Structures***, Vol. 32, No. 8, (2010), 2337-2351. https://doi.org/10.1016/j.engstruct.2010.04.009
37. Code, P., "Eurocode 3: Design of steel structures-part 1-2: General rules-structural fire design", London: European Committee for Standardisation, (2007).
38. Wald, F., Da Silva, L.S., Moore, D., Lennon, T., Chladna, M., Santiago, A., Beneš, M. and Borges, L., "Experimental behaviour of a steel structure under natural fire", ***Fire safety Journal***, Vol. 41, No. 7, (2006), 509-522.
39. AISC, "Seismic provisions for structural steel buildings, AISC Chicago., (2010).

Persian Abstract

چکیده

اتصال ابتکاری تاب آور در برابر آتش سوزی و زلزله بنام اتصال لوله ای با عملکرد بالا (HP-T)، در مقاله حاضر ارائه گردیده و اعتبار عددی آن تایید شده است. اتصال HP-T، شکل پذیری محوری و دورانی را افزایش داده و همچنین از گسیختگی ترد جلوگیری می کند. دوسری از مدل ها با موفقیت در نرم افزار آباکوس شبیه سازی شدند. تحلیل تنش حرارتی کوپله متوالی، در اولین مجموعه از مدل های طراحی برای شبیه سازی حرارت، جهت بررسی اثرات پارامترهای مختلف ازجمله ضخامت لوله و نسبت بار اعمالی انجام گردید. بمنظور شبیه سازی آسیب آتش سوزی، دو سناریو احتمالی آسیب لوله بال پایینی و آسیب جان تیر در معرض توام بارگذاری اولیه و حرارت در نظر گرفته شد. در مجموعه دوم مدل های شبیه سازی لرزه ای، مود گسیختگی، منحنی های چرخه ای و توزیع کرنش مورد تجزیه و تحلیل قرار گرفتند. با توجه به نتایج، اتصال مقاوم HP-T نه تنها افزایش شکل پذیری مناسب را در شرایط آتش سوزی متغیر نیرو فراهم می کند، بلکه حداقل ۸ درصد جابه جایی نسبی میان طبقه را بدون کاهش مقاومت قابل توجه تحمل می کند.

International Journal of Engineering

Journal Homepage: www.ije.ir

Design of Open Pit Mines using 3D Model in Two-element Deposits under Price Uncertainty

G. H. Kakha*

Faculty of Industry & Mining (Khash), University of Sistan and Baluchestan, Zahedan, Iran

PAPER INFO

Paper history:
Received 17 May 2022
Received in revised form 09 June 2022
Accepted 11 June 2022

Keywords:
Binomial Tree
Pricing Uncertainty
Pyramid Tree
Two-element Deposits
Three-dimensional Tree

ABSTRACT

When it comes to evaluating mining projects, uncertainty plays a significant role, particularly in the analysis of mining economic characteristics, which makes the assessment of a mining project erroneous and untrustworthy. The volatility of mineral prices is a major cause of economic ambiguity and concern. Economic uncertainty has extensively been examined in mining production project planning, but the majority of the study has focused on single-element deposits, with little emphasis devoted to the significance of pricing uncertainty in two-element deposits. Using a three-dimensional tree model, this study investigates how design could be affected by the pricing uncertainty of two different elements. In this model, not only annual volatility but also monthly volatility were considered due to momentary changes in the price of several elements. To authenticate the proposed model, a numerical example was resolved using discounted cash flow, binomial tree, pyramid tree, and three-dimensional modeling techniques. The results of each approach were compared to those of real-world data. Following the findings of the current investigation, it can be concluded that the values derived from the suggested model (a net present value of $ 324.2 thousand) are more precise than the values acquired from other approaches, and that they are just 8% out of step with reality. Other methods, on the other hand, come up with results that are at least 17% and at most 39% different from those that come from real data.

doi: *10.5829/ije.2022.35.10a.10*

1. INTRODUCTION

Design for open pit mines is a complex and significant issue that has been addressed by many researchers. The design process usually starts with a geological block model consisting of a group of imaginary regular blocks covering the surrounding ore and host rock resources. Then, a set of characteristics, including the grade, specific weight, and coordinates, are estimated or attributed to each block using drilling sample data. The geological features are combined with technical and economic parameters in the next step to determine the economic value of each block, forming the economic block model, which is a necessary input for the production planning.

Generally, production planning for an open-pit mine involves finding a sequence of blocks for optimized annual plans, which lead to the highest net present value (NPV) for the project cash flow while satisfying the technical limitations such as extraction capacity, processing capacity, block derivation sequence, and pit slope [1].

Design in mines can be categorized into deterministic and stochastic-based approaches. Deterministic open-pit production was first addressed in 1968 [2] and developed in many methods, such as integer programming [3, 4], complex integer programming [5, 6], dynamic programming [7], and metaheuristic approaches (e.g., genetic algorithms [8], particle swarm optimization [9], and ants colony algorithm [10, 11]. The main issue of this approach is the input parameter assumptions. The deterministic parameter assumption might lead to unrealistic and incorrect production planning because these parameters are associated with a significant uncertainty [12-14]. Most studies considered single-element deposit, and there have been few studies regarding the role of economic parameter uncertainty for two-element deposits [15-24]. To address the shortcomings of previous studies, the present study

*Corresponding Author Institutional Email: G.Kakha@eng.usb.ac.ir
(G. H. Kakha)

Please cite this article as: G. H. Kakha, Design of Open Pit Mines using 3D Model in Two-element Deposits under Price Uncertainty, ***International Journal of Engineering, Transactions A: Basics***, Vol. 35 No. 10, (2022), 1906-1917

investigates the design of two-element deposits under price uncertainty using the proposed 3D tree model.

2. EXPERIMENTAL PROCEDURE

Figure 1 depicts the stages that this article aims to take in order to accomplish the goals of this study.

2. 1. The Model Proposed for Modeling Pricing Uncertainty The binomial tree model is one of the most often used models for analyzing the discontinuously fluctuations of stock price. This model was first developed by Cox and Ross [25] to estimate the pricing stock uncertainty. Flexibility, accuracy, and speed in calculation are some of the advantages of the binomial tree model [26]. The structure of a binomial tree is formed of different branches and nodes. This model depicts all conceivable ways in which mineral prices might fluctuate throughout the project lifecycle. For each pricing node, it is seen how much the mineral was valued at that point in time. An illustration of a binomial tree is shown in Figure 2.

As can be seen, the number of nodes in each layer corresponds to the number of layers. These branches indicate various routes from one node to the next one, and every single one of them has its own probability and rate of rise or decline of related nodes. Ascending branches have a probability of realization of P_r, whereas descending branches have a chance of realization of 1-P_r. If a node is linked to the ascending branch, the value of that node is multiplied by u to get the node's value. By the same token, the value of the nodes linked to descending branches is derived by multiplying the value of the preceding node by d. For the purpose of illustration, if the value of the node in layer No. 1 of Figure 2 is S_0, the value of the node linked to the ascending branch and its probability of occurrence will be S_0u and P_r, respectively. Moreover, the value of the node connected to the descending branch and its probability of occurrence will be S_0d and 1-P_r in that order. The equations below show how to figure out u, d, and the probability of P_r [25].

$$u = \exp(\sigma\sqrt{\delta_t}) \quad (1)$$

$$d = \frac{1}{u} = \exp(-\sigma\sqrt{\delta_t}) \quad (2)$$

$$P_r = \frac{(1+r_f)-d}{u-d} \quad (3)$$

where σ is the Instability (unpredictability), u is the increasing rate of each node's value, r is the risk-free discount rate, d is the decreasing rate of each node's value, T is the life expectancy of a project in terms of time periods, and N is the number of time periods of a tree.

The binomial tree approach has a major limitation when it comes to analyzing the impact of many uncertainties simultaneously [27]. Using a pyramid tree model, Dehghani et al. [28] were able to remove this problem in the binomial tree technique. In their investigation, they looked at the impact of price and cost uncertainty on the evaluation of mining ventures. In the pyramid model, all possible prices and operating costs for minerals are taken into account (see Figure 3).

The pyramid tree model is capable of modeling and estimating both uncertainties simultaneously. Figure 4 illustrates a view of the pyramid tree.

It is made by multiplying the nodes of the economic value tree and the tree of probabilities, and then

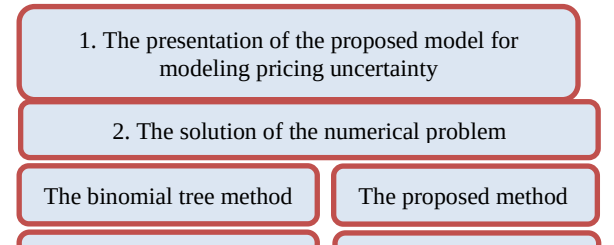

Figure 1. The process diagram

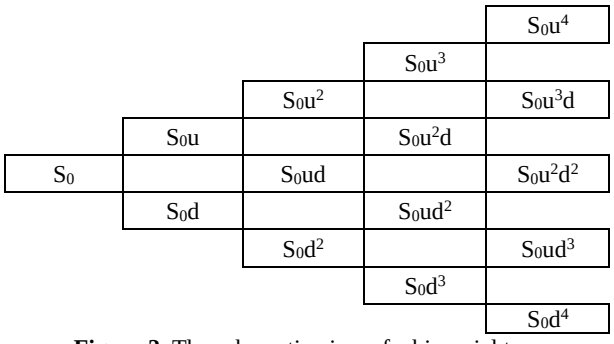

Figure 2. The schematic view of a binomial tree

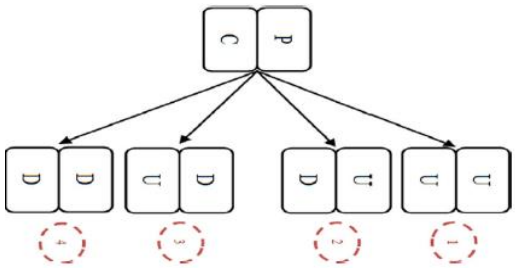

Figure 3. The pricing and operational cost variations (U: increasing and D: decreasing) [28]

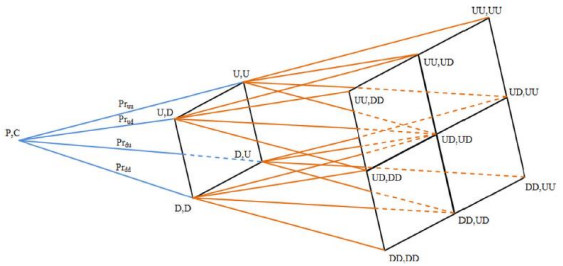

Figure 4. pyramid tree model (U: increasing and D: decreasing) [28]

discounting them using Equation (11). The net present value (NPV) will then be found by subtracting this tree from the other two trees and multiplying them.

$$Pr_{uu} = \frac{1}{4}\frac{(\Delta x_p \Delta x_c + \Delta x_c \vartheta_p \Delta t + \Delta x_p \vartheta_c \Delta t + \rho \sigma_p \sigma_c \Delta t)}{\Delta x_p \Delta x_c} \quad (4)$$

$$Pr_{uu} = \frac{1}{4}\frac{(\Delta x_p \Delta x_c + \Delta x_c \vartheta_p \Delta t - \Delta x_p \vartheta_c \Delta t - \rho \sigma_p \sigma_c \Delta t)}{\Delta x_p \Delta x_c} \quad (5)$$

$$Pr_{uu} = \frac{1}{4}\frac{(\Delta x_p \Delta x_c - \Delta x_c \vartheta_p \Delta t + \Delta x_p \vartheta_c \Delta t - \rho \sigma_p \sigma_c \Delta t)}{\Delta x_p \Delta x_c} \quad (6)$$

$$Pr_{uu} = \frac{1}{4}\frac{(\Delta x_p \Delta x_c - \Delta x_c \vartheta_p \Delta t - \Delta x_p \vartheta_c \Delta t + \rho \sigma_p \sigma_c \Delta t)}{\Delta x_p \Delta x_c} \quad (7)$$

$$Pr_{uu} + Pr_{ud} + Pr_{du} + Pr_{dd} = 1 \quad (8)$$

In the abovementioned relations, σ_P and σ_C denote the price and cost unpredictability, respectively. Moreover, Δt is the ratio of the life expectancy of a project to the number of time periods, ρ is the correlation between the price and cost data. It is worthy to note that ΔXp and ΔXc are calculated through the multiplication of volatilityin Δt [28].

$$\vartheta_p = \mathrm{r} - \frac{1}{2}\sigma_p^2 \quad (9)$$

$$\vartheta_c = \mathrm{r} - \frac{1}{2}\sigma_c^2 \quad (10)$$

$$DCF_{n,k}=BEV_{n,k}+(V/(1+i)) \quad (11)$$

$$V=Pr_{uu}.DCF_{n+1,uu}+Pr_{ud}.DCF_{n+1,ud}+ Pr_{du}.DCF_{n+1,du}+Pr_{dd}.DCF_{n+1,dd} \quad (12)$$

As previously stated, the binomial tree model was only capable of investigating one parameter under uncertainty and made the assumption that all other essential values remained constant. Dehghani et al. [28] employ just unpredictability, the yearly increasing and decreasing coefficients for prices in their pyramid tree, but the changes in mineral prices are on the spot and should be established upon the quantity of the blocks extracted in a year, unpredictability, and monthly increasing and decreasing coefficients to solve the model. Figure 5 shows an overview of the three-dimensional tree model.

The priority of the proposed model over the other two models is to simultaneously consider the monthly and annual unpredictability. In the proposed model, the price 3D trees are first created for two elements, as shown in Figure 5. A three-dimensional economic value tree is then generated for all price change situations utilizing pricing trees. Beginning in the second year, for example, there are two prices for every single element. As a result, four value possibilities may be found in the economic value tree. They include: 1) an increase in both elements' prices, 2) an increase in the price of the first element and a decrease in the price of the second element, 3) a decrease in the price of the first element and an increase in the price of the second element; and 4) a decrease in both elements' prices.

Following the construction of a three-dimensional economic value tree using Equations (4) to (10), a three-dimensional tree of probabilities is constructed, and in the following step, the corresponding multiplication tree is constructed by correspondingly multiplying the nodes of the two trees of economic value and probabilities. In the next phase, you can use Equation (11) to figure out how much the project will be value in the future by not taking into account the tree that you bought in the first phase.

2. 2. Numerical Example The blocks of a lead and zinc mine are shown in the following hypothetical cross-section where the lead and zinc cutoff grades are indicated by a number on the left and right side, respectively. Furthermore, the supplementary data is given in Table 1, in order to calculate the economic value of every single block.

The hypothetical grades model of a lead and zinc mine is shown in Figure 6.

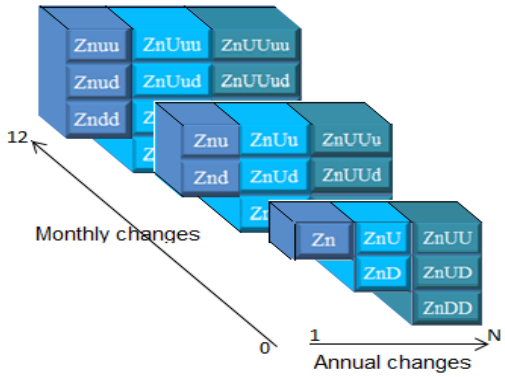

Figure 5. The 3D tree model for the price of zinc (ZN: The base price of zinc, U: The annual increasing coefficient, D: The annual decreasing coefficient, u: The monthly increasing coefficient, d: The monthly decreasing coefficient)

Figure 6. The Hypothetical Grades Model of a Lead and Zinc Mine

Osanloo and Ataei [29] examined the equivalent cutoff grade in multi-element deposits. The equations initiated from this research for two-element deposits are as follows:

$$BEV = TO * [\bar{G}_1 R_1(P_1 - r_1) + \bar{G}_2 R_2(P_2 - r_2) - C_r] - (TR * C_m) \quad (13)$$

where C_r is the cost of condensing and processing, C_m is the cost of the extraction of each ton ore, TO_i is the mineral tonnage in blocks, TR_i is the block tonnage, including tailings and minerals, P_2 is the price of the second element, r_2 is the cost of purifying and selling the second metal, R_2 is the total retrieval of the second metal, P_1 is the price of leading metal, r_1 is the cost of purifying and selling the leading metal, R_1 is the total retrieval of the leading metal, g_1 is the mean cutoff grade concerning the leading metal, and g_2 is mean cutoff grade concerning the second metal [30].

Equation (4) is initiated by factoring $R_1(P_1\text{-}r_1)$ in Equation (3).

$$BEV = TO * \left[R_1(P_1 - r_1)\left(\bar{G}_1 + \bar{G}_2 \frac{R_2(P_2 - r_2)}{R_1(P_1 - r_1)}\right) - C_r\right] - (TR * C_m) \quad (14)$$

$$f_{eq} = \frac{R_2(P_2 - r_2)}{R_1(P_1 - r_1)} \quad (15)$$

Equivalent factor f_{eq} is used to show the economic valueof the blocks for the two-element deposits as Equation (6).

$$BEV = TO * [R_1(P_1 - r_1)(\bar{G}_1 + f_{eq}\bar{G}_2) - C_r] - (TR * C_m) \quad (16)$$

On the basis of relations (13) and (17), Table 1 and considering zinc as the leading metal and lead as the second metal, one can turn the supposable cutoff grade model into the cutoff grade model equivalent to Figure 7.

Based on the data available in Table 1, the materials' mean density (3 ton/m^3), and the equivalent grade model, the block economic value model is in the form of Figure 8.

In this case, it is anticipated that it will take one year to extract each of the three blocks. As a result, the duration of this project will be three years. In Figure 9, Roman shows how to use his "dynamic planning" method to plan mining in this part.

Based on Figures 8 and 9 and Equation (17), a net present value of $291.53 thousand was derived using the discounted cash flow approach from the extraction of this cross-section.

$$NPV = \sum_{n=1}^{N} \frac{BEV_n}{(1+i)^n} \quad (17)$$

where BEV_n is the sum of economic value of the blocks in year n, i is the discount rate, and N is the project life.

TABLE 1. The information required for the problem.

Description	Amount for lead	Amount for zinc	unit
Total retrieval	80	85	%
Block dimension	10*10*5	10*10*5	Meter
Cut off limit	1.4	1.48	%
Density	10	7	Ton/m^3
Price in the beginning of 2013	2224.5	1986.21	Dollar/ton
The cost of extraction	1	1	Dollar/ton
Processing cost	63	63	Dollar/ton
Risk-free rate	7	7	%
F_{eq}	1.05	Equivalent cutoff grade	2.9

Figure 7. The equivalent grade model

Figure 8. The block economic value model(1000 dollars)

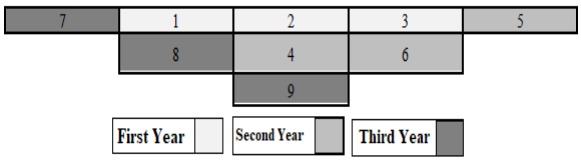

Figure 9. The order of mining

- **The binomial tree model**

Utilizing price data from 1990 to 2013, the binomial tree approach affecting by pricing uncertainty will be used to obtain the parameters needed to solve the numerical example (Tables 2 and 3).

The zinc and lead pricing trees are generated for 2013-2015 after calculating the binomial tree's necessary parameters and the base year price (Tables 4 and 5).

TABLE 2. The historical price data on zinc and lead between 1990 and the beginning of 2013 and the calculation of volatility[1]

Year	The price of lead	LN (Pn+1-pn)	The price of zinc	LN (Pn+1-pn)
1990	809.5	0.185207	1517.92	-0.0872
1991	557.8	-0.37242	1121.36	-0.3028
1992	543.51	-0.02595	1241.84	0.102052
1993	407.34	-0.2884	963.96	-0.2533
1994	548.72	0.29794	998.22	0.034924
1995	629.3	0.13702	1031.09	0.032398
1996	774.13	0.207132	1024.97	-0.00595
1997	623.06	-0.2171	1314.9	0.249097
1998	526.92	-0.16759	1024.29	-0.24976
1999	501.77	-0.04891	1075.8	0.049065
2000	454.17	-0.09967	1127.7	0.047116
2001	476.36	0.047702	886.82	-0.24029
2002	452.25	-0.05194	778.9	-0.12976
2003	514.21	0.128397	827.97	0.061094
2004	881.95	0.539504	1048.04	0.2357
2005	974.37	0.099656	1380.55	0.27556
2006	1288.42	0.279381	3266.18	0.861139
2007	2579.12	0.694032	3249.73	-0.00505
2008	2593.32	0.005491	1884.83	-0.54473
2009	1719.44	-0.41094	1658.39	-0.12799
2010	2148.19	0.222627	2160.36	0.264428
2011	2400.71	0.111139	2195.53	0.016149
2012	2063.56	-0.15133	1950.02	-0.11858
2013	0.0751	2224.50	0.018389	1986.21

TABLE 3. The information required to create binomial tree

The parameters of binomial tree	The price of zinc	The price of lead
Volatility	27.2%	26.1%
Increasing coefficient	1.60%	1.58
Decreasing coefficient	0.62%	0.63%
The probability of increase	45%	46%

TABLE 4. The tree of changes of zinc price

2013	2014	2015
1986.21	3182.399	5098.989
	1239.64	1986.21
		773.686

[1] https://www.ilzsg.org/static/statistics.aspx

TABLE 5. The tree of changes of lead price

2013	2014	2015
2224.5	3521.376	5574.327
	1405.246	2224.50
		887.7127

According to Equation (13) about the economic value of the block and the trees concerning the price of the two elements, the economic value tree has the following form, as shown in Tables 6 and 7.

Eventually, after discounting the economic value tree using Equation (18), the amount of net present value is determined.

$$DCF_{n,k} = BEV_{n,k} + \frac{P_r \times DCF_{n+1,k} + (1-P_r) \times DCF_{n+1,k+1}}{(1+r)} \quad (18)$$

This section's net present value will be $419.80 thousand dollars if it is extracted using the binomial tree approach to account for zinc and lead pricing uncertainty.

- **The pyramid tree model**

In light of what has been mentioned so far, a numerical example will be solved using the pyramid tree model in this part. Similar to the parameters of a two-dimensional binomial tree, these parameters already listed in Table 1 are needed to create trees. Afterwards, using price binomial trees for the two elements of lead and zinc (Tables 4 and 5), the economic value tree is created (Table 8).

In the next step, given the price historical data of lead and zinc in addition to Equations (4) to (10), the multivariable tree of probabilities is created (see Tables 9 and 10).

In the end, the discounted binomial tree for the model presented by Dehghani et al. will be shown in Table 11. As can be seen, using the pyramid tree developed by Dehghani et al., the net present value resulted from the extraction of the desired cross-section is equal to 215.23

TABLE 6. The economic value tree for each year ($1000)

2013	2014	2015
128.2807	240.4564	335.0613
	90.8831	128.2807
		46.65893

TABLE 7. The economic value discount tree ($1000)

2013	2014	2015
419.8029	468.5665	335.0613
	110.0699	128.2807
		46.65893

TABLE 8. The 3D economic value tree for each year

2013	2014	2015
128.2807	240.4564	335.0613
	174.9909	241.0051
	156.3486	204.3673
	90.8831	222.337
		128.2807
		91.6496
		177.3531
		83.29677
		46.65901

TABLE 9. The 3D tree of probabilities for each year

2013	2014	2015
1	0.472517	0.237791
	0.092562	0.068924
	0.087438	0.042277
	0.347483	0.16664
		0.182204
		0.013352
		0.051086
		0.111076
		0.12665

TABLE 10. A intermediate binomial tree obtained by multiplying the corresponding nodes of economic value and probabilities

2013	2014	2015
128.2807	113.6197	79.67441
	16.19749	16.61101
	13.67082	8.640079
	31.58033	37.05025
		23.37326
		1.223611
		9.060326
		9.252265
		5.909376

TABLE 11. The discounted binomial tree for pyramid model

2013	2014	2015
215.2318	184.9074	104.9255
	72.65671	61.64712
		24.22197

thousand dollars when considering the pricing uncertainty of zinc and lead.

- **The three-dimensional recommended model**

This study's model incorporates not just yearly volatility but also monthly volatility owing to the rapid shifts in the price of several elements in recent years, as previously mentioned. The suggested model is used to solve a numerical problem in this section. On average, one block is extracted every four months because the yearly extraction capacity in the given example is equal to three blocks. In order to make the suggested model trees, four-month data as well as yearly data must be used.

It is important to develop a pricing tree for the proposed model after computing the parameters associated with the model. For the suggested model in Tables 13 and 14, the lifetime of lead and zinc pricing trees and the mining capacity are assumed to be three years and three blocks each year.

In light of what has been discussed regarding the suggested model, the hypothetical scenario using the described model will now be resolved. The pricing tree for zinc and lead has been built for the proposed model, as shown in in Tables 15 and 16 (By using Table 12).

After establishing pricing trees for lead and zinc, it is time to develop a value tree. In this regard, for each price determined for a block associated with the first element, all prices associated with that block for the second element are included in the computation of the block's economic value, and the overall structure of the block's economic value tree is produced (see Table 17). Following the computation of the economic value tree for the desired example using the given model, a probability tree for this model should be generated. This is accomplished by the usage of Equations (4) to (10). Table 18 depicts the probability tree for each block, which corresponds to the economic value tree. Then, the intermediate binomial tree is made by multiplying the relevant nodes from the two trees of economic value and probability.

TABLE 12. The information required to create the proposed model

The parameters of annual binomial tree	The price of zinc	The price of lead
Volatility	27.2%	26.1%
Increasing coefficient	1.60%	1.58
Decreasing coefficient	0.62%	0.63%
The probability of increase	45%	46%
The parameters of four-month binomial tree	**The price of zinc**	**The price of lead**
Volatility	14.2%	14.8%`
Increasing coefficient	1.152%	1.158
Decreasing coefficient	0.86%	0.86%
The probability of increase	0.71%	0.7%

TABLE 13. The zinc pricing tree for the proposed model (ZN: The base price of zinc, U: The annual increasing coefficient, D: The annual decreasing coefficient, u: The 4-month increasing coefficient, d: The 4-month decreasing coefficient)

Zinc pricing tree for the first year			Zinc pricing tree for the second year			Zinc pricing tree for the third year		
BLOCK1	**BLOCK2**	**BLOCK3**	**BLOCK1**	**BLOCK2**	**BLOCK3**	**BLOCK1**	**BLOCK2**	**BLOCK3**
Zn	Znu	Znuu	ZnU	ZnUu	ZnUdd	ZnUU	ZnUUu	ZnUUuu
	Znd	Znud	ZnD	ZnUd	ZnUud	ZnUD	ZnUUd	ZnUUud
		Zndd		ZnDd	ZnUdd	ZnDD	ZnUDd	ZnUUdd
					ZnDdd		ZnDDd	ZnUDdd
								ZnDDdd

TABLE 14. The Lead pricing tree for the proposed model (Pb: The base price of Lead, U: The annual increasing coefficient, D: The annual decreasing coefficient, u: The 4-month increasing coefficient, d: The 4-month decreasing coefficient)

Lead pricing tree for the first year			Lead pricing tree for the second year			Lead pricing tree for the third year		
BLOCK1	**BLOCK2**	**BLOCK3**	**BLOCK3**	**BLOCK3**	**BLOCK3**	**BLOCK3**	**BLOCK3**	**BLOCK3**
Zn	Znu	Pbuu	PbUdd	PbUdd	PbUdd	PbUUuu	PbUUuu	PbUUuu
	Znd	Pbud	PbUud	PbUud	PbUud	PbUUud	PbUUud	PbUUud
		Pbdd	PbUdd	PbUdd	PbUdd	PbUUdd	PbUUdd	PbUUdd
			PbDdd		PbDdd	PbUDdd	PbUDdd	PbUDdd
						PbDDdd		PbDDdd

TABLE 15. The zinc pricing tree for the proposed model

Zinc pricing tree for the first year			Zinc pricing tree for the second year			Zinc pricing tree for the third year		
BLOCK1	**BLOCK2**	**BLOCK3**	**BLOCK1**	**BLOCK2**	**BLOCK3**	**BLOCK1**	**BLOCK2**	**BLOCK3**
1,986.21	2288.268	2636.261	3182.39	3666.37	4223.942	5098.989	5874.43	6767.798
	1724.025	1986.21	1239.64	2762.31	3182.399	1986.21	4425.909	5098.989
		1496.449		1076.00	2397.681	773.6886	1724.025	3841.677
					933.9689		671.5596	1496.449
								582.9119

TABLE 16. The lead pricing tree for the proposed model

Lead pricing tree for the first year			Lead pricing tree for the second year			Lead pricing tree for the third year		
BLOCK1	**BLOCK2**	**BLOCK3**	**BLOCK1**	**BLOCK2**	**BLOCK3**	**BLOCK1**	**BLOCK2**	**BLOCK3**
2,224.5	2578.172	2988.074	3521.376	4081.237	4730.111	5574.327	6460.585	7487.75
	1919.345	2224.5	1405.246	3038.316	3521.376	2224.5	4809.644	5574.327
		1656.05		1212.475	2621.522	887.7127	1919.345	4149.861
					1046.149		765.9368	1656.05
								660.8661

TABLE 17. The economic value tree for the proposed model ($1000)

First year			Second year			Third year		
BLOCK1	**BLOCK2**	**BLOCK3**	**BLOCK1**	**BLOCK2**	**BLOCK3**	**BLOCK1**	**BLOCK2**	**BLOCK3**
69.78	-1.5	82.001	130.375	-1.5	152.301	-1.5	181.538	243.3131
	-1.5	72.731	95.905	-1.5	135.684	-1.5	160.88	216.6879
	-1.5	65.746	84.962	-1.5	123.164	-1.5	122.347	196.628
	-1.5	70.269	50.493	-1.5	99.811	-1.5	107.337	159.2108
		60.998		-1.5	130.199	-1.5	156.171	144.6356
		54.014		-1.5	113.581	-1.5	135.513	208.3248

		61.535		-1.5	101.062	-1.5	96.98	181.6996
		52.264		-1.5	77.709	-1.5	81.97	161.6396
		45.279		-1.5	113.744	-1.5	111.762	124.2225
					97.127		91.104	109.6473
					84.607		96.98	182.2774
					61.254		37.561	155.6522
					84.938		94.039	135.5923
					68.32		73.381	98.17508
					55.8		34.848	83.59995
					32.447		19.838	136.6763
								110.0511
								89.99116
								52.57397
								37.99885
								118.4786
								91.85344
								71.79351
								34.37632
								19.8012

TABLE 18. The tree of probabilities for the proposed model

	First year			Second year			Third year		
BLOCK3	**BLOCK3**	**BLOCK3**	**BLOCK3**	**BLOCK3**	**BLOCK3**	**BLOCK3**	**BLOCK3**	**BLOCK3**
1	0.602733	0.359092	0.472517	0.359092	0.2533	0.237791	0.2533	0.194949
	0.096754	0.134216	0.092562	0.134216	0.014405	0.068924	0.014405	0.113992
	0.108246	0.040448	0.087438	0.040448	0.07406	0.184499	0.07406	0.080236
	0.192267	0.13931	0.347483	0.13931	0.095065	0.06664	0.095065	0.046479
		0.176649		0.176649	0.129678	0.111124	0.129678	0.059922
		0		0	0.150683	0.013352	0.150683	0.064091
		0.050663		0.050663	0.024188	0.179943	0.024188	0.042274
		0.09962		0.09962	0	0.011076	0	0.048318
		0		0	0.079806	0.126652	0.079806	0.014561
					0.027062		0.027062	0
					0.048067		0.048067	0.083913
					0		0	0.050157
					0.103685		0.103685	0.0636
					0		0	0
					0		0	0
					0		0	0.051995
								0.018239
								0
								0
								0
								0.067278
								0
								0
								0
								0

The intermediate binomial tree will be discounted in the following phase. This is done by converting the tree to a standard binomial tree, as shown in Tables 19 and 20. The probability value of the major element (zinc element) as well as the 4-month rate (2 percent) for 4-month periods will then be utilized to discount the standard binomial tree based on the main element (zinc element) and 4-month extraction periods for each block. They show the trees that were discounted each year and how much they were discounted at the end of each year, in Tables 21 and 22.

TABLE 19. The intermediate binomial tree obtained through multiplying the corresponding nodes of economic value and probabilities

First year			Second year			Third year		
BLOCK3	**BLOCK3**	**BLOCK3**	**BLOCK3**	**BLOCK3**	**BLOCK3**	**BLOCK3**	**BLOCK3**	**BLOCK3**
69.78	-0.9041	29.44605	61.60437	-0.53864	45.98363	-0.35669	45.98363	47.43364
	-0.14513	9.761619	8.877194	-0.20132	2.317477	-0.10339	2.317477	24.70068
	-0.16237	2.65929	7.428917	-0.06067	9.061012	-0.27675	9.061012	15.77664
	-0.2884	9.789181	17.54531	-0.20897	10.204	-0.09996	10.204	7.399957
		10.77529		-0.26497	20.25199	-0.16669	20.25199	8.666857
		0		0	20.41953	-0.02003	20.41953	13.35174
		3.117536		-0.07599	2.345754	-0.26991	2.345754	7.681168
		5.206542		-0.14943	0	-0.01661	0	7.810104
		0		0	8.919254	-0.18998	8.919254	1.808803
					2.465443		2.465443	0
					4.661541		4.661541	15.29544
					0		0	7.807047
					9.750485		9.750485	8.623668
					0		0	0
					0		0	0
					0		0	7.106483
								2.007222
								0
								0
								0
								7.971005
								0
								0
								0
								0

TABLE 20. The intermediate standard binomial tree obtained through multiplying the corresponding nodes of economic value and probabilities

First year			Second year			*Third year*		
BLOCK3	**BLOCK3**	**BLOCK3**	**BLOCK3**	**BLOCK3**	**BLOCK3**	**BLOCK3**	**BLOCK3**	**BLOCK3**
69.78	-1.42983	68.48029	70.48156	-1.3081	128.1587	-0.73682	147.9918	191.8403
	-0.07017	28.12907	24.97423	-0.63542	59.58691	-0.39329	70.69794	103.0542
		2.803223		-0.06833	17.11281	-0.47651	16.51065	51.88862
					8.440671		9.345174	13.95744
								7.53524

TABLE 21. The discounted binomial tree (4-month) for every single year

First year			Second year			Third year		
BLOCK3	**BLOCK3**	**BLOCK3**	**BLOCK3**	**BLOCK3**	**BLOCK3**	**BLOCK3**	**BLOCK3**	**BLOCK3**
113.38	54.2778	68.4802	156.5804	104.914	128.1587	260.5559	310.9210	191.8403
	20.3335	28.12907	60.90663	45.7519	59.58691	125.266	157.2383	103.0542
		2.803223		14.2524	17.11281	45.01529	56.63752	51.88862
					8.440671		21.20979	13.95744
								7.53524

As can be seen, the net present value resulted from the extraction of the desired cross-section to consider the pricing uncertainty of zinc and lead will be equal to 324.27 thousand dollars using the proposed model.

2. 3. Validation Using real prices from 2013 to 2015, the numerical example in this work was solved to test the model (see Table 23 and Figure 10).

Based on the real prices of zinc and lead for the years 2013 to 2015, the net present value of the extraction of the indicated section is 355.14 thousand dollars. The final results are presented in Table 24.

TABLE 22. The final discounted binomial tree

324.275	331.2886	260.5559
	137.1659	125.266
		45.01529

TABLE 23. The real pricing data for zinc and lead

Years	Real price for Zinc ($/ton)	Real price for Lead ($/ton)
2013(4-month 1)	1986.21	2224.50
2013(4-month 2)	1851.01	2088.10
2013(4-month 3)	1893.28	2106.66
2014(4-month 1)	2026.64	2097.84
2014(4-month 2)	2206.17	2158.59
2014(4-month 3)	2250.10	2029.95
2015(4-month 1)	2113.07	1859.16
2015(4-month 2)	2043.05	1821.98
2015(4-month 3)	1638.91	1682.32

Figure 10. The block economic value model based on real prices ($1000)

TABLE 24. The comparison of the evaluation results of different models

Column	Method	Net present value ($1000)	Difference from the real amount (D_i) ($1000)	Difference from the real amount (P_i) (%)
1	Real price DCF	355.14	0	0
2	Constant price DCF	291.53	63.61	17.9
4	Binomial tree	419.80	64.66	18.2
6	Pyramid tree	215.23	139.91	39.4
7	**Proposed model**	**324.27**	**30.87**	**8.6**

3. CONCLUSION

This paper adopted discounted cash flow, binomial tree, Pyramid tree, and our proposed method to predict the price in the future years. The results are presented in Table 24, and the following conclusions can be drawn.

- The proposed method is a practical and suitable approach to account for the price uncertainty of two-element deposits with the closest-to-reality output (8.6%).
- The second best method is the discounted cash flow, with a 17.9% difference from the real data. If the uncertainty is accounted for, the results will improve.
- The third and fourth-best methods are the binomial tree (18.2%) and Pyramid tree (39.4%), respectively.
- The result can be improved, provided that adequate methods are used to include the uncertainty.

- It is recommended that geological and economic uncertainties should be considered simultaneously in future research.

4. REFERENCES

1. Dagdelen, K., "Open pit optimization-strategies for improving economics of mining projects through mine planning", in 17th International Mining Congress and Exhibition of Turkey. Vol. 117, (2001), 121.
2. Johnson, T.B., "Optimum open pit mine production scheduling, University of California, Berkeley, (1968).
3. Dagdelen, K., "Optimum open pit mine production scheduling by lagrangian parameterization", Proc. of the 19th APCOM, (1986), 127-142.
4. Caccetta, L. and Hill, S.P., "An application of branch and cut to open pit mine scheduling", ***Journal of global optimization***, Vol. 27, No. 2, (2003), 349-365. doi: 10.1023/A:1024835022186.
5. Boland, N., Dumitrescu, I., Froyland, G. and Gleixner, A.M., "Lp-based disaggregation approaches to solving the open pit mining production scheduling problem with block processing selectivity", ***Computers & Operations Research***, Vol. 36, No. 4, (2009), 1064-1089. doi: 10.1016/j.cor.2007.12.006.
6. Elkington, T. and Durham, R., "Integrated open pit pushback selection and production capacity optimization", ***Journal of Mining Science***, Vol. 47, No. 2, (2011), 177-190. doi: 10.1134/S1062739147020055.
7. Wang, Q. and Sevim, H., "Enhanced production planning in open pit mining through intelligent dynamic search", ***Institute of Mining Metallurgy (ed)***, Vol. 23, (1992), 461-471. doi: 10.1007/s11771-018-3841-5.
8. Denby, B. and Schofield, D., "Open-pit design and scheduling by use of genetic algorithms", ***Transactions of the Institution of Mining and Metallurgy. Section A. Mining Industry***, Vol. 103, (1994).
9. Khan, A. and Niemann-Delius, C., "Production scheduling of open pit mines using particle swarm optimization algorithm", ***Advances in Operations Research***, Vol. 2014, (2014). doi: 10.1155/2014/208502.
10. Sattarvand, J., "Long-term open-pit planning by ant colony optimization", Aachen, Techn. Hochsch., Diss., 2009, (2012),
11. Shishvan, M.S. and Sattarvand, J., "Long term production planning of open pit mines by ant colony optimization", ***European Journal of Operational Research***, Vol. 240, No. 3, (2015), 825-836. doi: 10.1016/j.ejor.2014.07.040.
12. Abdel Sabour, S. and Poulin, R., "Mine expansion decisions under uncertainty", ***International Journal of Mining, Reclamation and Environment***, Vol. 24, No. 4, (2010), 340-349. doi: 10.1080/17480931003664991.
13. Dimitrakopoulos, R., Farrelly, C. and Godoy, M., "Moving forward from traditional optimization: Grade uncertainty and risk effects in open-pit design", ***Mining Technology***, Vol. 111, No. 1, (2002), 82-88. doi: 10.1179/mnt.2002.111.1.82.
14. Marcotte, D. and Caron, J., "Ultimate open pit stochastic optimization", ***Computers & Geosciences***, Vol. 51, (2013), 238-246. doi: 10.1016/j.cageo.2012.08.008.
15. Yazdani, M., Kabirifar, K., Fathollahi-Fard, A.M. and Mojtahedi, M., "Production scheduling of off-site prefabricated construction components considering sequence dependent due dates", ***Environmental Science and Pollution Research***, (2021), 1-17. doi: 10.1007/s11356-021-16285-0.
16. Tahernia, T. and Ataee-pour, M., "A model for determination of block economic value in underground mining", ***Iranian Journal of Mining Engineering***, Vol. 10, No. 28, (2015), 43-51. doi: 20.1001.1.17357616.1394.10.28.6.1.
17. Samis, M., Davis, G.A., Laughton, D. and Poulin, R., "Valuing uncertain asset cash flows when there are no options: A real options approach", ***Resources Policy***, Vol. 30, No. 4, (2005), 285-298. doi: 10.1016/j.resourpol.2006.03.003.
18. Shafiee, S., Topal, E. and Nehring, M., "Adjusted real option valuation to maximise mining project value–a case study using century mine", in Project Evaluation Conference, Citeseer. (2009), 125-134.
19. Dehghani, H. and Ataee-Pour, M., "Determination of the effect of operating cost uncertainty on mining project evaluation", ***Resources Policy***, Vol. 37, No. 1, (2012), 109-117. doi: 10.1016/j.resourpol.2011.11.001.
20. Dehghani, H. and Ataee-Pour, M., "The role of economic uncertainty on the block economic value–a new valuation approach", ***Archives of Mining Sciences***, Vol. 57, No. 4, (2012). doi: 10.2478/v10267-012-0066-6.
21. Mokhtarian Asl, M. and Sattarvand, J., "Integration of commodity price uncertainty in long-term open pit mine production planning by using an imperialist competitive algorithm", ***Journal of the Southern African Institute of Mining and Metallurgy***, Vol. 118, No. 2, (2018), 165-172. doi: 10.17159/2411-9717/2018/v118n2a10.
22. Souza, F.R., Câmara, T.R., Torres, V.F.N., Nader, B. and Galery, R., "Optimum mine production rate based on price uncertainty", ***REM-International Engineering Journal***, Vol. 72, (2019), 625-634. doi: 10.1590/0370-44672018720093.
23. Rimélé, A., Dimitrakopoulos, R. and Gamache, M., "A dynamic stochastic programming approach for open-pit mine planning with geological and commodity price uncertainty", ***Resources Policy***, Vol. 65, (2020), 101570. doi: 10.1016/j.resourpol.2019.101570.
24. Jamshidi, M. and Osanloo, M., "Multiple destination influence on production scheduling in multi-element mines", ***International Journal of Engineering, Transactions A: Basics,*** , Vol. 31, No. 1, (2018), 173-180. doi: 10.5829/ije.2018.31.01a.23.
25. Cox, J.C. and Ross, S.A., "The valuation of options for alternative stochastic processes", ***Journal of Financial Economics***, Vol. 3, No. 1-2, (1976), 145-166. doi: 10.1016/0304-405X(76)90023-4.
26. Cox, J.C., Ross, S.A. and Rubinstein, M., "Option pricing: A simplified approach", ***Journal of Financial Economics***, Vol. 7, No. 3, (1979), 229-263. doi: 10.1016/0304-405X(79)90015-1.
27. Copeland, T. and Antikarov, V., "Real options, Texere New York, (2001).
28. Dehghani, H., Ataee-pour, M. and Esfahanipour, A., "Evaluation of the mining projects under economic uncertainties using multidimensional binomial tree", ***Resources Policy***, Vol. 39, (2014), 124-133. doi: 10.1016/j.resourpol.2014.01.003.
29. Osanloo, M. and Ataei, M., "Using equivalent grade factors to find the optimum cut-off grades of multiple metal deposits", ***Minerals Engineering***, Vol. 16, No. 8, (2003), 771-776. doi: 10.1016/S0892-6875(03)00163-8.
30. Kakha, G. and Monjazi, M., "Push back design in two-element deposits incorporating grade uncertainty (research note)", ***International Journal of Engineering, Transactions, B: Applications***, Vol. 30, No. 8, (2017), 1279-1287. doi: 10.5829/ije.2017.30.08b.22.

Persian Abstract

چکیده

امروزه، عدم قطعیت‌ها نقش موثری در ارزیابی پروژه های معدنی بخصوص در بررسی پارامترهای اقتصادی معدنی ایفا می‌کنند، به گونه‌ای که ارزیابی یک پروژه معدنی بدون در نظر گرفتن عدم‌قطعیت‌های موجود غیرقابل اعتماد و نادرست است. یکی از مهمترین منابع عدم‌قطعیت‌های اقتصادی می‌توان به عدم‌قطعیت قیمت ماده معدنی اشاره نمود. محققین بسیاری به مطالعه بررسی نقش عدم‌قطعیت‌های اقتصادی در فرآیند برنامه‌ریزی تولید پروژه معدنی پرداخته‌اند اما بیشتر تحقیق‌های انجام شده در ذخایر تک عنصره بوده و کمتر به بررسی نقش عدم‌قطعیت قیمت در ذخایر دو عنصره توجه شده است. در این تحقیق به منظور لحاظ کردن همزمان عدم‌قطعیت قیمت دو عنصر در طراحی معادن، مدل درخت سه بعدی ارائه شده است. برای اعتبارسنجی مدل پیشنهادی یک مثال عددی با روش‌های جریان‌نقدی تنزیل یافته، درخت دوجمله‌ای، درخت هرمی و مدل سه بعدی حل شد و نتایج حاصل از همه روش‌ها با نتایج حاصل از داده‌های واقعی مقایسه گردید. نتایج تحقیق حاضر نشان می‌دهد، مقادیر حاصل از مدل پیشنهادی (ارزش خالص فعلی برابر با ۳۲٤/۲ هزار دلار)، نسبت به نتایج روش‌های دیگر از دقت بیشتری برخوردار بوده و فقط ۸٪ با واقعیت فاصله دارد. این در حالیست که نتایج حاصل از روش‌های دیگر حداقل ۱۷ و حداکثر ۳۹ درصد با نتایج حاصل از داده‌های واقعی اختلاف دارد.

IJE TRANSACTIONS A: Basics Vol. 35 No. 10, (October 2022) 1918-1928

International Journal of Engineering

Journal Homepage: www.ije.ir

Performance Evaluation of Onboard Wi-Fi Module Antennas in Terms of Orientation and Position for IoT Applications

T. Sridher*[a], A. D. Sarma[a], P. Naveen Kumar[b]

[a] *Chaitanya Bharathi Institute of Technology, Hyderabad, India*
[b] *Osmania University College of Engineering, Osmania University (OU), Hyderabad, India*

PAPER INFO

Paper history:
Received 03 Febraury 2022
Received in revised form 12 June 2022
Accepted 16 June 2022

Keywords:
Indoor Pathloss
Channel Modelling
Regression
IoT
Received Signal Strength
Node Micro Controller Unit ESP8266

ABSTRACT

With ever increasing demand of IoT based sensor systems, there is a need to assess the performance of wireless sensor networks especially in indoor environment. In these networks, antenna plays an important role. The performance of onboard antenna of the sensor module with respect to its height and orientation are examined in this paper. Several experiments were carried out mostly in indoor environment by changing orientation and height of the antennas. The performance is assessed on the basis of Received Signal Strength (RSS) and its modelling using linear, logarithmic and rational polynomial regression techniques which will characterize the channel in a particular environment. Out of all the combinations in terms of height of the antennas and their orientation, it is found for a given indoor environment, with transmitting antenna at a medium height facing upwards and receiving antenna with an inclination of 70^0 towards transmitter resulted in better performance with R^2_{poly} value of 86.81% and RMSE of 4dB. Therefore, this combination is suggested for wireless sensor networks in indoor environment for achieving the of cost-effective energy-efficient green IoT. The analysis would be useful for improving the efficiency and coverage of wireless sensor networks.

***doi**: 10.5829/ije.2022.35.10a.11*

1. INTRODUCTION

In the recent years it has been increasingly becoming common to have Internet-of-Things (IoT) enabled structures, environment and systems. IoT has become a key enabler for many applications like smart homes, cities, and smart farming. Many of these applications require good observability and controllability. The prominent problems faced by the IoT network are establishing an energy-efficient network and optimization in channel modelling for energy-efficient communication. Several researchers reported their work on techniques in IoT applications which saves power consumption of the modules [1, 2]. Easy implementation and commercial viability are the other primary important objectives of IoT manufacturers. Once the devices meet these objectives, they offer unparalleled flexibility for deployment within buildings without any hardwiring. Such devices minimizes the maintenance hassles and environmental impact [3].

As 5G communications have become order of the day, with the very large bandwidth at disposable, billions of IoT devices are coming up to make life convenient and comfortable. In wireless network, the communication channel performance is greatly affected by the surrounding environment. This is more true with indoor wireless networks. Even the small reflecting object can drastically affects the network's performance [4-7]. Among the various approaches to monitor and examine the surrounding environment, the most appropriate technique in recent years is wireless sensing [8]. There are wide coverage area networks and local area networks [9]. The former are expensive and do not offer easy deployment and movement [10]. The most popular short-range wireless networks are LoRa, ZigBee, Z-wave, Wi-Fi, and Bluetooth. Compared to other devices, Zig Bee,

*Corresponding Author Institutional Email: tsridhar_ece@cbit.ac.in
(T. Sridher)

Please cite this article as: T. Sridher, A. D. Sarma, P. Naveen Kumar, Performance Evaluation of Onboard Wi-Fi Module Antennas in Terms of Orientation and Position for IoT Applications, ***International Journal of Engineering, Transactions A: Basics***, Vol. 35 No. 10, (2022), 1918-1928

and Wi-Fi are being widely used in rapidly evolving IoT applications due to its low cost and easy deployment and use the same band of frequencies. Ibraheem and Hadi [11] investigated XBee devices data packets transmission paths and power consumption and proved that these modules offer high reliability having mesh topology and also multiple nodes can sleep whenever they are free.

Prediction of pathloss in a given environment using the IoT modules is more complex than with the conventional antennas operating with the same frequency band [12]. Therefore, more appropriate models are to be developed. The performance of line-of-sight and non-line of sight link are the functions of elevation angle between the transceiver module's antenna orientation and the communication environment's reflecting/ refracting/ diffracting / absorbing properties. The relative heights of the transmitting and receiving antennas plays a significant role in the modelling [13, 14]. This necessitates experimental data for various conditions for better channel modelling. Karimi Alavijeh et al. [15] proposed a statistical channel model based on the second moment of Received Signal Strength Indicator (RSSI) in a grass field outdoor scenario by placing a set of transciever antennas for different distances and orientations (0, 90, 180, 270 degrees). In their work, XBee-PRO 802.15.4 module at a 2.4 GHz omnidirectional antenna with 1.2dBi antenna is used. A statistical logarthemic regression channel model with RSSI variance and distance is developed and arrived an improvement of 22% localization accuracy when compared with constant covariance extended kalaman filter method with the same three nodes.

The development of the low-cost Wi-Fi missile telemetry system created remarkable financial savings during the training phase. Received Signal Strength, packet error rate, communication link quality were investigated in their work [16]. Indeed these low cost on board Wi-Fi module antennas are expected to be omnidirectional, but in practice they are not. We examined the effect of antenna orientation on RSS and found antenna offers the non-uniform radiation pattern. Brief details of the modules (Node MCU ESP8266 and Node MCU ESP8266 onboard WiFi Antenna) are given in Appendix A.

In the present work, we concentrated on the position and orientation of Wi-Fi antenna placed on the modules in the context of green energy-efficient IoT applications. As environment conditions such as building structures and wave propagation path cannot be changed, we considered only height, distance and oreintation of the antenna. To identify optimum position and orientation, we collected the Received Signal Strength (RSS) data from modules for nine different scenarios by changing the orientation and vertical position and modelled the indoor corridor propagation path. The corridor channel performance is evaluated using the linear regression, lognormal and polynomial regression models, and suggested the suitable one based on the received RSS values.

These results and analysis could be useful for optimum placement of sensors in indoor environment to avoid infrastructure issues, environmental and maintenance hassels. Further, the analysis is very much useful for localizing the source position even in the 11 to 22m region where severe multipath exists. In addition, the results can also be useful for assessing the performance of on board Wi-Fi anenna behaviour for Unmanned Aerial Vehicles (UAV).

2. IoT PROPAGATION PATHLOSS MODELS

There are several statistical pathloss models for predicting the behaviour of the wave propagation. Out of them three prominent models are considered in our work, namely linear, logarithmic regression and fourth order rational polynomial model. The most common statistical model is a linear regression model. It allows systematic interpretation on measured data to predict the wave propagation path in channel modelling. Still today many of the applications including predicting rice crop bio physical parameters in agriculture [17], research related to mammals [18] use this model. However, the model accurately predicts RSS values upto certain range in any of the polarization with respect to height after that the predicted values may not follow the real scenario measurements. Comparative analysis of Linear Regression, Lognormal along with ITUR and the Friis transmission model was made in our previous work [19]. The Present work is an extension of that work. In Friss equation, Pathloss exponent for free space assumes the value of '2'. However, in practical scenarios it can vary up to 5. The extension to this model where the plane of reflection with the environment is considered as the lognormal pathloss model [20]. The presented logarithmic regression model tends to follow the lognormal pathloss model and reasonably represents indoor experiments data.

As the Logarithmic Regression is parabolic shape, it emphasizes more closely on the RSS measurements for short distances. It is preferred because it fits well with measured data for a large variance [21]. The sensitivity of this model is examined by various authors with Root Mean Square Error (RMSE) and found that the results are stable [22, 23].

Whereas, rational polynomial coefficients are popular in photogrammetry and remote sensing applications. The rational polynomial model includes excess path loss due to diffractions from irregular heights between the transmitter and receiver [24].

These models are used to study the influence of change in the relative heights of modules and orientation

of onboard antenna on RSS. These linear (y_{linear}) and logarithmic (y_{log}) and polynomial (y_{poly}) regression models have the following standard forms [25]:

$$y_{linear} = \beta_0 + \beta_1 x \quad x = 1,2,3 \ldots..21 \tag{1}$$

$$y_{log} = \beta_0 + \beta_1 * \log(x) \quad x = 1,2,..21 \tag{2}$$

$$y_{poly} = \frac{\beta_0+\beta_1 x+\beta_2 x^2+\beta_3 x^3+\beta_4 x^4}{x+\gamma} = \frac{\sum_i \beta_i x^i}{x+\gamma} \quad i = 0,1,2,3,4 \tag{3}$$

where 'β_0' is an intercept / constant term / a RSS at a reference distance 'x_0', 'β_1' is slope/ regression coefficient, 'β_i' , 'γ' are the coefficients of polynomial and 'y' represents the modelled received signal strength at a distance of 'x'. Initially, we examined the measured data using the linear and logarithmic regression models. Suggested better height and orientation of antenna from findings. Later, for better channel modelling, we proposed the fourth order polynomial model that modifies the linear and logarithmic regression models. We used classic regression models in our work, because these modles can be easily combined with the latest machine learning algorithms (Linear, quadratic Support Vector Machine Learning, Gaussian Process, and Neural Regression Models). Classic models perform the surpervised machine learning by supplying a known set of observations of input data 'x', and known responses 'y'. Classic models are utilized to expand the traning data set and extended to employ error componesation in machine learning algorithms [26]. Regression analysis is a quantitative method applied to establish the relation between the known variables (distance (x), height (h)) to unknown parameter (β). Table 1 lists the summary of reviewed works and distinctive characterstics along with the present work.

3. EXPERIMENTAL SETUP

Initially, an experiment is conducted in both outdoor and indoor for evaluating the radiation behaviour of Wi-Fi transceiver modules (ESP8266). One module is considered for transmitting and the other one for receiving purpose. Operating frequency range is 2412M -2484MHz and 2412MHz frequency is considered in this experiment. A separate setup is made with two stands with rotation facility to create the energy efficient communication link without the need of additional hardware (Figure 1).

The gain of antenna is very important factor in pathloss modelling. The antenna gain of these low cost sensors is not necessarily be the same in all directions. So, we examined the antenna performance by considering experimental measurements. In outdoor environment for fixed distances (Ex. 1m, 2m and 5m etc.,), the orientations of transmitting and receiving antennas are varied in different directions and observed the effect on RSS values. Similar behaviour is noticed in indoor environment also. These observations show that on board antenna on IOT modules are not isotropic in their performance. For evaluating the channel behaviour we focused on the Received Signal strength values. Antennas with identical performance are chosen for our experiments. So antenna gain will not have any significant effect on the modelling.

For outdoor measurements propagation path link is 1m and the modules are placed at a height of 0.76m from the ground. Each module is powered by two AA batteries (3.0V). A program is developed to scan the desired Wi-Fi networks available in the environment and to estimate the received signal strength of each module. Signal strength values are recorded with a sampling rate of 1 s. For indoor measurements, ground floor corridor (3.57x21m) of the Research and Entrepreneurship (R & E) Hub of CBIT is considered. For changing height of the receiver portable 2.7m long PVC pipe is used. The sketch of experimental setup is shown in Figure 2. The PVC stand is designed in such a way that that the module position can be adjustable at any point along the pipe, by sliding movement (Figure 3). This type of experimental setup is convenient for the investigation of the effect of height on RSS values.

In Figure 2, Rx1, 2, and 3 represent the receiver positions. 'Tx' is transmitter located at the end of the corridor (21 m). Care is taken while designing the receiver module setup so that reflection are minimum.

4. RESULTS AND DISCUSSION

In this section, initially the modules' RSS performance is analysed interms of relative orientation of antennas in

Figure 1. Outdoor experimental setup consisting of PVC stands, IoT modules and system

TABLE 1. Summary of Reviewed works and Distinctive Characteristics along with present work

	Ibraheem and Hadi [11]	Investigated on the usage of low-cost off-the-shelf hardware modules (XBee) in vehicle tracking systems	XBee devices data packet transmission paths and power consumption are investigated	Proved that these modules offer high reliability having mesh topology and also multiple nodes can sleep whenever they are free
1.	Manuel Eichelberger [14]	Proposed a indoor localization system with Aircraft signals	Presented the advantages and challenges faced by aircraft signals in using for localization. Detailed description given for ground station requirement, server requirement with hardware modules.	Prototype implementation achieved localization accuracy of 25 meters.
2.	Catherwood et al., [16]	Investigated on the potential use of off-the-shelf hardware modules (Arduino Due Wi-Fi transmitter) as a replacement to the expensive missile test telemetry flight guidance system	Presented the design, development, and testing details of Wi-Fi- missile telemetry system. Received signal strength and packet error rate, indicators of communication link quality are investigated.	The proposed design will significantly save the money and identified limitations with selected low-cost equipment, including firmware, UDP data throughput, optimal alignment and elevation of antennas.
3.	Sumi and Ranga [27]	Proposed a solution for giving priority to emergency vehicles in smarty with Internet of Things (IoT) and Vehicular Ad Hoc Network (VANET)	In the proposed solution, emergency vehicles are given priority for smooth passage through traffics. Algorithms are presented to overcome the traffic signals.	With the concept of IoT and VANET the proposed system improved the quality in congestion avoidance, transmission delay, travel time and response time for overcoming the traffic signals.
4.	Shaohua Yang et al., [28]	Developed a room occupancy detection system based on sensor array.	The sensor arry(ESP-12S Wi-Fi module, MH-Z14A CO_2 sensor module, DHT22 temperature and humidity sensor) information is evaluated using the subset regression models.	The proposed system achieved detection accuracy of 97.32% with running time less than 30 s.
5.	T Sridher et al., (proposed work)	Evaluated the performance of Wi-Fi on board antenna in terms of Orientation, Position and Height.	The performance of on board antenna of the Wi-Fi sensor module with respect to its height and orientation are examined in this paper. Comparative analysis of Polynomial regression, Logarithmic Regression and Linear Regression models are made.	From the experimental results the optimum orientation and height are identified. Fourth order rational polynomial expression satisfies well for the whole corridor.

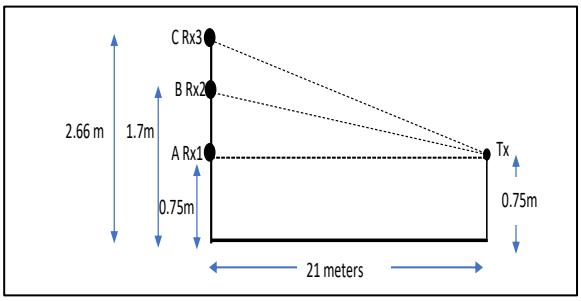

Figure 2. Sketch of experimental scenario at R&E Hub, CBIT, Hyderabad

Figure 3a. At 'A'

Figure 3b. At 'B'

Figure 3c. At 'C'

both outdoor and indoor environments. Later for a given indoor environment experiments are carried out with various antenna orientations and three receiver heights.

4. 1. Effects of Relative Orientation of Onboard Antennas As discussed in the previous section, for evaluating the performance of the module with respect to orientation of onboard 'F-Shaped' antenna the following procedure is implemented. Four scenarios arise with respect to the orientation of the transmitter (A) and receiver (B) antennas. In the first scenario both antennas face each other and is represented as (A+B+). In the second scenario Tx antenna faces the back side of Rx antenna(A+B-). In the third scenario, the Rx antenna sees the back side of the Tx antenna (A-B+). In the fourth and last scenario, the Rx antenna back side sees the back side of the Tx antenna (A-B-). '+' sign indicates the antenna is in the forward direction, and '-' indicates the reverse direction. The experimental sketch of transmitting and receiving antennas for a constant separation are shown in Figures 4 and 5. For a given transmitted power (-14dBm), the received power (RSS) at a distance of 1m is recorded and is shown in Figure 6 for outdoor environment. The sampling period is 1 sec. When the two antennas are

facing each other (A+B+) maximum power is obtained (-29.5dBm). Least power is observed when the back of one antenna sees the back of the other antenna (A-B-) (-46.7dBm). When the antennas see the same direction (A+B- and A-B+) power levels are more or less very similar (-37.5 and -36dBm).

When antennas are facing in opposite direction, it is clear that there is a significant effect on the received signal strength (Figure 6). Changing of orientation of either of the antennas effects the RSS considerably. These observations show that all IoT modules are not isotropic in their performance. Similar behaviour is noticed for other distances (2m and 5m) and indoor environment also (Figures 7 and 8).

However, as the distance between transmitter and receiver increases, the effect of antenna orientations are slightly less predominant in indoor environment. The measured average RSS values for all four scenarios in both indoor and outdoor are presented in Table 2.

At each location we have collected 60 samples, with sampling rate of 1 s. Increasing of sampling frequency will not have any significant effect on accuracy as the indoor environment is almost static. In dynamic conditions such as vehicle moving in ever changing environment, high sampling frequency may lead to improved accuracy. Table 2 presents the average of RSS samples (60) collected for each orientation for a given propagation path distance in indoor and outdoor environment. Increasing of sampling frequency will not

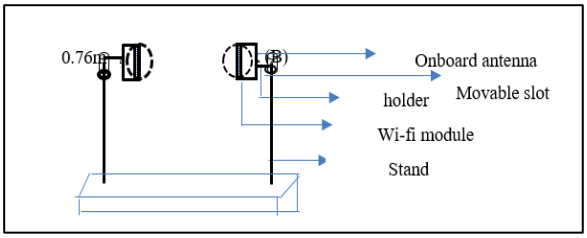

Figure 4. Sketch of transmitter and receiver antenna modules for experimentation

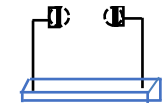

Figure 5a. (A+B+)

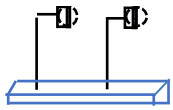

Figure 5b. (A+B-)

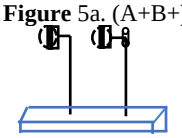

Figure 5c. (A-B+)

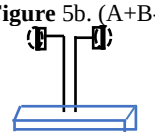

Figure 5d. (A-B-)

Figure 5. Different orientations of onboard transmitting and receiving

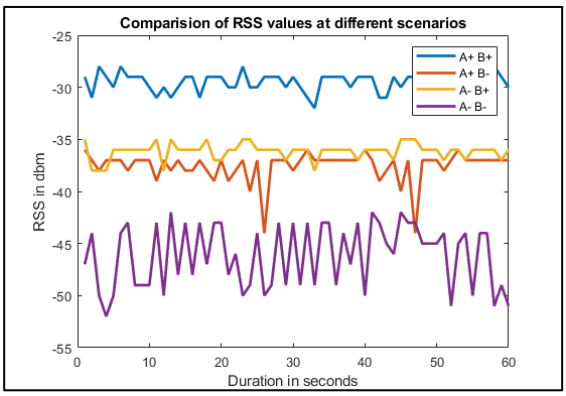

Figure 6. Comparison of RSS values with different orientations in outdoor environment

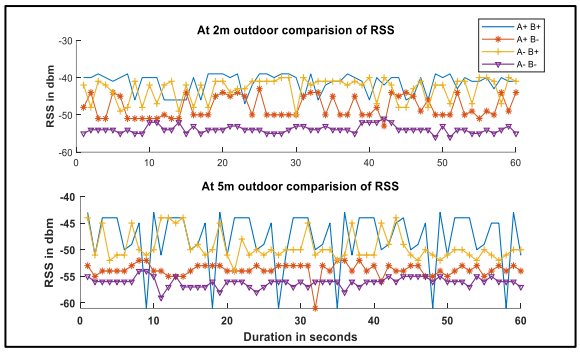

Figure 7. Outdoor RSS values for a path distance of a) 2m and b) 5m

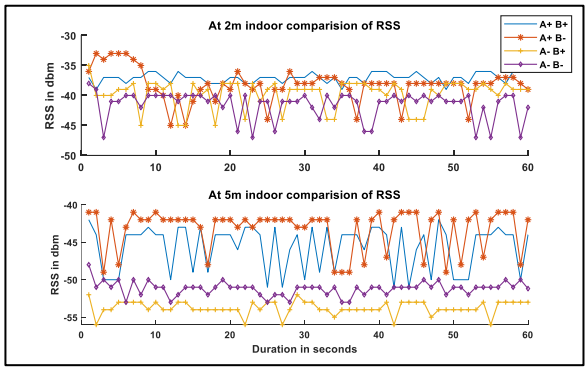

Figure 8. Indoor RSS values for a path distance of a) 2m and b) 5m

TABLE 2. Average RSS values of all scenarios in Indoor and Outdoor

Orientation of Modules	Indoor Received Power (dBm)			Outdoor Received Power (dBm)		
	1m	2m	5m	1m	2m	5m
A+ B+	-34.5	-37.1	-45.6	-29.5	-53.9	-47.7
A+ B-	-33.9	-38.3	-43.2	-37.5	-47.8	-53.4
A- B+	-32.8	-39.9	-53.7	-36.2	-43.1	-49.5
A- B-	-34.5	-41.5	-51.2	-46.7	-54.0	-56.1

have any significant effect on accuracy as the indoor environment is almost static. In dynamic conditions such as vehicle moving in ever changing environment, high samples may lead to improved accuracy.

Averaging the RSS values gives the smoothing the effect of the short term and long term fading. For any particular orientation of antenna, RSS is decreasing progressively with respect to distance in indoor and outdoor environment except for the scenario of (A+B+) in outdoor environment from 2m to 5m. For (A-B-) scenario the orientation effect is comparatively significant for the same distances. The effect of orientation on RSS values is less predominate in indoor, due to metallic structures of corridor such as doors, windows, wall obstructions and surface reflections [29].

4. 2. Effects of Height and Orientation of Receiving Antenna for a Given Height and Orientation of Transmitting Antenna in Indoor Environment

The modules' performance is evaluated using various heights and orientations of receiver inside a corridor (Figure 9). The sketch of position and orientation of Tx and Rx modules is shown in Figure 10. The transmitter module is facing upwards and is at a height of 0.76m and is moving in steps of 1m along centre line of the corridor. The receiver module along with the onboad antenna is placed at three different heights represented by A (0.75m), B (1.7m) and C(2.66m). For each height, measurements are taken for three receiver antenna orientations namely i) module facing towards source (Figures 10a, 10b and 10c) ii) module facing upwards (Figures 10d, 10e and 10f) and iii) module facing downwards (Figures 10g, 10h and 10i). This will result in 9 sets of recordings and details of each of these are as follows:

At each position (A, B or C), for each orientation of the receiving antenna, RSS values are measured for every 1m. Based on these values, linear and logarithmic regression models are developed and the same are shown in Figure 11(a-i) along with experimental data. The performance of regression models is evaluated in terms of statistical parameter 'coefficient of determination (R^2)'. The x-axis represents the source position in the corridor, and y-axis represents the RSS values. R^2 values are presented in each case.

It is clear from Figure 11, orientation and height of the module have significant effect on RSS for a given indoor environment. The data due to receiver positioned at location 'B' with the module facing down wards (Figure 10f) is well fitted to the logarithmic regression model better than any other described scenarios.

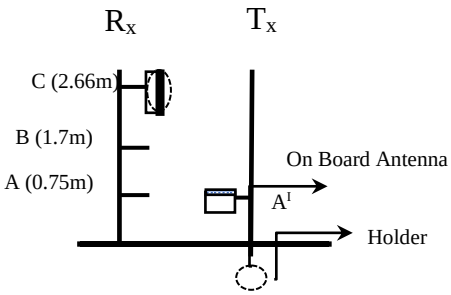

Figure 9. The Positions and Orientations of Tx and Rx modules

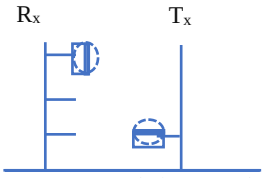

Figure 10a. Rx at 'C' facing towards source

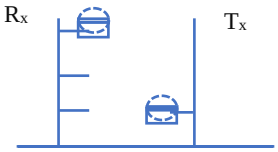

Figure 10b. Rx at 'C' facing upwards

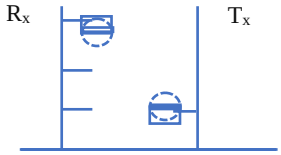

Figure 10c. Rx at 'C' facing downwards

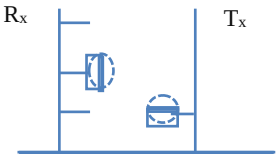

Figure 10d. Rx at 'B' facing towards source

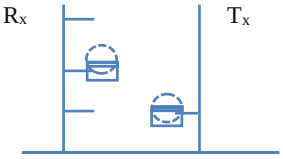

Figure 10e. Rx at 'B' facing upwards

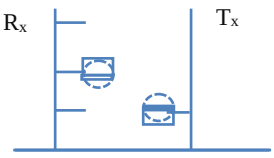

Figure 10f Rx at 'B' facing downwards

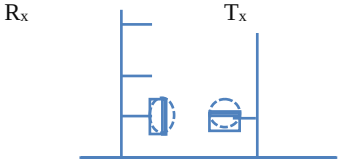

Figure 10g. Rx at 'C' faciing source

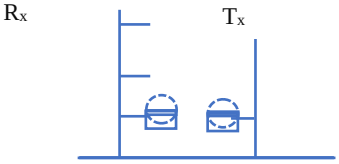

Figure 10h. Rx at 'C' facing upwards

Figure 10i Rx at 'C' facing downwards

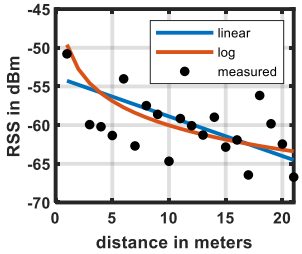

Figure 11a. Tx and Rx are as in Fig. 10a.
$model\ y_{linear} = -53.75 - 0.512x$
$model\ y_{log} = -49.598 - 4.53\ln(x)$
$R^2_{linear} = 32.8\%$
$R^2_{logarthemic} = 44.61\%$

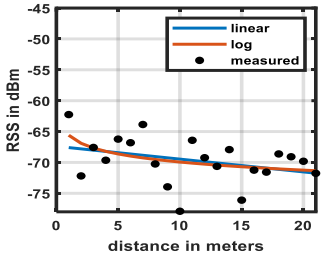

Figure 11b. Tx and Rx are as in Fig. 10b
$model\ y_{linear} = -67.38 - 0.207x$
$model\ y_{logarthemic} = -65.59 - 1.88\ln(x)$
$R^2_{linear} = 12.67\%$
$R^2_{logarthemic} = 17.35\%$

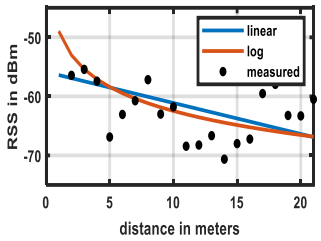

Figure 11c Tx and Rx are as in Fig.10c.
$model\ y_{linear} = -61.28 - 0.36x$
$model\ y_{logarthemic} = -56.02 - 4.3\ln(x)$
$R^2_{linear} = 17.62\%$
$R^2_{logarthemic} = 41.85\%$

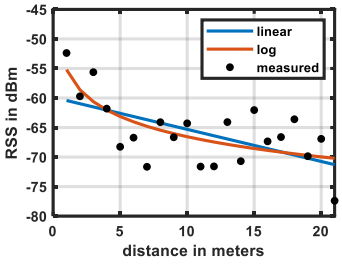

Figure 11d. Tx and Rx are as in Fig. 10d
$model\ y_{linear} = -55.864 + 2.815x$
$model\ y_{log} = -48.9548 - 5.8710\ln(x)$
$R^2_{linear} = 22.41\%$
$R^2_{logarthemic} = 48.61\%$

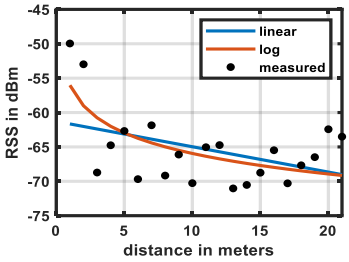

Figure 11e. Tx and Rx are as in Fig. 10e
$model: y_{linear} = -59.877 - 0.5432x$
$model\ y_{logerthemic} = -55.1963 - 4.9316\ln(x)$
$R^2_{linear} = 34.9\%$
$R^2_{logarthemic} = 49.87\%$

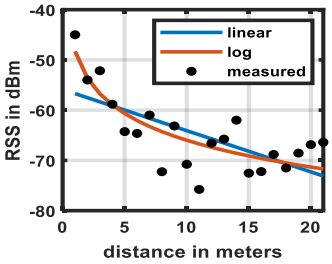

Figure 11f Tx and Rx are as in Fig. 10f
$model\ y_{linear} = -54.92 - 0.885x$
$model\ y_{logarthmic} = -46.31 - 8.49\ln(x)$
$R^2_{linear} = 44.18\%$
$R^2_{logarthemic} = 70.62\%$

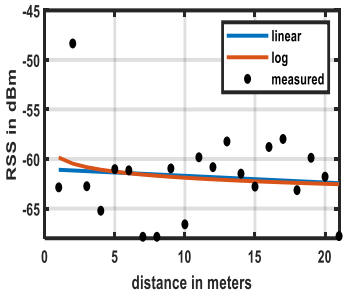

Figure 11g Tx and Rx are as in Fig.10g
$model\ \ y_{linear} = -61.023 - 0.0675x$
$model\ \ y_{log} = -59.85 - 0.8842\ln(x)$
$R^2_{linear} = 0.9\%$
$R^2_{logarthemic} = 2.78\%$

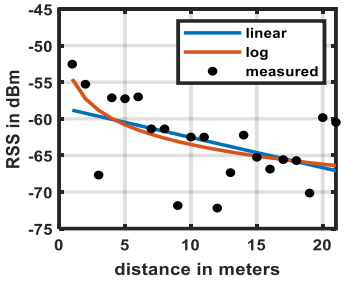

Figure 11h Tx and Rx are as in Fig.10h
$model\ y_{linear} = -58.4109 - 0.4134x$
$model\ y_{logarthemic} = -54.5641 - 3.8847\ln(x)$
$R^2_{linear} = 22.51\%$
$R^2_{logarthemic} = 34.51\%$

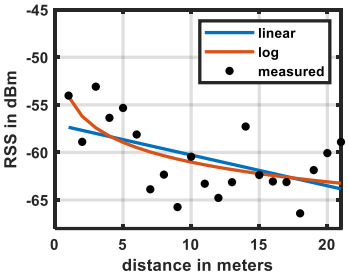

Figure 11i Tx and Rx are as in Figure 10i
$model\ y_{linear} = -61.28 - 0.36x$
$model\ y_{logarthemic} = -56.02 - 4.3\ln(x)$
$R^2_{linear} = 27.7\%$
$R^2_{logarthemic} = 41.14\%$

In the next set of experiments, we investigated the effect of inclination of the module and compared it with the other orientations. The position and orientation of the receiver antenna in 70^0 inclination at a height of 'B' is shown in Figure 12.

The measured RSS values along the corridor, for four receiver antenna orientations namely receiver antenna facing downwards, with the inclination of 70^0, facing towards the source, and facing upwards at a height of 'B' are presented in Figure 13.

The behaviour of RSS throughout the corridor is relatively better in antenna facing towards the source scenario (Figure 13). But, at the same time, the linear and logarithmic regression models are not satisfying the

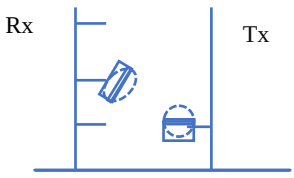

Figure 12. The Position of Receiver Antenna with 70^0 inclination

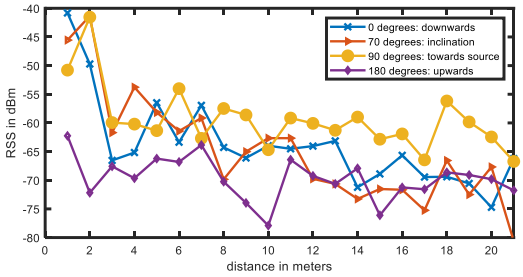

Figure 13. Comparison of RSS due to various orientations of Rx module

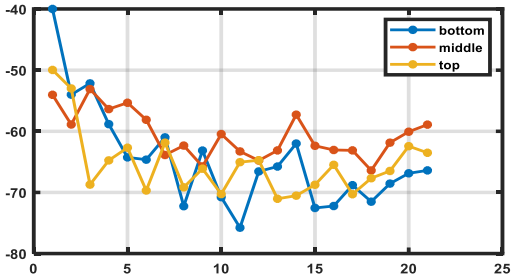

Figure 16. Comparison of RSS with respect to height

measured data (R^2: 22.41% and 48.61%). Whereas, with 70^0 orientation of receiver antenna satisfies logarithmic behaviour in an indoor environment with 79.56%.

It implies that the logarithmic model is well fitted with measured data at a height of 'B' with an inclination of 70^0 and provides the better indoor network coverage. The nonlinearities are well modelled at this height, with this inclination.

Similarly, we evaluated the performance of RSS with both transmitter and receiver module antennas facing each other as shown in Figure 14. It is noticed that, linear and logarithmic regression models are fitted only with 57% and 73.35% with the measured data (Figure 15).

There is no significant improvement in channel modelling as compared with the scenario of Figure 12.

Figure 16 is a comparison plot of measured RSS data with respect to the height for the scenarios of Figures 10a, 10d and 10g. 'x'-axis represents distance, and 'y'-axis represents RSS. It is obvious that at a height of 'B' measured RSS samples are stronger compared with the measured data due to other heights.

Table 3 compares linear and logarithmic regression models' R^2 for receiver at position 'B'. This helps in relating the performance of the models to the measured data due to different orientations of receiver antenna. Overall, when the transmitter and receiver are as in Figure 12, the estimated R^2 is better than other case. It indicates at the particular height of 'B' and when antennas inclined towards source provides good network coverage.

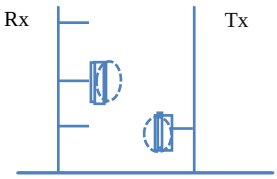

Figure 14. Both transmitting and receiving antennas are facing each other vertically

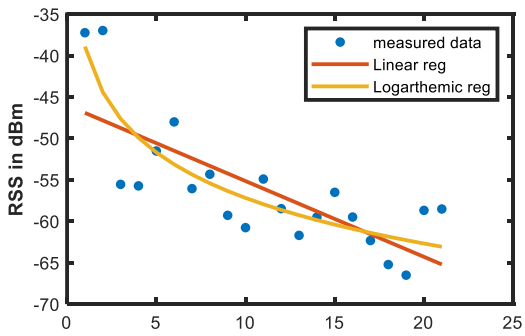

Figure 15. RSS measured data and Regression models when antennas facing each other

4. 3. Proposed Polynomial Pathloss Model

Keeping in view of the above mentioned results, especially with respect to height and orientation of the antenna, for a given set of conditions (receiver height of 1.7m, orientation of 70^0 and transmitter height of 0.75m) received signal strength of the radio signal at a frequency of 2.4 GHz , is modelled using the proposed fourth order polynomial model. The result of this model is presented in Figure 17. By increasing the order of the polynomial the skewness of the model will improve and it may follow the measured values. At the same time, the higher-order polynomial models increase the mathematical complexity in the selection of regression coefficients for prediction. In our case, it lead to the wrong position estimation in the 1-5 m region of the corridor. In the modelled data we have noticed spikes which are above the outliers for 1-5m region of the corridor and found its performance is degrading in terms of position accuracy. In our investigation we have tried even 5^{th} order polynomial which resulted in more spikes. So we

TABLE 3. Comparison of R^2 values for receiver antenna at height 'B' position with different orientations

Orientation of Modules	$R^2_{\_linear}$	$R^2_{\_logarthemic}$
0 degrees (Figure10f)	44.18%	70.62%
70 degrees (Figure12)	70.46%	79.56%
90 degrees (Figure10d)	22.41%	48.61%
180 degrees (Figure10e)	34.85%	49.87%

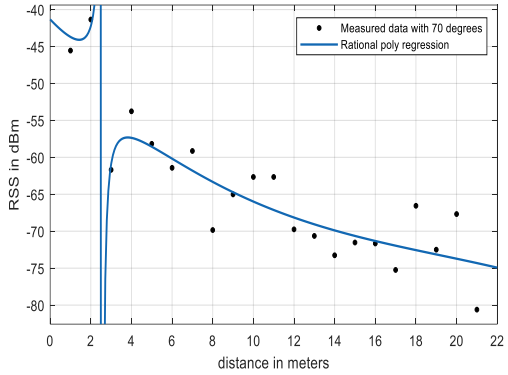

Figure 17. Measured and fourth order polynomial model

TABLE 4. Presents the values of coefficients of Linear, Logarithmic, and proposed fourth-order Rational Polynomial Regression model

Model	Expressions	Coefficients
Linear Regression (LR)	$RSS_{LR\ est} = \beta_0 + \beta_1(x)$ $where\ x = distance$	β_0 = -50.58 β_1 = -1.293
Logarithmic Regression (LN)	$RSS_{LN\ est} = \beta_0 + \beta_1(\log(x) + \log(\gamma))$ $where\ x = distance$ $\gamma = Rx.height$	β_0= -42.27 β_1 = -10.42 γ=1.7
Fourth Order Rational Polynomial Regression (Poly)	$RSS_{Poly\ est} = (\frac{\beta_0+\beta_1 x+\beta_2 x^2+\beta_3 x^3+\beta_4 x^4}{x+\gamma})$ $where\ x = distance$ $\gamma = Rx.height$	β_0 = 105.7 β_1 = -33.87 β_2 = -3.897 β_3 = 0.1577 β_4 = -0.003 γ = 1.7

considered 4th order polynomial as a better option which is valid throughout the corridor. The list of model equations and values of polynomial coefficients are presented in Table 4.

It is observed that the results due to the polynomial model matches well with the measurement data with a R^2 86.81% and RMSE of 4dB over the 5.3dB of linear and 4.4dB of logarithmic regression (Table 5).

For the given conditions, our proposed fourth order polynomial model agree well with measured data by Figure 17, Table 5. All the experimental observations are function of the environment which invariably includes doors and walls. In depth analysis of main factors that affect the variability of the received signal power is likely to improve the model accuracy. In our proposed statistical model, accuracy in 1-5 meters region where spikes exists can be further improved by smoothing techniques [5, 30-32]. Further collecting the large amount of data and by adopting the latest technologies such as machine learning algorithms the model accuracy can be improved in the whole corridor region [33].

TABLE 5. Comparison of various performance parameters

Performance parameter	Linear Regression Model	Logarithmic Regression	4th order Polynomial Regression
R^2	70.46%	79.56%	86.81%
RMSE	5.3dB	4.4dB	4dB

5. CONCLUSIONS

The performance of antennas plays an important role in efficient operation of wireless sensor networks. Several experiments are conducted in this context using Wi-Fi modules with different orientations and heights mostly in indoor environment. These two aspects influence considerably the RSS values. It is found that when the antennas face each other better RSS performance can be achieved. This is especially true for outdoor conditions and also if the propagation distance is less than 5m. With increasing distance, the effect of orientation is becoming less predominant. For indoor measurements, three heights are chosen. Results indicated that when the receiver antenna is placed at 1.7m and with 70^0 inclination facing towards source performance is better. Once the optimum orientation and height are identified (Figure 12), RSS modelling is carried out. For the given set of conditions (receiver height of 1.7m, orientation of 70^0 and transmitter height of 0.75m), out of the three regression techniques, the performance of proposed rational fourth order polynomial regression is better. Over all experimental results proved that appropriate onboard antenna orientation and its height significantly improve channel behaviour in a given environment. It can be concluded that, rational polynomial regression is a better choice for predicting the indoor path loss.

6. ACKNOWLEDGMENT

The research work presented in this paper is a by-product of the project entitled “A New Model for Short Term Forecasting of Scintillations using Machine Learning Approach and Generation of Regional Scintillation Maps” sponsored by Department of Science and Technology under SERB-CRG scheme, vide sanction letter no: CRG/2021/001660, dated:11 February, 2022.

7. REFERENCES

1. Saxena, A., Bhatt, A. and Patel, C., "Sstl io based wlan channel specific energy efficient ram design for internet of thing", in 2018 3rd International Conference On Internet of Things: Smart Innovation and Usages (IoT-SIU), IEEE. (2018), 1-5.
2. Song, H. and Gharpurey, R., "Digitally intensive transmitter employing rf pulse width modulation for iot applications", in 2015 IEEE Radio Frequency Integrated Circuits Symposium (RFIC), IEEE., (2015), 151-154.

3. Tamaddondar, M. and Noori, N., "Hybrid massive mimo channel model based on edge detection of interacting objects and cluster concept", ***International Journal of Engineering, Transactions B: Applications***, Vol. 35, No. 2, (2022), 471-480. doi: 10.5829/ije.2022.35.02b.23.
4. Wang, B., Xu, Q., Chen, C., Zhang, F. and Liu, K.R., "The promise of radio analytics: A future paradigm of wireless positioning, tracking, and sensing", ***IEEE Signal Processing Magazine***, Vol. 35, No. 3, (2018), 59-80. doi: 10.1109/MSP.2018.2806300.
5. Zanella, A., "Best practice in rss measurements and ranging", ***IEEE Communications Surveys & Tutorials***, Vol. 18, No. 4, (2016), 2662-2686. doi: 10.1109/COMST.2016.2553452.
6. Adebayo, S., Aweda, F., Ojedokun, I. and Olapade, O., "Refractive index perception and prediction of radio wave through recursive neural networks using meteorological data parameters", ***International Journal of Engineering, Transactions A: Basics***, Vol. 35, No. 4, (2022), 810-818. doi: 10.5829/ije.2022.35.04A.21.
7. Kramp, T., Kranenburg, R.v. and Lange, S., Introduction to the internet of things, in Enabling things to talk. 2013, Springer, Berlin, Heidelberg.1-10.
8. Liu, H., Darabi, H., Banerjee, P. and Liu, J., "Survey of wireless indoor positioning techniques and systems", ***IEEE Transactions on Systems, Man, and Cybernetics, Part C (Applications and Reviews)***, Vol. 37, No. 6, (2007), 1067-1080. doi: 10.1109/TSMCC.2007.905750.
9. Ferreira, A.F.G.G., Fernandes, D.M.A., Catarino, A.P. and Monteiro, J.L., "Localization and positioning systems for emergency responders: A survey", ***IEEE Communications Surveys & Tutorials***, Vol. 19, No. 4, (2017), 2836-2870. doi: 10.1109/COMST.2017.2703620.
10. Raza, U., Kulkarni, P. and Sooriyabandara, M., "Low power wide area networks: An overview", ***IEEE Communications Surveys & Tutorials***, Vol. 19, No. 2, (2017), 855-873. doi: 10.1109/COMST.2017.2652320.
11. Ibraheem, I.K. and Hadi, S.W., "Design and implementation of a low-cost secure vehicle tracking system", in 2018 International Conference on Engineering Technology and their Applications (IICETA), IEEE., (2018), 146-150.
12. Alobaidy, H.A., Singh, M.J., Behjati, M., Nordin, R. and Abdullah, N.F., "Wireless transmissions, propagation and channel modelling for iot technologies: Applications and challenges", ***IEEE Access***, Vol. 10, (2022), 24095-24131. doi: 10.1109/ACCESS.2022.3151967.
13. Colella, R., Catarinucci, L., Coppola, P. and Tarricone, L., "Measurement platform for electromagnetic characterization and performance evaluation of uhf rfid tags", ***IEEE Transactions on Instrumentation and Measurement***, Vol. 65, No. 4, (2016), 905-914. doi: 10.1109/TIM.2016.2516322.
14. Eichelberger, M., Luchsinger, K., Tanner, S. and Wattenhofer, R., "Indoor localization with aircraft signals", in Proceedings of the 15th ACM Conference on Embedded Network Sensor Systems. (2017), 1-14.
15. Alavijeh, A.K., Ramezani, M.H. and Alavijeh, A.K., "Localization improvement in wireless sensor networks using a new statistical channel model", ***Sensors and Actuators A: Physical***, Vol. 271, (2018), 283-289. https://doi.org/10.1016/j.sna.2018.01.015
16. Catherwood, P.A., Hughes, P. and McLaughlin, J., "Low-cost rf 802.11 g telemetry for flight guidance system development", ***The Journal of Engineering***, Vol. 2019, No. 12, (2019), 8496-8503. https://digitallibrary.theiet.org/content/journals/10.1049/joe.2018.5415
17. Wali, E., Tasumi, M. and Moriyama, M., "Combination of linear regression lines to understand the response of sentinel-1 dual polarization sar data with crop phenology—case study in miyazaki, japan", ***Remote Sensing***, Vol. 12, No. 1, (2020), 189. https://doi.org/10.3390/rs12010189
18. O'Connell-Rodwell, C.E., Freeman, P.T., Kinzley, C., Sandri, M.N., Berezin, J.L., Wiśniewska, M., Jessup, K. and Rodwell, T.C., "A novel technique for aging male african elephants (loxodonta africana) using craniofacial photogrammetry and geometric morphometrics", ***Mammalian Biology***, (2022), 1-23. https://doi.org/10.1007/s42991-022-00238-2
19. Sridher, T., Sarma, A., Kumar, P.N. and Lakshmanna, K., "Results of indoor localization using the optimum pathloss model at 2.4 ghz", in 2020 XXXIIIrd General Assembly and Scientific Symposium of the International Union of Radio Science, IEEE. 1-4.
20. Phillips, C., Sicker, D. and Grunwald, D., "A survey of wireless path loss prediction and coverage mapping methods", ***IEEE Communications Surveys & Tutorials***, Vol. 15, No. 1, (2012), 255-270. doi: 10.1109/SURV.2012.022412.00172.
21. Aneuryn-Evans, G. and Deaton, A., "Testing linear versus logarithmic regression models", ***The Review of Economic Studies***, Vol. 47, No. 1, (1980), 275-291.
22. Christensen, R., "Log-linear models and logistic regression, Springer Science & Business Media, (2006).
23. Bendat, J.S. and Piersol, A.G., "Random data: Analysis and measurement procedures, John Wiley & Sons, (2011).
24. Long, T., Jiao, W. and He, G., "Rpc estimation via $\ell_1 $-norm-regularized least squares (l1ls)", ***IEEE Transactions on Geoscience and Remote Sensing***, Vol. 53, No. 8, (2015), 4554-4567. doi: 10.1109/TGRS.2015.2401602.
25. Montgomery, D.C., Peck, E.A. and Vining, G.G., "Introduction to linear regression analysis, John Wiley & Sons, (2021).
26. Zhang, Y., Wen, J., Yang, G., He, Z. and Wang, J., "Path loss prediction based on machine learning: Principle, method, and data expansion", ***Applied Sciences***, Vol. 9, No. 9, (2019), 1908. https://doi.org/10.3390/app9091908
27. Sumi, L. and Ranga, V., "Intelligent traffic management system for prioritizing emergency vehicles in a smart city", ***International Journal of Engineering, Transactions B: Applications***, Vol. 31, No. 2, (2018), 278-283. doi: 10.5829/ije.2018.31.02b.11.
28. Yang, S., Huang, Z., Wang, C., Ran, X., Feng, C. and Chen, B., "A real-time occupancy detection system for unoccupied, normally and abnormally occupied situation discrimination via sensor array and cloud platform in indoor environment", ***Sensors and Actuators A: Physical***, Vol. 332, (2021), 113116.
29. Series, P., "Effects of building materials and structures on radiowave propagation above about 100 mhz", ***Recommendation ITU-R***, (2015), 2040-2041.
30. Yedukondalu, K., Sarma, A. and Kumar, A., "Mitigation of gps multipath error using recursive least squares adaptive filtering", in 2010 IEEE Asia Pacific Conference on Circuits and Systems, IEEE., (2010), 104-107.
31. Kamatham, Y., Sarma, A., Kumar, A. and Satyanarayana, K., "Spectral analysis and mitigation of gps multipath error using digital filtering for static applications", ***IETE Journal of Research***, Vol. 59, No. 2, (2013), 156-166. doi: 10.4103/0377-2063.113036.
32. Jo, H.-S., Park, C., Lee, E., Choi, H.K. and Park, J., "Path loss prediction based on machine learning techniques: Principal component analysis, artificial neural network, and gaussian process", ***Sensors***, Vol. 20, No. 7, (2020), 1927. https://doi.org/10.3390/s20071927
33. Cho, K. and Gharpurey, R., "A digitally intensive transmitter/pa using rf-pwm with carrier switching in 130 nm cmos", ***IEEE Journal of Solid-State Circuits***, Vol. 51, No. 5, (2016), 1188-1199. doi: 10.1109/JSSC.2015.2512932.

8. APPENDIX A

Brief details of node MCU Wi-fi Module and Wi-fi Antenna

A. NodeMCU ESP 8266

Node Micro Controller Unit (MCU) is an open-source software and works on 802.11b/g/n protocols. A product of Espressif in which analog wireless modulation technique is used to create a short-range line of sight device to device communication. It offers Pulse Width Modulation (PWM). RSS amplitude information is a function of the duty cycle, and phase information is a function of the pulse position [32]. Pulse width modulation maintains the uniform amplitude with a good Signal to Noise Ratio. The receiver sensitivity varies from -91dBm to -72dBm conforming the protocols of IEEE 802.11 b to 802.11 n, which is far better than the sensitivity of digital Long Range (LoRa) modules (-148dbm). The small compact size Printed Circuit Board (PCB) module integrates Wi-Fi antenna, RF balun, Power amplifier, Low noise receiver amplifier, filters, and power management modules. Configured NodeMCU modules maintains the channel space with at least 20 MHz between two modules to avoid the air interface.

B. NodeMCU ESP 8266 onboard WiFi Antenna

The inverted 'F' shape PCB trace onboard antenna plays an important role in channel characterization. These antennas are generally omnidirectional to offer wide coverage area advantage and tolerance to its rotation. Even though it is an omnidirectional antenna, in practice, it provides non-uniform radiation pattern. The radiated energy in the form of toroidal geometry is perpendicular to the antenna's longitudinal direction. The gain of the antenna is typically 2dBi.

Persian Abstract

چکیده

با افزایش تقاضا برای سیستم های حسگر مبتنی بر اینترنت اشیا، نیاز به ارزیابی عملکرد شبکه های حسگر بی سیم به ویژه در محیط داخلی وجود دارد. در این شبکه ها آنتن نقش مهمی دارد. عملکرد آنتن پردازنده ماژول حسگر با توجه به ارتفاع و جهت آن در این مقاله مورد بررسی قرار گرفته است. چندین آزمایش بیشتر در محیط داخلی با تغییر جهت و ارتفاع آنتن ها انجام شد. عملکرد بر اساس قدرت سیگنال دریافتی (RSS) و مدل‌سازی آن با استفاده از تکنیک‌های رگرسیون چند جمله‌ای خطی، لگاریتمی و منطقی ارزیابی می‌شود که کانال را در یک محیط خاص مشخص می‌کند. از بین تمام ترکیبات از نظر ارتفاع آنتن ها و جهت گیری آنها، برای یک محیط داخلی مشخص یافت می شود که آنتن فرستنده در ارتفاع متوسط رو به بالا و آنتن گیرنده با شیب 700 به سمت فرستنده عملکرد بهتری با R2poly دارد. مقدار ۸۶.۸۱٪ و RMSE 4dB بنابراین، این ترکیب برای شبکه‌های حسگر بی‌سیم در محیط داخلی برای دستیابی به اینترنت اشیا سبز مقرون‌به‌صرفه پیشنهاد می‌شود. تجزیه و تحلیل برای بهبود کارایی و پوشش شبکه های حسگر بی سیم مفید خواهد بود.

International Journal of Engineering

Journal Homepage: www.ije.ir

Challenges and Prospects of Widespread Adoption of Pozzolans for Building Construction: A Statistical Assessment

O. O. Omotayo*, C. Arum

Department of Civil Engineering, Federal University of Technology, Akure, Nigeria

P A P E R I N F O

Paper history:
Received 27 May 2022
Received in revised form 14 June 2022
Accepted 18 June 2022

Keywords:
Concrete
Construction Industry
Pozzolan
Supplementary Cementitious Materials

A B S T R A C T

Pozzolans are supplementary cementitious materials (SCMs) that many researchers have found suitable for partial replacement of cement in concrete in order to reduce the environmental hazards and energy consumption involved in the production of concrete. However, these materials have been seldomly used in the present day construction industry especially in Nigeria, in spite of notable research efforts on them over the past decade and abundance of evidence to support their tremendous benefits. A question therefore naturally arises: What is responsible for the hesitation in applying pozzolans widely in the construction industry? This paper investigated by means of a research survey the reasons for their low acceptance and adoption by stakeholders in the construction industry. Opinions from 82 respondents of impressive involvement in the construction industry were collated and statistically analyzed using non-parametric tests, namely Cronbach's Alpha Reliability, Kruskal-Wallis H and Mann-Whitney U tests. The results of the analyses affirmed that pozzolans are effective in mitigating the negative environmental effects caused by using conventional cement in concrete. It further revealed that notable factors militating against their adoption in the construction industry include unavailability of relevant mixture design standards for pozzolanic concrete, lack of commercial production of pozzolanic concrete, unavailability of sufficiently skilled professionals on pozzolan application, inadequate public awareness, lack of policies recommending and guiding its use, and fears on results achievable with use of pozzolans. Respondents generally agreed that development of proper guidelines and standards, as well as adequate public awareness will favour wide acceptance and industrial application of pozzolans.

***doi**: 10.5829/ije.2022.35.10a.12*

1. INTRODUCTION

Over the years, the need for production of clean energy resources and building materials has driven several researchers into sourcing for alternatives for cement. Cement constitutes an integral component in the production of concrete, and it has for long been and remains a valuable resource for development of buildings and infrastructure all over the world. However, its production has constituted a menace to the environment that several researchers are battling to solve it today. Production of 1 ton of ordinary Portland cement (OPC) has been found to be accompanied with the release of 1 ton of carbon dioxide (CO_2) into the atmosphere [1]. Furthermore, the cement industry requires close to 1.7 tons of limestone in production of cement and generates approximately 3.2-6.3 GJ amount of energy, amounting to about 11% of the total energy consumption for all industries [2, 3]. These key issues have brought about the need for alternatives for cement. Pozzolans have been identified as supplementary cementitious materials for partial replacement of ordinary Portland cement in concrete, and many research activities on the subject-matter are still ongoing [4-11]. Examples of pozzolans include fly ash, ground granulated blast furnace slag (GGBS), rice husk ash (RHA), palm oil fuel ash (POFA), bamboo leaf ash (BLA) and many more. Indeed, pozzolans have been found effective in production of different types of concrete, including normal strength, high strength, and lightweight concrete. Although the use of fly-ash has already gained ground in application by the construction industry in a number of developed countries,

*Corresponding Author Institutional Email: ooomotayo@futa.edu.ng (Omotayo O. O.)

Please cite this article as: O. O. Omotayo, C. Arum, Challenges and Prospects of Widespread Adoption of Pozzolans for Building Construction: A Statistical Assessment, ***International Journal of Engineering, Transactions A: Basics***, Vol. 35 No. 10, (2022), 1929-1940

other sustainable industrial and/or agro-based supplementary cementitious materials, such as rice husk ash, palm oil fuel ash, sugar-cane bagasse ash are yet to enjoy similar popularity in many countries especially in developing countries typified by Nigeria. Many researches conducted both within and outside Nigeria on utilization of agro-based pozzolans have shown that when used to partially substitute Portland cement in concrete, the resulting concrete exhibits similar strengths as when 100% Portland cement is employed and has the added advantage of enhancing the resistance of concrete to aggressive media and reduces alkali-silica reactions, in addition to being environmentally more friendly [10, 12-14]. Furthermore, in countries such as Nigeria where housing is beyond the reach of many families owing to the high cost of Portland cement component of concrete, preliminary studies have shown that partial replacement of cement with pozzolans obtained from some commonly available agricultural and other waste materials, have the potential to make housing more affordable [9,15]. In spite of the positive results, the use of the research outputs have not been embraced by the construction industry in many countries. This is what motivated the study reported in this paper. This study aimed at examining the reasons pozzolans have not been adopted in the construction industry, and anticipates prospects for the future applications of these materials based on broad-based statistical analyses of a comprehensive survey and recommendations from notable stakeholders in the construction industry. This paper gives an introduction on the research paper, reviewed literature on supplementary cementitious materials, highlights the research method, presents the results from the study and discusses the implications of the results from the study, after which appropriate conclusions are drawn and recommendations made.

2. SUPPLEMENTARY CEMENTITIOUS MATERIALS (POZZOLANS)

There are several types of supplementary cementitious materials (SCMs) that have good prospects of improving the properties of concrete at specific contents. Different researches have shown notable mechanical and chemical properties of SCMs when used in concrete, some of which include reduction in cement required, decreased water absorption, permeability and binder porosity. Pozzolans may be classified into two broad groups; natural pozzolans and artificial pozzolans. Artificial pozzolans can be further subdivided into pozzolans from industrial processes and pozzolans from organic matter [16]. Artificial pozzolans that have been subjects of research by different authors include fly ash, rice husk ash, bamboo leaf ash, palm oil fuel ash, corn cob ash etc. Being by-products of industrial and agricultural sectors, the use of these pozzolans is considered very sustainable and attractive.

2. 1. Fly Ash This is one of the pozzolans that has been widely used in concrete with tremendous results and wide acceptability in several countries today. Fly ash, which generally has a smooth and spherical shape, is a by-product obtained from the combustion of coal in thermal power plants [17]. The annual generation of fly ash in different countries like USA, China and India is in the range of 75 to 120 million tonnes [18-19]. Tremendous benefits offered by fly ash in fresh concrete include improved workability, lower water demand and reduced heat of hydration. Meanwhile in hardened concrete, it improves the ultimate strength and long-term durability, and lowers the permeability. It has also been observed that the use of fly ash in concrete suppresses alkali-silica reaction, and improves resistance to corrosion and sulfate attack [20-21]. According to Dhadse et al. [22], a cut of about 25 MT can be achieved in production of CO_2 when 25MT/year of fly ash is applied to production of Portland Pozzolana Cement (PPC), hence, it is environmentally sustainable. Fly ash has also been discovered as an effective material in production of high performance concrete [23-24]. However, in recent times, market trends have shown that there is a gradual short-fall in the supply of fly-ash due to a gradual retirement of coal-fired power plants, and this trend is likely to continue over the next 20 years [25-26]. Hence there is a need for development of standards and specifications on other supplementary cementitious materials that can be used in place of fly-ash.

2. 2. Metakaolin Metakaolin is another pozzolan with potential application in partial replacement of cement in concrete. It has been known to be effective in producing concrete with very high strength. Metakaolin is produced from the calcination of purified kaolinite, the main mineral present in clay, at a temperature of 700 to 800^{o}C [27]. At this temperature, the octahedral alumina and tetrahedral silica lamellae structure of kaolinite gets broken down due to de-hydroxylation [16]. This causes the formation of a material possessing very high silica (SiO_2) and alumina (Al_2O_3) content, which could be in the range of 50 to 60% and 40 to 50%, respectively. This in turn enhances the formation of calcium silicate hydrates (CSH) and calcium aluminate hydrates (CAH) in concrete. Güneyisi et al. [28] showed that the compressive and splitting tensile strengths of metakaolin modified concrete have positive effects on strength with up to 30% higher strength than plain concrete. For the most suitable compressive strength and durability performance, an optimal replacement level of 10% has been recommended [29-31]. Metakaolin is also highly regarded for its durability performance. It has good water absorption properties, improves pore structure of

concrete, remarkably resistant to acid and sulphate attack, possesses good thermal properties, good chloride binding capacity, and improved corrosion resistance [27, 31-32]. However, the major drawback to the use of metakaolin is its high cost, which can be attributed to low rate of production, disappointing response from the construction industry, and sometimes environmental legislations against the exploration of kaolinite deposits [12].

2. 3. Ground Granulated Blast Furnace Slag Blast furnace slag is a byproduct generated when pig iron is being produced from a blast furnace, in the presence of iron ore, coke and limestone. When dried and ground into fine particles, this slag is referred to as Ground granulated blast furnace slag (GGBS). GGBS can be used in replacement of cement from a range of 30 to 70%, producing concrete with very high compressive strength and significant gain in strength with time [33]. Gao et al. [34] observed that the microstructural properties of concrete significantly improves with finer GGBS particles, as it results in an increase in surface area and a strengthening of the interfacial transition zone between the aggregate and cement paste. In a study by Lee et al. [35], GGBS was found to possess high bond strength, flexural strength and shear strength values compared to conventional concrete. It was also discovered that it can be used as an admixture in precast concrete without any problem in structural performance. GGBS is also effective in reducing porosity and chloride ion penetration, and improving acid and sulphate resistance [36], as well as decreasing the heat of hydration [6]. The disadvantage of GGBS production is the problem of insufficient steel production industries in Nigeria. Ikpeseni et al. [37] observed that quite a number of steel industries within the country are either moribund or operating below expectation. Hence, the steel industry is still largely dependent on imports. Alberici et al. [38] also noted that the availability of slag in the UK is declining due to the decreasing level of iron and steel production. This is, therefore, a major drawback to the availability of GGBS.

2. 4. Rice Husk Ash Rice husk ash (RHA) is another viable pozzolan which has been used in replacement of OPC and other varied applications. Rice husk is obtained from the milling process of paddy rice. Reports have indicated that approximately 600 million tons of rice paddy is produced annually, which is made up of about 25% rice husks on the average [39]. Hence, rice husk ash is widely available and can be easily produced through burning of rice husk under controlled or uncontrolled conditions [40]. Several researchers have observed that RHA contains high percentage of silica (over 70%) and hence high pozzolanic reactivity. This enables it to form a highly dense calcium silicate hydrate (CSH) gel when the amorphous silica combines with free lime ($Ca(OH)_2$) resulting in tremendous strength gain [41]. RHA generally results in an improvement in compressive strength, split tensile strength, and flexural strength at an optimal percentage addition of 8-10% [8, 42]. Arum *et al.* [10] also observed that RHA increases the setting time of concrete and improves its workability and porosity. The durability properties are very impressive, as it improves concrete corrosion resistance, decreases chloride penetration and reduces the permeability [14]. The relatively low cost of obtaining this material compared to several others makes it a very attractive solution for cement replacement.

2. 5. Palm Oil Fuel Ash Palm oil fuel ash is obtained from the burning of palm oil fibres, bunches and shells under a temperature of about 800 to 1000ºC. In palm oil mill boilers, about 85% fibre, 15% shell and palm fruit bunches are burned, generating the required energy for the extraction of crude palm oil [13]. Several researchers have discovered that palm oil fuel ash (POFA) has promising potentials in producing lightweight concrete with improved compressive strength. Oyejobi et al. [43] in a study observed that partial replacement of cement with 10% POFA in concrete significantly improves the compressive strength and durability of concrete. Rajesh et al. [44] observed a similar trend with optimum at 20% POFA addition. They also found out that POFA improved the flexural quality and split tensile strength of normal concrete. POFA has also been used in making self-consolidating high-strength concrete with encouraging results. Research by Salam et al. [45] revealed that POFA has good filling ability with satisfactory segregation resistance, and in content up to 20% gives improved durability indices such as reduced water absorption and permeable porosity.

2. 6. Bamboo Leaf Ash The significant capabilities of Bamboo Leaf Ash (BLA) as a pozzolanic material have been revealed by several researchers in the past decade and is yet undergoing exploration. In order to obtain this ash, dried bamboo leaves are heated and burnt in a furnace at 600ºC for 2 hours. The ash produced has been found to possess pozzolanic properties. Singh et al. [46] studied the mechanism of BLA during hydration of OPC, and observed that BLA reacts with calcium hydroxide ($Ca(OH)_2$) to form calcium silicate hydrate (C-S-H), with progression of pozzolanic activity as temperature increases. Considering the strength properties of concrete produced from BLA, [47-48], among others found out that cement could be replaced with BLA up to 15%, although with some compromise in the desirable strength. They also observed that they have tremendous durability properties such as improved acid and chloride resistance, reduced porosity and improved permeability properties. Umoh and Ujene [49] also

observed that the splitting tensile strength values obtained using BLA can be up to 75% of that of the OPC concrete.

As reported from these researches, pozzolans have great potentials to be used in concrete. However, they are yet to be widely adopted in the construction industry. The reason for this has been scarcely looked into by researchers. Botchway and Masoperh [50] investigated the reason for low application of pozzolana cement in the Ghanian construction industry. Results from the study revealed that inadequte awareness, lack of commercial availability of pozzolans, limited market and absence of active support from the government are major factors mitigating against the patronage of pozzolanic cement. Adisa [15] examined the effect of partially substituting RHA in cement for a low-cost housing unit. Results revealed that cement is responsible for up to 42% of the total construction cost, and when partially replaced with 15% RHA, about 7% of the total building cost can be saved. Anigbogu [51] studied the means of developing and efficiently applying pozzolan cement in Nigeria, and suggested strategies for establishing a viable basis for their application. Some of the strategies advanced include development of national standards for production and use of Pozzolanic cements in Nigeria, creation of data bank on available pozzolans in Nigeria, encouragement of further research into effective local pozzolans and academia-industry cooperation on its production. Some of these researches and the research gaps are summarized in Table 1.

TABLE **1.** Summary of literature review

S/N	Author	Research focus	Research gap
1.	Reddy and Rao [6]	Used fly ash and GGBS in replacement of cement	Application of this in industrial context is not known
2.	Shafabakhsh and Ahmadi [8]	Evaluated performance of coal waste ash and rice husk ash in improving properties of pervious concrete pavement	Application of this in industrial context is not known
3.	Ikumapayi [11]	Examined effect of Bamboo Leaf Ash and Locust Bean Pod Ash on crystal and microstructure properties of concrete	Application of this in industrial context is not known
4.	Kanthe et al. [13]	Fly ash and rice husk ash were blended with cement to improve shrinkage properties of concrete	Application of this in industrial context is not known
5.	Sudha [14]	Evaluated the effect of lime sludge and fly ash in partially replacing fine aggregate in concrete	Application of this in industrial context is not known
6.	Botchway and Masoperh [50]	Examined low utilization of pozzolans in Ghanian construction industry	The Nigerian context has not been studied
	and so on.		

Seeing the great possibilities achieveable with the use of pozzolans when applied in concrete and the variety of researches that have delved into proving its value, it has been a matter of concern that pozzolans have not been in use in the construction industry in Nigeria. From Table 1, it is clear that none of the research works investigated why pozzolans are not widely in use across the world and not in use almost totally in countries such as Nigeria. This has created a knowledge gap, hence, the present study was conducted in order to ascertain what is responsible for this seeming apathy to the use of pozzolans. This general objective was achieved by gathering information from different stakeholders in the construction industry on the subject matter. The information obtained were subsequently analyzed using appropriate statistical tools to obtain insightful revelations.

3. RESEARCH METHODOLOGY

An online survey was conducted and responses were gathered from eighty-two (82) different respondents who are quite visible in the civil engineering and construction industry. This was done through the use of Google forms. In the questionnaire, general data was first collected about the respondents, their areas of specialization and number of years of practice. Opinions of the respondents were then gathered based on the use of ordinary Portland cement concrete, its benefits, and challenges involved with its use. Thereafter, information was collected on the availability of pozzolans, their use, merits and demerits, and reasons for their non-applicability in the present day construction industry in many developing countries including Nigeria. Statistical analysis of the results of the survey was done using SPSS Statistical Analysis software package. The questions asked on the opinions of respondents on the use of concrete and pozzolans were coded as presented in Table 2.

Cronbach's Alpha Reliability test was done to ascertain the level of reliability of the results obtained from the collected data. The Cronbach's Alpha is a tool used to evaluate the internal consistency of a test or scale, and is usually expressed as a number between 0 and 1. The internal consistency explains the inter-relationship between items within a test, or the extent to which the items in a test evaluate a particular concept. It therefore assists in ensuring that a test is valid and reliable for research purposes. When items in a test are well correlated to each other, the alpha value increases. Acceptable values of alpha range between 0.7 to 0.95 [52]. The formula for Cronbach's alpha is given by Glen [53]:

TABLE **2.** Survey Questions and their respective codes

What is your opinion on the following advantages and disadvantages of concrete	C1	Concrete is a very good material for construction?
	C2	In terms of ease of construction, concrete is more preferred than other construction materials
	C3	In terms of accessibility as a construction material, concrete is more readily available than other construction materials (e.g. Steel, timber)
	C4	Use of concrete is more economical compared to other types of materials
	C5	Concrete is more effective in handling complex designs
	C6	More skilled professionals are available in the construction industry involved with concrete
	C7	Concrete contributes largely to the problem of global warming
	C8	Production of ordinary portland cement (opc) incessantly poses a serious environmental threat
	C9	Alternative materials for cement for use in tackling the issue of environmental sustainability caused by cement productions have not been discovered
What are your opinions on the use of pozzolans in concrete?	P1	Pozzolans have been widely accepted and applicable in the construction industry
	P2	Pozzolans have been found comparatively effective in concrete production when used in replacement of cement
	P3	Pozzolans are easily obtainable and available
	P4	Use of pozzolans brings an overall improvement in environmental sustainability by curbing cement production
	P5	The use of pozzolans from local materials offers an effective means of managing waste
	P6	Use of pozzolans can bring an overall reduction in the cost of using cement as a binder in concrete production
	P7	The unavailability of relevant design mix standards places a limitation on the use of pozzolans in the current day industry
	P8	Lack of commercial production of pozzolans for use in the industry has limited its applicability to the construction industry
	P9	Lack of professionals involved with the use of pozzolans presents another limitation to its use
	P10	Inadequate public awareness on the effectiveness of pozzolanic cement concrete has limited its wide-spread acceptance
	P11	Fears on the results achievable with the use of pozzolans prevents designers and contractors from considering the option of pozzolans for use
	P12	Lack of policies and standards on the use of pozzolans has limited its acceptability in the construction industry
	P13	With proper guidelines on use of pozzolans and public awareness, they can effectively be applied to the modern day construction industry

$$\alpha = \frac{N \cdot \bar{c}}{\bar{v} + (N-1) \cdot \bar{c}} \quad (1)$$

where N is the number of items, $\bar{c}$ represents average covariance between item-pairs, $\bar{v}$ represents average variance.

A Kruskal-Wallis H test was performed to see if there was a significant difference between the opinions of the respondents on concrete and pozzolans based on the number of years of practice, central area of practice and which branch of construction industry the repondent is mostly involved in. Kruskal-Wallis test is a non-parametric test that checks if samples are originated from the same distribution. In other words, we are able to ascertain by this test if the differences between more than two groups are so large and unlikely to have occurred accidentally [54]. In this case, consideration is given to the number of years of practice. The null hypothesis of the Kruskal-Wallis test supposes that the groups have the same mean ranks. It is the non-parametric equivalent of one-way ANOVA, in which data are jointly ranked from low to high or vice-versa. It also assumes that the underlying data is not normally distributed. The H statistic is mathematically represented by Kothari and Garg stated below [55]:

$$H = \left[\frac{12}{N(N+1)} \sum_{i=1}^{k} \frac{{R_i}^2}{n_i}\right] - 3(N+1) \quad (2)$$

where N is the total number of participants in all groups combined, R_i is the total rank for the i-th group and n_i is the number of participants in the i-th group. The value of H is tested in comparison with the chi-square distribution for k-1 degrees of freedom, where k is the number of groups.

A Mann-Whitney U test was also conducted to see if there was a difference in the opinions on the use of concrete as well as pozzolans between respondents in Nigeria and those in other countries. It was also conducted to check if familiarity of respondents with pozzolans affect their opinions. Mann-Whitney U test is the non-parametric equivalent of the independent t-test, which is used in testing for differences between the dependent variable for two independent groups.

The U statistic, which measures the difference between the ranked observations of the two groups is

mathematically expressed by the following exptession [55]:

$$U = n_1 \cdot n_2 + \frac{n_1(n_1+1)}{2} - R_1 \quad (3)$$

where n_1 and n_2 are the group sizes and R_1 is the sum of ranks assigned to values of the first group.

The flow chart of the adopted methodology is presented in Figure 1. The results of the statistical analyses are presented and discussed in the next section.

4. RESULTS AND DISCUSSION

4. 1. General Information on Respondents

Majority of the respondents are resident in Nigeria (69.5%) while other respondents are from sixteen (17) other different countries as shown in Figure 2. Eighty-three per cent (83%) of the respondents recorded that they were in the civil engineering profession and among the remaining; only 2 of the respondents were not in a field related to civil engineering and/or building construction. Figure 3 shows that most of the respondents had their central area of practice in the academia, construction and consultancy, with 24% having more than one central area of practice. Considering the branches of civil engineering with higher concentration of respondents, it was observed that majority of the respondents were involved in structural engineering, civil engineering and construction engineering and management or combinations of these. Some other respondents are based in geotechnical engineering, environmental engineering, water resources and waste-water engineering. This can be observed in Figure 4. Furthermore, Figure 5 shows that many of the respondents were in the practice of civil engineering between 0 to 5 years. However, majority (over 50%) of the respondents had practiced the profession for over 6 years. This indicates a quite experienced set of respondents.

Majority (84%) of the respondents were involved in the use of concrete in construction, with several of them also involved in use of alternative materials such as steel and timber. This is presented in Figure 6. Other materials

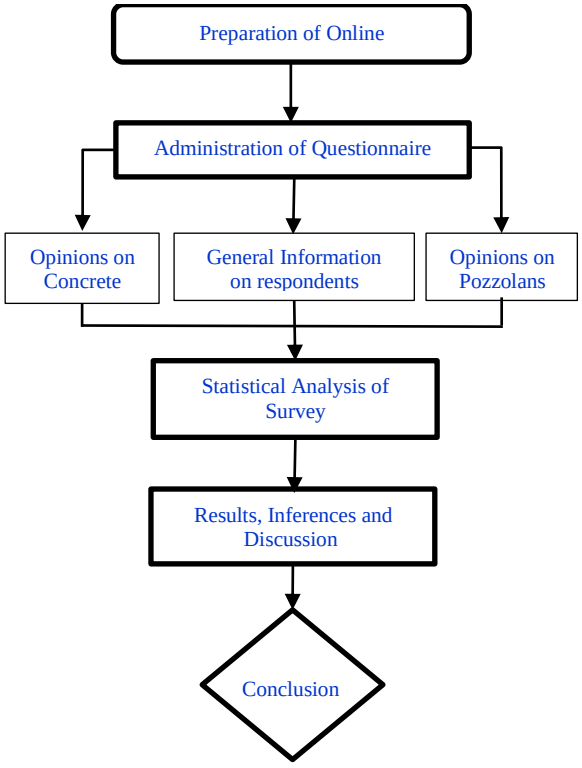

Figure 1. Flow chart showing methodology

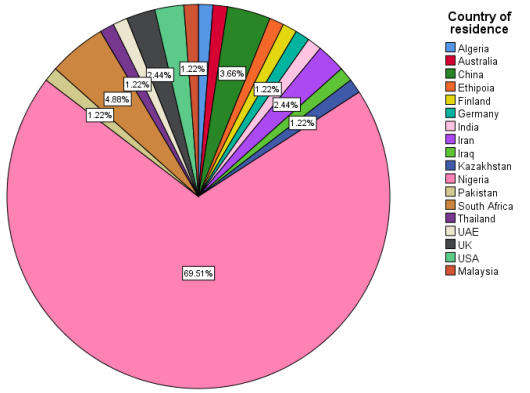

Figure 2. Country of residence

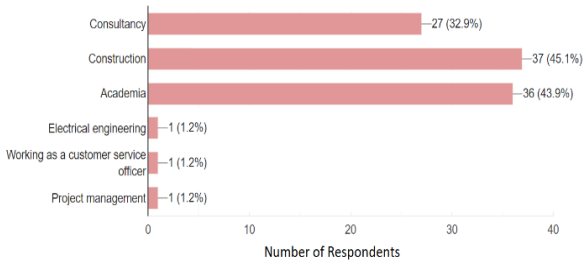

Figure 3. Central Area of Practice in the Industry

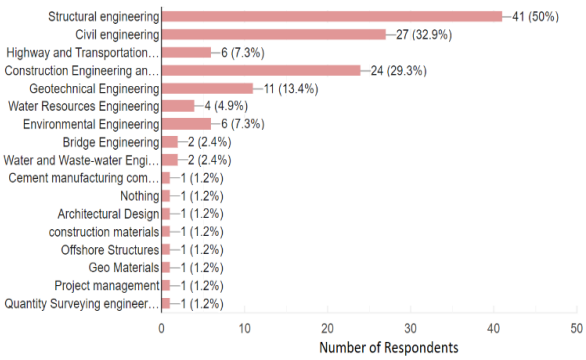

Figure 4. Branch of Civil engineering/construction mostly involved in

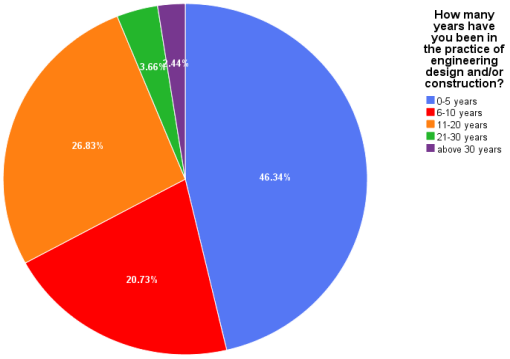

Figure 5. Years of Practice of respondents

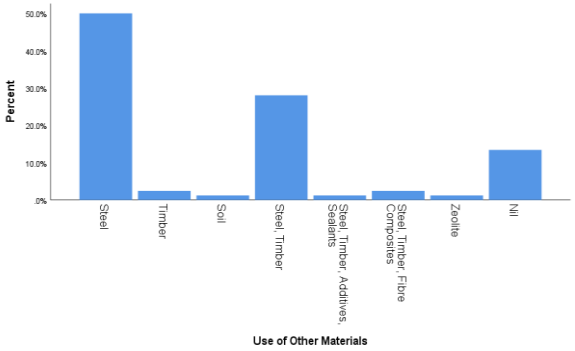

Figure 6. Use of other materials

used include soil, fibre-reinforced polymer (FRP) composites, unplasticized polyvinyl chloride (UPVC). It can be inferred that majority of the respondents are involved in the use of concrete due to its availability, economy compared with other materials, and its ease of construction, as seen from the opinions gathered on the use of concrete.

4. 2. Opinions on the Use of Concrete The responses from the survey alluded to the fact that concrete is a good construction material. Majority (84%) of the respondents also agreed that concrete is preferred to other construction materials. Similarly, the responses from the survey indicate that concrete is more readily available than other construction materials (e.g. steel, timber etc.). It was also noted that most respondents (69%) believe that the use of concrete is more economical compared to other types of materials, and is more effective in handling complex designs. In addition, majority (83%) of the respondents alluded to the fact that there are more skilled professionals working with concrete than other materials in the construction industry. However, a large number of respondents also supported the fact that concrete contributes largely to the problem of global warming, and poses a serious environmental threat to the environment. One crucial issue discovered from the responses is that quite a number of stakeholders were not aware of alternative materials for cement. However, some noted that they were aware of the use of pozzolans (such as Ground granulated blast furnace slag (GGBS), fly ash, volcanic ash etc.) and biopolymers (such as Xanthan gum). These foregoing questions led to a further enquiry on the general knowledge of the stakeholders about pozzolans and their application in the construction industry.

4. 3. Opinions on the Use of Pozzolans Upon introducing the concept of pozzolans, it became clearer that only a few were not really familiar with pozzolanic materials (10%). Results of the survey, however, showed that the pozzolans have only been fairly applicable in the construction industry. Most of the respondents (65%) agreed that pozzolans are comparatively effective in concrete production when used in replacement of cement. It was also agreed that pozzolans generally bring an overall improvement in environmental sustainability by reducing the environmental effects involved in cement production. There were relatively indistinct opinions about the availability and obtainability of pozzolans (with only 45% consenting to their availability). The fact that the use of pozzolans brings an overall improvement in environmental sustainability was largely admitted by most of the respondents (78%). It was also the popular view of majority of the respondents (93%) that using pozzolans in concrete is an effective waste management approach. The survey shows that in spite of these tremendous qualities of pozzolans, the application of pozzolans to the construction industries has been limited due to lack of commercial production, with many respondents (73%) consenting to this fact. Another observed limitation is that the level of available skilled professionals within the construction industry presently applying pozzolans in their construction activities is low, 75.6% consenting to this fact. Majority (87.6%) of the respondents also believe that inadequate public awareness on the effectiveness of pozzolanic cement concrete has not allowed them to be widely accepted. The fears and doubts largely exercised by designers and contractors on the results achievable with the use of pozzolans, and lack of adequate policies and standards on pozzolan use are also factors limiting their use in the industry. As seen from the survey, most of the respondents (approximately 75.7%) allude to these opinions. Generally, it was observed by majority of the respondents (89%) that the applicability of pozzolans to the industry can be improved upon by adequate public awareness and development of proper guidelines on their use.

4. 4. Statistical Analyses

4. 4. 1. Cronbach's Alpha Reliability Analysis In order to ascertain the reliability of the test results obtained from all respondents, statistical analyses were

performed based on the collected data. The results of Cronbach's Alpha Reliability test are presented in Tables 3 and 4. The Cronbach's alpha value for the opinions on the use of concrete and the use of pozzolans were 0.736 and 0.779, respectively. This shows that the results from this survey are very reliable and well correlated, since these values fall between the acceptable range of 0.70 to 0.95, as recommended by Tavakol and Dennick [52].

4. 4. 2. Kruskal-Wallis H Test The Kruskal-Wallis H test results of opinions on concrete and pozzolans based on number of years of practice, central area of pracice and branch of involvement in civil engineering are presented in Tables 5-8. The null hypothesis was that there is no significant difference in the opinions of respondents based on their number of years in practice, central area of practice or branch of civil engineering they are involved in.

TABLE 3. Reliability results on the Opinions concerning the Use of Concrete

Reliability Statistics		
Cronbach's Alpha	**Cronbach's Alpha Based on Standardized Items**	**N of Items**
0.723	0.736	9

TABLE 4. Reliability results on the Opinions concerning the Use of Pozzolans

Reliability Statistics			
Cronbach's Alpha	**Cronbach's Alpha Based on Standardized Items**	**N of Items**	**Cronbach's Alpha**
0.767	0.779	13	0.767

TABLE 5. Kruskal-Wallis H Test on opinions concerning Use of Concrete Based on Number of Years of Practice

Test Statistics[a,b]									
	C1	**C2**	**C3**	**C4**	**C5**	**C6**	**C7**	**C8**	**C9**
Kruskal-Wallis H	1.591	8.290	5.678	4.189	6.065	3.487	2.431	2.716	2.672
Df	4	4	4	4	4	4	4	4	4
Asymp. Sig.	0.810	0.082	0.225	0.381	0.194	0.480	0.657	0.606	0.614

a. Kruskal Wallis Test

b. Grouping Variable: How many years have you been in the practice of engineering design and/or construction?

TABLE 6. Kruskal-Wallis H Test on opinions concerning Use of Pozzolans Based on Number of Years of Practice

Test Statistics[a,b]													
	P1	**P2**	**P3**	**P4**	**P5**	**P6**	**P7**	**P8**	**P9**	**P10**	**P11**	**P12**	**P13**
Kruskal-Wallis H	2.174	2.735	3.625	4.907	7.658	2.572	4.323	1.285	1.031	2.135	5.389	2.858	6.664
Df	4	4	4	4	4	4	4	4	4	4	4	4	4
Asymp. Sig.	0.704	0.603	0.459	0.297	0.105	0.632	0.364	0.864	0.905	0.711	0.250	0.582	0.155

a. Kruskal Wallis Test

b. Grouping Variable: How many years have you been in the practice of engineering design and/or construction?

TABLE 7. Kruskal-Wallis H Test on opinions concerning Use of Pozzolans Based on Central Area of Practice

Test Statistics[a,b]													
	P1	**P2**	**P3**	**P4**	**P5**	**P6**	**P7**	**P8**	**P9**	**P10**	**P11**	**P12**	**P13**
Kruskal-Wallis H	3.247	6.032	3.759	4.663	0.752	1.363	6.274	5.922	6.397	5.551	7.736	2.603	3.545
Df	4	4	4	4	4	4	4	4	4	4	4	4	4
Asymp. Sig.	0.517	0.197	0.440	0.324	0.945	0.851	0.180	0.205	0.171	0.235	0.102	0.626	0.471

a. Kruskal Wallis Test

b. Grouping Variable: Which of this is your central area of practice in the industry?

TABLE 8. Kruskal-Wallis H Test on opinions on Use of Pozzolans Based on Branch of Civil Engineering involved in

Test Statistics[a,b]													
	P1	**P2**	**P3**	**P4**	**P5**	**P6**	**P7**	**P8**	**P9**	**P10**	**P11**	**P12**	**P13**
Kruskal-Wallis H	0.797	6.108	2.657	4.881	3.034	4.174	2.466	3.040	5.141	2.861	4.695	4.174	3.454
Df	4	4	4	4	4	4	4	4	4	4	4	4	4
Asymp. Sig.	0.939	0.191	0.617	0.300	0.552	0.383	0.651	0.551	0.273	0.581	0.320	0.383	0.485

a. Kruskal Wallis Test

b. Grouping Variable: In which of these branches of civil engineering and/or construction are you mostly involved?

TABLE 9. Mann-Whitney U test on the Use of concrete based on Country of residence

	Test Statistics[a]								
	C1	**C2**	**C3**	**C4**	**C5**	**C6**	**C7**	**C8**	**C9**
Mann-Whitney U	595.500	689.000	694.000	610.000	651.000	543.000	533.000	604.500	662.000
Wilcoxon W	895.500	2400.000	2405.000	2321.000	2362.000	843.000	2244.000	2315.500	962.000
Z	-1.332	-.077	-.022	-.919	-.482	-1.687	-1.731	-.994	-.356
Asymp. Sig. (2-tailed)	0.183	0.938	0.982	0.358	0.630	0.092	0.083	0.320	0.722

a. Grouping Variable: Country of residence

TABLE 10. Mann-Whitney U test on the Use of Pozzolans based on Country of residence

	Test Statistics[a]												
	P1	**P2**	**P3**	**P4**	**P5**	**P6**	**P7**	**P8**	**P9**	**P10**	**P11**	**P12**	**P13**
Mann-Whitney U	590.0	621.0	620.0	689.5	686.0	610.0	485.5	442.0	472.5	480.0	451.5	456.0	596.0
Wilcoxon W	2301.0	921.0	2331.0	989.5	986.0	910.0	785.5	742.0	772.5	780.0	751.5	756.0	896.0
Z	-1.124	-0.825	-0.806	-0.073	-.114	-.967	-2.316	-2.781	-2.528	-2.483	-2.684	-2.685	-1.124
Asymp. Sig. (2-tailed)	0.261	0.410	0.420	0.942	0.909	0.333	0.021	0.005	0.011	0.013	0.007	0.007	0.261

a. Grouping Variable: Country of residence

TABLE 11. Mann-Whitney U test on the Use of Pozzolans based on Familiarity with Pozzolans

	Test Statistics[a]												
	P1	**P2**	**P3**	**P4**	**P5**	**P6**	**P7**	**P8**	**P9**	**P10**	**P11**	**P12**	**P13**
Mann-Whitney U	258.0	286.5	293.0	165.0	80.0	196.0	278.0	218.0	154.5	194.5	169.0	130.0	154.5
Wilcoxon W	3033.0	322.5	329.0	201.0	116.0	232.0	314.0	254.0	190.5	230.5	205.0	166.0	190.5
Z	-0.618	-0.160	-0.049	-2.251	-3.773	-1.725	-0.304	-1.309	-2.455	-1.789	-2.138	-2.848	-2.438
Asymp. Sig. (2-tailed)	0.537	0.873	0.961	0.024	0.000	0.085	0.761	0.190	0.014	0.074	0.033	0.004	0.015

a. Grouping Variable: Are you familiar with the word pozzolans?

The Kruskal-Wallis H test results showed that the number of years of practice of respondents did not cause any significant difference in their opinions on concrete and pozzolans, $H(4) = 1.59$ to 8.29, all $p_s > 0.05$ (Mean ranks for all groups range from 19.75 to 65.5), hence we accept the null hypothesis. This suggests that there was a universal agreement in the opinions of the respondents on the use of concrete and pozzolans considering their

experience in the construction industry. The respondents were classified according to their central area of practice into 5 broad groups which include "academia", "construction", "consultancy", "combined" (where respondents are involved in 2 or more areas), and "others". It was also discovered that there was no significant difference between these groups, H(4) = 0.754 to 7.736, all $p_s > 0.05$ (Mean ranks for all groups range from 20.17 to 55.33). Another classification of the respondents was into the major branches of civil engineering and construction they were involved in. Five (5) broad groups were identified "Civil & Structural Engineering", "Construction Engineering & Project management", "Geotechnical, Highway & Transportation Engineering", "Water & Environmental Engineering" and "Others". The test showed similar trend as in the other two tests above, H(4) = 0.797 to 5.141, all $p_s > 0.05$), hence we accept the null hypothesis.

4. 4. 3. Mann-Whitney U Test The results of the Mann-Whitney U test are presented in Tables 9-11. The null hypothesis was that no significant difference exists between the opinions of respondents in Nigeria and outside the country on concrete and pozzolans. The results interestingly reveal that the general opinions on concrete (C1 - C9) and on the ability of pozzolans (P1 – P6) were the same, that is there was no significant difference (U = 533.0 to 694.0, all $p_s > 0.05$). However, the opinions on the challenges preventing the adoption of pozzolans (P7 – P12) were significantly different (U = 442.0 to 485.5, all $p_s < 0.05$). In other words, it can be inferred that respondents from Nigeria differed in opinions from respondents outside Nigeria on the reasons for poor adoption of pozzolans in the construction industry. The factors represented by these codes (P7 to P12) include "use of pozzolans can bring an overall reduction in the cost", "the unavailability of relevant design mix standards places a limitation on the use of pozzolans", "lack of commercial production of pozzolans", "lack of professionals involved with the use of pozzolans", "inadequate public awareness", and "fears on the results achievable with the use of pozzolans". This difference in opinions can be explained by the fact that unlike Nigeria, several developed countries are already putting pozzolans into industrial application. Hence, the issues perceived as major factors inhibiting pozzolan application in Nigeria may not be the same as in some other countries. One critical factor generally agreed upon, however, is that provision of proper guidelines, standards and adequate public awareness improves the adoption of pozzolans for industrial applications. Another U-test was conducted based on the null hypothesis that no significant difference exists between the opinions of those familiar with pozzolans (74) and those that are not (8). The results of the test showed that there was significant difference in some opinions, represented by codes P4, P5, P6, P9, P11, P12 (U = 80 to 169, $p_s < 0.05$). This suggests that there needs to be improved awareness on the potential benefits of pozzolans and means of application will significantly improve its acceptance within the construction industry. The major factors responsible for the low level of adoption of pozzolans proven by this research are similar to those reported by Botchway and Masoperh [50] and Anigbogu [51].

5. SUMMARY AND CONCLUSION

This research sought to examine the probable reasons behind the low level of adoption of these SCMs in the Nigerian construction industry. It has explored the different potentials of some supplementary cementitious materials (SCMs) in concrete as well as their effectiveness. In order to understand the reason behind the low level of their acceptance in the construction industry, an online survey was carried out, which revealed that although concrete is a very good material for construction, its adverse environmental impacts require the partial replacement of its ordinary Portland cement fraction with supplementary cementitious materials in order to mitigate the negative environmental effects and in some cases, to also reduce cost. The study also confirmed that pozzolans have been comparatively effective in concrete production when used in partial replacement of cement. However, the research revealed that the most significant factors mitigating against their widespread adoption, especially in the Nigerian construction industry include: unavailability of relevant design mix standards for pozzolanic concrete, lack of commercial production of pozzolanic concrete, unavailability of sufficiently skilled professionals involved with the use of pozzolans, inadequate public awareness, lack of policies recommending and guiding its use, and fears on results achievable with use of pozzolans. It was generally agreed that the provision of guidelines and adequate public awareness on the use of pozzolans will improve their acceptance and adoption in the contemporary construction industry.

6. ACKNOWLEDGEMENT

The authors wish to acknowledge the Federal University of Technology, Akure for the support of present research through its staff development programme.

7. REFERENCES

1. Hafizyar, R. and Dheyaaldin, M. H., "Concrete Technology and Sustainably Development from Past to Future." ***Sustainable Structures and Materials, An International Journal***, Vol. 2, No. 1, (2019), 1-13. https://doi.org/10.26392/SSM.2019.02.01.001

2. Hasanbeigi, A., Price, L., Lu, H. and Lan, W., "Analysis of energy-efficiency opportunities for the cement industry in Shandong Province, China: A case study of 16 cement plants." ***Energy***, Vol. 35, No. 8, (2010), 3461-3473. https://doi.org/10.1016/j.energy.2010.04.046
3. Verma, Y. K., Mazumdar, B. and Ghosh, P. "Thermal energy consumption and its conservation for a cement production unit," ***Environmental Engineering Research***, Vol. 26, No. 3, (2021). https://doi.org/10.4491/eer.2020.111
4. Chikouche Hamina, M. and Naceri, A. "Effects of Pozzolanic Admixture (Waste Bricks) on Mechanical Response of Mortar." ***International Journal of Engineering***, ***Transactions B: Applications***, Vol. 21, No. 1, (2008), 1-8.
5. Becerra-Duitama, J. A. and Rojas-Avellaneda, D. "Pozzolans: A review." ***Engineering and Applied Science Research***, Vol. 49, No. 4, (2022), 495-504. https://ph01.tci-thaijo.org/index.php/easr/article/view/247697
6. Sai Giridhar Reddy, V. and Ranga Rao, V. "Eco-friendly blocks by blended materials." ***International Journal of Engineering***, ***Transactions B: Applications***, Vol. 30, No. 5, (2017), 636-642. doi: 10.5829/idosi.ije.2017.30.05b.02
7. Pachideh, G., Gholhaki, M. and Moshtagh, A. "Performance of porous pavement containing different types of pozzolans." ***International Journal of Engineering Transactions C: Aspects,*** Vol. 32, No. 9, (2019), 1277-1283. doi: 10.5829/ije.2019.32.09c.07
8. Shafabakhsh, G. and Ahmadi, S. "Evaluation of coal waste ash and rice husk ash on properties of pervious concrete pavement." ***International Journal of Engineering***, ***Transactions B: Applications***, Vol. 29, No. 2, (2016), 192-201. doi: 10.5829/idosi.ije.2016.29.02b.08
9. Kanthe, V., Deo, S. and Murmu, M. "Combine Use of Fly Ash and Rice Husk Ash in Concrete to Improve its Properties (Research Note)." ***International Journal of Engineering***, ***Transactions B: Applications***, Vol. 31, No. 7, (2018), 1012-1019. doi: 10.5829/ije.2018.31.07a.02
10. Arum, C., Ikumapayi, C. M. and Aralepo, G. O. "Ashes of Biogenic Wastes—Pozzolanicity, Prospects for Use, and Effects on Some Engineering Properties of Concrete." ***Materials Sciences and Applications***, Vol. 2013, No. 4, (2013), 521-527. doi: 10.4236/msa.2013.49064
11. Ikumapayi, C. M. "Crystal and Microstructure Analysis of Pozzolanic Properties of Bamboo Leaf Ash and Locust Beans Pod Ash Blended Cement Concrete." ***Journal of Applied Sciences and Environmental Management***, Vol. 20, No. 4, (2016), 943-952. doi: 10.4314/jasem.v20i4.6
12. Bakera, A. T. and Alexander, M. G. "Use of metakaolin as supplementary cementitious material in concrete, with focus on durability properties." ***RILEM Technical Letters***, Vol. 4, (2019), 89-102. https://doi.org/10.21809/rilemtechlett.2019.94
13. Bamaga, S. O., Hussin, M. W. and Ismail, M. A. "Palm Oil Fuel Ash: Promising Supplementary Cementing Materials," ***KSCE Journal of Civil Engineering***, Vol. 17, No. 7, (2013), 1708-1713. https://doi.org/10.1007/s12205-013-1241-9
14. Saraswathy, V. and Song, H. W. "Corrosion performance of rice husk ash blended concrete." ***Construction and Building Materials***, Vol. 21, No. 8, (2007), 1779-1784. https://doi.org/10.1016/j.conbuildmat.2006.05.037
15. Adisa, O. K. "Economy of RHA (Rice Husk Ash) in Concrete for Low-Cost Housing Delivery in Nigeria," ***Journal of Civil Engineering and Architecture***, Vol. 7, No. 11, (2013), 1464-1470.
16. Becerra-Duitama, J. A. and Rojas-Avellanda, D. "Pozzolans: A review." ***Engineering and Applied Science Research (EASR)***, Vol. 49, No. 4, (2022), 495-504. https://ph01.tci-thaijo.org/index.php/easr/article/view/247697
17. Kanthe, V. N., Deo, S. V. and Murmu, M. "Early age shrinkage behavior of triple blend concrete." ***International Journal of Engineering***, ***Transactions B: Applications***, Vol. 33, No. 8, (2020), 1459-1464. doi: 10.5829/ije.2020.33.08b.03
18. Sudha, S. "Durability and Strength Character of Concrete Using Lime Sludge and Flyash as Partial Replacement of Fine Aggregate." ***International Research Journal of Engineering and Technology***, Vol. 03, No. 07, (2016), 1724-1729.
19. Dwivedi, A. and Jain, M. K. "Fly ash - Waste management and Overview: A Review." ***Recent Research in Science and Technology***, Vol. 6, No. 1, (2014), 30-35.
20. American Coal Ash Association, "Fly Ash Facts for Highway Engineers [2003]." United States. Federal Highway Administration. Office of Technology Applications, 2003.
21. Ha, T. Muralidharan, S., Bae, J., Ha, Y., Lee, H., Park, K. and Kim, D. "Accelerated short-term techniques to evaluate the corrosion performance of steel in fly ash blended concrete," ***Building and Environment***, Vol. 42, No. 2007, (2007), 78-85. https://doi.org/10.1016/j.buildenv.2005.08.019
22. Dhadse, S., Kumari, P. and Bhagia, L. J. "Fly ash characterization, utilization and Government initiatives in India - A review." ***Journal of Scientific & Industrial Research***, Vol. 67, (2008), 11-18.
23. Karim, M. R., Zain, M. F. M., Jamil, M., Lai, F. C. and Islam, M. N. "Strength development of mortar and concrete containing fly ash: A review." ***International Journal of the Physical Sciences***, Vol. 6, No. 17, (2011), 4137-4153. doi: 10.5897/IJPS11.232
24. Kayali, O. "Fly ash lightweight aggregates in high performance concrete." ***Construction and Building Materials***, Vol. 22, No. 12, (2008), 2393-2399. https://doi.org/10.1016/j.conbuildmat.2007.09.001
25. NPCA, "Fly Ash Trends Downwards," *Utility Structures*, 2017. https://precast.org/2017/03/fly-ash-trends-downward/ (accessed Oct. 27, 2021).
26. Sutter, L. L., Hooton, R. D. and Schlorholtz, S. "Methods for evaluating fly ash for use in highway concrete", Vol. 749. Transportation Research Board, 2013.
27. Al-Akhras, N. "Durability of metakaolin concrete to sulfate attack," ***Cement and Concrete Research,*** Vol. 36, No. 2006, (2006), 1727-1734. https://doi.org/10.1016/j.cemconres.2006.03.026
28. Güneyisi, E., Gesoğlu, M. and Mermerdaş, K. "Improving strength, drying shrinkage, and pore structure of concrete using metakaolin." ***Materials and structures***, Vol. 41, No. 5, (2008), 937-949. https://doi.org/10.1617/s11527-007-9296-z
29. Dinakar, P., Sahoo, P. K. and Sriram, G. "Effect of Metakaolin Content on the Properties of High Strength Concrete." ***International Journal of Concrete Structures and Materials***, Vol. 7, No. 3, (2013), 215-223. https://doi.org/10.1007/s40069-013-0045-0
30. Dhinakaran, G., Thilgavathi, S. and Venkataramana, J. "Compressive Strength and Chloride Resistance of Metakaolin Concrete," ***KSCE Journal of Civil Engineering***, Vol. 16, No. 7, (2012), 1209-1217. https://doi.org/10.1007/s12205-012-1235-z
31. Vejmelková E., Pavlíková, M., Keppert, M., Keršner, Z., Rovnaníková, P., Ondrácek, M., Sedlmajer, M. and Cerny, R. "High performance concrete with Czech metakaolin: Experimental analysis of strength, toughness and durability characteristics," ***Construction and Building Materials***, Vol. 24, No. 2010, (2010), 1404-1411. https://doi.org/10.1016/j.conbuildmat.2010.01.017
32. Parande, A. K., Babu, B. R., Karthik, M. A., Kumaar, K. D. and Palaniswamy, N. "Study on strength and corrosion performance for steel embedded in metakaolin blended concrete/mortar." ***Construction and Building Materials***, Vol. 22, No. 3, (2008), 127-134. https://doi.org/10.1016/j.conbuildmat.2006.10.003

33. Thavasumony, D., Subash, T. and Sheeba, D. "High Strength Concrete using Ground Granulated Blast Furnace Slag (GGBS)." ***International Journal of Scientific & Engineering Research***, Vol. 5, No. 7, (2014), 1050-1054.
34. Gao, J. M., Qian, C. X., Liu, H. F., Wang, B. and Li, L. "ITZ microstructure of concrete containing GGBS," ***Cement and Concrete Research***, Vol. 35, No. 7, (2005), 1299-1304. https://doi.org/10.1016/j.cemconres.2004.06.042
35. Lee, Y. J., Kim, H. G., and Kim, K. H. "Effect of Ground Granulated Blast Furnace Slag Replacement Ratio on Structural Performance of Precast Concrete Beams." ***Materials***, Vol. 14, No. 23, (2021), 7159. https://doi.org/10.3390/ma14237159
36. Duży, P., Sitarz, M., Adamczyk, M., Choińska, M. and Hager, I. "Chloride ions' penetration of fly ash and ground granulated blast furnace slags-based alkali-activated mortars." ***Materials***, Vol. 14, No. 21, (2021), 6583. https://doi.org/10.3390/ma14216583
37. Ikpeseni, S. C., Owebor, K. and Owamah, H. I. "Developing the Nigerian Steel Sector: The Economic and Industrial Implications," ***NIPES Journal of Science and Technology Research***, Vol. 3, No. 1, (2021), 202-211.
38. Alberici, S., de Beer, J. G., van der Hoorn, I. and Staats, M. "Fly ash and blast furnace slag for cement manufacturing." *BEIS Research Paper*, 2017.
39. Jhatial, A. A., Goh, W. I., Mo, K. H., Sohu, S. and Bhatti, I. A. "Green and sustainable concrete–the potential utilization of rice husk ash and egg shells." ***Civil Engineering Journal***, Vol. 5, No. 1, (2019), 74-81.
40. Hadipramana, J., Riza, F. V., Rahman, I. A., Loon, L. Y., Adnan, S. H. and Zaidi, A. M. A. "Pozzolanic characterization of waste Rice husk ash (RHA) from Muar, Malaysia," in IOP Conference Series: Materials Science and Engineering, Vol. 160, (2016), 012066.
41. Sivakumar, G. and Ravibaskar, R. "Investigation on the hydration properties of the rice husk ash cement using FTIR and SEM." ***Applied Physics Research***, Vol. 1, No. 2, (2009), 71-77.
42. Krishna, N. K., Sandeep, S. and Mini, K. M. "Study on concrete with partial replacement of cement by rice husk ash," IOP Conference. Series: Materials Science and Engineering, Vol. 149, No. 2016, (2016), 1-11.
43. Oyejobi, D. O., Abdulkadir, T. S. and Ahmed, A. T. "A Study of Partial Replacement of Cement with Palm Oil Fuel Ash in Concrete Production." ***Journal of Agricultural Technology***, Vol. 12, No. 4, (2016), 619-631.
44. Rajesh, Ch., Sameer, G. N., Reddy, M. S. M., Jagarapu, D. C. K. and Jogi, P. K. "Consumption of palm oil fuel ash in producing lightweight concrete." ***Materials Today: Proceedings***, Vol. 33, No. 2020, (2020) 1073-1078. https://doi.org/10.1016/j.matpr.2020.07.096
45. Salam, M. A., Safiuddin, M. and Jumaat, M. Z. "Durability Indicators for Sustainable Self-Consolidating High-Strength Concrete Incorporating Palm Oil Fuel Ash." ***Sustainability***, Vol. 2018, No. 10, (2018), 1-16. https://doi.org/10.3390/su10072345
46. Singh, N. B., Das, S. S., Singh, N. P. and Dwivedi, V. N. "Hydration of bamboo leaf ash blended Portland cement," ***Indian Journal of Engineering & Materials Sciences***, Vol. 14, (2007), 69-76.
47. Asha, P., Salman, A. and Kumar, R. A. "Experimental Study on Concrete with Bamboo Leaf Ash." ***International Journal of Engineering and Advanced Technology***, Vol. 3, No. 6, (2014), 46-51.
48. Dhinakaran, G. and Chandana, G. H. "Compressive Strength and Durability of Bamboo Leaf Ash Concrete." ***Jordan Journal of Civil Engineering***, Vol. 10, No. 3, (2016), 279-289.
49. Umoh, A. A. and Ujene, A. O. "Empirical Study on Effect of Bamboo Leaf Ash in Concrete," ***Journal of Engineering and Technology***, Vol. 5, No. 2, (2014), 71-82.
50. Botchway, E. A. and Masoperh, A. "Investigating the Low Utilization of Pozzolana Cement in the Ghanian Construction Industry." ***International Journal of Advance Research in Engineering and Technology***, Vol. 10, No. 4, (2019), 55-62.
51. Anigbogu, N. A. "Framework for efficient development and application of pozzolan cement in Nigeria," in ***P***roceedings of NBRRI stakeholders' forum, Abuja, 24th–25th (2011).
52. Tavakol, M. and Dennick, R. "Making sense of Cronbach's alpha," ***International Journal of Medical Education***, Vol. 2, (2011), 53-55. doi: 10.5116/ijme.4dfb.8dfd
53. Glen, S. "Cronbach's Alpha: Definition, Interpretation, SPSS," *StatisticsHowTo.com: Elementary Statistics for the rest of us!*, 2022. https://www.statisticshowto.com/probability-and-statistics/statistics-definitions/cronbachs-alpha-spss/ (accessed Jun. 09, 2022).
54. Hole, G. "The Kruskal-Wallis test." Research methods 1 Handouts, (2000).
55. Kothari, C. R. and Garg, G. *Research methodology: Methods and techniques*, Third. India: New Age International, (2014).

Persian Abstract

چکیده

پوزولان ها مواد سیمانی تکمیلی (SCM) هستند که بسیاری از محققان آن را برای جایگزینی جزئی سیمان در بتن به منظور کاهش خطرات زیست محیطی و مصرف انرژی در تولید بتن مناسب می دانند. با این حال، علیرغم تلاش های تحقیقاتی قابل توجه در دهه گذشته و شواهد فراوان برای حمایت از مزایای فوق العاده آنها، این مواد به ندرت در صنعت ساخت و ساز امروزی به ویژه در نیجریه استفاده می شود. بنابراین به طور طبیعی یک سؤال مطرح می شود: چه چیزی باعث تردید در کاربرد گسترده پوزولان ها در صنعت ساختمان می شود؟ این مقاله با استفاده از یک بررسی تحقیقاتی به بررسی دلایل پذیرش و پذیرش کم آنها توسط ذینفعان صنعت ساختمان پرداخته است. نظرات ۸۲ پاسخ دهنده در مورد مشارکت چشمگیر در صنعت ساخت و ساز با استفاده از آزمون های ناپارامتریک، یعنی قابلیت اطمینان آلفای کرونباخ، آزمون Kruskal-Wallis H و Mann-Whitney U، گردآوری و مورد تجزیه و تحلیل آماری قرار گرفت. نتایج آنالیزها تایید کرد که پوزولان ها در کاهش اثرات منفی محیطی ناشی از استفاده از سیمان معمولی در بتن موثر هستند. علاوه بر این، فاکتورهای قابل توجهی که مخالف پذیرش آنها در صنعت ساختمان است عبارتند از: در دسترس نبودن استانداردهای طراحی مخلوط مربوطه برای بتن پوزولانی، عدم تولید تجاری بتن پوزولانی، در دسترس نبودن متخصصان با مهارت کافی در کاربرد پوزولان، آگاهی ناکافی عمومی، فقدان سیاست های توصیه کننده. و راهنمایی استفاده از آن و ترس از نتایج قابل دستیابی با استفاده از پوزولان ها. پاسخ دهندگان به طور کلی موافق بودند که توسعه دستورالعمل ها و استانداردهای مناسب و همچنین آگاهی عمومی کافی به پذیرش گسترده و کاربرد صنعتی پوزولان ها کمک می کند.

International Journal of Engineering

Journal Homepage: www.ije.ir

Fall Detection using Deep Learning Algorithms and Analysis of Wearable Sensor Data by Presenting a New Sampling Method

R. Keramati Hatkeposhti, M. Yadollahzadeh Tabari*, M. GolsorkhtabariAmiri

Department of Computer Engineering, Islamic Azad University, Babol Branch, Babol, Iran

P A P E R I N F O

Paper history:
Received 01 May 2022
Received in revised form 01 June 2022
Accepted 14 June 2022

Keywords:
Deep Learning
Fall Detection
Health Monitoring
Sisfall
Wearable Sensors

A B S T R A C T

Fall is one of the most critical health challenges in the community, which can cause severe injuries and even death. The primary purpose of this study is to develop a deep neural network using wearable sensor data to detect falls. Most datasets in this field suffer from the problem of data imbalance so that the instances belonging to the Fall classes are significantly less than the data of the normal class. This study offers a dynamic sampling technique for increasing the balance rate between the samples belonging to fall and normal classes to improve the accuracy of the learning algorithms. The Sisfall dataset was used in which human activity is divided into three categories: normal activity (BKG), moments before the fall (Alert), and role on the ground (Fall). Three deep learning models, CNN, LSTM, and a hybrid model called Conv-LSTM, were implemented on this dataset, and their performance was evaluated. Accordingly, the Conv-LSTM hybrid model presents 96.23%, 98.59%, and 99.38% in the Sensitivity parameter for the BKG, Alert, and Fall classes, respectively. For the accuracy parameter, we have managed to reach 97.12%. In addition, by using noise smoothing and removal techniques, we can hit a 97.83% accuracy rate. The results indicate the proposed model's superiority compared to other similar studies.

***doi**: 10.5829/ije.2022.35.10a.13*

1. INTRODUCTION

Increasing life expectancy and social change have increased the population of the elderly living alone in their homes. Falling is a significant danger to the lives of these people. According to reliable sources, a sudden fall is the leading cause of fatal injuries and the most common cause of hospitalization. After road traffic injuries, falling is the second leading cause of death due to unintentional injuries[1]. On the other hand, the medical expenses for the fall accident are also increasing [1].

In addition to physical injury, falls can cause much psychological damage, especially to the elderly. They can cause other side effects such as decreased physical activity, fear of falling, depression, anxiety, loneliness, and loss of confidence in independent living [2].

Of course, the elderly are not the only group affected by the fall; anyone with any disability or hospitalized patients will frequently experience the fall. The incidence of falls is higher in people suffering from chronic diseases such as Parkinson's, osteoarthritis, and osteoporosis [3].

Response and relief time are critical in preventing the most severe possible consequences of fall-related side effects and injuries. In the meantime, fall detection systems (FDS) can provide rapid services and assistance to the individual to reduce the consequences of the fall and ensure the well-being of the elderly at home and better patient management. Despite fall detection systems, a person can be saved by timely warning or calling for help.

FDSs can be classified into two general groups. The first group is systems based on sensors located around the user and are mainly based on machine vision (Context-Aware System). Using these tools may have high accuracy in fall detection, but there are also

*Corresponding Author Institutional Email: m_tabari@baboliau.ac.ir (M. Yadollahzadeh Tabari)

[1] http://www.who.int/mediacentre/factsheets/fs344/en/

Please cite this article as: R. Keramati Hatkeposhti, M. Yadollahzadeh Tabari, M. GolsorkhtabariAmiri, Fall Detection using Deep Learning Algorithms and Analysis of Wearable Sensor Data by Presenting a New Sampling Method, ***International Journal of Engineering, Transactions A: Basics***, Vol. 35 No. 10, (2022), 1941-1958

challenges. These systems are effective for use in a fixed area. In this particular range, changes in factors such as lighting, furniture arrangement, or the presence of unexpected elements and various noises may have a negative impact on the performance of these systems. It also violates people's privacy [4].

The existence of these challenges, on the one hand, and the advancement of new technologies and wearable sensors, such as accelerometers, gyroscopes, and magnetometers, on the other, led to falling detection systems moving toward the second group, namely wearable and inertial sensors (Inertial Measurement Units: IMUs). By analyzing the data of these sensors, they can detect the fall in real-time. Wearable fall detection systems are portable and do not have privacy issues. They are very accurate and can identify people's activities and send warning messages to third parties for help before or after the fall to reduce the negative consequences of the fall [5, 6].

A typical sensor in wearable devices is the three-axis accelerometer, which is widely used due to its low cost, small size, and installation in all smartphones.

Developers of fall detection systems are currently facing many challenges. One of the most important is the lack of access to real data. Obtaining actual data from people's behavior in everyday life is not an easy task. Falling is a sudden and unpredictable behavior. Therefore, we are required to use datasets with simulated movements in laboratories that, due to the high risk, most public data available to the target population of the elderly are not tested. This reduces the accuracy of the results of these systems in real life [7].

Another challenge is the unbalanced data used in deep learning algorithms. In this case, the number of samples belonging to one class is very different from the number of samples belonging to another class. In such cases, the system is usually biased for the majority class, and the probability of incorrectly detecting the fall increases.

Accordingly, this study aims to design an effective algorithm based on deep learning using wearable sensor data for fall detection. With relatively simple architecture, while increasing the balance rate between the data, can detect the fall directly on the sensor current with high accuracy.

The article is categorized as follows:

After the introduction in the first section, which discusses related issues and challenges, the second part refers to the classification of fall detection systems and a review of studies conducted in this field. The third section describes the conditions for selecting a database. Then in the fourth section, the proposed method of how to sample the data with the proposed models is mentioned. In the fifth section, the experiments and evaluations resulting from the implementation of the models are shown and compared with other studies. In the sixth section, a general discussion and conclusion are made.

2. RELATED WORKS

The review of past studies can be divided into two parts: datasets and algorithms used. The trend of using sensors used in FDSs before and after 2014 has been reported in literature [8]. The report shows that the number of FDSs using cameras has greatly decreased since 2014, and the use of accelerometers is expanding.

Chen et al. [9] demonstrated that accelerometer data are mainly crucial for fall detection, and about 85% of the selected features are related to accelerometers, about 10% are related to gyroscopes, and the rest are related to other sensors.

Özdemir [10] has conducted a study on the effect of sensor location on fall detection accuracy. They performed experiments with six different traditional machine learning algorithms. They showed that the sensors, which are located close to the center of gravity of the human body (like the chest and waist), are the most effective place.

The results of studies showed that when a system combines several types of sensors, its performance is significantly improved because each of the sources and sensors can independently provide excellent and sufficient information about different aspects of human activities and balance characteristics of individuals [11].

Since 2014, the trend of using algorithms has changed from threshold algorithms to machine learning algorithms and, in these recent years, has shifted to deep learning algorithms [12, 13].

In 2017, Aziz et al. [14] made a detailed comparison of ten fall detection algorithms that use accelerometer-based sensor data. Five of them used threshold-based methods, and the remaining methods were based on machine learning algorithms. The final comparison showed that machine learning-based fall detection methods perform better than threshold-based algorithms [14].

Ozdemir and Barshan [15] used 2520 experiments to create a large dataset of 14 volunteers and performed a set of standard movements that included 20 fall behaviors and 16 Activities of Daily Living (ADL). Using multilayer perceptron (MLP) for binary classification between normal behavior and fall, their fall detection system provided 95% accuracy [15].

Of course, traditional machine learning algorithms need to extract appropriate features from the data. Feature extraction must be done before any learning and must be manually determined that their effectiveness depends on the researcher's knowledge and genius. This can make feature extraction and selection very complex and significantly affect the efficiency and performance of the machine learning model [16].

But deep learning methods can automatically perform the representations needed to detect and classify raw data without human intervention and the need for specialized knowledge and automatically select the appropriate features [17].

Along with the rapid advancement of deep learning, data enhancement, and the promotion of computing hardware, deep learning models to identify human movements and activities, including fall behavior, have grown significantly [18].

Chen et al. [19] designed a Convolutional Neural Network (CNN) model consisting of three layers of Convolutional and three layers of dense and used it to detect falls. They used a dataset consisting of 31,688 samples and eight types of activities for analysis. This study compared Support Vector Machine (SVM) and Deep Belief Network (DBN) methods with the CNN method, which CNN model provided the best accuracy with 93.8%.

Tao and Yun [20] proposed the Long Short Term Memory (LSTM) model and Skeleton Data, recorded by Kinect, to predict the fall. This model reports a value of 91.7% for the sensitivity parameter and 75% for the specificity parameter, which indicates that this model can detect most pre-impact falls but has a high false alarm rate [30].

Torti et al. [21] used the sliding windowing technique and the Sisfall dataset to detect a fall, classifying the fall process into three stages: "non-fall, Alert, and fall." They reported a high sensitivity value for the fall class (98.73%). But they obtained lower accuracy regarding non-fall and Alert (88.39% and 91.08%). Only the LSTM model has been used in this study, and no comparison has been made with other deep learning structures [21].

Musci et al. [22] proposed a Recurrent Neural Network (RNN) model for fall detection using accelerometer data. The core of their neural network architecture is a fully connected layer that processes raw data, followed by two LSTM layers. They trained and tested their model with the Sisfall dataset. Their model achieved 97.16% accuracy in fall behavior and 94.14% in ADL behavior.

3. DATASET SELECTION

Choosing the suitable dataset for training and validating models has always been an important and influential issue. Due to the emergence and development of intelligent sensors, it was decided to use the data of laboratory wearable hybrid sensors for this study and finally selected the Sisfall dataset for this study.

In 2017, Sucerquia et al. [23], instead of using smartphones, introduced a handheld device to perform various experiments to identify normal and falling behaviors; thus providing the Sisfall dataset. The device consisted of two 3D accelerometers and a gyroscope, and sampled sensor data were at a frequency of 200 Hz. As a result, it also takes advantage of hybrid sensors, which can effectively deliver results.

The dataset was produced with the help of 38 volunteers, including 19 men and 19 women in the age range of 19 to 75 years, divided into two groups the elderly and adults. The elderly group consisted of 15 participants (eight males and seven females between 60 and 75 years old). The adult group had 23 participants (11 males and 12 females between 19 and 30 years old) who recorded more than 4,500 experiments. The data included 19 normal behaviors and 15 types of falls. One of the advantages of this data is the simultaneous use of young and older adults to test and prepare data, which is close to reality. Table 1 presents the types of fall behaviors defined in the Sisfall dataset and their descriptions.

In 2018, Musci and colleagues [22] did more labeling on the Sisfall dataset, which includes the following three classes:

BKG (Back-ground)**:** The class is the default, and the person behaves normally and has control over their situation.

Alert: The interval is the time when a person loses his balance and goes from normal to falling.

Fall: Specify the position in which the person is completely lying on the ground.

Unlike other datasets, Sisfall has a third class called "Alert, " a normal behavior close to falling. This class, which has also been considered in this study, can be used to modify the assessments of fall detection systems and identify fall behavior before impact.

Figure 1 shows an example of a data sequence with temporary annotations from Sisfall. This figure shows the status of the first three-axis accelerometer signals in the three regions. In the first few seconds, the person behaves normally and is moving, labeled BKG (blue color range). The initial imbalance is marked as Alert in yellow and the Fall range in red. The person then gets up and continues to move. These intervals are marked with the Alert and BKG labels, respectively.

Figure 2a shows an example signal of a fall behavior where a red circle indicates the moment of fall. Figure 2b also shows the falling behavior discretely in three classes, BKG, Alert, and Fall.

4. THE PROPOSED METHOD

4. 1. Structure of the Models Used In this study, a deep learning approach was used in which two models of CNN, LSTM, and a combined model of the two called Conv-LSTM, were examined.

Numerous experiments were performed to determine the best structure for each model. In these experiments, the performance of the models was evaluated with

TABLE 1. Fall behaviors defined in the Sisfall database

Code	Activity	Trials	Duration
F01	Fall forward while walking caused by a slip	5	15s
F02	Fall backward while walking caused by a slip	5	15s
F03	Lateral fall while walking caused by a slip	5	15s
F04	Fall forward while walking caused by a trip	5	15s
F05	Fall forward while jogging caused by a trip	5	15s
F06	Vertical fall while walking caused by fainting	5	15s
F07	Fall while walking, with use of hands in a table to dampen fall, caused by fainting	5	15s
F08	Fall forward when trying to get up	5	15s
F09	Lateral fall when trying to get up	5	15s
F10	Fall forward when trying to sit down	5	15s
F11	Fall backward when trying to sit down	5	15s
F12	Lateral fall when trying to sit down	5	15s
F13	Fall forward while sitting, caused by fainting or falling asleep	5	15s
F14	Fall backward while sitting, caused by fainting or falling asleep	5	15s
F15	Lateral fall while sitting, caused by fainting or falling asleep	5	15s

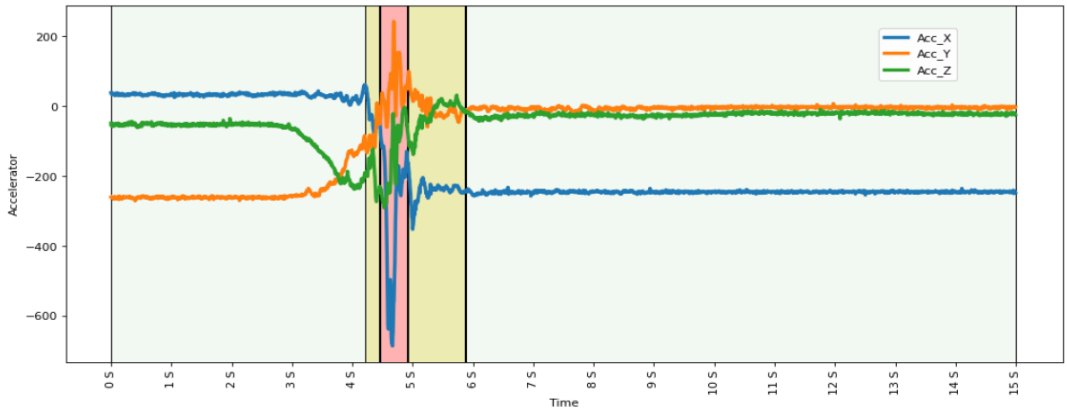

Figure 1. Sample labeling SA01/F10_R01 showing the ranges of the three classes BKG, Alert, and Fall in blue, yellow, and red, respectively

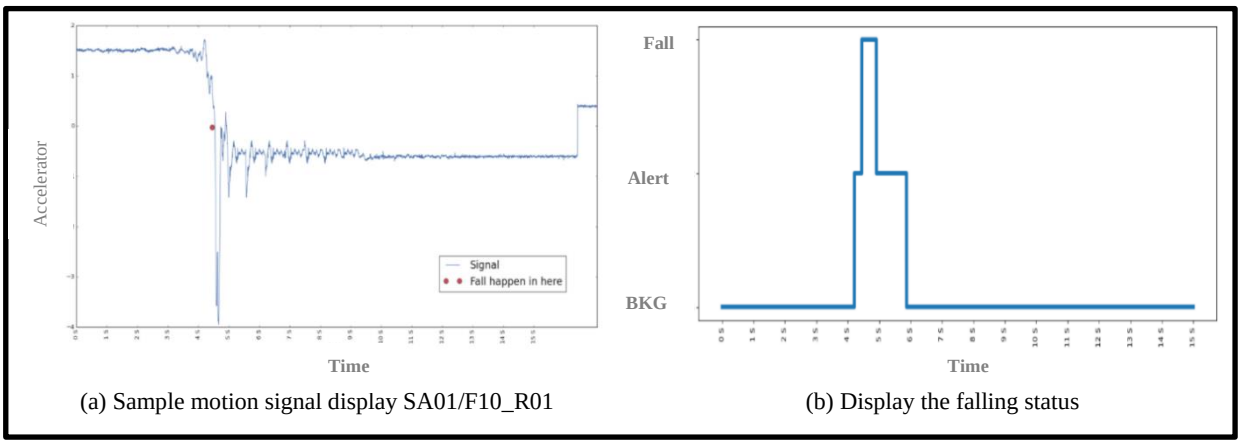

(a) Sample motion signal display SA01/F10_R01 (b) Display the falling status

Figure 2. An example of a fall status signal

different numbers and sizes of layers such as Convolutional, LSTM, Dropout, and Fully Connected. Finally, the best structure was obtained for each model shown in Figures 3 and 4.

Models with different parameters were trained, and the stage (Epoch) with the lowest "Loss Validation" error was considered the best mode. Based on the nature of the data and the experience of working with deep networks, various hyperparameters were adjusted and examined in the model construction and how to train them. These parameters include the number of layers, the size of each layer filter, the number and size of the dropout layer, the number and size of the Fully Connected Layer, the Activation Function, the Optimizer Function, the Kernel Size, and the Learning Rate, BatchSize value, Decay parameters, and Epoch number.

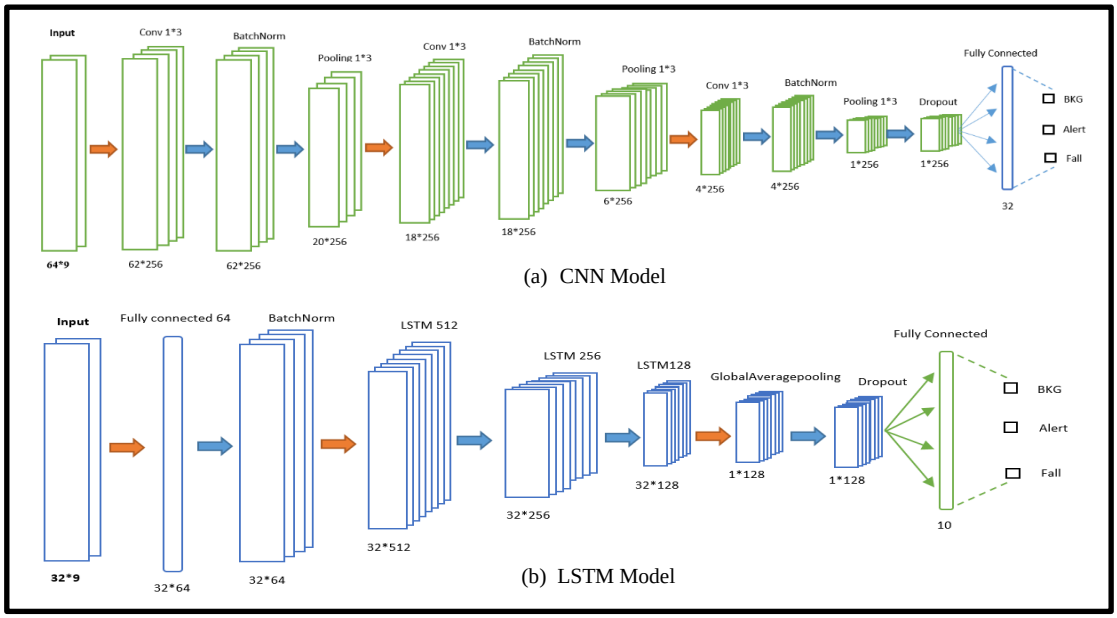

Figure 3. The structure of CNN and LSTM networks with the layers used

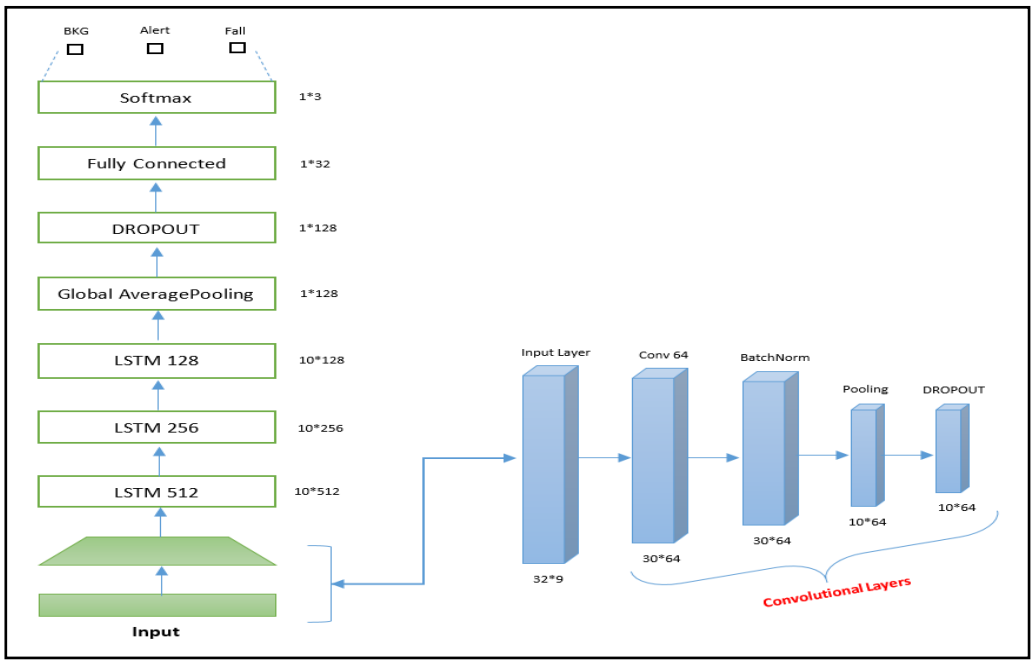

Figure 4. Conv-LSTM hybrid network structure with the number and status of its conv and LSTM layers

As shown in Figure 3, the best CNN model is when three Convolutional layers with sizes 256 are used. The LSTM Network also provided the best results when three layers of LSTM were used, with sizes 512, 256, and 128, respectively.

In the hybrid model, an attempt has been made to design a combination of the best modes of the CNN and LSTM models to achieve better results and incorporate the advantages of using CNN and LSTM. Using the CNN algorithm, appropriate features are extracted automatically, but it ignores long-term time relationships in the time series that are important for identifying behaviors and movements. LSTM, on the other hand, uses memory cells to learn long-term dependencies on time series data and dependencies between extracted properties. Of course, due to its complex structure, it has a long and very time-consuming execution time.

Therefore, in the Conv-LSTM hybrid model, CNN layers first extract the raw data properties and send them to the LSTM layers to identify temporal relationships. Compared to the single LSTM method, this technique saves a lot of time and execution calculations.

As shown in Figure 4, a combination grid of a one-dimensional convolutional layer of size 64 starts, which performs the input processing. After identifying essential and practical features, the three layers of LSTM with sizes 512, 256, and 128 are sent.

In addition, the Batchnormalize layer is used to help normalize data and adjust input data after the convolutional layer. Due to the network structure, the adopted solution also includes two Dropout layers with a rate of 50%. Of course, in the meantime, the MaxPooling technique has also been used to adjust and reduce the data and select the best option for the next round. The activation function used in layers is also a modified Rectified Linear Unit (ReLU). However, functions such as Scaled exponential linear unit (SeLU) can also be used, and repeated experiments have shown that the two functions have almost the Similar performance.

4. 2. Preparation and Preprocessing of Data

• Standardization

All machine learning architectures have one thing in common, and that is the issue of normalization and standardization of data input to the network. Using standardization, data is scaled, and data distribution is normalized. Standardizing is to obtain values with a mean of zero and a standard variance or deviation of one. If the mean of the original data is equal to μ and their standard deviation is also σ, the value of Z is obtained based on Equation (1), where xi is a data point in between (x1, x2,…, xn)[1].

$$Z = \frac{X_i - \mu}{\sigma} \tag{1}$$

and based on this conversion, we will have:

$$\bar{Z} = \frac{1}{n}\sum_{i=1}^{n} Z_i = \frac{1}{n}\sum_{i=1}^{n}\left(\frac{x_i-\mu}{\sigma}\right) = \frac{\bar{x}-\mu}{\sigma} = 0 \tag{2}$$

On the other hand, we have to calculate the variance:

$$\sigma_z^2 = \frac{1}{n}\sum_{i=1}^{n}(Z_i - \bar{Z})^2 = \frac{1}{n}\sum_{i=1}^{n} Z_i^2 = \sum_{i=1}^{n}\left(\frac{x_i-\mu}{\sigma}\right)^2 = \frac{1}{\sigma^2}\frac{1}{n}\sum_{i=1}^{n}(x_i-\mu)^2 = \frac{\sigma^2}{\sigma^2} = 1 \tag{3}$$

Therefore, in standardization, the conversion $\sim(\mu.\sigma^2) \rightarrow \sim(0.1)$ takes place. Standardization is essential and effective when dealing with many features and data at different scales. Standardization causes functions to be in saturated areas later, and as a result, the training process encounters problems such as Vanishing Gradient later.

• Smoothing Data

In addition to standardization, one of the essential steps in signal processing is removing noise and unwanted factors that filters can do. Filters are divided into analog and digital. Digital filters have advantages over analog filters that make them more widely used. These include high reliability, high performance, and no need for unique settings. Digital filters are divided into two general categories Infinite Impulse Response (IIR) and Finite Impulse Response (FIR)[2].

At a glance, if the Y(z) function represents a digital filter,

$$Y(z) = X(z)\,H(z) = \frac{b(1)+b(2)z^{-1}+\ldots\ldots+b(n+1)z^{-n}}{a(1)+a(2)z^{-1}+\ldots\ldots+a(m+1)z^{-m}} \tag{4}$$

Then:

1) If n = 0, we will have an IIR filter.

2) If m = 0, we will have an FIR filter.

FIR filters have an utterly linear phase, which is very effective in image and audio processing applications, while IIR filters are nonlinear. FIR filters are non-reversible, but IIR filters have a feedback path. One of the advantages of IIR filters over FIR filters is that analog filters can be converted to digital IIR filters.

According to the nature of the data, the IIR 1st order low-pass filter was used to remove noise. This filter was chosen because of its simplicity, and at the same time, it has provided similar results to other filters. The relationship of this filter is shown in Equation (5) [9].

$$S^*[n] = \alpha\, S[n-1] + (1-\alpha)S[n]. where\ 0 \le \alpha \le 1 \tag{5}$$

[1] https://towardsdatascience.com/how-and-why-to-standardize-your-data-996926c2c832

[2] https://towardsdatascience.com/how-and-why-to-standardize-your-data-996926c2c832

However, after the α coefficient is infiltrated, it can be converted to the relation $S^*[n] = S[n] + \alpha\,(S[n-1] - S[n])$. In this case, $S^*[n]$ is the current filtered signal, $S\,[n]$ is the current instantaneous signal, and $S\,[n-1]$ is the previous order signal.

Here α is an adaptive coefficient in the range [0, 1] that can have the following states:

1) If $\alpha \neq 0$, then it will be an IIR filter.

2) If $\alpha = 0$, then the output is exactly equal to the input; in fact, no filter is applied.

3) If $\alpha \rightarrow 1$, the output moves towards a constant value and eventually becomes linear.

If the value of the α coefficient is close to 1, many of the signal behaviors may be lost, and the classification task may be difficult. "Alert" labels may even be identified as "BKG". If α is considered too small, no noise may be detected or eliminated. Given the conditions of the data and repeated experiments, the best option for the α coefficient value (0.9) was considered. Figure 5 shows the results of applying the filter to the three-axis signals of the first accelerometer.

Signal magnitude area (SMA), which describes changes in human activity, has been used to determine falls. This parameter is represented by Equation 6, where x_t, y_t and z_t represent the accelerometer sensor readings on the x, y, and z axes, respectively.

$$SMA = \sqrt{X_t^2 + Y_t^2 + Z_t^2} \quad (6)$$

For a better comparison, the SMA mode of the signals is shown in Figure 5. Figure 5(a) shows the normal behavior of the signal, which was transformed into Figure 5(b) by applying a filter and removing noise. Figure 5(c) also indicates the status of the signals simultaneously in SMA and SMA filtered mode, and the effectiveness of filtering in this mode is quite visible.

In this study, a standardization method was used for data preprocessing, and IIR filtering was used to remove noise. The models were trained once without noise cancellation and again with noise cancellation, and the results were evaluated.

4. 1. Dynamic Sampling of Data with the Approach of Increasing the Alignment Rate

Using a proper data sampling method can ensure the success of learning algorithms in generalizing the training to the experimental stage. In solving the issue of imbalanced data, a new technique with a data amplification approach for sampling and increasing the number of minority class samples is proposed and has been operational.

Ordinally, for data sampling, the input data sequence must be adjusted for each training, validation, and testing set with fixed-size windows (w). Of course, the window size of w is a hyperparameter, the precise adjustment of which is significant for the effectiveness of the network architecture. On the other hand, when calculating data flow, the data should be placed at the edge of a sliding window. Accordingly, determining the degree of overlap and the choice of movement steps (Stride) is also very important and influential.

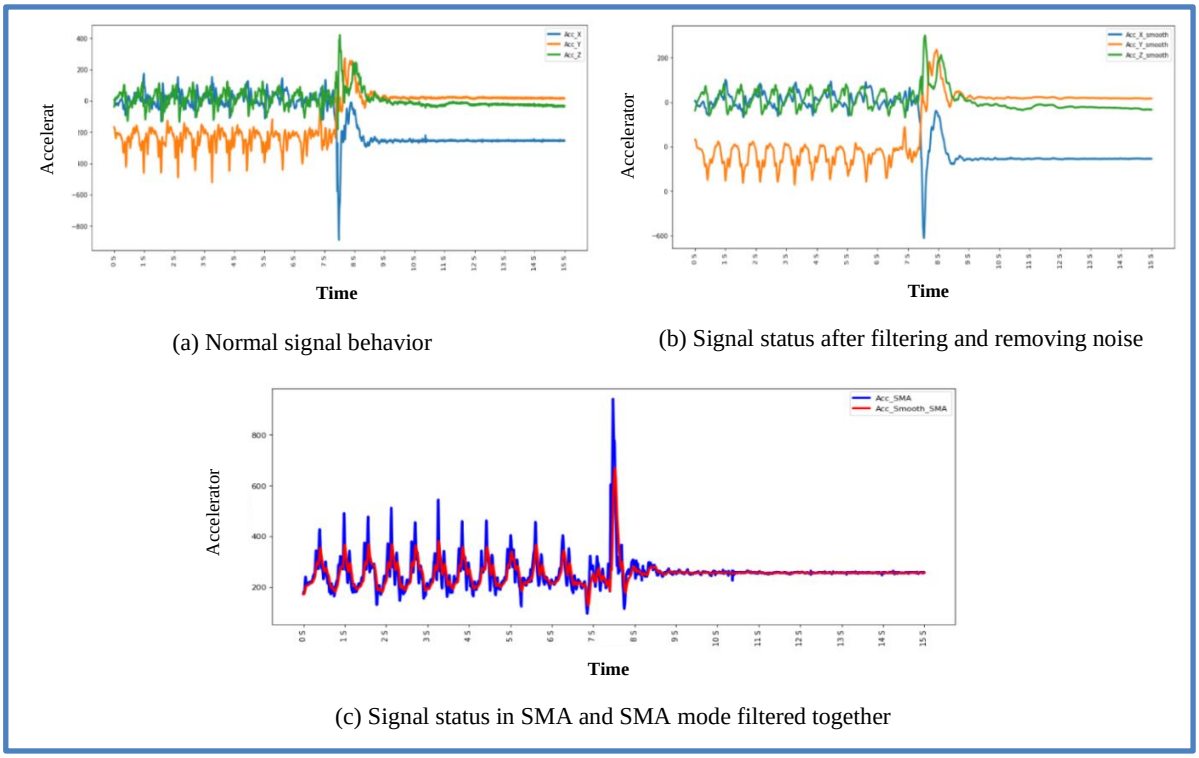

(a) Normal signal behavior

(b) Signal status after filtering and removing noise

(c) Signal status in SMA and SMA mode filtered together

Figure 5. Display the three-axis signals of the first accelerometer corresponding to the sample SA02/F03_R01 in three positions

To move the slider in the data, according to Equation (7), because it always starts with the BKG label, we first use a 50% overlap rate, and as soon as we reach the first Fall label, we increase the overlap percentage. For simplicity, we used overlaps 75, 90, and 95. Then, after finishing the fall label and reaching the BKG label again, a 50% overlapping window is used. Figure 6, illustrates this approach, where the compaction and increase of overlap in the Fall range are evident.

$$Stride = \begin{cases} 50\% & lable = BKG \\ 75\% \ or \ 90\% \ or \ 95\% & lable \neq BKG \end{cases} \quad (7)$$

As shown in Figure 7, based on the average_sensititvity parameter, the best accuracy in 64-width windowing was on CNN. But in LSTM and Conv-LSTM networks, the best result is obtained in the w=32 with 95% overlap for the Alert and Fall sections.

The best values for the window width and overlap parameters were determined by examining the sensitivity criterion, which is shown in Tables 2, 3, and 4. As it turns out, as the overlap increases, the results improve, and the classification error decreases. The best result is the Conv-LSTM hybrid model, which uses a window width of w=32 and 95% overlap in the Fall and Alert classes.

Figure 8 shows the sampling status with windowing w = 32 and dynamic overlaps, and it is clear that at 95% overlap status, a better balance is established between classes. The initial dataset was unbalanced; with a normal overlap of 50%, the equilibrium rate (ratio of the number of falling samples to the number of normal behavior samples) was less than 1%, with a 95% overlap in the Fall and Alert sections, this value reached 13.92%, which almost increased 14 times. This data increase in the minority class can be very effective in system performance and accuracy improvement.

So with the same technique, without much increase for the BKG class, a lot of new data from the Alert and Fall class was added to the collection, which significantly improved the imbalance problem.

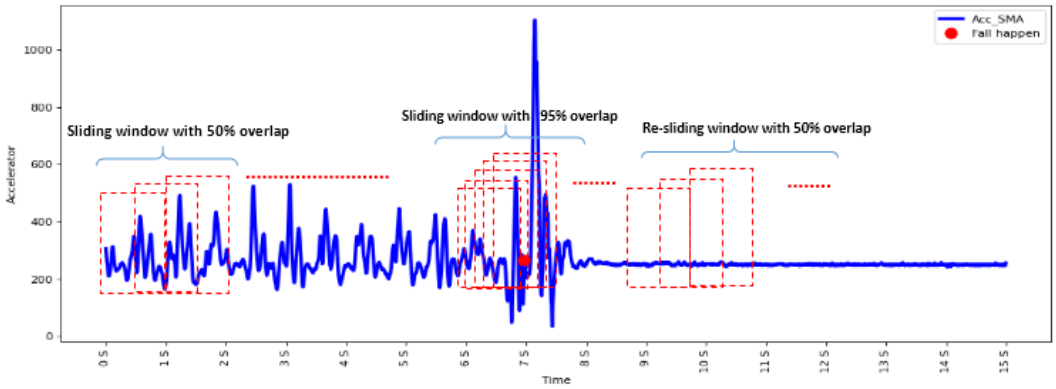

Figure 6. Sampling process and overlap in different classes related to sample SA01/F10_ R01

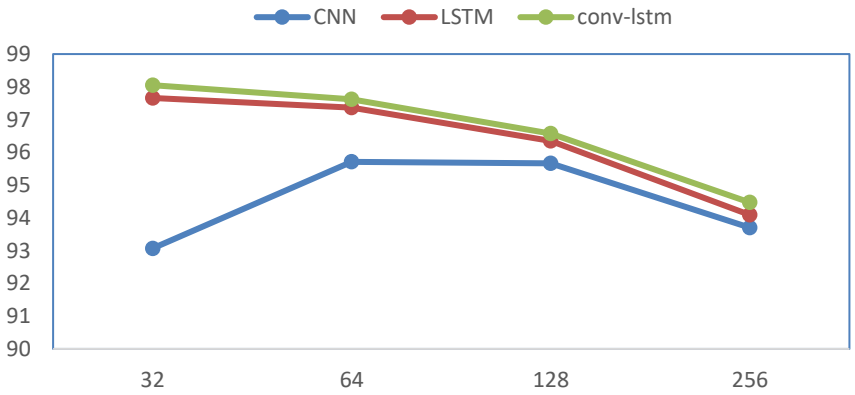

Figure 7. Status diagram of the Average_sensititvity average parameter in three models with different windowing

TABLE 2. Status of window values and overlap in sampling in the CNN model

ROW	Window size (W)	degree of overlap (S%)	Accuracy	CNN: Sensitivity (%)			
				BKG	Alert	Fall	Average_sensititvity
1	32	50	87.33	87.69	73.89	86.03	82.54
2	32	75	89.67	90.31	77.24	88.64	85.40
3	32	90	91.08	92.01	83.69	92.03	89.24
4	32	95	92.57	93.33	89.16	96.71	93.07
5	64	50	90.48	90.83	77.36	87.33	85.17
6	64	75	90.45	90.89	81.26	91.03	87.73
7	64	90	93.54	93.71	92.41	93.07	93.06
8*	**64**	**95**	**94.98**	**94.68**	**95.53**	**96.92**	**95.71**
9	128	50	92.44	92.81	77.15	93.22	87.73
10	128	75	92.61	92.96	79.79	91.78	88.18
1	128	90	92.89	93.26	89.43	94.45	92.38
12	128	95	95.39	95.26	95.76	95.97	95.67
13	256	50	92.11	92.24	64.73	95.35	84.11
14	256	75	92.07	92.49	81.96	86.86	87.11
15	256	90	92.76	93.10	89.11	91.86	91.36
16	256	95	93.93	94.06	93.26	93.78	93.70

TABLE 3. Status of windowing values and overlap in sampling in LSTM model

ROW	Window size (W)	degree of overlap (S%)	Accuracy	LSTM: Sensitivity (%)			
				BKG	Alert	Fall	Average_sensititvity
1	32	50	88.90	89.28	73.87	89.48	84.21
2	32	75	90.90	91.47	79.62	90.95	87.35
3	32	90	95.02	95.14	93.58	96.27	94.99
4*	**32**	**95**	**96.61**	**95.85**	**98.08**	**99.06**	**97.66**
5	64	50	91.46	91.82	78.29	88.81	86.31
6	64	75	93.27	93.85	81.36	93.31	89.51
7	64	90	95.84	96.61	93.75	96.49	95.62
8	64	95	97.07	97.01	96.95	98.14	97.37
9	128	50	91.88	92.37	75.36	94.72	87.48
10	128	75	93.27	93.91	77.99	94.71	88.87
11	128	90	95.49	95.96	91.40	94.51	93.96
12	128	95	95.98	96.20	95.52	97.34	96.35
13	256	50	92.86	93.31	74.86	84.88	84.35
14	256	75	91.87	92.59	82.65	85.40	86.88
15	256	90	92.99	93.07	89.73	93.90	92.23
16	256	95	94.78	95.00	93.85	93.43	94.09

TABLE 4. Status of windowing values and overlap in sampling in Conv-LSTM hybrid model

ROW	Window size (W)	degree of overlap (S%)	Accuracy (%)	Conv-Lstm: Sensitivity (%)			
				BKG	Alert	Fall	Average_sensititvity
1	32	50	90.15	90.57	73.87	89.48	84.64
2	32	75	91.84	92.38	81.25	90.86	88.16
3	32	90	84.77	94.70	94.65	96.58	95.31
4*	32	95	97.12	96.23	98.59	99.38	98.07
5	64	50	92.65	93.06	77.57	89.50	86.71
6	64	75	93.06	93.56	83.01	92.53	89.70
7	64	90	96.47	96.42	94.08	96.64	95.71
8	64	95	97.41	97.31	97.62	97.94	97.62
9	128	50	93.46	93.95	78.43	93.22	88.53
10	128	75	93.58	94.22	81.64	93.98	89.95
11	128	90	96.06	96.45	93.56	93.62	94.54
12	128	95	96.39	96.33	96.51	96.87	96.57
13	256	50	92.38	92.39	72.98	93.02	86.13
14	256	75	90.93	91.41	82.31	84.67	86.13
15	256	90	93.48	93.60	89.83	92.54	91.99
16	256	95	94.56	94.82	94.80	93.78	94.47

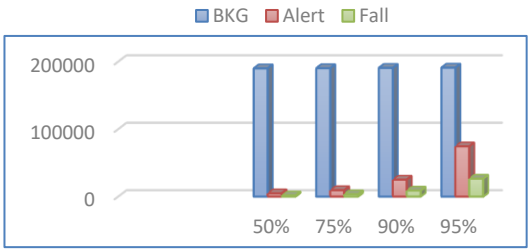

Degree of overlap	Number of BKG	Number of Alert	Number of Fall	Total data	Balance rate (Fall to BKG ratio)
50%	190041	4855	1777	196673	0.94 %
75%	190360	9486	3481	203327	1.83 %
90%	190745	25071	8936	224752	4.68 %
95%	191085	74549	26599	292233	13.92 %

Figure 8. Status of samples number in different classes by dynamic overlap method

5. IMPLEMENTATION AND EVALUATION

5. 1. Implementation In this study, as shown in the flowchart of Figure 9, after selecting the data set, the data were pre-processed, and a new approach was used for data sampling. Due to the structure of the Sisfall dataset and the use of two accelerometers and a three-axis gyroscope, nine channels can be used to receive data. For implementation, all available 9-channel data have been used.

The dataset was divided into three smaller and independent sets, entitled Train with a ratio of 60%, Validation with a ratio of 20%, and Test with a ratio of 20%. The model is trained with Train data and its learning level experiments with validation data. Next, the model's performance is evaluated with test data that it has not seen before.

5. 2. Evaluation Criteria As shown in Figure 10, the data identification and classification results are classified into the following four groups.

Of course, the main challenge of fall detection systems is to reduce false positive (FP) warnings and also to reduce false negative (FN) warnings [24-27]. There are various criteria for evaluating the performance of machine learning algorithms for classification problems; the following parameters can be mentioned [28-30].

$$Accuracy\ (\%) = 100 * \frac{TP+TN}{TN+FN+TP+FP} \quad (8)$$

$$precision\ (\%) = 100 * \frac{TP}{TP+FP} \quad (9)$$

$$Sensitivity\ (\%) = 100 * \frac{TP}{TP+FN} \quad (10)$$

$$Specificity\ (\%) = 100 * \frac{TN}{TN+Fp} \quad (11)$$

$$F - Score\ (\%) = \frac{2*Recal*precision}{Recal+precision} \quad (12)$$

The sensitivity criterion describes the ability to detect a fall, and the specificity criterion describes the FDS's ability to prevent false alarms. The goal is for the model to accurately detect a fall, which implies a fall detection model with a high sensitivity value. We also do not want to have too many false warnings. Therefore, the main criteria for evaluating the models in this study are the sensitivity and specificity parameters, and we will look at other parameters as well.

5. 2. Experiments and Evaluation Results

Figure 11 shows the general laboratory process of this study. All training and testing steps are performed on a system equipped with an Intel Core i7 processor and NVIDIA GeForce 930MX graphics, and 8 GB of main memory with the Windows 10 operating system.

We performed three general experiments to evaluate the proposed models and approach. In the first experiment, the method which was presented in by Musci et al. [22] in 2018, every window that contains at least 10% of the Fall class is labeled Fall. Every non-Fall window in which most samples are in the Alert class is labeled Alerts, and the remaining windows are labeled in the BKG class. Of course, we considered the overlap rate constant and the value of 50%.

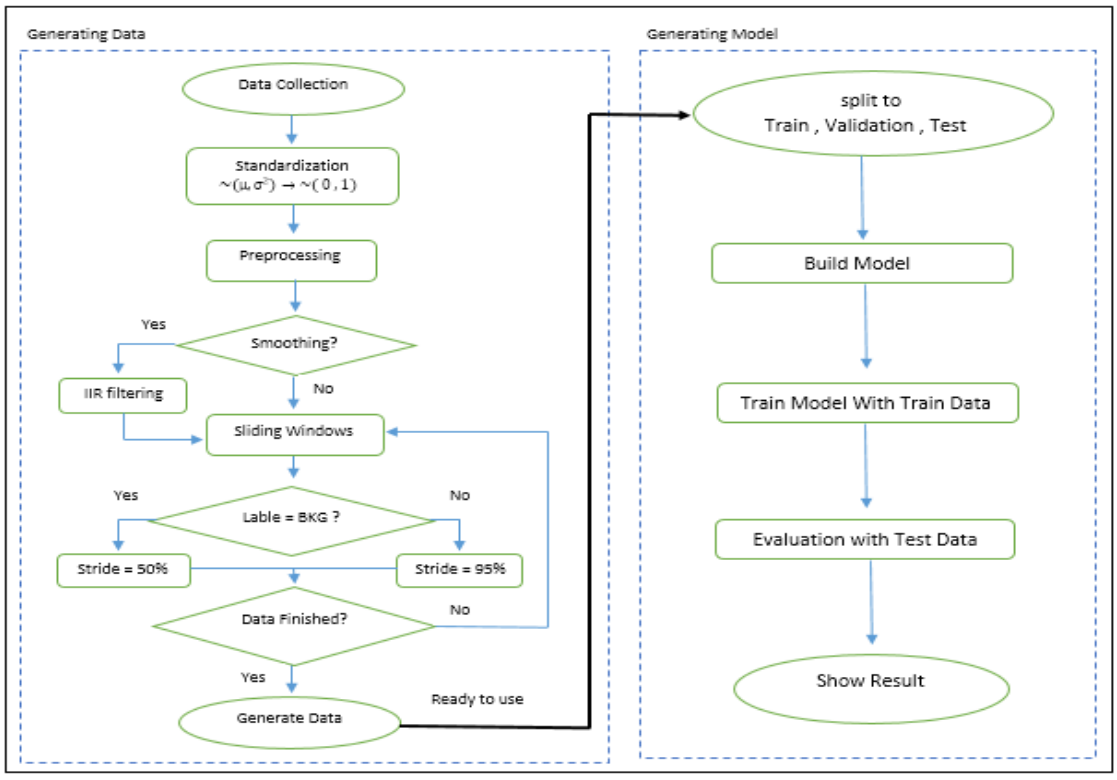

Figure 9. Flowchart of the fall detection process

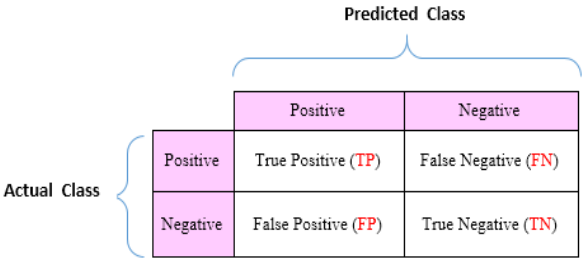

Figure 10. Classification of real and predicted classes into four groups

In the second experiment, we considered the overlap rate during sampling constant, and 50% and the majority vote approach were used for labeling.

In the third experiment, which is the proposed method of this study, the dynamic overlap was used. We first used a 50% overlap for sampling and increased the overlap to 95% as soon as we reached the first Alert and then the first drop. This process continued until we reached the first normal state (BKG) again, after which we sampled the path again with 50% overlap.

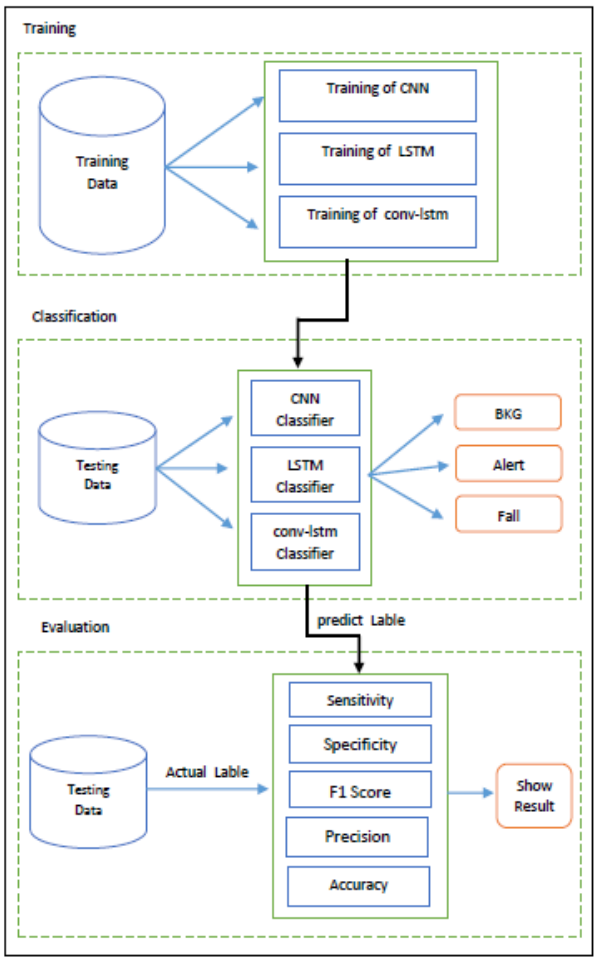

Figure 11. General laboratory process

Tables 5, 6, and 7 summarized the results of these experiments separately for the three proposed algorithms based on sensitivity and specitifity criteria.

The experimental results were also compared with the data reported by Yu et al. [31] studied in 2020 and in 2019 by Torti et al. [21].

Yu et al. [31] studied two models of CNN, LSTM, and a combined model of these two called Conv-LSTM were used to detect the fall, and their performance was evaluated on the Sisfall dataset. Torti et al. [21] also used the sliding windowing technique and the Sisfall dataset to detect falls. They classified the fall process into three stages: "no fall, Alert and fall" and used the LSTM model to classify the three classes.

And as it turns out, the proposed method with 32-width windowing and 95% overlap, compared to other methods, has shown the best accuracy in most classes.

As shown in Table 5, the value of the Accuracy parameter of the proposed method in the CNN model is 94.98%. More importantly, in this model, the value of the Sensitivity parameter in the proposed method in the BKG, Alert, and Fall classes is 94.68%, 95.53 %, and 96.92%, respectively, the best result in all classes compared to other methods.

Of course, only the sensitivity value of the fall class in the torti method is higher than the proposed method. But in this research, only the LSTM model is used, and in the other two classes, the results are weaker than the proposed method.

Also, the value of the specificity parameter in these three classes is 98.93%, 95.13%, and 99.15%, respectively; which is the best result compared to other cases.

According to Table 6, the accuracy parameter of the proposed method in the LSTM model shows a value of 96.61%. The value of the sensitivity parameter in the proposed method for the BKG, alert, and fall classes are 95.85, 98.08, and 99.06, respectively, which is still the best compared to other methods in all classes. At the same time, there is a relative balance between the results of all three classes. Also, the value of the specificity parameter in these three classes is 99.48%, 97.26%, and 99.39%, respectively, which is the best result compared to other cases. On the other hand, a review of the two tables shows that the results of the LSTM model performed much better than the CNN model in all classes.

TABLE 5. Comparison of the performance results of the proposed method with the results of some similar studies in the CNN model

CNN - Best ACC : 94.98%						
Evaluation criteria	**Class**	**Study results Torti -2019**	**Study results Yu -2020**	**Experimental results of the proposed method**		
				With study approach Musci-2018	**Fixed overlap 50%**	**overlap 95%**
Sensitivity	BKG	88.39	89.9	93.19	90.83	94.68
	Alert	91.08	90.33	94.60	77.36	95.53
	Fall	98.73	93.76	94.42	87.33	96.92
Specificity	BKG	97.85	95.05	98.34	93.45	98.93
	Alert	90.77	91.52	94.4	92.05	95.13
	Fall	97.93	98.42	98.82	98.44	99.15

TABLE 6. Comparison of the performance results of the proposed method with the results of some similar studies in the LSTM model

LSTM - Best ACC : 96.61%						
Evaluation criteria	**Class**	**Study results Torti -2019**	**Study results Yu -2020**	**Experimental results of the proposed method**		
				With study approach Musci-2018	**Fixed overlap 50%**	**overlap 95%**
	BKG	88.39	91.5	93.21	sensitivity	BKG
Sensitivity	Alert	91.08	91.48	91.37	77.36	Alert
	Fall	98.73	96.22	91.82	87.33	Fall
	BKG	97.85	95.93	96.96	specificity	BKG
Specificity	Alert	90.77	94	94.39	92.05	Alert
	Fall	97.93	97.54	98.78	98.44	Fall

TABLE 7. Comparison of the performance results of the proposed method with the results of some similar studies in the Conv-Lstm hybrid model

Conv-Lstm – Best ACC : 97.12%						
Evaluation criteria	**Class**	**Study results Torti -2019**	**Study results Yu -2020**	**Experimental results of the proposed method**		
				With study approach Musci-2018	**Fixed overlap 50%**	**overlap 95%**
	BKG	88.39	93.15	92.61	93.06	**96.23**
Sensitivity	Alert	91.08	93.78	94.6	77.57	**98.59**
	Fall	98.73	96	92.07	89.5	**99.38**
	BKG	97.85	96.59	98.62	93.64	**99.60**
Specificity	Alert	90.77	94.49	93.88	93.89	**96.82**
	Fall	97.93	98.69	98.68	98.81	**99.59**

According to Table 7, the accuracy parameter of the proposed method in the Conv-LSTM hybrid model shows a value of 97.12%. The sensitivity parameter values in the proposed method in the BKG, Alert, and Fall classes are 96.23, 98.59, and 99.38, respectively, known as the best in all classes compared to other methods. Also, the values of the specificity parameter in these three classes are 99.60%, 96.82%, and 99.59%, respectively, as the best result compared to other cases. Meanwhile, there is a balance between the results of the classes.

On the other hand, an examination of the three tables, the summary chart of which is presented in Figure 12, shows that the results of the Conv-LSTM hybrid model performed better than the CNN model in all classes. Also, the hybrid model results were better than the LSTM model, and the training time in the hybrid model was much shorter than in the LSTM Network (78 seconds vs. 143 seconds per Epoch).

Therefore, the hybrid model was able to detect the fall with high accuracy, and even the alert class was able to identify with high accuracy, which helps to announce the necessary warning with high confidence before the fall. There was also a balance between the accuracy values of each class in all three models, which could indicate the good quality of the models and good network training with the proposed method. On the other hand, although the number of samples in the fall

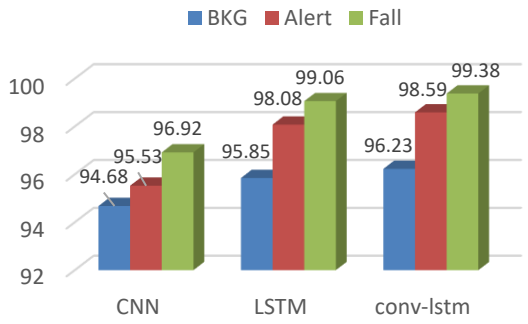

Figure 12. Status diagram of Sensitivity parameter values in three models and in three classes

and alert classes was much lower than in the BKG class, a review of all three models shows that higher sensitivity and specificity values were obtained in these classes. This could result from the approach of dynamic overlap in this study.

Therefore, these comparisons show that the hybrid model has performed better with the proposed approach to fall detection using the Sisfall dataset.

Also, the graphs of sensitivity/specificity values and loss/accuracy parameters related to the hybrid model can be seen in Figures 13 and 14, respectively. The process of improvement of these parameters is clearly observed.

Examining the results obtained in the Confusion Matrix and observing the results of other evaluation criteria such as Precision and F-score, it is observed that in these parameters, high accuracy is provided. These results are presented in Figure 15. As can be seen, the Precision parameter values in all classes are higher than 90%, with an average value of 95.72%. In the F-Score criterion, all classes have values close to 1.

On the other hand, in the continuation of the work, removing noise from the data was performed, for which the first-time low-pass IIR filter was used. After preprocessing and noise removal from the data, the networks were re-implemented on them. The status of the values of the three criteria, Sensitivity, Precision,

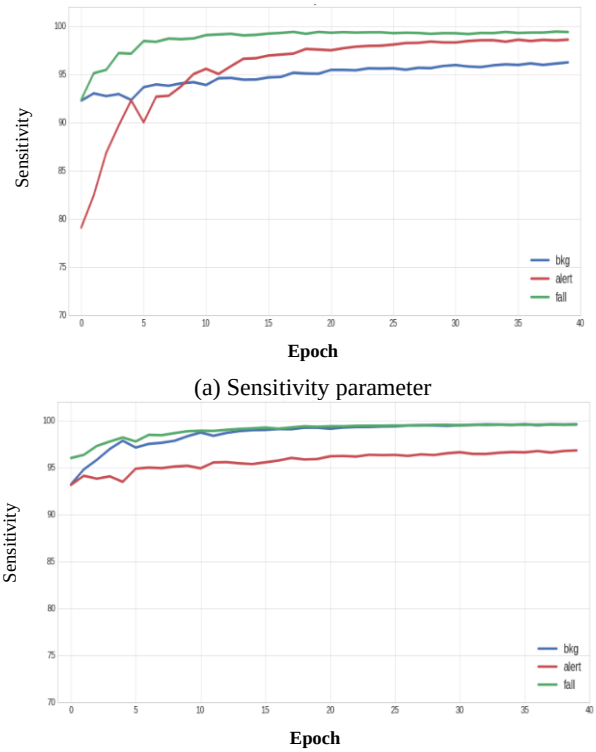

(a) Sensitivity parameter

(b) Specificity parameter

Figure 13. Status diagrams of Sensitivity and Specificity parameter values related to the Conv-Lstm hybrid model

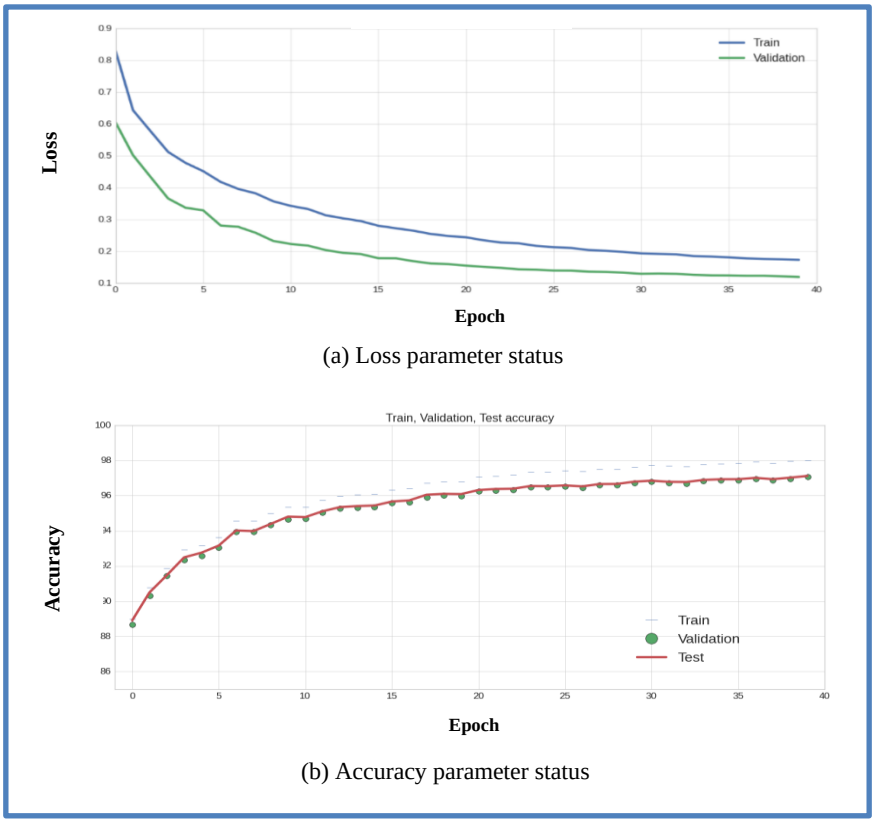

(a) Loss parameter status

(b) Accuracy parameter status

Figure 14. Status diagram of Loss parameter and Accuracy parameter in Conv-Lstm hybrid model

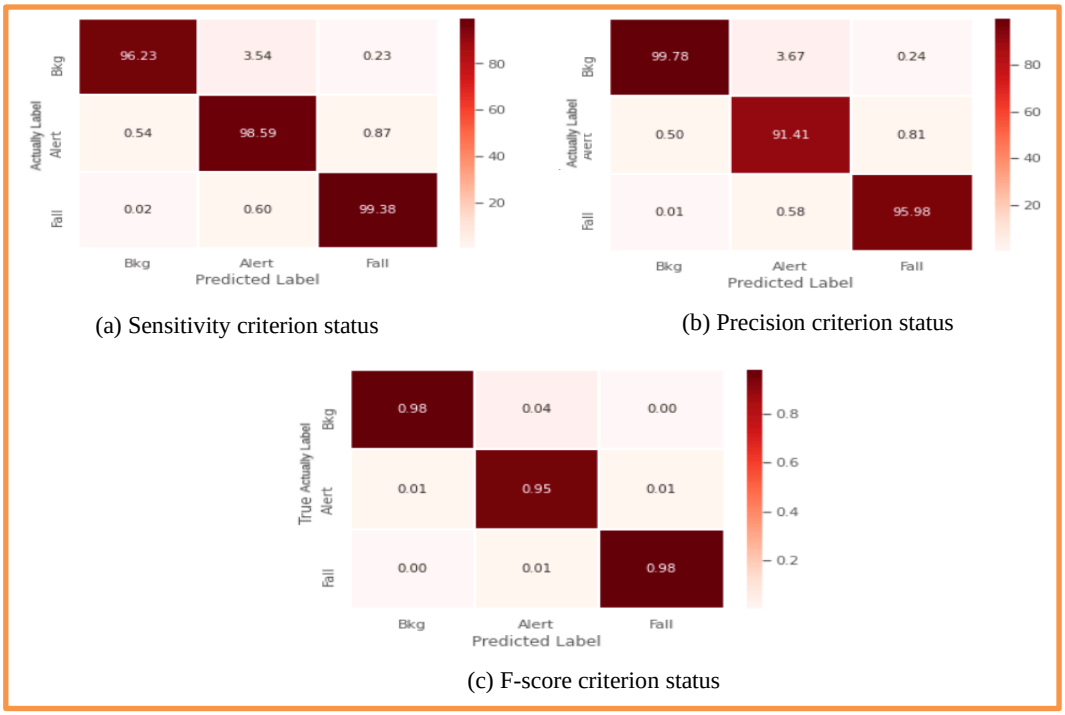

(a) Sensitivity criterion status

(b) Precision criterion status

(c) F-score criterion status

Figure 15. Confusion Matrix values in the Conv-Lstm hybrid model

and F-score, based on the Confusion Matrix table, is shown in Figure 16. Based on the results, high accuracy has been achieved in all classes. In the hybrid model, by removing noise from the data, the sensitivity criterion in the three classes of BKG, Alert, and Fall has presented 97.13%, 99.05%, and 99.36%, respectively, which is a relative improvement compared to before.

Also, the results obtained with the smoothed data are compared with the initial data without noise removal, the results of which are shown in Table 8 and their status diagram in Figure 17.

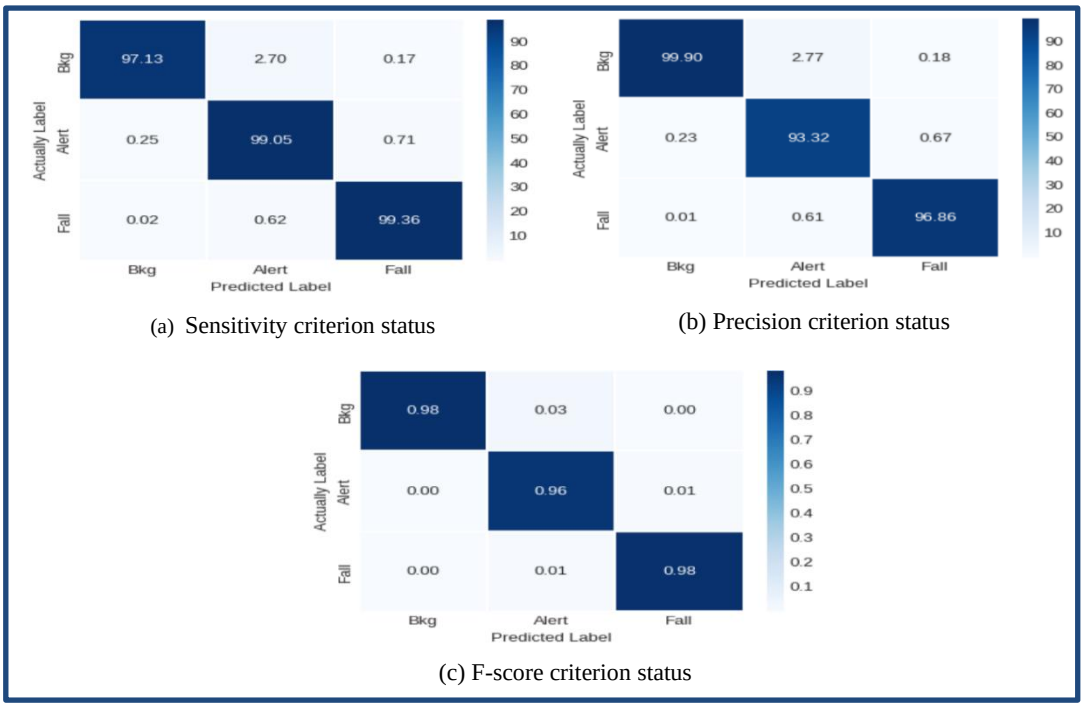

(a) Sensitivity criterion status

(b) Precision criterion status

(c) F-score criterion status

Figure 16. Confusion matrix values of the Conv-Lstm hybrid model with Smooth data

TABLE 8. Comparison of performance results of three models, without noise removal and with noise removal (smooth) from the data

°	Class	CNN	CNN_Smooth	LSTM	LSTM_Smooth	Conv-Lstm	Conv-Lstm_Smooth
	BKG	94.68	95.90	95.85	97.44	96.23	97.13
Sensitivity	Alert	95.53	96.73	98.08	98.75	98.59	99.05
	Fall	96.92	96.84	99.06	99.35	99.38	99.36
	BKG	98.93	99.20	99.48	99.65	99.60	99.81
Specificity	Alert	95.13	96.17	97.26	97.70	96.82	97.56
	Fall	99.15	99.38	99.39	99.47	99.59	99.68
Accuracy		94.98	96.11	96.61	97.91	97.12	97.83

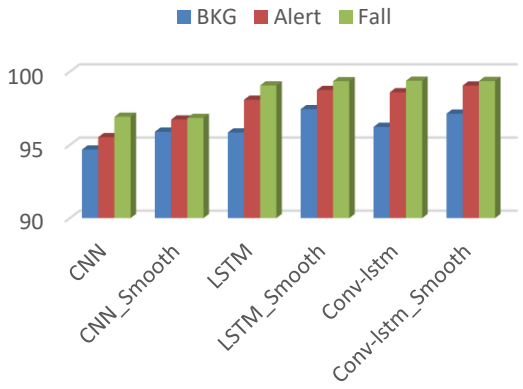

Figure 17. Performance diagram of three models with noise removal from the data and compare it the noise-free mode based on Sensitivity parameter

As shown in Figure 17, noise cancellation from data has improved performance in almost all models and all classes. But among the models, it had the most impact on the CNN model. Also, the BKG and Alert classes were more affected by noise cancellation than the Fall class, which could be due to the number of instances of the classes or more smoothing of the signals of these classes than the Fall class due to filtering.

6. DISCUSSION AND CONCLUSION

The problems of the aging population worldwide are becoming more and more, and the fall is one of the significant health challenges among the elderly and the disabled, which can cause great harm and even death. However, falls can happen to anyone, including young people. Therefore, early detection of falls is one of the essential components of improving the quality of life for people, especially the elderly.

This study presented a framework for identifying fall behavior using deep learning neural networks based on wearable sensor data. Based on this, a three-class Sisfall dataset is used, in which two accelerometer sensors and a gyroscope sensor are used. Studies have shown that accelerometer data are essential for fall detection and are widely used. The data included 34 falls and normal behavior activities performed by 38 participants with a wearable device attached to their waist.

Due to the imbalance between the number of data class samples in data science projects, this study aims to provide a new approach to data sampling and data windowing to increase the accuracy of fall detection. Many experiments were performed, and finally, it was shown that sampling the data with 32 widths and 95% overlap gives the best results.

Three architectures, CNN, LSTM, and the Conv-LSTM hybrid model, have also been applied to the dataset to determine the best model. The results showed that the LSTM and Conv-LSTM models performed better than the CNN model.

Also, in most cases, the Conv-LSTM hybrid model has better performance than the LSTM model, and better results have been obtained based on evaluation criteria. Accordingly, the Conv-LSTM hybrid model in the three classes of BKG, alert, and fall with sensitivity values of 96.23%, 98.59%, and 99.38%, as well as 97.12% in the Accuracy parameter, could provide the best result. Good results have been obtained in other criteria as well.

We also compared our approach with other similar tasks, which, according to the results, were superior to them in all classes.

The noise cancellation process was also performed with a first-time low-pass IIR filter, and retesting showed that it could have a positive effect, especially on the CNN model, and also improved the accuracy of the Fall and Alert classes. In the combined model, the sensitivity parameter values for the BKG, alert, and fall classes are 97.13%, 99.05%, and 99.36%, respectively. For the Accuracy parameter, an accuracy of 97.83% has been obtained.

Therefore, the Conv-LSTM hybrid model with filtered data can provide the best accuracy in all classes and in all evaluation criteria.

The proposed approach for dynamic data sampling led to a more excellent balance between the number of samples in different classes. This has increased accuracy and reduced false alarms. Also, the combination of CNN and LSTM algorithms and using the advantages of these two algorithms have greatly improved the accuracy of fall detection.

However, among the various methods, there is no clear evaluation framework. So it is a bit difficult to evaluate and compare the results somewhat. Lack of access to actual data was one of the limitations of this study, which required us to use datasets with simulated movements in laboratories. This may reduce the accuracy of the results of these systems in real life.

On the other hand, parameters such as age, gender, height, and weight of people and external factors affecting the signals are also effective in the accuracy of fall detection. The impact of these parameters can be seriously considered in future studies of fall detection systems.

7. REFERENCES

1. Florence, C.S., Bergen, G., Atherly, A., Burns, E., Stevens, J. and Drake, C., "Medical costs of fatal and nonfatal falls in older adults", ***Journal of the American Geriatrics Society***, Vol. 66, No. 4, (2018), 693-698. doi: 10.1111/jgs.15304.
2. Qiu, H. and Xiong, S., "Center-of-pressure based postural sway measures: Reliability and ability to distinguish between age, fear of falling and fall history", ***International Journal of Industrial Ergonomics***, Vol. 47, (2015), 37-44. doi: 10.1016/j.ergon.2015.02.004.
3. Organization, W.H., Ageing, W.H.O. and Unit, L.C., "Who global report on falls prevention in older age, World Health Organization, (2008).
4. Zhang, D., Wang, H., Wang, Y. and Ma, J., "Anti-fall: A non-intrusive and real-time fall detector leveraging csi from commodity wifi devices", in International Conference on Smart Homes and Health Telematics, Springer., (2015), 181-193.
5. Santos, G.L., Endo, P.T., Monteiro, K.H.d.C., Rocha, E.d.S., Silva, I. and Lynn, T., "Accelerometer-based human fall detection using convolutional neural networks", ***Sensors***, Vol. 19, No. 7, (2019), 1644. doi: 10.3390/s19071644.
6. Casilari, E., Lora-Rivera, R. and García-Lagos, F., "A study on the application of convolutional neural networks to fall detection evaluated with multiple public datasets", ***Sensors***, Vol. 20, No. 5, (2020), 1466. doi: 10.3390/s20051466.
7. Pannurat, N., Thiemjarus, S. and Nantajeewarawat, E., "Automatic fall monitoring: A review", ***Sensors***, Vol. 14, No. 7, (2014), 12900-12936. doi: 10.3390/s140712900.
8. Xu, T., Zhou, Y. and Zhu, J., "New advances and challenges of fall detection systems: A survey", ***Applied Sciences***, Vol. 8, No. 3, (2018), 418. doi: 10.3390/app8030418.
9. Chen, X., Xue, H., Kim, M., Wang, C. and Youn, H.Y., "Detection of falls with smartphone using machine learning technique", in 2019 8th International Congress on Advanced Applied Informatics (IIAI-AAI), IEEE., (2019), 611-616.
10. Özdemir, A.T., "An analysis on sensor locations of the human body for wearable fall detection devices: Principles and practice", ***Sensors***, Vol. 16, No. 8, (2016), 1161. doi: 10.3390/s16081161.
11. Ren, L. and Peng, Y., "Research of fall detection and fall prevention technologies: A systematic review", ***IEEE Access***, Vol. 7, (2019), 77702-77722. doi: 10.1109/ACCESS.2019.2922708.
12. Liang, S., Chu, T., Lin, D., Ning, Y., Li, H. and Zhao, G., "Pre-impact alarm system for fall detection using mems sensors and hmm-based svm classifier", in 2018 40th Annual International Conference of the IEEE Engineering in Medicine and Biology Society (EMBC), IEEE., (2018), 4401-4405.
13. Wu, Y., Su, Y., Feng, R., Yu, N. and Zang, X., "Wearable-sensor-based pre-impact fall detection system with a hierarchical classifier", ***Measurement***, Vol. 140, (2019), 283-292. doi: 10.1016/j.measurement.2019.04.002.
14. Aziz, O., Musngi, M., Park, E.J., Mori, G. and Robinovitch, S.N., "A comparison of accuracy of fall detection algorithms (threshold-based vs. Machine learning) using waist-mounted tri-axial accelerometer signals from a comprehensive set of falls and non-fall trials", ***Medical & Biological Engineering & Computing***, Vol. 55, No. 1, (2017), 45-55. doi: 10.1007/s11517-016-1504-y.
15. Özdemir, A.T. and Barshan, B., "Detecting falls with wearable sensors using machine learning techniques", ***Sensors***, Vol. 14, No. 6, (2014), 10691-10708. doi: 10.3390/s140610691.
16. Wang, J., Chen, Y., Hao, S., Peng, X. and Hu, L., "Deep learning for sensor-based activity recognition: A survey", ***Pattern Recognition Letters***, Vol. 119, (2019), 3-11. doi: 10.1016/j.patrec.2018.02.010.
17. LeCun, Y., Bengio, Y. and Hinton, G., "Deep learning", ***nature***, Vol. 521, No. 7553, (2015), 436-444. doi: 10.1038/nature14539.
18. Ordóñez, F.J. and Roggen, D., "Deep convolutional and lstm recurrent neural networks for multimodal wearable activity recognition", ***Sensors***, Vol. 16, No. 1, (2016), 115. doi: 10.3390/s16010115.
19. Chen, Y. and Xue, Y., "A deep learning approach to human activity recognition based on single accelerometer", in 2015 IEEE international conference on systems, man, and cybernetics, IEEE., (2015), 1488-1492.
20. Tao, X. and Yun, Z., "Fall prediction based on biomechanics equilibrium using kinect", ***International Journal of Distributed Sensor Networks***, Vol. 13, No. 4, (2017), doi: 10.1177/1550147717703257.
21. Torti, E., Fontanella, A., Musci, M., Blago, N., Pau, D., Leporati, F. and Piastra, M., "Embedding recurrent neural networks in wearable systems for real-time fall detection", ***Microprocessors and Microsystems***, Vol. 71, (2019), 102895. doi: 10.1016/j.micpro.2019.102895.
22. Musci, M., De Martini, D., Blago, N., Facchinetti, T. and Piastra, M., "Online fall detection using recurrent neural networks", arXiv preprint arXiv:1804.04976, (2018). doi: 10.48550/arXiv.1804.04976.
23. Sucerquia, A., López, J.D. and Vargas-Bonilla, J.F., "Sisfall: A fall and movement dataset", ***Sensors***, Vol. 17, No. 1, (2017), 198. doi: 10.3390/s17010198.
24. Rastogi, S. and Singh, J., "A systematic review on machine learning for fall detection system", ***Computational Intelligence***, Vol. 37, No. 2, (2021), 951-974. doi: 10.1111/coin.12441.
25. Usmani, S., Saboor, A., Haris, M., Khan, M.A. and Park, H., "Latest research trends in fall detection and prevention using machine learning: A systematic review", ***Sensors***, Vol. 21, No. 15, (2021), 5134. doi: 10.3390/s21155134.
26. Syed, A.S., Sierra-Sosa, D., Kumar, A. and Elmaghraby, A., "A deep convolutional neural network-xgb for direction and severity aware fall detection and activity recognition", ***Sensors***, Vol. 22, No. 7, (2022), 2547. doi: 10.3390/s22072547.
27. Bourjandi, M., Yadollahzadeh Tabari, M. and Golsorkhtabaramiri, M., "Fuzzy centralized coordinate learning

and hybrid loss for human activity recognition", ***International Journal of Engineering, Transactions A: Basics,***, Vol. 35, No. 1, (2022), 130-141. doi: 10.5829/IJE.2022.35.01A.12.

28. Siddharth, D., Saini, D. and Singh, P., "An efficient approach for edge detection technique using kalman filter with artificial neural network", ***International Journal of Engineering, Transactions C: Aspects,***, Vol. 34, No. 12, (2021), 2604-2610. doi: 10.5829/IJE.2021.34.12C.04.
29. Bourjandi, M., Yadollahzadeh-Tabari, M. and Golsorkhtabaramiri, M., "Combined deep centralized coordinate learning and hybrid loss for human activity recognition", ***Concurrency and Computation: Practice and Experience***, (2022), e6870. doi: 10.1002/cpe.6870.
30. Bourjandi, M., Yadollahzadeh-Tabari, M. and GolsorkhtabariAmiri, M., "Predicting user's movement path in indoor environments using the stacked deep learning method and the fuzzy soft-max classifier", ***IET Signal Processing***, (2022). doi: 10.1049/sil2.12125.
31. Yu, X., Qiu, H. and Xiong, S., "A novel hybrid deep neural network to predict pre-impact fall for older people based on wearable inertial sensors", ***Frontiers in Bioengineering and Biotechnology***, Vol. 8, (2020), 63. doi: 10.3389/fbioe.2020.00063.

Persian Abstract

چکیده

سقوط یکی از مهم‌ترین چالش‌های سلامتی در جامعه است که می‌تواند باعث صدمات شدید و حتی مرگ افراد شود. هدف اصلی این مطالعه، توسعه شبکه‌های عصبی عمیق با استفاده از داده‌های سنسورهای پوشیدنی برای شناسایی سقوط می‌باشد. اکثر مجموعه داده‌ها در این زمینه از مشکل عدم توازن رنج می برند به طوری که نمونه‌های متعلق به کلاس‌های Fall به طور قابل توجهی کمتر از داده‌های کلاس عادی هستند. این مطالعه یک تکنیک نمونه گیری پویا برای افزایش نرخ تعادل بین نمونه های متعلق به کلاس های سقوط و عادی ارائه می دهد تا دقت الگوریتم های یادگیری را بهبود بخشد. از مجموعه داده Sisfall استفاده شده است که در آن، فعالیت انسان‌ها به سه دسته فعالیت عادی(BKG) ، لحظات قبل از سقوط (Alert) و نقش روی زمین (Fall) تقسیم می شود. سه مدل یادگیری عمیق CNN، LSTM و یک مدل ترکیبی به نام-Conv Lstmبر روی این مجموعه داده پیاده‌سازی شدند و عملکرد آنها مورد ارزیابی قرار گرفت. بر این اساس، مدل ترکیبی Conv-Lstm مقادیر ۹۶.۲۳٪، ۹۸.۵۹٪ و ۹۹.۳۸٪ را در پارامتر Sensitivity برای کلاس‌هایBKG، Alert و Fall ارائه می‌کند. برای پارامتر Accuracy نیز موفق شدیم به نرخ ۹۷.۱۲٪ برسیم. علاوه بر این، با استفاده از تکنیک‌های هموارسازی و حذف نویز، می‌توان به میزان دقت ۹۷.۸۳ درصد نیز رسید. نتایج حاکی از برتری مدل پیشنهادی نسبت به سایر مطالعات مشابه دارد.

IJE TRANSACTIONS A: Basics Vol. 35 No. 10, (October 2022) 1959-1966

International Journal of Engineering

Journal Homepage: www.ije.ir

Analytical and Experimental Investigation of Recycled Aggregate Concrete Beams Subjected to Pure Torsion

N. Masne*, S. Suryawanshi

Department of Civil Engineering, S. V. National Institute of Technology, Surat, India

PAPER INFO

Paper history:
Received 29 May 2022
Received in revised form 25 June 2022
Accepted 27 June 2022

Keywords:
Atena-3D
Natural Aggregates Concrete
Nonlinear Analysis
Pure Torsion
Recycled Concrete Aggregates
Replacement Ratio

ABSTRACT

This study presents the ATENA-3D simulation of natural aggregate concrete (NAC) and recycled aggregate concrete (RAC) beams subjected to pure torsion and the beam was validated by the experimental results with corresponding outputs. All the test specimens were 150 mm wide, 250 mm, deep and 1800 mm long. The natural coarse aggregate (NCA) were replaced by coarse recycled concrete aggregate (RCA) at three replacement ratios of 0 %, 50 %, and 100 % to prepare concrete. All the beam specimens were simulated and tested to assess the parameters like torque, twist, crack pattern, stiffness, and toughness in pure torsion. The comparison of ATENA-3D and experimental results showed that torque resistance capacity, stiffness, and toughness of beams decreased as the % of RCA increased in the concrete. A similar torque-twist curve pattern was observed in simulation and experimental studies. All the specimens failed due to torsional cracking. The torsional capacity of the beams in ATENA-3D software was higher by 9.80 %, 10.67 %, and 12.80 % than the experimental results. The results reveal that varying the quantity of RCA in RAC does not compromise the pure torsional behavior of the beam in both methods. Also, it can be concluded that the use of RCA in RAC is acceptable for structural concrete beams in pure torsion.

doi: *10.5829/ije.2022.35.10a.14*

1. INTRODUCTION

Crushing of concrete to generate the coarse aggregate for the manufacturing of fresh concrete is a typical method for producing environment friendly concrete for new infrastructure. This conserves natural resources and eliminates the need for waste concrete dumps. The total availability of RCA in India is about 1.8 million tonnes per year[1]. As a new structural material RAC will help practicing as well as a research engineers to predict not only its bearing capacity but also its deformation capability during the course of loading. Under the uniaxial compression, the behavior of normal-strength RAC develops a stress-strain relationship for the same and there is an empirical expression for RAC [1]. The toughness and ductility index of the RAC decreases as the percentage of RCA increases in the concrete. In addition to this, the test results indicated the RCA content has a remarkable influence on the compressive strength of the concrete [2]. The comparison between experimental and numerical results confirmed that the criterion of failure and mechanical behavior of standard concrete will be applicable to RAC and concluded that the performance dependent failure criterion was suitable for concretes with RCA [3]. The RAC made from the tested cubes and precast concrete columns performed satisfactorily and did not vary considerably from the control concrete performance [4]. The mechanical behavior of wall beams made of RAC showed better structural integrity than conventional brick wall beams [5]. According to Sarsam et al. [6], the torsional behavior of RAC beams was found satisfactory when compared to NAC beams and concluded that the use of RAC in structural beams is practically possible in pure torsion. The experimental seismic torsional behavior of the NAC and RAC beams was found satisfactory [7]. The numerical (Abaqus) and experimental analysis of NAC and RAC beams confirm that both the types of the concrete beam were perform well in seismic torsion [8]. With the increased usage of finite element analysis (FEA)

*Corresponding Author Institutional Email: *nsmasne@gmail.com* (N. Masne)

[1] https://cpcb.nic.in/openpdffile.php?id=TGF0ZXN0RmlsZS8xNTlfMTQ5NTQ0NjM5N19tZWRpYXBob3RvMTkyLnBkZg

Please cite this article as: N. Masne, S. Suryawanshi, Analytical and Experimental Investigation of Recycled Aggregate Concrete Beams Subjected to Pure Torsion, ***International Journal of Engineering, Transactions A: Basics***, Vol. 35, No. 10, (2022), 1959-1966

to address complicated issues ANSYS, ABAQUS, ATENA-3D, and some other FEA software were utilized to analyze the structural concrete elements under a variety of loading reported in the literature [9-13]. The ATENA-3D FEM software was also used to investigate the flexural capacity of a slab, and the results were found consistent with experimental data [14]. Except for the investigation by Sarsam et al. [6], there is a shortage of information in the literature on a pure torsional test of RAC beams in analytical and experimental works. The primary purpose of this comparative study was to examine the effect of RCA in RAC beams on the pure torsional behavior under static loading conditions. This objective was accomplished in two stages. The first stage was a structural laboratory test of NAC and RAC beams, where the deflection and load carrying capacity of all beams were measured and translated into torque-twist curves for further investigation. In the second stage, the experimental results were compared with ATENA-3D software results under pure torsion, for which the model for RAC behavior is used from the literature [1].

2. ATENA-3D ANALYSIS- FINITE ELEMENT MODELLING

ATENA-3D is a FEM-based software used to simulate and analyse reinforced concrete structural elements. All processes to generate model geometry, assign material specifications, simulate loading and support conditions, and monitor structural member reaction under applied force are given in detail. The basic idea of FEM modeling is to divide the mathematical model into non-overlapping geometric components. All of the elements' responses are given in the form of a fixed number of degrees of freedom that are described by an unknown function or a collection of nodes. The mathematical model's answer is then a discrete model, formed by linking or assembling all the pieces. As part of the finite element approach, reinforced concrete may either be modelled as a composite (i.e., the concrete and embedded steel) or as a discrete material model (i.e., the concrete and the reinforcing steel). The finite element approach is particularly suited for superimposing material models for composite material components. In ATENA-3D, numerous constitutive models that account for these effects are established. ATENA-3D's graphical user interface (GUI) provides an efficient and potent environment for solving a wide variety of anchoring problems. ATENA-3D enables computer-based simulations of structural tests. This is the current trend in the area of research and development. Material models of this type can be utilized for virtually all forms of reinforced concrete structural components, and they are particularly useful in the design of structures.

3. MATERIAL MODELS

ATENA-3D's material models can be used with different materials. It also allows to use user defined material models which are very helpful to model the material that is not available in its library.

3. 1. Concrete There are several material models in ATENA-3D's library that depict concrete behavior, but the software allows users to define their own material models. The stress-strain relationship of the structural member's concrete is calculated by testing a specimen under compression. This measured data or any other stress-strain relationship from the literature can be entered into "3D NonlinearCementitious 2 User" to model concrete behavior. Figure 1 shows the user-defined material definition window and the resulting stress-strain curve.

In this study, the 3D FEM simulation software ATENA-3D was utilized to model the experimental results. In order to replicate the behavior of concrete, a smeared crack model, i.e. total strain crack, was chosen since it gives a variable stress-strain relationship for both compression and tension. As illustrated in Figure 1, and Equation (1) the Suryawanshi et al. [2] model was chosen to represent the nonlinear behavior of the concrete in compression for both NAC and RAC.

$$\bar{\sigma} = a(\bar{\varepsilon}) + b(\bar{\varepsilon})^2 + c(\bar{\varepsilon})^3 + d(\bar{\varepsilon})^4 \quad (1)$$

where, $\bar{\sigma}$ (The normalized stress) is the ratio of the stress level under consideration to the peak stress (σ/f_c') and $\bar{\varepsilon}$ (The normalized strain) is the ratio of the strain corresponding to σ and the strain at peak stress$(\varepsilon/\varepsilon_0)$.

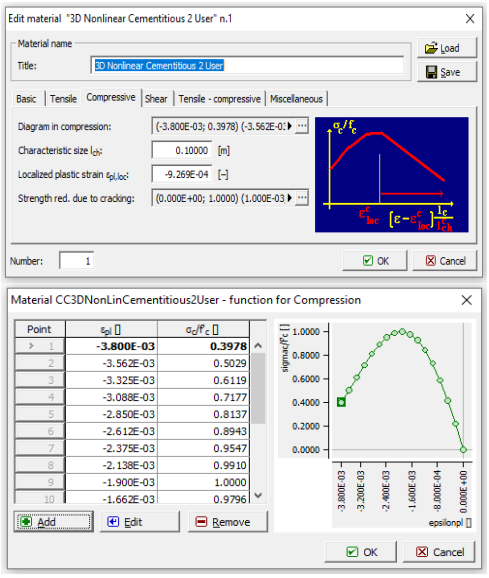

Figure 1. Material model used for concrete

Coefficient a represents the ratio of the initial tangent modulus and the secant modulus corresponding to peak stress (E_{itm}/E_p) and is defined in terms of the RCA replacement level. R is percentage replacement of NCA by RCA.

3. 2. Steel Reinforcement ATENA-3D software allows users to give input actual stress-strain curves of steel reinforcement to mimic its behavior. This provision obviously gives more accurate results compared to that because of the use of an idealized stress-strain relationship for steel. Figure 2 shows the experimental stress-strain curve used as input data for ATENA-3D.

As a result, Figure 3 depicts a comparable stress-strain relationship obtained using ATENA-3D software. It should be noted that additional qualities, such as elastic modulus, are eventually taken care of by ATENA-3D itself on the basis of input data in the form of a stress-strain relationship or empirically determined values.

3. 3. Loading and Supporting Steel Plates 3D Elastic Isotropic material model properties were applied for simulation as shown in Figure 4. This 3D Elastic Isotropic Material model is suggested for the support and loading steel plates because, it is commonly required to avoid any unrealistic stress concentration in nonlinear analysis. As this may cause early cracking or failure in

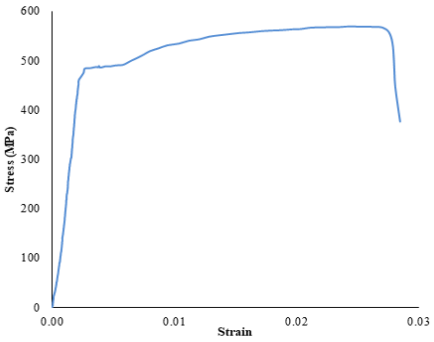

Figure 2. Measured stress-strain relationship for steel rebar, 12 mm diameter

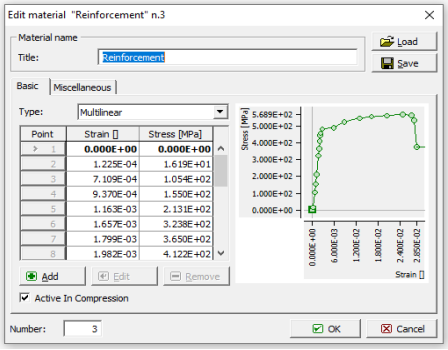

Figure 3. Experimental stress-strain relationship for steel reinforcement

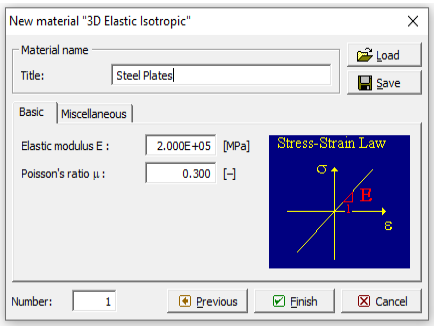

Figure 4. Material properties used for steel plates

the supporting and loading steel plates. If the support conditions are applied at single nodes, this may create strong stress concentrations affecting the analysis results [10]. The same properties of steel plates were also reported in literature [10, 14].

3. 4. Geometry Definition Figure 5 shows the geometry of the concrete beam and it was generated with the reinforcement (both longitudinal and transverse) modeled as bar (truss) elements in ATENA-3D software. Thermo-Mechanically Treated deformed steel reinforcement bars were used in the experiments and the same bars were modeled in ATENA-3D. The 2 bars of 10 mm diameter for the top and 3 bars of 12 mm diameter at bottom and 8 mm diameter bar for stirrups at 100 mm spacing were used for all the beam. The 3 bars of 12 diameters were used in the top and bottom of lever arms with 8 mm diameter stirrups with 50 mm spacing, as shown in Figure 6. Steel plates of small thickness were used for loading the beam to simulate the small contact (theoretically line contact) of the loading rollers. At support also steel plates were used as the channel caps were used upon the supporting rollers.

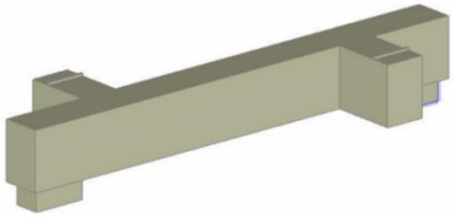

Figure 5. Geometry of the beam specimen in ATENA-3D

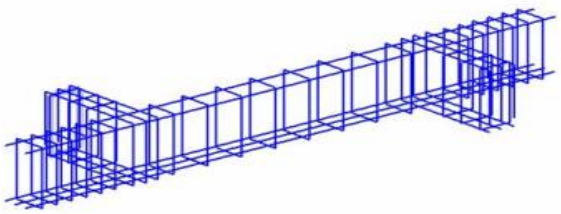

Figure 6. Reinforcement created in ATENA-3D

3. 5. Finite Element Mesh and Element Type Isoperimetric formulations with linear and/or quadratic interpolation functions are used for the majority of ATENA-3D components. The isoperimetric formulation of one-dimensional, two-dimensional, and three-dimensional elements is considered to be one of the "classic" formulations of elements. This is very important, particularly in nonlinear analysis. In ATENA-3D software, 3D solid brick hexahedron and tetrahedron elements can be used to construct FE mesh. The element type (i.e. shape function) is linear or quadrilateral depending on the needed accuracy. Figure 7 depicts the use of tetrahedral elements of 50 mm size in this study.

3. 6. Boundary Conditions, Loading and Monitoring Points The load was applied to the beam models as "prescribed deformation" located in the middle of the loading plate's upper surface. The vertical (i.e., z-direction) movement of the support plate was restrained by line support positioned along the middle line of the plate's bottom surface. As the rollers were free to rotate about the longitudinal axis (i.e. x-direction) only end nodes of the line support were restrained against translation. The monitoring point to record the load was positioned in the center of the top surface of the load plates, where the specified deformation was applied, as depicted in Figure 8. The point of the deflection observers was at the same point where the deflection was considered. After creating the geometry and necessary inputs analysis of the model is done in the processing (run) mode.

4. EXPERIMENTAL INVESTIGATION

4. 1. Materials Grade 53 ordinary portland cement following the requirements of IS: 12269-2013 [15], was used during the experiment. Locally available white river sand complying with zone II of standard IS 383: 1970 (reaffirmed in 2016) [16], was used as fine aggregate (FA) (fineness modulus = 2.85). NCA of nominal maximum size 20 mm conforming to the definite coarse aggregate grading limits of IS 383:1970 (reaffirmed 2016) [16], were used. The RCA was acquired by treating laboratory-tested concrete samples using a mechanical breaker and jaw crusher. RCA was manually blended within the coarse aggregate grading limitations established in IS 383-1970. (Reaffirmed 2016) [16]. There were two size fractions of coarse aggregate: 4.75–10 mm and 10–20 mm used in the experimental work for concrete. The 0 %, 50 %, and 100 % replacement of RCA consider as R0, R50, and R100 concrete for beams. Thermo-Mechanically Treated deformed steel reinforcement bars used in the experiment and simulation were discussed in section 3.4. According to IS 10262 [17], the absolute volume method was used to design all three types of M30 grade NAC and RAC mixture, and IS 456 [18] was followed for the casting of concrete. According to the IS 456 [18], potable tap water was used for the purpose of mixing and curing the concrete. A commercially available polycarboxylic ether-based High-Range Water Reducing admixture (HRWRA), conforming to IS 9103:1999 (1999b) [19], was used to achieve the desired workability of the concrete in this experimental work. Plastic-coated plywood forms were used for torsion beams. 150 mm diameter and 300 mm in length cylinders were used to cast the concrete cylinder for compression and tensile tests. All the beam specimens were covered with gunny bags in the lab on a level surface for 28 days curing. All the cylinders were immersed in a water tank for curing until tested.

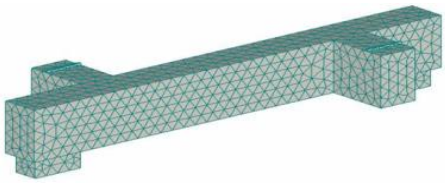

Figure 7. FE mesh of tetrahedral elements

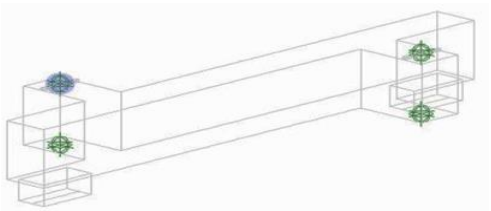

Figure 8. Position of monitoring points to record load and deflection

4. 2. Test Setup and Instrumentation The test setup was designed to test the beam in pure torsion. Figure 9 shows the experimental test setup for testing beams in pure torsion. The tested beams were progressively loaded into the center of the steel spreader beam with a small load increment till failure by a 1000 kN capacity of hydraulic jack. Two lever arms of 250 mm in length,150 mm wide, and 250 mm in depth were provided at 1000 mm distance on the opposite sides of the beam to apply the load at the top and to measure the deflection at the bottom. The beams were supported by rollers and the load was applied through a spreader steel beam resting on loading rollers. Vertical deformations in the reinforced concrete beam were recorded by dual linear variable displacement transducers (LVDTs) located below the lever arms of the torsion span. The data from LVDT and the load sensor were attached to the data acquisition system (DAS). The recorded data were a crack pattern, ultimate torque, and angle of twist for all beams. The ropes were used to tie the hydraulic jack, load cell, and spreader beam for safety purposes which was not affecting the reading, at any stage of testing.

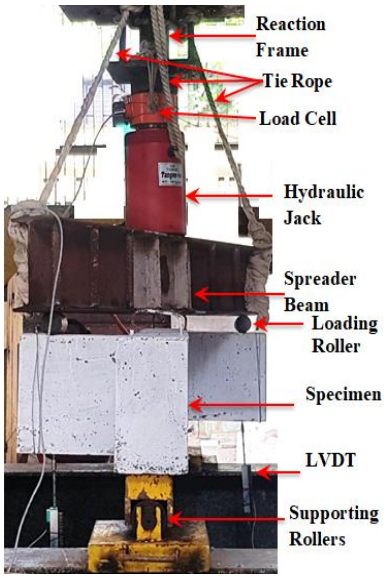

Figure 9. Experimental test set-up for testing beams in pure torsion

5. RESULTS AND DISCUSSION

In ATENA-3D software, a simulation of the NAC and RAC beam was performed using a modified version of the Newton–Raphson method. This modified method maintains equilibrium in the tolerance for displacement iteration and keeps the load increase constant, allowing for accurate loading values. This method creates a set of nonlinear equations using incremental step-by-step analysis, where the stiff matrix of the first equation is used to save time [14]. For optimal results, a mixture of the full and modified Newton–Raphson techniques has been used in practice. Finally, the behavior of modeled beams was studied, including torque-twist behavior, crack patterns and these models results were compared with experimental work in pure torsion.

5. 1. Effect of RCA on Compressive and Tensile Strength of RAC The mean of the three-cylinder test data was used to calculate the compressive and tensile strengths of all three types of concrete. With an increases the percentage of RCA in concrete, compressive and tensile strength decreases, and a similar trend was reported in the literature [6]. Figure 10 compares NCA and RCA concrete compressive and tensile strengths. The results were as expected, i.e., reducing compressive and tensile strength decreased ultimate torque, and confirmed the findings in this work. When the compressive strength of all simulated beams was reduced, the torque resistance capacity significantly changed.

5. 2. Cracking Behavior of NAC and RAC Beams in Pure Torsion The propagation of cracks and

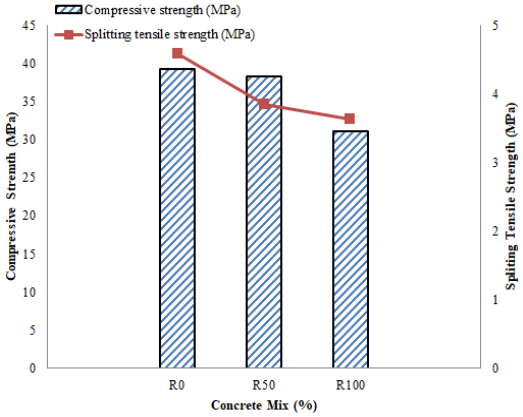

Figure 10. Effect of RCA replacement on compressive strength and tensile strength of concrete

failure patterns were observed as part of this study. At the start of the simulation and experimental test, when the load increased linearly, no cracks were observed in the both methods. The behavior of the beam was generally elastic until it cracked, and torsion mostly resisted by concrete. The cracking patterns generated in ATENA-3D analysis and experientially obtained cracking patterns are existing in Figure 11. It was seen that in all the beams with different percentage of replacement of RCA, the cracking pattern more or less similar, the same failure pattern reported in the literature [8]. The first crack has been generated practically at constant load in the range of 34 to 36 KN in all beam specimens. The first diagonal torsional crack was initiated from the center of longer side of all beams in both method. All the propagated cracks were inclined at an angle of 45° to the longitudinal axis of beam [8]. Number of cracks observed in NAC beams less than the number of cracks in 50 % and 100 % RCA in RAC beams when test was finished. The failure became in the beam with the widening of one of these cracks in both test. However, the peak load was decreased with an increase in the percentage of RCA in concrete. This shows that RAC and NAC beams were behave similarly in ATENA-3D and experiment.

5. 3. Effect on Torsional Strength and Angle of Twist of NAC and RAC Beams Each beam specimen was tested in a load frame in order to measure the torsional capacity and angle of twist and to study the effect of RCA on the RAC beam in pure torsion. The continuous monitoring of each load increment and the corresponding deflection was carried out. The load-deflection data was transformed into torque-twist data and the test results have been compiled for further analysis. The torque resisting capacity and the angle of twist of the tested NAC and RAC beams are reported in Table 1, based on ATENA-3D and experimental data.

The torsional capacity of the beams in ATENA-3D software was higher by 9.80 %, 10.67 %, and 12.80 %,

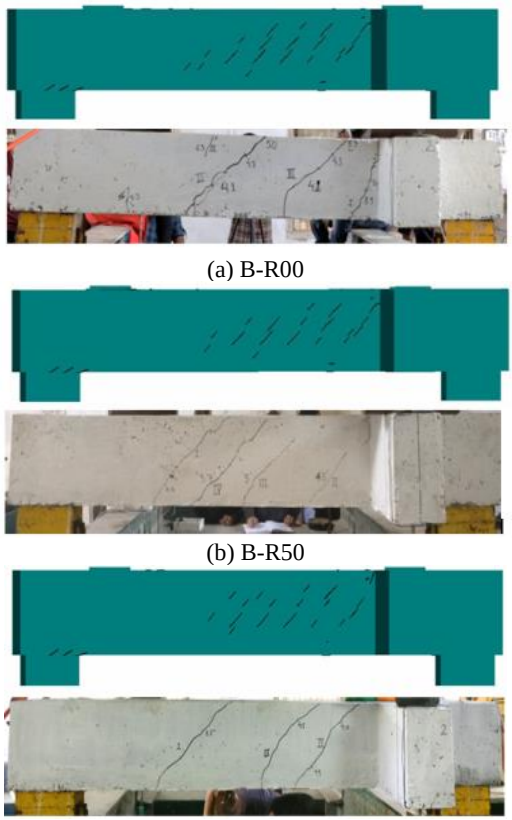

(a) B-R00

(b) B-R50

(c) B-R100

Figure 11. Comparison of measured and ATENA-3D simulated crack patterns at peak load

respectively than the experimental value for 0%, 50%, and 100% replacement of RCA in RAC beams. It should be noted that the torsional capacity of the beam was higher in ATENA-3D than the experimental value. This is because of idealized support conditions. Moreover, the roller supports which were actually used in the experiment could not be modeled in ATENA-3D due to its limitations regarding establishing the line contacts [10].

5. 4. Effect on Torque-Twist Curve of NAC and RAC Beams For all the tested beams, the relationship between torque and angle of twist was as usual, with almost linear behavior followed by nonlinear behavior until failure, as illustrated in Figure 12. It has been observed that the torque-twist curves obtained from the software analysis and experiments were almost similar for NAC and RAC beams, parallel tendency described in the prior works [9]. The experimental and numerical recorded peak value of torsional moment was 9.20 kN.m and 10.20 kN.m for the beam specimen with 0% replacement of RCA, 8.95 kN.m, and 10.02 kN.m for 50% replacement of RCA, and 7.50 kN.m and 8.60 kN.m for 100% replacement of RCA, respectively. The

TABLE 1. Comparison of torque-twist of NAC and RAC beams

Method/Beam ID		B-R00	B-R50	B-R100
Measured	Torque (kN.m)	9.20	8.95	7.50
	Twist (rad/m)	0.044	0.045	0.048
ATENA-3D	Torque (kN.m)	10.20	10.02	8.60
	Twist (rad/m)	0.023	0.023	0.024

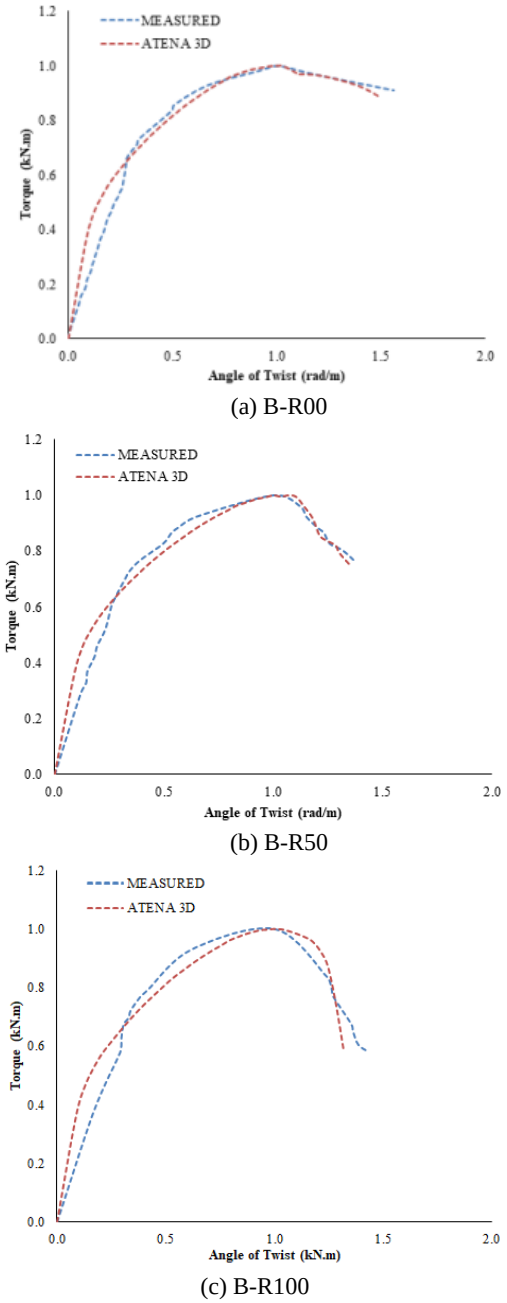

(a) B-R00

(b) B-R50

(c) B-R100

Figure 12. Torque-Twist curve for all beam specimens (in normalized form)

measured corresponding angle of twist was 0.044 rad/m and 0.023 rad/m, 0.045 rad/m and 0.023 rad/m and 0.048 rad/m and 0.024 rad/m, respectively. The following salient observations can be placed on record in light of this study. The torque-twist behavior of beams B-R00 and B-R50 were identical until cracking and had an approximately similar trend up to the maximum torque. Then, the B-R50 beam curve turns as the curve of B-R100. The area under the torque-twist curve drops as the level of RCA replacement rises. An addition of RCA in concrete leads to a decrease in slopes of torque-twist curves after the peak, indicating the brittleness nature of the RAC than NAC.

5. 5. Effect on Torsional Stiffness and Toughness of NAC and RAC Beams The torsional stiffness of all the beams was evaluated at ultimate states for analytical and experimental methods, which shown as the % of RCA increases in the concrete the stiffness of RAC beams decreases [7] as shown in Table 2. Because of decreasing the stiffness of beams, the angle of twist increases after the ultimate state in pure torsion for the entire specimen. The analytical stiffness higher than the measured stiffness was observed for all the beams. The toughness is the property of the strength and ductility of beams. It was appropriately considered from the entire area in the torque-twist curve. The toughness was reduced as the % of RCA increased [2] in concrete as depicted in Table 2 for both methods. The experimental torsional toughness was found lower than the analytical values for all the beams.

5. 6. Comparison of Torsional Moment Using Standards In order to assess whether current code provisions on the design of pure torsional members made of NAC are applicable to the RAC members in their present form or not, widely accepted codes such as IS: 456 [18] based on Skew Bending Theory [18, 20] and ACI: 318 [21] which is based on Space Truss Analogy [21-23] and have been considered for comparison. The experimentally measured and ATENA-3D obtained values of ultimate torsional moments were compared with international standards. The outcome of this limited exercise is presented in Figure 12. It has been seen that the entire method gives safe values with varying degrees

TABLE 2. Torsional stiffness and toughness for measured and analytical method

Method/Beam ID		B-R00	B-R50	B-R100
Stiffness	Measured (kNm^2)	209.09	198.89	156.25
	ATENA-3D (kNm^2)	443.47	435.65	358.33
Toughness	Measured (kNm/m)	1.263	1.039	1.038
	ATENA -3D (kNm/m)	1.303	1.053	1.048

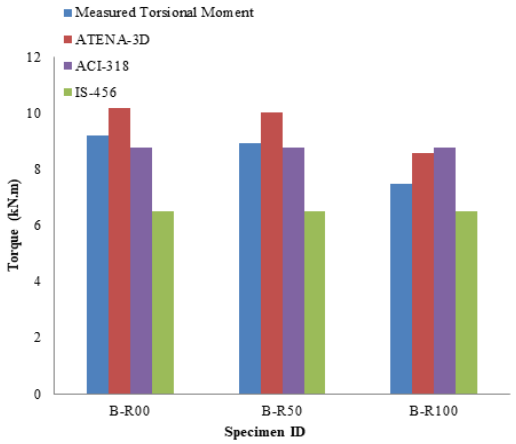

Figure 12. Comparison of torsional moment with different methods

of accuracy. FEA can be used to predict the behavior of reinforced NAC and RAC beams. Finally, the results reveal that varying the quantity of RCA in the RAC beam does not compromise pure torsional behavior in both methods.

6. CONCLUSION

In this comparative work, the effect of RCA on the pure torsional behavior of RAC beams was numerically investigated and compared with the outcomes of experimental work.

- As the percentage of RCA increased in concrete, the compressive and tensile strength decreased.
- The experientially obtained cracking patterns and cracking patterns generated in ATENA-3D analysis have been compared. It was seen that in all beams with different percentage of replacement of RCA, the cracking patterns were more or less comparable.
- The torsional capacity of the beams in ATENA-3D software was higher by 9.80 %, 10.67 %, and 12.80 %, respectively than the experimental value for 0 %, 50 %, and 100 % replacement of RCA in RAC beams. Both the studies have confirmed that the torsional capacity of the RAC beam was marginally less than the NAC beams.
- The comparison of experimentally obtained torque-twist curves and ATENA-3D analysis torque-twist curves was found similar, however, not identical in nature.
- The stiffness and toughness were reduced as the percentage of RCA increased in RAC in both methods.
- After comparing the torsional moment of the beam with international standards, all beams were given safe values with varying degrees of accuracy.

- The ATENA-3D simulation program can be used to predict the behavior of NAC and RAC beams in pure torsion with due care.
- When comparing these two approaches, the usage of RCA in RAC is suitable for structural concrete beams in pure torsion.

7. REFERENCES

1. Suryawanshi, S., Singh, B. and Bhargava, P., "Equation for stress–strain relationship of recycled aggregate concrete in axial compression", ***Magazine of Concrete Research***, Vol. 70, No. 4, (2018), 163-171. https://doi.org/10.1680/jmacr.16.00108
2. Suryawanshi, S., Singh, B. and Bhargava, P., Characterization of recycled aggregate concrete, in Advances in structural engineering. 2015, Springer.1813-1822.
3. Folino, P. and Xargay, H., "Recycled aggregate concrete–mechanical behavior under uniaxial and triaxial compression", ***Construction and Building Materials***, Vol. 56, No., (2014), 21-31. doi. https://doi.org/10.1016/j.conbuildmat.2014.01.073
4. Malešev, M., Radonjanin, V. and Marinković, S., "Recycled concrete as aggregate for structural concrete production", ***Sustainability***, Vol. 2, No. 5, (2010), 1204-1225.
5. Zhang, M., Fu, X.J., Wu, Y. and Sun, H., "Test study on the mechanical behavior of recycled aggregate concrete wall-beam", in Applied Mechanics and Materials, Trans Tech Publ. Vol. 351, No. Issue, (2013), 260-263.
6. Sarsam, K.F., Salih, N. and Hussein, M., "Assessment of reinforced recycling aggregate concrete beams under torsional moment", ***International Journal of Engineering & Technology***, Vol. 7, No. 4.20, (2018), 623-628. doi: 10.14419/ijet.v7i4.20.27403.
7. Wang, X., Liu, B. and Zhang, C., "Seismic behavior of recycled aggregate concrete beams under cyclic torsion", ***Construction and Building Materials***, Vol. 129, (2016), 193-203. doi. http://dx.doi.org/10.1016/j.conbuildmat.2016.10.101
8. Fu, J.L., Liu, B.K., Ma, J.W. and Zhou, H., "Experimental study on seismic behavior of recycled aggregate concrete torsion beams with abaqus", in Advanced Materials Research, Trans Tech Publ. Vol. 1079, (2015), 220-225.
9. Cervenka, V. and Cervenka, J., "Atena program documentation–part 2-2: User's manual for atena3d", ***Prague, República Theca***, (2003).
10. Červenka, J., Procházková, Z. and Sajdlova, T., "Atena program documentation, part 4-2, tutorial for program atena 3d", ***Cervenka Consulting, Prag***, (2013).
11. Phani Prasanthi, P., Sivaji Babu, K. and Eswar Kumar, A., "Waviness effect of fiber on buckling behavior of sisal/carbon nanotube reinforced composites using experimental finite element method", ***International Journal of Engineering***, ***Transactions C: Aspects,*** Vol. 34, No. 12, (2021), 2617-2623. https://doi.org/10.5829/ije.2021.34.12C.06
12. Shadmand, M., Hedayatnasab, A. and Kohnehpooshi, O., "Strengthening of rc beams using steel plate-fiber concrete composite jackets (finite element simulation and experimental investigation)", ***International Journal of Engineering***, ***Transactions A: Basics,*** Vol. 35, No. 1, (2022), 73-92. https://doi.org/10.5829/ije.2022.35.01a.07
13. Beiram, A. and Al-Mutairee, H., "Effect of using waste rubber as partial replacement of coarse aggregate on torsional strength of square reinforced concrete beam", ***International Journal of Engineering***, ***Transactions B: Applications***, Vol. 35, No. 2, (2022), 397-405. https://doi.org/10.5829/ije.2022.35.02b.16
14. Kaur, S., Kaur, P., Kaur, I. and Gupta, S., "Nonlinear analysis of two-layered shcc and reinforced concrete composite slabs", ***Innovative Infrastructure Solutions***, Vol. 7, No. 1, (2022), 1-11. https://doi.org/10.1007/s41062-021-00654-2
15. "Bis is12269-13, ordinary portland cement, 53 grade-specification, bureau of indian standards", (2013).
16. "Bis is383-1970 [reaffirmed 2016], specification for coarse and fine aggregates from natural sources for concrete, bureau of indian standards, " (2016).
17. "Bis is10262-09, concrete mix proportioning-guidelines, bureau of indian standards, " (2009).
18. "Bis (bureau of indian standards) is 456: 2007 'indian standard plain and reinforced concrete code of practice', bureau of indian standards, new delhi ", (2007).
19. "Bis is9103-99, concrete admixtures specification, bureau of indian standards," (1999).
20. Subramanian, N., "Design of reinforced concrete structures.1st ed. , Oxford University Press:, (2013), 306-333.
21. Wight, J., Barth, F., Becker, R., Bondy, K., Breen, J., Cagley, J., Collins, M., Corley, W., Dolan, C. and Fiorato, A., "Aci committee 318," building code requirements for structural concrete (aci 318-05) and commentary (aci 318r-05)", ***Am. Concr. Institute, Farmingt. Hills, MI***, (2003), 430.
22. Wight, J.K. and MacGregor, J.G., "Reinforced concrete, Pearson Education UK, (2016).
23. Pillai., S., U. and Menon, D., "Reinforced concrete structures., Tata mcgraw-hill, (2009).

Persian Abstract

چکیده

این مطالعه شبیه‌سازی ATENA-3D از بتن سنگدانه طبیعی (NAC) و تیرهای بتن سنگدانه بازیافتی (RAC) را ارائه می‌دهد که در معرض پیچش خالص قرار گرفته‌اند و تیر با نتایج تجربی با خروجی‌های مربوطه تأیید شد. تمام نمونه های آزمایشی دارای عرض ۱۵۰ میلی متر، عمق ۲۵۰ میلی متر و طول ۱۸۰۰ میلی متر بودند. سنگدانه درشت طبیعی (NCA)با سنگدانه بتن بازیافتی درشت (RCA)در سه نسبت جایگزینی ۰٪، ۵۰٪ و ۱۰۰٪ برای آماده سازی بتن جایگزین گردید. تمام نمونه‌های تیر برای ارزیابی پارامترهایی مانند گشتاور، پیچش، الگوی ترک، سختی و چقرمگی در پیچش خالص، شبیه‌سازی و آزمایش شدند. مقایسه ATENA-3D و نتایج تجربی نشان داد که ظرفیت مقاومت گشتاور، سختی و چقرمگی تیرها با افزایش درصد RCA در بتن کاهش می‌یابد. الگوی منحنی گشتاور–پیچش مشابهی در شبیه‌سازی و مطالعات تجربی مشاهده شد. تمام نمونه ها به دلیل ترک خوردگی پیچشی شکست خوردند. ظرفیت پیچشی تیرها در نرم افزار ATENA-3D به میزان ۹/۸۰ درصد، ۱۰/۶۷ درصد و ۱۲/۸۰ درصد بیشتر از نتایج تجربی بود. نتایج نشان می‌دهد که تغییر مقدار RCA در RAC رفتار پیچشی خالص تیر را در هر دو روش به خطر نمی‌اندازد. همچنین می توان نتیجه گرفت که استفاده از RCA در RAC برای تیرهای بتنی سازه ای در پیچش خالص قابل قبول است.

IJE TRANSACTIONS A: Basics Vol. 35 No. 10, (October 2022) 1967-1980

International Journal of Engineering

Journal Homepage: www.ije.ir

Glutaraldehyde: Introducing Optimum Condition for Cross-linking the Chitosan/Gelatin Scaffolds for Bone Tissue Engineering

F. Banafati Zadeh, A. Zamanian*

Department of Nanotechnology and Advanced Materials, Materials and Energy Research Center, Karaj, Iran

PAPER INFO

Paper history:
Received 24 January 2022
Received in revised form 18 May 2022
Accepted 15 June 2022

Keywords:
Bone Tissue Engineering
Chitosan
Cross-linking
Gelatin
Glutaraldehyde

ABSTRACT

Large bone defects caused by trauma or disease needs extra intervention. Gelatin/chitosan complex is one of the most valuable compositions for bone healing, but fast degradation in aqueous solution and low mechanical properties increase the need for cross-linking agent. The cross-linker concentration and cross-linking method had a significant effect on the properties of fabricated scaffolds. Here, three different cross-linking methods of Glutaraldehyde (GA), including addition to the solution, vapor exposure, and immersion, were studied by different in-vitro analyses to find the best GA cross-linker concentration and cross-linking method. Scanning electron microscopy showed homogeneous microstructures in all samples. Fourier transform infrared spectrophotometry revealed cross-linking reactions in all samples. Swelling ratio and biodegradation ratio was reduced by increasing cross-linking concentration and exposure time. Nonetheless, higher cross-linker concentration and exposure time improved mechanical properties, while it seems the cross-linking exposure time had more effect than concentration. Accordingly, GA (1 wt%) cross-linked scaffold with solution addition method showed suitable performance with 39.3° contact angle, 1.45±0.05 MPa compressive strength, 22.31±1.3 (%) swelling ratio, and 26.33±4.47 (%) biodegradation ratio. In-vitro experiments indicated cells were spread all over the scaffolds with higher than 80 (%) cell viability in all time points. The expression of alkaline phosphatase (ALP) and osteo-related genes (osteocalcin and related transcription factor 2) were improved during 14 days of cell incubation and showed the high capacity of the scaffold support in mineralization and osto-differentiation. Therefore GA (1 wt%) cross-linked scaffold with solution addition was introduced as the best candidate for bone repair and further studies.

doi: *10.5829/ije.2022.35.10A.15*

1. INTRODUCTION

The growing older population increased the need for bone replacement all around the world [1]. Bone is known as the most frequently transplanted organ after blood [2]. Large bone defects cannot be regenerated naturally and required external intervention [3, 4]. Drawbacks of autografts and allografts such as additional defect sites, low number of donors, and disease transmission limited their usage and introduced tissue engineering as a novel proper substitution [5]. Tissue engineering combines cell, scaffolds, and biological factors to mimic the defect site's extracellular matrix (ECM) [6, 7].

A favorable scaffold should be biocompatible, biodegradable, highly porous with interconnected pores for nutrition and oxygen flow with sufficient mechanical strength, and provide a suitable microenvironment for cell adhesion, proliferation, and growth [8, 9]. To date, several polymers have been used for different biomedical applications and the fabrication of bone tissue engineering scaffolds [10-15]. Chitosan, a biocompatible, biodegradable natural polysaccharide derived from chitin of crustaceans exoskeletons, has gained a lot of attention in tissue engineering [16]. The advantage of chitosan, such as biocompatibility, biodegradability, antibacterial properties, and non-toxicity, made it popular for bone tissue engineering and drug delivery [17-19]. However, chitosan cannot provide

*Corresponding Author Institutional Email: a-zamanian@merc.ac.ir (A. Zamanian)

Please cite this article as: F. Banafati Zadeh, A. Zamanian, Glutaraldehyde: Introducing Optimum Condition for Cross-linking the Chitosan/Gelatin Scaffolds for Bone Tissue Engineering, ***International Journal of Engineering, Transactions A: Basics***, Vol. 35, No. 10, (2022), 1967-1980

a suitable mimicked-substrate for cell functionalization; accordingly, composite structure fabrication can compensate for this problem. Therefore, gelatin, a natural and water-soluble biopolymer that is obtained from the denaturation of collagen [20, 21], can be the suitable choice for fabrication of regenerative bone substitutes due to the presence of Arg-Gly-Asp (RGD)-like sequences which can enhance cell adhesion and proliferation [22].

Although chitosan/gelatin composition has been previously used as the scaffold compound in bone tissue engineering applications [23], it should be cross-linked before usage to enhance mechanical and chemical stability as well as long-lasting the scaffolds [20]. Cross-linking is chemical or physical bonds between polymer chains to modify mechanical, biological, and degradation properties [24]. There are different techniques typically in three physical, chemical, enzymatic categories for cross-linking chitosan and gelatin [25]. The physical cross-linking revealed some drawbacks such as low cross-linking degree and mechanical properties. Lee et al. [26] used e-beam physical cross-linking, while the higher e-beam dose reduced the molecular weight and as a result decreased previous cross-linking effects. Furthermore, it was not satisfying in bulk gelatin samples. In addition, enzymatic cross-linking may show low cross-linking efficiency. Chemical agents addition is the most often method among the mentioned methods due to its easiness and high output crosslinking [27, 28]. As a result, here we used chemical cross-linking manner of gelatin and chitosan. Among different kinds of gelatin and chitosan cross-linkers, glutaraldehyde (GA) is one of the most popular cross-linkers due to its inexpensive, availability, and high efficiency [29]. Cross-linking chitosan and gelatin with GA is very efficient because of the large number of the amine and hydroxyl groups in their chemical composition [30]. Different kinds of cross-linking manners suggested for GA such as solution addition [31], vapor [32], and immersion [33]. Badawy et al. [20] added different concentrations of GA to chitosan/alginate/gelatin gel spheres. Higher GA concentration formed more rigid constructs with lower swelling capacity. The other cross-linking method is vapor cross-linking, which is one of the favorable methods due to its easy control and inhibiting structure collapsing of the scaffolds [34]. Zhu et al. [34] used GA vapor for cross-linking carboxyethyl chitosan and polyvinyl alcohol scaffolds. Their results demonstrated that the constructs' stability improved after vapor cross-linking while maintaining their high cell viability. In another study, the freeze-dried scaffolds were soaked in 1 wt.% GA for cross-linking followed by deionized water immersion to remove the extra amount of GA. The cellular and mechanical investigations revealed that GA cross-linked gelatin/chitosan/nanobioglass had proper durability with favorable cellular adhesion [35, 36].

Although several articles have been presented on the cross-links of gelatin and chitosan, as far as we know, there is no reference article comparing different cross-linking methods when using GA for bone tissue engineering applications and the need for a comprehensive article to examine and compare cross-linkers concentration and cross-linking method is felt. In this study, biocompatible gelatin/chitosan scaffolds fabricated by freeze-drying technique and the effect of cross-linker concentration and three different GA cross-linking methods (solution addition, vapor cross-linking, and cross-linking immersion) on gelatin/chitosan scaffolds have been investigated. For this, the effect of cross-linker on the morphological and pore size was evaluated. Then, the chemical interactions, swelling, degradation, and mechanical behavior of each scaffold were studied. Contact angle measurement was conducted on the selected scaffold with more favorable properties for bone tissue replacement. Finally, optimum GA cross-linked scaffolds' capacity for cell adhesion, proliferation, and differentiation was studied.

2. MATERIALS AND METHODS

2. 1. Aterials Gelatin (M_w =40–50 KDa), glutaraldehyde (25%, d = 1.058 g/cm^3), ethanol (M_w=46.07 g/mol), and acetic acid ($M_{w=}$ 60.05 g/mol) were purchased from Merck Co. Ltd. (Darmstadt, Germany). Chitosan (M_w= 190–310 kDa, DD=75– 85%), thiazolyl blue tetrazolium bromide (MTT, M_w= 414.32 g/mol), p-nitrophenyl phosphate (pNPP, tablet), and dimethyl sulfoxide (DMSO, 1X) were purchased from Sigma Co. Ltd. (Massachusetts, USA). Phosphate buffer saline powder (PBS, pH 7.2– 7.4) was purchased from Aprin advanced technology development Co. Ltd. (Tehran, Iran). Alkaline phosphatase kit (ALP) was purchased from MAN Co. Ltd. (Tehran, Iran). Dulbecco's Modified Eagle's medium (DMEM), fetal bovine serum, penicillin-streptomycin were purchased from Gibco-BRL, Life Technologies Co. Ltd. (N.Y., USA). All the chemicals were analytical grade and were used without any purification. All aqueous solutions were prepared with deionized (DI) water.

2. 2. Fabricating of GA Cross-linked Scaffolds To prepare chitosan/gelatin (2 wt.%) solution, chitosan powder (3g) was added to the acetic acid (2 M, 300 ml) under the stirring condition at 35 ℃ for 24 h. Then, gelatin (3g) was added to the solution under stirring conditions, and stirring was continued for 5 h at 35 ℃ to prepare a homogenous solution.

In order to fabricate GA cross-linked scaffolds, three cross-linking manners (solution addition, immersion, and vapor) were applied. For solution addition GA cross-linking, 0/5 and 1 (wt.%), GA was added to 30 ml

chitosan/gelatin solution under stirring condition for 0.5 h to obtain a homogeneous solution. Then, the cross-linked contained solution was transferred to the freeze-drier. For this purpose, the as-prepared solutions (contained or non-contained cross-linking agent**)** were poured into aluminum cylinders made of aluminum sheets with a diameter of 1.0 mm and height of 170 mm and kept at -20 ℃ for 24 h then freeze-dried at -50 ℃ and 0.5 torr for 48 h (Pishtaz Equipment Engineering co., Iran). The freeze-dried samples were then cut as discs with 10 mm in diameter and 15 mm in height.

For vapor and immersion cross-linking, the prepared gelatin-chitosan solution was freeze-dried to create chitosan/gelatin scaffolds at the first step. The applied freeze-drying conditions were the same as the earlier mentioned conditions. Then, some cross-linker free scaffolds were selected for GA vapor cross-linking and moved to a sealed desiccator containing 10 ml of 25% aqueous GA solution in a Petri dish. The scaffolds were placed on a shelf in the desiccator in the exposure of GA vapor for 6, 24, and 48 h at room temperature. After cross-linking, the cross-linked scaffolds were placed in a hood for 2 h followed by deionized water soaking at 37◦C for 1 day. The final scaffolds were dried at 60°C for 24 h.

The other freeze-dried scaffolds were cross-linked by GA immersion. So, the scaffolds were immersed in 0.5, 1, and 2 wt. % GA solution for 1 and 24 h at 37 °C. Then, the scaffolds were washed with deionized water for 2 min followed by 1 h immersion in ethanol for unreacted GA removing. The samples were dried at room temperature for 24 h. The prepared sample codes were summarized in Table 1.

TABLE 1. The compositions of fabricated scaffolds

Code	Base	GA Concentration (wt. %)	Method	Time (h)
Control	2.0 wt.% chitosan/gelatin	----	----	-
GA0.5S		0.5 wt. %	Adding to the solution	0.5
GA1S		1 wt. %	Adding to the solution	0.5
GAV-6		25 wt. %	Vapor	6
GAV-24		25 wt. %	Vapor	24
GAV-48		25 wt. %	Vapor	48
GA0.5I-1		0.5 wt. %	Immersion	1
GA0.5I-24		0.5 wt. %	Immersion	24
GA1I-1		1 wt. %	Immersion	1
GA1I-24		1 wt. %	Immersion	24
GA2I-1		2 wt. %	Immersion	1
GA2I-24		2 wt. %	Immersion	24

2. 3. Characterization

Morphology observations: The morphology of the fabricated scaffolds was observed using scanning electron microscopy (SEM, Vega, Czech Republic) at an accelerating voltage of 5 kV. A thin layer of gold was coated on the samples before SEM observation.

Fourier transform infrared spectroscopy (FTIR): In order to investigate the chemical functional groups of the prepared scaffolds, FTIR spectroscopy was performed. Therefore, a Perkin-Elmer Spectrum 400 Fourier transfer infrared (FTIR) spectrophotometer in the wavenumber range of 400–4,000 cm^{-1} was used.

Water-scaffold interactions: The swelling (water absorption) capacity of the prepared scaffolds was calculated using Equation (1) after immersion of the round samples for 5, 30, 60, 120 min in 15 ml in the PBS solution at 37 ± 0.5 °C [37]:

$$Absorption(\%) = \left|(W_w - W_d)/W_d\right| \times 100 \quad (1)$$

where W_d is the weight of the dried scaffold and W_w is the weight of the scaffold after being placed in PBS. The test was repeated on five samples and the average result was reported.

Biodegradation ratio: The biodegradation ratio of the prepared scaffolds was calculated using Equation (2) after soaking of the scaffolds for 2 weak in phosphate-buffered saline (PBS) at 37 ± 0.5 °C [38]:

$$\text{Biodegradation}(\%) = \left|(W_w - W_d)/W_d\right| \times 100 \quad (2)$$

where W_w is the initial weight of the scaffold (before immersion in PBS) and W_d is the weight of scaffold after immersion in PBS. The test was repeated on five samples and the average result was reported.

Mechanical strength: The Mechanical properties of the scaffolds were measured by a compression strength test system (Santam, STM 20, Iran) with a crosshead speed of 0.5mm/min. All the specimens were cut into 10 mm [39]. The test was repeated on five samples and the average result was reported.

Contact angle: In addition, the wettability of the selected scaffolds was analyzed by water contact angle measurements. The sessile drop method (Kruss DSA 100, Germany) used the water contact angle assay at room temperature. The droplet size was set to 1.0 ml [40]. The test was repeated on five samples and the average result was reported.

2. 4. Cells-Scaffold Interactions

Cell morphology: Adhered cell morphology observation investigated the capability of the optimum scaffolds to cell attachment. So, 5×10^4 cells/ml (rat bone marrow mesenchymal stem cells (BMSCs, supplied by Fudan University Hospital Medical Center) were seeded on the surfaces of each sterilized scaffolds, and DMEM with 15% (v/v) FBS and 100 mg/ml penicillin-streptomycin

were added to each well. The cells were incubated for 3 days at 37 ± 0.5 °C and 5 % CO_2. After 3 days, the DMEM was removed, and each sample was washed by PBS solution. The fixation was performed by glutaraldehyde and 1 % osmium tetroxide. The ascending ethanol concentration (10, 30, 50, 79, 90, 95, and 100) was added to each sample for dehydration. After drying in air condition, the morphology of adhered cells was observed by FE-SEM.

MTT: Viability of the cells was obtained 2, 4, and 7 days after cell culture. MTT test was conducted with L929 fibroblast cells. After determined time points of cell cultures, the DMEM was removed and was replaced by fresh 10 μ L MTT contained culture medium. The cells were incubated by a fresh medium. After 2 h incubation at 37 °C with 5% CO_2, the culture medium and MTT were removed, and 100 μl of DMSO was added to each well plate. The optical density was measured at 570 nm wavelength [41, 42]. The cell viability was calculated using the Equation (3).

$$Cell Viability\ (\%) = (ODsample / ODcontrol) \times 100 \quad (3)$$

Alkaline phosphatase (ALP) assay: In order to determine the ALP activity as an indicator of osteo-differentiation, p-nitrophenol from p-nitrophenyl phosphate (p-NPP) releasing level was measured after 0, 7, and 14 days of cell culture. Lysing was performed by the addition of 0.1 % Titron X-100 followed by freeze-thawing at 37±0.5°C. ALP level was determined using ALP kit, so the reaction was stopped by NaOH (1N), and the absorbance was investigated at 405 nm [43].

Cell differentiation: The expression level of Osteogenic-related genes such as osteocalcin (OC) and runt-related transcription factor 2 (RUNX2) was evaluated using Real-time (RT) polymerase chain reaction (PCR). For this purpose, BMSCs cells were cultured for 72 h on the surface of the scaffolds. Then, the osteogenic medium was replaced, and cells were cultured for 7 and 14 days. Every 2 days, the osteogenic medium was refreshed. At the end of each time point (0, 7, and 14 days), the total RNA was extracted using TRIzol Reagent (Invitrogen Pty Ltd, Australia). cDNA was synthesized from the RNA of each sample by SuperScript II First-Strand cDNA synthesis kit. The relative gene expression was calculated at 95 °C for 3 min followed by 40 cycles of 95 °C for 3 s and 60 °C for 30 s using specific primers. OC: Forward, GGGAGACAACAGGGAGGAAAC; Reverse, TCGGTCATGCTCTCTCCAAAC. RUNX2: Forward, CCCAGCCACCTTTACCTACA; Reverse, TATGGAGTGCTGCTGCTGGTCTG. Results normalized with housekeeping gene GAPDH as a control. GAPDH: Forward, GCCCAATACGACCAAATCC; Reverse, AGCCACATCGCTCAGACA. All the cell investigations were repeated on five samples and the average result was reported.

2. 5. Statistical Analyzes The results were presented as the mean ± standard deviation of 5 experiments using Microsoft Excel 2016 software (Microsoft, Redmond, WA, USA). Statistical analysis was performed by using one-way ANOVA and Tukey test with significance reported when $P < 0.05$.

3. RESULTS AND DISCUSSION

3. 1. Morphology Observation Figures 1 and 2 demonstrate the SEM micrographs and pore size distribution of prepared scaffolds with different concentrations of GA and various cross-linking methods. As can be seen, the open pores are uniformly formed, and thin walls separate the pores in all samples. Figures 1(a) and (b) shows SEM micrographs of GA0.5S and GA1S samples, respectively, Figure 1 (c-e) indicates the SEM micrographs of GAV-6, GAV-24, and GAV-48 scaffolds, respectively, and Figure 1(f) presents mean pore size. The pore size samples were in the range of 50-400 μm. Here, GA0.5S and GA1S showed the average pore diameter of 233.00±7.64 and 140.16±5.64 μm, respectively. But pore size of the GAV-6, GAV-24, and GAV-48 scaffolds was calculated 232.41±8.43, 187.14±7.7, and 75.26±5.56 μm, respectively. Figure 2 (a-f) shows the SEM micrographs of GA0.5I-1, GA0.5I-24, GA1I-1, GA1I-24, GA2I-1, and GA2I-24, respectively. Figure 2(g) demonstrate the average pore size of GA immersion cross-linked samples. Here, the pore diameter mean was calculated 160.95±7.02, 154.92±6.9, 160.31±6.9, 99.25±3.28, 141.26, and 72.78±29.92 μm for GA0.5I-1, GA0.5I-24, GA1I-1, GA1I-24, GA2I-1, and GA2I-24, respectively. All GA cross-linked samples with different methods such as vapor, immersion, and solution addition, exhibited porosity between 20-80%. In the case of pore size, increasing the cross-linking time and concentration decreased the average pore size in all samples.

As a critical parameter for biomedical applications, the microstructure of the scaffolds should provide the suitable geometry for better cell migration, cellular proliferation, and proper vascularization for transportation of nutrients and removal of waste products [44]. According to the morphology observations and average pore size of samples cross-linked by the GA immersion method, a more irregular pore shape was observed than other scaffolds. It should be noted that although these samples had more scattered values, the average pore diameter of all GA immersed samples was in the range of 50-200 μm. The optimum pore size for BMSCs growth was found to be in the range of 100-500 μm, which can be approximately matched with the pore

size range in prepared GA cross-linked scaffolds [45, 46]. Small pores restrict cell migration and infiltration into the 3D structure of the scaffolds, while large pores with better cell responses reduce the mechanical properties [47]. Accordingly, a range of small and large pores is required for observing better results, as achieved in currently modified scaffolds. A proper bone tissue engineering scaffold should have porosity in the range of 20-90 % depends on the cortical and cancellous bone structure [48]. The all samples had porosity in the mentioned range. However, pore sizes were in the range of 50-400 µm which were in the proper range for bone replacement [45, 46]. The pore size results demonstrated that the GA vapor cross-linked scaffolds had a primarily homogenous morphology. The samples cross-linked by GA vapor exposure had a more uniform structure than samples cross-linked with other methods. Although there was slight pore morphology deformation, the pores were still open with suitable size, and this change can be negligible.

3. 2. Fourier Transform Infrared Spectroscopy (FTIR) FTIR spectroscopy investigated the chemical composition of the freeze-dried scaffolds, and the results are demonstrated in Figures 3(a)-(c). Chitosan/gelatin scaffolds without any cross-linker were considered as the control sample. The characteristic peaks of chitosan and gelatin were detected in all FTIR samples. The wide absorption band at around 3100-3600 cm^{-1} was attributed to the stretching vibration of O-H bonded to N-H in all samples [49]. The specific chitosan peaks were

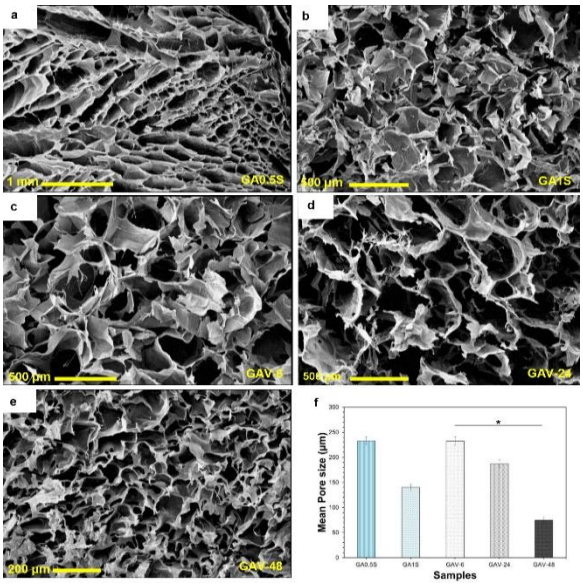

Figure 1. SEM micrographs of (a) GA0.5S; (b) GA1S; (c) GAV-6; (d) GAV-24; (e) GAV-48 scaffolds. (f) The mean pore size measurements of GA0.5S, GA1S, GAV-6, GAV-24, and GAV-48 scaffolds

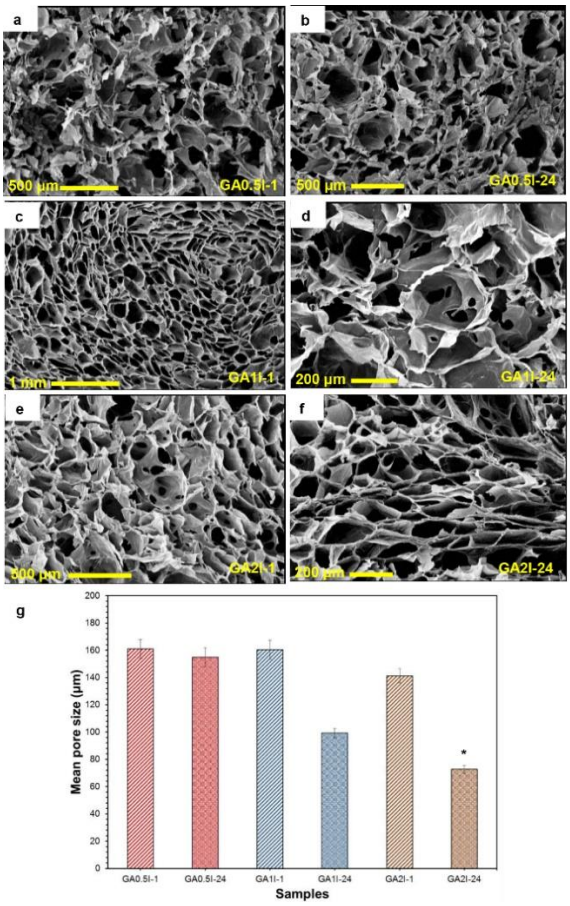

Figure 2. SEM micrographs of (a) GA0.5I-1; (b) GA0.5I-24; (c) GA1I-1; (d) GA1I-24; (e) GA2I-1; (f) GA2I-24 scaffolds. (g) The mean pore size measurements of GA0.5I-1, GA0.5I-24, GA1I-1, GA1I-24, GA2I-1, and GA2I-24 scaffolds

detected at around 1651 cm^{-1}, 1542 cm^{-1}, and 1381 cm^{-1}, due to C=O stretching (amide I), N-H bending (amide II), and N-H bending and C-N stretch (amide III), respectively [50]. Figure 4(a) illustrates the proposed schematic of GA cross-linking reaction process of chitosan and gelatin using solution addition (a), vapor exposure (b), and immersion (c) methods, respectively, and Figure 4(b) shows the schematic of cross-linking techniques for chitosan/gelatin scaffolds.

Chitosan/gelatin crosslinking mechanism by GA has been performed through nucleophile addition-type reaction by the aldehyde functional groups with free non-protonated ε-amino groups of chitosan and gelatin reactions [51]. GA cross-linking created covalent linkage imine bonds (-C=N) between aldehyde groups of GA and amine group of gelatin and chitosan at around 1651 cm^{-1} and merged with amid I bonds of gelatin and chitosan [52]. Amine-containing compounds such as polysaccharides can easily react with aldehyde functionalities such as used GA here and create Schiff base compound [53], also this Schiff base mechanism

was demonstrated in a previous study by Patel et al. [54]. According to the achieved FTIR results, the higher GA cross-linker or higher exposure time intensified C=N related peak and confirmed the higher cross-linking percentage of chitosan and gelatin. These results were incontinence with a previous study performed by Nguyen et al. [31]. Accordingly, GA was considered a creep cross-linking, and in the early hours, GA could not completely cross-linked gelatin and chitosan due to the environment's acidity. However, the acid had been evaporated during the time, and as a result, the cross-linking process of the sample was better performed in samples with higher immersion time.

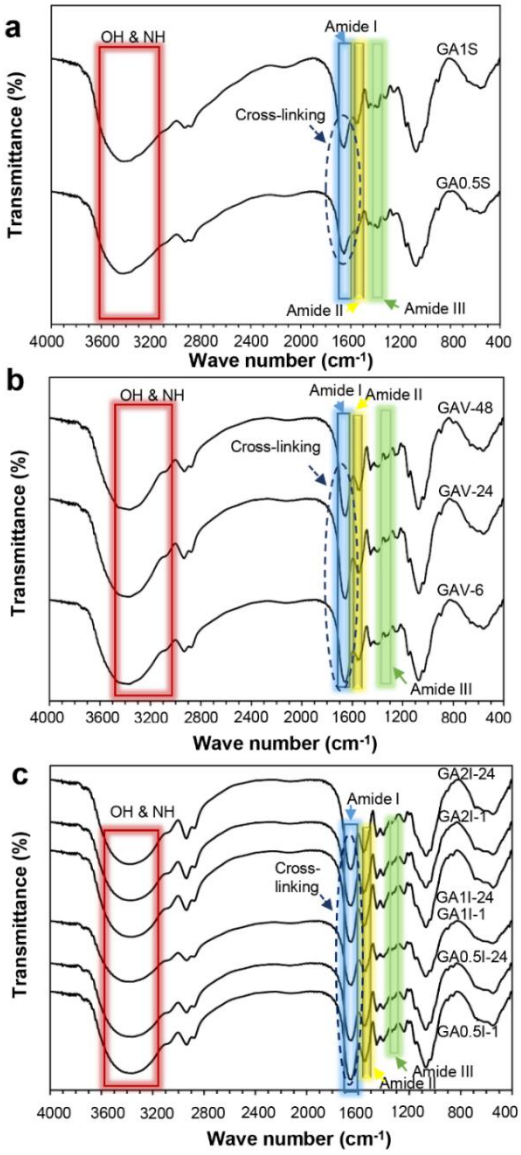

Figure 3. FTIR spectra of GA cross-linked gelatin/chitosan scaffolds with addition to (a) solution; (b) vapor exposure; and (c) immersion techniques

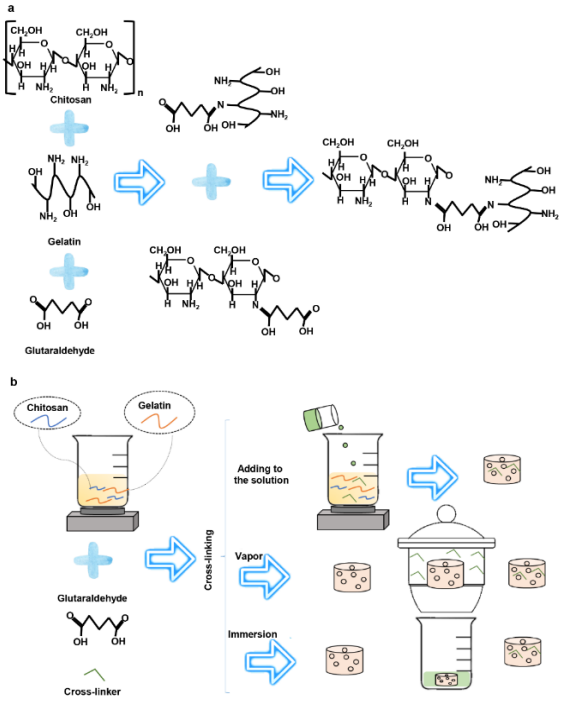

Figure 4. (a) Proposed schematic of the reaction between GA cross-linked gelatin and chitosan; (b) the schematic of scaffold preparation using different cross-linking methods

3. 3. Water-Scaffolds Interactions Herein, the swelling capability of all fabricated scaffolds was measured by soaking in PBS solution. The swelling ratio of GA cross-linked scaffolds with different methods of addition to the solution, vapor exposure, and immersion technique are demonstrated in Figure 5(a-c), respectively. As can be seen in Figure 5, GA cross-linking method affected the swelling ratio, besides GA concentration and time. In the solution addition method, the GA1S absorbed lower fluid than GA0.5S samples, and the swelling ratio was reduced from 35.55±3.1 to 22.31±1.3 (%) in 120 min PBS solution soaking. GAV-6, GAV-24, and GAV-48 scaffolds showed 33.12±0.21, 31.13±0.97, and 19.37±1.98 swelling capacity after 120 min immersion in PBS solution, respectively. In addition, after 120 min, swelling ratio was reached 26.59±3.97, 23.82±4.97, 26.23±0.13, 20.10±1.79, 22.49±2.89, and 16.55±0.57, for GA0.5I-1, GA0.5I-24, GA1I-1, GA1I-24, GA2I-1, and GA2I-24 scaffolds, respectively. Uncross-linked Gelatin/chitosan scaffold was considered as a control sample.

Swelling ratio is an essential factor in cell-scaffolds interactions, biodegradation ratio, and bioactivity in tissue engineering. A high swelling ratio leads to scaffolds' weight loss and structural deformation [34]. Gelatin is a hydrogel with a high capacity to absorb water and should be cross-linked before usage to regulating gelatin swelling capacity [55]. According to the achieved

results, the swelling ratio of each GA cross-linked sample was increased during 120 min. In general, GA cross-linking concentration and swelling time addition decreased the swelling ratio compared with control sample independence of crosslinking method. The higher GA concentration leads to the cross-linking bridge in the structure, especially with amine groups of chitosan. On the other hand, the higher cross-linked volume compacts the structure and limits chain movement [23]. In addition, high cross-likening duration increases the chance of cross-linker to react with the functional groups. Both cross-linked solution samples had lower swelling capacity compared with vapor cross-linked samples for 6 and 24 h. Whereas GA vapor cross-linked scaffolds for 48 h demonstrated lower swelling capacity. GA exposure duration influenced the swelling ratio in vapor cross-linked scaffolds. As the duration of cross-linking increased, the cross-linker had more opportunity to penetrate the structure and thus cross-linked the larger structure volume. Therefore, these achieved results were in line with a previous study by Kulkarni et al. [56], which showed that crosslinking exposure time led to a lower swelling ratio. The same trend was found in immersion samples and the 24 h immersed scaffolds had a lower than 1 h swelling ratio. In addition, the higher cross-link ratio reduced the swelling capacity. There was a slight irregularity in the decreasing trend of these samples, which can be attributed to the irregularity of the pores in the freezing process, which can be ignored. The more interesting result was that according to the results it seemed the cross-linking duration had more effect on swelling ratio than cross-linking concentration in immersion technique.

3. 4. Biodegradation Ratio In this study, scaffolds were immersed in PBS solution to evaluate biodegradability. The results are shown in Figure 5(d-f). Cross-inker free control sample demonstrated the most biodegradation ratio and had 51.16 ± 2.16 (%) biodegradation ratio after 2 weeks. GA1S, GAV-48, GAI-24 scaffolds with biodegradation ratio of 26.33±4.47, 22.53±4.44, and 21.72±72, respectively, demonstrated the lowest biodegradation ratio compared with other samples.

To allow new bone formation, bone tissue-engineered scaffolds must be biodegradable with a match biodegrading ratio with new bone tissue growth. Therefore, one of the critical parameters that are studied in bone tissue engineering is biodegradability [30]. The high biodegradation ratio in control sample was not unexpected as both chitosan and gelatin are hydrophilic and have a high degradation rate. Gelatin usually hydrolyzes in the presence of water quickly [57]. In GA cross-linked samples, the higher cross-linker concentration and exposure time decreased the biodegradation ratio. This phenomenon is consistent with the data previously published by Zhu et al. [34], where the higher exposure time to GA vapor cross-linker led to a lower biodegradation ratio. In general, the increasing cross-linker concentration reduced the biodegradation rate regardless of cross-linking method. In GA cross-linked samples, GA2I-24 indicated the lowest biodegradation and swelling ratio among all scaffolds. GA vapor cross-linked scaffolds showed the most biodegradation ratio even though they did not have the highest swelling ratio. This phenomenon may arise from low mechanical stability and insufficient penetration of the cross-linker into the inner layers of the structure. Because after the biodegradation of the initial layers, the bio-degradation process has been accelerated within two weeks. In general, the increasing cross-linker concentration reduced the biodegradation rate regardless of cross-linking method.

Due the presence of hydrophilic groups such as amide and carboxyl in gelatin structures, it hydrolyzed quickly in the presence of water. In addition, other studies indicated that *in-vivo* gelatin biodegradation was conducted by both hydrolysis and enzymatic manners [38, 58]. Besides, the PBS soaking of chitosan can lead to the 1,4 N-acetyl-glucosamine groups hydrolysis and created amino sugars. In the body environment, the degradation products can follow glycosaminoglycans and glycoprotein metabolic pathways or excreted from body [59]. GA cross-linking decreases biodegradation ratio by limitation of fluidic penetration and increasing the hydrophobicity. This low permeability of the aqueous solution delays the formation of smaller polymer residues, which are usually rapidly hydrolyzed in water. During the time, cross-link bonding breaks and facilities fluid penetration, which terminate to degradation of scaffolds [57, 60]. Here, the higher concentration and GA exposure time provided more favorable degradation ratio for bone replacement, while the other properties should be considered for introducing the best bone candidate.

3. 5. Mechanical Strength Here, the GA cross-linked scaffolds' mechanical properties were investigated, and the results are summarized in Figure 6. Figure 6(a) shows the compressive strength and (b) elastic modulus of the scaffolds. The lowest elastic modulus and compressive strength were achieved for the control group with 0.02 ± 0.15 MPa and 0.058±0.004 MPa, respectively. The compressive strength of the scaffolds were 0.06±0.013, 1.45±0.05, 0.08±0.01, 0.94±0.07, 1.12±0.18, 0.07±0.01, 1.03±0.08, 1.36±0.19, 1.87±0.22, 1.42±0.03, 2.24±0.09 MPa for GA0.5S, GA1S, GAV-6, GAV-24, GAV-48, GA0.5I-1, GA0.5I-24, GA1I-1, GA1I-24, GA2-1, GA2I-24, respectively and the elastic modulus was achieved 0.13±0.01, 3.87±1.01, 0.50±0.01, 1.03±0.54, 2.53±0.09, 0.45±0.046, 1.67±0.90, 2.88±0.04, 5.63±0.87, 3.75±0.07, 11.49±,0.41 MPa, respectively.

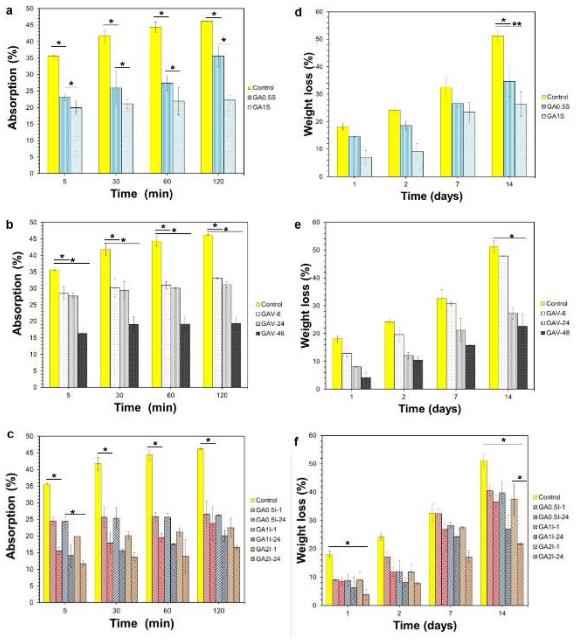

Figure 5. Swelling capacity of GA cross-linked gelatin/chitosan scaffolds with (a) addition to solution; (b) vapor exposure; and (c) immersion techniques during 120 min soaking in PBS solution. Weight loss of the GA cross-linked gelatin/chitosan scaffolds with (d) addition to solution; (e) vapor exposure; and (f) immersion techniques during 2 week immersion in PBS solution

The mechanical properties measurements of the fabricated scaffolds were necessary to estimate the scaffolds' load-bearing capacity in the bone defects [61]. The material type, cross-linker degree, and pore size influenced the compressive moduli of the scaffold [62]. The cross-linking of the composition increased the modulus and compressive strength compared to the control sample. In GA1S scaffolds, the elastic modulus and compressive strength was higher than GA0.5S. These results were in line with previous reports, introducing the cross-linker concentration as one of the influential factors on the stronger mechanical properties [53]. In addition in another study, Putri et al. [63] demonstrated the addition of GA with the concentration of 5 vol% relative to the total mixture to the chitosan and gelatin solution increased the compressive strength to 3.3 ± 0.3 MPa in comparison with non-cross-linked sample with 1.7 ± 0.2 MPa, compressive strength; whereas the relative higher compressive modulus in their study can be related to the β-tricalcium phosphate addition to the gelatin and chitosan composites. On the other hand, in the GA vapor cross-linking method, 48 h exposing increased the elastic modulus. According to the achieved data in the immersion technique, the more GA concentration and cross-linker soaking time increased the elastic module of the scaffolds. It seems the cross-linking exposure time had more effect than concentration. According to the compressive strength of natural trabecular and cortical bone (0.1–16 MPa and 130–200 MPa [64]), the scaffolds with higher compressive strength were more favorable for bone regeneration. Therefore, GA1S, GAV-48, GA1I-1, GA1I-24, GA2I-1, GA2I-24 scaffolds with higher compressive strength and elastic modulus were chosen for further investigations.

3. 6. Contact Angle Water-drop contact angle of the GA1S, GAV-48, GA1I-1, GA1I-24, GA2I-1, GA2I-24 scaffolds was measured as an indicator of hydrophilic/hydrophobic behavior. The results are demonstrated in Figure 7. Water contact angle of control, GA1S, GAV-48, GA1I-1, GA1I-24, GA2I-1, GA2I-24 was measured as 39.3°, 58.3°, 76.9°, 42.2°, 76.7°, 59.0°, and 106.4°, respectively.

More hydrophilic surfaces demonstrate lower contact angle and show enhanced cell adhesion and proliferation [65]. Although chitosan and gelatin have hydrophilic functional groups, blending the chitosan with gelatin reduces hydrophilicity [66]. This effect can be related to the interaction between the functional groups of gelatin and chitosan with different charge side chains and neutralize charge complex formation with reduced charge density and polarity. The non-cross-linked scaffolds demonstrated the lowest contact angle. This can be related to the lower compact volume and free

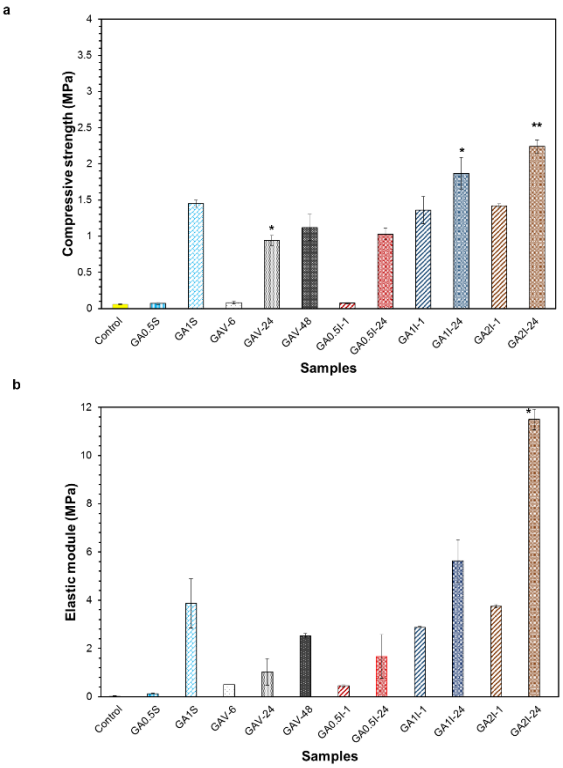

Figure 6. (a) The compressive strength and (b) elastic modulus of all samples

hydrophilic functional groups of chitosan and gelatin. In general, the scaffolds' contact angle was reduced by adding cross-linker concentration and exposing time in GA cross-linked sample. It was expected according to the results of swelling ratio and biodegradation properties. The high swelling and biodegradation property of the chitosan/gelatin scaffolds can be attributed to the gelatin dissolution in watery fluids and opening the interacted functional groups of chitosan and gelatin followed by interaction with H_2O molecules during the soaking time in addition to the lower compact and non-cross-linked volume. It should be noted that the scaffolds with a contact angle in the range of approximately 20-70 ° are more favorable for cell interactions [67, 68]. Therefore, it is expected GA1S, GA1I-1, and GA2I-1 demonstrate the best cell behavior. Among these three samples and according to the achieved physicochemical results, GA1S sample was selected as the optimum sample and introduced for more cellular investigations.

3. 7. Cell-Scaffold Behavior This study performed cell studies on the optimum sample (GA1S) based on the above results to evaluate the BMSCs morphology, proliferation, and cell differentiation. As shown in Figure 8(a), cells were well attached to the surface of the sample. Also, cells were created filopodia and well spread all over the scaffold. According to the MTT results (Figure 8(b)), the GA1S showed lower cell viability than the control sample in 2 and 4 days, but after 7 days GA1S scaffold showed accelerated cell proliferation and demonstrated higher cell viability compared with the control sample. According to ALP relative expression results of GA1S sample (Figure 8(c)), ALP level was approximately equal with control specimen, while after 7 days, there was an increase in ALP expression compared with the control scaffold. After 14 days, the ALP expression was accelerated and significantly higher than the control scaffold. To further investigate the bone differentiation of cultured cells, OC and RUNX2 expression was measured in GA1S scaffold, and the results are shown in Figure 8 (d and e), respectively. There was a similar trend in OC expression, and there was a significantly higher expression in GA1S sample compared with the control. A relatively lower RUNX2 expression was detected in GA1S scaffold in 7th and 14th days of incubation.

The well cell adhesion and filopodia formation on GA1S scaffold can be due to the biocompatibility nature of both polymers, and on the other hand, the glycine, proline, and hydroxyproline residues of gelatin [69, 70]. The relatively lower cell viability in first days may be related to absorbed GA on the surface. According to Figure 8 (b, insert), it should be

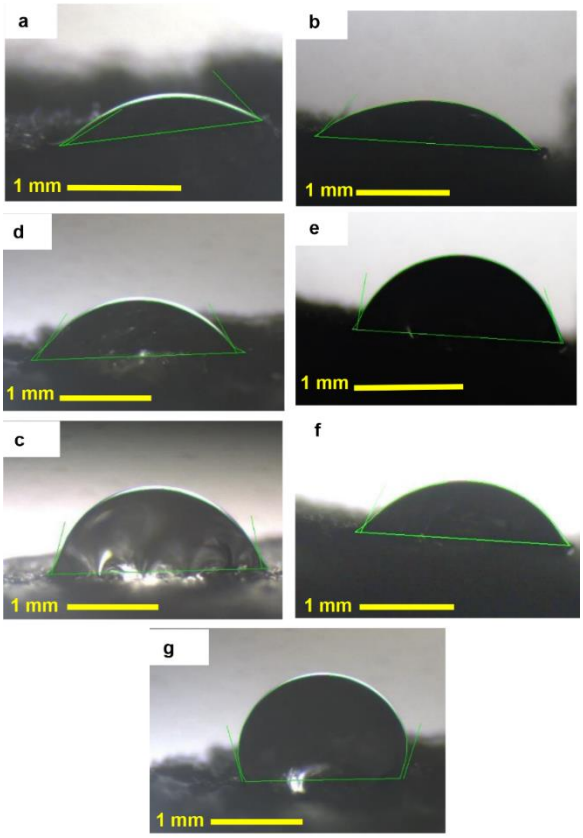

Figure 7. The contact angle of the (a) control; (b) GA1S; (c) GAV-48; (d) GA1I-1; (e) GA1I-24; (f) GA2I-1; and (g) GA2I-24 gelatin/chitosan scaffolds

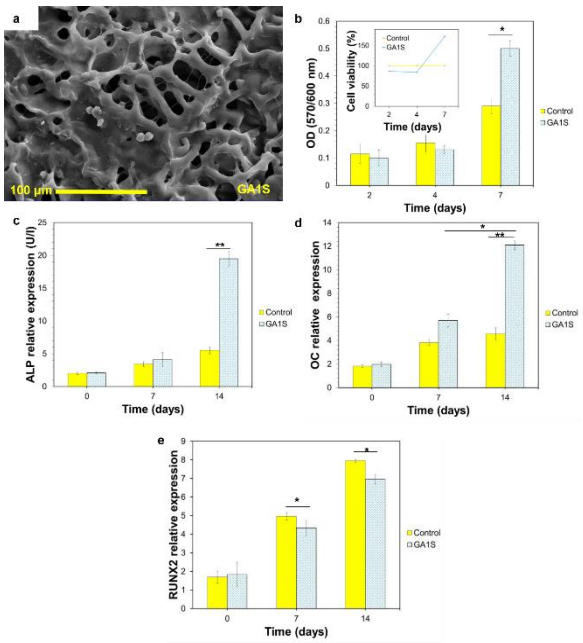

Figure 8. (a) FESEM micrograph of cell cultured morphology on the surface of GA1S scaffold; (b) the results of cell viability during 7 days of cell culturing. (c) ALP; (d) OC; and (e) RUNX2 expression level during 14 days of cell incubation on the surface of GA1S scaffold

noted that although the GA1S sample showed a slight decrease in cell viability compared to the control sample in the early days, it was in the acceptable range and had more than 80% cell viability on all days.

ALP is an osteoblastic activity and mineralization indicator, an initial osteoblastic differentiation marker [71]. The ALP expression was increased during 14 days and showed higher values in compare to the control sample. OC and RUNX2 are essential genes of osteoblastic differentiation [72]. RUNX2 is a middle and OC is a late-stage marker of osteogenic differentiation [73]. OC as a noncollagenous protein in bone ECM increases bone formation and has a high affinity for calcium ions in mineralization and apatite deposition [74]. Therefore, high expression of OC in GA1S scaffold could help mineralization and bone formation. However, a relatively lower RUNX2 expression was detected in GA1S scaffold in 7th and 14th days of incubation, while the RUNX2 expression proved the osteoblastic differentiation.

4. CONCLUSIONS

Cross-linking concentration, exposure time, and applied technique had a lot of effect on the properties of GA cross-linked gelatin/chitosan scaffolds. In general, according to the morphological observation, the obtained freeze-dried structure was porous with open porosity in all the used techniques. The average pore sizes were in the suitable range for bone tissue engineering. The samples cross-linked by GA vapor exposure had a more uniform structure than samples cross-linked with other methods. On the other hand, it was demonstrated that the higher GA cross-linker or higher exposure time intensified C=N related peak and confirmed the higher cross-linking percentage. Also, the higher GA cross-linking exposing duration and concentration decreased swelling ratio and biodegradation ratio while improved the mechanical properties. It was revealed that the cross-linking exposure time had more effect than concentration on mechanical properties and only higher GA concentration or longer GA exposure time showed an acceptable mechanical properties for bone regeneration. Contact angle results of the candidate samples confirmed the swelling results and the contact angle was reduced by cross-linker concentration and exposure time increasing and GA1S sample demonstrated a 39.3° contact angle. The cellular studies was performed on the selected specimen (GA1S) for further investigations. Cell adhesion, and viability results demonstrated the high cell supporting behavior of GA1S scaffolds. In addition, the GA1S scaffold led to the osteo-related genes expression such as ALP, OC, and RUNX2. As the result of all experiments, the GA1S sample was introduced as the optimum scaffold, and it can be useful for bone tissue engineering applications.

Author Contributions: Ideas and evolution of overarching goals, development and creation of models, conducting an investigation process, and preparation of the manuscript were done by FB. DL cooperate in in-vitro data collection and analysis procedures. Leadership responsibility for the activity planning and execution, including mentorship external to the core team and acquisition of the financial support for the project leading to this publication, were performed by CY and AZ.

Funding: This work was supported by the Scientific Research Foundation provided by Pudong Hospital affiliated to Fudan University (Project no. YJRCJJ201906), the Talents Training Program of Pudong Hospital affiliated to Fudan University (Project no. PX202001), the Youth Science and Technology Project of Health Commission of Shanghai Pudong New Area (Project no. PW2020B-5), the Outstanding Clinical Discipline Project of Shanghai Pudong (Grant No. PWYgy2018-09).

Data Availability Statement: The datasets generated for this study are available on request to the corresponding author

Acknowledgments: Special thanks must go to Dr. Farnaz Ghorbani from the institute of Biomaterials, University of Erlangen-Nuremberg. Her expert knowledge in the field of tissue engineering scaffolds is a worthy addition to this text.

Conflicts of Interest: The authors whose names are listed certify that they have NO affiliations with or involvement in any organization or entity with any financial interest, or non-financial interest in the subject matter or materials discussed in this manuscript.

5. REFERENCES

1. Koons, G.L., Diba, M. and Mikos, A.G., "Materials design for bone-tissue engineering", ***Nature Reviews Materials***, Vol. 5, No. 8, (2020), 584-603. https://doi.org/10.1038/s41578-020-0204-2
2. Guillaume, O., Geven, M., Sprecher, C., Stadelmann, V., Grijpma, D., Tang, T., Qin, L., Lai, Y., Alini, M. and De Bruijn, J., "Surface-enrichment with hydroxyapatite nanoparticles in stereolithography-fabricated composite polymer scaffolds promotes bone repair", ***Acta Biomaterialia***, Vol. 54, (2017), 386-398. https://doi.org/10.1016/j.actbio.2017.03.006
3. Pereira, H.F., Cengiz, I.F., Silva, F.S., Reis, R.L. and Oliveira, J.M., "Scaffolds and coatings for bone regeneration", ***Journal of Materials Science: Materials in Medicine***, Vol. 31, No. 3, (2020), 1-16.
4. Hassanzadeh Nemati, N. and Mirhadi, S.M., "Synthesis and characterization of highly porous TiO_2 scaffolds for bone defects", ***International Journal of Engineering, Transactions A: Basics***, , Vol. 33, No. 1, (2020), 134-140. https://doi.org/10.5829/ije.2020.33.01a.15
5. Liu, D., Nie, W., Li, D., Wang, W., Zheng, L., Zhang, J., Zhang, J., Peng, C., Mo, X. and He, C., "3d printed pcl/srha scaffold for enhanced bone regeneration", ***Chemical Engineering Journal***, Vol. 362, (2019), 269-279. https://doi.org/10.1016/j.cej.2019.01.015

6. Sadeghinia, A., Soltani, S., Aghazadeh, M., Khalilifard, J. and Davaran, S., "Design and fabrication of clinoptilolite–nanohydroxyapatite/chitosan–gelatin composite scaffold and evaluation of its effects on bone tissue engineering", ***Journal of Biomedical Materials Research Part A***, Vol. 108, No. 2, (2020), 221-233. https://doi.org/10.1002/jbm.a.36806
7. Sultana, N., Hassan, M., Ridzuan, N., Ibrahim, Z. and Soon, C., "Fabrication of gelatin scaffolds using thermally induced phase separation technique", ***International Journal of Engineering***, Vol. 31, No. 8, (2018), 1302-1307. https://doi.org/10.5829/ije.2018.31.08b.19
8. Raja, N. and Yun, H.-s., "A simultaneous 3d printing process for the fabrication of bioceramic and cell-laden hydrogel core/shell scaffolds with potential application in bone tissue regeneration", ***Journal of Materials Chemistry B***, Vol. 4, No. 27, (2016), 4707-4716. https://doi.org/10.1039/C6TB00849F
9. Sarparast, Z., Abdoli, R., Rahbari, A., Varmazyar, M. and Reza Kashyzadeh, K., "Experimental and numerical analysis of permeability in porous media", ***International Journal of Engineering***, ***Transactions B: Applications,*** Vol. 33, No. 11, (2020), 2408-2415. https://doi.org/10.5829/ije.2020.33.11b.31
10. Ilyas, R. and Sapuan, S., "The preparation methods and processing of natural fibre bio-polymer composites", ***Current Organic Synthesis***, Vol. 16, No. 8, (2019), 1068-1070. https://doi.org/10.2174/1570179416082001201056l6
11. Ilyas, R., Sapuan, S., Harussani, M., Hakimi, M., Haziq, M., Atikah, M., Asyraf, M., Ishak, M., Razman, M. and Nurazzi, N., "Polylactic acid (PLA) biocomposite: Processing, additive manufacturing and advanced applications", ***Polymers***, Vol. 13, No. 8, (2021), 1326. https://doi.org/10.3390/polym13081326
12. Ilyas, R.A., Sapuan, S.M., Ibrahim, R., Abral, H., Ishak, M., Zainudin, E., Asrofi, M., Atikah, M.S.N., Huzaifah, M.R.M. and Radzi, A.M., "Sugar palm (arenga pinnata (wurmb.) merr) cellulosic fibre hierarchy: A comprehensive approach from macro to nano scale", ***Journal of Materials Research and Technology***, Vol. 8, No. 3, (2019), 2753-2766. https://doi.org/10.1016/j.jmrt.2019.04.011
13. Ilyas, R., Sapuan, S., Ishak, M. and Zainudin, E., "Sugar palm nanofibrillated cellulose (arenga pinnata (wurmb.) merr): Effect of cycles on their yield, physic-chemical, morphological and thermal behavior", ***International Journal of Biological Macromolecules***, Vol. 123, No., (2019), 379-388. https://doi.org/10.1016/j.ijbiomac.2018.11.124
14. Ilyas, R., Zuhri, M., Aisyah, H., Asyraf, M., Hassan, S., Zainudin, E., Sapuan, S., Sharma, S., Bangar, S. and Jumaidin, R., "Natural fiber-reinforced polylactic acid, polylactic acid blends and their composites for advanced applications", ***Polymers***, Vol. 14, No. 1, (2022), 202. https://doi.org/10.3390/polym14010202
15. Ilyas, R., Zuhri, M., Norrrahim, M.N.F., Misenan, M.S.M., Jenol, M.A., Samsudin, S.A., Nurazzi, N., Asyraf, M., Supian, A. and Bangar, S.P., "Natural fiber-reinforced polycaprolactone green and hybrid biocomposites for various advanced applications", ***Polymers***, Vol. 14, No. 1, (2022), 182. https://doi.org/10.3390/polym14010182
16. Tang, G., Tan, Z., Zeng, W., Wang, X., Shi, C., Liu, Y., He, H., Chen, R. and Ye, X., "Recent advances of chitosan-based injectable hydrogels for bone and dental tissue regeneration", ***Frontiers in Bioengineering and Biotechnology***, Vol. 8, (2020), 587658. https://doi.org/10.3389/fbioe.2020.587658
17. Prakash, J., Prema, D., Venkataprasanna, K., Balagangadharan, K., Selvamurugan, N. and Venkatasubbu, G.D., "Nanocomposite chitosan film containing graphene oxide/hydroxyapatite/gold for bone tissue engineering", ***International Journal of Biological Macromolecules***, Vol. 154, (2020), 62-71. https://doi.org/10.1016/j.ijbiomac.2020.03.095
18. Vaidhyanathan, B., Vincent, P., Vadivel, S., Karuppiah, P., AL-Dhabi, N.A., Sadhasivam, D.R., Vimalraj, S. and Saravanan, S., "Fabrication and investigation of the suitability of chitosan-silver composite scaffolds for bone tissue engineering applications", ***Process Biochemistry***, Vol. 100, (2021), 178-187. https://doi.org/10.1016/j.procbio.2020.10.008
19. De Witte, T.M., Wagner, A.M., Fratila-Apachitei, L.E., Zadpoor, A.A. and Peppas, N.A., "Immobilization of nanocarriers within a porous chitosan scaffold for the sustained delivery of growth factors in bone tissue engineering applications", ***Journal of Biomedical Materials Research Part A***, Vol. 108, No. 5, (2020), 1122-1135. https://doi.org/10.1002/jbm.a.36887
20. Badawy, M.E., Taktak, N.E., Awad, O.M., Elfiki, S.A. and El-Ela, N.E.A., "Preparation and characterization of biopolymers chitosan/alginate/gelatin gel spheres crosslinked by glutaraldehyde", ***Journal of Macromolecular Science, Part B***, Vol. 56, No. 6, (2017), 359-372. https://doi.org/10.1080/00222348.2017.1316640
21. Sharma, S., Sudhakara, P., Singh, J., Ilyas, R., Asyraf, M. and Razman, M., "Critical review of biodegradable and bioactive polymer composites for bone tissue engineering and drug delivery applications", ***Polymers***, Vol. 13, No. 16, (2021), 2623. https://doi.org/10.3390/polym13162623
22. Choi, Y.-J., Park, H., Ha, D.-H., Yun, H.-S., Yi, H.-G. and Lee, H., "3d bioprinting of in vitro models using hydrogel-based bioinks", ***Polymers***, Vol. 13, No. 3, (2021), 366. https://doi.org/10.3390/polym13030366
23. Zarif, M.-E., "A review of chitosan-, alginate-, and gelatin-based biocomposites for bone tissue engineering", ***Biomater. Tissue Eng. Bull***, Vol. 5, (2018), 97-109.
24. Oryan, A., Kamali, A., Moshiri, A., Baharvand, H. and Daemi, H., "Chemical crosslinking of biopolymeric scaffolds: Current knowledge and future directions of crosslinked engineered bone scaffolds", ***International Journal of Biological Macromolecules***, Vol. 107, (2018), 678-688. https://doi.org/10.1016/j.ijbiomac.2017.08.184
25. Ehrmann, A., "Non-toxic crosslinking of electrospun gelatin nanofibers for tissue engineering and biomedicine—a review", ***Polymers***, Vol. 13, No. 12, (2021), 1973. https://doi.org/10.3390/polym13121973
26. Lee, J.B., Ko, Y.-G., Cho, D., Park, W.H. and Kwon, O.H., "Modification and optimization of electrospun gelatin sheets by electron beam irradiation for soft tissue engineering", ***Biomaterials Research***, Vol. 21, No. 1, (2017), 1-9. https://doi.org/10.1186/s40824-017-0100-z
27. Campiglio, C.E., Contessi Negrini, N., Farè, S. and Draghi, L., "Cross-linking strategies for electrospun gelatin scaffolds", ***Materials***, Vol. 12, No. 15, (2019), 2476. https://doi.org/10.3390/ma12152476
28. Yang, G., Xiao, Z., Long, H., Ma, K., Zhang, J., Ren, X. and Zhang, J., "Assessment of the characteristics and biocompatibility of gelatin sponge scaffolds prepared by various crosslinking methods", ***Scientific Reports***, Vol. 8, No. 1, (2018), 1-13. https://doi.org/10.1038/s41598-018-20006-y
29. Pauly, M.P., Tucker, L.-Y., Szpakowski, J.-L., Ready, J.B., Baer, D., Hwang, J. and Lok, A.S.-F., "Incidence of hepatitis b virus reactivation and hepatotoxicity in patients receiving long-term treatment with tumor necrosis factor antagonists", ***Clinical Gastroenterology and Hepatology***, Vol. 16, No. 12, (2018), 1964-1973. e1961. https://doi.org/10.1016/j.cgh.2018.04.033
30. Liu, Y., Ma, L. and Gao, C., "Facile fabrication of the glutaraldehyde cross-linked collagen/chitosan porous scaffold for skin tissue engineering", ***Materials Science and Engineering: c***, Vol. 32, No. 8, (2012), 2361-2366. https://doi.org/10.1016/j.msec.2012.07.008

31. Nguyen, T.-H. and Lee, B.-T., "Fabrication and characterization of cross-linked gelatin electro-spun nano-fibers", ***Journal of Biomedical Science and Engineering***, Vol. 3, No. 12, (2010), 1117. https://doi.org/10.4236/jbise.2010.312145
32. Destaye, A.G., Lin, C.-K. and Lee, C.-K., "Glutaraldehyde vapor cross-linked nanofibrous pva mat with in situ formed silver nanoparticles", ***ACS Applied Materials & Interfaces***, Vol. 5, No. 11, (2013), 4745-4752. https://doi.org/10.1021/am401730x
33. Yang, Y., Ritchie, A.C. and Everitt, N.M., "Comparison of glutaraldehyde and procyanidin cross-linked scaffolds for soft tissue engineering", ***Materials Science and Engineering: c***, Vol. 80, (2017), 263-273. https://doi.org/10.1016/j.msec.2017.05.141
34. Zhu, B., Li, W., Chi, N., Lewis, R.V., Osamor, J. and Wang, R., "Optimization of glutaraldehyde vapor treatment for electrospun collagen/silk tissue engineering scaffolds", ***ACS Omega***, Vol. 2, No. 6, (2017), 2439-2450. https://doi.org/10.1021/acsomega.7b00290
35. Kaczmarek, B., Sionkowska, A., Monteiro, F., Carvalho, A., Łukowicz, K. and Osyczka, A., "Characterization of gelatin and chitosan scaffolds cross-linked by addition of dialdehyde starch", ***Biomedical Materials***, Vol. 13, No. 1, (2017), 015016. https://doi.org/10.1088/1748-605X/aa8910
36. Maji, K., Dasgupta, S., Pramanik, K. and Bissoyi, A., "Preparation and evaluation of gelatin-chitosan-nanobioglass 3d porous scaffold for bone tissue engineering", ***International Journal of Biomaterials***, Vol. 2016, (2016). https://doi.org/10.1155/2016/9825659
37. Nokoorani, Y.D. and Shamloo, A., "Comparison of the effect of edc and glutaraldehyde as cross-linkers on morphology and swelling ratio of gelatin/chitosan scaffolds for use in skin tissue engineering", in 2018 25th National and 3rd International Iranian Conference on Biomedical Engineering (ICBME), IEEE. (2018), 1-4.
38. Rezaei, H., Asefnejad, A., Joupari, M.D. and Joughehdoust, S., "The physicochemical and mechanical investigation of siloxane modified gelatin/sodium alginate injectable hydrogels loaded by ascorbic acid and β-glycerophosphate", ***Materials Today Communications***, Vol. 26, (2021), 101914. https://doi.org/10.1016/j.mtcomm.2020.101914
39. Ghorbani, F., Zamanian, A. and Sahranavard, M., "Mussel-inspired polydopamine-mediated surface modification of freeze-cast poly (ε-caprolactone) scaffolds for bone tissue engineering applications", ***Biomedical Engineering/Biomedizinische Technik***, Vol. 65, No. 3, (2020), 273-287. https://doi.org/10.1515/bmt-2019-0061
40. Ghorbani, F., Sahranavard, M. and Zamanian, A., "Immobilization of gelatin on the oxygen plasma-modified surface of polycaprolactone scaffolds with tunable pore structure for skin tissue engineering", ***Journal of Polymer Research***, Vol. 27, No. 9, (2020), 1-12. https://doi.org/10.1007/s10965-020-02263-6
41. Hassanzadeh Nemati, N., Ghasempour, E. and Zamanian, A., "Effect of dual releasing of β-glycerophosphate and dexamethasone from ti nanostructured surface for using in orthopedic applications", ***International Journal of Engineering, Transactions A: Basics,***, Vol. 32, No. 10, (2019), 1337-1344. https://doi.org/10.5829/ije.2019.32.10a.01
42. Ghorbani, F., Ghalandari, B., Sahranavard, M., Zamanian, A. and Collins, M.N., "Tuning the biomimetic behavior of hybrid scaffolds for bone tissue engineering through surface modifications and drug immobilization", ***Materials Science and Engineering: c***, Vol. 130, (2021), 112434. https://doi.org/10.1016/j.msec.2021.112434
43. Ghorbani, F., Zamanian, A., Behnamghader, A. and Joupari, M.D., "Microwave-induced rapid formation of biomimetic hydroxyapatite coating on gelatin-siloxane hybrid microspheres in 10x-sbf solution", ***e-Polymers***, Vol. 18, No. 3, (2018), 247-255. https://doi.org/10.1515/epoly-2017-0196
44. Ghafari, R., Jonoobi, M., Amirabad, L.M., Oksman, K. and Taheri, A.R., "Fabrication and characterization of novel bilayer scaffold from nanocellulose based aerogel for skin tissue engineering applications", ***International Journal of Biological Macromolecules***, Vol. 136, (2019), 796-803. https://doi.org/10.1016/j.ijbiomac.2019.06.104
45. Thein-Han, W., Saikhun, J., Pholpramoo, C., Misra, R. and Kitiyanant, Y., "Chitosan–gelatin scaffolds for tissue engineering: Physico-chemical properties and biological response of buffalo embryonic stem cells and transfectant of gfp–buffalo embryonic stem cells", ***Acta Biomaterialia***, Vol. 5, No. 9, (2009), 3453-3466. https://doi.org/10.1016/j.actbio.2009.05.012
46. Lee, J.H., Park, T.G., Park, H.S., Lee, D.S., Lee, Y.K., Yoon, S.C. and Nam, J.-D., "Thermal and mechanical characteristics of poly (l-lactic acid) nanocomposite scaffold", ***Biomaterials***, Vol. 24, No. 16, (2003), 2773-2778. https://doi.org/10.1016/S0142-9612(03)00080-2
47. Sattary, M., Rafienia, M., Khorasani, M.T. and Salehi, H., "The effect of collector type on the physical, chemical, and biological properties of polycaprolactone/gelatin/nano-hydroxyapatite electrospun scaffold", ***Journal of Biomedical Materials Research Part B: Applied Biomaterials***, Vol. 107, No. 4, (2019), 933-950. https://doi.org/10.1002/jbm.b.34188
48. Abbasi, N., Hamlet, S., Love, R.M. and Nguyen, N.-T., "Porous scaffolds for bone regeneration", ***Journal of Science: Advanced Materials and Devices***, Vol. 5, No. 1, (2020), 1-9. https://doi.org/10.1016/j.jsamd.2020.01.007
49. Chen, H., Xing, X., Tan, H., Jia, Y., Zhou, T., Chen, Y., Ling, Z. and Hu, X., "Covalently antibacterial alginate-chitosan hydrogel dressing integrated gelatin microspheres containing tetracycline hydrochloride for wound healing", ***Materials Science and Engineering: c***, Vol. 70, (2017), 287-295. https://doi.org/10.1016/j.msec.2016.08.086
50. Ding, Y., Yin, H., Shen, S., Sun, K. and Liu, F., "Chitosan-based magnetic/fluorescent nanocomposites for cell labelling and controlled drug release", ***New Journal of Chemistry***, Vol. 41, No. 4, (2017), 1736-1743. https://doi.org/10.1039/C6NJ02897G
51. Baniasadi, H., SA, A.R. and Mashayekhan, S., "Fabrication and characterization of conductive chitosan/gelatin-based scaffolds for nerve tissue engineering", ***International Journal of Biological Macromolecules***, Vol. 74, (2015), 360-366. https://doi.org/10.1016/j.ijbiomac.2014.12.014
52. Sharma, C., Dinda, A.K., Potdar, P.D., Chou, C.-F. and Mishra, N.C., "Fabrication and characterization of novel nano-biocomposite scaffold of chitosan–gelatin–alginate–hydroxyapatite for bone tissue engineering", ***Materials Science and Engineering: c***, Vol. 64, (2016), 416-427. https://doi.org/10.1016/j.msec.2016.03.060
53. Hospodiuk, M., Dey, M., Sosnoski, D. and Ozbolat, I.T., "The bioink: A comprehensive review on bioprintable materials", ***Biotechnology Advances***, Vol. 35, No. 2, (2017), 217-239. https://doi.org/10.1016/j.biotechadv.2016.12.006
54. Patel, S., Srivastava, S., Singh, M.R. and Singh, D., "Preparation and optimization of chitosan-gelatin films for sustained delivery of lupeol for wound healing", ***International Journal of Biological Macromolecules***, Vol. 107, (2018), 1888-1897. https://doi.org/10.1016/j.ijbiomac.2017.10.056
55. Luo, Y., Li, Y., Qin, X. and Wa, Q., "3d printing of concentrated alginate/gelatin scaffolds with homogeneous nano apatite coating for bone tissue engineering", ***Materials & Design***, Vol. 146, (2018), 12-19. https://doi.org/10.1016/j.matdes.2018.03.002
56. Kulkarni, A.R., Soppimath, K.S., Aminabhavi, T.M., Dave, A.M. and Mehta, M.H., "Glutaraldehyde crosslinked sodium alginate beads containing liquid pesticide for soil application", ***Journal of***

Controlled Release, Vol. 63, No. 1-2, (2000), 97-105. https://doi.org/10.1016/S0168-3659(99)00176-5

57. Alizadeh, M., Abbasi, F., Khoshfetrat, A. and Ghaleh, H., "Microstructure and characteristic properties of gelatin/chitosan scaffold prepared by a combined freeze-drying/leaching method", ***Materials Science and Engineering: c***, Vol. 33, No. 7, (2013), 3958-3967. https://doi.org/10.1016/j.msec.2013.05.039
58. Bacakova, L., Zikmundova, M., Pajorova, J., Broz, A., Filova, E., Blanquer, A., Matejka, R., Stepanovska, J., Mikes, P. and Jencova, V., "Nanofibrous scaffolds for skin tissue engineering and wound healing based on synthetic polymers", ***Applications of Nanobiotechnology***, (2019), 1. https://doi.org/10.5772/intechopen.88744
59. Iqbal, H., Ali, M., Zeeshan, R., Mutahir, Z., Iqbal, F., Nawaz, M.A.H., Shahzadi, L., Chaudhry, A.A., Yar, M. and Luan, S., "Chitosan/hydroxyapatite (ha)/hydroxypropylmethyl cellulose (hpmc) spongy scaffolds-synthesis and evaluation as potential alveolar bone substitutes", ***Colloids and Surfaces B: Biointerfaces***, Vol. 160, (2017), 553-563. https://doi.org/10.1016/j.colsurfb.2017.09.059
60. Kavya, K., Dixit, R., Jayakumar, R., Nair, S.V. and Chennazhi, K.P., "Synthesis and characterization of chitosan/chondroitin sulfate/nano-sio2 composite scaffold for bone tissue engineering", ***Journal of Biomedical Nanotechnology***, Vol. 8, No. 1, (2012), 149-160. https://doi.org/10.1166/jbn.2012.1363
61. Kouhi, M., Morshed, M., Varshosaz, J. and Fathi, M.H., "Poly (ε-caprolactone) incorporated bioactive glass nanoparticles and simvastatin nanocomposite nanofibers: Preparation, characterization and in vitro drug release for bone regeneration applications", ***Chemical Engineering Journal***, Vol. 228, (2013), 1057-1065. https://doi.org/10.1016/j.cej.2013.05.091
62. Ji, C., Annabi, N., Khademhosseini, A. and Dehghani, F., "Fabrication of porous chitosan scaffolds for soft tissue engineering using dense gas co2", ***Acta Biomaterialia***, Vol. 7, No. 4, (2011), 1653-1664. https://doi.org/10.1016/j.actbio.2010.11.043
63. Putri, T.S., Rianti, D., Rachmadi, P. and Yuliati, A., "Effect of glutaraldehyde on the characteristics of chitosan–gelatin–β-tricalcium phosphate composite scaffolds", ***Materials Letters***, Vol. 304, (2021), 130672. https://doi.org/10.1016/j.matlet.2021.130672
64. Gerhardt, L.-C. and Boccaccini, A.R., "Bioactive glass and glass-ceramic scaffolds for bone tissue engineering", ***Materials***, Vol. 3, No. 7, (2010), 3867-3910. https://doi.org/10.3390/ma3073867
65. Nalvuran, H., Elçin, A.E. and Elçin, Y.M., "Nanofibrous silk fibroin/reduced graphene oxide scaffolds for tissue engineering and cell culture applications", ***International Journal of Biological Macromolecules***, Vol. 114, (2018), 77-84. https://doi.org/10.1016/j.ijbiomac.2018.03.072
66. Zhang, Z., Cheng, X., Yao, Y., Luo, J., Tang, Q., Wu, H., Lin, S., Han, C., Wei, Q. and Chen, L., "Electrophoretic deposition of chitosan/gelatin coatings with controlled porous surface topography to enhance initial osteoblast adhesive responses", ***Journal of Materials Chemistry B***, Vol. 4, No. 47, (2016), 7584-7595. https://doi.org/10.1039/c6tb02122k
67. Huang, Y., Hao, M., Nian, X., Qiao, H., Zhang, X., Zhang, X., Song, G., Guo, J., Pang, X. and Zhang, H., "Strontium and copper co-substituted hydroxyapatite-based coatings with improved antibacterial activity and cytocompatibility fabricated by electrodeposition", ***Ceramics International***, Vol. 42, No. 10, (2016), 11876-11888. https://doi.org/10.1016/j.ceramint.2016.04.110
68. Schnell, G., Staehlke, S., Duenow, U., Nebe, J.B. and Seitz, H., "Femtosecond laser nano/micro textured ti6al4v surfaces—effect on wetting and mg-63 cell adhesion", ***Materials***, Vol. 12, No. 13, (2019), 2210. https://doi.org/10.3390/ma12132210
69. Mahnama, H., Dadbin, S., Frounchi, M. and Rajabi, S., "Preparation of biodegradable gelatin/pva porous scaffolds for skin regeneration", ***Artificial Cells, Nanomedicine, and Biotechnology***, Vol. 45, No. 5, (2017), 928-935. https://doi.org/10.1080/21691401.2016.1193025
70. Liu, C., Kou, Y., Zhang, X., Dong, W., Cheng, H. and Mao, S., "Enhanced oral insulin delivery via surface hydrophilic modification of chitosan copolymer based self-assembly polyelectrolyte nanocomplex", ***International Journal of Pharmaceutics***, Vol. 554, (2019), 36-47. https://doi.org/10.1016/j.ijpharm.2018.10.068
71. Trivedi, S., Srivastava, K., Gupta, A., Saluja, T.S., Kumar, S., Mehrotra, D. and Singh, S.K., "A quantitative method to determine osteogenic differentiation aptness of scaffold", ***Journal of Oral Biology and Craniofacial Research***, Vol. 10, No. 2, (2020), 158-160. https://doi.org/10.1016/j.jobcr.2020.04.006
72. Hashemi, S.F., Mehrabi, M., Ehterami, A., Gharravi, A.M., Bitaraf, F.S. and Salehi, M., "In-vitro and in-vivo studies of pla/pcl/gelatin composite scaffold containing ascorbic acid for bone regeneration", ***Journal of Drug Delivery Science and Technology***, Vol. 61, (2021), 102077. https://doi.org/10.1016/j.jddst.2020.102077
73. Rozila, I., Azari, P., Munirah, S.b., Safwani, W.K.Z.W., Pingguan-Murphy, B. and Chua, K.H., "Polycaprolactone-based scaffolds facilitates osteogenic differentiation of human adipose-derived stem cells in a co-culture system", ***Polymers***, Vol. 13, No. 4, (2021), 597. https://doi.org/10.3390/polym13040597
74. Du, X., Yu, B., Pei, P., Ding, H., Yu, B. and Zhu, Y., "3d printing of pearl/caso 4 composite scaffolds for bone regeneration", ***Journal of Materials Chemistry B***, Vol. 6, No. 3, (2018), 499-509. https://doi.org/10.1039/c7tb02667f

Persian Abstract

چکیده

نقایص شایع استخوانی بزرگ معمولا به خودی خود خوب نمی شوند و کمپلکس ژلاتین/کیتوسان یکی از بهترین ترکیبات برای مهندسی بافت استخوان است، اما تجزیه سریع در محلول آبی و خواص مکانیکی کم نیاز به پیوند عرضی را افزایش می دهد. غلظت پیوند عرضی و روش پیوند عرضی بر خواص داربست ها تأثیر زیادی دارند. در اینجا، سه روش مختلف پیوند عرضی با گلوتارآلدئید (GA)، افزودن به محلول، قرار گرفتن در معرض بخار و غوطه وری با آنالیزهای مختلف برای یافتن بهترین تکنیک و غلظت مورد مطالعه قرار گرفتند. میکروسکوپ الکترونی روبشی ریزساختار متخلخل همگن را در تمامی نمونه ها نشان داد. درصد تورم و زیست تخریب پذیری با افزایش غلظت و زمان پیوند عرضی کاهش یافت اما خواص مکانیکی بهبود یافته است، همچنین تاثیر زمان نسبت به غلظت بیشتر بوده است. داربست پیوند داده شده با روش افزودن به محلول (1 wt .%) عملکرد بهتری نسبت به سایر نمونه ها داشته است و از خود زاویه تماس ۳۹/۳°، استحکام فشاری ۱/٤٥±۰/۰٥ مگاپاسکال، درصد تورم ۱/۳±۲۲/۳۱ (٪) و زیست تخریب پذیری ٤/٤۷±۲٦/۳۳ (٪)نشان داد. همچنین این نمونه زنده مانی سلولی بالاتر از ۸۰ (٪)داشته است و بیان آلکالین فسفاتاز (ALP) و استئوژن ها در طی ١٤ روز انکوباسیون سلولی بهبود یافته است که نشان دهنده ی ظرفیت بالای این نمونه در تمایز استخوانی می باشد. بنابراین این داربست به عنوان بهترین کاندید برای ترمیم استخوان و مطالعات بیشتر مهندسی بافت استخوان پیشنهاد می شود.

International Journal of Engineering

Journal Homepage: www.ije.ir

Digital Communication Based on Image Security using Grasshopper Optimization and Chaotic Map

K. S. Khalaf, M. A. Sharif*, M. S. Wahhab

Electronic and Control Engineering Techniques Department, Technical Engineering College – Kirkuk, Northern Technical University, Iraq

P A P E R I N F O

Paper history:
Received 22 August 2021
Received in revised form 05 July 2022
Accepted 06 July 2022

Keywords:
Chaotic Map
Communication
Grasshopper Optimization
Image Encryption Optimization
Image Pixel Correlation
Security

A B S T R A C T

Encryption is very important to protect sensitive data, especially images, from any illegal access and infringement. This research is presented to provide an image encryption optimization method for communication based on image security. This method uses the grasshopper optimization algorithm to perform optimal encryption and irregular logical mapping. Initially, this approach creates multiple encrypted images and a chaotic map, in which the session key for the initial conditions of the map depends on a simple suspended image. After that, the encrypted images work as an initial and particles set for optimization through the grasshopper optimization algorithm. The optimized encoded image with the correlation coefficient of the continuous pixels is expressed as a function of proportion. The results from Matlab simulation of the proposed encoding method show that the encrypted images are the same, and the adjacent pixels are highly correlated with other outstanding encoding rows, such as planar histogram entropy and effective pixel rate of change average correction strength.

***doi**: 10.5829/ije.2022.35.10a.16*

NOMENCLATURE

DFT	Discrete Fourier Transform	DICOM	Digital Imaging and Communications in Medicine
WDICA	Discrete Weight Imperial Competitive Algorithm	DNA coding	Genetic coding
PSO	Particle Swarm Optimization	GOA	Grasshopper Optimization Algorithm

1. INTRODUCTION

With the expansion of the communication in the computer network technologies, it is easy to access digital images over the network process and use, produce and distribute them further. On the one hand, digital technology brings a lot of convenience to people, but on the other hand, due to the transmission of a lot of video data through non-standard and unreliable channels, issues of confidentiality and privacy are contradictory, and it poses a risk when communicating and gives attackers or illegal users a chance to abuse. Therefore, the security and protection of digital data storage and transfer is more important than ever [1].

In particular, image security helps the application layer protect data sent from unwanted leaks or changes during delivery. There are various ways to protect the personal information of the current image and prevent unauthorized access to the image content. It uses image encryption methods to convert simple images into undetectable hidden formats to ensure airtightness with authenticated end users [2]. In general, two main ways are available to protect digital image or multiple images. The first way by hiding information that includes display, steganography, anonymity, and channel range. In other cases, it is encryption that includes other items such as contract encryption and chaotic encryption [3].

Today, the need for image encryption to securely transmit images over the internet and wireless networks is increasing, with special features such as overloading of digital image data and strong correlation between adjacent pixels, desensitization (i.e. slight variations) to text data. .The characteristics of pixels of the image, it cannot significantly reduce the quality and bulk of the

*Corresponding Author Institutional Email: msharif@ntu.edu.iq
(M. A. Sharif)

Please cite this article as: K. S. Khalaf, M. A. Sharif, M. S. Wahhab, Digital Communication Based on Image Security using Grasshopper Optimization and Chaotic Map, ***International Journal of Engineering, Transactions A: Basics***, Vol. 35 No. 10, (2022), 1981-1988

data). This is because encryption is slow for large amounts of data and stronger correlation between image pixel, so the implementations of these conventional image encryption algorithms are more complex when using commercial software's. For real-time video encryption, only encryption that does not compromise security and consumes less time at the same time is recommended. Although very slow cryptography sometimes provides improved security, real-time processes have few practical applications [2]. In various encryption algorithms, there are more advantages to chaos encryption technology, and these technologies are represented suitable for empirical use to provide an excellent combinations of high security, speed, complexity, and reasonable computational cost. However, the image encryption method using the chaos system still has many disadvantages, such as destruction of irregularities and low defense against simple text-based attacks. To get rid of these shortcomings and problems, the threats of the security and inefficiencies observed in image encryption can be enhanced by using optimization algorithms.

A chaotic algorithm is a well-defined nonlinear system with a variety of properties, including high-sensitivity self-assertion to initial conditions. The irregular order produced by the irregular map is a quasi-random sequence. Its structure is difficult to analyze, difficult to predict, and very complex. Chaos system can easily improve/ enhance the security of cryptographic systems. Based on the irregular map, the existing cryptographic algorithms can be siplitted into two types: permutation or modification and propagation. The first approach (permutation) algorithm depends on a random order or transformation of the matrix where the pixels positions in the original images. The encryption effect of the permutation algorithm is good, but if you don't change the pixels values, histogram of the encrypted images is created, and the original pictures are copied. So, security can threaten statistical analysis [3].

Irregularity theory is the part of mathematics that governs dynamic systems. In particular, it confirms a high sensitivity to the smallest changes in the initial conditions, thereby dramatically leading to large changes - a reaction commonly refer to the butterfly effects [4]. These minor changes produce the consequences of widespread distortion of such dynamic systems, making them unpredictable in the long run [5]. In addition to the advantages described in the previous section, these chaotic systems are easy to implement and exhibit confusing and spreading behavior in the iterative process of moving cryptosystems. The proposed approach in this paper for the optimal encoding of images due to the correlation of the pixels, using irregular mapping and grasshopper optimization algorithm is proposed. The irregularity function is utilized as the initial way of encryption to create the population, and then the locust optimization approach is utilized to guarantee the progress of the encryption process through the optimization operation. The results obtained in relation to the correlation coefficient of the image in comparisons with other recently introduced images encryption approaches show the optimal results of the proposed method.

2. RELATED WORKS

There are two main methods of chaotic cryptography: Block encryption and sequential encryption. Chaotic encryption methods provide a good balance between security, speed, and flexibility.

With the emergence of a new approach called chaos theory and the clarification of its scientific and theoretical dimensions, today chaos is no longer considered a concept of disorganization and disarray with the negative meaning concept, rather, it refers to the existence of unpredictable and accidental aspects in dynamic phenomena. One of the definitions of this theory states: "Chaos is a kind of regular irregularity or irregular in irregularity [6].

Logistic mapping is the most common and simple chaotic system that is widely used as an example of a low-dimensional chaotic mapping [7]. Logistic mapping involves a second order nonlinear differential equation. The dynamic relationship of this system was first introduced by Robert and defined as follows:

$$u_{n-1} = r \times u_n(1 - u_n) \quad (1)$$

where r is the logistic coefficient. The range of changes r is between zero to 4, but by changing r in this area it gives different properties to the function.

Chaotic tent mapping: Equation (2) represents the tent mapping equation:

$$f(x_n) = x_{n+1} = \begin{cases} \frac{x_n}{p} & 0 \le x_n \le p \\ \frac{1-x_n}{1-p} & p \le x_n \le 1 \end{cases} \quad (2)$$

So that $x_n \in [0,1]$, where p represents one of the control parameters that is very influential in the system behavior and x_0: the initial values. If the control parameters is in the range [0,1], the mapping of the tent becomes chaotic.

Hannon Mapping: A two-dimensional inverted chaotic mapping introduced by Hannon in 1976. Hannon mapping already introduced as a method for producing quasi-random sequence [8]. This mapping is defined as follows:

$$\begin{cases} x_{n+1} = 1 + y_n - \alpha x_n^2 \\ y_{n+1} = \beta x_n \end{cases} \quad (3)$$

Thus (X_0, Y_0) is the starting point and even (X, Y) represent a 2-dimension state of the proposed systems. Note that, $\alpha = 1.4$ and $\beta = 0.3$, this system will be in turbulence.

Conventional encryption requires that the encrypted text be the same size as the simple text. This is not a hindrance to similar images. Apart from the existing standards, the method used for encryption of images is to use affine transforms and bit performance. However, these methods cannot provide sufficient security for images as they cannot reduce the high correlation of pixels [7]. Another notable method utilized to encode images are based the random symmetry of the pixels in the images. The symmetric operation can significantly reduce the correlation, but it has little effects on the histograms of the encrypted images and other statistical attributes. Finally, you can expose a lot of information about simple images that are very vulnerable to histogram-based statistical attacks and other attacks [9-11].

Naskar et al. [12] presented a new approach that provides both purpose of encrypting both gray scale and binary images for harmless compression. Scanning methods are integrated to generate patterns utilized in encryption techniques and compression. Ravichandran et al. [13] have integrated irregular logical mappings to encrypt images and used them to meet the prerequisites for secure image transfer. Its cryptographic method involves the execution of two-irregular logical maps and a secret eighty-bit foreign key.

Talarposhti et al. [14] proposed in their paper an image encoding method using the differential evolution, discrete fourier transform (DFT), and differential evolution (DE). By utilizing differential evolution DE through crossover operations and mutations of chosen components whose selection indicators are generated by the linear feedback shift register (LFSR), this system manipulates the size and procedure of images from the DFT domain. Adleman [15] expressed that distortion within the 01 image extended using a single arch mapping generated arbitrary sequences, resetting the gray values of the image, and confusion. It demonstrates how to encode modern images to create the required release. Zhang et al. [16] reported a method of image encryption using irregular mapping and discrete weight imperial competitive algorithm (WDICA). They used arch mapping as a random source and WDICA as an evolutionary technique for designing cryptographic processes based on infiltration diffusion architecture. A method for encoding images using crystal particle optimization is introduced by Zhang et al. [17]. This method alters the ARNOLD image and then uses the key using the modified PSO to next transform the pixel position.

Özkaynak and Yavuz [18] have discussed symmetric image encoding using linear geometry. This approach involves consolidating alternatives with transfer techniques. The proposed image encryption scheme includes a combination of irregular arch mapping, sinusoidal mapping, and logical mapping to ensure further the safe transmission of medical DICOM images. Shiu et al. [19] achieved proper encoding, the dissemination of image pixels is achieved using cross-inspired biological mutations in the image encryption systems. Ravichandran et al. [20] also achieved image encryption by combining dynamic harmony search and irregular mapping.

Ravichandran et al. [20] showed that image encryption algorithms are easily selected by simple text attacks based on randomness and fixed encryption rules. Improved image encoding is provided using DNA coding and irregular mapping [21]. This is done by using a very irregular system to change positions and pixel values to do things like DNA using DNA coding rules and finally using images encoded by DNA. decoding. Ravihandran Pujari et al. [22] presented image encoding using a DNA encoding and irregularity system to encode medical images; DNA has a natural compatibility with the functions of DNA and genetic algorithms that determine the genetic properties of these organisms.

These approaches are utilized to encrypt images from an optimization point of view. In this work, images of genetic algorithms are shared and distributed by genetic operators.

Cryptographic algorithms using the randomness system provide a high level of security that can compensate for the shortcomings of traditional cryptographic algorithms. The proposed method in this work uses a combination of a chaos-based images encryption methods and a grasshopper optimization algorithm. The detail is explained in the following sections.

3. PROPOSED METHOD

The concept of optimization is to look for values between the parameters of a function that minimize or maximize the function. One of the optimization algorithms is meta-heuristic algorithms. Meta-heuristic algorithms have methods for getting out of local optimization and have high capability of development and scope. According to the studies, meta-heuristic algorithms have better results than accurate algorithms, which are able to find the optimal answer in a quantitative way, but are not suitable for complex and difficult problems. Meta-heuristic optimization algorithms are also known among engineering for four reasons: First, they are based on simple concepts and are easily implemented, second, they do not require much information, third, they can bypass the desired local state, and fourth they can cover different issues with different mechanisms.

One of the newest optimization algorithms introduced by grasshopper optimization algorithm [23]. The grasshopper algorithm is a nature-inspired meta-heuristic algorithm that simulates the behavior of grasshopper in

nature and the group movement of grasshoppers toward food sources.

The grasshopper algorithm was introduced by Coello [24]. The steps of the grasshopper algorithm are as follows:

$$X_i = S_i + 2G_i + A_i \quad (4)$$

X_i indicates the positions of the grasshoppers, S_i indicates social interactions, G_i the gravitational forces on the grasshopper, and A_i the horizontal force.

$$X_i = r_1 S_i + r_2 2G_i + r_3 A_i \quad (5)$$

r_1, r_2 and r_3 are random numbers. This is considered a black box.

The following equations are used to calculate S_i (social interactions).

$$d_{ij} = |x_j - x_i| \quad (6)$$

$$S_i = \sum_{j=1}^{N} s(d_{ij}) d_{ij} \quad (7)$$

The parameters i and j are grasshopper i and grasshopper j.

$$d_{ij} = x_j - x_i)/d_{ij} \quad (8)$$

That d_{ij} is a single vector from grasshoppers i to grasshoppers j, and the function s will be obtained as follows.

$$S(r) = f e^{\frac{-r}{l}} - e^{-r} \quad (9)$$

The parameter l indicates the scale of gravity and f indicates the intensity of gravity. Figure 1 shows the s function showing how it can affect the social interactions (gravity and repulsion) of the grasshopper.

Figure 2 shows a conceptual model of gravity and repulsion and comfort area.

Here are details of the steps of the proposed method. Its general flowchart is shown in Figure 3.

The steps that describe the proposed method are as follows:

- **Step 1:** In this step, we first give the parameters of the logistics mapping function, which includes two parameters r (the variable parameter of the logistics function) and u_0 (the initial value of the logistics function) as the initial population to the grasshopper algorithm to obtain the optimal value of each parameter. Of course, the value of r should be considered in the range of 3.57 to 4. However, in this study, we considered the value of r as a conformity so that the resulting encrypted image has the lowest correlation between pixels or the highest entropy. So each grasshopper is considered as x = [r, u_0].
- **Step 2:** In this step, the relevant image is entered into the system and the cost function is calculated. First, the relevant image must be encrypted using logistic mapping, which parameters are being optimized by the grasshopper algorithm; Then we get the cost function for each grasshopper.
- **Step 3:** After obtaining the cost function of the images or the same amount of grasshoppers, the best amount that has the highest value according to the cost function is selected as the superior grasshopper in the relevant iteration. During the implementation of the grasshopper optimization algorithm, the best grasshopper that attracts other grasshoppers is selected and then the best grasshopper with the values of parameters R and u_0 with the highest entropy in the encrypted image is selected.
- **Step 4:** In this step, after obtaining the optimal value for the parameters r and u_0 as the key, they must be converted to binary code. It should be noted that because the numbers are decimal, we used to convert decimal numbers to binary. The conversion is such that the integer parts of the numbers u_0 and r will remain and we will convert only the decimal part of them. In conversion, the size of the binary part is not fixed and is variable, so we choose the number so that it is a maximum of 64 bits for each of the parameters; As a result, the key length becomes 128 bits.
- **Step 5:** In this step, we encrypted the corresponding image using the optimized logistics function. The cryptographic method is performed in two steps. Change the parameter values of the pixels and the permutation of the pixels.

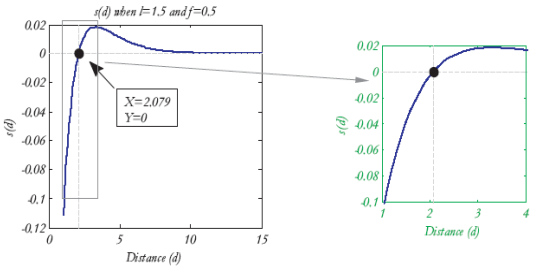

Figure 1. The function (s) (left); when l = 1.5; f = 0.5 (in the right Figure); The amplitude of the function (s), when x is in [1, 4]

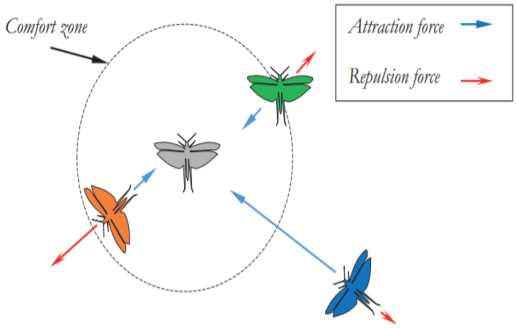

Figure 2. Conceptual model of the areas of gravity, repulsion and comfort [23]

❖ **Step 6:** In this step, the encrypted image will be generated as output.

Change the value of the pixels: First, according to Equations (3-11) the logistics function and the values of its optimized parameters to the number of pixels in the image; We produced the value of u_n, so the length of the matrix U is equal to M * N; and M is the length; N is the width of the corresponding image. Then multiply each element of the matrix by the number 255 (pixel color change area) and then XOR the corresponding pixel of the image to change its value. This process continues until all the pixels in the image are changed.

In Equation (11) U_i is any vector U and $\oplus$ means xor.

We changed the location of the pixels to increase the quality of the encryption and make the cryptographic system more secure, as well as to minimize the correlation between adjoining or adjacent pixels. For this purpose, we have used the Noth algorithm [25-28] to matrix permutation. Although the rand function is used to generate random numbers in this Note algorithm, but for cryptography and decryption that can reproduce the generated random number under certain conditions, we use functions that have quasi-random properties. Because in the decoding section to find the image, you must first change the location of the pixels to the original state. In this paper, we have used the logistic function instead of the rand function in the Noth algorithm.

$$u_{n+1} = r * u_n (1 - u_n) \quad (10)$$

$$newValue = round(U_i * 255) \oplus oldValue \quad (11)$$

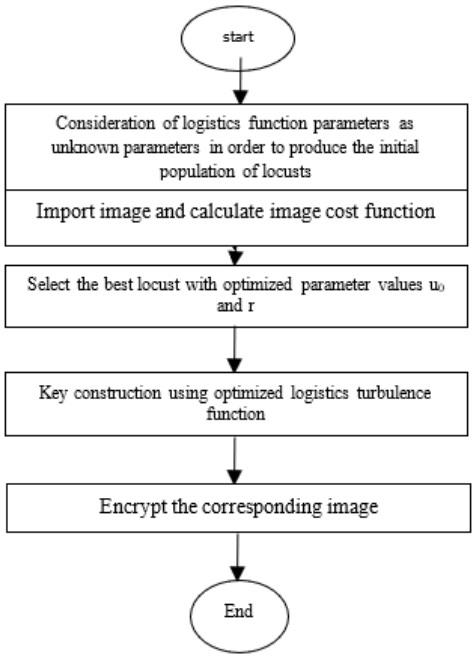

Figure 3. Flowchart of the proposed algorithm

4. EVALUATED THE PROPOSED METHOD

This section simulates the proposed method on standard images such as boat and Lena, peppers. We have also examined the proposed method with the methods available in literature [26, 29, 30].

To implement the method mentioned in this article, standard images with a size of 512 x 512 have been used. Also, the optimization operation has been done in 100 repetitions with MATLAB software. The encryption processes on the lena images is based on the correlation between adjoined pixels and the entropy-based optimization is performed. Of course, it should be noted that the diagrams shown are the average of the simulations during different iterations. Chaos-based image encryption is very sensitive to changes in specified parameters, so there is no single answer in optimizing this problem so that the set of answers converges to it, but the optimization operation can be terminated by determining the minimum value for correlation and the maximum value required for entropy or the maximum repetition.

In various articles, 1000 pairs of neighboring pixels are randomly selected for simplicity and speed of calculation, but in this study, we consider the value of N equal to all image pixels so that the correlation coefficient is constant each time the calculation covers the whole image. The original image and Lena: the encrypted image is shown in Figure 4.

The maximum correlation coefficient is one and refer to a high correlation between adjoining pixels. An excellent encryption algorithm must encrypt the image in such a way that the correlation coefficients between adjoining pixels in the encrypted image are pretty small and near to zero, here the attacker does not have access to any information through analysis.

The main images and the encrypted images and the histograms diagram of the original and encrypted images as well as the distribution of the correlations of the adjacent pixels in the horizontal direction in the main image and the encrypted images of Lena and the Boat image are shown in Figures 4 and 5. The original image histograms; and the encrypted image histograms is illustrated in Figure 6. In addition, the correlation of

Figure 4. Lena**:** The original image and Lena: the encrypted image

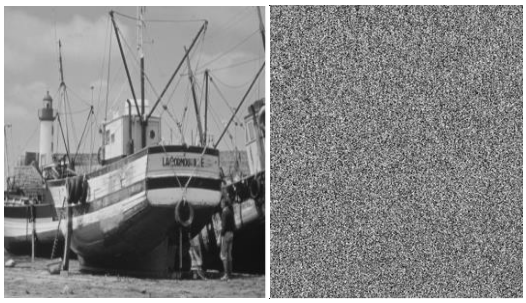

Figure 5. Boat: the original image and the encrypted image

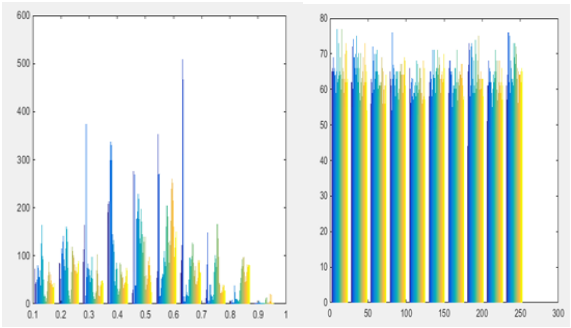

Figure 6. The original image histograms; and The Encrypted image histograms

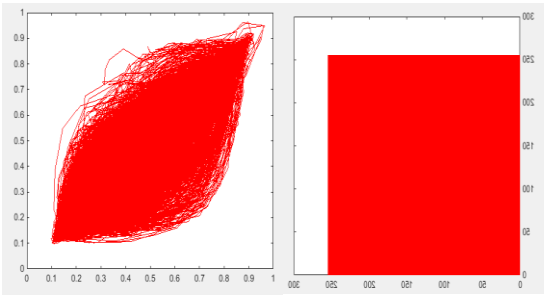

Figure 7. Correlation of adjoined pixels of the original images and encoded images

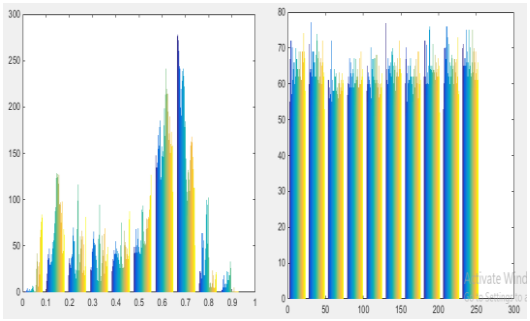

Figure 8. Boat main image histogram and encoded image histogram

adjoined pixels of the original images and encoded images are shown in Figure 7.

The boat main image histogram and encoded image histogram is also shown in Figure 8

Table 1 summarized the values obtained from the correlation coefficient between adjoined pixels in the images. From Table 2, the NPCR values are at the highest values and also the UACI values are better than the reference value reported in literature [27-29]. The results showed that the image encrypted by this work's approach has the lowest correlation between the available methods and the appropriate entropy.

TABLE 1. Correlation value of adjacent pixel

	Main image	Encrypted image with the proposed method	Encrypted image in reference [26]	Encrypted image in reference [29]	Encrypted image in reference [30]
Boat	0.9751	0.0000085	0.00000144	NA	NA
Lena	0.9718	0.000003226	0.00000682	NA	NA
Peppers	0.9732	0.0001017	0.00024591	0.0003	0.0114

TABLE 2. UACI and NPCR criteria

	NPCR proposed method	NPCR Reference [26]	UACI proposed method	UACI Reference [26]
Boat	99.65	99.191	42.152	31.159
Lena	99.43	99.22	58.12	30.147
Peppers	99.79	99.16	38.71	30.667

5. CONCLUSION

Today, image encryption represents as one of the important methods to achieve security. Conventional encryption methods cannot be utilized because of the correlations between adjoining pixels of large amounts of information and time-consuming processing. Among the proposed methods for image encryption, the turbulence functions have been used due to its properties like quasi-

randomness, sensitivity to and simplicity and initial conditions, reduction of computation time, and simple of implementations. Using the proposed method in this work, we were able to encode the images in a way that has the highest entropy and the lowest possible correlation by the logistic turbulence function using the grasshopper algorithm (GOA). The results show high accuracy, quality, and security against attacks, so that the correlation values of the encrypted images are significantly lower than the studied methods. For future solutions, we can point by fuzzy grasshopper parameters to improve the grasshopper algorithm and use it in image encryption.

5. REFERENCES

1. Nickel, S., Karimi, H. and Bashiri, M., "Capacitated single allocation p-hub covering problem in multi-modal network using tabu search", ***International Journal of Engineering, Transactions C: Aspects***, Vol. 29, No. 6, (2016), 797-808. doi: 10.5829/idosi.ije.2016.29.06c.09.
2. Su, Z., Zhang, G. and Jiang, J., "Multimedia security: A survey of chaos-based encryption technology", ***Multimedia-A Multidisciplinary Approach to Complex Issues***, (2012). doi: 10.5772/36036
3. Norouzi, B., Seyedzadeh ,S.M., Mirzakuchaki, S. and Mosavi, M.R., "A novel image encryption based on hash function with only two-round diffusion process", ***Multimedia Systems***, Vol. 20, No. 1, (2014), 45-64. doi: 10.1007/s00530-013-0314-4
4. Furht, B. and Kirovski, D., "Multimedia security handbook, CRC press.(2004)
5. Wu, Y., Zhou, Y., Noonan, J.P. and Agaian, S., "Design of image cipher using latin squares", ***Information Sciences***, Vol. 264, (2014), 317-339. doi: 10.1016/j.ins.2013.11.027.
6. Hua, Z. and Zhou, Y., "Image encryption using 2d logistic-adjusted-sine map", ***Information Sciences***, Vol. 339, (2016), 237-253. doi: 10.1016/j.ins.2016.01.017.
7. Hassan, M.A.S. and Abuhaiba, I.S.I., "Image encryption using differential evolution approach in frequency domain," arXiv preprint arXiv:1103.5783, (2011). doi: 10.48550/arXiv.1103.5783.
8. Schneier, B., "Applied cryptography: Protocols, algorithms, and source code in c, john wiley & sons, (2007).
9. Ye, R., Zeng, S., Lun, P., Ma, J. and Lai, C., "An image encryption scheme based on bit circular shift and bi-directional diffusion", ***Int J Inform Technol Comput Sci (IJITCS)***, Vol. 6, No. 1, (2014), 82-92. doi: 10.5815/ijitcs.2014.01.10.
10. Enayatifar, R., Abdullah, A.H. and Lee, M., "A weighted discrete imperialist competitive algorithm (wdica) combined with chaotic map for image encryption", ***Optics and Lasers in Engineering***, Vol. 51, No. 9, (2013), 1066-1077. doi: 10.1016/j.optlaseng.2013.03.010.
11. Sabarinath, R., Jegadeesan, S. and Venkatalakshmi ,K., "Image encryption using modified particle swarm optimization", ***IJRCCT***, Vol. 3, No. 2, (2014), 241-246. doi: 10.1007/s41870-018-0099-y
12. Naskar, P.K., Chaudhuri, A. and Chaudhuri, A., "A secure symmetric image encryption based on linear geometry ,"in 2014 Applications and Innovations in Mobile Computing (AIMoC), IEEE., (2014), 67-74.
13. Ravichandran, D., Praveenkumar, P., Rayappan, J.B.B. and Amirtharajan, R., "Chaos based crossover and mutation for securing dicom image", ***Computers in Biology and Medicine***, Vol. 72, (2016), 170-184. doi: 10.1016/j.compbiomed.2016.03.020
14. Talarposhti, K.M. and Jamei, M.K., "A secure image encryption method based on dynamic harmony search (dhs) combined with chaotic map", ***Optics and Lasers in Engineering***, Vol. 81, (2016), 21-34. doi: 10.1016/j.optlaseng.2016.01.006.
15. Adleman, L.M., "Molecular computation of solutions to combinatorial problems", ***Science***, Vol. 266, No. 5187, (1994), 1021-1024. doi: 10.1126/science.7973651.
16. Zhang, X., Zhou, Z. and Niu, Y., "An image encryption method based on the feistel network and dynamic DNA encoding", ***IEEE Photonics Journal***, Vol. 10, No. 4, (2018), 1-14.
17. Zhang, J., Fang, D. and Ren, H., "Image encryption algorithm based on DNA encoding and chaotic maps", ***Mathematical Problems in Engineering***, Vol. 2014, (2014). doi: 10.1155/2014/917147.
18. Özkaynak, F. and Yavuz, S., "Analysis and improvement of a novel image fusion encryption algorithm based on DNA sequence operation and hyper-chaotic system", ***Nonlinear Dynamics***, Vol. 78, No. 2, (2014), 1311-1320. doi: 10.1007/s11071-014-1517-8.
19. Shiu, H.-J., Ng, K.-L., Fang, J.-F., Lee, R.C. and Huang, C.-H., "Data hiding methods based upon DNA sequences", ***Information Sciences***, Vol. 180, No. 11, (2010), 2196-2208. doi: 10.1016/j.ins.2010.01.030
20. Ravichandran, D., Praveenkumar, P., Rayappan, J.B.B. and Amirtharajan, R., "DNA chaos blend to secure medical privacy", ***IEEE Transactions on Nanobioscience***, Vol. 16, No. 8, (2017), 85 .858-0doi: 10.1109/TNB.2017.2780881.
21. Wang, X. and Zhang, H.-l., "A novel image encryption algorithm based on genetic recombination and hyper-chaotic systems", ***Nonlinear Dynamics***, Vol. 83, No. 1, (2016), 333-346. doi: 10.1007/s11071-015-2330-8.
22. Pujari, S.K., Bhattacharjee, G. and Bhoi, S., "A hybridized model for image encryption through genetic algorithm and DNA sequence", ***Procedia Computer Science***, Vol. 125, (2018), 165-171. doi: 10.1016/j.procs.2017.12.023.
23. Sezavar, A., Farsi, H .and Mohamadzadeh, S., "A modified grasshopper optimization algorithm combined with cnn for content based image retrieval", ***International Journal of Engineering, Transactions A: Basics***, Vol. 32, No. 7, (2019), 924-930. doi: 10.5829/ije.2019.32.07a.04.
24. Coello, C.A.C., "Theoretical and numerical constraint-handling techniques used with evolutionary algorithms: A survey of the state of the art", ***Computer Methods in Applied Mechanics and Engineering***, Vol. 191, No. 11-12, (2002), 1245-1287. doi: 10.1016/S0045-7825(01)00323-1.
25. Knuth, D.E., *Theartofcomputerprogramming: Sortingandsearching*. 1973, Addison-Wesley, Reading, Massachusetts.
26. Hussain, I., Azam, N.A. and Shah, T., "Stego optical encryption based on chaotic s-box transformation", ***Optics & Laser Technology***, Vol. 61, (2014), 50-56. doi: 10.1016/j.optlastec.2014.01.018.
27. Ahmad, M., Alam, M.Z., Umayya, Z., Khan, S. and Ahmad, F., "An image encryption approach using particle swarm optimization and chaotic map", ***International Journal of Information Technology***, Vol. 10, No. 3, (2018), 247-255. doi: 10.1007/s41870-018-0099-y.
28. Jolfaei, A. and Mirghadri, A., "A new approach to measure quality of image encryption", ***International Journal of Computer and Network Security***, Vol. 2, No. 8, (2010), 38-44, doi: 10.12928/TELKOMNIKA.v17i6.10488.

29. Norouzi, B., Mirzakuchaki, S., Seyedzadeh, S.M. and Mosavi, M.R., "A simple, sensitive and secure image encryption algorithm based on hyper-chaotic system with only one round diffusion process", ***Multimedia Tools and Applications***, Vol. 71, No. 3, (2014), 1469-1497. doi: 10.1007/s11042-012-1292-9.

30. Farwa, S., Muhammad, N., Shah, T. and Ahmad, S., "A novel image encryption based on algebraic s-box and arnold transform", ***3D Research***, Vol. 8, No. 3, (2017), 1-14, doi: 10.1007/s13319-017-0135-x

Persian Abstract

چکیده

رمزگذاری برای محافظت از داده های حساس، به ویژه تصاویر، در برابر هرگونه دسترسی غیرقانونی و نقض بسیار مهم است. این تحقیق به منظور ارائه یک روش بهینه سازی رمزگذاری تصویر برای ارتباطات مبتنی بر امنیت تصویر ارائه شده است. این روش از الگوریتم بهینه سازی ملخ برای انجام رمزگذاری بهینه و نگاشت منطقی نامنظم استفاده می کند. در ابتدا، این رویکرد چندین تصویر رمزگذاری شده و یک نقشه آشفته ایجاد می کند که در آن کلید جلسه برای شرایط اولیه نقشه به یک تصویر ساده معلق بستگی دارد. پس از آن، تصاویر رمزگذاری شده به عنوان یک اولیه و ذرات برای بهینه سازی از طریق الگوریتم بهینه سازی ملخ تنظیم می شوند. تصویر کدگذاری شده بهینه شده با ضریب همبستگی پیکسل های پیوسته به عنوان تابعی از نسبت بیان می شود. نتایج شبیه‌سازی متلب روش کدگذاری پیشنهادی نشان می‌دهد که تصاویر رمزگذاری‌شده یکسان هستند و پیکسل‌های مجاور با سایر ردیف‌های رمزگذاری برجسته، مانند آنتروپی هیستوگرام مسطح و نرخ پیکسل مؤثر تغییر میانگین قدرت تصحیح همبستگی بالایی دارند.

International Journal of Engineering

Journal Homepage: www.ije.ir

Investigating the Effect of Soil Layering on Soil-structure Interaction under Seismic Load

M. Zarinfar*

Department of Civil Engineering, Bu-Ali Sina University, Hamedan, Iran

PAPER INFO

Paper history:
Received 24 April 2022
Received in revised form 05 July 2022
Accepted 07 July 2022

Keywords:
Rock Layer
Seismic Analysis
Steel Moment
Soft Soil
Soil and Structure Interaction

ABSTRACT

Considering soil layering is a crucial and effective issue in investigating the seismicity of structures. However, previous studies have not examined the presence of a rock layer in soft soil. So, in the present paper, the effect of the rock layer in soft soil on the forces and displacements created in the low-and mid-rise steel moment frame was investigated. Thus, several numerical calculations were performed on 12 different sizes of rock layers at three different depths. Finite element models were analyzed using ABAQUS Software and considering the interaction of structure and soil. Results of the studies showed that the value of force and displacement depends on the frequency of the structure, the frequency of the soil-structure system, dominant earthquake frequency, the rock weight, and the stiffness of the structure. Two new parameters are defined that have a linear relationship with force and displacement. Results show that the thickness and length of the rock layer affect the value of force and displacement. Also, the presence of a rock layer in the soil may not be reliable and may increase the shear force by up to 27%, the axial force by up to 10%, and the moment by up to 19%. The effect of the presence of a rock layer on the displacement is more than on the force and increases the lateral displacement by up to 31% and the relative vertical displacement of the foundation by up to 59%.

***doi**: 10.5829/ije.2022.35.10a.17*

1. INTRODUCTION

The damage to artificial structures caused by earthquakes has long been a matter of concern, and earthquakes of different intensities significantly impact human production and life [1, 2]. Macroseismic vulnerability and seismic damage are important issues in the field of seismic safety. Vulnerability analysis of typical structures has been studied in the literature [3-5].

Without considering the interaction of structure and soil, dynamic structure analysis will not correspond to reality. The movement transmitted from the earthquake to the structure depends not only on the characteristics of the earthquake, the earthquake route, and the local conditions of the site but also on the interaction of soil and structure. The presence of soil increases the acceleration of the earthquake transmitted to the structure and increases the flexibility of the structure [6]. The first factor is the cause of more seismic damage in structures built on soft soil than in structures built on hard soil, so that the performance of the structure may change from the life-safe to a near-collapse without considering the interaction of the structure and the soil [7, 8]. The second factor reduces the frequency of the soil-structure system. Propagating waves from the structure increase the damping of the soil-structure system because of the radiation of energy in the soil [6].

Past studies on the structure and soil interaction were analytical [9], numerical [7, 10], and laboratory [11]. Aydin et al. [12] investigated the influence of soil-structure interaction on the optimal design of damping devices. The structure and soil interaction can be ignored for flexible structures built on hard soils. However, in the presence of stiff structures on soft soils, the interaction has particular importance and should be considered in the analysis of the structure. This issue has been shown by Kim and Roesset [13] by analyzing the system of one degree of freedom and by other researchers by analyzing

*Corresponding Author Institutional Email: zarinfar@basu.ac.ir (M. zarinfar)

Please cite this article as: M. Zarinfar, Investigating the Effect of Soil Layering on Soil-structure Interaction under Seismic Load, ***International Journal of Engineering, Transactions A: Basics***, Vol. 35 No. 10, (2022), 1989-2006

the structure of the moment frame [10]. Fatahi et al. [14] showed that the lateral displacement of the structure and the period of the soil-structure system increase with increasing bedrock depth. Tabatabaiefar et al. [10] showed that ignoring the interaction does not necessarily lead to the design of safe moment frames with moderate height. For the structures built on soft soil, the motion transmitted to the structure is different from the free field movement because the structure and soil interaction create additional dynamic deformation [8]. Mostly by considering the structure and soil interaction, the base shear will decrease, and the storey displacement will increase.

Although several studies have been conducted on the soil and structure interaction, the effect of the presence of a rock layer in soft soil has not been examined. The importance of including soil layering in seismic analysis has been reported in past studies. Damages reported from the Northridge Earthquake in 1994 indicate that soil layering can affect the dynamic response of the entire system [15]. Rayhani and El Naggar [16] examined the impact of soil profile thickness, soil layering, buried depth of the structure, and lateral boundary distance on the results of soil and structure interaction analysis. They showed that considering an equivalent layer could not provide an accurate prediction of reality, and soil layering should be considered in the analysis. Past studies have not been referred to the size of the rock layer and how it affects the force and displacement created in the structure under the effect of the earthquake. The aim of this article is to investigate the effect of the presence of the rock layer in soft soil on the force and displacement created in the structure by considering the interaction of soil and structure. For this purpose, the results of numerical modeling with shaking table experiments presented in the study conducted by Hokmabadi et al. [8] and Tabatabaiefar et al. [10] were first compared. Then, the rock layers were modeled in 12 different sizes, at three depths, and under three steel moment frames with different heights in ABAQUS Software. By applying records of the Kobe earthquake (near-field earthquake) and El Centro earthquake (far-field earthquake), the value of axial force, shear force, moment, and displacement in the structure are calculated, and the effect of the rock layer on the results is analyzed.

2. NUMERICAL MODEL VALIDATION

The shaking table test mentioned in the studies conducted by Hokmabadi et al. [8] and Tabatabaiefar et al. [10] was used to validate the model. In the two papers, they used dynamic similarities to scale the earthquake record. The advantage of using dynamic similarity in experiments is that the same value of gravity acceleration and density are considered in reality and the model. However, other parameters such as time, force, acceleration, etc., should be used in a scaled manner. The scaled records of the El Centro and Kobe earthquakes are shown in Figures 1 and 2. Experiments were performed on the structure fixed to the shaking table and the structure built on the shallow foundation to examine the impact of soil-structure interaction.

The width of the structure is 0.4 m, the height of the structure is 1.5 m, and the number of the storey is 15. The shear wave velocity in the soil is 36 m per second. Not only the shear wave velocity in the soil must be scaled, but also the soil bearing capacity must also be sufficient. For this purpose, a combination of kaolinite, bentonite, lime, and volcanic ash was used in these articles. More details on the way of performing the experiment and the parameters used to model the soil and structure can be found in the mentioned articles.

The time history of horizontal acceleration at the 15th storey obtained from a two-dimensional plane strain analysis for a structure fixed to the shaking table and a structure placed on the soil by applying a scaled El Centro earthquake is shown in Figures 3 and 4. The results obtained for the lateral displacement of the 15th storey as a result of applying the scaled Kobe earthquake are shown in Figures 5 and 6. The value of lateral

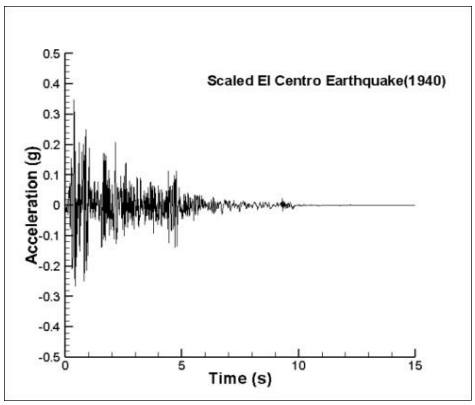

Figure 1. The scaled El Centro earthquake record

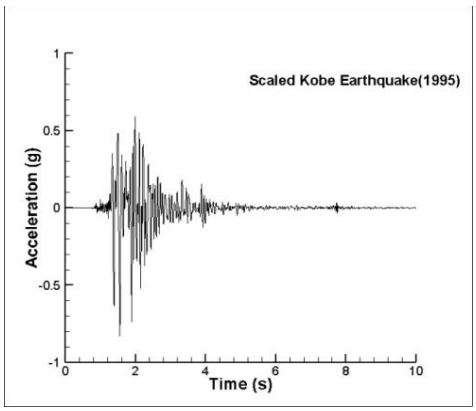

Figure 2. The scaled Kobe earthquake record

displacement is obtained by deducting the shaking table motion from the lateral displacement of the stories. The maximum lateral displacement of the stories measured in the laboratory by applying the El Centro earthquake and the value estimated by the numerical model are presented in Figure 7.

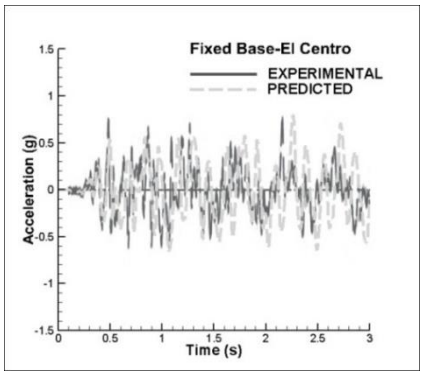

Figure 3. Time-history acceleration at the roof level of the structure under the El Centro earthquake for the fixed-base structure

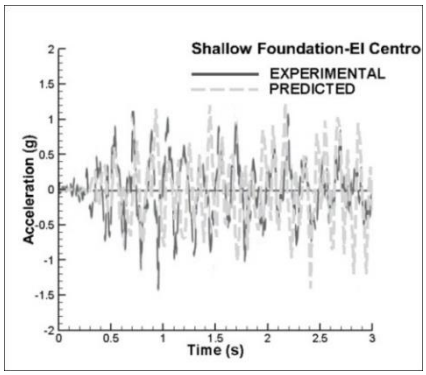

Figure 4. Time-history acceleration at the roof level of the structure under the El Centro earthquake for the structure with shallow foundation

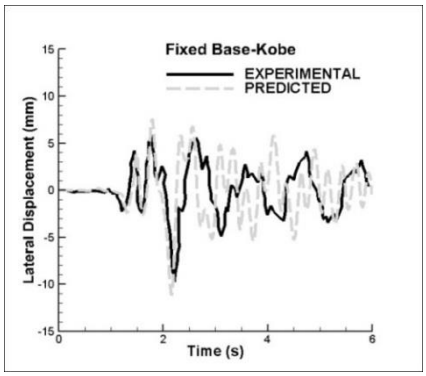

Figure 5. Time-history displacement at the roof level of the structure under the Kobe earthquake for the fixed-base structure

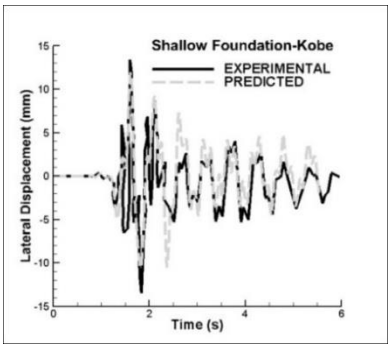

Figure 6. Time-history displacement at the roof level of the structure under the Kobe earthquake for the structure with shallow foundation

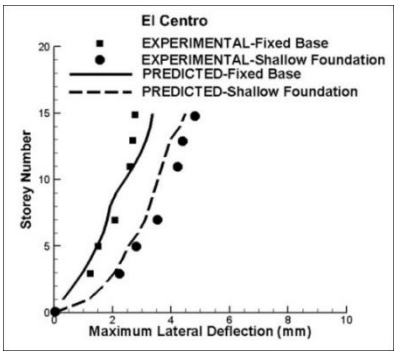

Figure 7. Comparison of experimental and numerical predictions of maximum lateral displacements

There is a good agreement between the results obtained from the laboratory and the numerical analysis, which includes the history of lateral displacement, lateral acceleration, and maximum lateral displacement of the stories in terms of trend and value. Since; the analyses are performed in the structure with a fixed base and the structure on the soil, this numerical analysis can be used as an alternative to the structure and soil system for further studies.

The next simulation includes the soil-structure model problem illustrated by Zienkiewicz et al. [17]. Homogeneous soil properties are assumed, and the incoming seismic wave is considered El Centro. The comparison of displacement, acceleration, and stress histories of control points indicates the validity of the numerical simulations (Figures 8 to 13).

3. MODEL DESCRIPTION AND ASSUMPTIONS

In this section, the effect of the rock layer in soft soil on the force and lateral displacement created in the low-and mid-rise steel structures is examined. For this purpose, the interaction of steel moment frames of 6-, 9- and 12-storey and soft clay was considered. The characteristics of the studied frames are shown in Table 1.

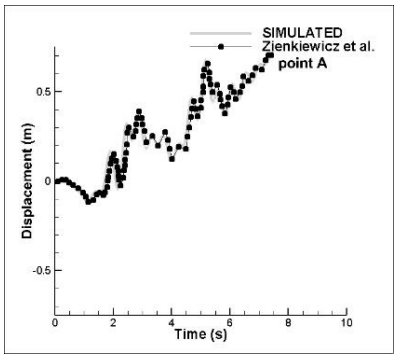

Figure 8. Comprision of displacement history at point A

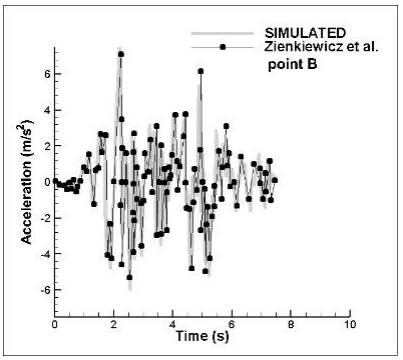

Figure11. Comprision of acceleration history at point B

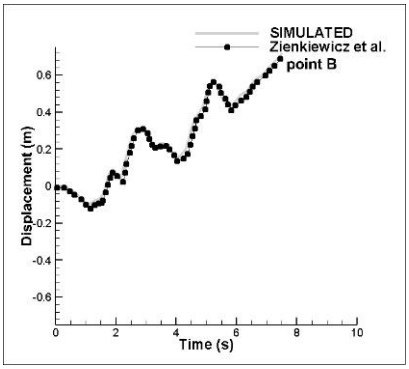

Figure 9. Comprision of displacement history at point B

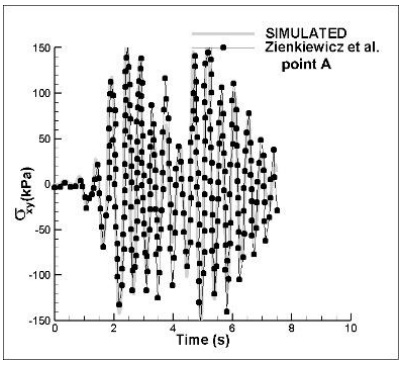

Figure 12. Comprision of stress history at point A

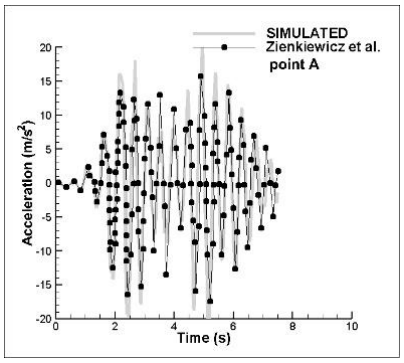

Figure 10. Comprision of acceleration history at point A

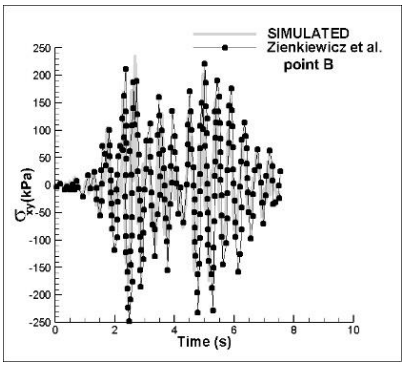

Figure 13. Comprision of stress history at point B

The characteristics of the numerical models, for the 12-storey structure include the location of the bedrock, the dimensions of the structure, and the soil medium are shown in Figure 14. The numerical models of 6- and 9-storey structures are constructed in exactly the same way. In this paper, it is assumed that the bedrock is located at a depth of 30 m below the soil surface. The results presented by Rayhani and El Naggar [16] show that the

TABLE 1. Characteristics of the steel frames

Name	Number of stories	Number of bays	Storey height (m)	Bay width (m)	Total height (m)	Total width (m)
S6	6	3	3	3	18	9
S9	9	3	3	3	27	9
S12	12	3	3	3	36	9

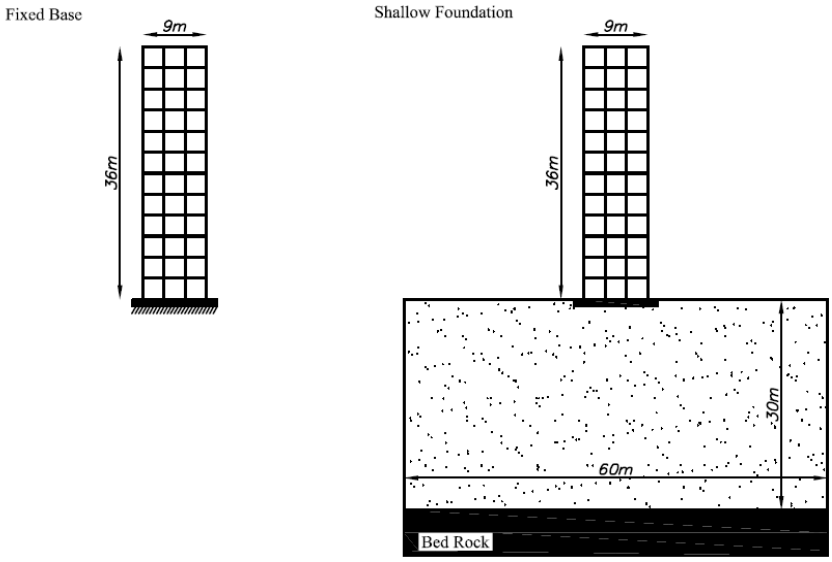

Figure 14. 12-storey steel structure with the fixed-base foundation and shallow foundation

maximum acceleration transmitted to the soil surface increases with increasing the thickness of the soil profile from 10 to 70 m. The maximum increase in acceleration occurs at a depth of 30 m. As a result, considering the thickness of 30 m of soil in soil-structure interaction analyses is a reasonable assumption.

The preliminary analysis of the structure was first performed in ETABS software. The design in ETABS was done in such a way that the stress ratio in beams was less than 0.8 and more than 0.6, and in columns, it was less than 0.4. The dead load and the live load of the floors were considered at 600 and 200 kg/m^2, respectively.

A mat foundation with dimensions of 12x12x1m was considered in numerical analyses. ABAQUS software was used for numerical modeling of soil-structure interaction. The damping of the structure was selected as Rayleigh type, and the damping value was considered at 5%. The damping coefficients were calculated using the frequency of the first and second modes, which are shown in Table 2. The beam and column elements were selected as the second-order one-dimensional element type, and the foundation and soil elements were selected as the Serendipity quadratic type. The sections used for beams and columns in 6-, 9- and 12- storey structures are shown in Table 3.

Von Mises constitutive model with isotropic hardening was selected for steel, and the damaged plasticity model was chosen for concrete. The concrete damage plasticity model is one of the most widely used constitutive models for concrete simulation in ABAQUS software, which has been used in various articles [7]. This model simulates the mechanism of failure in tension and compression in a continuum space using the damage parameter, which is a function of non-elastic strain.

TABLE 2. Rayleigh coefficient for steel structures

Name	Frequency of the first mode	Frequency of the second mode	α	β
S6	0.966	2.930	0.456	0.004
S9	0.836	2.201	0.380	0.005
S12	0.702	2.068	0.329	0.006

TABLE 3. Typical sections of 6,9 and 12-storey structures

Number of stories	Levels	Beam section	Column section
6	1-3	IPE220	Box 220x16mm
	4-6	IPE200	Box 200x16mm
9	1-3	IPE270	Box 280x16mm
	4-6	IPE240	Box 240x16mm
	7-9	IPE200	Box 200x16mm
12	1-4	IPE300	Box 300x16mm
	5-8	IPE270	Box 280x16mm
	9-12	IPE240	Box 240x16mm

The value of the internal dilation angle for concrete is obtained by fitting the model results to laboratory data, which are usually assumed to be between 30 and 40 degrees [18]. The values of the parameters used for concrete and steel are shown in Tables 4 and 5.

The properties considered for the soil are effective in the modeling of soil-structure interaction. The interaction between soil and structure decreases with increasing the stiffness of the soil. The properties of soft clay are selected from real geotechnical explorations, which are

shown in Table 6. The constitutive model used for soil is the Mohr-Coulomb model. Due to the difference between the rock layer and the soft soil in terms of stiffness, the elastic behavior for the rock layer is used, which is shown in Table 7.

The elastic modulus of the rock is 100 times the elastic modulus of the soil. Numerical modeling was performed to examine the effect of thickness, length, and position of the rock layer in soft soil. Therefore, three thicknesses of 1.5, 3, and 6m and four lengths of 7.5, 15, 30, and 60 m were considered for the rock layer. Soft soil was divided into three parts, including upper, middle, and lower, with a thickness of 10 m, and the rock layer was placed at 8, 16, and 24 m depths.

TABLE 4. Constitutive parameters of concrete

Parameter	Value
Mass density	$\rho(kg/m^3)=2350$
Poisson's ratio	$\nu=0.3$
Elastic modulus	$E(MPa)=28284$
Compressive strength	$f_c'(MPa)=32$
Tensile strength	$f_t'(MPa)=3.4$
Dilation angle	31
Eccentricity	0.1
The ratio of initial equibiaxial compressive yield stress to initial uniaxial compressive yield stress	$\sigma_{b0}/\sigma_{c0}=1.16$
The ratio of the second stress invariant on the tensile meridian	$K_c=0.67$

TABLE 5. Constitutive parameters of steel

Parameter	Value
Mass density	$\rho(kg/m^3)=7850$
Poisson's ratio	$\nu=0.3$
Elastic modulus	$E(GPa)=200$
Yield stress	$f_y(MPa)=280$

TABLE 6. Constitutive parameters of the soft soil

Parameter	Value
mass density	$\rho(kPa)=1550$
Poisson's ratio	$\nu=0.4$
Elastic modulus	$E_{\max}(kPa)=7.5e4$
Shear wave velocity	$V_s(m/s)=131$
Cohesion	$c(kPa)=100$
Angle of internal friction	$\phi=14$
Plastic index	$PI=16$

TABLE 7. Constitutive parameters of the rock layer

Parameter	Value
Mass density	$\rho(kPa)=2600$
Poisson's ratio	$\nu=0.25$
Elastic modulus	$E(kPa)=7.5e6$

Considering a large distance between the lateral boundaries of the numerical model increases the computational effort, but the model's width should not be selected so small as to lead to a computational error. In previous studies, it has been recommended to consider the model's width 3 to 5 times the frame width. Rayhani and El Naggar [16] showed that increasing the distance of a boundary from five times the width of the structure to ten times the width has a small effect (5% change) on the seismic response of the models.

An important issue to consider in soil-structure interaction problems is the way of modeling the lateral boundary condition. Lateral boundary conditions must be defined in such a way that waves reaching the lateral boundaries can cross the boundaries. If the waves reaching the lateral boundaries are reflected in the model, they will cause modeling errors. There are different methods for modeling boundaries. The first research in this area was presented by Lysmer and Kuhlemeyer [19]. These authors suggested that boundaries have been modeled as energy absorbers or viscous boundaries. Zienkiewicz et al. [17] proposed the free field boundary model and the lateral boundary model with tied degrees of freedom. Li et al. [20] compared different lateral boundary conditions for soil-structure interaction models. The results showed that if the viscous-spring (VS) boundary condition is used, the small model cannot be used to investigate the interaction. However, the tied degrees of freedom (TDOF) boundary conditions model the interaction with good performance, and the model's size can be considered up to 6 times smaller. In this paper, the condition of the lateral boundary with tied degrees of freedom and the width of 60 m for soil was used to model the problem of soil-structure interaction. The boundary condition of the lower part of the soil layer is defined in such a way that the movement of the soil relative to the bedrock is zero.

Damping in the structure was considered constant (5%) during the analysis. However, damping and shear modulus depend on the value of the shear strain. It is observed that with increasing shear strain, the damping increases and the shear modulus decreases. A study

conducted by Sun et al. [21] was used to model a decrease in shear strength and an increase in soil damping due to the earthquake. By examining laboratory data, Sun et al. [21] showed that changes in shear modulus depend on confining pressure, consolidation history, loading frequency, plasticity, and porosity. Soil plasticity was introduced as the most important factor affecting the change of shear modulus during earthquake loading. These authors presented five curves for different ranges of the plastic index. In this paper, the curve for the plastic index in the range of 10 to 20 was used, as shown in Figures 15 and 16. The equivalent linear method was used to estimate the value of shear modulus and damping. In this method, a linear analysis with initial shear modulus and damping is performed. Then, based on shear strain value, shear modulus value and damping coefficient are estimated.

The contact surface between soil and foundation or between soil and rock has been modeled in the form of traction/separation laws using the Mohr-Coulomb criterion and considering normal and tangential stiffness.

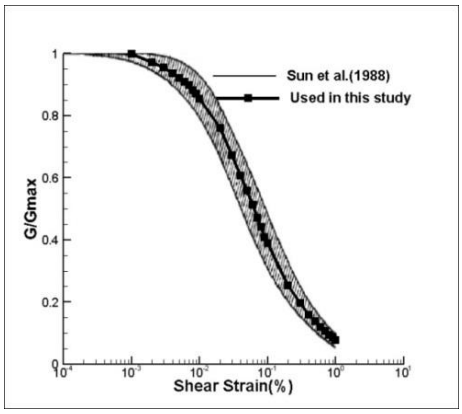

Figure 15. Relationships between G/Gmax and cyclic shear strain

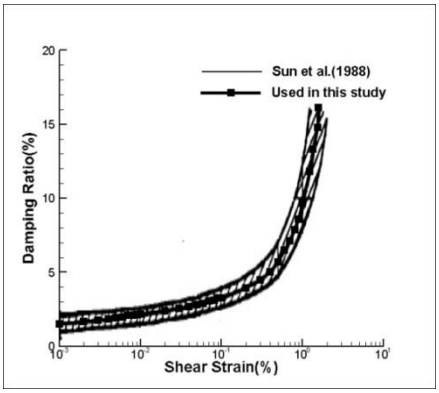

Figure 16. Relationships between the material damping ratio and cyclic shear strain

In this model, the friction is inactive until the adhesion is reduced. If the adhesion decreases, the friction model is activated and contributes to the shear strength. Before the onset of damage, the shear strength is the combination of adhesion and friction. After damage, the adhesion participation is zero, and the shear strength is entirely due to the frictional resistance. Previous studies have recommended that the maximum value of normal and shear stiffness be estimated using the following equation [8, 16].

$$k_n(\max) = k_s(\max) = 10 \times \max\left(\frac{K + 4/3G}{\Delta z_{\min}}\right) \quad (1)$$

In this equation, K and G are the bulk and shear modulus. $\Delta z_{\min}$ is the smallest width of an adjoining zone in the normal direction. The value of contact surface stiffness was considered constant during the analysis. K_n and K_s values for soft clay were selected at $1.07 \times 10^5 kPa/m$. Selecting lower values led to higher estimates of lateral deformation, and higher values did not affect lateral deformation.

4. NUMERICAL SIMULATIONS

Two earthquake records were applied to each of the studied frames. The normal and shear stress contours of 9 storey structure are presented in Figures 17-19 as an example. These figures are obtained by applying the Kobe earthquake. Factors influencing the choice of the earthquake are the intensity, duration, and frequency of the earthquake. The Kobe earthquake is considered in the category of near-field earthquakes, and the El Centro earthquake is considered in the classification of far-field earthquakes. These records have been used in various references to study the interaction of soil and structure. The magnitude of the Kobe earthquake was 6.8, and the magnitude of the El Centro earthquake was 6.9 [22]. Based on the earthquake record, the dominant period of the Kobe earthquake is 0.36, and the dominant period of the El Centro earthquake is 0.56 (Table 8). Figures 20 and 21 show the acceleration records of the El Centro and Kobe earthquakes.

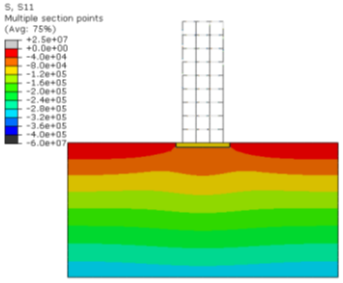

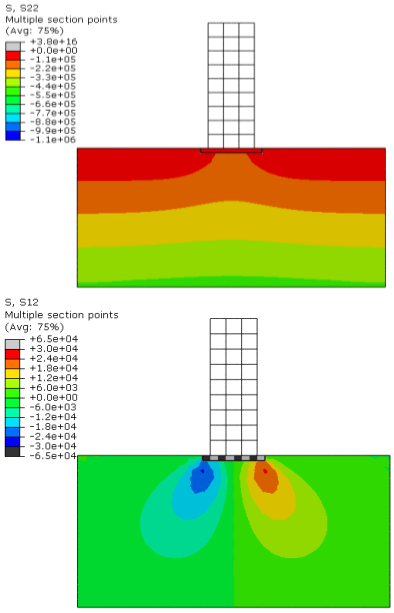

Figure 17. The distribution of normal and shear stress after static analysis

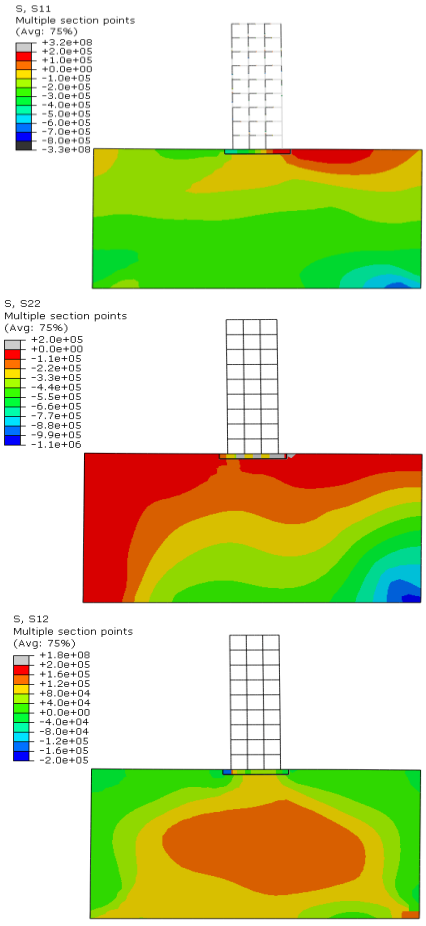

Figure 18. The distribution of normal and shear stress at 4s after beginning of the earthquake

TABLE 8. Ground motion parameters

Parameter	Kobe	El Centro
Magnitude of earthquake	6.8	6.9
Maximum horizontal acceleration	0.834g	0.349g
Predominant period(s)	0.36	0.56
Significant duration(s)	8.4	24.58
Arias intensity(m/s)	8.389	1.758

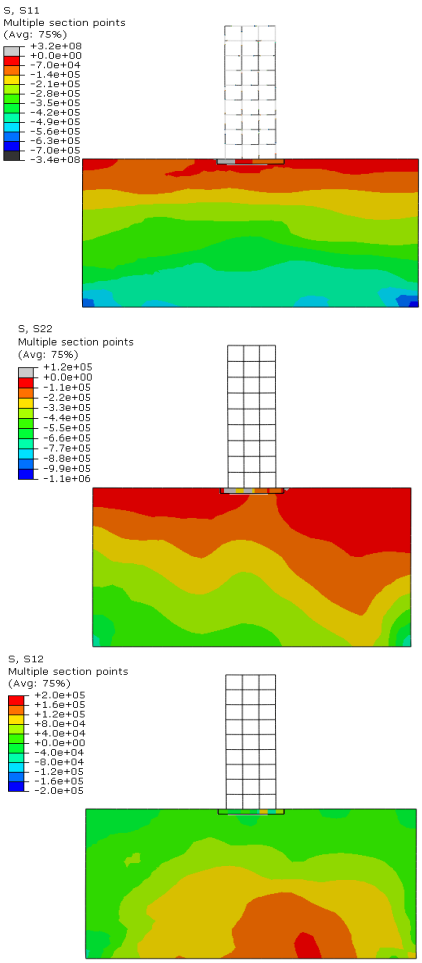

Figure 19. The distribution of normal and shear stress at 8s after beginning of the earthquake

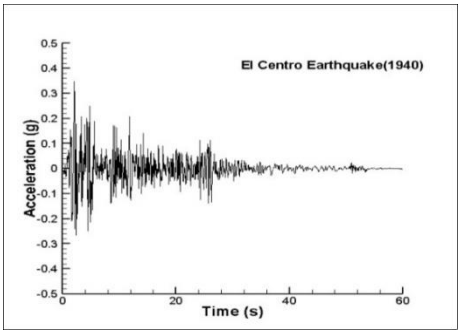

Figure 20. El Centro earthquake record

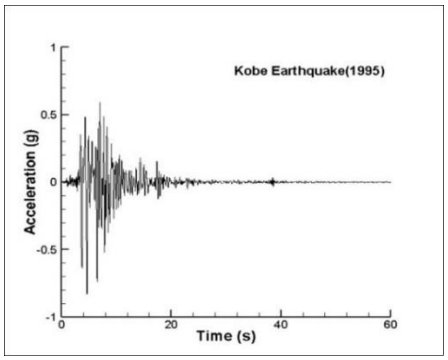

Figure 21. Kobe earthquake record

After analyzing the value of axial force, moment, shear force, base shear, and lateral displacement in the stories were calculated. The mentioned parameters were obtained from the modeling during the time history of the earthquake. The maximum value obtained for each parameter is recorded and investigated in this study. The shear force created in the j-th column of the storey i is displayed by v_j^i. Shear, moment, and axial force created in the 1st column of the storey 15, are shown in Figures 22-24. Displacement and acceleration history at the 15th storey are shown in Figures 25 and 26. The result shows

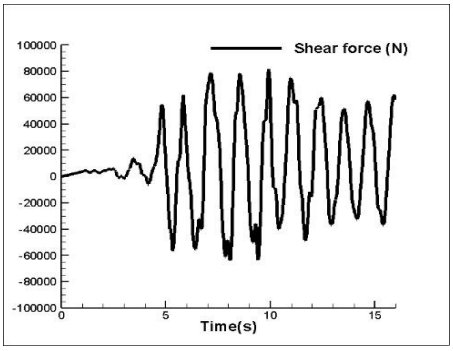

Figure 22. Shear force history in a 1-th column of the storey 15

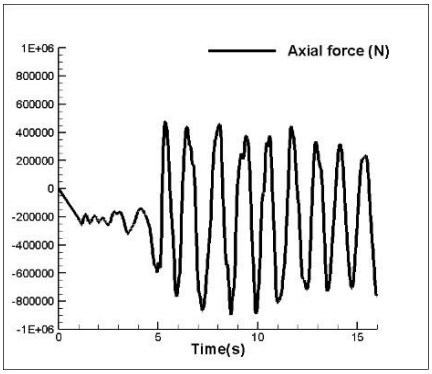

Figure 23. Axial force history in a 1-th column of the storey 15

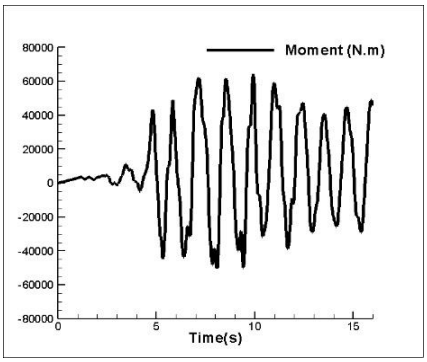

Figure 24. Moment history in a 1-th column of the storey 15

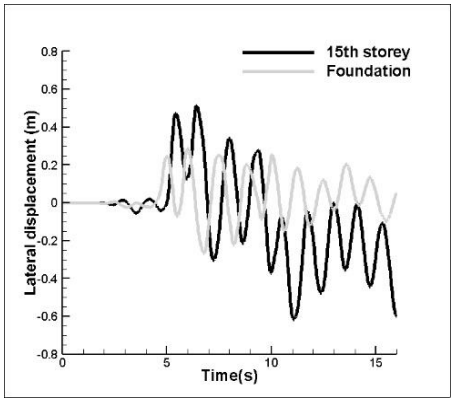

Figure 25. Displacement history at the 15th storey and foundation

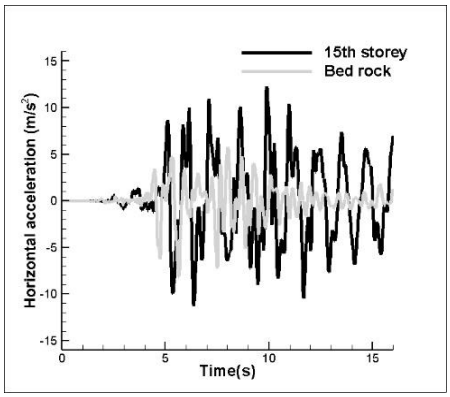

Figure 26. Acceleration history at the 15th storey and bed rock

that the acceleration transmitted to the structure increases. Since; there are four columns in each storey of the structure, the value of j varies from 1 to 4. The maximum value of shear force created in the columns of the storey is recorded and displayed with a parameter $v_{\max}^i$. The mean and maximum values of the parameter $v_{\max}^i$ are displayed with $\bar{V}$ and $V_{\max}$, respectively (Figures 27 and 28).

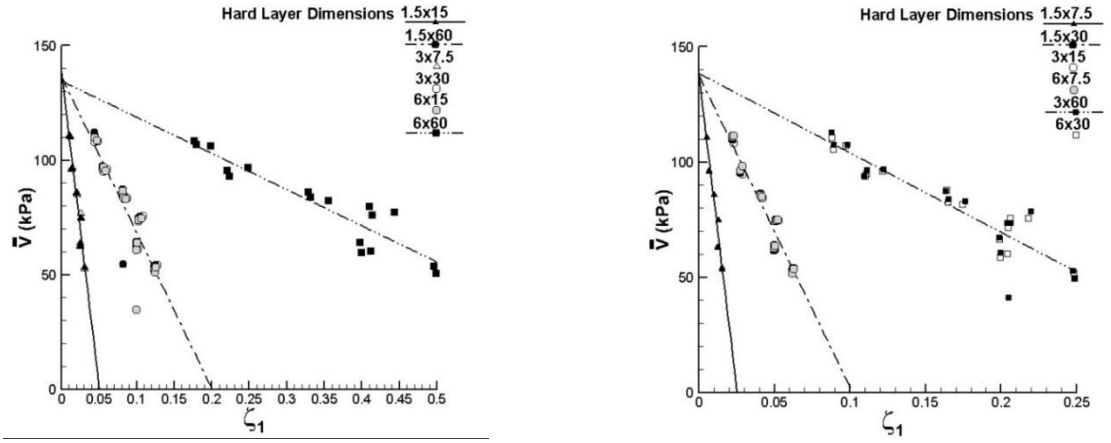

Figure 27. Average shear force of the columns $\bar{V}$

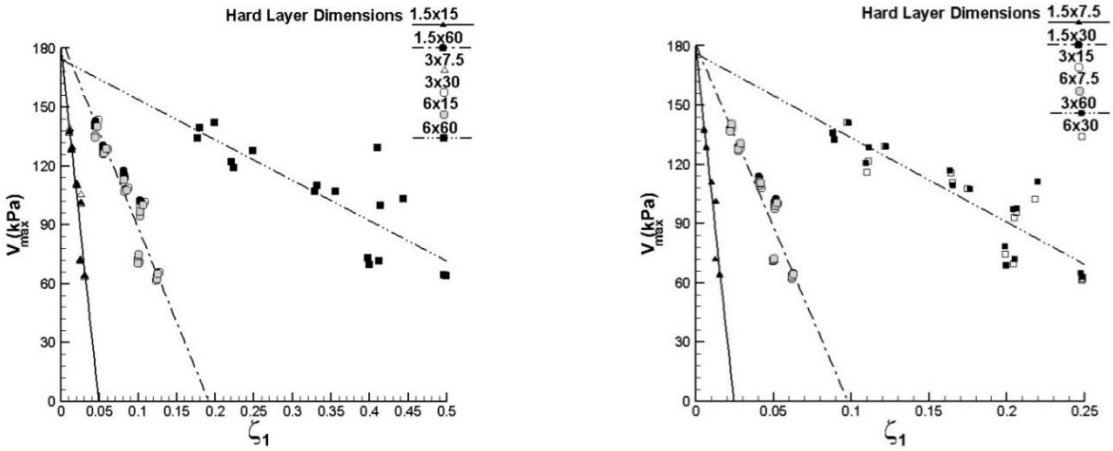

Figure 28. Maximum shear force of the columns $V_{\max}$

$$v_{\max}^{i} = \max(v_j^i) \tag{2}$$

$$\bar{V} = \frac{\sum_{i=1}^{n} v_{\max}^{i}}{n} \tag{3}$$

$$V_{\max} = \max(v_{\max}^{i}) \tag{4}$$

In the above formula, n is the number of stories of the structure.

Similarly, for the moment created in the column of stories, two parameters of $\bar{M}$ and $M_{\max}$ have been defined (Figures 29 and 30), for the axial force, two parameters of $\bar{P}$ and $P_{\max}$ have been defined (Figures 31 and 32), for the lateral displacement of stories, the parameter of $\Delta_{h(\max)}$ has been defined (Figure 33), and for the relative vertical displacement of foundation, the parameter Δ_v (Figure 34) has been defined. Since; the base shear value is considered an important parameter in seismic analysis, two parameters of $\bar{V}_t$ and $V_{t(\max)}$ (Figures 35 and 36) have been used, which are calculated in the following formula.

$$\bar{V}_t = \frac{\sum_{i=1}^{n} \max\left(\sum_{j=1}^{4} v_j^i\right)}{n} \tag{5}$$

$$V_{t(\max)} = \max\left(\max\left(\sum_{j=1}^{3} v_j^i\right)\right) \tag{6}$$

The rock layer dimensions for one parameter are plotted in two diagrams to make the diagrams more straightforward. Dimensions 7.5 x 1.5, 30 x 1.5, 15 x 3, 7.5 x 6, 60 x 3, 30 x 6 (m) are shown in one diagram, and the rest of the size of rock layers is shown in another diagram.

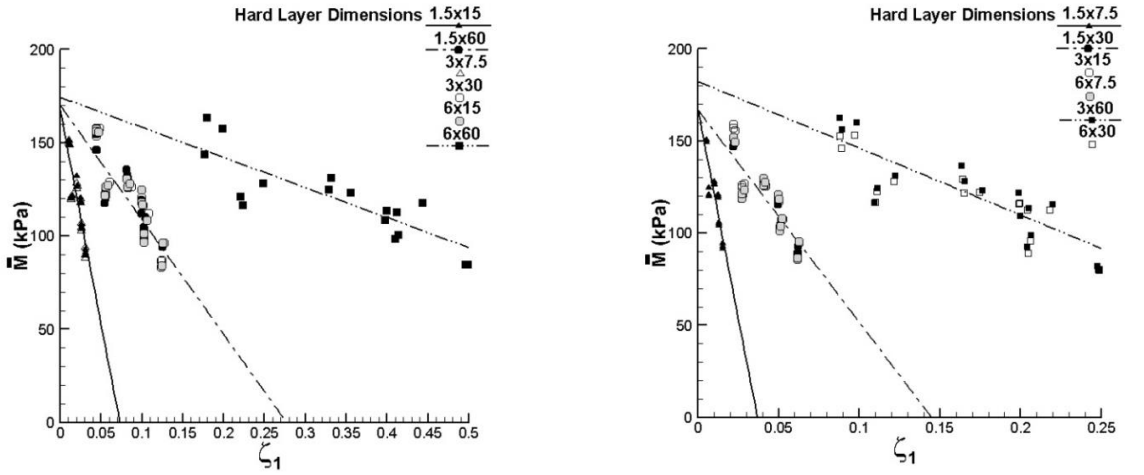

Figure 29. Average moment of the columns $\overline{M}$

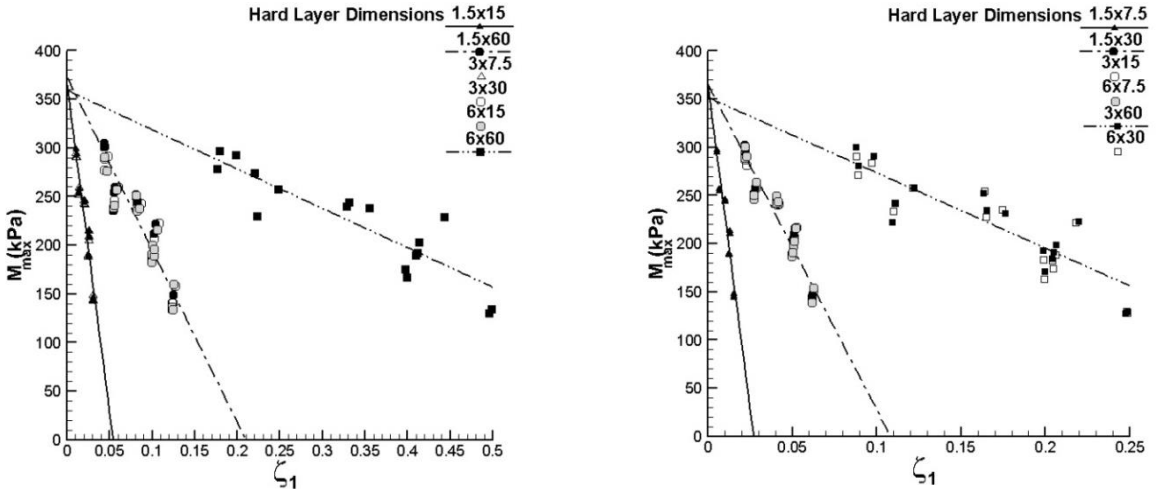

Figure 30. Maximum moment of the columns $M_{\max}$

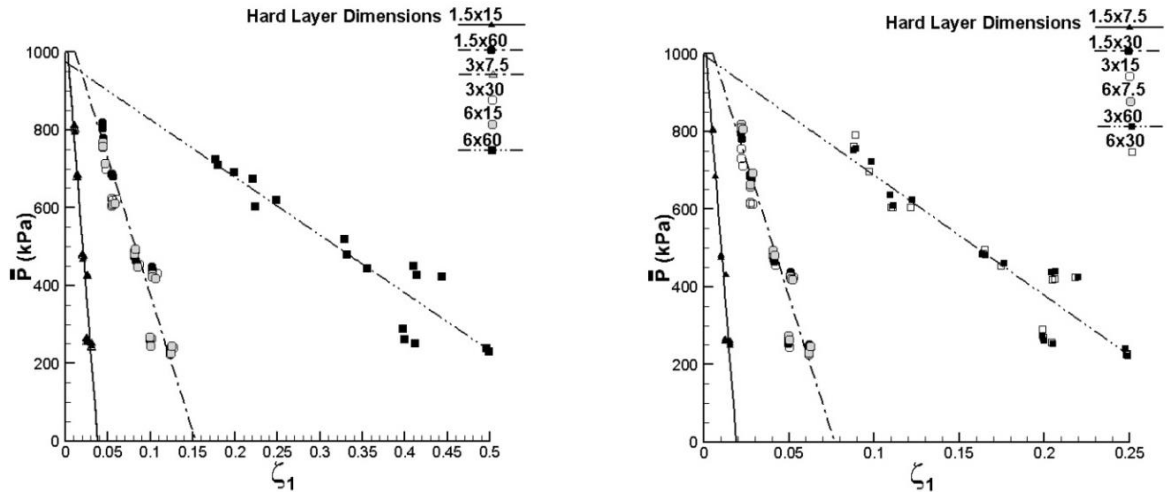

Figure 31. Average axial force of the columns $\overline{P}$

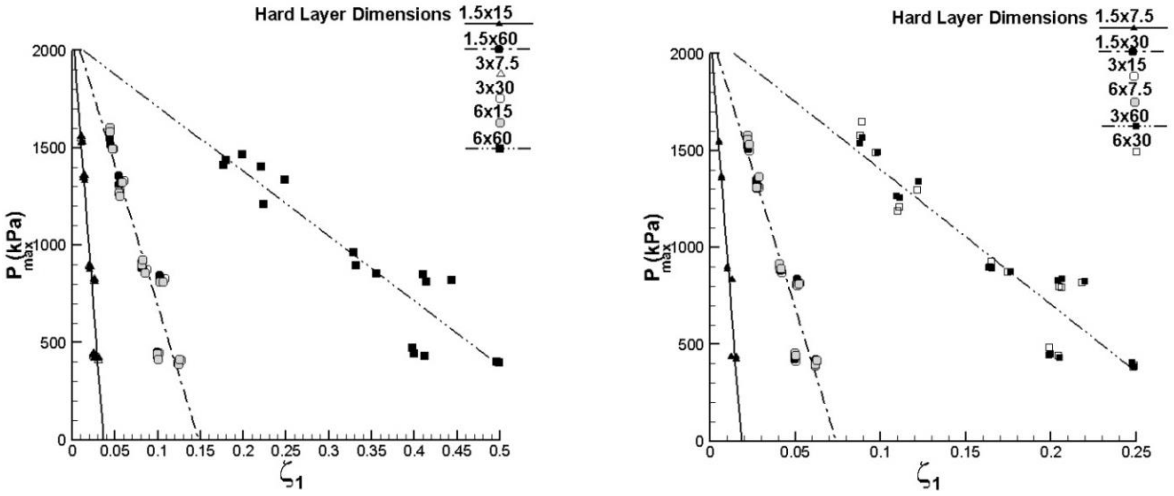

Figure 32. Maximum axial force of the columns $P_{\max}$

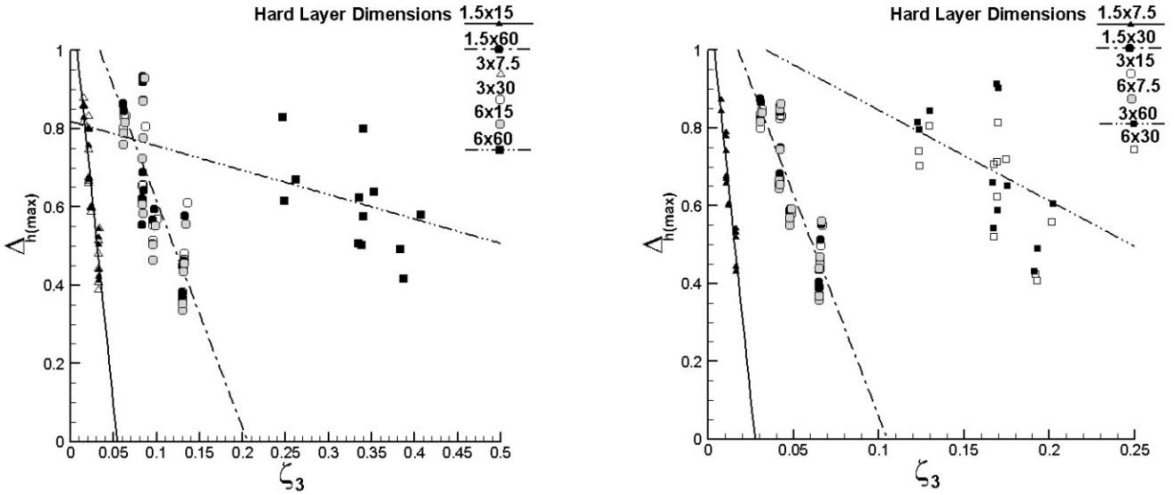

Figure 33. Maximum lateral displacement $\Delta_{h(\max)}$

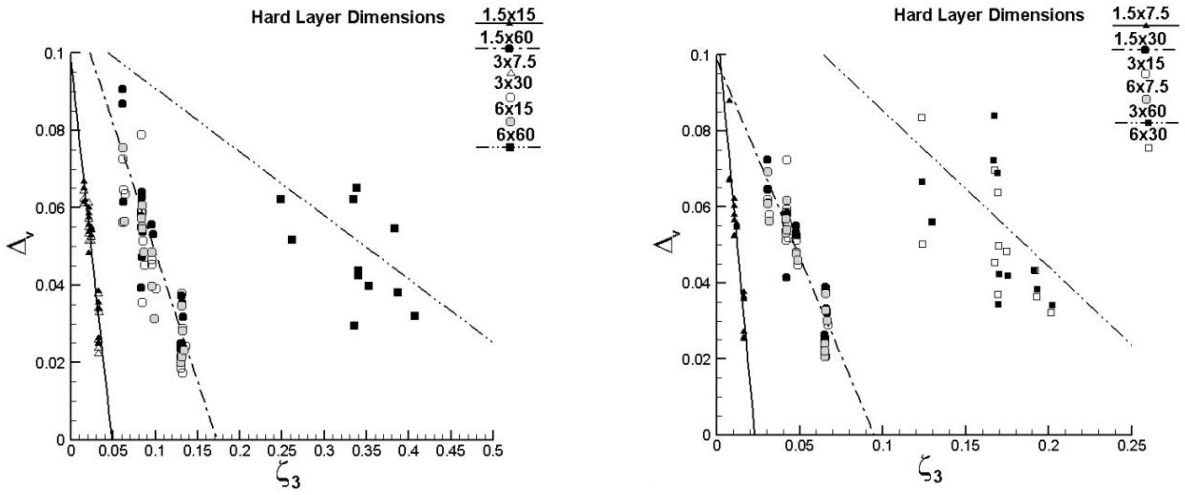

Figure 34. Maximum relative vertical displacement of the foundation Δ_v

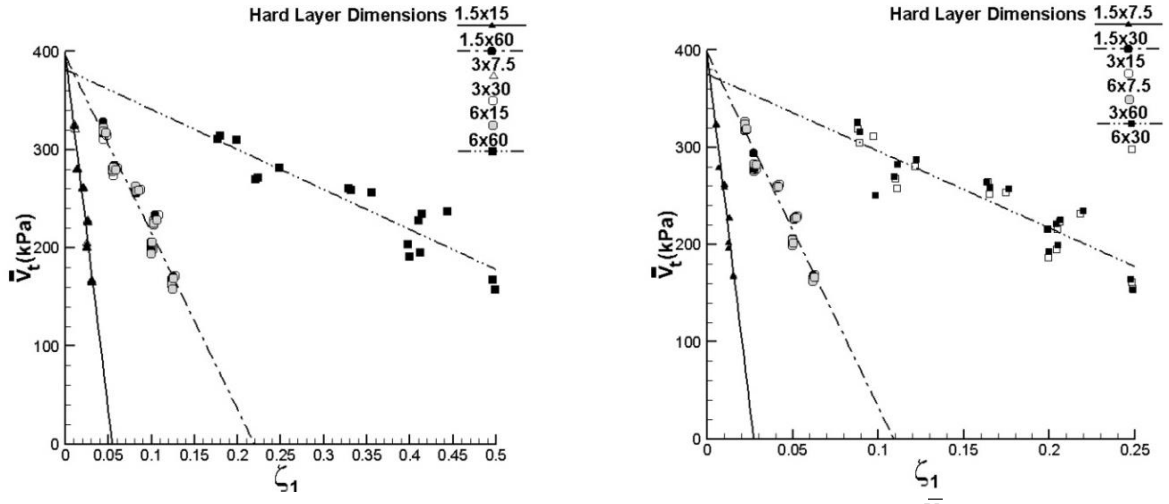

Figure 35. Average of the total shear force of the columns in a storey $\bar{V}_t$

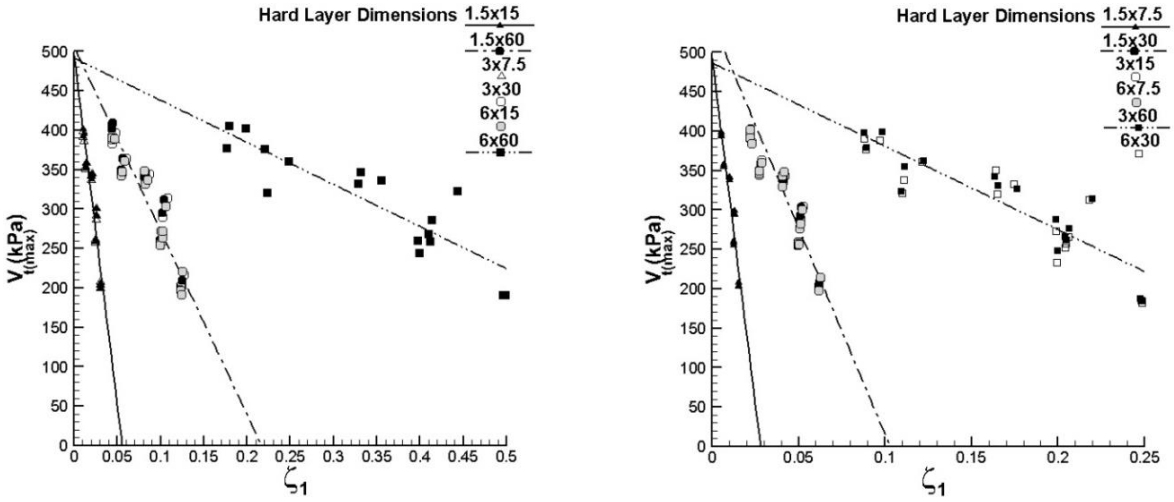

Figure 36. Base shear force $V_{t(\max)}$

In this paper, parameters ξ_1, ξ_3 are introduced to analyze the data. The results showed a correlation coefficient of more than 0.85 with introduced parameters. However, as the mass of the rock layer increases, the data dispersion increases. ξ_1 has been used in force and moment diagrams, and ξ_3 has been used in lateral displacement and relative vertical displacement diagrams.

$$\xi_1 = f_{SS}^2 \times \sqrt{\frac{f_S}{f_E}} \frac{W}{K_S} \tag{7}$$

$$\xi_3 = \frac{f_{SS}}{f_E} \times \frac{W}{K_S} \tag{8}$$

where f_{SS} is the frequency of the soil-structure system, f_S is the frequency of the structure, f_E is the dominant frequency of the earthquake, W is the weight of the rock layer, and K_S is the stiffness of the structure. In estimating the introduced parameters (ξ_1, ξ_3), the values in Tbale 9 are used. The f_S and f_{SS} values were calculated by performing modal analysis in ABAQUS software for each model.

By examining the changes in ξ_1, ξ_3, we can have a better understanding of the effect of the rock layer on the items that are important in the design of structures. One of the important factors affecting the design of structures is the characteristics of the earthquake, which is reflected as the dominant frequency in the ξ_1, ξ_3 parameters. The

TABLE 9. Parameters used in the estimation of ξ_1, ξ_3

Parameter		Value
f_E	Kobe	2.78
	El Centro	1.78
f_S	S6	0.97
	S9	0.84
	S12	0.70
$K_S(N)$	S6	732089
	S9	632903
	S12	700714

Kobe earthquake is a near-field earthquake that has a larger dominant frequency and shorter period than the far-field El Centro earthquake. It should be noted that these earthquakes were selected due to the proximity of magnitude. The magnitude of the El Centro earthquake was 6.9, and the magnitude of the Kobe earthquake was 6.8. Another important factor that should be considered is the frequency of the structure and the frequency of the soil-structure system. If the natural frequency is close to the frequency of the applied force, it is possible for the occurrence of a resonance phenomenon. In the numerical simulation of this paper, the structure and the soil-structure system frequency was less than the dominant frequency of the earthquake, so the f_S / f_E ratio varies between 0.25 and 0.5. The value of the f_{SS} varies between 0.51 and 0.74.

Figures 27 to 36 show that the forces and deformations obtained for rock layers of the same mass (or dimensions) are closely and linearly related to the ξ_1, ξ_3 parameters. In other words, the thickness of the rock layer alone does not affect the interaction of soil and structure, and the length of the rock layer also affects the behavior of the structure and soil. For example, the value of force- obtained for the rock layer in the dimensions of 30 x 1.5, 15 x 3, 7.5 x 6(m) with a good approximation are related linearly to ξ_1. This issue indicates that the presence of a rock layer with a thickness of more than 3 is not necessarily more conservative than a rock layer with a thickness of 1.5 m. In some cases, it can provide worse conditions in terms of force and displacement.

Based on Figures 27 to 36, it can be seen that if the size of the rock layer is constant, if the ξ_1 and ξ_3 value decrease, due to the linear relationship of force with ξ_1 and displacement with ξ_3, the force and displacement caused by the earthquake will increase. For example, since the dominant frequency of the Kobe earthquake is greater than the dominant frequency of the El Centro earthquake, ξ_1 and ξ_3 decrease if the other parameters are constant. As a result, the force and displacement caused by the Kobe earthquake will be greater than that of the El Centro earthquake.

Tables 10 and 11 show the maximum and minimum effect of the presence of a rock layer on the value of force and displacement. In the case of the presence of a rock layer, the mean and maximum axial force is 1.1 times compared to the homogeneous layer of soft clay (from now on, called the reference state).

TABLE 10. Ratios of force and moment relative to the reference value

Record			$\frac{V_{t(\max)}}{V_{t(ref)}}$	$\frac{\overline{V}_t}{\overline{V}_{t(ref)}}$	$\frac{V_{\max}}{V_{\max(ref)}}$	$\frac{\overline{V}}{\overline{V}_{ref}}$	$\frac{M_{\max}}{M_{\max(ref)}}$	$\frac{\overline{M}}{\overline{M}_{ref}}$	$\frac{P_{\max}}{P_{\max(ref)}}$	$\frac{\overline{P}}{\overline{P}_{ref}}$
S6	Kobe	Maximum	1.11	1.07	0.96	0.94	1.05	1.03	1.10	1.10
		Minimum	0.90	0.92	1.06	1.02	0.86	0.90	0.94	0.93
	El Centro	Maximum	1.15	1.06	0.95	0.93	1.19	1.11	1.03	1.03
		Minimum	0.91	0.92	1.06	1.02	0.88	0.88	0.90	0.87
S9	Kobe	Maximum	1.03	1.01	0.96	0.95	1.03	1.07	1.07	1.08
		Minimum	0.95	0.96	1.27	1.06	0.93	0.95	0.95	0.93
	El Centro	Maximum	1.08	1.04	0.92	0.95	1.07	1.12	1.01	1.03
		Minimum	0.86	0.95	1.05	1.02	0.82	0.84	0.96	0.96
S12	Kobe	Maximum	1.04	1.02	0.97	0.95	1.03	1.09	1.03	1.02
		Minimum	0.95	0.77	1.02	1.02	0.92	0.96	0.95	0.86
	El Centro	Maximum	1.06	1.06	0.90	0.97	1.07	1.09	1.00	1.01
		Minimum	0.90	0.93	1.09	1.06	0.87	0.97	0.88	0.88

TABLE 11. Ratios of displacement relative to the reference value

Record			$\frac{\Delta_v}{\Delta_{v(ref)}}$	$\frac{\Delta_{h(\max)}}{\Delta_{h(\max)(ref)}}$
S6	Kobe	Maximum	1.59	1.07
		Minimum	0.56	0.75
	El Centro	Maximum	1.01	1.20
		Minimum	0.56	0.73
S9	Kobe	Maximum	1.15	1.31
		Minimum	0.67	0.65
	El Centro	Maximum	1.04	1.27
		Minimum	0.64	0.76
S12	Kobe	Maximum	1.56	1.02
		Minimum	0.73	0.71
	El Centro	Maximum	0.98	1.00
		Minimum	0.55	0.67

The maximum axial force is related to the rock layer with dimensions of 30 x 6, which is located at a depth of 24 m. The minimum value of the axial force is 0.86 of the reference state and is related to the 60x6 rock layer, which is located at a depth of 8 m. For other parameters, similar information is given in Tables 10 and 11. As can be seen, the value of axial force with a thickness of 1.5 m is between the maximum and minimum value, indicating that the assumption of the presence of a rock layer with less thickness is not necessarily reliable.

The presence of a rock layer causes the maximum axial force to increase by 1.1, the shear force to increase by 1.27, and the moment force to increase by 1.19 compared to the reference state.

Increasing the value of maximum forces indicates that there is a possibility of failure of structural members. The largest increase is related to the shear force. The mean axial force increased by 1.1, the shear force increased by 1.06, and the moment increased by 1.12 compared to the reference state. Since; the mean force and moment value can be considered as a criterion for estimating the construction cost, it has been considered in this paper. The construction cost increases with increasing the mean force and moment. The maximum difference of 12% shows that with optimal design, the cost of constructing the structure will not increase much. It should be noted that there are conditions in which the rock layer reduces the force and moment. The positive effect of the presence of the rock layer on the value of force and moment is a maximum of 18%. Its effect on the mean value of force and moment is 16%.

The value of base shear force with the $V_{t(\max)}$ is shown in Table 10. The presence of a 60 x 6 rock layer, which is located at a depth of 8 m, increases the value of base shear force by 15%. The maximum reducing effect of the presence of the lock layer for the base shear force is 14%, which occurs if there is a 30 x 6 rock layer located at a depth of 24 m. The mean shear force of the storey also varies from 0.77 to 1.07 compared to the reference state. In short, it can be concluded that the presence of a rock layer can increase the value of base shear and the mean shear force of the structure.

The value of horizontal displacement shown in Table 11 indicates that a rock layer with dimensions of 30 x 3(m) located in the middle of the soft soil layer will lead to a 31% increase in lateral displacement caused by the Kobe earthquake. The El Centro earthquake for a rock layer with a dimension of 60x3(m) also causes a 27% increase in lateral displacement. Increased lateral displacement causes the structure's performance to exceed life safety and approach near collapse. In Figures 37 and 38, the relative lateral displacements created in the 9-storey structure are compared in the two cases. As seen, in the presence of a rock layer, for both the Kobe and El

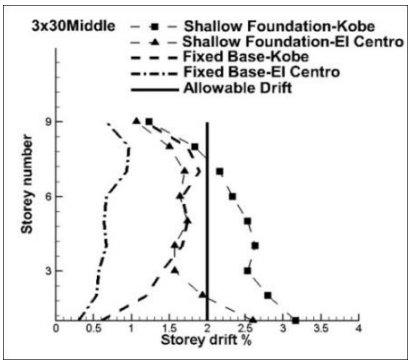

Figure 37. Inter-storey drift Comparison between soil with the rock layer (3x30) and fixed base

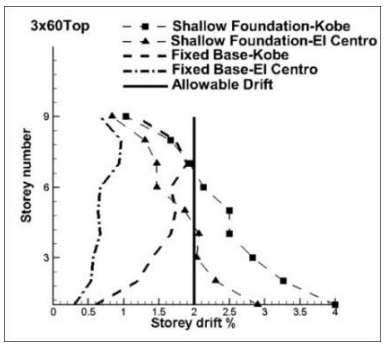

Figure 38. Inter-storey drift Comparison between soil with the rock layer (3x60) and fixed base

Centro earthquakes, the relative lateral displacement has exceeded the value of life safety performance and is close to the collapse level. This condition occurs when the relative lateral displacement with fixed support is within the allowable range.

The maximum value obtained for the relative vertical displacement of the foundation is equal to 1.59 times the reference state and is related to the Kobe earthquake and 60x3(m) rock layer dimensions. This indicates that the presence of a rock layer can also cause the overturning of the structure.

Finally, the statistical study on the dimensions and location of the rock layer and its effect on the maximum force and displacement are shown in Figures 39-42. As seen, 60 x 6(m) dimensions with a distribution of 33% had the greatest effect on increasing, and 30 x 6 dimensions with a distribution of 44% had the greatest effect on decreasing the value of force and moment.

Placement of the rock layer in the last third of the soil layer with a distribution of 61% had the greatest effect on increasing the force and moment, and placement of the rock layer in the middle of soft soil with a distribution of 48% had the greatest effect on reducing the value of force and moment. The area of 180 square meters for the rock layer with a distribution of 64% has the least force and moment, and the area of 360 square meters has the highest value of force and moment. Placement in the upper third of the soil layer with a distribution of 67% has the greatest effect on increasing lateral displacement, and placement in the lower third of the soft soil layer has the greatest effect on reducing lateral displacement.

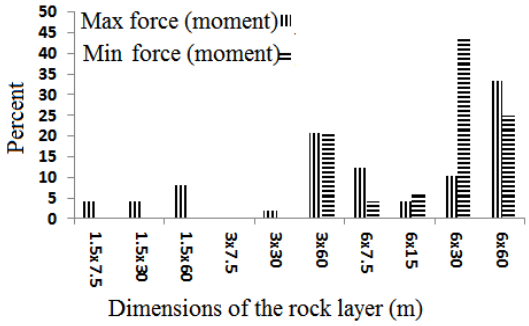

Figure 39. Effect of the rock layer dimension on the force and moment

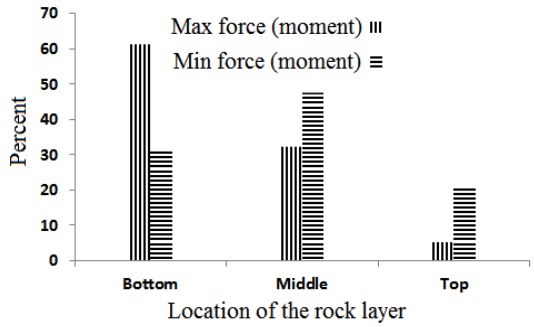

Figure 40. Effect of the rock layer location on the force and moment

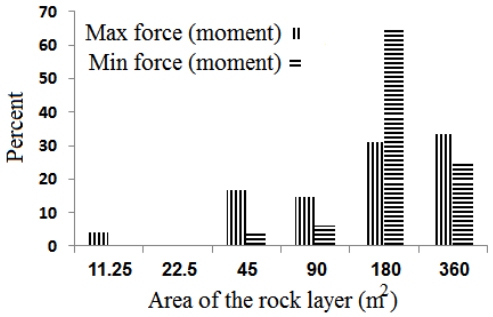

Figure 41. Effect of the rock layer area on the force and moment

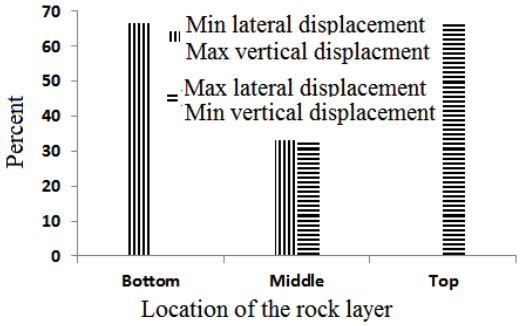

Figure 42. Effect of the rock layer location on the vertcal and lateral displacement

5. CONCLUSION

In this paper, ABAQUS software was used to investigate the effect of a rock layer on the seismic behavior of steel moment frames. In the first step, the shaking table experiment was modeled, and the accuracy of the results was examined. The agreement of the obtained results with the laboratory results shows the accuracy and efficiency of the numerical model. In the next step, three structures of 6-, 9- and 12-storey steel moment frames, which are placed on soft clay, were analyzed. Rock layers with a thickness of 1.5, 3, and 6 m and lengths of 7.5, 15, 30, and 60 m were selected. The elastoplastic constitutive model was selected for soil, steel, and concrete. For the rock layer, the elastic behavior is used. The mean and maximum axial force, shear force, and moment force in the columns were calculated. The obtained results show that the relationship between the force with the introduced parameter ξ_1 and the displacement with parameter ξ_3 is linear. These two parameters depend on the frequency of the structure, the frequency of the soil-

structure system, the dominant frequency of the earthquake, the weight of the rock layer, and the stiffness of the structure. The advantage of using these two parameters is that the location of the rock layer, the height of the structure, and the type of earthquake are specified in the definition of these parameters, and the obtained results can be generalized for other structures and other earthquakes. The results obtained for rock layers with the same weight (or the same dimensions) have a linear relationship with ξ_1 and ξ_3. It reflects the fact that the length of the rock can be as important as the thickness of the rock. As the size of the rock layer increases, the correlation decreases, but the relationship can be considered linear. For rock layers of the same weight, the force and the lateral displacement decrease with increasing ξ_1 and ξ_3. The effect of the rock layer on displacement is more than the force. The presence of a rock layer can increase the maximum value of lateral displacement by up to 31% and the relative vertical displacement of the foundation by up to 59%. Increased lateral displacement causes the performance of the structure to exceed life safety and approach near collapse. The rock layer with dimensions of 60 x 6(m) has the highest value of force (moment), and the rock layer with dimensions of 30 x 6 has the lowest value of force (moment). Placement of the rock layer in the lower third of the soil layer increases the force and reduces lateral displacement, and placement of the rock layer in the middle of the soil reduces the force. Placement of the rock layer in the upper third of the soil increases lateral displacement. The location and dimensions of the rock layer have the most important effect on the force and displacement. The presence of a rock layer can increase the maximum value of axial force, shear force, and moment in the columns of the structure. This suggests that not considering the rock layer in soft soil does not necessarily reliable. The mean value of force and moment increased by a maximum of 12%, which indicates that the cost of construction does not increase significantly with the rock layer.

6. REFERENCES

1. Li, S.-Q. and Liu, H.-B., "Vulnerability prediction model of typical structures considering empirical seismic damage observation data", ***Bulletin of Earthquake Engineering***, (2022), 1-43. doi: 10.1007/s10518-022-01395-y.
2. Li, S.-Q. and Liu, H.-B., "Comparison of vulnerabilities in typical bridges using macroseismic intensity scales", ***Case Studies in Construction Materials***, Vol. 16, (2022), e01094. doi: 10.1016/j.cscm.2022.e01094.
3. Li, S., Chen, Y. and Yu, T., "Comparison of macroseismic-intensity scales by considering empirical observations of structural seismic damage", ***Earthquake Spectra***, Vol. 37, No. 1, (2021), 449-485. doi: 10.1177/8755293020944174.
4. Li, S.-Q., Liu, H.-B. and Chen, Y.-S., "Vulnerability models of brick and wood structures considering empirical seismic damage observations", in Structures, Elsevier. Vol. 34, (2021), 2544-2565.
5. Li, S.-Q. and Liu, H.-B., "Statistical and vulnerability prediction model considering empirical seismic damage to masonry structures", in Structures, Elsevier. Vol. 39, (2022), 147-163.
6. Wolf, J.P., "Dynamic soil structure interaction, PrenticeHall. Inc., Englewood Cliffs, New Jersey, (1985).
7. Bagheri, M., Jamkhaneh, M.E. and Samali, B., "Effect of seismic soil–pile–structure interaction on mid-and high-rise steel buildings resting on a group of pile foundations", ***International Journal of Geomechanics***, Vol. 18, No. 9, (2018), 04018103. doi: 10.1061/(ASCE)GM.1943-5622.0001222.
8. Hokmabadi, A.S., Fatahi, B. and Samali, B., "Assessment of soil–pile–structure interaction influencing seismic response of mid-rise buildings sitting on floating pile foundations", ***Computers and Geotechnics***, Vol. 55, (2014), 172-186. doi: 10.1016/j.compgeo.2013.08.011.
9. Mulliken, J.S. and Karabalis, D.L., "Discrete model for dynamic through-the-soil coupling of 3-d foundations and structures", ***Earthquake Engineering & Structural Dynamics***, Vol. 27, No. 7, (1998), 687-710. doi: 10.1002/ (SICI)1096-9845(199807)27:7<687::AID-EQE752>3.0.CO;2-O.
10. Tabatabaiefar, S.H.R., Fatahi, B. and Samali, B., "Numerical and experimental investigations on seismic response of building frames under influence of soil-structure interaction", ***Advances in Structural Engineering***, Vol. 17, No. 1, (2014), 109-130. doi: 10.1260/1369-4332.17.1.109.
11. Kitada, Y., Hirotani, T. and Iguchi, M., "Models test on dynamic structure–structure interaction of nuclear power plant buildings", ***Nuclear Engineering and Design***, Vol. 192, No. 2-3, (1999), 205-216. doi: DOI: 10.1016/S0029-5493(99)00109-0.
12. Aydin, E., Ozturk, B., Bogdanovic, A. and Farsangi, E.N., "Influence of soil-structure interaction (ssi) on optimal design of passive damping devices", in Structures, Elsevier. Vol. 28, (2020), 847-862.
13. Kim, Y.-S. and Roesset, J.M., "Effect of nonlinear soil behavior on inelastic seismic response of a structure", ***International Journal of Geomechanics***, Vol. 4, No. 2, (2004), 104-114. doi: 10.1061/(ASCE)1532-3641(2004)4:2(104).
14. Fatahi, B., Far, H., Sadeghi Hokmabadi, A. and Samali, B., "Significance of bedrock depth in dynamic soil-structure interaction analysis for moment resisting frames", in International Conference on Performance-Based Design in Earthquake Geotechnical Engineering, Associazione Geotecnica Italiana-Roma., (2012).
15. Holzer, T.L., Bennett, M.J., Ponti, D.J. and Tinsley III, J.C., "Liquefaction and soil failure during 1994 northridge earthquake", ***Journal of Geotechnical and Geoenvironmental Engineering***, Vol. 125, No. 6, (1999), 438-452. doi: 10.1061/(ASCE)1090-0241(1999)125:6(438).
16. Rayhani, M. and El Naggar, M.H., "Numerical modeling of seismic response of rigid foundation on soft soil", ***International Journal of Geomechanics***, Vol. 8, No. 6, (2008), 336-346. doi: 10.1061/(ASCE)1532-3641(2008)8:6(336).
17. Zienkiewicz, O., Bicanic, N. and Shen, F., Earthquake input definition and the trasmitting boundary conditions, in Advances in computational nonlinear mechanics. 1989, Springer.109-138.
18. Jankowiak, T. and Lodygowski, T., "Identification of parameters of concrete damage plasticity constitutive model", ***Foundations of Civil and Environmental Engineering***, Vol. 6, No. 1, (2005), 53-69.
19. Lysmer, J. and Kuhlemeyer, R.L., "Finite dynamic model for infinite media", ***Journal of the Engineering Mechanics***

Division, Vol. 95, No. 4, (1969), 859-877. doi: 10.1061/JMCEA3.0001144.

20. Li, Y., Zhao, M., Xu, C.-s., Du, X.-l. and Li, Z., "Earthquake input for finite element analysis of soil-structure interaction on rigid bedrock", ***Tunnelling and Underground Space Technology***, Vol. 79, (2018), 250-262. doi: 10.1016/j.tust.2018.05.008.
21. Sun, J.I., Golesorkhi, R. and Seed, H.B., "Dynamic moduli and damping ratios for cohesive soils, Earthquake Engineering Research Center, University of California Berkeley, (1988).
22. PEER, *Peer ground motion database*. 2014, Univ. of California Berkeley, CA.

Persian Abstract

چکیده

در نظرگرفتن لایه‌بندی خاک در بررسی لرزه‌ای سازه‌ها مقوله‌ای مهم و اثرگذاراست. در پژوهش‌های پیشین، وجود لایه‌سنگی درون خاک نرم موردتوجه قرار نگرفته‌است. در مقاله حاضر، تاثیر لایه‌ای از سنگ درون خاک نرم بر نیروها و تغییرمکان‌های بوجودآمده در قاب فولادی خمشی کوتاه و متوسط بررسی می‌شود. از این‌رو محاسبات عددی متعددی بروی ۱۲ نوع اندازه متفاوت لایه‌سنگی در سه عمق مختلف انجام شده‌است. مدل‌های عددی بااستفاده از نرم افزار آباکوس در قالب المان محدود و با لحاظ کردن اثرات متقابل سازه و خاک تحلیل شده‌اند. نتیجه بررسی‌های انجام‌شده نشان می‌دهد که مقدار نیرو و تغییرمکان به فرکانس سازه، فرکانس مجموعه سازه و خاک، فرکانس غالب زلزله، وزن لایه‌سنگی و سختی سازه وابسته هستند. در این مقاله، دو پارامتر جدید به‌نحوی تعریف شده‌اند که رابطه‌ای خطی با نیرو و تغییرمکان داشته باشند. نتایج بدست‌آمده گویای آن‌است که ضخامت و طول لایه‌سنگی بر مقدار نیرو و تغییرمکان اثرگذاراست. علاوه براین، وجود لایه‌ای از سنگ درون خاک ممکن‌است در جهت اطمینان نباشد و موجب افزایش نیروی‌برشی تا ۲۷ درصد، نیروی‌محوری تا ۱۰ درصد و لنگر تا ۱۹ درصد شود. تاثیر وجود لایه‌ی سنگی بر تغییرمکان بیش از نیرواست و موجب افزایش تغییرمکان جانبی تا ۳۱ درصد و تغییرمکان نسبی قائم پی تا ۵۹ درصد می‌شود.

International Journal of Engineering

Journal Homepage: www.ije.ir

Effect of Tubular Solar Absorber on Performance of Counterflow Double Pass Solar Air Heater: Experimental and Numerical Studies

N. F. Hussein*[a], S. T. Ahmed[b], A. L. Ekaid[a]

[a] *University of Technology, Baghdad, Iraq.*
[b] *Bilad Alrafidain University College, Diyala, Iraq*

PAPER INFO

Paper history:
Received 09 June 2022
Received in revised form 06 July 2022
Accepted 10 July 2022

Keywords:
Solar Air Heaters
Thermal Storage
Double Pass
Tthermos-hydraulic Efficiency
Tubular Capsules

ABSTRACT

The problem of solar radiation intermittency can significantly affect the thermal performance of solar air heaters (SAHs). The efficient solution for this problem is utilizing thermal storage to store the thermal energy and using it again in off sunshine hours. The present study analyzed the thermal performance of two configurations of counterflow double pass solar air heater. The first configuration included a conventional flat plate solar absorber, while the second configuration involved tubular capsules that are filled with water as a sensible thermal storage material. The tubular capsules have been installed longitudinally in parallel to the direction of airflow. The study involved numerical and experimental parts. The results showed a remarkable enhancement in useful energy production when using the tubular capsules. Moreover, the SAH with tubular capsules can produce useful energy for a longer time due to the presence of the thermal storage material within capsules. It is found that the total useful energy in the case of tubular capsules is about 4082, 4295.3, 4426, 4584, and 4693 W at a mass flow rate of 0.03, 0.025, 0.02, 0.015, and 0.01 kg/s, respectively, with an increment of 39.1, 51.2, 59.4, 74.8, and 89.6%, respectively as compared with the flat-plate absorber. In addition, the average thermo-hydraulic efficiency in the case of tubular capsules are higher than those values which are achieved in flat plate case by about 9.3, 15, 19.6, 28.2, and 40% at a mass flow rate of 0.03, 0.025, 0.02, 0.015, and 0.01 kg/s, respectively.

***doi**: 10.5829/ije.2022.35.10a.18*

NOMENCLATURE

A_c	Collector area (m^2)	Tair,out	Outlet air temperature (^{0} C)
Cp_{air}	Specific energy of air (J/kg^{0}K)	Tair,in	Inlet air temperature (^{0}C)
Cp_w	Specific energy of water (J/kg^{0}K)	Tw2-Tw1	Water temperature rise (^{0}C)
I	Solar radiation (W/m^2)	t	Time period between two measurements (s)
m_{air}	Air mass flow rate (kg/s)	$\eta_{th,charge}$	Thermal efficiency in charge period.
m_w	Water mass (kg)	$\eta_{th,discharge}$	Thermal efficiency in discharge period.
Q_{in}	Received energy (W)	$\eta_{eff,charge}$	Thermo-hydraulic efficiency in charge period
$Q_{mechanecal}$	Pumping power (W)	$\eta_{eff,discharge}$	Thermo-hydraulic efficiency in charge period
Q_{useful}	Useful energy gain (W)	P	Pressure drop (Pa)
Q_s	Stored energy (W)	ρ_{air}	Air density (kg/m^3)
$T_{air,in}$	Inlet air temperature (^{0}C)		

1. INTRODUCTION

Conventional energy sources such as fossil fuels are limited and affected by supply problems and unstable prices [1]. Moreover, burning fossil fuels produce harmful emissions that are associated with many respiratory diseases and are responsible for environmental pollution and global warming [2]. These

*Corresponding Author Institutional Email: 50153@uotechnology.edu.iq (N. F. Hussein)

Please cite this article as: N. F. Hussein, S. T. Ahmed, A. L. Ekaid, Effect of Tubular Solar Absorber on Performance of Counterflow Double Pass Solar Air Heater: Experimental and Numerical Studies, ***International Journal of Engineering, Transactions A: Basics***, Vol. 35 No. 10, (2022), 2007-2017

serious problems and challenges pushed the world to invest effectively in other alternative sources such as renewable energies. Solar energy is a promising source of unlimited and clean energy. Solar energy can be invested directly either in electrical energy generation by using photovoltaic systems [3] or in thermal energy generation by utilizing various systems for instance solar air dryers [4], solar water collectors [5], solar towers [6], solar chimneys [7], etc. Solar air heaters are simple in their design and installation. The conventional solar air heaters consist of a transparent cover which is usually made from glass material to minimize the top heat losses to the surroundings [8], solar absorber plate that is usually made from metal to absorb solar energy in thermal energy form, air channels, an electric air blower to supply air to the system, and thermal insulation to reduce thermal losses from back and sides of the collector [9]. Solar air heaters are utilized in many applications that work under low or mild temperatures [10], for instance drying textile, agricultural, and marine products, in addition to dehumidifying and heating the interiors of buildings to create a comfortable environment, especially in the winter season or in cold zones [11]. However, solar air heaters suffer from some drawbacks represented by energy losses, a low thermal performance due to the low convective heat transfer coefficient between the airflow and the surface of the solar absorber plate, and the solar intermittency problem that make the conventional solar air heaters cannot meet the application's requirements after the sunset or during off-sunshine hours [12]. Research is continuously conducted to find the best solutions for these drawbacks. Regarding reducing the lost energy, Kumar and Subhash [13] studied the effect of glass cover number, and they concluded that increasing the cover layers can reduce the top heat loss, but at the expense of the amount of solar radiation reaching the absorbing surface, Kumar et al. [14] used a number of low-cost thermal insulating materials (bubble wrap and ceramic wool) and tested their influence on the collector's performance. They revealed that using ceramic wool can reduce the thermal losses from the collector's body and rise the thermal efficiency by approximately 5.6%. Abdelkader et al. [15] studied the effect of painting the solar absorber plates with paints based on nanoparticles technology. The researchers showed that mixing nanoparticles with paint led to an increase in the outlet air temperature by approximately 20% because of enhancing the optical characteristics of paint. On the other hand, many researchers focused on solving the problem of low convective heat transfer coefficient by adopting various techniques. For example, Das et al. [16] enhanced the convective heat transfer coefficient by up to 17% by creating artificial roughness by mixing the sand particles with the black paint. Jalil et al. [17] tested the effect of installing wavy fins of 3 and 7 waves on the solar flat plate absorber, and they succeeded in improving the thermal performance by about 84% as compared with the conventional collector. Sudhakar and Cheralathan [18] improved the thermal performance by up to 17.4% by replacing the conventional flat plate absorber with V- groove absorber with pin fins on its two sides. Mesgarpour [19] studied numerically enhancing the thermal performance by creating a helical flow path by replacing the conventional flat plate absorber with helical channels. The results showed that these helical channels increased the heat transfer area up to 24.18%, hence, enhancing thermal performance. In addition, a new technology that involved replacing conventional flat plate absorbers with novel configurations that can be filled with thermal storage materials was adopted by many researchers to solve the problem of solar energy intermittency. Jalil and Ali [20] studied the effect of adding steel wool as a sensible thermal storage material in the lower channel of the collector. The thermal performance is enhanced by about 79.82% when using steel wool at a porosity of 0.9625.

Sajawal et al. [21] replaced the conventional flate-plate absorber with finned tubes filled with phase change material (RT44HC and RT18HC). The study outcomes revealed that the thermal performance rise to 71.6% by using a mixture of (RT44HC and RT18HC) instead of using them separately. Muthukumaran and Senthil [22] tested new designs of solar absorbers which are straight tubes and spiral coiled that are filled with a mixture of paraffin wax and glycerol. The results showed that the spiral coiled absorber offered superior thermal performance than the straight tubes and the conventional flat plate absorbers. Moreover, integrating thermal storage with the solar collector can stores thermal energy for a short time during off-sunshine hours or after sunset, hence enhancing the uniformity of outlet air temperature. Raju and Kumar [23], Sudhakar and Cheralathan [24] adopted encapsulated phase change material technology to improve thermal performance. Using this technique can enhance thermal efficiency in the range of 9-15%. Abed [25] used a mixture of paraffin wax and sand as new thermal storage material, different mixing ratios have been tested, and the outcomes revealed that mixing 20% of paraffin wax with sand raise the air temperature rise up to 9.2% and gives the best thermal performance. Using built-in thermal storage technology within the double-pass solar air heaters is still under development and requires more research. Moreover, the three-dimensional mathematical models that adopt finite volume schemes and are related to forced convection turbulent flow inside a counterflow double-pass solar air heater with built-in thermal storage are very few. Therefore, this study offers a new design of the solar absorber within the counterflow double-pass solar air heater that is tubular capsules filled with a sensible thermal storage material.

2. NUMERICAL METHOD

2. 1. Geometry The two configurations are created by using CFD software ANSYS Fluent version (2021 R2). The geometry of the two configurations is performed by a designed modeler of the ANSYS workbench. Generally, the two configurations included glass cover, solar absorber (flat plate for the first configuration and tubular capsules for the second configuration), backplate, and thermal insulation. The generated configurations are presented in Figure 1.

2. 2. Meshing The meshing process for the two configurations was performed by using the meshing tool in the ANSYS workbench (2021 R2) as shown in Figure 2. Structured mesh with mesh element size equal to 1365379 has been generated, and the dependency of mesh on the solution's accuracy was achieved by doing an independent mesh test, where the mesh concentration is gradually increased until the variation in outlet temperature becomes less than 1% as shown in Figure 3.

2. 3. Assumptions The case is assumed three-dimensional (3D), and the airflow through the upper and lower channels is assumed forced convection turbulent incompressible flow. In addition, the thermophysical characteristics of the airflow are assumed constant. The fluid inside the tubular capsules is selected liquid water. The solar rate is assumed uniform and equals 1000 W/m^2, and the inlet thermal condition equals 25 ^{0}C. Moreover, both the back and side walls of the collector are assumed insulated.

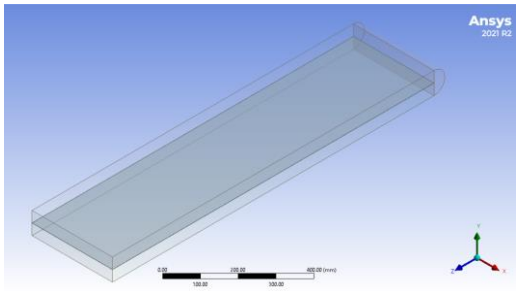

(a) First configuration

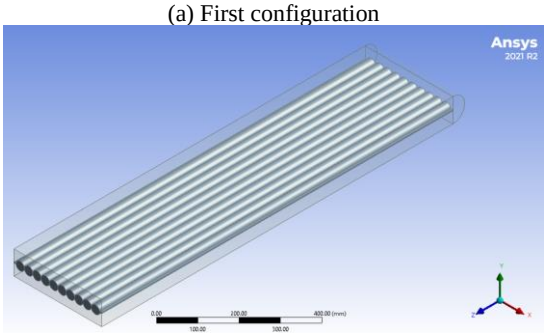

(b) Second configuratioon

Figure 1. The geometry of the configurations

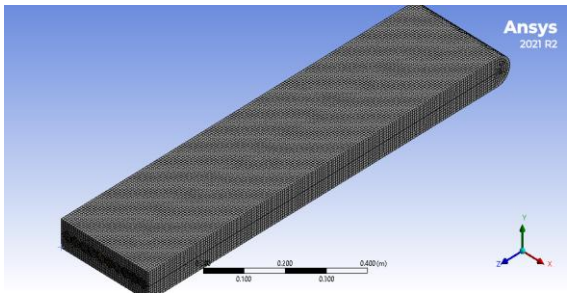

Figure 2. Meshing configurations

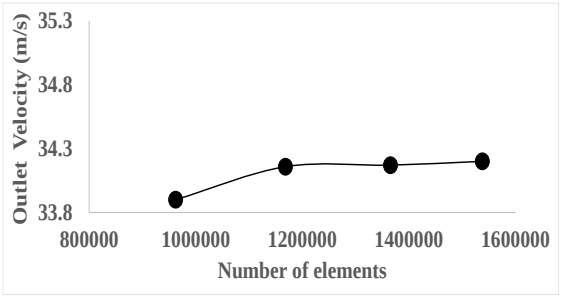

Figure 3. Mesh independence test's outcomes

2. 4. Boundary Conditions and Operating Parameters The operating parameters and boundary conditions that are applied in the simulation are listed in Table 1. In addition, the properties of both glass cover, backplate, and tubular capsules are listed in Table 2.

2. 5. Solution Method The finite-volume method with a semi-implicit pressure-linked algorithm (SIMPLE) has been used to solve the governing equations. In addition, a second-order upwind scheme is

TABLE 1. Operating parameters and boundary conditions

Boundary condition	Value
Solar rate	1000 W/m^2
Mass flow rate	0.01, 0.015, 0.02, 0.025 and 0.03 kg/s.
Inlet air temperature	25 ^{0}C
Wind velocity	1 m/s

TABLE 2. Properties of the glass cover, backplate, and absorber.

Property	Glass cover	Backplate	Absorber
Thermal conductivity (W/m.K)	1.4	80	387.6
Specific heat (J/kg.K)	770	450	381
Density (kg/m^3)	2540.4	8013	8978

applied for discretizing the governing equations. The renormalization group (RNG)- k-ε model which is the most common model for describing turbulent flow behaviors. Kumar et al. [26] have chosen for simulating turbulent flow as well as heat transfer since this model gives approximately the same results as both the Blasius empirical correlation and the Dittus-Boelter empirical correlation [27]. The convergence criteria for continuity, momentum, and energy equations are set to 1e-03, 1e-03, and 1e-06, respectively.

3. EXPERIMENTAL SETUP

3. 1. General Description The main components of the experimental setup as shown schematically in Figure 4 are a counterflow double pass solar air heater (CFDPSAH), an artificial solar simulator, an electrical air blower, U-tube manometer, orifice meter, thermocouples, and a data logger.

The body of the solar air heater is constructed as a rectangular box from a 1.8 cm thick plywood sheet. The collector body is divided into upper and lower channels which are separated by a solar absorber. The collector's projected area is 1200 × 300 mm. The upper channel is covered by a glass cover with a thickness of 4 mm and a transmittance of 88% for the purpose of allowing maximum solar radiation rate to fall on the solar absorber and preventing long-wave radiation to escape to the surrounding. The galvanized plate of 1 mm thick has been placed in the lower channel to invest some of the thermal losses. Two configurations of solar absorber as shown in Figure 5 have been used, the first configuration is a flat plat absorber as a reference, and the second configuration is a set of tubular capsules which are fitted in parallel to the direction of airflow.

The upper side of solar absorbers is coated with black paint to enhance the absorptivity of absorbers for solar radiation. The tubular capsules have been filled with a sensible thermal storage medium (water). An electrical air blower is utilized to supply air to the solar air heater, and a manual valve which is attached to the pump side of the air blower is used to adjust the air mass flow rate. Different mass flow rates (0.01-0.03 kg/s) with increment of 0.005 are adopted in experiments. The artificial solar radiation rate (average value equal to 1000 w/m^2) is achieved by using an artificial solar simulator which is controlled by utilizing variac transformation. The pressure difference through the solar heater is measured by connecting the measuring device to two tapes which are fixed at the inlet and outlet of the solar heater. Thirty-eight thermocouples (type K) were used to monitor the temperature distribution in the solar heater during the experiment time. These thermocouples were installed in different locations which are: four thermocouples were fitted in each of glass cover, the middle height of the upper and lower channels, the upper and lower side of the solar absorber, and the upper side of the backplate, as well as twelve thermocouples inside the tubular capsule. Moreover, two thermocouples were mounted at the inlet and outlet of the solar heater. The positions of measuring points are shown in Figure 6. The dimensions and specifications of solar air heater configurations as well as the details of the materials that are used in the experimental setup are listed in Table 3.

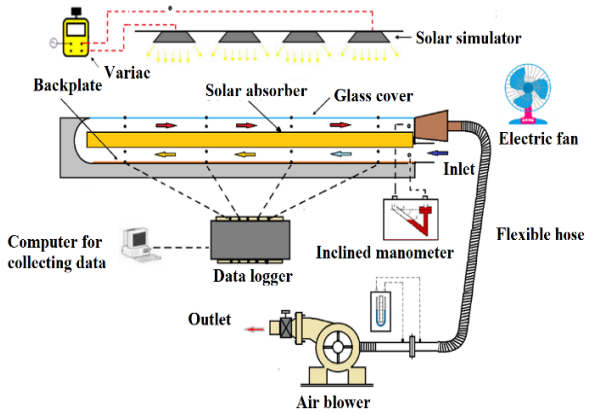

Figure 4. Schematic of the experimental setup

Figure 5. Solar absorber configurations

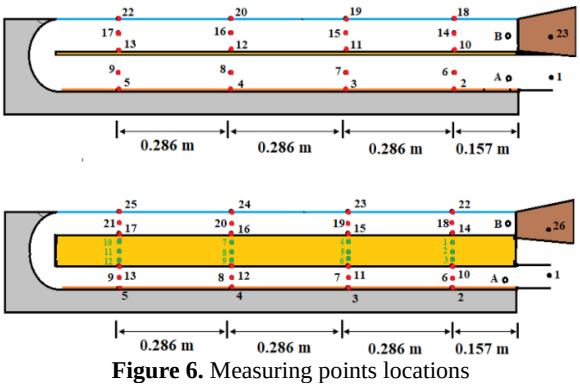

Figure 6. Measuring points locations

TABLE 3. Dimensions and specifications of solar air heater configurations

Item	Details
Double pass solar air heater	
Total length	1260 mm
Total width	340 mm
Total height	80.9 mm
Effective length	1200 mm
Effective width	300 mm
First absorber configuration (copper flat plate)	
Height of upper & lower channels	40 mm
Plate thickness	0.9 mm
Plate length	1200 mm
Plate width	30 mm
Second absorber configuration (copper tubular capsules)	
Height of upper & lower channels	32.15 mm
Length	1200 mm
Outer Diameter	28.6 mm
Inner Diameter	26.7 mm
Thickness	0.9 mm
Number of capsules	10
Insulation (Polyurethane foam)	
Thickness	50 mm
Absorber coating (black paint Rust-oleum)	
Absorptivity	92%

3. 2. Instruments and Measuring Devices The details and specifications of instruments and measuring devices that are used in experiments are summarized in Table 4.

TABLE 4. Details and specifications of instruments and measuring devices

Instrument type	Model	Purpose of usage	Accuracy level
Solar power meter	SPM-1116SD	Measuring solar intensity	±5%
Orifice meter + U tube manometer	-	Measuring mass flow rate	±5%
Data logger	AT-4524	Measuring temperatures	$\pm 0.8^0$C
Digital Thermometer	HT-9815	Measuring temperatures	$\pm 2^0$C
Inclined manometer	-	Measuring pressure drop	±2%

3. 3. Experimental Procedure and Data Analysis

3. 3. 1. Experimental Procedure The temperature of all thermocouples at the beginning of the experiment should be equal to 25 ^{0}C which is the same temperature as the room. After that, the electric air blower and the artificial solar simulator are switched on at the desired value. Then, the system is kept running until the system reaches a steady-state, and during this time, the readings of all thermocouples are measured every 5 minutes. Finally, when the steady-state is achieved at the end of the charge period after 1 hour, all temperatures and the pressure drop across the solar air heater are recorded. After that, the solar simulator is switched off and the discharge period starts. During the discharge period, measuring of all temperatures continues. The discharge period ends when the temperature difference between the inlet and the outlet equals approximately zero.

3. 3. 2. Data Analysis Depending on the first law of thermodynamics, the solar air heater's performance can be evaluated by the following formulas [28, 29]:

$$\eta_{th,charging} = \frac{Q_{useful}+Q_s}{Q_{in}} \quad (1)$$

$$\eta_{th,discharging} = \frac{Q_{useful}}{Q_s} \quad (2)$$

where Q_{useful}, Q_{in}, and Q_s represent the useful energy gained from solar air heater, received energy from solar source and stored energy which can be represented by the following formulas:

$$Q_{useful} = \dot{m}_{air} . Cp_{air}(T_{air,out} - T_{air,in}) \quad (3)$$

$$Q_{in} = A_c . I \quad (4)$$

$$Q_s = m_w . Cp_w(T_{w,2} - T_{w,1})/t \quad (5)$$

For the first configuration, the stored energy (Q_s) is assumed zero due to the absence of thermal storage material. The term thermo-hydraulic efficiency or effective efficiency is used to take into account the influence of pressure drop on the solar air heater performance which can be calculated as follows [30]:

$$\eta_{eff,charge} = \frac{Q_{useful}+Q_s-Q_{mechanical}}{Q_{in}} \quad (6)$$

$$\eta_{eff,discharge} = \frac{Q_{useful}-Q_{mechanical}}{Q_s} \quad (7)$$

$$Q_{mechanical} = \frac{\dot{m}_{air}\times\Delta p}{\rho_{air}} \quad (8)$$

where $Q_{mechanical}$ is the needed pumping power for supplying air through the system.

4. RESULTS AND DISCUSSION

The numerical and experimental outcomes show the effect of replacing the conventional flat plate absorber with the tubular capsules on the thermal performance of the solar air heater. The validation between the numerical and experimental results has been made. In addition to that, a comparison between the conventional and proposed absorber in terms of total useful power and average thermo-hydraulic efficiency is presented.

4. 1. Validation between Experimental and Numerical Work The validation between experimental and numerical work is carried out, and the result is presented in Figures 7(a) and 7(b). The deviation within the acceptable agreement in ranges between 4% to 8.2 %.

4. 2. Experimental Results

4. 2. 1. Temperature Distribution The principal purpose of SAHs is supplying hot air to use it in housings heating, industrial applications, etc. The assessment of the temperature distribution of outlet airflow for the two configurations at different mass flow rates is shown in Figure 8. The results indicate that the outlet air temperature in the first configuration is greater than those temperature values in the second configuration, and this result can be attributed to saving part of absorbed solar energy by the absorber in the thermal storage material, in addition to decreasing the reflected solar radiation from the absorber through the glass cover to the surrounding (top heat loss) due to the special design of tubular capsules that causes internal reflections between the curvature surfaces of the absorber [31]. However, it can be noted that the second configuration can produce hot air for a longer time due to the presence of thermal storage material inside the tubular capsules which acts as an energy source that supply the airflow by energy during the discharge period. In addition, it can be seen from these figures that the outlet temperature also decreases with rising air mass flowrate due to increasing the convection process. It is found that at the end of the charge period, the outlet air temperature at a mass flow rate of 0.03 kg/s for second and first configurations is 32.7 ^{0}C, and 33.9 ^{0}C, respectively, and these temperatures increased by 24.7%, and 47% at 0.01 kg/s to become 40.7 ^{0}C, and 50 ^{0}C,

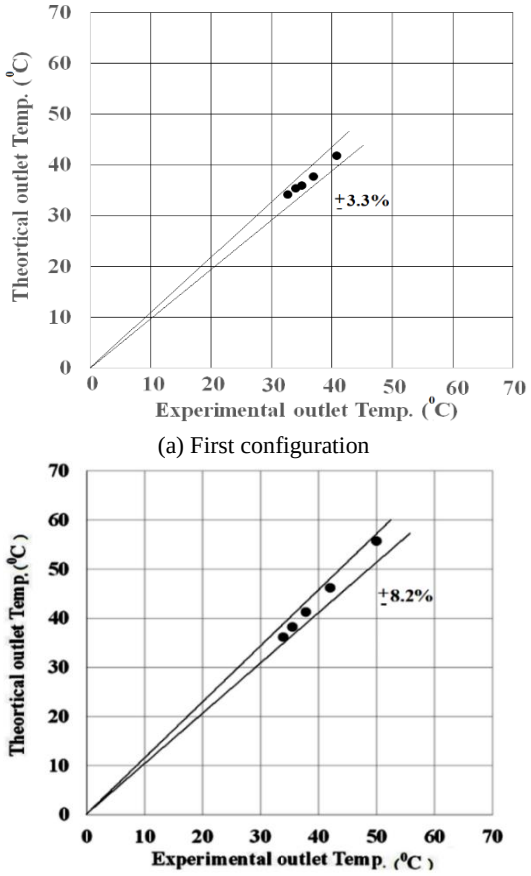

(a) First configuration

(b) Second configuration

Figure 7. Validation between experimental and numerical work

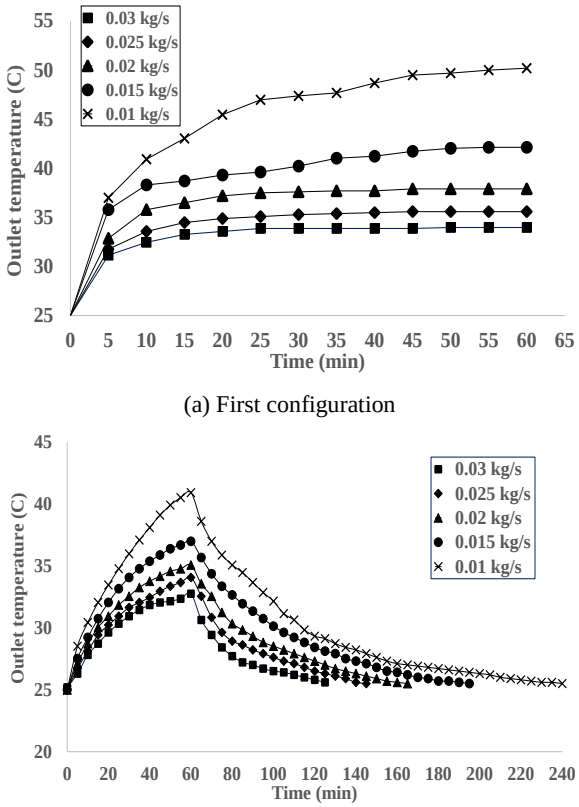

(a) First configuration

(b) Second configuration

Figure 8. Temperature distributions

respectively. Hence, this means that the percentage of rising outlet air temperature increases with decreasing the mass flow rate due to an increase in heat transfer rates from the absorber to airflow [32].

4. 2. 2. Total Useful Energy The total useful energy represents an important parameter in calculating the thermal performance of a solar air heater. Figure 9 displays the total values of the useful energy that is extracted from the solar absorber via the airflow at different mass flow rates. It can be seen from this figure that there is a significant increase in useful energy production when using the tubular capsules. It is found that the second configuration produces total useful energy of about 4082, 4295.3, 4426, 4584, and 4693 W at a mass flow rate of 0.03, 0.025, 0.02, 0.015, and 0.01 kg/s, respectively. The findings also show that the total useful energy that is extracted by the second configuration is significantly higher than the extracted useful energy in the first configuration by about 89.6, 74.8, 59.4, 51.2, and 39.1% for mass flow rates of 0.01, 0.015, 0.02, 0.025, and 0.03, respectively. This can be attributed to accumulated energy in the thermal storage medium which is invested in the discharge period.

4. 2. 3. Average Thermo-hydraulic Efficiency The thermo-hydraulic efficiency is a general parameter that is used not only for evaluating the SAHs performance but also for indicating the future research enhancement of SAHs performance. The assessment of the average thermo-hydraulic efficiency of both first and second configurations at various mass flow rates is stated in Figure 10. This figure reveals that the average thermo-hydraulic efficiency in the second configuration increases despite the decrease in mass flow rate values. This result can be attributed to the presence of thermal storage material (water) inside the proposed absorber that in turn feeds the airflow by the thermal energy during the discharge period, and this discharge period increases

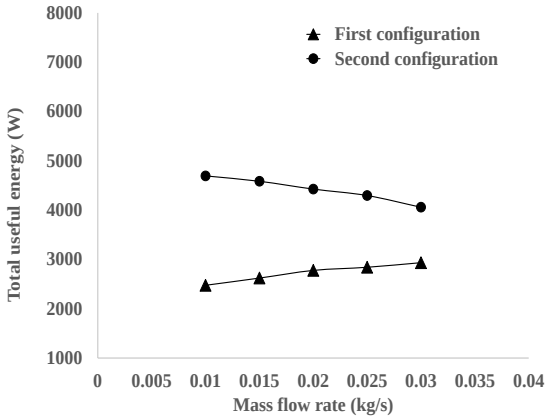

Figure 9. Total useful energy

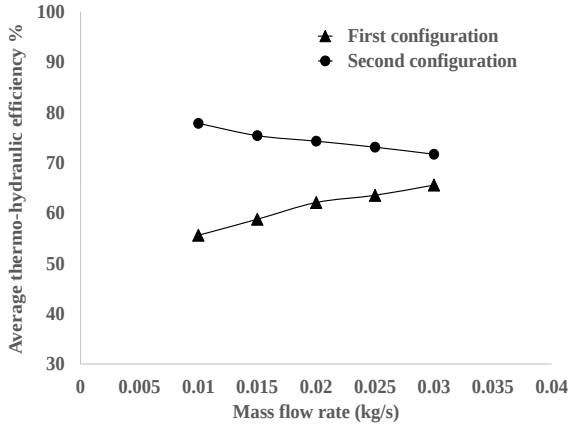

Figure 10. Average thermo-hydraulic efficiency

more and more as the air mass flow rate decreases, hence, producing useful energy for a longer time. Moreover, it is found that the average thermo-hydraulic efficiency for the second configuration is higher than the efficiency values of the first configuration because of the extra energy that is supplied to airflow in the discharge period which is not available in the first configuration case. The average thermo-hydraulic efficiency of the second configuration is about 71.7, 73.1, 74.3, 75.4, and 77.85% at air mass flow rates of 0.03 kg/s, 0.025 kg/s, 0.02 kg/s, 0.015 kg/s, and 0.01 kg/s, respectively, with increment of about 9.3, 15, 19.6, 28.2, and 40% at a mass flow rate of 0.03, 0.025, 0.02, 0.015, and 0.01 kg/s, respectively as compared with first configuration.

4. 3. Numerical Results

4. 3. 1. Temperature Distribution Contours The temperature distribution of airflow at a minimum and maximum flow rates for the two configurations is presented in Figures 11(a)-11(d). It can be observed that the temperature of airflow increases as the air moves forwards through the path of the collector's channels, and this increase in airflow temperature can be attributed to the stored thermal energy in the solar absorber, which in turn transfers to the airflow when it passes over the absorber surfaces. In addition, the outlet air temperature

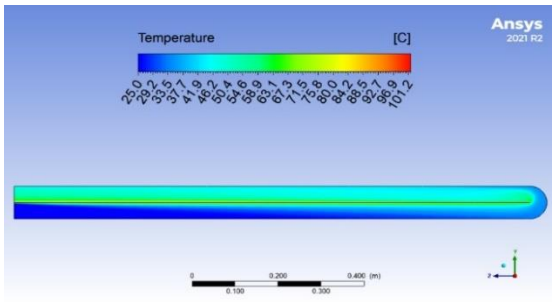

(a) (First configuration), $\dot{m}$=0.01 kg/s

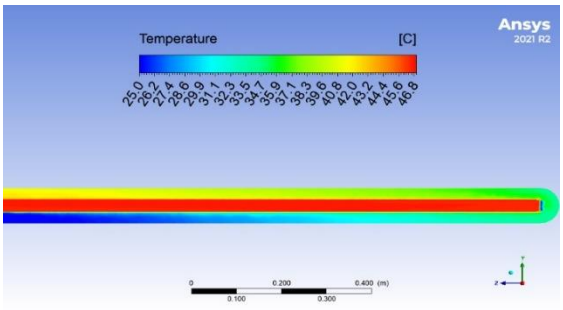

(b) (Second configuration), $\dot{m}$=0.01 kg/s

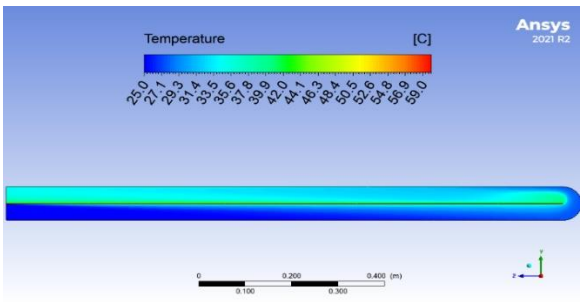

(c) (First configuration), $\dot{m}$=0.03 kg/s

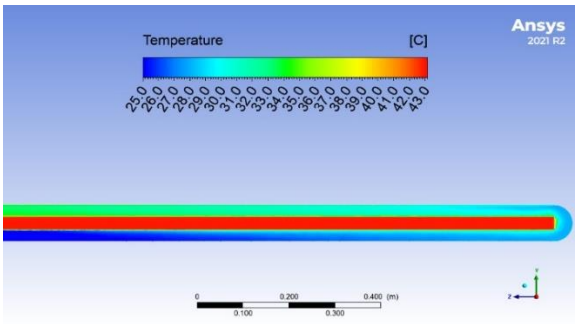

(d) (Second configuration), $\dot{m}$=0.03 kg/s

Figure 11. Temperature distribution of airflow

decreases as the mass flow rate increases because the convection exchange decreases as the airflow speed increases [33]. Furthermore, it can be noted that the airflow temperature in the second configuration is less than the airflow temperature in the first configuration because part of the absorbed energy is stored in the thermal storage material.

Figures 12(a)-12(d) show the temperature distribution of the absorber for the two configurations at the end of the charge period. It can be observed that the temperature distribution increases towards the middle point of the solar collector and decreases beyond this point to the end of the collector, and this result may be attributed to the role of vortices that are created at the start zone of the upper channel which in turn cause mixing up the airflow, hence, rising heat transfer rate between the absorber and the airflow [34]. Moreover, these figures indicate to the inverse relationship between airflow rate and absorber temperature.

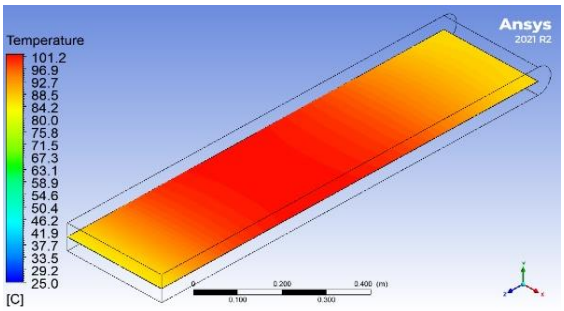

(a) (First configuration), $\dot{m}$=0.01 kg/s

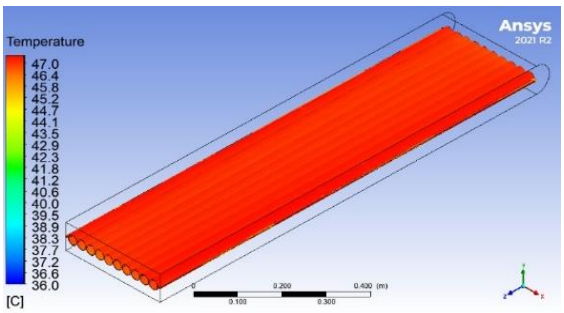

(b) (Second configuration), $\dot{m}$=0.01 kg/s

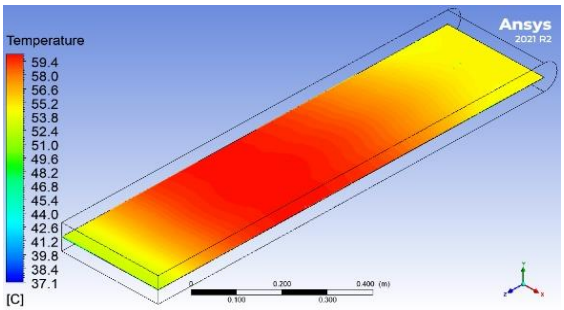

(c) (First configuration), $\dot{m}$=0.03 kg/s

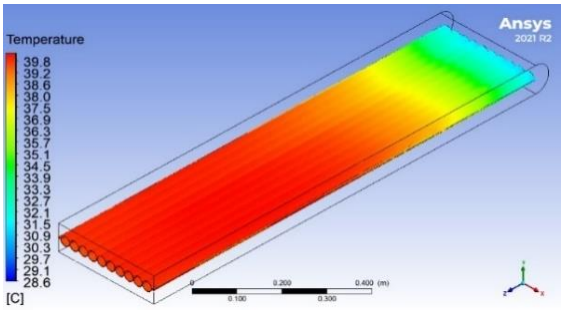

(d) (Second configuration), $\dot{m}$=0.03 kg/s

Figure 12. Temperature distribution of solar absorber configurations

4. 3. 2. Air Velocity Vectors Figures 13(a)-13(d) describe the velocity vectors at minimum and maximum mass flow rates for the two configurations. The maximum velocity is located at the end of the lower channel, and the flow separation occurs at the beginning of the upper channel. Moreover, the flow separation increases as the air mass flow rate increases.

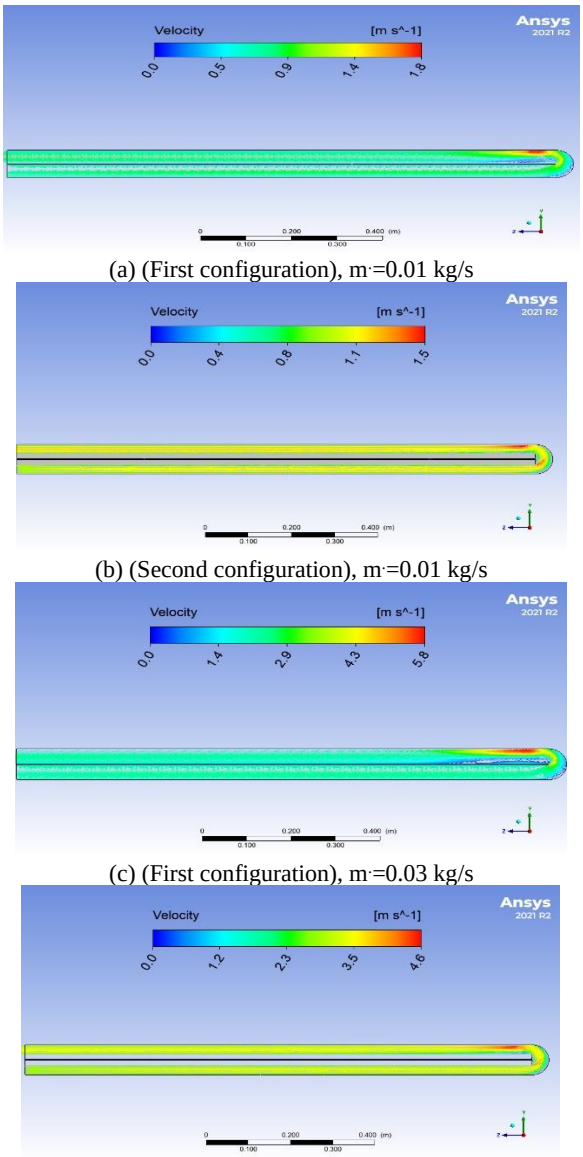

(a) (First configuration), m·=0.01 kg/s

(b) (Second configuration), m·=0.01 kg/s

(c) (First configuration), m·=0.03 kg/s

(d) (Second configuration), m·=0.03 kg/s

Figure 13. Velocity vectors of airflow

5. CONCLUSIONS

The outcomes of the present work can be summarized in the following brief points:

1. the second configuration can supply useful power for a longer time as compared with the first configuration due to the presence of thermal storage material.
2. The total useful energy generated by the second configuration is greater than those values that are achieved by the first configuration by an increment of 39.1, 51.2, 59.4, 74.8, and 89.6% at mass flow rates of 0.03, 0.025, 0.02, 0.015, and 0.01, respectively.
3. The second configuration offers higher average thermal performance compared to the first configuration with an increment of about 9.3, 15, 19.6, 28.2, and 40% at a mass flow rate of 0.03, 0.025, 0.02, 0.015, and 0.01 kg/s, respectively.
4. Depending upon the findings of this work, it can be claimed that the feasibility of using the tubular capsules solar absorber as a thermal performance enhancer.

6. ACKNOWLEDGMENT

The authors are thankful to the University of Technology- Iraq for providing help in completing this work.

7. REFERENCES

1. Chaichan, M.T., Abass, K.I. and Kazem, H.A., "The impact of thermal storage materials on the heating and storage efficiencies of a solar air heater", ***World Wide Journal of Multidisciplinary Research and Development,*** Vol. 4, (2018), 121-128.
2. Jasim Mahmood, A., "Thermal evaluation of a double-pass unglazed solar air heater with perforated plate and wire mesh layers", ***Sustainability,*** Vol. 12, (2020), 1-15. https://doi.org/10.3390/su12093619.
3. Shiravi, A.H., Firoozzadeh, M. and Lotfi, M., "Experimental study on the effects of air blowing and irradiance intensity on the performance of photovoltaic modules, using Central Composite Design", ***Energy,*** Vol. 238, (2022), 121633.
4. Lakshmi, D.V.N., Muthukumar, P. and Nayak, P.K., "Experimental investigations on active solar dryers integrated with thermal storage for drying of black pepper", ***Renewable Energy,*** Vol. 167, (2021), 728-739. https://doi.org/10.1016/j.renene.2020.11.144.
5. Shafiee, M., Farbeh, A.M. and Firoozzadeh, M., "Experimental Study on Using Oil-Based Nanofluids in a Vacuumed Tube Solar Water Heater; Exergy Analysis", ***International Journal of Ambient Energy,*** (2022), 1-24. https://doi.org/10.1080/01430750.2022.2073267.
6. Sorgulu, F. and Dincer, I., "Design and analysis of a solar tower power plant integrated with thermal energy storage system for cogeneration" ***International Journal of Energy Research***, Vol. 43, (2019), 6151-6160. https://doi.org/10.1002/er.4233.
7. Karimipour-Fard, P. and Beheshti, H., "Performance enhancement and environmental impact analysis of a solar chimney power plant: Twenty-four-hour simulation in climate condition of isfahan province, iran" ***International Journal of Engineering, Transactions B: Applications,*** Vol. 30, (2017), 1260-1269. doi: 10.5829/ije.2017.30.08b.20.
8. Kouhikamali, R. and Hassani, M., "The Possibility of using Flat Plate Solar Collector Based on the Best Calculated Tilt Angle in the City of Rasht as a Case Study", ***International Journal of Engineering, Transactions B: Applications,*** Vol. 27, No. 8, 2014, 1297-1306. https://doi: 10.5829/idosi.ije.2014.27.08b.16.
9. Goel, V., Hans, V.S., Singh, S., Kumar, R., Pathak, S.K., Singla, M., Bhattacharyya, S., Almatrafi, E., Gill, R.S. and Saini, R.P., "A comprehensive study on the progressive development and applications of solar air heaters", ***Solar Energy***, Vol. 229, (2021), 112-147. https://doi.org/10.1016/j.solener.2021.07.040.
10. Rayeni, A.D. and Nassab, S.A., "Effects of gas radiation on thermal performances of single and double flow plane solar heaters", ***International Journal of Engineering, Transactions***

C: Aspects Vol. 33, No. 6, 2020, 1156-1166. https://doi: 10.5829/ije.2020.33.06c.14.

11. Razak, A.A., Majid, Z.A.A., Azmi, W.H., Ruslan, M.H., Choobchian, S., Najafi, G. and Sopian, K., "Review on matrix thermal absorber designs for solar air collector", ***Renewable and Sustainable Energy Reviews***, Vol. 64, (2016), 682-693. https://doi.org/10.1016/j.rser.2016.06.015.
12. Salih, S.M., Jalil, J.M. and Najim, S.E., "Experimental and numerical analysis of double-pass solar air heater utilizing multiple capsules PCM", ***Renewable Energy***, Vol. 143, (2019), 1053-1066. https://doi.org/10.1016/j.renene.2019.05.050.
13. Kumar, A. and Subhash, K., "Effect of roughness and glass cover on solar air heater performance-A review", ***International Research Journal of Advanced Engineering and Science***, Vol. 2, (2017), 46-58.
14. Kumar, P.G., Balaji, K., Sakthivadivel, D., Vigneswaran, V.S., Meikandan, M. and Velraj, R., "Effect of using low-cost thermal insulation material in a solar air heating system with a shot blasted V- 14 corrugated absorber plate", ***Thermal Science and Engineering Progress***, Vol. 14, (2019), 100403. https://doi.org/10.1016/j.tsep.2019.100403.
15. Abdelkader, T.K., Zhang, Y., Gaballah, E.S., Wang, S., Wan, Q., Fan, Q., "Energy and exergy analysis of a flat-plate solar air heater coated with carbon nanotubes and cupric oxide nanoparticles embedded in black paint", ***Journal of Cleaner Production***, Vol. 250, (2020), 1-11. https://doi.org/10.1016/j.jclepro.2019.119501.
16. Das, B., Mondol, J.D., Debnath, S., Pugsley, A., Smyth, M. and Zacharopoulos, A., "Effect of the absorber surface roughness on the performance of a solar air collector: An experimental investigation", ***Renewable Energy***, Vol. 152, (2020), 567-578. https://doi.org/10.1016/j.renene.2020.01.056.
17. Jalil, J.M., Nothim, R.F. and Hameed, M.M., "Effect of Wavy Fins on Thermal Performance of Double Pass Solar Air Heater", ***Engineering and Technology Journal***, Vol. 39, (2021), 1362-1368. http://doi.org/10.30684/etj.v39i9.1775.
18. Sudhakar, P. and Cheralathan, M., "Thermal performance enhancement of solar air collector using a novel V-groove absorber plate with pin-fins for drying agricultural products: an experimental study", ***Journal of Thermal Analysis and Calorimetry***, Vol. 140, (2020), 2397-2408. https://doi.org/10.1007/s10973-019-08952-9.
19. Mesgarpour, M., Heydari, A. and Wongwises, S., "Geometry optimization of double pass solar air heater with helical flow path", ***Solar Energy***, Vol. 213, (2021), 67-80. https://doi.org/10.1016/j.solener.2020.11.015.
20. Jalil, J.M. and Ali, S.J., "Thermal Investigations of Double Pass Solar Air Heater with Two Types of Porous Media of Different Thermal Conductivity", ***Engineering and Technology Journal***, Vol. 39, (2021), 79-88. http://dx.doi.org/10.30684/etj.v39i1A.1704.
21. Sajawal, M., Rehman, T.U., Ali, H.M., Sajjad, U., Raza, A. and Bhatti, M.S., "Experimental thermal performance analysis of finned tube-phase change material based double pass solar air heater", ***Case Studies in Thermal Engineering***, Vol. 15, (2019), 1-25. https://doi.org/10.1016/j.csite.2019.100543.
22. Muthukumaran, J. and Senthil, R., "Experimental performance of a solar air heater using straight and spiral absorber tubes with thermal energy storage", ***Journal of Energy Storage***, Vol. 45, (2022), 103796. https://doi.org/10.1016/j.est.2021.103796.
23. Raju, G. and Kumar, M. M., "Experimental study on solar air heater with encapsulated phase change material on its absorber plate", ***Energy Storage***, Vol. 3, (2021), 1-16. https://doi.org/10.1002/est2.256.
24. Sudhakar, P. and Cheralathan, M., "Encapsulated PCM based double pass solar air heater: A comparative experimental study", ***Chemical Engineering Communications***, Vol. 208, (2021), 788-800. https://doi.org/10.1080/00986445.2019.1641701.
25. Abed, A.H., "Thermal storage efficiency enhancement for solar air heater using a combined SHSm and PCM cylindrical capsules system: experimental investigation", ***Engineering and Technology Journal***, Vol. 34, (2016), 999-1011.
26. Kumar, K., Kaushik, S. and Bisht, V.S., "CFD analysis on solar air heater with artificial roughened broken curved ribs", ***International Journal of Scientific & Engineering Research***, Vol. 8, (2017), 264-275.
27. Yadav, A. S. and Bhagoria, J. L., "Modeling and simulation of turbulent flows through a solar air heater having square-sectioned transverse rib roughness on the absorber plate", ***The Scientific World Journal,*** Vol. 2013, (2013), 1-12. https://doi.org/10.1155/2013/827131.
28. Sharol, A. F., Razak, A. A., Majid, Z. A., Azmi, M. A. and Tarminzi, M. A., "Evaluation on the performance of cross-matrix absorber double-pass solar air heater (CMA-DPSAH) with and without thermal energy storage material", ***Journal of Advanced Research in Fluid Mechanics and Thermal Sciences,*** Vol. 70, No. 2, (2020), 37-49. https://doi.org/10.37934/arfmts.70.2.3749.
29. Sharol, A. F., Abdul Razak, A., Abdul Majid, Z. A. and Fudholi, A., "Experimental study on performance of square tube absorber with phase change material", ***International Journal of Energy Research***, Vol. 44, No. 2, (2020), 1-12. https://doi.org/10.1002/er.4971.
30. Hussien, S.Q. and Farhan, A. A., "The effect of metal foam fins on the thermo-hydraulic performance of a solar air heater", ***International Journal of Scientific & Engineering Research,*** Vol. 9, No. 2, (2019), 840-847.
31. Hassan, H., Abo-Elfadl S. and El-Dosoky MF., "An experimental investigation of the performance of new design of solar air heater (tubular)", ***Renewable Energy,*** Vol. 151, (2020), 1055-1066. https://doi.org/10.1016/j.renene.2019.11.112.
32. Bergman, T.L., and Incropera, F.P., "Fundamentals of heat and mass transfer", John Wiley & Sons, (2011).
33. Salih, S.M., Jalil, J.M. and Najim, S.E., "Double-Pass Solar air Heater (DP-SAH) utilizing Latent Thermal Energy Storage (LTES)" in 2nd International Conference on Sustainable Engineering Techniques, Baghdad, Iraq, (2019), 32001-32010, https://doi:10.1088/1757-899X/518/3/032038.
34. Mohammed, A. "Study of Double Pass Solar Air Heater Integrated with A Thermal Storage Material", PhD thesis, University of Technology, Baghdad, Iraq, (2017).

Persian Abstract

چکیده

مشکل تابش خورشیدی متناوب می تواند به طور قابل توجهی بر عملکرد حرارتی بخاری های هوای خورشیدی (SAHs) تأثیر بگذارد. راه حل کارآمد برای این مشکل استفاده از ذخیره سازی حرارتی برای ذخیره انرژی حرارتی و استفاده مجدد از آن در ساعات غیر آفتابی است. مطالعه حاضر عملکرد حرارتی دو پیکربندی از گرمکن هوای خورشیدی دو گذری جریان مقابل تحلیل کرد. پیکربندی اول شامل یک جاذب خورشیدی صفحه تخت بود، در حالی که پیکربندی دوم شامل کپسول های لوله ای است که با آب به عنوان یک ماده ذخیره حرارتی معقول پر می شود. کپسول های لوله ای به صورت طولی و موازی جهت جریان هوا نصب شده اند. این مطالعه شامل بخش های عددی و تجربی بود. نتایج افزایش قابل توجهی را در تولید انرژی مفید هنگام استفاده از کپسول های لوله ای نشان داد. علاوه بر این، SAH با کپسول‌های لوله‌ای به دلیل وجود مواد ذخیره‌سازی حرارتی درون کپسول‌ها، می‌تواند برای مدت طولانی‌تری انرژی مفید تولید کند. مشخص شده است که کل انرژی مفید در مورد کپسول های لوله ای در حدود ٤٠٥٨، ٤٢٩٥.٣، ٤٤٢٦، ٤٥٨٤، و ٤٦٩٣ (W) با سرعت جریان جرمی ۰.۰۳، ۰.۰۲۵، ۰.۰۲، ۰.۰۱۵، و ۰.۰۱ کیلوگرم بر ثانیه است. با افزایش ۳۸.۳، ۵۱.۲، ٥٩.٤، ٧٤.٨ و ٨٩.٦ درصد نسبت به صفحه تخت. علاوه بر این، متوسط راندمان ترموهیدرولیک در مورد کپسول های لوله ای بیشتر از مقادیری است که در صفحه تخت در حدود ۹.۳، ۱۵، ۱۹.٦، ۲۸.۲ و ٤٠ درصد در نرخ جریان جرمی ۰.۰۳، ۰.۰۲۵ به دست می آید. به ترتیب ۰.۰۲، ۰.۰۱۵ و ۰.۰۱ کیلوگرم بر ثانیه است.

International Journal of Engineering

Journal Homepage: www.ije.ir

Evaluation of Steel Fiber Reinforced Geopolymer Concrete Made of Recycled Materials

H. A. Goaiz*[a], H. A. Shamsaldeen[a], M. A. Abdulrehman[b], T. S. Al-Gasham[a]

[a] *Department of Civil Engineering, Wasit University, Wasit, Iraq*
[b] *Department of Materials Engineering, Mustansiriyah University, Baghdad, Iraq*

PAPER INFO

Paper history:
Received 15 June 2022
Received in revised form 20 July 2022
Accepted 21 July 2022

Keywords:
Geopolymer Concrete
Recycled Steel Fiber
Tensile Strength
Waste Glass

ABSTRACT

In the last few decades, the geopolymer concrete presented an evolution in civil engineering field. The current study aims to produce a low cost steel fiber reinforced geopolymer concrete with an ecceptable tensile properties. The experimental program aims to investigate the tensile behaviour of geopolymer concrete reinforced with steel fiber and made of recycled materials. The primary ingredients of the steel fiber reinforced geopolymer concrete in this study were waste materials. The recycled steel fiber was extracted from tires and chopped into tiny fibers with an average length of 20 mm and an average diameter of 0.7 mm. The geopolymer concrete in this study consisted of coarse aggregate, which was crushed recycled concrete. Also, the fine aggregate was crushed waste glass. In addition to the compressive strength, tensile test procedures such as splitting tensile strength, double punch tensile strength, and flexural tensile strength were all investigated in this study. Recycled steel fiber was compared to a new hooked-end steel fiber and hybrid steel fiber (50% new + 50% recycled) with three different volumetric percentages of steel fiber (0.5%, 1.0%, and 1.5%). The new steel fiber geopolymer concrete mix with 1.5% of steel fiber showed the highest test results among other mixes, as the tensile strength was increased by nearly 50% in the case of the double punch test. This conduct could be explained as the new steel fiber having a uniform, straight shape with hooked ends, increasing the anchorage between the fly ash binder and the steel fiber. In addition, the recycled steel fiber was contained some rubber crumbs that could be another reason that negatively affected the tensile properties of the geopolymer concrete.

doi:*10.5829/ije.2022.35.10a.19*

1. INTRODUCTION

Conventional concrete is the most used construction material worldwide for its cost effectiveness and reliable mechanical properties. This very high consumption of the general purposes cement concrete, more than 8.8 billion tons per year [1], is now considered one of the carbon dioxide emission sources to the atmosphere that causes dramatic climate changes. Thus, geopolymer concrete (GC) was introduced by Davidovits in 1994 [2] to be an alternative to Portland cement concrete for environmental considerations. Instead of Portland cement, by-product materials such as fly ash or new materials such as metakaolin were used to develop an inorganic alumina-silica polymer that works as cementing material [3-5]. Both ordinary concrete and GC are weak under tensile stresses and for this reason, the concrete in tension is neglected in many international codes [6]. However, in some structural applications (such as hydraulic structures and airport pavements), tensile strength could be a critical mechanical property of GC, and then it should be taken into account [7]. One solution to enhance the tensile behaviour of the GC is to add a steel fiber to the concrete mix. The cracking triggering and propagation behavior of fiber-reinforced geopolymer concrete (FRGC) can be controlled by using the optimum dose of steel fiber that depends on many factors such as shape and aspect ratio (length/diameter) of steel fiber and aggregate/binder ratio of GC. In the current study, some recycled materials were used to enhance the tensile

*Corresponding Author Institutional Email: hussam@uowasit.edu.iq
(H. A. Goaiz)

Please cite this article as: H. A. Goaiz, H. A. Shamsaldeen, M. A. Abdulrehman, T. S. Al-Gasham, Evaluation of Steel Fiber Reinforced Geopolymer Concrete Made of Recycled Materials, ***International Journal of Engineering, Transactions A: Basics***, Vol. 35 No. 10, (2022), 2018-2026

properties of the GC in order to produce a low cost building material with reliable mechanical properties.

To assess the tensile behaviour of concrete, several test methods have been adopted for this purpose. The most widely used test procedure: the splitting test or the Brazilian test. Many international standards have adopted this method, such as American Standard for Testing Materials C 469-04 [8]; Australian Standard (AS) 1012.10 [9], because of its ease to perform and reliable results of tensile strength for plain concrete. The splitting test procedure is also applicable for steel fiber reinforced concrete (SFRC), as stated by many studies [10-13]. On the other hand, Olesen et al. [14], Goaiz et al. [15] and Goaiz et al. [16] stated that the splitting test procedure is not recommended to evaluate the tensile strength of SFRC because of the overestimated results recorded by this test method in comparison with the results of the direct tensile test method. Another indirect tensile strength test was suggested by Chen [17], commonly called Double Punch Test (DPT). Several studies were then assessed the Double Punch Test procedure reported in literature [18-21]. The DPT has the advantage of a smaller size of concrete sample and a more straightforward test procedure than the splitting test. Goaiz et al. [16] found that the results of the DPT and the direct tensile test were closer to each other. Thus, the tensile behaviour of the GC that reinforced with different types of steel fiber in this study was evaluated by three different test procedures.

Recently, many experimental studies were conducted in order to investigate the behaviour if fiber reinforced geopolymer concrete [22-24]. However, for the Steel Fiber Reinforced Geopolymer Concrete (SFRGC) to be valuable construction material, it must compete economically with the existing reinforcing system. The current study aims to produce a low cost steel fiber reinforced geopolymer concrete with an acceptable tensile properties. Therefore, one of the best options for getting low-cost SFRGC is to find recycled materials that could be used to produce this type of concrete.

2. EXPERIMENTAL PROGRAM

The experimental program included three different test procedures (splitting test, double punch test, and flexural test) that have been conducted to evaluate the tensile behaviour of the SFRGC specimens. In addition to the reference concrete mix made of plain GC, nine SFRGC mixes have been prepared with volumetric steel fiber percentages 0.5%, 1.0%, and 1.5%. Also, the experimental program of this work included three different types of steel fiber; new steel fiber, recycled steel fiber, and hybrid steel fiber (50% new + 50% recycled).

2. 1. Materials Ten GC mixes were prepared using class F fly ash. This type of fly ash was chosen in this study due to the better performance compare to other types when cured at 60 °C. The coarse aggregate of recycled crushed concrete (5-20 mm), the fine aggregate of recycled crushed glass with a grade of Zone No. 3, according to the Iraq standard No. 45:1985 [25]. In addition, alkaline solution ($NaOH+Na_2SiO_3$), water, a water-reducing admixture (superplasticiser), and steel fiber were used. Table 1 shows the mixed design of the fly ash-based GC used in this study. The steel fiber was in two types; the first type was end-hooked steel fiber of 25 × 0.5 mm (long × diameter). The second type was recycled steel fiber extracted from cars tier, with an average length of 20 mm and average diameter of 0.7 mm; some of the materials used in this study are shown in Figure 1. The SFRGC included 0.5%, 1.0%, and 1.5% steel fiber by volume of concrete for all mixes. The hybrid mix contains 50% of new steel fiber and 50% recycled steel fiber.

2. 2. Mixing of SFRGC Specimens In this study, sodium hydroxide was prepared with a molarity of 10 by dissolving the NaOH flakes in distilled water. Then, sodium hydroxide solution was mixed with sodium silicate for several minutes to form the alkali liquid left for 24 hours before use. The recycled crushed gravel, crushed glass, and fly ash were mixed in a dry condition for 2-3 minutes by a pan-type concrete mixer. Then, the alkali liquid was mixed with additional water and for 4-5 minutes until homogeneity is reached. The reference mix (0% steel fiber) was ready to be cast. In the case of SFRGC, the steel fiber was added little by little to the fresh GC mix and in order to avoid any blockage of the steel fiber during the last 3 minutes of mixing. All of the GC samples were cured at a temperature of 60 ˚C in the oven for 28 days.

TABLE 1. Concrete mix design adopted for the current study

Component	Dosage			
	GC	**S0.5X***	**S1.5X***	**S1.5X***
Fly ash (FA) [kg/m^3]	350	350	350	350
Alkaline solution by wt.% of FA	0.5	0.5	0.5	0.5
Recycled coarse aggregate [kg/m^3]	1050	1050	1050	1050
Recycled fine aggregate [kg/m^3]	900	900	900	900
NaOH molarity	10	10	10	10
Superplasticiser by wt.% of FA	2.25	2.25	2.25	2.25
Steel Fibres [kg/m^3]	-----	40	80	120
Water by wt. % of FA	0.1	0.1	0.1	0.1
Na_2SiO_3/NaOH	1:1.5	1:1.5	1:1.5	1:1.5

*Note: X letter refers to any type of steel fiber reinforcement

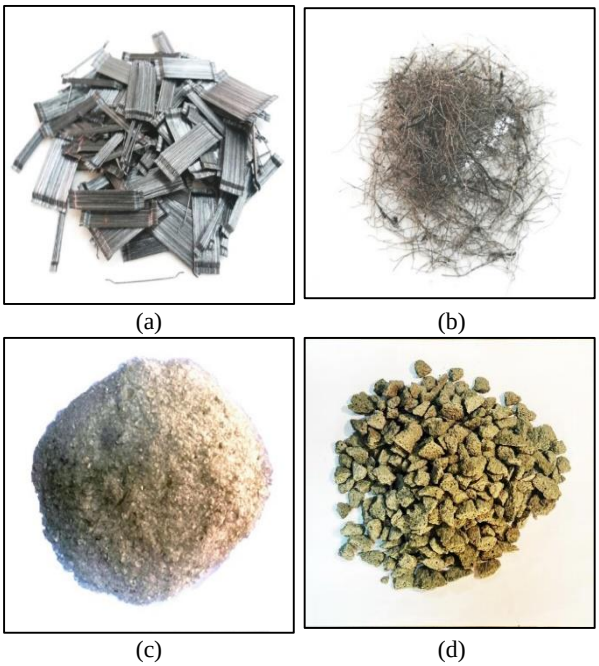

Figure 1. Some materials: (a) New steel fiber; (b) Recycled steel fiber; (c) Recycled crashed glass and (d) Recycled crashed concrete

2. 3. Test setup and Procedure

2. 3. 1. Compression Test To determine the compressive strength of the GC cubes, a Matest compression testing machine with a loading capacity of 1500 kN was used. For each mix, three cubes were tested under a constant loading of 20 MPa/min according to BS EN 12390-3:2019 [26] at the age of 28 days.

2. 3. 2. Splitting Tensile Test The American standard ASTM C496-02 [2] was adopted to evaluate the splitting strength of the GC cylinders. For each mix, three cylinders were prepared with 150 mm × 300 mm (diameter × height). According to the standard, the load must be applied at a rate of 1.5 MPa/min. Therefore, the splitting tensile strength of the specimens can be calculated according to ASTM C496-02 [2].

2. 3. 3. Double Punch Test (DPT) The DPT was conducted according to the test method proposed by Chen [17], see Figure 2. Based on this test method, the tensile strength of GC specimens can be determined by preparing three cylinders with 150 mm ×150 mm (diameter × height). The applied load is transferred from the loading heads of the compression machine to the specimens through steel punches with 37.5 × 25 mm (diameter × height) located between the loading plates and the two surfaces of the specimen. Two-dimensional guides were used to ensure that the steel punches were located at the center of the specimens to prevent any loading eccentricity during the test. The load was applied at a 1.4 MPa/min rate on the specimen until the maximum load was reached. The tensile strength can be calculated according to Chen [17].

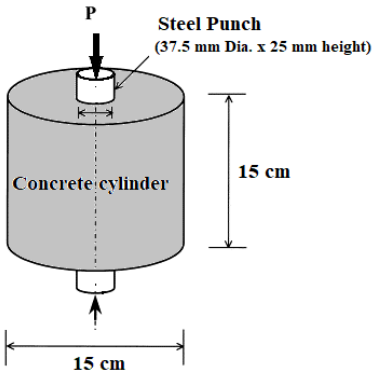

Figure 2. Double Punch Test as suggested by Chen [17]

2. 3. 4. Flexural Test The flexural strength in this study is conducted according to ASTM C 78-16 [27] to calculate the modulus of rupture by using simple beam with a third-point loading test procedure. The flexural strength of the geopolymer concrete is obtained by averaging the results of two specimens since the values obtained are very close. Test prisms of SFRGC are made with dimensions of 100 × 100 × 500 mm.

3. RESULTS AND DISCUSSION

3. 1. Concrete Compressive Strength Table 2 shows the test results for the compressive strengths of the plain GC mix and SFRGC with new steel fiber, recycled steel fiber, and hybrid steel fiber. The results showed an average strength of the four concrete mixes between 31 MPa to 36 MPa. Also, it can be seen that the type of the steel fiber had a considerable impact on the strength of SFRGC.

Mixes S0.5N, S0.5R, and S0.5H were achieved an increment of 7%, 0%, and 5% higher compressive strength than Mix GC. It can be seen that there is no increment of the compressive strength was recorded for GC mix with 0.5% of recycled steel fiber or even slight decrease and this could be attributed to the presence of the rubber crumbs within the recycled steel fibers. Mixes S1.0N, S1.0R, and S1.0H were achieved an increment of 12%, 1%, and 9% higher compressive strength than Mix GC. For example, mixes S1.5N, S1.5R, and S1.5H were achieved an increment of 16%, 3%, and 13% higher compressive strength than Mix GC. The higher average 28-d compressive strength was obtained by Mix S1.5N (SFRGC made with new steel fiber) which is 36 MPa, see Figure 3.

To demonstrate the effect using recycled aggregate, the results of this study were compared to another study conducted by Zhang et al. [24] which had nearly the same aggregate/cementitious materials ratio but with natural river aggregate. For the same content of steel fiber ranging from 0% to 1.5%, Zhang et al. [24] obtained GC mixes with compressive strength between 43 MPa to 50 MPa. Taking in consideration other differences between the mixes of the two studies, it can be seen that the use of recycled aggregate lead to a reduction of nearly 30% of the compressive strength of the GC mixes.

3. 2. Splitting Tensile Strength Test Figure 4 presents the splitting strength of GC mix and SFRGC mixes with different types of steel fiber. The splitting strength of mixes S0.5N, S0.5R and S0.5H was respectively increased by 49%, 9% and 30% compared to GC mix. Mixes S1.0N, S1.0R and S1.0H was respectively increased by 61%, 28% and 44% compared to GC mix. Also, the splitting strength of mixes S1.5N, S1.5R and S1.5H was respectively increased by 85%, 46% and 56% compared to GC mix. Mix S1.5N that included new steel fiber had recorded the highest splitting strength of 4.9 MPa which contained the highest compressive strength and new steel fiber.

3. 3. Double Punch Test Figure 5 shows the DPT failure pattern of the GC samples with new, recycled, and hybrid steel fiber. Figure 5(a) present the failure mode of GC specimens (no steel fiber added). It can be observed that the failure pattern showed three radial cracks on the upper and the lower surfaces of the specimen that having an angle of 120° between each crack. According to previous studies, this pattern of failure was commonly reported in the literature [15-21]. However, as the percentage of the steel fiber increased up to 1.5%, more radial cracks can be seen. On the other hand the width of the radial cracks was reduced, as presented in Figures 5(b) and 5(c). Therefore, by using steel fibre in the GC mixes, more minor radial failure cracks can be seen in different directions of the surface of the specimens.

TABLE 2. Average strength results of all mixes.

Mix ID	Compressive [MPa]		Splitting [MPa]		DPT [MPa]		Flexural [MPa]	
	Mean	SD	Mean	SD	Mean	SD	Mean	SD
GC	31.3	1.1	2.65	0.23	2.24	0.22	4.86	0.44
S0.5N	33.6	1.88	3.95	0.35	2.91	0.28	6.92	0.75
S0.5R	31.2	2.66	2.88	0.41	2.36	0.33	5.08	1.06
S0.5H	32.8	2.42	3.44	0.44	2.5	0.38	6.11	0.97
S1.0N	35.1	2.32	4.28	0.48	3.18	0.36	8.15	0.93
S1.0R	31.7	3.28	3.4	0.36	2.55	0.46	6.19	1.31
S1.0H	34.1	2.94	3.82	0.38	2.8	0.39	6.83	1.18
S1.5N	36.2	3.14	4.9	0.42	3.31	0.43	8.36	1.26
S1.5R	31.9	4.2	3.86	0.61	2.65	0.44	6.51	1.68
S1.5H	35.4	3.44	4.12	0.54	3.16	0.49	7.10	1.38

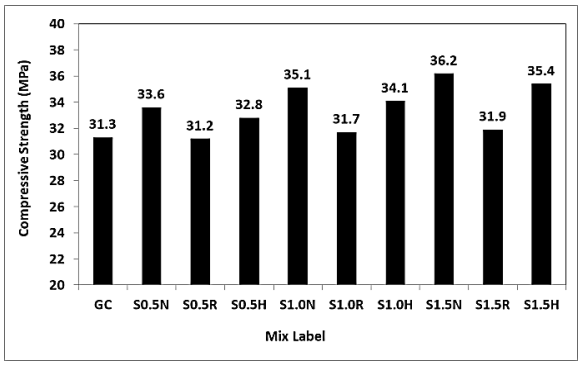

Figure 3. 28-day results of compressive strength

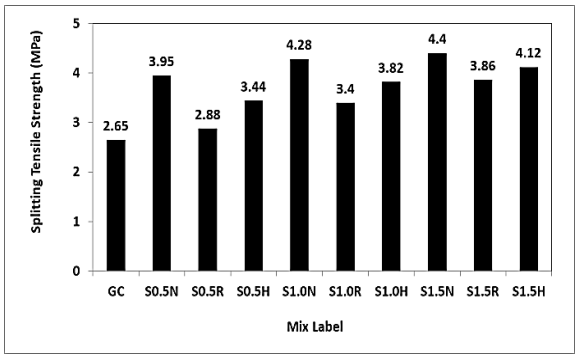

Figure 4. 28-day results of splitting strength

Figure 6 shows the DPT results, according to this figure, the tensile strength of S0.5N, S0.5R, and S0.5H was increased by 30%, 5%, and 17%, respectively, compared to GC. Also, the DPT tensile strength of S1.0N, S1.0R, and S1.0H was increased by 42%, 14%, and 25%, respectively, compared to GC. Finally, the tensile strength of S1.5N, S1.5R, and S1.5H was increased by 48%, 25%, and 41%, respectively, compared to PC. The highest tensile result of 3.31 MPa was recorded by S1.5N that had the highest GC compressive strength and contained the new steel fiber. This behaviour is quite similar to the splitting strength test because of the influence of the increment in steel fiber content.

3. 4. Flexural Strength Test Figure 7 shows the flexural failure modes of the GC samples with new, recycled and hybrid steel fiber. Figure 7(a) present the failure pattern of plain GC samples (no steel fiber added).

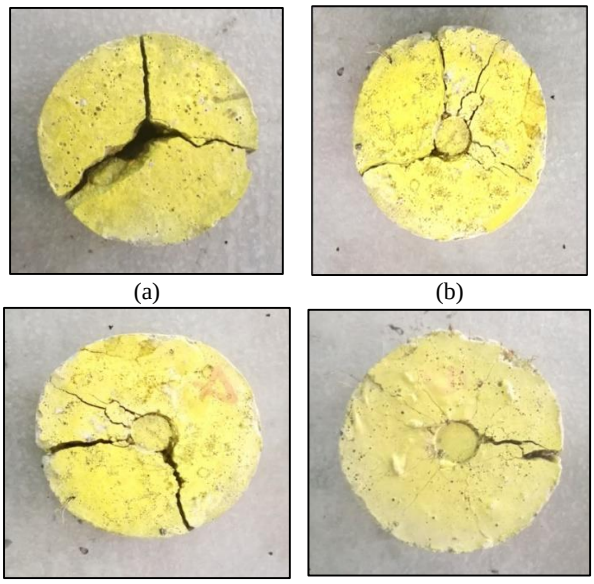

Figure 5. Failure pattern of double punch test for different steel fiber content

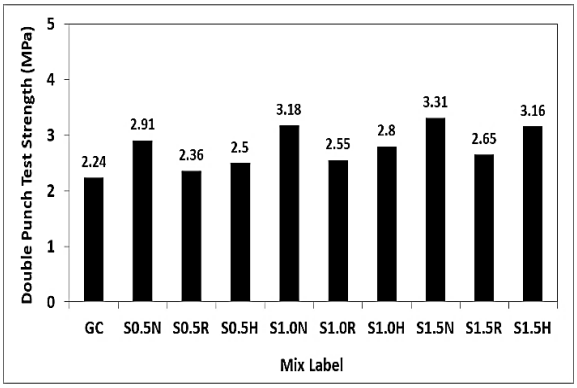

Figure 6. 28-day results of DPT tensile strength

As shown in this figure, the prism sample was utterly split into two parts near the centerline of the specimen by one crack. This mode of failure is reported as a standard failure mode of the flexural strength test. The failure mode was tended to show more cracks near the centerline of the specimen due to the increase of the steel fiber percentage up to 1.5%. The two parts of the specimen in this case, however, were still attached to each other by the presence of the steel fiber, as shown in Figures 7(b), 7(c), and 7(d). Thus, using of steel fiber in the GC could be the reason to see more centerline cracks in the failure mode.

The results of the flexural strength are presented in Figure 8. This figure shows an increase of the flexural strength of mixes S1.5N, S1.5R, and S1.5H was respectively increased by 72%, 34%, and 44%, in comparison with the GC mix. The highest flexural tensile strength (8.36 MPa) was recorded by mix S1.5N,

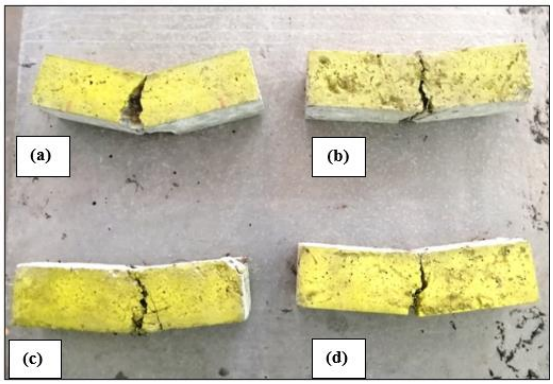

Figure 7. Failure mode of flexural test for different steel fiber content

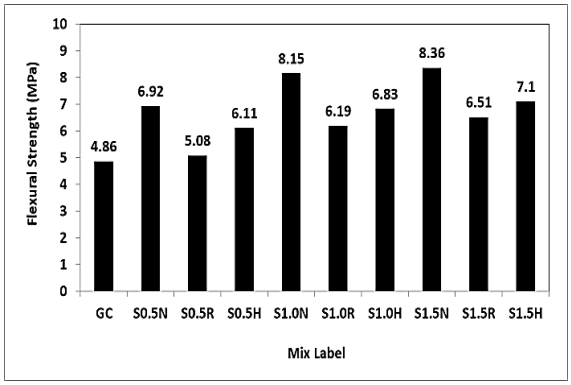

Figure 8. 28-days results of flexural tensile strength

where the highest steel fiber content and the new steel fiber were used.

3. 5. Comparison of Tensile Strength Tests

Figure 9 shows the tensile test results for three different test procedures (splitting test, double punch test, and flexural test). As expected, the Flexural test shows the highest tensile results among other test methods, and mix S1.5N obtained the highest tensile strength of 8.36 MPa. On the other hand, splitting and double punch tests are both indirect tensile test methods, although the splitting test is not appropriate for SFRGC mixes because the

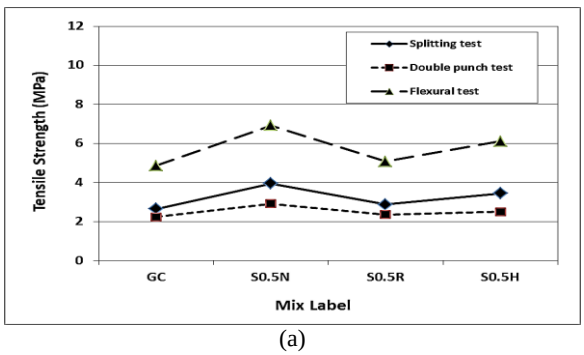

(a)

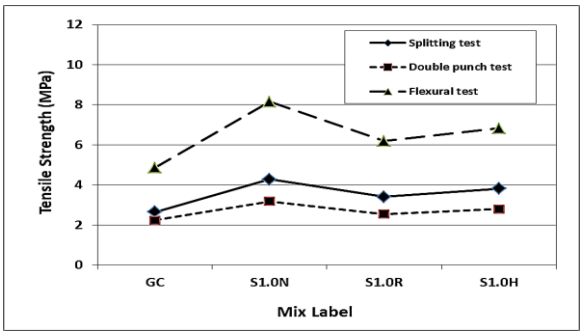

(b)

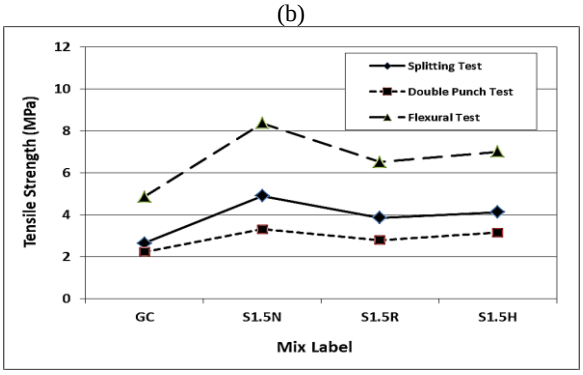

(c)

Figure 9. Tensile strength results of different test methods and different steel fiber content: (a) 0.5% steel fibre content; (b) 1.0% steel fibre content and (c) 1.5% steel fibre content

failure crack was not visual and the SFRGC samples was intact post the ultimate failure was achieved. The presence of the steel fiber is the only reason for this ductile behaviour because the applied load was spread along multiple surfaces of failure which prohibited the splitting failure. Also, the applied load was non-uniformly extended in the direction of load due to the compressive zone that created under the loading strip. Also, according to the tensile test results of different test procedures that were used in this study, it can be seen the type and the amount of the steel fiber had a dramatic effect of the tensile behaviour. The recycled steel fiber has the lower effect on tensile strength compared to the new steel fiber and the hybrid steel fiber. The main reason behind this behaviour was the small amount of the rubber that attached to the surface of the recycled steel fiber which affects the bond between the steel fiber and the surrounded GC matrix. Another reason could be the non-uniform shape and distribution of the recycled steel fiber within the GC mix which causes weak bonding between the steel fiber and the GC mix.

4. COMPRESSIVE-TENSILE STRENGTH RELATIONSHIP

The tensile strength could be an important design parameter in different types of structures such as hydraulic structures or airports pavement. For this reason, international building codes suggested some equations to predict the value of the tensile strength by only knowing the compressive strength of the concrete. However, these empirical equations are limited to Portland cement concrete with a specific range of compressive strength. In this study, two equations, Equations (1) and (2) proposed by the ACI 363R-92 [28] and CEB-FIP 199 1[29] respectively were used to verify the experimental tensile strength of the steel fibre geopolymer concrete.

$$f_t = 0.59\, f_c^{\,0.5} \quad (1)$$

$$f_t = 0.3\, f_c^{\,0.66} \quad (2)$$

Then, the predicted tensile strength was compared to the experimental results of each individual test procedure in Table 3 shown below. From this table, it can be seen that Equation (2) shows a lower predicted values of the tensile strength than Equation (1) and this conservative model could be more suitable and preferable in the structural design. Moreover, Equation (2) yielded predicted values of the tensile strength which are very close to the experimental values of the double punch test procedure as can be seen in Table 4. As mentioned above in many previous studies [15-21], the double punch test showed very reliable results in terms of determining the tensile strength of steel fibre reinforced concrete. For this reason, an equation was suggested to show the relationship between the compressive strength and the double punch tensile strength of SFRGC. Although, the equation is limited number of data in this study but it could be a promising start for future studies to find a reliable model for the relationship between the compressive and the tensile strength of SFRGC. A polynomial equation from the second order was obtained using MS Excel program to represent the best fit with the higher R-squared value of 0.91 for the double punch tensile strength, see Figure 10. In addition, Equation (3) is shown below:

$$f_t = 0.0016\, f_c^{\,2.0} + 0.084\, f_c - 1.83 \quad (3)$$

5. COST EFFECTIVENESS

In general, the cost of a geopolymer concrete vary from country to another around the world depending on many factors such as the target compressive strength of the concrete, prices of the raw materials, the labor cost and the regulations of the country due to carbon taxation. Locally in Iraq, the cost of ordinary Portland cement concrete production for compressive strength of 30s MPa is nearly $80 per cubic meter and it can be up to $120 for steel fiber reinforced concrete. However, the cost of the GC production is unknown because there is no constructional demand on this type of concrete yet. One advantage of any new proposed material is the cost

effectiveness so that it can be potentially used the construction industry. Table 4 shows the estimated cost of GC locally produced per cubic meter. The total price of nearly $107 per cubic meter of can be expected to locally produce a recycled steel fiber reinforced geopolymer concrete. This price is 12% lower than those of conventional concrete with advantage of using friendly environment construction material.

TABLE 3. Experimental and predicted values of the tensile strength

Mix ID	Splitting [MPa]	Double Punch [MPa]	Flexural [MPa]	Predicted Strength Eq. (1)	Predicted Strength Eq. (2)
GC	2.65	2.24	4.86	3.30	2.97
S0.5N	3.95	2.91	6.92	3.42	3.12
S0.5R	2.88	2.36	5.08	3.30	2.97
S0.5H	3.44	2.5	6.11	3.38	3.07
S1.0N	4.28	3.18	8.15	3.50	3.21
S1.0R	3.4	2.55	6.19	3.32	3.00
S1.0H	3.82	2.8	6.83	3.45	3.15
S1.5N	4.9	3.31	8.36	3.55	3.28
S1.5R	3.86	2.65	6.51	3.33	3.01
S1.5H	4.12	3.16	7.10	3.51	3.23

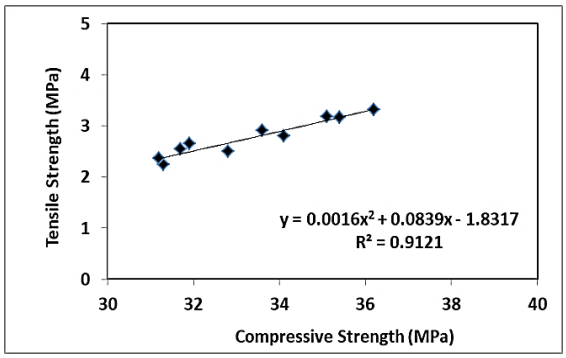

Figure 10. Compressive-tensile relationship of SFRGC based on double punch tensile test procedure

TABLE 4. Cost per cubic meter for locally produced GC

Component	Price per (kg)	Amount (kg/m^3)	Cost per (m^3)
Fly ash (class F) [kg/m^3]	0.1	350	35
Alkaline solution [kg/m^3]	0.05	175	8.75
Recycled coarse aggregate [kg/m^3]	0.01	1050	10.5
Recycled fine aggregate [kg/m^3]	0.05	600	30
Superplasticiser [kg/m^3]	0.4	7.8	3.12
Steel Fibres [kg/m^3]	0.5	40	20
		Total	$107.4

6. CONCLUSIONS

This study experimentally investigated the tensile behaviour of three different types of steel fiber geopolymer concrete (SFRGC) mixes. A total number of 120 specimens were tested under compression, splitting tensile, double punch and flexural tests. Each result shown in this study was an average of three individual readings. The SFRGC mixes were compared to a reference plain geopolymer concrete (GC) mix to examine the efficiency of using recycled steel fiber in making concrete.

1. In this study, geopolymer concrete was produced with reliable compressive strength of nearly 30 MPa by using waste filler (recycled crashed concrete, and recycled crushed glass). Accordingly, with more research work on the durability of this type of concrete, it can be recommended to use it as a reinforced concrete in the construction field. However, compared to a previous research, the replacement of natural river aggregate with recycled aggregate could lead to a compressive strength reduction of nearly 30%.
2. The compressive strength of concrete was slightly increased by using recycled steel fiber (an increment of 3% for 1.5% of recycled steel fiber concrete). However, an increment of 16% was achieved for the compressive strength when new steel fiber is used with 1.5% volume content. Also, attention should be given to the geopolymer concrete's workability by using the proper amount of alkaline solution and superplasticiser. The higher average 28-d compressive strength was obtained by SFRGC made with new steel fiber which is 36 MPa.
3. The highest splitting tensile strength of GC of 4.9 MPa was achieved by using new steel fiber with 1.5% of steel fiber content. Because this type of steel fiber has some advantages such as uniform aspect ratio (length/diameter) and straight shape with a hooked end to increase the anchorage with the cement paste. On the other hand, the highest splitting tensile strength of GC with recycled steel fiber was 3.86 MPa. This is because that the recycled steel fiber was contained some rubber crumbs which may negatively affected the mechanical properties of the geopolymer concrete.
4. The splitting test method was inadequate to evaluate the tensile strength of SFRGC in both cases of new steel fiber and recycled steel fiber. This is because the failure surface of the specimen was more than one and it is a conflict with the equation used to calculate the tensile strength in this method. However, for tensile strength assessment of SFRGC, a double punch test procedure can be adopted with reliable adequacy.
5. The highest flexural strength (8.36 MPa) of GC mixes was achieved by involving 1.5% of steel fiber content. New steel fiber recycled steel fiber, and

hybrid steel fiber was respectively increased by 72%, 34%, and 44%, in comparison with the GC without steel fiber. Also, as expected, the flexural test method obtained the highest tensile strength results among other tensile strength test procedures, nearly 16% of the compressive strength.

6. In terms of cost effectiveness, locally the cost of producing recycled steel fiber geopolymer concrete is nearly 12% lower than the cost of conventional steel fiber reinforced concrete.

7. REFERENCES

1. Habert G., D'Espinose De Lacaillerie J.B. and Roussel N., "An environmental evaluation of geopolymer based concrete production: reviewing current research trends", ***Journal of Clean Production***, Vol. 19, (2011), 1229-1238, doi: 10.1016/j.jclepro.2011.03.012
2. Davidovits, J., "High-alkali cements for 21st century concretes", ***ACI Symposium Publication***, Vol. 144, No. 1, (1994), 383-398. doi: 10.14359/4523.
3. Noori, A.S., Oweed, K.M., Raouf, R.M. and Abdulrehman, M.A., "The relation between destructive and non-destructive tests of geopolymer concrete", ***Materials Today: Proceedings***, Vol. 42, (2021), 2125-2133. doi: 10.1016/j.matpr.2020.12.296.
4. Al-Sultani, S., Al-Hydary, I. and Al-dujaili, M., "Taguchi-grey relational analysis for optimizing the compressive strength and porosity of metakaolin-based geopolymer", ***International Journal of Engineering, Transactions B: Applications***, Vol. 34, No. 11, (2021), 2525-2533. doi: 10.5829/IJE.2021.34.11B.15.
5. Raj, S., Arulraj, P., Anand, N., Balamurali, K. and Gokul, G., "Influence of various design parameters on compressive strength of geopolymer concrete: A parametric study by taguchi method", ***International Journal of Engineering, Transactions A: Basics***, Vol. 34, No. 10, (2021), 2351-2359. doi: 10.5829/IJE.2021.34.10A.16.
6. Bernal, S., De Gutierrez, R., Delvasto, S. and Rodriguez, E., "Performance of an alkali-activated slag concrete reinforced with steel fibers", ***Construction and Building Materials***, Vol. 24, No. 2, (2010), 208-214. doi: 10.1016/j.conbuildmat.2007.10.027.
7. Zain, M.F.M., Mahmud, H.B., Ilham, A. and Faizal, M., "Prediction of splitting tensile strength of high-performance concrete", ***Cement and Concrete Research***, Vol. 32, No. 8, (2002), 1251-1258. doi: 10.1016/S0008-8846(02)00768-8.
8. " Concrete, A.I.C.C.o. and Aggregates, C., "Standard test method for splitting tensile strength of cylindrical concrete specimens1, ASTM international, (2017).
9. Standard, A., "Method 10: Determination of indirect tensile strength of concrete cylinders (brazil 'or splitting test)", ***Methods of Testing Concrete, AS***, (2000).
10. Behnood, A., Verian, K.P. and Gharehveran, M.M., "Evaluation of the splitting tensile strength in plain and steel fiber-reinforced concrete based on the compressive strength", ***Construction and Building Materials***, Vol. 98, No. 1, (2015), 519-529. doi: 10.1016/j.conbuildmat.2015.08.124.
11. Kmiecik P. and Kaminski M. "Modelling of reinforced concrete structures and composite structures with concrete strength degradation taken into consideration", ***Archives of Civil and Mechanical Engineering,*** Vol. 11, No. 3, 623-636 (2011), doi: 10.1016/S1644-9665(12)60105-8.
12. Molins, C., Aguado, A. and Saludes, S., "Double punch test to control the tensile properties of frc (barcelona test)", ***Materials and Structures***, Vol. 42, No. 4, (2009), 415-425. doi: 10.1617/s11527-008-9391-9.
13. Abrishambaf, A., Barros, J.A. and Cunha, V.M., "Tensile stress–crack width law for steel fibre reinforced self-compacting concrete obtained from indirect (splitting) tensile tests", ***Cement and Concrete Composites***, Vol. 57, (2015), 153-165. doi: 10.1016/j.cemconcomp.2014.12.010
14. Olesen, J.F., Østergaard, L. and Stang, H., "Nonlinear fracture mechanics and plasticity of the split cylinder test", ***Materials and Structures***, Vol. 39, No. 4, (2006), 421-432. doi: 10.1617/s11527-005-9018-3.
15. Goaiz Hussam, A., Yu, T. and Hadi Muhammad, N.S., "Quality evaluation tests for tensile strength of reactive powder concrete", ***Journal of Materials in Civil Engineering***, Vol. 30, No. 5, (2018), 1-9. doi: 10.1061/(ASCE)MT.1943-5533.0002257
16. Goaiz, H.A., Farhan, N.A., Sheikh, M.N., Yu, T. and Hadi, M.N., "Experimental evaluation of tensile strength test methods for steel fibre-reinforced concrete", ***Magazine of Concrete Research***, Vol. 71, No. 8, (2019), 385-394. doi: 10.1680/jmacr.17.00516
17. Chen, W.F. and Colgreve, T.A., "Double punch test for tensile strength of concrete", ***ACI Materials Journal***, Vol. 67, No. 2, (1970), 993-1005.
18. Carmona Malatesta, S., Aguado de Cea, A. and Molins Borrell, C., "Generalization of the barcelona test for the toughness control of frc", ***Materials and Structures***, Vol. 45, No. 7, (2012), 1053-1069. doi: 10.1617/s11527-011-9816-8.
19. Chen, W.F. and Yuan, R.L., "Tensile strength of concrete: Double-punch test", ***Journal of the Structural Division***, Vol. 106, No. 8, (1980), 1673-1693. doi: 10.1061/JSDEAG.0005493.
20. Marti, P., "Size effect in double-punch tests on concrete cylinders", ***ACI Materials Journal***, Vol. 86, No. 6, (1989), 597-601. doi: 10.14359/2261.
21. Kim, J., Kim, D.J., Park, S.H. and Zi, G., "Investigating the flexural resistance of fiber reinforced cementitious composites under biaxial condition", ***Composite Structures***, Vol. 122, (2015), 198-208. doi: 10.1016/j.compstruct.2014.11.055.
22. Dawood E.T., Ahmed A.A. and Hassan A.M., "Production of geoploymer mortar reinforced with sustainable fibers", ***Journal of the Mechanical Behavior of Materials***, Vol. 29, No.1, (2020), 114-23. doi: 10.1515/jmbm-2020-0012.
23. Nagajothi S. and Elavenil S., "Parametric studies on the workability and compressive strength properties of geopolymer concrete", ***Journal of the Mechanical Behavior of Materials***, Vol. 27, (2018), 3-4. doi: 10.1515/jmbm-2018-0019.
24. Zhang P., Wang J., Li Q., Wan J. and Ling Y., "Mechanical and fracture properties of steel fiber-reinforced geopolymer concrete", ***Science and Engineering of Composite Materials***, Vol. 28, No. 1, (2021), 299-313. doi: 0.1515/secm-2021-0030.
25. No, I.S., "For aggregates of natural resources used for concrete and construction", Baghdad, Iraq, (1984).
26. Standard, B., "Testing hardened concrete", Compressive Strength of Test Specimens, BS EN, (2009), 12390-12393.
27. ASTM, C., "Standard test method for flexural strength of concrete (using simple beam with third-point loading)", in American society for testing and materials. Vol. 100, (2010), 19428-12959.
28. "American Concrete Institute. "State of the art report on high-strength concrete." ACI 363R-92, Farmington Hills, MI (1992).
29. MC90, C., "Comite euro-international du beton-federation international de la pre-contrainte (ceb-fip), model code 90 for concrete structures", ed: Thomas Telford, London, (1993).

Persian Abstract

چکیده

در چند دهه اخیر، بتن ژئوپلیمری تحولی در زمینه مهندسی عمران ارائه کرده است. هدف مطالعه حاضر تولید یک بتن ژئوپلیمری تقویت شده با الیاف فولادی کم هزینه با خواص کششی قابل قبول است. هدف این برنامه آزمایشی بررسی رفتار کششی بتن ژئوپلیمری تقویت شده با الیاف فولادی و ساخته شده از مواد بازیافتی است. مواد اولیه بتن ژئوپلیمری تقویت شده با الیاف فولادی در این مطالعه مواد زائد بودند. الیاف فولادی بازیافتی از لاستیک ها استخراج و به الیاف ریز با طول متوسط ۲۰ میلی متر و قطر متوسط ۰٫۷ میلی متر خرد شد. بتن ژئوپلیمری در این مطالعه شامل سنگدانه های درشت بود که بتن بازیافتی خرد شده بود. همچنین، سنگدانه ریز خرد شده شیشه زباله بود. علاوه بر مقاومت فشاری، روش‌های تست کششی مانند استحکام کششی شکافتن، مقاومت کششی دو پانچ و استحکام کششی خمشی همگی در این مطالعه بررسی شدند. الیاف فولادی بازیافتی با الیاف فولادی با انتهای قلاب‌دار جدید و الیاف فولادی هیبریدی (۵۰٪ جدید + ۵۰٪ بازیافت شده) با سه درصد حجمی مختلف الیاف فولادی (۰٫۵٪، ۱٫۰٪ و ۱٫۵٪) مقایسه شد. مخلوط بتن ژئوپلیمر الیاف فولادی جدید با ۱٫۵ درصد الیاف فولادی بالاترین نتایج آزمایش را در میان سایر مخلوط ها نشان داد، زیرا مقاومت کششی در مورد آزمایش پانچ دوبل افزایش یافته است. این رفتار را می توان به این صورت توضیح داد که الیاف فولادی جدید دارای یک شکل یکنواخت و مستقیم با انتهای قلاب شده است که باعث افزایش لنگر بین چسب خاکستر بادی و الیاف فولادی می شود. علاوه بر این، الیاف فولادی بازیافتی حاوی خرده های لاستیکی بود که می تواند دلیل دیگری باشد که بر خواص کششی بتن ژئوپلیمری تأثیر منفی می گذارد.

International Journal of Engineering

Journal Homepage: www.ije.ir

Measuring and Benchmarking the Quality Culture Maturity of Construction Companies in Indonesia

R. A. Karim*[a], Y. Latief[a], T. Y. Zagloel[b]

[a] *Department of Civil and Environmental Engineering, Faculty of Engineering, Universitas Indonesia, Depok, Indonesia*
[b] *Department of Industrial Engineering, Faculty of Engineering, Universitas Indonesia, Depok, Indonesia*

PAPER INFO

Paper history:
Received 21 April 2022
Received in revised form 21 July 2022
Accepted 23 July 2022

Keywords:
Quality Culture Maturity
Construction Companies
Benchmarking

ABSTRACT

In February 2018, Indonesian government suspended all big-scale elevated construction projects underway in Indonesia for several months to conduct a thorough investigation. The temporary suspension was triggered because of the prevalent construction accidents, most of which were due to construction failures. Previous studies stated that companies should implement a quality culture to carry out quality management properly. This study aims to measure the maturity level of the quality culture of state-owned, private, and foreign construction companies and compare them using gap analysis. In order to do so, this study has developed a measurement instrument adapted for construction companies based on previous studies, expert judgment, and input from respondents. The results showed that the maturity level of state-owned, foreign, and private construction companies in Indonesia were 64%, 70%, and 53% of the expected condition, respectively. In addition, this study observed eight priority indicators to have a significant relationship with construction failure, whose maturity level needs to be improved to reduce the construction failure rate. Those priority indicators included Inspiration & Motivation, Horizontal Alignment, Progress Monitoring, Feedback from Costumer, Staff Empowerment, Attitude to Quality Improvement, Attitude to Staff, and Training Provision.

doi: *10.5829/ije.2022.35.10a.20*

1. INTRODUCTION

In Indonesia, quality failures, either in the form of construction failures or defects that cause owner dissatisfaction, are still common in construction projects. For example, several Indonesian news websites/portals reported that from July 2017 to Oct 2019, there were more than thirty construction failure incidents on large-scale construction projects in Indonesia, as shown in Figure 1. These incidents occurred almost every month, most of which were conducted by state-owned construction companies. Due to the prevalence of these incidents, in February 2018, Indonesian government suspended all ongoing large-scale elevated construction projects for several months to conduct a thorough investigation.

From the data, it can be concluded that construction quality failures still occur in large-scale construction projects in Indonesia. Large-scale projects are carried out by large construction companies, and large construction

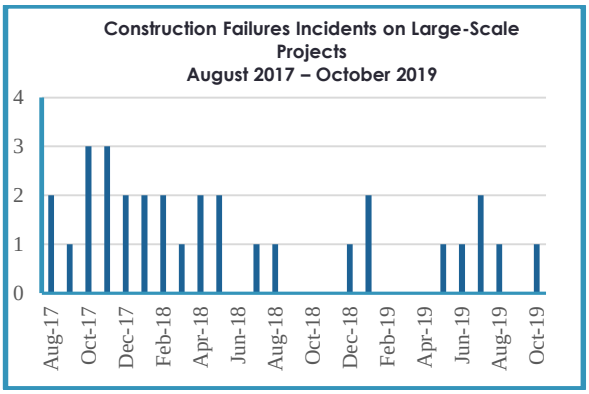

Figure 1. Construction Failures Data on Large-Scale Projects in Indonesia between August 2017 and October 2019

*Corresponding Author Email: rully.a.karim@gmail.com (R. A. Karim)

Please cite this article as: R. A. Karim, Y. Latief, T. Y. Zagloel, Measuring and Benchmarking the Quality Culture Maturity of Construction Companies in Indonesia, ***International Journal of Engineering, Transactions A: Basics***, Vol. 35 No. 10, (2022), 2027-2039

companies are required to have a quality management system certificate, which Indonesian government requires ISO 9001 certification.

It proves that having a certification of ISO 9001 does not guarantee that a construction company implements a Quality Management System (QMS) properly [1]. Based on a summary of several previous studies, although quality management implementation has been widely applied since 1980s in Japan and 1990s in the American construction industry, it has not been successful in some developing countries [2]. Construction companies complained about several implementation problems, including expensive certification costs, preventing them from establishing a quality management system [3]. Hoonakker et al. [4] stated that the most significant barrier to implementing quality management in a construction company was the culture within the company itself. Every organization that wants to implement or manage a quality program needs a cultural shift and develops an appropriate quality culture [1, 4, 5]. Because of the barriers in the quality system can be reduced if the organization can develop a strong quality culture [5].

However, Willar et al. [6] stated that it is difficult for a company to change its old habits and behavior to assimilate a new quality culture. To be able to form a new culture, the existing internal culture must be reviewed first [7]. Therefore, it is necessary to formulate an appropriate strategy to implement a quality culture in a construction company. Wilson [8] suggested that in the process of change towards a quality culture, a maturity approach is needed as a road map, a framework for developing prioritization of action, a tool for assessment, and a common language and shared vision. The quality culture maturity approach will help organizations assess their current quality culture and identify the actions needed to increase their maturity level [9].

From the results of the literature review that has been carried out, no previous research has measured the quality culture level or quality culture maturity of construction companies. Therefore, this study aims to measure the maturity level of quality culture of the three types of construction companies in Indonesia, which are state-owned, private, and foreign construction companies whose construction quality is known to be very good. In order to do that, a measurement instrument suitable for use in the construction sector must be developed first. The measurement instrument can be used to measure the condition of a quality culture within a company. It can also be used as a basis for comparing conditions between one company to another. In this study, the measurement result of the three types of construction companies was benchmarked to identify the potential improvement to formulate the appropriate strategy to implement a quality culture in state-owned construction companies, which is expected to reduce the number of construction failures.

2. LITERATURE REVIEW

2. 1. Quality Culture in Construction Company

A quality culture was defined as an enterprise environment where quality had become a personal value for all employees. As a result, everyone consistently abided by quality guidelines and felt the quality around them, not just obeying orders from above [10]. This was a condition where quality-focused actions became the behavior of every employee within the company.

Based on previous studies, Mahmood & Mohammed [5] have identified thirteen important dimensions of quality culture, which include: Top management leadership and commitment, Customer focus, Continuous improvement, Education and training, Teamwork, Employee engagement, Empowerment, Partnership with suppliers, Awards and recognition, Communication, Motivation, Organizational structure, and Strategic & quality policy. Meanwhile, according to Saha & Hardie [11], quality culture can be described as a culture that: Prioritizes leadership over supervision; Inspires staff commitment to selected quality activities; Uses the team as the primary management style; Allow the staff at all levels to participate in work-related decisions; Increase pride in work results; Eliminate fear, and; Inspire people to seek continuous improvement.

2. 2. Maturity Level of Quality Culture

The maturity level of a company is defined as a state of completion, perfection, or readiness to fulfill the work that can measure the effectiveness, skills, and competence in managing company activities and programs [12]. Several studies have examined the maturity levels of construction companies in various subjects such as risk management [13], knowledge management [12], project management [14], and process improvement [15].

For quality culture maturity, two previous studies have been obtained, but none have been conducted in construction companies. Both of them have developed a tool to measure quality culture maturity in an organization, which were in the library organization conducted by Wilson [8], and in the Aviation company conducted by Spiak [9]. Wilson formulated the Quality Maturity Model (QMM) to determine the library organization's position and prioritize actions toward achieving a quality culture [8]. Wilson observed 41 factors in describing the formation of quality culture. Those factors are grouped into eight facets, namely: “organization’s management”, “environmental sensing”, “attributes of learning organization”, “attitude to change”, “attitude to quality”, “leadership”, “investment in staff”, and, “alignment” [8]. Meanwhile, Spiak [9] has also compiled a Quality Culture Maturity Model (QCMM) for aviation companies which are grouped into five groups, namely: Foundation, Structure,

Process/Tools, Key Enablers, and Quality Values. These two studies are used as the basis for developing quality culture measurement tools in this study by adapting them to the needs of construction companies. Each of the previous studies has gaps, some of which are not for construction companies, and some are not specifically for measuring quality culture maturity. The complete comparison can be seen in Table 1.

It was first checked whether all elements of the quality culture in the construction company described by Saha & Hardie [11] and Mahmood & Mohammed [5] had been accommodated in the quality culture maturity model from Wilson [8] and Spiak [9]. The following approach was by studying the previous literature on quality maturity in construction companies and comparing it with those elements of the quality culture and Wilson and Spiak's quality culture maturity model. In their research on the project management maturity model (PMMM) in construction companies, Machado et al. [14] have compared the various existing maturity models and concluded that the best PMMMs for construction companies are OPM3 and MMGP Prado.

Both PMMM are sourced from the Project Management Body of Knowledge of PMI, but it is also stated that OPM3 is the most frequently referred to in many studies [14] and is also considered the best stand out because it is published by PMI [16]. In addition, OPM3 also divides the maturity questions based on the project management knowledges, one of which is quality management [16]. Therefore OPM3 is used as a source in this study.

A further study conducted by Permatasari et al. [16] has also compiled various sources, including 42 questions on Quality Management in OPM3, and proposed an assessment model of Contractor Quality Management. Another research that has also produced a maturity model related to construction quality is the Construction Industry Macro Maturity Model (CIM3). As the name suggests, this model is made for the macro scale of the construction industry, not the scale of a company [17]. However, several of its indicators can be categorized at the company level. This study used these maturity models as references to adapt the existing quality culture model related to its application in construction companies. The first step was to check whether the elements or indicators of these models have been included in the quality culture maturity model that Wilson and Spiak have developed. The comparative meta-analysis of these previous studies can be seen in Table 2.

TABLE 1. Gap Comparison of the Main References

References	for Quality Culture Maturity	for Construction Companies
Quality Culture Maturity Model [9]	yes	no
Quality Maturity Model [8]	yes	no
Construction Industry Maturity Model [17]	quality maturity	construction industry
Knowledge Management Maturity [12]	no	yes
Quality Management System (QMS) Maturity [18]	QMS maturity	yes
Contractor Quality Management Maturity [16]	QM maturity	yes

TABLE 2. Main References of Quality Culture Maturity Model

Variables/Indicators	Wilson	Spiak
Element of Quality Culture		
Top management leadership and commitment [5, 11]	x	x
Customer focus [5]	x	x
Continuous improvement [5]	x	x
Education and Training [5]	x	x
Teamwork [5, 11]		x
Involvement [5, 11],	x	
Empowerment [5]	x	x
Supplier partnership [5],		x
Reward and recognition [5]	x	x
Communication [5]	x	x
Motivation [5]	x	
Organization Structure [5]	x	x
Strategic and Quality Policy [5]	x	x
Inspires staff commitment [11]	x	x
Increase pride in work results [11]		x
Eliminate fear [11]		x
Quality Maturity in Construction Company		
People and Customer Management [16]	x	x
Supplier Partnership [16]		x
Communication of Improvement Information [16]	x	x
Customer Satisfaction Orientation [16]	x	x
External Interface Management [16]	x	
Strategic Quality Management [16, 17]	x	x
Team Work Structures [16]		x
Operational Quality Planning [16, 17]		x
Quality Improvement Measurement System [16]	x	x
Corporate Quality Culture [16]	x	x
Reliability [16]		x

Conformance [16]		x
Perceived Quality [16, 17]	x	
Responsiveness [16]		x
Assurance [16]		x
Report [17]		x

In addition to the elements or indicators in Table 2, there are several other indicators added from the Wilson and Spiak model themselves, namely Knowledge Management, Optimization, Documentation, Proactive/preventive, Staff encouragement to innovate [9], Consistency [8, 9], Alignment, and Attitude [8].

2. 3. Construction Failure Construction failure or also known as the defect, is a condition where the whole or part of the construction results does not comply with the required contractual specifications [19], based on the function, performance, as well as legal and user requirements, regarding the structures, services, or other facilities [20]. The construction failure rate was often indicated by the cost and amount of rework [21-23]. Therefore, this study used the Cost of Rework (Y1) and the Number of Rework (Y2) as the indicators of the Construction Failure variable.

3. RESEARCH METHODOLOGY

This research was conducted by collecting data regarding the existing condition of the quality culture maturity of three types of large construction companies in Indonesia, namely state-owned, private, and foreign construction companies, and then comparing each of them and also to the expected condition by conducting a gap analysis. The existing condition was taken from the perceptions of the respondents who are employees of the three types of companies. The expected conditions were collected from the perceptions of expert practitioners from large construction companies with at least managerial positions and more than ten years of experience. The complete flowchart of this study method is presented in Figure 2.

Of all the referred previous studies about maturity in construction companies, three of them make comparisons among the construction companies. All three studies were carried out by distributing questionnaire instruments to respondents who were employees of construction companies. Two of them only compare the companies' final maturity score/level [12, 18] but did not compare them by the indicators/elements. The other one has compared by the indicator level, but the companies being compared are individual companies in the same category, not a group of companies representing different categories [16]. One study has compared the companies by grouping them into categories, such as the core business, annual revenue, number of quality staff, number of employees, and location, but only comparing the final maturity score [18]. This study measured the quality culture maturity of construction companies grouped by a category, which is by their ownership and then compared them by their quality culture maturity indicators score. By benchmarking, the company can identify its position compared to other companies and the potential factors that can be developed [18].

The existing conditions were identified by collecting data on respondents' perceptions about the quality culture maturity level of the company they work for, using a questionnaire instrument. The questionnaire questions were derived from the quality culture maturity variables and indicators identified from the literature review and validated by external experts serving as practitioners or academicians with more than 15 years of experience in the construction industry. During content and construct validation, there were several variables and indicators proposed by the experts to be combined, and the constructs were adjusted accordingly. There is also an indicator, namely punishment added by the expert. They think that punishment is still needed in the Indonesian construction industry. The list of the variables and indicators is presented in Table 3.

After that, for each indicator, a question item was provided with five options of answers which described

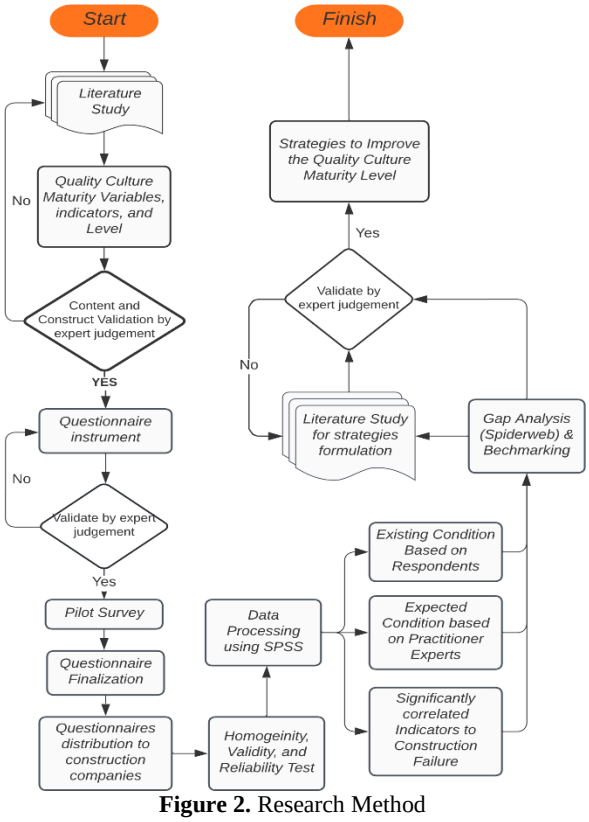

Figure 2. Research Method

TABLE 3. Research Variables

Code	Variables	Code	Indicator	Reference
X1	Leadership	X1.1	Vision and value setting	[8, 9]
		X1.2	Trust	[8, 9]
		X1.3	Inspiration & motivation	[8]
		X1.4	Decision making	[9]
		X1.5	Leadership Commitment	[9, 13]
		X1.6	Setting expectations / common language	[9, 13, 16]
X2	Management & Communication	X2.1	Knowledge Management	[9, 12]
		X2.2	Process Management	[8, 9, 13, 24]
		X2.3	Vertical alignment	[8]
		X2.4	Horizontal alignment	[8]
		X2.5	Optimization	[9]
		X2.6	Strategic plan generation	[8, 13, 16, 17]
		X2.7	Progress monitoring	[8]
		X2.8	Performance measurement	[8, 9, 16]
		X2.9	Documentation / Report	[9]
		X2.10	Communication flow	[8, 9, 13, 16]
		X2.11	Consistency	[8, 9]
		X2.12	Compliance	[9]
		X2.13	Proactive / preventive	[9]
		X2.14	Root cause analysis / corrective action	[9]
		X2.15	Staff structure	[8]
		X2.16	Feedback from Customer	[8, 16]
X3	Staff Participation & Empowerment	X3.1	Staff empowerment	[8, 9, 16]
		X3.2	Learning level	[8, 9]
		X3.3	Staff encouragement to innovate	[8, 9, 16]
		X3.4	Contribution	[8]
		X3.5	Teamwork	[9, 16]
X4	Attitude	X4.1	Attitude to risk	[8, 13]
		X4.2	Attitude to Quality	[8, 16]
		X4.3	Attitude to quality improvement	[8, 16]
		X4.4	Attitude to Change	[8]
		X4.5	Perception of drivers of change	[8]
		X4.6	Type of quality improvement initiatives	[8, 9]
		X4.7	Perception of responsibility for the quality	[8, 9, 13]
		X4.8	Attitude to mistakes	[8]
		X4.9	Fairness/justice	[9]
		X4.10	Functional excellence / capability	[9, 16]
		X4.11	Customer service	[8, 9, 16]
X5	Investment in Human Resources	X5.1	Attitude to staff	[8, 9]
		X5.2	Training provision	[8, 9, 13]
		X5.3	Development of staff	[8, 9, 16]
		X5.4	Recognition of staff	[8, 9, 16]
		X5.5	Punishment of Staff	Experts

the levels of quality culture maturity. These levels were based on several previous studies and inputs from external experts and are shown as follows [25],

- Level 1 (Ad hoc): The implementation of quality culture is still non-existent or chaotic [8].
- Level 2 (Repeatable): Quality culture implementation is already in existence, with some being continuously carried out, although it is not well-defined or structured [8].
- Level 3 (Defined): The implementation of quality culture is already well-defined but not routinely conducted [8, 26].
- Level 4 (Managed): The quality culture implementation is well-defined and already routinely executed but not regularly evaluated, or when adequately assessed, the results are not accompanied by corrective improvement [8, 12, 25].
- Level 5 (Continuous): The implementation of quality culture is well-defined, regularly implemented, evaluated, and continuously improved [8, 12].

The five answer options for each indicator were formulated based on previous studies, representing the five levels of quality culture maturity adapted to construction company operations, which the experts also validated. Examples of the answer options are shown in Table 4.

The next step is to conduct a pilot survey to 15 respondents who are also employees of large construction companies. The result stated that the questionnaire was understandable, with some editorial-related inputs. After the questionnaire was corrected according to the input from the pilot survey, the questionnaire was distributed to respondents.

TABLE 4. Example of Quality Culture Maturity Indicator and Its Levels

Maturity Level	Indicator
	X1.1. Vision and Mission Setting
Level 1 (Ad-Hoc)	Upper management has not set a vision and values.
Level 2 (Repeatable)	Upper management has defined the company's vision and values, but still difficult to understand for the employees.
Level 3 (Defined)	Upper management has clearly defined the company's vision and values and communicated them to all employees through various media, including dialogue sessions and the induction of new employees.
Level 4 (Managed)	The company's vision and values have been defined and communicated to all employees and become the basis for formulating all policies, procedures, targets, performance indicators / KPIs, and employee development plans.
Level 5 (Continuous)	Upper management has defined, communicated, and aligned the company's vision and values. All employees have implemented it, and it has become a daily behavior that is always tried to be maintained.

Respondents were asked to select the level that best describes the current condition of their company for each indicator question and also the relative influence each indicator has on construction failure. Construction failure is represented by the cost of rework and the number of reworks. To obtain the expected conditions data, the same instrument was provided to twenty-six contributing external practitioner experts to identify the required maturity level to establish a quality culture in a construction company. These practitioners were also from the large state-owned construction companies with managerial positions and above. The twenty-six experts' and respondents' answers were then compared for a gap analysis. From the gap analysis results, it can be known how far the current condition of quality culture maturity has met the expected conditions.

The results of the data collection were assessed first with Data Adequacy Test (KMO & Bartlett), Comparative Homogeneity Test (Independent T Sample & Anova), Validation Test (Product moment Pearson Correlation), and Reliability Test (Cronbach's Alpha), using the SPSS software. The results of those tests were valid and reliable data on the existing condition of quality culture maturity level in construction companies. With this data, a gap analysis was carried out between the existing and optimum/expected conditions. The gap analysis results were represented in the form of a spiderweb diagram.

4. RESULTS AND DISCUSSION

4. 1. Existing Condition Quality Culture Maturity of Construction Company A total of 214 respondents contributed to the survey. They were employees of 31 big-grade construction companies in Indonesia, of which 71 were from state-owned companies, 71 were from private companies, and 72 were from foreign companies.

The results of the Kaiser-Meyer-Olkin Measure of Sampling Adequacy test showed a result of 0.962 which means that the sample is sufficient with a significance value of <0.05, which means that there is a correlation between variables and is feasible for the next process. The results of the homogeneity test with the Kruskal Wallis H Non-Parametric Test also stated that the sample was homogeneous based on the categories of Work Experience, Education, and Position. The validity test with the Pearson Correlation test also stated that with an alpha of 5%, all question items were valid. Likewise, the Cronbach Alpha test results stated that the instrument is reliable with a value of 0.971. After the data were proven

sufficient, homogeneous, valid, and reliable, it was followed by data processing and analysis.

The data processing is conducted to determine two findings. The first is a comparison between the existing and expected conditions of quality culture maturity level based on the data obtained from respondents. The second is the relationship between the X variable (from each indicator) and the Construction Failure Variable, namely the Cost of Rework and the Number of Rework, based on the Pearson Correlation Test of the respondent data.

Regarding the expected condition, the answers obtained from the expert practitioners were dominated by Levels 4 and 5. However, the answers to level 5 were more prevalent. Since the information was based on ordinal data, the selected answer that occurred more frequently was observed in Level 5. Only one indicator was considered sufficient at Level 4, namely Attitude to Risk (X4.1). The following in Figure 3 is the gap analysis of construction companies' quality culture maturity level in Indonesia. The gap analysis showed the indicators that needed to be improved to achieve the expected condition and the comparison with the other types of companies. Suppose the condition in one type of company is better. In that case, it indicates that the indicator is improvable in other companies, and its better implementation can be used as a reference for improvement strategies.

According to the data analysis result of the state-owned construction companies, only 6 of the 43 indicators met the expected condition, with four being the Management and Communication variable indicators. The remaining indicators were below Level 5, with one only reaching Level 2, namely the X5.4. Recognition of Staff in the Investment in Human Resources variable.

Four indicators also had a gap of 2 levels from the expected condition, namely X1.5. Leaders Commitment, X1.6. Expectation Setting, X2.10. Communication Flow' X3.2. Level of Learning, and X4.1. Attitude to Risk. The remaining 32 indicators have only one gap with the expected condition.

Based on Figure 3, it was observed that there was one (and the only) quality culture maturity level indicator that was expected to be sufficient at level 4, namely X4.1. Attitude to Risk. Although, the existing condition of this indicator in the state-owned companies has not met the expected conditions, which is only at Level 3 (Defined). This means that the attitude of employees in handling risks has not been managed and evaluated regularly. In the state-owned companies, the variable with the highest level of maturity was the Organizational Attitude, accompanied by Management and Communication. On the other hand, the lowest was the Investment in Human Resources, followed by the Leadership variable. This indicated that the respondents who are construction company employees feel that the investment in employees provided by their company was still insufficient. In addition, they also feel the lack of leadership from their company leaders regarding the quality programs.

Regarding the correlation with construction failure, only seven indicators did not correlate with the Cost of Rework (Y1) and the Number of Rework (Y2) in state-owned companies. The remaining 36 indicators

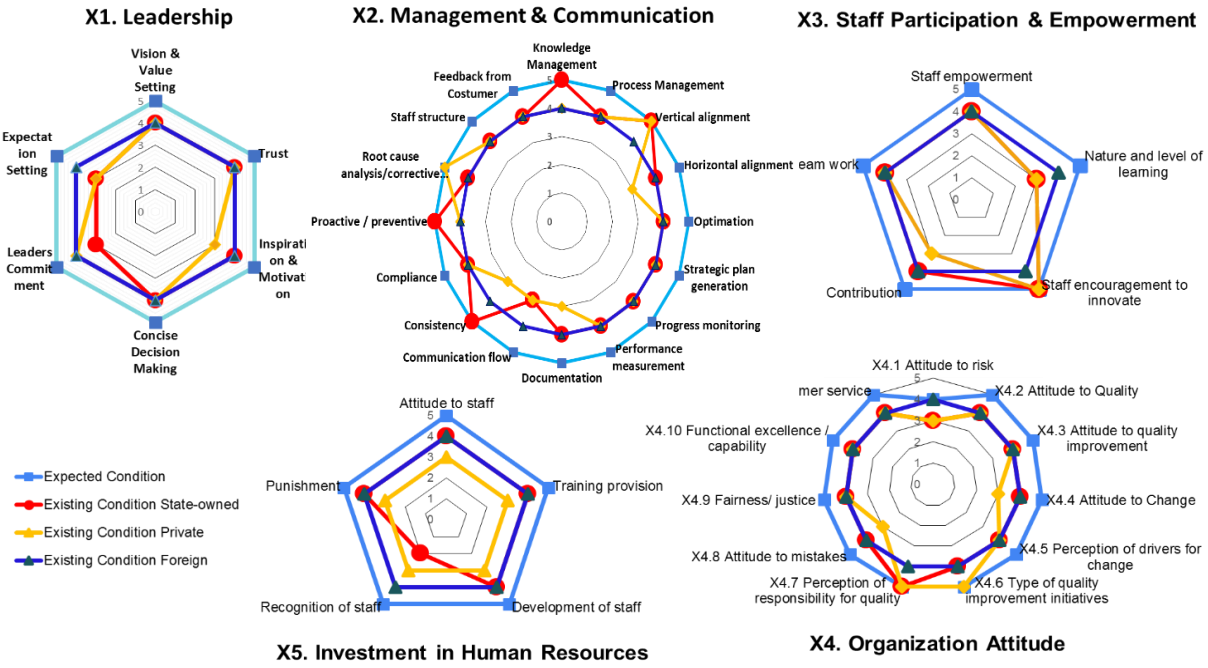

Figure 3. Gap Analysis of the Quality Culture Maturity Level of Construction Companies in Indonesia

correlated with construction failure, where 27 correlated with Y1 or Y2, and the other 9 correlated with Y1 and Y2, respectively. In this study, the indicators that have a significant correlation with the two construction failure indicators were categorized as high significance, and those that correlated only with one of them were classified as low significance. Those nine indicators that have a high significance with the construction failure are described in Table 5. Among the nine indicators that significantly affected construction failure, only one of them has reached the expected level of maturity, namely X2.3. Vertical Alignment. The other eight have one gap level with the expected condition (Level 5). This indicated that the eight high significant indicators required maturity improvement to achieve the expected conditions. The comparison of the significant indicators of the three types of construction companies is presented in Figure 4.

4. 2. Benchmarking the Quality Culture of Indonesian Construction Companies Based on the answers from the external experts, the ideal maturity conditions were found within the range of Levels 4 and 5. Suppose the respondent's response value at Levels 4 and 5 was classified as a mature condition, and the value at Levels 1 and 2 was classified as a poor condition, then the percentage of the mature condition can be calculated.

TABLE 5. The High Significance Indicators of State-Owned Construction Company

Variable		Indicator	Expect. Level	Exist. Level	G a p	Correlation	
						Y1	Y2
Leadership	X1.3.	Inspiration & Motivation	**5**	4	1	0.265*	0.305**
	X2.3.	**Vertical alignment**	**5**	5	**0**	0.319**	0.278*
Management & Communication	X2.4.	Horizontal alignment	**5**	4	1	0.304**	0.298*
	X2.7.	Progress monitoring	**5**	4	1	0.374**	0.240*
	X2.16.	Customer Feedback	**5**	4	1	0.268*	0.352**
Staff Participation & Empowerment	X3.1.	Staff empowerment	**5**	4	1	0.240*	0.370**
Organization Attitude	X4.3.	Attitude to quality improvement	**5**	4	1	0.305**	0.358**
Investment in Human Resources	X5.1.	Attitude to staff	**5**	4	1	0.325**	0.325**
	X5.2.	Training provision	**5**	4	1	0.252*	0.242*

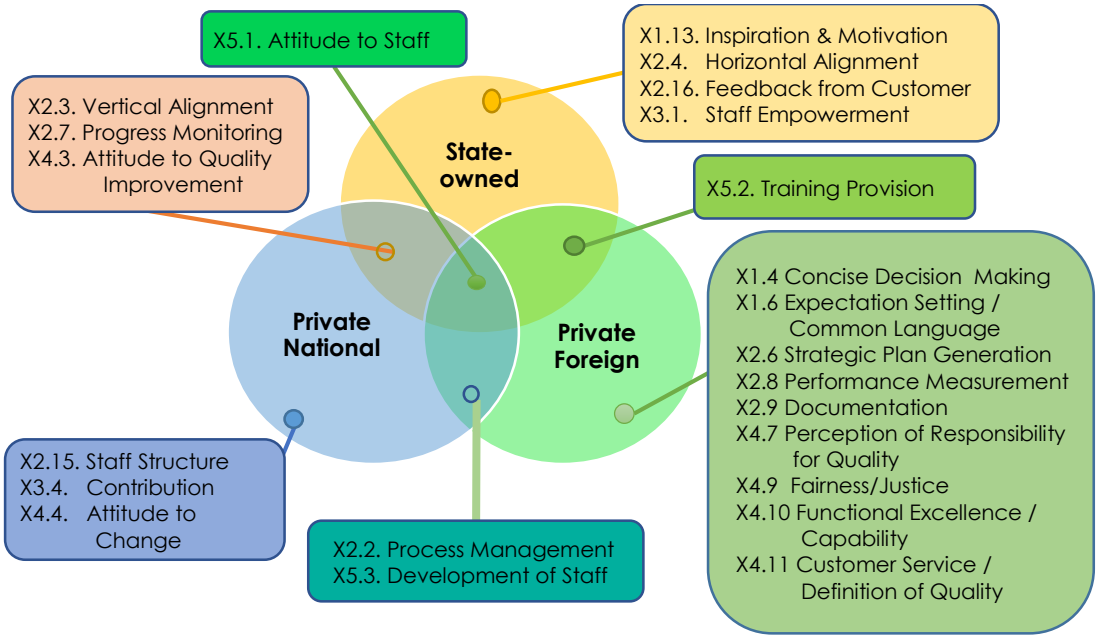

Figure 4. Priority Strategy of Quality Culture to Reduce the Construction Failure Rate

The data obtained in this study included state-owned, private, and foreign private companies. The results found in the state-owned company were juxtaposed with those obtained at two other companies, as shown in Table 6.

The data in Table 6 shows the existing maturity conditions of quality culture by assuming all indicators have the same weight. The highest and lowest were foreign and national private companies with 70% and 53% of the expected condition, respectively. While state-owned companies account for 64%, indicating that many improvements were required to develop the quality culture properly and to reduce the construction failure rate.

From the prioritized indicators in Figure 4, it can be seen that there is one same indicator that is considered significant to be improved by the three types of construction companies, namely X5.1 Attitude to Staff. It implies that this indicator is a common problem in Indonesian construction companies. Regarding the eight significant indicators of state-owned construction companies, as seen in the spider web diagram in Figure 3, it can be seen that the conditions in the other two types of companies are at the same level or lower, so they cannot be used as a reference for better implementation. However, there are several other indicators that are not considered to have an effect on construction failure, whose level is still below foreign companies and even private companies. In the state-owned companies, all the prioritized indicators are at Level 4, meaning that all the companies already have standards and procedures related to all those prioritized indicators. However, it remains the implementation that should be maintained and carried out consistently, including for their system of periodic evaluation and continuous improvement.

Furthermore, for the prioritized indicators, based on literature review and experts advise, there were recommended strategies for increasing the maturity level. State-owned construction companies were advised to view employees as the company's main asset with commitment and guarantee of employee welfare. This aimed to make employees company's assets that are committed to running the organization system [8]. Large state-owned construction companies are big organizations which had already invested in their employees, as part of government regulation or as the organization's effort. Based on the external experts' suggestion, the employees of large state-owned construction companies are likely to feel undervalued when they do not understand the additional benefits that the organization has provided or what they received is not what they expected or needed. This indicates that the companies should survey the benefits being expected by the employees to support their work and welfare. Companies should also review their employees' needs for continuous development of skills due to the rapid development of the business environment [27].

Company leaders are advised to reformulate expectations for employees, usually in the form of a Key Performance Index, that are clear and measurable. Employees should mutually agree on these KPIs and are regularly evaluated [9]. Companies should also define a complete improvement measurement system to evaluate the impact of each improvement activity [28]. Also, to define a collaborative strategy orientation for the improvement program to be integrated across all company elements [9], because one of the main problems encountered in continuous improvement was the lack of a comprehensive company-wide planned strategy [28]. The external experts also suggested that companies evaluate the coordination system between work units/departments, using the internal customer's concept to improve the management qualities continuously. This should subsequently be carried out to conduct a 360-degree performance appraisal by collecting feedback from employees' subordinates, colleagues, supervisors, and self-evaluation by themselves.

The company should also establish a customer feedback system that should have at least seven components [29], such as service indicators, performance targets and standards, feedback collection tools and process management, and reporting and IT systems. Additionally, the company should campaign the importance of customer complaint information to improve the organization's image, disseminate procedures for reporting customer complaints,

TABLE 6. Benchmarking of Quality Culture Maturity in Constructions Company

Variable	State-Own Company			Private Company			Foreign Company		
	Poor	**Medium**	**Mature**	**Poor**	**Medium**	**Mature**	**Poor**	**Medium**	**Mature**
X1. Leadership	12%	29%	59%	16%	32%	52%	11%	25%	64%
X2. Management & Communication	11%	21%	68%	10%	31%	58%	5%	21%	74%
X3. Staff Participation & Empowerment	9%	26%	64%	11%	35%	54%	6%	26%	68%
X4. Organization Attitude	11%	20%	69%	12%	31%	57%	7%	17%	76%
X5. Investment in Human Resources	19%	24%	57%	16%	41%	44%	12%	19%	69%
Quality Culture Maturity Level Existing Condition	**12%**	**24%**	**64%**	**13%**	**34%**	**53%**	**8%**	**22%**	**70%**

implement an incentive system for reporting customer problems, and non-usage of customer complaints to evaluate the personal performance of certain employees [30].

For staff empowerment, companies are advised to facilitate employees to share learning, information, and knowledge [9]. They should also provide opportunities for employees to propose suggestions at open meetings and implement a reward and punishment system. The measurement, assessment, and adjustment of the quality improvement plan based on employees' inputs are very important, as well as communicating the performance results and impacts to all involved individuals [9]. Company leaders should provide the employees with an understanding of the limits of the decision-making authority and that they can always return to their direct leaders if they do not want to or worry that they have crossed their authority limits. This gives employees the opportunity and trust to contribute to decision-making and, simultaneously, acknowledge the direct leaders about their power over their subordinates [31]. Company leaders should always provide recognition and appreciation to excellent employees for them to feel valued by the organization. This fosters pride and confidence in job performances, increases the sense of belonging to the company, as well as creates enthusiasm and motivation for quality improvement [8, 9, 32, 33].

The problems with employee attitudes towards quality improvement are often caused by the changes in work patterns, which occur due to the quality improvement programs, such as document congestion, difficulties in measuring job results, and unsupportive subcontractors [34]. This indicates that employees need to understand the importance of quality improvement programs, which should be preceded explicitly by the role of top management, and to be involved in quality improvement programs to establish good communication, relationships, and motivation [34].

Several studies also stated that one of the methods of changing the attitude of employees was by conducting training and workshops on the importance of quality improvement programs [8, 9, 32, 35]. The company should conduct regular training that should be aimed at the staff and leaders' levels, such as motivational training to inspire employees, including those in the management position. The leaders should be provided with adequate training related to the knowledge of company quality management, as well as motivational and inspirational skills [36]. The training should not only be related to the technical areas of work but also related to the methods of dealing with customers in obtaining feedback and maintaining expectations [29, 30]. According to the involved experts, an effective training program should be developed based on employee management plans. It should also be appropriately structured with working hours, such as 60% and 40% for job progress and training, respectively.

The experts in this study also suggested the need to implement a reward and punishment system to spur employees towards implementing quality improvement programs. Subsequently, they also recommended the need to launch a company rebranding campaign if necessary. A rebranding campaign can increase the employees' and customers' awareness of the proclaimed organizational quality culture [36].

5. CONCLUSION

This research has developed a tool to assess the maturity level of the quality culture of construction companies. By conducting an assessment and gap analysis, it can be identified which indicators still need to be improved in maturity to reduce the failure rate of construction. After that, benchmarking can also be carried out by measuring the quality culture maturity condition of other types of construction companies and using it to identify the potential improvement and as a lesson if they had better conditions. By identifying which indicators need to be improved, studying how to improve them, and seeing examples of better implementation in other companies, the formulation of a quality culture improvement plan in an organization will be more focused and directed. In this paper, the indicators discussed for improvement are only those related to construction failure, while this tool can be used for other purposes related to quality performance.

This research is only limited to the case study of construction companies in Indonesia. Therefore, further research should be developed for larger data samples. The limitation of this research is to analyze the gap between the existing and the expected conditions on the maturity level of quality culture in construction companies in Indonesia. Further research is suggested to develop more technical strategies or systems to increase the maturity level of the quality culture to reduce construction failures in Indonesia.

6. ACKNOWLEDGMENT

The author would like to thank the financial support provided by the University of Indonesia through PUTI Doctor of the Fiscal Year 2020 with the contract number: NKB-698 / UN2.RST / HKP.05.00 / 2020 managed by the Directorate of Research and Community Engagement (DRPM) Universitas Indonesia.

7. AUTHORS' NOTE

The authors declare that there is no conflict of interest regarding the publication of this article, and also confirmed that the article is free of plagiarism.

8. REFERENCES

1. Willar, D., "Improving quality management system implementation in indonesian construction companies", Queensland University of Technology, (2012),
2. Jraisat, L., Jreisat, L. and Hattar, C., "Quality in construction management: An exploratory study", ***International Journal of Quality & Reliability Management***, Vol. 33, No. 7, (2016), 920-941. doi.
3. Tang, S., Ahmed, S.M., Aoieong, R.T. and Poon, S., "Construction quality management, Hong Kong University Press, Vol. 1, (2005).
4. Hoonakker, P., Carayon, P. and Loushine, T., "Barriers and benefits of quality management in the construction industry: An empirical study", ***Total Quality Management***, Vol. 21, No. 9, (2010), 953-969. doi: 10.1080/14783363.2010.487673.
5. Mahmood, W.Y.W. and Mohammed, A.H., "A conceptual framework for the development of quality culture in the construction industry", in Assoc. Res. Constr. Manag. ARCOM 2008-Proc. 24th Annu. Conf. Vol. 1, (2008), 247-256.
6. Willar, D., Coffey, V. and Trigunarsyah, B., "Examining the implementation of iso 9001 in indonesian construction companies", ***The TQM Journal***, Vol. 27, No. 1, (2015), 94-107. doi: 10.1108/TQM-08-2012-0060.
7. Willar, D., Trigunarsyah, B. and Coffey, V., "Organisational culture and quality management system implementation in indonesian construction companies", ***Engineering, Construction and Architectural Management***, (2016). doi: 10.1108/ECAM-02-2015-0026.
8. Wilson, F., "The quality maturity model: Your roadmap to a culture of quality", ***Library Management***, Vol. 36, No. 3, (2015), 258-267. doi: 10.1108/LM-09-2014-0102.
9. Spiak, M., "Quality culture maturity model: Theoretical development", Faculty of the National Graduate School & University of Quality Systems Management, (2012).
10. Srinivasan, A. and Kurey, B., "Creating a culture of quality", ***Harvard Business Review***, Vol. 92, No. 4, (2014), 23-25. doi: 10.1891/9780826129673.0012.
11. Saha, S. and Hardie, M., "Culture of quality and the australian construction industry", Proceedings IGLC-13, (2005).
12. Wibowo, M.A. and Waluyo, R., "Knowledge management maturity in construction companies", ***Procedia Engineering***, Vol. 125, (2015), 89-94. doi: 10.1016/j.proeng.2015.11.014.
13. Zhao, X., Hwang, B.-G. and Low, S.P., "Developing fuzzy enterprise risk management maturity model for construction firms", ***Journal of Construction Engineering and Management***, Vol. 139, No. 9, (2013), 1179-1189. doi: 10.1061/(asce)co.1943-7862.0000712.
14. Machado, F., Duarte, N., Amaral, A. and Barros, T., "Project management maturity models for construction firms", ***Journal of Risk and Financial Management***, Vol. 14, No. 12, (2021), 571. doi. https:// doi.org/10.3390/jrfm14120571
15. Finnemore, M., Sarshar, M., Aouad, G., Barrett, P., Minnikin, J. and Shelley, C., *Standardised process improvement for construction enterprises (spice)*. 2002, Citeseer.
16. Permatasari, F.L., Adi, T.J.W. and Wiguna, I.P.A., "Assessment model of contractor quality management maturity", ***IPTEK Journal of Proceedings Series***, Vol. 3, No. 6, (2017).
17. Willis, C.J. and Rankin, J.H., "The construction industry macro maturity model (cim3): Theoretical underpinnings", ***International Journal of Productivity and Performance Management***, Vol. 61, No. 4, (2012), 382-402. doi: 10.1108/17410401211212652.
18. Smith, J., Carrey, B., Fuller, P. and Dudley, N., "Benchmarking the maturity of quality management system in western australia", (2018). doi: 10.32738/CEPPM.201509.0014.
19. "Indonesia government, government regulation of the republic of indonesia number 29 year 2000 concerning provision of construction services. ", (2000).
20. Forcada, N., Macarulla, M., Gangolells, M. and Casals, M., "Assessment of construction defects in residential buildings in spain", ***Building Research & Information***, Vol. 42, No. 5, (2014), 629-640. doi: 10.1080/09613218.2014.922266.
21. Josephson, P.-E. and Hammarlund, Y., "The causes and costs of defects in construction: A study of seven building projects", ***Automation in Construction***, Vol. 8, No. 6, (1999), 681-687.
22. Love, P.E., Irani, Z. and Edwards, D.J., "A rework reduction model for construction projects", ***IEEE Transactions on Engineering Management***, Vol. 51, No. 4, (2004), 426-440.
23. Love, P.E., Teo, P. and Morrison, J., "Revisiting quality failure costs in construction", ***Journal of Construction Engineering and Management***, Vol. 144, No. 2, (2018), 05017020. doi: 10.1061/(ASCE)CO.1943-7862.0001427.
24. Andersen, E.S. and Jessen, S.A., "Project maturity in organisations", ***International Journal of Project Management***, Vol. 21, No. 6, (2003), 457-461. doi: 10.1016/S0263-7863(02)00088-1.
25. Pratama, F.H., Andhika, R. and Latief, Y., "The framework of quality culture maturity in indonesian construction company to reduce the construction failure rate", in IOP Conference Series: Earth and Environmental Science, IOP Publishing. Vol. 794, (2021), 012027.
26. Dadashi Haji, M., Taghaddos, H., Sebt, M., Chokan, F. and Zavari, M., "The effects of bim maturity level on the 4d simulation performance: An empirical study", ***International Journal of Engineering***, ***Transactions C: Aspects,*** Vol. 34, No. 3, (2021), 606-614. doi: 10.5829/ije.2021.34.03c.03.
27. Lee, C.H. and Bruvold, N.T., "Creating value for employees: Investment in employee development", ***The International Journal of Human Resource Management***, Vol. 14, No. 6, (2003), 981-1000. doi: 10.1080/0958519032000106173.
28. Jurburg, D., Viles, E., Jaca, C. and Tanco, M., "Why are companies still struggling to reach higher continuous improvement maturity levels? Empirical evidence from high performance companies", ***The TQM Journal***, (2015). doi: 10.1108/TQM-11-2013-0123.
29. Wirtz, J. and Tomlin, M., "Institutionalising customer-driven learning through fully integrated customer feedback systems", ***Managing Service Quality: An International Journal***, (2000). doi: 10.1108/09604520010341654.
30. Wirtz, J., Tambyah, S.K. and Mattila, A.S., "Organizational learning from customer feedback received by service employees: A social capital perspective", ***Journal of Service Management***, (2010). doi: 10.1108/09564231011050814.
31. Greasley, K., Bryman, A., Dainty, A., Price, A., Soetanto, R. and King, N., "Employee perceptions of empowerment", ***Employee Relations***, (2005). doi: 10.1108/01425450510605697.
32. Holt, G.D., Love, P.E. and Nesan, L.J., "Employee empowerment in construction: An implementation model for process improvement", ***Team Performance Management: An International Journal***, (2000). doi: 10.1108/13527590010343007.
33. Godfrey, T., "The relationship between perceived organisational support and turnover intentions in a developing country: The mediating role of organisational commitment", ***African Journal of Business Management***, Vol. 4, No. 6, (2010), 942-952. doi.
34. Haupt, T.C. and Whiteman, D.E., "Inhibiting factors of implementing total quality management on construction sites",

The TQM Magazine, Vol. 16, No. 3, (2004), 166-173. doi: 10.1108/09544780410532891.

35. Field, L., "Training and learning in small business. Issues for research, ERIC, (1997).

36. Gao, Z., Ye, J. and Huang, Y., "Study on the construction of enterprise quality culture for brand strategy", ***iBusiness***, Vol. 4, No. 3, (2012), 260-264. doi: 10.4236/ib.2012.43033.

9. Appendix-Questionnaire sample

	Variable	Sub Variable		Question & Multiple Answer Choices	Choose one of the conditions that best describes your company
2	**Management & Communication**	7	Progress monitoring	13	**How does the company monitor progress towards achieving company goals?**	
				a	*The progress towards achieving company goals is never monitored.*	
				b	*The progress of achieving company goals has been monitored, but not done routinely and programmed.*	
				c	*There is already a program/system for monitoring the progress of achieving company goals, but the monitoring results have never been followed up.*	
				d	*There is already a progress monitoring program in the achievement of company goals, and corrective actions are in place if needed.*	
				e	*Progress in achieving company goals is closely monitored by a monitoring system, and corrective actions are taken and documented if needed. This monitoring program is evaluated regularly and improved.*	
		8	Performance measurement	14	**How is the performance measurement process in your company?**	
				a	*Don't know/no performance measurement.*	
				b	*Performance measurement uses only mathematical measures like volume per day, percentage of weight, etc.*	
				c	*Performance measurement uses mathematical measures and client feedback.*	
				d	*The performance of several processes is measured using performance indicators based on the expectations of the client, while several others have used KPI as a reference.*	
				e	*All performance measurements have used KPI references which are prepared based on the company's strategic objectives which are evaluated and improved regularly.*	

	Variable	Sub Variable		Question & Multiple Answer Choices	Choose one of the conditions that best describes your company
5	**Investment in Human Resources**	3	Development of staff	41	**Do you feel that the company supports the self-development of its employees?**	
				a	*There is no Employee development program.*	
				b	*Employees are supported to develop themselves.*	
				c	*There are already skills development programs prepared by the company for employees in certain sections and levels.*	
				d	*Employees are supported in developing their skills, there is already a skill development program prepared by the company for all employees.*	
				e	*All Employees are encouraged to develop their careers and talents. The company already has a clear development path. Employee development is evaluated to determine the cadre of future company leaders.*	

4	Recognition of staff	42	**Did you get a reward or recognition for your best work?**
		a	*No, not even getting any attention.*
		b	*Some get rewards, some don't, depending on their respective managers.*
		c	*Yes, there is a company commitment to employee recognition, although not in a clear specific system.*
		d	*Yes, there are systems, structures and processes for employee recognition and/or rewards and/or development.*
		e	*Yes, employees feel valued for recognition and/or rewards and/or development systems, structures and processes that are clearly and consistently implemented and developed.*

Persian Abstract

چکیده

در فوریه ۲۰۱۸، دولت اندونزی تمام پروژه های ساخت و ساز در مقیاس بزرگ را که در اندونزی در دست اجرا بود، به مدت چند ماه به حالت تعلیق درآورد تا تحقیقات کاملی را انجام دهد. تعلیق موقت به دلیل حوادث ساخت‌وساز رایج که بیشتر آن‌ها به دلیل خرابی‌های ساخت‌وساز بود، آغاز شد. مطالعات قبلی بیان می‌کردند که شرکت‌ها باید فرهنگ کیفیت را پیاده‌سازی کنند تا مدیریت کیفیت را به درستی انجام دهند. این مطالعه با هدف سنجش میزان بلوغ فرهنگ کیفیت شرکت‌های ساختمانی دولتی، خصوصی و خارجی و مقایسه آنها با استفاده از تحلیل شکاف انجام شده است. برای انجام این کار، این مطالعه یک ابزار اندازه گیری را برای شرکت های ساختمانی بر اساس مطالعات قبلی، قضاوت کارشناسان و ورودی پاسخ دهندگان ایجاد کرده است. نتایج نشان داد که سطح سررسید شرکت‌های ساختمانی دولتی، خارجی و خصوصی در اندونزی به ترتیب ٦٤، ۷۰ و ۵۳ درصد شرایط مورد انتظار است. علاوه بر این، این مطالعه هشت شاخص اولویت دار را مشاهده کرد که رابطه معنی داری با شکست ساخت و ساز دارند که سطح بلوغ آنها برای کاهش نرخ شکست ساخت و ساز نیاز به بهبود دارد. این شاخص های اولویت شامل الهام و انگیزه، تراز افقی، نظارت بر پیشرفت، بازخورد از مشتری، توانمندسازی کارکنان، نگرش به بهبود کیفیت، نگرش به کارکنان، و ارائه آموزش بودند.

International Journal of Engineering

Journal Homepage: www.ije.ir

New Framework Based on a Multi-criteria Decision-making Model of Technology Transfer in the Auto-battery Manufacturing Industry under Uncertainty

A. H. Latifian[a], R. Tavakkoli-Moghaddam*[b], M. A. Keramati[a]

[a] *Department of Technology Management, Central Tehran Branch, Islamic Azad University, Tehran, Iran*
[b] *School of Industrial Engineering, College of Engineering, University of Tehran, Tehran, Iran*

PAPER INFO

Paper history:
Received: 16 April 2022
Received in revised form: 30 June 2022
Accepted: 04 July 2022

Keywords:
Technology Transfer
Automotive Battery Industry
World-class Manufacturing
Bi-objective Mathematical Model
Multi-criteria Decision-making Method
Epsilon-constraint Method

ABSTRACT

This research builds a decision-based optimization model to evaluate and decide on the methods of technology transfer in the auto-battery industry under uncertainty. This research is conducted based on the needs of the country's battery industry and shows the impact of technology transfer on world-class manufacturing. At first, the effective indices in the assessment of a technology transfer method are singled out through reviewing the literature and the experts' judgment. The sample population in this research consists of experts from eight auto-battery manufacturing companies. Then, each of the approved indices is assessed via the best-worst method, and in continuation, the technology transfer methods are evaluated and prioritized using an MOORA method as multi-criteria decision-making under uncertainty. The gray theory is also used to deal with uncertainty. According to the results obtained from the best-worst method, the five significant indices (i.e., improving style management, business strategy, cost-effectiveness, how to communicate with the organization, and competitiveness) are considered to select the technology transfer methods in the auto-battery production industry. Finally, to implement the proposed framework in the state auto-battery manufacturing industries, a dual-purpose mathematical model is introduced for optimized world-class technology transfer methods. To solve the proposed model, the developed ε-constraint method is used. Finally, based on the results of the proposed method, the transfer method of joint investment is recognized as the most suitable technique for technology transfer in this industry.

***doi**: 10.5829/ije.2022.35.10a.21*

NOMENCLATURE

P_i	Cost of implementing the *i*-th method in manufacture *j*	L_{ij}	Reliability of the *i*-th method for implementation in manufacture *j*
W_{ij}	Weight of implementing the *i*-th method in manufacture *j*	D_j	Number of authorized methods that manufacturer *j* can choose
x_{ij}	Random numbers between 0 and 1		

1. INTRODUCTION

Globalization along with the development of technology has had a great impact on national competitiveness, improvements influence organizational strategies, tactics, and operative decisions. The applications of technology transfer and commercialization are vital issues in a highly competitive global market [1]. Due to the very low rate of technology products in developing countries, they are forced to import technology from pioneer countries to achieve the development and improvement of their products [2]. Technology management leads to everyday competition between companies, which results in increasing prices and complicating products and services [3, 4]. Global changes and processes mainly lead to the development and invention of new technologies and more than 50% new products and their processes have an important theoretical and practical background under the title of technology transfer.

Recent studies emphasize the importance of international research and development to increase domestic productivity as one of the global factors of increasing technology transfer between countries,

*Corresponding Author's Email: tavakoli@ut.ac.ir (R. Tavakkoli-Moghaddam)

Please cite this article as: A. H. Latifian, R. Tavakkoli-Moghaddam, M. A. Keramati, New Framework Based on a Multi-criteria Decision-making Model of Technology Transfer in the Auto-battery Manufacturing Industry under Uncertainty, ***International Journal of Engineering, Transactions A: Basics***, Vol. 35 No. 10, (2022), 2040-2055

especially among developed countries that help each other to develop. Today, only a handful of countries are independent in terms of technological needs, even the United States, which has long been at the forefront of technology development, is in many ways dependent on international resources. But developing countries are more dependent on external resources and technical know-how than other developed countries [5]. On the other hand, long-term prediction of technology and economic development is very important for Asian developing countries (e.g., Iran, Pakistan, and India) [6]. Technology transfer is a process that takes place to achieve the progress of companies or countries in various fields (e.g., competitiveness and financial profit) [7, 8]. It is about transferring technology from one place to another, for example, from one organization to another or from one country to another [9].

Technological pressure (through research) or market pull (through industry) leads to this transfer. The international scope of technology commercialization may include developed countries, developing countries, and other countries with economic transition [10].

The demand for batteries continues to grow worldwide, with the market for (rechargeable) batteries was 62 billion dollars in 2014[2] and reached 90 billion dollars in 2020 and by 2030, it is projected to increase to $150 billion[3]. Of this revenue in 2020, $35.5 billion came from automative battery sales[4], and as per a recent study by Global Market Insights INC, the global market for starter batteries is expected to exceed $47 billion by 2025.

Therefore, the purpose of this study is to present three-step mathematical modeling to evaluate and select transfer of technology methods in the automotive battery industry. It is based on multi-criteria decision-making (MCDM) techniques under conditions of information uncertainty. First, the best-worst method (BWM) is used to determine the optimal weight of the factors affecting technology transfer. Then a gray MOORA rating method is used to rank technology transfer methods, which are identified as the most important methods for managers. Then a multi-objective mathematical scheduling model is presented to select optimal methods aiming for world-class manufacturing. Finally, due to the multi-objective nature of the proposed model, the augmented ε-constraint method is used to solve the mathematical model. The following detailed objectives will be mainly considered in this research:

- Designing an optimal decision-based approach for technology transfer in the automotive battery industry under uncertain criteria.
- Identifying the factors affecting the evaluation of technology transfer methods
- Identifying appropriate technology transfer methods in the automotive battery industry, with a view to costs minimizing and maximizing reliability.

At the end of the first section (i.e., introduction), the structure of the research is divided as follows: the second section reviews the research literature, the third section describes the research method, the fourth section presents the research case study, and also the framework of proposed criteria, the fifth section discusses the computational results, the sixth part at the end presents a general conclusion and some suggestions for future researches.

2. LITERATURE REVIEW

In this section, the theoretical basis, research background, and research gaps are studied.

2. 1. World Class Manufacturing In the dynamic and complex environment 21st-century environment, organizations, businesses, and industries compete internationally, and global production is a vital element of success in competing around the world [11]. As a result, a country's production & manufacturing capacity at a globally-competitive level as well as achieving high GDP growth rates are essential components of national identity and pride.

The world-class manufacturing (WCM) process focuses on deploying the following objectives:

- Gradual increase of quality and efficiency in industrial processes.
- Eliminating waste and losses.
- Improvement in data/information.
- Effective/efficient utilization of time resources.
- Increasing flexibility
- Development of customer service [12].

WCM refers to techniques/technologies enabling companies/businesses to correlate their performance with their leading competitors [13]. It creates a new paradigm consistent with rapidly-evolving customer requirements. Due to market changes (production diversity, quantity, etc.), by providing new and specific solutions, WCM possesses the ability to direct, guide, and organize businesses towards excellence with optimal flexibility [11].

One of the most significant requisite tools for accomplishing WCM accesses to the most up-to-date and advanced technologies in the world, providing the basis for producing products according to customer needs, highest quality achievable, cost-effectiveness, minimum waiting times, maximum flexibility, and optimal after-sales service. However, because access to new technologies is a time-consuming and costly process,

[2] https://www.grandview reserch .com/industry-analysis/battery-market/segmentation

[3] https://www.eurobat.org/

[4] https://batteryinnovation.org/

many countries use the technology transfer process.

2. 2. Technology Transfer Technology transfer is a method in which governmental research institutes transfer the technologies they have developed to private companies and try to stimulate and improve the commercialization of technology transfer. The main purpose of this method is to increase public awareness of such technologies to strengthen industrial and technological competition, which in turn leads to increased competitiveness at the national level [1]. This concept originates from the management of innovation and research and development and has become more prominent with the introduction of technology transfer between developed and developing countries and the design of its legal and contractual dimensions [14]. For an efficient and effective Technology transfer into the country, it is necessary to use appropriate routes and methods to the internal conditions of the country and the industry to achieve a competitive advantage in the market and industry. Advanced technologies of developed countries are essential for the industrialization of developing countries. Many of the countries that are now developed have benefited greatly from advanced imported technologies [15].

2. 3. Literature Review There are few empirical studies in the field of technology transfer and innovative performance in developing countries [1, 7]. Given that Iran is a developing country, technology transfer is a hot topic among domestic researchers, and various types of research have been done in this field, each of which has looked at the issue from one perspective. This section mentions some of the domestic and foreign research conducted in recent years.

Din Mohammadi and Shafiei [16] used a hybrid multi-criteria decision-making model based on Analytic Hierarchy Process (AHP) and TOPSIS method to rank the technology transfer factors in the wind turbine industry. This model is used to determine the most appropriate wind turbine transmission strategy from four options including reverse engineering, technical skills training, key contracts, and technology license for Iran's renewable energy sector. The results are compared with the outputs of classical decision-making models.

Arabzadeh [17] studied how organizations have maintained their growth through the use of technology transfer factors. In his study, some of the most important oil industry companies were evaluated using the fuzzy analytic hierarchy process (FAHP) and fuzzy TOPSIS (FTOPSIS). The results of both methods show that the oil pipeline and the telecommunication company are more important than the National Gas Company and the Petroleum Products Distribution Company. Also, the results of the FAHP technique show that the technological aspects of the oil industry are more prominent than its organizational, personnel, and industrial aspects. Lee et al. [1] studied the technology transfer of IT equipment and introduced a comprehensive framework for factors affecting the timely completion of technology transfer between suppliers and buyers according to technology transfer agreements. They used the Analytic Hierarchy Process (AHP) method to determine the factors affecting the timely completion of technology transfer.

Distanont et al. [18] investigated the factors affecting the technology transfer performance in the Thai petrochemical industry using exploratory factor analysis (EFA) and structural equation modeling (SEM). Research findings show important factors affecting the technology transfer performance are: 1) absorption capacity, 2) characteristics of partners, 3) complexity of technology and 4) inter-organizational relationships. Kraujalienė [19] studied appropriate tools for evaluating the efficiency of the technology transfer process in higher education institutions using TOPSIS, COPRAS, Multi-MOORA, and DEA methods. The results approved FARE to identify critical factors for the technology transfer process and their weights. Lavoie and Daim [20] introduced a methodology to evaluate an organization's technology transfer capabilities. Their proposed approach is a combination of practical research in the first stage. They used an analytic hierarchy process (AHP) method in the second stage, and instead of focusing on a single technology, project, or program, concentrates on the evaluation of the organization as a whole, i.e. this model provides an insight into the extent to which the organization is ready for successful technology transfer from the research phase to the operational phase.

Amini et al. [21] studied the factors affecting technology transfer at the University of Tehran. They used Analytic Hierarchy Process (AHP) to rank and evaluate the factors. Political, economic, and environmental conditions were identified as the most important factors in technology transfer. Amir-Ghodsi et al. [22] presented a new integrated method based on the Shannon-projection attribute function (PAF) using gray interval numbers, to analyze technology transfer methods in the construction industry. The results showed that reverse engineering and import of capital goods and machinery are the best methods of technology transfer, respectively. Naeeni Bonyadi et al. [23], in a study to select the best provider, best technology, and best transfer method, used the gray DEMATEL and the Best-Worst methods to determine the weights of the criteria, and the gray network analysis method to determine the priority of the options.

Nouri et al. [24] examined the impact of technology transfer on employment. Among the methods examined in this study, unity and joint ventures on ineffective employment and the effect of integration and acquisition methods, foreign direct investment, franchises, operating licenses, multinational enterprises, research and

development, and reproducing enterprises on positive employment have been identified. In the second phase, the TOPSIS method was used to rank the technology transfer methods according to the criterion of impact on the employment of ordinary and skilled workers. Accordingly, the franchise method was identified as the most suitable method for creating employment among unskilled workers, and the research and development, foreign direct investment, and reproducing enterprise methods were identified as the most suitable method for creating employment among skilled workers. Iroegbu et al. [25] investigated the challenges affecting technology transfer between the two sides by creating a platform through which reliable solutions can be generated. Using the case study analysis and the Fuzzy AHP approach, several problems are identified in this study, including management and strategic issues, marketing concerns, technical issues, environmental difficulties, and regulatory concerns.

Durak et al. [26] identified the criteria that the companies in the technoparks in Istanbul take into consideration in their technopark preferences and then select the most appropriate technopark based on these criteria. The criteria used in the study are proposed for the first time for the selection of technoparks by authors. The sample studied is also used for the first time for the technopark selection. For this purpose, the current data obtained from the managers of the companies in the technoparks in Istanbul are used. In the application part, AHP and TOPSIS are used separately in the selection of the most appropriate facility location for the companies in Istanbul Technoparks. The result of the study shows that the most suitable facility location was the ITU by two different MCDM methods.

Mohammadi et al. [27] identified and prioritized the critical success factors in technology transfer projects by using an integrated approach based on the fuzzy Delphi method and the Additive Ratio Assessment (ARAS) method. The results show that experience in technology transfer in the transferee company, the existence of experienced technology transfer managers, sufficient organizational infrastructure, and documenting project problems, achievements, and experiences are four critical success factors of the technology transfer projects.

Ravi and Janodia [10] attempted to answer the research question of whether current dynamics within Indian universities create an environment for enabling knowledge transfer/commercialization and propose plausible suggestions to enable academia-industry technology transfer. They have tried to cover three key aspects: (1) the awareness and practice of patents and research commercialization among Indian academia, (2) comprehending strategies adapted to commercialize research activities, and (3) barriers in a university-industry technology transfer.

Dahooie et al. [28] considered selecting the most appropriate method of television technology acquirement for Irancell MTN Telecommunication Company using a combinational model consisting of MCDM methods. In the first phase of structuring the model, they defined the list of criteria and options based on a literature review. Then, in the evaluation phase, they used the fuzzy Delphi technique to finalize the list of criteria and options, and then they used a fuzzy group hierarchical best-worst method to determine the weights of the criteria and evaluate the options. Finally, in the ranking phase, the options were ranked using fuzzy multiple attribute decision-making (F-MADM) methods including ARAS-F, fuzzy TOPSIS, fuzzy WASPAS, fuzzy VIKOR, fuzzy MABAC, and fuzzy SAW. Then, the integer linear program (ILP) model was used to summarize the ranking. Based on the results, the main criteria in terms of importance are technological factors, environmental and market factors, organizational factors, and partner or vendor factors. The most important sub-criteria can also be considered in order: the rate of innovation in the industry, the degree of the strategic importance of technology, the need for access to technology, and the ability to divide assets. The final ranking results showed that turnkey contracts, stock ownership, and outsourcing are the top three options in order of priority.

Marznaki et al. [29] presented a study that delved into the dynamism of the variables impacting technology transfer capacities by following a system dynamics approach, examining similar studies, and interviewing experts in the downstream petrochemical industries in the polymer pipe and fittings domain. Then, causal loop diagrams are delineated and the causal relationships among variables are examined, and the VENSIM software is used for analyzing the causal loops.

2. 4. Research Gap Currently, 22 companies are operating in Iran that produce automotive batteries, of which 8 companies produce batteries and the rest are assemblers. The actual capacity of these companies in automotive battery production is about 15 million units and is increasing to about 18 million units. Considering the traffic volume of about 22 million vehicles in the country and the annual increase of about one million units and taking into account the average life of each battery of about 20 months, we need about 12 million batteries annually. In addition to all the above factors (the presence of excess capacity in relation to the country's needs), seasonal sales of batteries, the impossibility of battery maintenance, and factors (e.g., sanctions), the only way for companies to stay in the market is to switch to world-class manufacturing.

One of the most important tools for companies to globalize is the process of technology transfer, which can not only produce new products but also provide higher quality and lower prices to enter competitive markets (at home and abroad) and lead to:

– Improvement of the standard of living in developing countries, restructuring their industries, creating jobs,

and improving their economies;

- Laying the foundation for eliminating the technological gap with the developed countries and reaching sustainable development by improving the level of technology in a country.

As can be seen in the literature review, the world-class manufacturing and technology transfer issue is one of the most important scientific challenges in Iran. Therefore, in this study, we intend to provide a new framework based on the best-worst, gray MOORA (G-MOORA) and Multi-Objective Optimization (MOO) to explore and select technology transfer methods in the automotive battery industry aiming to enter global markets.

3. FRAMEWORK OF THE PROPOSED APPROACH

In this section, the basic definitions related to the proposed decision-making approach are summarized. A mixed-integer bi-objective programming model is also being formulated. Based on these main concepts, a new approach consisting of fuzzy MCDM and mathematical optimization is proposed.

3. 1. Best-Worst Method The BWM is one of the powerful methods in solving MCDM problems used to obtain the weights of selected options and criteria [28, 30]. This method compensates the weaknesses of methods for based on couple comparison (e.g., AHP and ANP) and incompatibility. Also, it significantly decreases the number of couple comparisons, just by doing reference comparisons. In recent years, researchers in various fields used the BWM to define weights and rank options [31-33]. Generally, the BWM consists of the following steps:

Step 1: Establishing a decision benchmark system: The decision benchmark system composes of a set of criteria identified by assessing the comments and views of experts and calculated by $\{c_1,c_2,\ldots,c_n\}$. The values of the decision criteria can reflect the performance of various alternatives.

Step 2: Determining the best/worst from the primary criteria as well as the sub-criteria: Consistent with the decision criteria system, the best/worst criteria should be identified by the decision-makers. The best criterion is designated by the symbol c_B and the worst criterion is denominated by the symbol w_B.

Step 3: Conducting reference comparisons for the best criterion: In this step, the best criterion is prioritized over other criteria by using numbers between 1 and 9. The results of this vector are shown as follows:

$$A_B=(a_{B1},a_{B2}, \ldots, a_{Bn}) \quad (1)$$

where the a_{Bj} denotes the priority of the best-selected criterion of B over each j criterion. It is clear/obvious that $a_{BB}=1$

Step 4: Performing reference comparisons for the worst criteria: Similarly, via utilizing numbers between 1&9, the priority of all criteria over the worst selected criterion is calculated. The findings of this vector are demonstrated as follows:

$$A_w=(a_{1W},a_{2W}, \ldots, a_{nW})^T \quad (2)$$

where a_{jW} denotes the priority of each j criterion over the worst selected W criterion. It is clear/obvious that $a_{WW}=1$.

Step 5: Determining the optimal eights $(W_1,W_2,\ldots,W_n)$. In this step, to achieve the optimal weights of the criteria, the maximum absolute difference $\{|w_B-a_{Bj}w_j|, |w_j-a_{jW}w_W|\}$ for all j must be minimized. It is formulated as the below-mentioned optimization problem.

$$\min \max_j \{|w_B-a_{Bj}w_j|, |w_j-a_{jW}w_W|\} \min \xi^L$$
$$\sum_j w_j=1 \quad (3)$$
$$w_j\geq 0, \text{ for all } j$$

Problem (3) can be converted to the following model:

$$\min \xi^L$$
$$\text{s.t.}$$
$$|w_B-a_{Bj}w_j|\leq \xi^L, \text{ for all } j$$
$$|w_j-a_{jW}w_W|\leq \xi^L, \text{ for all } j \quad (4)$$
$$\sum_j w_j=1$$
$$w_j\geq 0, \text{ for all } j$$

A 4-line model and the panswer is unique. Therefore, by solving this model, optimal weights $(w_1,w_2,\ldots,w_n)$, and quantities ξ^{L*} are obtained. Regarding the above model, the close to zero values of ξ^{L*} reveal a high level of compatibility [34].

3. 2. Gray MOORA Method A gray system theory is one of the most effective methods used to solve indeterminate problems in terms of discrete and incomplete information. As compared to other MADM methods, the MOORA method is very easy, simple, and comprehendible to use in any decision-making environment. These methods require less computing time because they require a minimum number of mathematical steps as well as being useful to the decision-makers who have less command in mathematics. For this reason, the MOORA method is very robust for different decision-making problems [36]. In general, a gray system theory is an algorithm that can analyze the uncertain relationships of members of a system with a reference member and also can be used in multi-criteria groups [35].

A gray number ($\otimes G$) is displayed as an $\otimes G=\left[\underline{a}, \overline{a}\right]$ an interval, in such a manner where a & a of real numbers are members of the (R) group, and possess the ability to have unlimited values.

If $\otimes G_1=\left[\underline{a_1}, \overline{a_1}\right]$ & $\otimes G_2=\left[\underline{a_2}, \overline{a_2}\right]$

are two gray numbers, henceforth the lgebraic calculations on $\otimes G_1$ & $\otimes G_2$ can be displayed as follows [37]:

$$\otimes G_1+\otimes G_2=\left[\underline{a_1}+\underline{a_2}, \overline{a_1}+\overline{a_2}\right] \quad (5)$$

$$-\otimes G_2=\left[-\overline{a_2}, -\underline{a_2}\right] \quad (6)$$

$$\otimes G_1-\otimes G_2=\otimes G_1+\left(-\otimes G_2\right)=\left[\underline{a_1}-\overline{a_2}, \overline{a_1}-\underline{a_2}\right] \quad (7)$$

$$\otimes G_1\times\otimes G_2=\begin{bmatrix}\min\left(\underline{a_1a_2}, \underline{a_1}\overline{a_2}, \overline{a_1}\underline{a_2}, \overline{a_1a_2}\right),\\ \max\left(\underline{a_1a_2}, \underline{a_1}\overline{a_2}, \overline{a_1}\underline{a_2}, \overline{a_1a_2}\right)\end{bmatrix} \quad (8)$$

$$\otimes G_2^{-1}=\left[\frac{1}{\overline{a_2}}, \frac{1}{\underline{a_2}}\right] \quad (9)$$

$$\otimes G_1\div\otimes G_2=\left[\underline{a_1}, \overline{a_1}\right]\times\left[\frac{1}{\overline{a_2}}, \frac{1}{\underline{a_2}}\right]=\left[\min\left(\frac{\overline{a_1}}{\overline{a_2}}, \frac{\overline{a_1}}{\underline{a_2}}, \frac{\underline{a_1}}{\overline{a_2}}, \frac{\underline{a_1}}{\underline{a_2}}\right), \max\left(\frac{\overline{a_1}}{\overline{a_2}}, \frac{\overline{a_1}}{\underline{a_2}}, \frac{\underline{a_1}}{\overline{a_2}}, \frac{\underline{a_1}}{\underline{a_2}}\right)\right] \quad (10)$$

$$k.\otimes G=\left[k\underline{a}, k\overline{a}\right],\ k>0 \quad (11)$$

The MOORA method is one of the multi-criteria decision-making methods developed by Brauers and Zavadskas [38]. In 2010, they made this method more stable and added the full multiplication form to it [39].

The MOORA method consists of two parts: the ratio system and the reference point approach to evaluate the options. In this study, gray numbers are integrated into the MOORA method and Table 1 is used as a Verbal scale evaluation of options based on the G-MOORA method.

Step 1: Forming the initial gray decision matrix X according to Equation (12) by using the verbal scale listed in Table 1.

$$X=\begin{bmatrix}[x_{11},u_{11}] & [x_{12},u_{12}] & \cdots & [x_{1n},u_{1n}]\\ [x_{21},u_{21}] & [x_{22},u_{22}] & \cdots & [x_{2n},u_{2n}]\\ \vdots & \vdots & \ddots & \vdots\\ [x_{m1},u_{m1}] & [x_{m2},u_{m2}] & \cdots & [x_{mn},u_{mn}]\end{bmatrix}; \quad (12)$$

i=1, …, m; j=1, …, n

So that m represents the total number of options and n is equal to the total number of criteria. Each element $[x_{ij}, u_{ij}]$ of X that is consisted of two components x_{ij} as the lower limit and u_{mn} as the upper limit, indicates the importance of the ith option to the jth criterion.

TABLE 1. Verbal scale evaluation of options based on the G-MOORA method

Verbal expressions	Gray numbers
Very poor (VP)	[0, 1]
Poor (P)	[1, 3]
Medium poor (MP)	[3, 4]
Fair (F)	[4, 5]
Medium important (MI)	[5, 6]
Important (I)	[6, 9]
Very important (VI)	[9, 10]

Step 2: Obtaining the normal gray decision matrix $\bar{X}$ according to Equation (13). The elements of the matrix X are converted to scaleless numbers in the range of zero and one, using Equations (14) and (15).

$$\bar{X}=\begin{bmatrix}[\bar{x}_{11},\bar{u}_{11}] & [\bar{x}_{12},\bar{u}_{12}] & \cdots & [\bar{x}_{1n},\bar{u}_{1n}]\\ [\bar{x}_{21},\bar{u}_{21}] & [\bar{x}_{22},\bar{u}_{22}] & \cdots & [\bar{x}_{2n},\bar{u}_{2n}]\\ \vdots & \vdots & \ddots & \vdots\\ [\bar{x}_{m1},\bar{u}_{m1}] & [\bar{x}_{m2},\bar{u}_{m2}] & \cdots & [\bar{x}_{mn},\bar{u}_{mn}]\end{bmatrix}; \quad (13)$$

i=1, …, m; j=1, …, n

$$[\bar{x}]_{m\times n}=\frac{2x_{ij}}{\left(\sum_{i=1}^{m}x_{ij}+\sum_{i=1}^{m}u_{ij}\right)} \quad (14)$$

$$[\bar{u}]_{m\times n}=\frac{2u_{ij}}{\left(\sum_{i=1}^{m}x_{ij}+\sum_{i=1}^{m}u_{ij}\right)} \quad (15)$$

Step 3: Calculating the weighted normal gray decision matrix $\hat{X}$ according to Equation (16). The weights obtained by the best-worst method are multiplied by each element of the normal gray decision matrix $\bar{X}$ according to Equations (17) and (18). So, the weighted normal gray decision matrix results as follows:

$$\hat{X}=\begin{bmatrix}[\hat{x}_{11},\hat{u}_{11}] & [\hat{x}_{12},\hat{u}_{12}] & \cdots & [\hat{x}_{1n},\hat{u}_{1n}]\\ [\hat{x}_{21},\hat{u}_{21}] & [\hat{x}_{22},\hat{u}_{22}] & \cdots & [\hat{x}_{2n},\hat{u}_{2n}]\\ \vdots & \vdots & \ddots & \vdots\\ [\hat{x}_{m1},\hat{u}_{m1}] & [\hat{x}_{m2},\hat{u}_{m2}] & \cdots & [\hat{x}_{mn},\hat{u}_{mn}]\end{bmatrix}; \quad (16)$$

i=1, …, m; j=1, …, n

$$\hat{x}_{ij}=\bar{x}_{ij}\times w_j \quad (17)$$

$$\hat{u}_{ij}=\bar{u}_{ij}\times w_j \quad (18)$$

where w_j is the defuzzied weight of the jth criterion through the best-worst method.

Step 4: Calculating the normalized performance values by subtraction of the cost criteria (when the desired value of criteria is the maximum value) from the utility criteria (when the desired value of criteria is the minimum) as

stated in Equation (19).

$$\hat{y}_i = \sum_{j=1}^{g} \hat{v}_{ij} - \sum_{j=g+1}^{n} \hat{v}_{ij} \quad (19)$$

where $\sum_{j=1}^{g} \hat{v}_{ij}$ is the sum of the total ascending criteria for (1,…,g) and $\sum_{j=g+1}^{n} \hat{v}_{ij}$ is the sum of the total descending criteria for (g+1,…,n). g is the number of utility criteria and n-g is the number of cost criteria.

Step 5: Attaining the best non-gray performance (BNGP) of the $\hat{y}_i$ characteristic by:

$$BNGP_i(\hat{y}_i) = \frac{\hat{x}_{ij} + \hat{u}_{ij}}{2} \quad (20)$$

Finally, the options are ranked according to the value of $\mathrm{BNGP_i}(\hat{y}_i)$, so that the option with a high value of $\mathrm{BNGP_i}(\hat{y}_i)$ is optimal and ranks first.

3. 3. Proposed Mathematical Model In this section, a two-objective mathematical model is proposed to allocate technology transfer methods considering cost and reliability objectives. Generally, implementing any of these methods is costly for the company. Therefore, only a part of them can be executed due to budget constraints. Reducing costs and increasing reliability are two of the main goals of this problem. As with other mathematical models, modeling the problem requires some hypotheses. The assumptions of this study are as follows:

- The number of technology transfer methods is specified and limited.
- The number of battery manufacturers is specified and limited.
- The cost of implementation and the degree of reliability of each method and the total budget for the methods are different and specific amounts.
- The order of implementation of methods is not desired.
- Several methods can be chosen for each manufacturer.
- The values of model parameters are definite.

Each method of the model has an importance coefficient which is a specific number between zero and one and is resulted in the gray MOORA method.

Indices:

$i=\{1, ..., m\}$ i technology transfer methods

$j=\{1, ..., n\}$ j battery producer

3. 3. 1. Mathematical Model

$$\min Z_1 = \sum_{i=1}^{m} \sum_{j=1}^{n} W_{ij} x_{ij} \quad (21)$$

$$\max Z_2 = \sum_{i=1}^{m} \sum_{j=1}^{n} P_i L_{ij} x_{ij} \quad (22)$$

s.t.

$$\sum_{i=1}^{n} x_{ij} \le D_j \quad \forall j \quad (23)$$

$$\sum_{i=1}^{n} x_{ij} \ge 1 \quad \forall j \quad (24)$$

$$x_{ij} \in \{0,1\} \quad \forall i,j \quad (25)$$

The proposed model has two objectives under uncertain conditions (elucidated hereinafter). Objective function (21) minimizes the costs of implementing technology transfer methods. Objective function (22) maximizes the reliability of implementing technology transfer methods in manufacturing plants. The model also has three constraints. Constraint (23) guarantees that the number of methods assigned to each manufacturer does not exceed the limit. Constraint (24) ensures that at least one method is assigned to each manufacturer. Finally, Constraint (25) also determines the type of variables used in the problem.

3. 3. 2. Epsilon-constraint Method In multi-objective programming, evaluated problems are concerned with mathematical optimization involving more than one objective function, in which the objectives need to be optimized simultaneously or sequentially. In particular, in the literature, the Pareto or efficient frontier function has been used to illustrate the trade-offs among conflicts between multiple objectives. Various techniques concerning exact and heuristic procedures have been proposed to analyze the trade-offs among these conflicting objectives, one of which is ε-constraint programming. The advantages of ε-constraint programming include being able to obtain exact Pareto solutions, instead of approximated solutions, using a series of single-objective subproblems, in which all but one objective is transformed into constraints [40]. The formula of the ε-constraint method is as follows, wherein the first objective is introduced as the primary objective.

$$\min f_1(X) \quad (26)$$

$$x \in X \quad (27)$$

$$f_2(X) \le \varepsilon_2 \quad \vdots \quad f_n(X) \le \varepsilon_n \quad (28)$$

In the proposed query of this study, the initial objective is considered the primary objective, and other objectives are viewed as secondary objectives. Hence, according to the ε-constraint method, the new formula of the proposed model culminates in the following optimization problem.

$$\min \mathrm{Obj}_1 \quad (29)$$

$$\mathrm{Obj}_2 \ge \varepsilon_2 \quad (30)$$

Equation (9) represents the main objective function of the problem, and Equation (10) adds to the problem's set of constraints

4. CASE STUDY

Today, the battery industry has become one of the most important industries in the world, and one of the reasons is the use of portable electrical devices. On the other hand, the growth of the automotive industry has led to the growth of battery manufacturing. The studied population of this research consists of experts of battery companies, named 1. Saba Battery, 2. Borna Battery, 3. Pasarghad Battery, 4. Dorna Battery, 5. Sepahan Battery, 6. Azar Battery, 7. Niru Gostaran Khorasan Battery, and Vaya Battery. There are many indicators and criteria for evaluating technology transfer methods. The classification presented in this research has put together the indicators that were conceptually closer to the problem. This can help managers to have a more coherent view of the effective indicators while choosing the appropriate collaboration method. To this end, in this step, a list of relevant criteria for evaluating technology transfer methods is identified according to a review and revision of previous research and face-to-face interviews with experts, which is presented in Figure 1.

Technology transfer methods are defined as a set of activities in which the technology required by the applicant is provided for him, in exchange for the supplier's satisfaction. Technology transfer methods vary depending on the type of technology and transfer conditions and in some cases are very diverse. The transfer methods evaluated in this study are described in Table 2.

5. RESULTS

In this section, the results of using the proposed.

5. 1. Defining the Weights of Criteria: Best-Worst Method In this section, the relative importance of the criteria presented in Figure 1 was obtained using the best-worst method. After defining criteria and sub-criteria, a committee of experts compared criteria and sub-criteria through numbers between 1 to 9.

The best and worst criteria for evaluating technology transfer methods were selected from all the main criteria, through a collective and mutual agreement. Accordingly, managerial factors and technical factors were selected as the best and the worst criteria, respectively. Then, the experts prioritized the best criterion over other criteria (BO) and also the priority of other criteria over the worst criterion (OW).

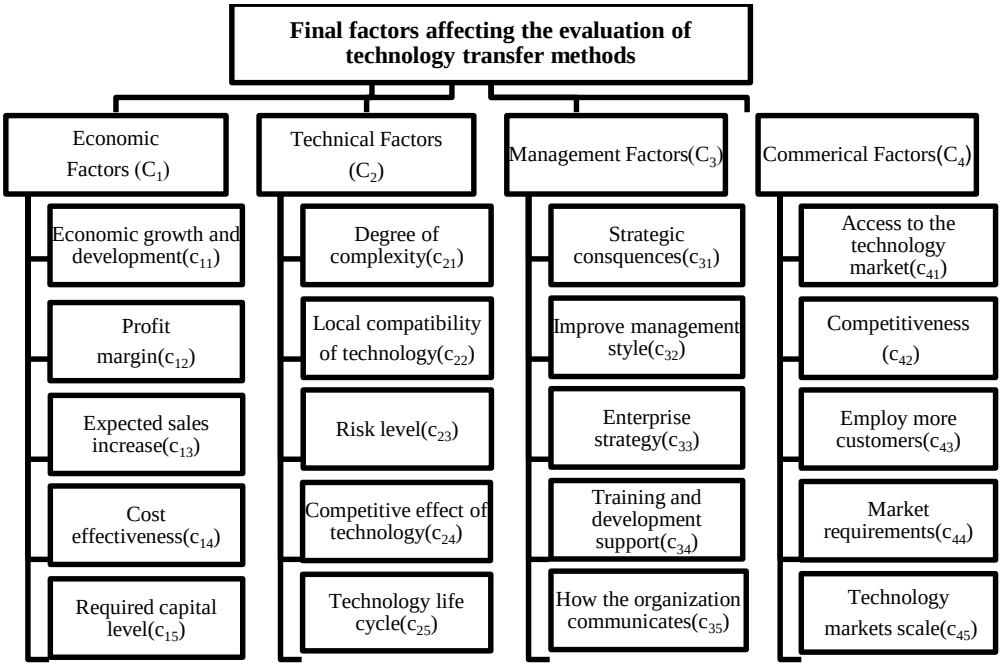

Figure 1. Factors influencing in evaluate the of technology methods in the automotive battery industry

Hence the vectors of best-other criteria and other criteria-worst obtained are presented in Table 3.

After obtaining the priorities of the main criteria, the relative weights were obtained using Model (4), which is presented in Table 4. According to the following table, the comparisons are very consistent because its value is 0.036 which is close to zero.

Similarly, pairwise comparisons of the sub-criteria of the main criteria are presented. Finally, the final weights of criteria affecting the evaluation of technology transfer methods in battery companies are presented in Table 5. As can be seen from the results, the criteria of management style improvement, the business strategy, cost-effectiveness, how to communicate with the organization, and competitiveness are the five primary criteria affecting the evaluation of technology transfer methods in battery companies.

5. 2. Evaluation of Technology Transfer Methods: Gray MOORA Method

After obtaining optimal weights of criteria, in the next step, the technology transfer methods are evaluated using the proposed gray MOORA method. All the experts were asked individually to evaluate the options based on criteria, using a verbal scale presented in Table 1. After obtaining the priority level of each expert, in the next step, the average of the degrees is calculated and the average gray decision matrix is obtained according to Table 6.

TABLE 2. Methods of technology transferrin auto-battery manufacturing industry

Technology Transfer Methods	Row
Buy royalties (A1)	1
Education and training (A2)	2
Foreign Direct Investment (A3)	3
Reverse Engineering (A4)	4
Recruitment and exchange of manpower (A5)	5
Franchise Method (A6)	6
Licensing (A7)	7
Joint R&D(A8)	8
External supply (A9)	9
Joint Venture(A10)	10

TABLE 3. Paired comparison between principal components

BO	Economic Factors (C1)	Technical Factors (C2)	Management Factors (C3)	Commercial Factors (C4)
Management Factors (C3)	2	8	1	4
OW			**Technical Factors (C2)**	
Economic Factors(C1)			3	
Technical Factors(C2)			1	
Management Factors(C3)			8	
Commercial Factors(C4)			2	

TABLE 4. Relative weight of the main dimension in evaluating technology transfer methods

Criterion	Relative normalized weight	ξ^{L^*}
Economic Factors (C1)	0.250	0.036
Technical Factors (C2)	0.071	
Management Factors(C3)	0.536	
Commercial Factors(C4)	0.143	

TABLE 5. Final weight of effective indicators in evaluating technology transfer methods

Final weight	Relative weight	Sub-criteria	Criterion
0.051	0.204	Economic growth and development (c11)	Economic factors (0.250)
0.042	0.166	Profit margin (c12)	
0.031	0.125	Expected sales increase (c13)	
0.113	0.453	Cost effectiveness (c14)	
0.013	0.053	Required capital level (c15)	
0.016	0.219	Degree of complexity (c21)	Technical factors (0.071)
0.012	0.164	Local compatibility of technology (c22)	
0.031	0.438	Risk level (c23)	
0.004	0.055	Competitive effect of technology (c24)	
0.009	0.123	Technology life cycle (c25)	
0.056	0.105	Strategic consequences (c31)	Management factors (0.536)
0.254	0.474	Improve management style (c32)	
0.113	0.211	Enterprise strategy (c33)	
0.028	0.053	Training and development support (c34)	
0.085	0.158	How the organization communicates (c35)	
0.016	0.111	Access to the technology market (c41)	Commercial factors (0.143)
0.032	0.222	Employ more customers (c43)	
0.008	0.056	Technology markets scale (c45)	

TABLE 6. Initial decision matrix gray option-criterion

	C11	C12	C13	C14	C15	C21	C22	C23	C24	C25
A1	[3.21, 6.7]	[3.5, 4.83]	[4.42, 5.92]	[2.75, 4.25]	[4.17, 5.83]	[3.67, 5.25]	[2.92, 4.42]	[2.5, 3.83]	[4.25, 5.83]	[3.67, 5]
A2	[4.83, 7.24]	[3.75, 5.25]	[3.17, 4.75]	[1.92, 3.33]	[3.08, 4.67]	[3.58, 4.75]	[4.17, 5.5]	[4.25, 5.83]	[4.75, 6]	[4.58, 6]
A3	[4.2, 7.61]	[3.92, 5.25]	[3.83, 5.33]	[4.67, 6.25]	[2.92, 4.17]	[4, 5.17]	[4.08, 5.33]	[2.58, 3.83]	[2.25, 3.92]	[4.58, 5.75]
A4	[3.71, 5.9]	[4.33, 5.83]	[3, 4.33]	[2.58, 4]	[4.08, 5.08]	[3.25, 4.58]	[2.83, 4.17]	[3.33, 4.75]	[2.75, 4.08]	[3.5, 4.83]
A5	[3.9, 7.27]	[4.33, 5.92]	[3.17, 4.33]	[4, 5.17]	[4.92, 6.67]	[4.17, 5.58]	[4.67, 6.08]	[2.75, 4.33]	[2.83, 4.25]	[3.17, 4.67]
A6	[4.18, 5.78]	[6.67, 8]	[4.08, 5.67]	[4.42, 6.17]	[4.17, 5.58]	[4.17, 5.83]	[4, 5.17]	[4.83, 6]	[3.33, 4.67]	[3.83, 5.33]
A7	[2.76, 5.68]	[4.17, 5.83]	[3.17, 4.67]	[3.92, 5.25]	[4.17, 5.33]	[4.42, 5.58]	[4.67, 6.25]	[5, 6.25]	[4.17, 5.25]	[3.42, 4.58]
A8	[3.66, 6.56]	[5.33, 6.5]	[3.5, 5.17]	[3.42, 5.08]	[4, 5.58]	[4, 5.33]	[3.83, 5.5]	[5.08, 6.75]	[4, 5.67]	[3.58, 4.92]
A9	[3.05, 7.05]	[4.33, 5.75]	[3.75, 5.08]	[6, 7]	[5.33, 6.5]	[4, 5.58]	[4.83, 6.42]	[3.25, 4.75]	[4.08, 5.83]	[3.83, 5.17]
A10	[3.86, 6.39]	[4.44, 6.86]	[3.05, 6.59]	[4.44, 5.6]	[4.55, 7.47]	[3.98, 5.6]	[4.34, 7.16]	[4.49, 5.93]	[4.09, 6.06]	[4.39, 7.56]
	C31	**C32**	**C33**	**C34**	**C35**	**C41**	**C42**	**C43**	**C44**	**C45**
A1	[3.5, 4.92]	[3.83, 5.33]	[3.67, 5.33]	[4.58, 6.33]	[5.17, 6.42]	[3.58, 4.92]	[2.33, 3.58]	[4.42, 5.83]	[3.33, 4.67]	[4.5, 5.83]
A2	[4.25, 5.5]	[4.08, 5.67]	[2.75, 4.33]	[3.75, 4.92]	[3, 4.25]	[4, 5.42]	[2.75, 4.25]	[3.67, 5.17]	[4.42, 5.75]	[5, 6.67]
A3	[3.58, 5.25]	[3.83, 5.08]	[4.5, 6.08]	[4.08, 5.42]	[4, 5.5]	[4.58, 6.17]	[4.67, 6.17]	[2.75, 4]	[4.25, 5.58]	[4.75, 6.5]
A4	[4.5, 6]	[4.33, 5.58]	[3.17, 4.33]	[4.08, 5.67]	[3.42, 4.67]	[5.25, 6.67]	[2.33, 3.5]	[3.75, 5.33]	[5.67, 6.83]	[5.5, 7.25]
A5	[4, 5.17]	[3.92, 5.33]	[3.92, 5.5]	[4.58, 6]	[3.75, 5.25]	[4, 5.17]	[3.33, 4.75]	[4, 5.08]	[3.25, 4.83]	[3.33, 4.75]
A6	[3.75, 5.25]	[4.5, 6.42]	[4.25, 5.58]	[4.33, 5.75]	[4.17, 6]	[4.58, 6.25]	[3.75, 5.25]	[3.75, 5.25]	[2.67, 4.25]	[3.33, 4.5]
A7	[4.92, 6.42]	[3.42, 4.58]	[4.25, 5.5]	[4.33, 6]	[2.42, 4]	[3.5, 5.08]	[5.25, 6.83]	[3.83, 5]	[4.17, 5.5]	[4.83, 5.92]
A8	[3.83, 5.17]	[3.25, 4.92]	[5.5, 6.5]	[4.42, 5.83]	[5.58, 6.92]	[4.67, 6.08]	[3.83, 5.5]	[3.33, 5]	[2.58, 3.67]	[2.33, 3.67]
A9	[4.42, 5.58]	[3.75, 5]	[4.58, 5.92]	[5.17, 6.83]	[3.42, 4.92]	[4, 5.5]	[3.75, 5.08]	[4.08, 5.33]	[3.17, 4.67]	[5.42, 7.25]
A10	[3.75, 6.9]	[3.93, 7.3]	[4.36, 5.8]	[3.86, 7.21]	[4.43, 7.08]	[3.7, 7.56]	[3.66, 5.97]	[3.63, 5.54]	[4.11, 6.26]	[3.64, 6.39]

To ensure consistency of the evaluation criteria, the initial gray decision matrix should be converted to a comparable scale. Hence the normal gray decision matrix is obtained using Equations (13) – (15) as shown in Table 7.

Then, the weights of each criterion are multiplied in the normalized gray decision matrix based on Equations (16) - (18), and the weighted gray matrix is created as shown in Table 8.

Finally, the normalized performance values are obtained by subtracting the cost criteria from the utility criteria, and also the best non-gray performance (i.e., the characteristic $BNGP_i(\hat{y}_i)$) is calculated (using Equations (12) (19) and (20), respectively), as shown in Table 9.

Studied input parameters are shown in Tables 10-12. Generally, the input Information used in the mathematical model can be divided into these three sections:

- Information such as the prioritization of appropriate methods of technology transfer in the automotive battery industry, which was reviewed and specified in the first part of the article;
- Information such as the cost of implementing different methods of technology transfer in companies (Table 10) and the number of methods allowed for allocation to manufacturers (Table 12). This part was collected from automotive battery companies that have generally carried out the technology transfer process in recent years; and
- Information such as the reliability of the implementation of each method of technology transfer in the companies obtained by creating a questionnaire and asking for expert opinions (Table 11).

5. 3. Optimal Allocation of Methods: Solve The Mathematical Model In this section, a set of technology transfer methods is assigned to each manufacturer by solving a mathematical programming model. It should be noted that the set of manufacturers consists of 1. Saba Battery, 2. Borna Battery, 3. Pasarghad Battery, 4. Dorna Battery, 5. Sepahan Battery, 6. Azar Battery, 7. Niru Gostaran Khorasan Battery, and Vaya Battery. To solve the proposed mathematical model, the ε-constraint method is used in the GAMS software environment version 24.3 and CPLEX solver. In the following, the results of how the technology transfer methods are assigned to each manufacturer after solving the problem are reported.

TABLE 7. Normal gray decision matrix option-criteria

	C11	C12	C13	C14	C15	C21	C22	C23	C24	C25
A1	[0.06, 0.13]	[0.07, 0.09]	[0.1, 0.14]	[0.06, 0.09]	[0.08, 0.12]	[0.08, 0.11]	[0.06, 0.09]	[0.06, 0.08]	[0.1, 0.13]	[0.08, 0.11]
A2	[0.09, 0.14]	[0.07, 0.1]	[0.07, 0.11]	[0.04, 0.07]	[0.06, 0.1]	[0.08, 0.1]	[0.09, 0.11]	[0.09, 0.13]	[0.11, 0.14]	[0.1, 0.13]
A3	[0.08, 0.15]	[0.07, 0.1]	[0.09, 0.12]	[0.1, 0.14]	[0.06, 0.08]	[0.09, 0.11]	[0.08, 0.11]	[0.06, 0.08]	[0.05, 0.09]	[0.1, 0.12]
A4	[0.07, 0.11]	[0.08, 0.11]	[0.07, 0.1]	[0.06, 0.09]	[0.08, 0.1]	[0.07, 0.1]	[0.06, 0.09]	[0.07, 0.11]	[0.06, 0.09]	[0.08, 0.1]
A5	[0.08, 0.14]	[0.08, 0.11]	[0.07, 0.1]	[0.09, 0.11]	[0.1, 0.14]	[0.09, 0.12]	[0.1, 0.13]	[0.06, 0.1]	[0.06, 0.1]	[0.07, 0.1]
A6	[0.08, 0.11]	[0.13, 0.15]	[0.09, 0.13]	[0.1, 0.14]	[0.08, 0.11]	[0.09, 0.13]	[0.08, 0.11]	[0.11, 0.13]	[0.08, 0.11]	[0.08, 0.12]
A7	[0.05, 0.11]	[0.08, 0.11]	[0.07, 0.11]	[0.09, 0.12]	[0.08, 0.11]	[0.1, 0.12]	[0.1, 0.13]	[0.11, 0.14]	[0.09, 0.12]	[0.07, 0.1]
A8	[0.07, 0.13]	[0.1, 0.12]	[0.08, 0.12]	[0.08, 0.11]	[0.08, 0.11]	[0.09, 0.12]	[0.08, 0.11]	[0.11, 0.15]	[0.09, 0.13]	[0.08, 0.11]
A9	[0.06, 0.14]	[0.08, 0.11]	[0.09, 0.12]	[0.13, 0.16]	[0.11, 0.13]	[0.09, 0.12]	[0.1, 0.13]	[0.07, 0.11]	[0.09, 0.13]	[0.08, 0.11]
A10	[0.07, 0.12]	[0.08, 0.13]	[0.07, 0.15]	[0.1, 0.12]	[0.09, 0.15]	[0.09, 0.12]	[0.09, 0.15]	[0.1, 0.13]	[0.09, 0.14]	[0.1, 0.16]
	C31	**C32**	**C33**	**C34**	**C35**	**C41**	**C42**	**C43**	**C44**	**C45**
A1	[0.07, 0.1]	[0.08, 0.11]	[0.08, 0.11]	[0.09, 0.12]	[0.11, 0.14]	[0.07, 0.1]	[0.05, 0.08]	[0.1, 0.13]	[0.07, 0.1]	[0.09, 0.12]
A2	[0.09, 0.11]	[0.09, 0.12]	[0.06, 0.09]	[0.07, 0.1]	[0.06, 0.09]	[0.08, 0.11]	[0.06, 0.1]	[0.08, 0.12]	[0.1, 0.13]	[0.1, 0.13]
A3	[0.07, 0.11]	[0.08, 0.11]	[0.09, 0.13]	[0.08, 0.11]	[0.08, 0.12]	[0.09, 0.12]	[0.11, 0.14]	[0.06, 0.09]	[0.09, 0.12]	[0.09, 0.13]
A4	[0.09, 0.12]	[0.09, 0.12]	[0.07, 0.09]	[0.08, 0.11]	[0.07, 0.1]	[0.1, 0.13]	[0.05, 0.08]	[0.08, 0.12]	[0.13, 0.15]	[0.11, 0.14]
A5	[0.08, 0.11]	[0.08, 0.11]	[0.08, 0.11]	[0.09, 0.12]	[0.08, 0.11]	[0.08, 0.1]	[0.08, 0.11]	[0.09, 0.11]	[0.07, 0.11]	[0.07, 0.09]
A6	[0.08, 0.11]	[0.1, 0.14]	[0.09, 0.12]	[0.08, 0.11]	[0.09, 0.13]	[0.09, 0.12]	[0.09, 0.12]	[0.08, 0.12]	[0.06, 0.09]	[0.07, 0.09]
A7	[0.1, 0.13]	[0.07, 0.1]	[0.09, 0.11]	[0.08, 0.12]	[0.05, 0.08]	[0.07, 0.1]	[0.12, 0.16]	[0.09, 0.11]	[0.09, 0.12]	[0.1, 0.12]
A8	[0.08, 0.11]	[0.07, 0.1]	[0.11, 0.14]	[0.09, 0.11]	[0.12, 0.15]	[0.09, 0.12]	[0.09, 0.13]	[0.08, 0.11]	[0.06, 0.08]	[0.05, 0.07]
A9	[0.09, 0.12]	[0.08, 0.11]	[0.1, 0.12]	[0.1, 0.13]	[0.07, 0.1]	[0.08, 0.11]	[0.09, 0.12]	[0.09, 0.12]	[0.07, 0.1]	[0.11, 0.14]
A10	[0.08, 0.14]	[0.08, 0.16]	[0.09, 0.12]	[0.07, 0.14]	[0.09, 0.15]	[0.07, 0.15]	[0.08, 0.14]	[0.08, 0.12]	[0.09, 0.14]	[0.07, 0.13]

TABLE 8. Normalized gray decision weight matrix option-criteria

	C11	C12	C13	C14	C15	C21	C22	C23	C24	C25
A1	[0.003, 0.007]	[0.003, 0.004]	[0.003, 0.004]	[0.007, 0.011]	[0.001, 0.002]	[0.001, 0.002]	[0.001, 0.001]	[0.002, 0.003]	[0, 0.001]	[0.001, 0.001]
A2	[0.005, 0.007]	[0.003, 0.004]	[0.002, 0.003]	[0.005, 0.008]	[0.001, 0.001]	[0.001, 0.002]	[0.001, 0.001]	[0.003, 0.004]	[0, 0.001]	[0.001, 0.001]
A3	[0.004, 0.007]	[0.003, 0.004]	[0.003, 0.004]	[0.012, 0.016]	[0.001, 0.001]	[0.001, 0.002]	[0.001, 0.001]	[0.002, 0.003]	[0, 0]	[0.001, 0.001]
A4	[0.004, 0.006]	[0.003, 0.005]	[0.002, 0.003]	[0.006, 0.01]	[0.001, 0.001]	[0.001, 0.002]	[0.001, 0.001]	[0.002, 0.003]	[0, 0]	[0.001, 0.001]
A5	[0.004, 0.007]	[0.003, 0.005]	[0.002, 0.003]	[0.01, 0.013]	[0.001, 0.002]	[0.001, 0.002]	[0.001, 0.002]	[0.002, 0.003]	[0, 0]	[0.001, 0.001]
A6	[0.004, 0.006]	[0.005, 0.006]	[0.003, 0.004]	[0.011, 0.015]	[0.001, 0.001]	[0.001, 0.002]	[0.001, 0.001]	[0.003, 0.004]	[0, 0]	[0.001, 0.001]
A7	[0.003, 0.006]	[0.003, 0.005]	[0.002, 0.003]	[0.01, 0.013]	[0.001, 0.001]	[0.002, 0.002]	[0.001, 0.002]	[0.003, 0.004]	[0, 0]	[0.001, 0.001]
A8	[0.004, 0.006]	[0.004, 0.005]	[0.002, 0.004]	[0.009, 0.013]	[0.001, 0.001]	[0.001, 0.002]	[0.001, 0.001]	[0.003, 0.005]	[0, 0.001]	[0.001, 0.001]
A9	[0.003, 0.007]	[0.003, 0.005]	[0.003, 0.004]	[0.015, 0.018]	[0.001, 0.002]	[0.001, 0.002]	[0.001, 0.002]	[0.002, 0.003]	[0, 0.001]	[0.001, 0.001]
A10	[0.004, 0.006]	[0.004, 0.006]	[0.002, 0.005]	[0.011, 0.014]	[0.001, 0.002]	[0.001, 0.002]	[0.001, 0.002]	[0.003, 0.004]	[0, 0.001]	[0.001, 0.001]

	C31	C32	C33	C34	C35	C41	C42	C43	C44	C45
A1	[0.004, 0.006]	[0.021, 0.029]	[0.009, 0.013]	[0.002, 0.003]	[0.009, 0.012]	[0.001, 0.002]	[0.004, 0.006]	[0.003, 0.004]	[0.001, 0.002]	[0.001, 0.001]
A2	[0.005, 0.006]	[0.022, 0.031]	[0.006, 0.01]	[0.002, 0.003]	[0.005, 0.008]	[0.001, 0.002]	[0.005, 0.007]	[0.003, 0.004]	[0.002, 0.002]	[0.001, 0.001]
A3	[0.004, 0.006]	[0.021, 0.027]	[0.011, 0.014]	[0.002, 0.003]	[0.007, 0.01]	[0.001, 0.002]	[0.008, 0.01]	[0.002, 0.003]	[0.002, 0.002]	[0.001, 0.001]
A4	[0.005, 0.007]	[0.023, 0.03]	[0.007, 0.01]	[0.002, 0.003]	[0.006, 0.008]	[0.002, 0.002]	[0.004, 0.006]	[0.003, 0.004]	[0.002, 0.002]	[0.001, 0.001]
A5	[0.005, 0.006]	[0.021, 0.029]	[0.009, 0.013]	[0.002, 0.003]	[0.007, 0.009]	[0.001, 0.002]	[0.006, 0.008]	[0.003, 0.004]	[0.001, 0.002]	[0.001, 0.001]
A6	[0.004, 0.006]	[0.024, 0.035]	[0.01, 0.013]	[0.002, 0.003]	[0.008, 0.011]	[0.001, 0.002]	[0.006, 0.009]	[0.003, 0.004]	[0.001, 0.002]	[0.001, 0.001]
A7	[0.006, 0.007]	[0.018, 0.025]	[0.01, 0.013]	[0.002, 0.003]	[0.004, 0.007]	[0.001, 0.002]	[0.009, 0.011]	[0.003, 0.004]	[0.001, 0.002]	[0.001, 0.001]
A8	[0.004, 0.006]	[0.018, 0.027]	[0.013, 0.015]	[0.002, 0.003]	[0.01, 0.012]	[0.001, 0.002]	[0.006, 0.009]	[0.002, 0.004]	[0.001, 0.001]	[0, 0.001]
A9	[0.005, 0.006]	[0.02, 0.027]	[0.011, 0.014]	[0.003, 0.004]	[0.006, 0.009]	[0.001, 0.002]	[0.006, 0.008]	[0.003, 0.004]	[0.001, 0.002]	[0.001, 0.001]
A10	[0.004, 0.008]	[0.021, 0.039]	[0.01, 0.014]	[0.002, 0.004]	[0.008, 0.013]	[0.001, 0.002]	[0.006, 0.01]	[0.003, 0.004]	[0.001, 0.002]	[0.001, 0.001]

TABLE 9. Best non-gray performance in technology transfer methods

Technology transfer method	$\hat{v}_{ij}^{+}$	$\hat{v}_{ij}^{-}$	$\hat{y}_i$	$BNGP_i(\hat{y}_i)$	RANK
Buy royalties (A1)	[0.073, 0.104]	[0.004, 0.006]	[0.069, 0.098]	0.084	7
Education and training (A2)	[0.069, 0.099]	[0.005, 0.007]	[0.064, 0.092]	0.078	10
Foreign Direct Investment (A3)	[0.082, 0.113]	[0.004, 0.006]	[0.078, 0.107]	0.093	3
Reverse Engineering (A4)	[0.073, 0.1]	[0.004, 0.006]	[0.068, 0.094]	0.081	9
Recruitment and exchange of manpower (A5)	[0.077, 0.107]	[0.005, 0.007]	[0.073, 0.1]	0.086	6
Franchise Method (A6)	[0.086, 0.119]	[0.006, 0.008]	[0.08, 0.111]	0.096	2
Licensing (A7)	[0.076, 0.105]	[0.006, 0.008]	[0.07, 0.097]	0.084	8
Joint R&D (A8)	[0.08, 0.111]	[0.006, 0.008]	[0.074, 0.103]	0.089	5
External supply (A9)	[0.084, 0.113]	[0.005, 0.007]	[0.079, 0.106]	0.092	4
Joint Venture (A10)	[0.081, 0.132]	[0.006, 0.008]	[0.075, 0.124]	0.099	1

TABLE 10. Cost of implementing technology transfer method *i* in company *j*

W_{ij}	M1	M2	M3	M4	M5	M6	M7	M8
A1	2,089	2,574	2,063	3,429	1,932	3,383	2,179	3,162
A2	2,987	2,862	2,168	3,345	2,177	3,199	3,316	1,971
A3	2,194	1,853	3,148	3,172	2,062	2,558	2,604	2,696
A4	2,169	2,178	1,817	2,780	1,844	2,523	3,138	2,536
A5	3,245	3,236	1,995	2,279	2,376	2,510	2,973	1,845
A6	3,043	2,331	2,532	1,925	2,965	2,797	2,742	3,332
A7	2,165	3,076	2,716	3,224	3,300	3,061	2,375	2,115
A8	2,173	2,028	2,251	3,300	3,280	2,000	2,687	2,838
A9	2,792	3,300	2,098	3,244	2,661	2,665	2,999	1,824
A10	1,909	2,046	2,212	2,531	3,450	3,172	2,518	2,584

TABLE 11. Reliability of implementing technology transfer method *i* in company *j*

L_{ij}	M1	M2	M3	M4	M5	M6	M7	M8
A1	0.895	0.973	0.895	0.974	0.905	0.981	0.851	0.887
A2	0.940	0.959	0.892	0.942	0.933	0.873	0.933	0.851
A3	0.905	0.976	0.911	0.871	0.979	0.936	0.943	0.932
A4	0.907	0.984	0.870	0.931	0.882	0.914	0.850	0.983
A5	0.983	0.897	0.896	0.892	0.903	0.963	0.938	0.854
A6	0.857	0.956	0.962	0.965	0.903	0.852	0.901	0.875
A7	0.885	0.904	0.878	0.862	0.864	0.968	0.934	0.862
A8	0.919	0.884	0.959	0.938	0.864	0.984	0.876	0.913
A9	0.916	0.879	0.976	0.878	0.925	0.864	0.925	0.983
A10	0.855	0.900	0.977	0.875	0.897	0.949	0.854	0.948

TABLE 12. Number of methods allowed for allocation to manufacturer *j*

	M1	M2	M3	M4	M5	M6	M7	M8
D_j	3	4	2	3	2	2	3	2

Based on this information, the mathematical problem designed for 100 iterations of the ε-Constraint Method was solved and the Pareto front was obtained from two objective functions.

The results are shown in Figure 2. The results were presented to the experts. They agreed on choosing the best answer from the 101 points on the Pareto front, based on the values obtained for the objective functions. The results are shown in Table 13. Also, how the technology transfer methods are assigned to each manufacturer is described in Table 14.

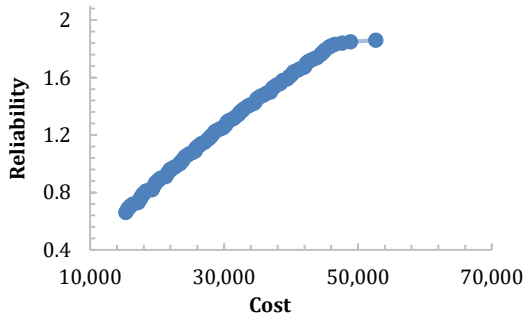

Figure 2. Pareto front created based on target functions

TABLE 13. Optimal goal function based on expert opinion

Cost (Z1)	Reliability (Z2)
30,756	1.3

TABLE 14. How to assign the technology transfer method to each company

Technology transfer method	Company							
	1	2	3	4	5	6	7	8
A1					✓			
A2								
A3		✓			✓			
A4								
A5								✓
A6		✓		✓				
A7								
A8	✓	✓				✓		
A9			✓					✓
A10	✓	✓	✓				✓	

6. CONCLUSION

One of the key success factors for international competition in companies is the accumulation of technology-based advantages. Enterprises use different ways to access technology. Technology transfer is known as one of the main shortcuts for developing countries to reduce the technology gap with developed countries. However, companies and countries face different challenges in this journey. In this regard, the development of intelligent and facilitating laws that are appropriate to the characteristics and challenges of each country can help improve the level of technology transfer.

In this study, we attempted to follow theoretical and research principles and frameworks to provide a model to identify the factors affecting technology transfer

methods to improve company performance. For this purpose, at first, we reviewed domestic and foreign research and proposed a set of 20 factors in four categories of economic, technical, managerial, and commercial factors which were localized according to the judgments of an expert committee composed of expertise from battery companies. Then the best-worst method (BWM)was used to determine the effective weight of each factor and prioritize technology transfer methods. The conclusion of best-worst showed that the indicators of “improving management style”, “firm strategy”, “cost effectiveness” “how to communicate with the organization” and “competitiveness” are among the effective indicators in the evaluation of technology transfer methods, considering the company's performance improvement.

Also, the “joint venture” approach achieved the best performance in three indicators of “risk level”, "management style improvement” and “competitiveness”, which indicates that if the company intends to compete in the world-class and take a step in the development and progress direction, the joint venture method is of the most importance. Because the company can benefit from the direct and continuous help and cooperation of large companies to improve its business, move towards modernization of production methods, increase efficiency and productivity, and as a result increase the capacity and production rate of its business. The other notable result of this study mentions the low rank of the training and teaching method. This indicates that the experts of the relevant companies believe that a technology transfer method such as training and teaching is time-consuming and the results do not greatly improve the company's competitive position and production capacity. They were not sure about the efficiency of methods like training and teaching, hiring, or exchanging of human forces. Finally, a two-objective mathematical model (zero and one type) was presented and solved to assign each method to the most important battery manufacturers in the country. According to the obtained results, the technology transfer method of "joint venture" had the most frequency in companies.

Research limitations include access to company experts, intrinsic limitations of the questionnaire, the possibility of a conservative response from the experts, the time-consuming distribution, completion, and collection of the questionnaires due to administrative barriers, and the wide variation in the experts' views on factors affecting technology transfer. In future research, the following can be considered:

- To cover all aspects of the problem more comprehensively and to avoid conservative responses from experts, it is recommended that a combination of interview and questionnaire be used at all stages of future research; because more useful information can usually be obtained during the interview due to two-way communication.
- Using a heuristic algorithm or other MCDM models, such as VICOR, TOPSIS, VASPAS, etc. to analyze the sensitivity of the results obtained from the Best-Worst method is effective in prioritizing options.
- Evaluating and ranking technology transfer methods based on the variables of transfer speed, transfer cost, adaptability, and self-sufficiency;

More activity of the company's research and development department not only in terms of technology adoption but also in terms of development activities.

7. REFERENCES

1. Lee, S., Kim, B.S., Kim, Y., Kim, W. and Ahn, W., "The framework for factors affecting technology transfer for suppliers and buyers of technology in korea", ***Technology Analysis & Strategic Management***, Vol. 30, No. 2, (2018), 172-185. doi: 10.1080/0953 .7325.2017.1297787
2. Bertsch, G.K., "After the revolutions: East-west trade and technology transfer in the 1990s, Routledge..(2019)
3. Buzás, N., From technology transfer to knowledge transfer: An institutional transition, in Linking industries across the world. 2019, Routledge.109-124.
4. Günsel, A., "Research on effectiveness of technology transfer from a knowledge based perspective", ***Procedia-Social and Behavioral Sciences***, Vol. 207, No., (2015), 777-785. doi: 10.1016/j.sbspro.2015.10.165.
5. Kaimoneitz, D., "Making the link: Agricultural research and technology transfer in developing countries", ***Westview Special Studies in Agriculture Science and Policy.***, (1990). doi: 10.1201/9780429044410.
6. Hsiao, C.-T. and Liu, C.-S., "Dynamic modeling of the development of the dram industry in taiwan", ***Asian Journal of Technology Innovation***, Vol. 20, No. 2, (2012), 277-293. doi: 10.1080/ 19761597.2012.741396.
7. Hsu, D.W., Shen, Y.-C., Yuan, B.J. and Chou, C.J., "Toward successful commercialization of university technology: Performance drivers of university technology transfer in taiwan", ***Technological Forecasting and Social Change***, Vol. 92, (2015), 25-39. doi: 10.1016/ j.techfore.2014.11.002.
8. Bigliardi, B., Galati, F., Marolla, G .and Verbano, C., "Factors affecting technology transfer offices' performance in the italian food context", ***Technology Analysis & Strategic Management***, Vol. 27, No. 4, (2015), 361-384. doi: 10.1080/09537325.2014.1002464.
9. Bozeman, B., Rimes, H. and Youtie, J., "The evolving state-of-the-art in technology transfer research: Revisiting the contingent effectiveness model", ***Research Policy***, Vol. 44, No. 1, (2015), 34-49. doi: 10.1016/j.respol.2014.06.008.
10. Ravi, R. and Janodia, M.D., "Factors affecting technology transfer and commercialization of university research in india: A cross-sectional study", ***Journal of the Knowledge Economy***, Vol. 13, No. 1, (2022), 787-803. doi: 10.1007/s13132-021-00747-4.
11. Khorasgani, G.H., Modiri, M. and Farsijani, H" ,.Designing a sustainable world class manufacturing model in the automotive industry in iran", ***Tehnički Glasnik***, Vol. 14, No. 2, (2020), 143-153. doi: 10.31803/tg-20200131192955 .

12. Malindzakova, M. and Malindzak, D., "Linking the world class manufacturing system approach with a waste management", ***Tem Journal***, Vol. 9, No. 2, (2020), 750. doi: 10.18421/TEM92-43.
13. Kalantari, H., Nikabadi, M.S. and Zarei, A., "Identification of world-class manufacturing strategies and their implementation requirements in food industry (case study: Olive product)", doi: 10.1504/ijBEX..2020.10032841.
14. Majidpour, M., "International technology transfer and the dynamics of complementarity: A new approach", ***Technological Forecasting and Social Change***, Vol. 122, (2017), 196-206. doi: 10.1016/j.techfore.2016.03.004 .
15. Christensen, H.B., Lee, E., Walker, M. and Zeng, C., "Incentives or standards: What determines accounting quality changes around ifrs adoption?", ***European Accounting Review***, Vol. 24, No. 1, (2015), 31-61. doi: 10.1080/09638180.2015.1009144.
16. Dinmohammadi, A. and Shafiee, M., "Determination of the most suitable technology transfer strategy for wind turbines using an integrated ahp-topsis decision model", ***Energies***, Vol. 10, No. 5 , .642 ,(2017)doi: 10.3390/en10050642 .
17. Arabzadeh, S., "Ranking of companies regarding the effective factors on technology transfer using fahp and fuzzy topsis techniques", ***International Journal of Industrial and Systems Engineering***, Vol. 28, No. 4, (2018), 468-493, doi: 10.1504/IJISE.2018.090447 .
18. Distanont, A., Khongmalai, O. and Kritpipat, P., "Factors affecting technology transfer performance in the petrochemical industry in thailand: A case study", ***WMS Journal of Management***, Vol. 7, No. 2, (2018), 23-35.
19. Kraujalienė, L., "Comparative analysis of multicriteria decision-making methods evaluating the efficiency of technology transfer", ***Business, Management and Economics Engineering***, Vol. 17, No. 1, (2019), 72-93. doi: 10.3846/bme.2019 .11014.
20. Lavoie, J.R. and Daim, T., Technology transfer assessment: An integrated approach, in R&d management in the knowledge era. (2019), Springer. 439-460.
21. Amini, E., Baniasadi, M., Vahidi, H., Nematollahi, H., Khatami, M., Amandadi, M., Malekyan ,L. and Safarpour, H., "Affecting factors of knowledge-based companies using fuzzy ahp model, case study tehran university enterprise park", ***Journal of the Knowledge Economy***, Vol. 11, No. 2, (2020), 574-592. doi: 10.1007/s13132-018-0554-9.
22. Amirghodsi, S., Bonyadi Naeini, A. and Roozbehani, B., "An integrated shannon-paf method on gray numbers to rank technology transfer strategies", ***Engineering Management Journal***, Vol. 32, No. 3, (2020), 186-207. doi: 10.1080/10429247.2020.1738879 .
23. Bonyadi Naieni, A., Amirghodsi, S. and Makui, A., "Simultaneous selection of the technology and its transfer method from the preferred supplier applying bwm and grey anp methods", ***Industrial Management Studies***, Vol. 18, No. 56, (2020), 209-243. https://dx.doi.org/10.22054/jims.2019.36668.2182
24. Noori, F., Delangizan, S. and Rezaee, B., "The employment effect of technology transfer methods: A systematic review", ***Journal of Entrepreneurship Development***, Vol. 14, No. 2, (2021), 341-360. https://dx.doi.org/10.22059/jed.2021.312036.653485
25. Iroegbu, U.F., Ushie, M.A. and Otiala, B.P., "A fuzzy ahp approach for technology transfer problems: A case study of africa and china partnerships", (2021). doi: 10.4236/ajibm.2021.116042.
26. Durak, İ., Arslan, H.M. and Özdemir, Y., "Application of AHP–topsis methods in technopark selection of technology companies: Turkish case", ***Technology Analysis & Strategic Management***, (2021), 1-15. https://doi.org/10.1080/09537325.2021.1925242
27. Mohammadi, N., Dahooie, J.H. and Khajevand, M., "A hybrid approach for identifying and prioritizing critical success factors in technology transfer projects (case study: Diesel locomotive manufacturing)", ***Journal of Engineering, Design and Technology***, (2021). https://doi.org/10.1108/JEDT-07-2021-0345
28. Dahooie, J.H., Qorbani, A.R. and Daim, T., "Providing a framework for selecting the appropriate method of technology acquisition considering uncertainty in hierarchical group decision-making: Case study: Interactive television technology", ***Technological Forecasting and Social Change***, Vol. 168, (2021), 120760. doi: 10.1016/j.techfore.2021.120760 .
29. Marznaki, Y.S., Khamseh, A. and Shakib, M.H., "A system dynamics approach for investigating technology transfer capacities in iranian polymer pipe and fittings industry", ***Technology Analysis & Strategic Management***, (2022), 1-17. https://doi.org/10.1080/09537325.2022.2037544
30. Rezaei, J., "Best-worst multi-criteria decision-making method", ***Omega***, Vol. 53, (2015), 49-57. doi. https://doi.org/10.1016/j.omega.2014.11.009
31. Afrasiabi, A., Chalmardi, M.K. and Balezentis, T., "A novel hybrid evaluation framework for public organizations based on employees' performance factors", ***Evaluation and Program Planning***, Vol. 91, (2022), 102020. https://doi.org/10.1016/j.evalprogplan.2021.102020
32. Afrasiabi, A., Tavana, M. and Di Caprio, D., "An extended hybrid fuzzy multi-criteria decision model for sustainable and resilient supplier selection", ***Environmental Science and Pollution Research***, Vol. 29, No. 25, (2022), 37291-37314. https://doi.org/10.1007/s11356-021-17851-2
33. Kannan, D., Moazzeni, S., mostafayi Darmian, S. and Afrasiabi, A., "A hybrid approach based on mcdm methods and monte carlo simulation for sustainable evaluation of potential solar sites in east of iran", ***Journal of cleaner production***, Vol. 279, (2021), 122368. https://doi.org/10.1016/j.jclepro.2020.122368
34. Rezaei, J., "Best-worst multi-criteria decision-making method: Some properties and a linear model", ***Omega***, Vol. 64, (2016), 126-130. https://doi.org/10.1016/j.omega.2015.12.001
35. Chithambaranathan, P., Subramanian, N., Gunasekaran, A. and Palaniappan, P.K., "Service supply chain environmental performance evaluation using grey based hybrid mcdm approach", ***International Journal of Production Economics***, Vol. 166, (2015), 163-176. doi: 10.1016/j.ijpe.2015.01.002.
36. Patel, S.S. and Prajapati, J., "Multi-criteria decision making approach: Selection of blanking die material", ***International Journal of Engineering, Transactions B: Applications,***, Vol. 30, No. 5, (2017), 800-806. doi: 10.5829/idosi.ije.2017.30.05b.21 .
37. Parkouhi, S.V. and Ghadikolaei, A.S" ,.A resilience approach for supplier selection: Using fuzzy analytic network process and grey vikor techniques", ***Journal of Cleaner Production***, Vol. 161, (2017), 431-451. https://doi.org/10.1016/j.jclepro.2017.04.175
38. Brauers, W.K. and Zavadskas, E.K., "The moora method and its application to privatization in a transition economy", ***Control and Cybernetics***, Vol. 35, No. 2, (2006), 445-469. http://eudml.org/doc/209425
39. Brauers, W.K.M. and Zavadskas, E.K., "Project management by multimoora as an instrument for transition economies", ***Technological and Economic Development of Economy***, Vol. 16, No. 1, (2010), 5-24. doi: 10.3846/tede.2010.01.
40. Wattanasaeng, N. and Ransikarbum, K., "Model and analysis of economic-and risk-based objective optimization problem for plant location within industrial estates using epsilon-constraint algorithms", ***Computation***, Vol. 9, No. 4, (2021), 46. https://doi.org/10.3390/computation9040046

Persian Abstract

چکیده

هدف از این پژوهش طراحی یک مدل مبتنی بر تصمیم‌گیری-بهینه‌سازی به‌منظور ارزیابی و تخصیص شیوه‌های انتقال تکنولوژی در صنایع باتری‌سازی خودرو تحت شرایط عدم قطعیت است. این تحقیق بر مبنای نیاز صنعت باتری کشور انجام گرفته و نشان دهنده تاثیر به سزای انتقال تکنولوژی بر تولید در کلاس جهانی است. ابتدا شاخص‌های مؤثر در ارزیابی شیوه‌های انتقال تکنولوژی از طریق بررسی مرور ادبیات و همچنین نظرات خبرگان شناسایی می‌شوند. جامعه آماری این پژوهش را خبرگان هشت شرکت تولیدکننده باتری خودرو تشکیل می‌دهند. سپس هر یک از شاخص‌های تأییدشده از طریق به‌کارگیری روش بهترین-بدترین وزن دهی می‌گردند و در ادامه شیوه‌های انتقال تکنولوژی با استفاده از روش تصمیم‌گیری چندمعیاره مورا تحت شرایط عدم قطعیت مورد ارزیابی و اولویت‌بندی واقع شدند. بمنظور در نظر گرفتن عدم قطعیت نیز از تئوری خاکستری بهره گرفته شد. مطابق نتایج به‌دست‌آمده از روش بهترین-بدترین شاخص‌های "بهبود سبک مدیریتی"، "استراتژی بنگاه"، "اثربخشی هزینه‌ای"، "نحوه ارتباط با سازمان" و "رقابت‌پذیری" پنج شاخص اولیه مؤثر در ارزیابی روش‌های انتقال تکنولوژی در صنعت باتری‌سازی هستند. در نهایت به منظور پیاده‌سازی چارچوب پیشنهادی در صنایع باتری‌سازی کشور از طریق حل یک مدل ریاضی دوهدفه بهینه‌سازی شیوه‌های بهینه انتقال تکنولوژی با هدف تولید در سطح جهانی، برای هر یک از تولیدکنندگان مشخص گردید. جهت حل مدل پیشنهادی از رویکرد اپسیلون-محدودیت تکامل یافته بهره گرفته شد، مطابق نتایج به دست آمده از رویکرد پیشنهادی، شیوه انتقال "سرمایه‌گذاری مشترک" مناسب‌ترین روش جهت انتقال فناوری در صنایع باتری سازی است.

International Journal of Engineering

Journal Homepage: www.ije.ir

A Repetitive Bipolar Pulsed Power Generator Based on Switched-capacitor Concept

M. Mohammadzade[a], A. R. Nateghi[b], H. Zare*[c]

[a] *Department of Electrical and Computer Engineering, Babol Noshirvani University of Technology, Babol, Iran*
[b] *Faculty of Electrical and Computer Engineering Shahid Sattari University, Tehran, Iran*
[c] *Department of Electrical Engineering, Technical and Vocational University (TVU), Iran*

PAPER INFO

Paper history:
Received 25 March 2022
Received in revised form 09 July 2022
Accepted 24 July 2022

Keywords:
Pulse Power Generator
Repetitive Bipolar Pulse Generator
Multi-Level Switching
Avalanche Breakdown

ABSTRACT

This paper presents a pulsed-power generator that can produce a high voltage bipolar pulse from a relatively low-voltage input source, based on the switched-capacitor concept. The circuit boosts the input voltage by storing energy in several capacitors in a predefined pattern and simultaneously releasing it to the load. It is worth noting that the structure can short-circuit its output terminal while charging the capacitors without using any switches across the load. This topology is mainly suitable for applications requiring a high voltage pulse and only having access to low voltage input sources. Moreover, thee structure can generate a combination of wide and narrow pulses by alteranting its output voltage between two different values. Precise calculation and employment of capacitors ensure that the structure can properly generate the intended output pulses with an acceptable ever-so-slight voltage drop. Finally, MATLAB Simulink was used to evaluate the circuit's operation, and experimental tests were conducted on a laboratory setup, where the results confirmed the proper performance of the circuit.

doi: *10.5829/ije.2022.35.10a.22*

1. INTRODUCTION

High voltage pulsed power supply with repetitive rate has found widespread use in industrial, medical, and environmental applications [1]. In this regard, the following utilizations have been reported in the literature: plasma source for ion implantation, microwave generation, metal forming, water purification, food sterilization, eye surgery, cancer treatment, and reducing muscle contractions during irreversible electroporation [2-8]. Considering the vast application of these pulse generators, optimizing their circuit design is crucial. Applying the avalanche breakdown property of transistors is one of the methods to achieve an ideal design for generating pulses [9]. The other important design issue of such circuits is the switching process of the components [10]. These circuits are mainly composed of several switching states, each providing a part of the overall output voltage waveform. The switches used in these generators are of different types, such as electronic switches and fast diodes, including MOSFET, BJT, and IGBT.

Depending on the type of switches used, the structure, its control, and maintenance can be more complicated and costly. Therefore, achieving high- voltage high-energy pulses at an acceptable cost should be addressed for the aforementioned applications. Employing BJT transistors with avalanche breakdown for generating voltage pulses is one of the approaches to achieving a compact design [11]. However, the blocking voltage of semiconductor switches is one of their most significant limitations. Employing either a series connection of switches or a step-up transformer has been proposed in different configurations to overcome this issue [12]. Nevertheless, transformer losses, size, and difficulties in matching it with load impedance lead to a decline in the system's reliability and efficiency. Additionally, the probability of a switch failure in these two methods is significantly higher due to the absence of proper protection circuits.

Another method of achieving a pulsed power generator is using the Marx structure. In this structure, similar switches are used to charge capacitors in parallel and discharge them in series across the load. Marx generators (MGs) require a significantly high input voltage to merely

*Corresponding Author Institutional Email: hszare@tvu.ac.ir (H. Zare)

Please cite this article as: M. Mohammadzade, A. R. Nateghi, and H. Zare, A Repetitive Biboplar Pulse Power Generator Based on Switched-capacitor Concept, ***International Journal of Engineering, Transactions A: Basics***, Vol. 35 No. 10, (2022), 2056-2064

produce a high voltage pulse (without any transformers). However, it obliges a specific triggering circuit to precisely control the switches. Despite sufficient rise time, this structure suffered from low efficiency and repetition rate due to the need of too many circuit elements. Additionally, short life time of the circuit was the other disadvantage the traditional Marx pulse generators. Turning to the applications that use low voltage power supplies as an input source, using Marx structure requires too many modules. This feature results in higher size, cost and control complexity of the circuit.

In recent years, MG has had dual functions by combining repetitive rate of semiconductor switches with voltage adder from Marx principle, which helps decrease the pulse's rising time compared to the conventional circuits, leading to a more precise and better-formed pulse. However, MG structures may employ many modules for applications requiring low-voltage input sources, resulting in increased control complexity and cost. Multistage and/ or modular switched-capacitor circuits (using low-voltage semiconductors) were developed to address the abovementioned limitations, besides easing the design and control process. The fundamental building block of these circuits is based on MG sub-modules, in which the majority of the circuit components can withstand a voltage similar to the input voltage [13]. A repetitive Marx-type generator based on half and full-bridge Switched-Capacitor (SC) cells is introduced by Sakamoto et al. [14], facilitating independent control of pulsed power parameters. The modularity of the generator not only has led to an easily adjustable pulse signal but also more output voltage levels for reaching higher voltages. However, it requires numerous capacitors and switches to generate the intended pulse. A cascaded H-bridge multilevel inverter for liquid food sterilization eliminating bulky transformer requirements is proposed by Jambari et al. [4]. Although this sturcutre and its performance are straighforward, it suffers from using several independent input sources. A bipolar high-frequency narrow pulse generator based on two independent solid-state unipolar positive MGs positioned back to back for medical application was suggested by Redondo et al. [15]. Notably, each side of the converter is used only in half of the time of a cycle. This feature obliges using a high number of circuit component. Despite having a simple operation control, this pulse generator implements two separate input sources for its two sides.

In general, bipolar high-voltage pulses can be generated with several techniques using semiconductor switches, of which the most common approach is to combine a unipolar pulse generator and an H-bridge on the load side [16]. Besides, using a single primary-side multiple secondary-side transformer-based topology was introduced by Lee et al. [16] in which the number of secondary windings is dependant to the multiplying ratio of the pulse generator. Although this feature helps isolating the input side from the output side, it increases the overall size, weight and cost of the converter. Additionally, the high current stress on the primary side of the transformer makes it vulnerable to failure, reducing the reliability of the circuit. Yet, the main disadvantage of this structure is a large number of H-bridge inverter switches, inflexibility of the pulse, constraints of the required modulator.

Another type of bipolar modular structure is a multistage structure in which a low voltage submodule is stacked in series to generate a high voltage. Two unipolar modulators are used to construct a bipolar pulse power modulator by Liu et al. [17]. Hence, compared to a unipolar pulse power modulator, this requires twice the number of modules to configure the same output voltage level. A multistage modulator structure using several bipolar sub-modules was proposed by Yao et al. [8] and Gholamalitabar et al. [18]. Bipolar sub-modules capable of generating both positive and negative outputs are stacked in series to generate high voltage bipolar pulses. Additionally, the number of components required to construct this complex module can be reduced. As an extension to the research presented by Gholamalitabar et al. [18], a uni/ bipolar high-voltage pulse generator based on a side bridge has been proposed. The primary advantage of this method is its ability to generate various high-voltage unipolar and bipolar pulse waveforms with a relatively low-voltage dc power supply. Using relatively low-voltage IGBT for implementing submodules of the full-bridge is the other advantage of this structure. Unlike the Marx generator that simultaneously charges the capacitors, this topology benefits from the sequential charge of the capacitors. This feature helps ensure a lower current on the IGBTs of the submodules. Furthermore, a modular controllable bipolar pulse generator based on the Capacitor Switch Voltage Multiplier (CS-VM) was introduced by Alijani et al. [19]. In this strategy, capacitors are charged with a predetermined pattern and discharged across the load in a specified sequence.

Accordingly, introducing a pulse generator circuit based on SC Voltage Multiplier (SC-VM) is presented in this study. In this method, similar to CS-VM, several capacitors are charged in predetermined time intervals while the load is short-circuited. Then, all or several of these capacitors are discharged into the load in the final stages. Consequently, a multiplied pulsed voltage is formed from a low-voltage DC source. To further discuss the proposed concept, the rest of this article is organized as follows: Section II describes the topology and its operating principles, such as charging and discharging paths and bipolar pulse generation. It also provides capacitance calculations and a brief comparison with similar works. Then, the circuit structure is evaluated through simulation and experiment where the results are added in section III. Finally, the paper is concluded in section IV.

2. PROPOSED CIRCUIT

2. 1. Principles of Operation The fundamental idea of the proposed circuit is to charge several capacitors via the SC-VM network and then connect them in series to generate high voltage pulses at the output. The proposed structure is depicted in Figure 1. The circuit comprises six electrolyte capacitors and 23 power switches, including 13 unidirectional and five bidirectional ones. The switches S6, S9, S10, S11, and S15 are bidirectional switches that utilize the same control signal for both switches. As a result, the overall structure necessitates using only 18 driver circuits.

Three distinct patterns (P_n) for voltage multiplication are applicable to the circuit. As summarized in Table 1, each pattern charges the capacitors up to a predetermined amount that yields a specific voltage amplitude. Since the third pattern (P_3) results in the highest voltage amplitude, the rest of the paper is based on applying this pattern to the circuit. This pattern charges the circuit capacitors in a way that V_{C5} is four times the input voltage (V_{in}), which is twice the V_{C1} and four times V_{C3}. Nonetheless, as shown in Figure 2, the proposed structure is extendable to produce higher voltages where the highlighted part is repeated n-times to reach the intended voltage amplitude. In that case, the main part of the circuit operates with any of the abovementioned patterns. However, based on the application and user's preferences, the extension part can either double the capacitors' voltage in every step or charge all of them with the same voltage as C5 and C6. However, there are a few limiting factors in both approaches, such as the amplitude of input voltage and the rating of semiconductor devices in the circuit. As a result, the intended output waveform for the basic circuit of Figure 1, is achieved by using the operating sequence presented in Table 2 where the corresponding current path of each stage illustrated in Figure 3. Accordingly, all capacitors are charged during the first six stages of operation. In steps 7 and 9, negative and positive voltage pulses are generated by a specific combination of capacitors and applied to the load.

During the first (Figure 3a) and second (Figure 3b) stages of the circuit's operation, capacitors C_3 and C_4 are directly charged by the input source up to V_{in}. As shown in Figure 3c, these two capacitors are connected in series with C1 causing it to charge to a maximum of 2Vin in the third stage. Similarly, capacitor C2 undergoes the same process in the fourth stage (Figure 3d). Then, C1, C3, and C4 charge C6 up to 4Vin (Figure 3e). Likewise, capacitor

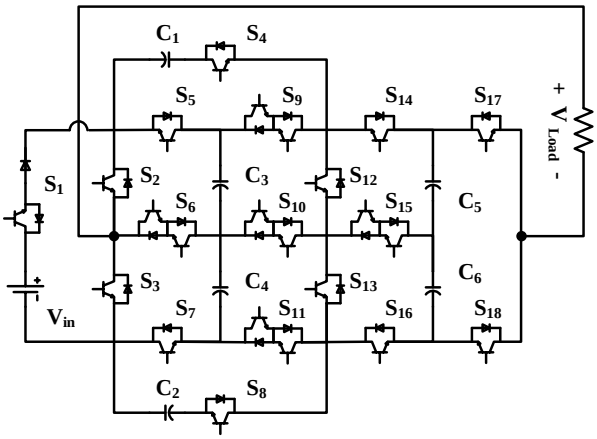

Figure 1. General structure of the proposed pulse generator

TABLE 1. Possible charging patterns

Charging Pattern	Capacitors' Voltage			Max. Output Voltage
	C_3, C_4	C_1, C_2	C_5, C_6	
P_1	V_{in}	V_{in}	V_{in}	$5V_{in}$
P_2	V_{in}	$2V_{in}$	$2V_{in}$	$8V_{in}$
P_3	V_{in}	$2V_{in}$	$4V_{in}$	$12V_{in}$

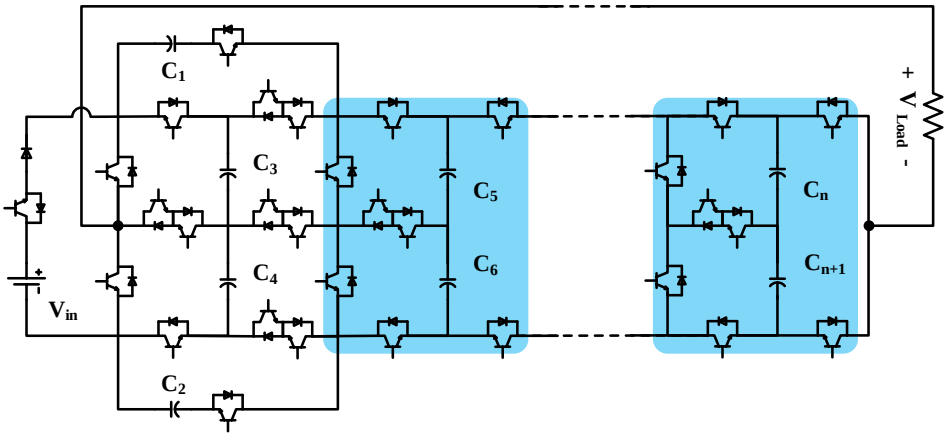

Figure 2. Extension of the presented topology

TABLE 2. Operational sequence considering pattern P3

Stage	Description	V_{out}
1	Charging C_3	0
2	Charging C_4	0
3	Charging C_1	0
4	Charging C_2	0
5	Charging C_6	0
6	Charging C_5	0
7	Discharging C_2, C_3, C_4, C_5, C_6 to the load	$-12\times V_{in}$
8	Charging C_4	0
9	Discharging C_1, C_3, C_4, C_5, C_6 to the load	$+12\times V_{in}$
10	Charging C_3	0

C5 is charged to the same voltage level in the sixth stage (Figure 3f). It is worth noting that the load is short-circuited while the capacitors are being charged, so the output voltage is kept at zero. Finally, as presented in Figure 3g, the charged capacitors C2, C5, C4, C6, and C3, are coupled in the seventh stage to generate a final voltage of -12Vin. This results in the generation of a negative voltage pulse. Again, the load is short-circuited in the eighth stage (Figure 3b). Afterwards, capacitors C1, C5, C4, C3, and C6 are discharged into the load in the ninth stage, producing a positive voltage pulse with an amplitude of 12Vin (Figure 3h). The tenth stage is a repetition of the first stage where the load voltage becomes zero (Figure 3a). For instance, switches 1, 3, 5, 6, 10, 12, 14, and 17 should be turned on to implement the first stage, and other switches should remain off. The time sequence required by all switches for one cycle of the output voltage is shown in Figure 4.

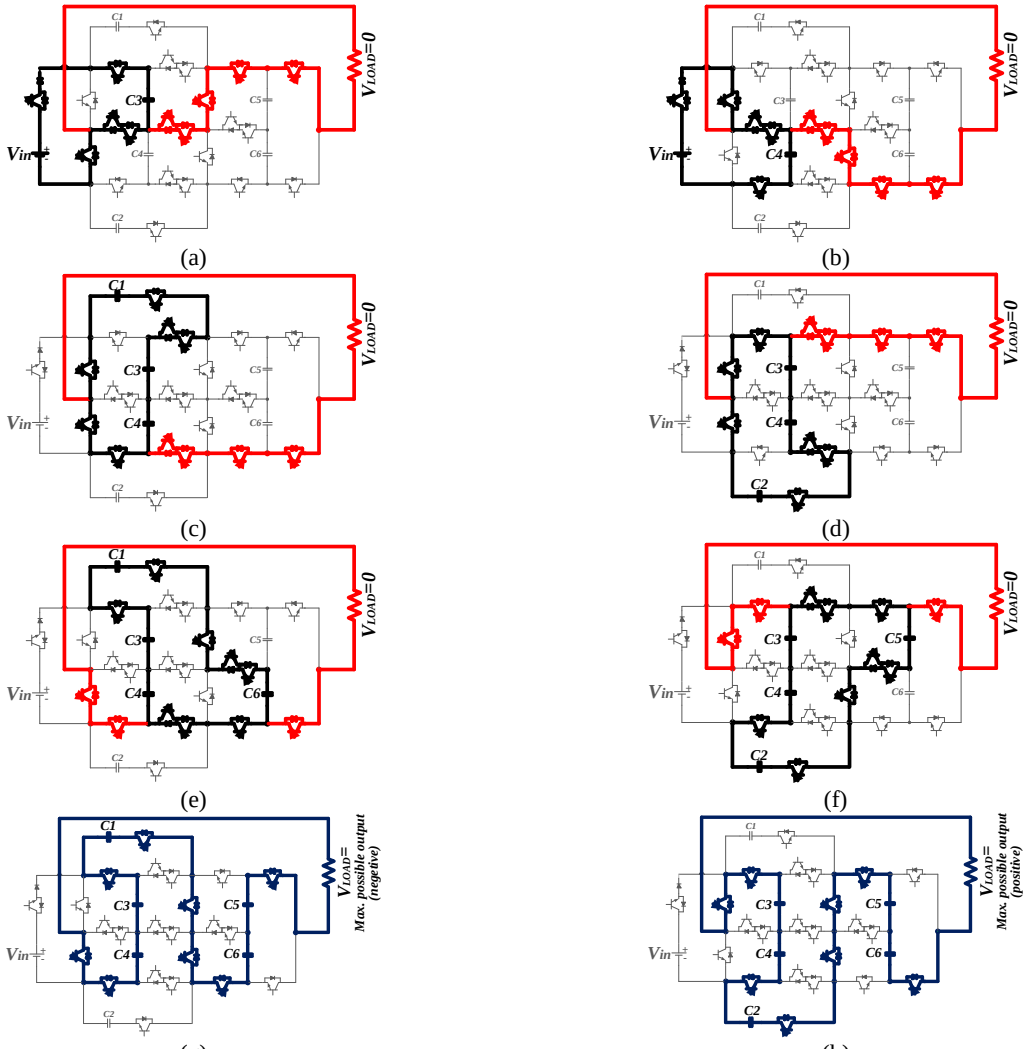

Figure 3. Various current paths regarding ten stages of Table 2 (black=charging path of the capacitors, red=current path of the load, blue=discharging path of the capacitors to the load) (a) stages 1 and 10, (b) 2 and 8, (c) 3, (d) 4, (e) 5, (f) 6, (g) 7, and (h) 9

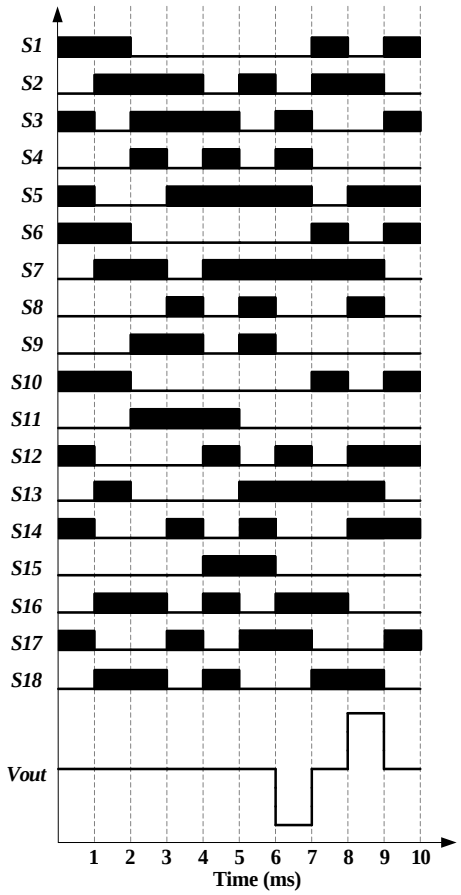

Figure 4. Time sequence of all switches and the corresponding output voltages

2. 2. Capacitance Determination It is essential to select proper capacitances to keep their voltage drop at a specific amount during the whole pulse generation process. Considering the charging pattern of P_3, as some capacitors are charging others, they experience a k percent voltage drop (0<k<1). For instance, C1 is charged by the series connection of C3 and C4, where their total charge is shared with C1. This process consumes some energy that C3 and C4 should provide. So, a part of their voltage (or energy) is always devoted to this charge sharing and not transferred to C1. This phenomenon is modeled and presented in its voltage by parameter k. Therefore, instead of reaching 2Vin, C1 can only get to 2(1-k)Vin. Hence, based on the operational sequence of Figure 4, each capacitor's voltage equals [18]:

$$\begin{cases} V_{C3} = V_{C4} = V_{in} \\ V_{C1} = V_{C2} = 2(1-k)V_{in} \\ V_{C5} = V_{C6} = 4(1-k)^2 V_{in} \end{cases} \quad (1)$$

Hence, the amplitude of the output voltage reaches:

$$V_{out-max} = \left(2+2(1-k)+8(1-k)^2\right) V_{in} = 2\left(4k^2-9k+6\right)V_{in} \quad (2)$$

Which, equals to $12V_{in}$ in ideal conditions (k=0). Accordingly, the required capacitances are determined:

$$C_i \geq \frac{V_{out}.\Delta t}{R.a.V_{Ci}} \qquad i=1,2,\ldots,6 \quad (3)$$

Where Δt is the total pulse width, aV_{Ci} is the voltage drop of each capacitor while discharging, and R is the load impedance. Accordingly:

$$C_{3,4} \geq 2C_{1,2} \geq 4C_{5,6} \quad (4)$$

Thus, each capacitance can be designed for a given voltage drop, maximum pulse width and load impedance. Figure 5 presents the changes in the circuit capacitances versus variations of these parameters.

2. 3. Comparison Table 3 briefly compares the proposed circuit to the ones presented by Sakamoto et al. [14], Gholamalitabar et al. [18] Alijani et al. [19] and Redondo [20] ,where the maximum operating voltage in all of them is within the same range. For sake of fairness, the comparison is made among structures that benefit from a similar gain of 12, defined as the ratio of the output voltage amplitude to the input one ($V_{out-max}/V_{in}$). This factor implies that in the case of using the same input source with the same amplitude, all of these topologies produce a pulsed voltage whose amplitude is 12 times the input one. Nevertheless, the input voltage directly dictates the choice of circuit elements, especially switching devices. So, these topologies may differ in their choice of elements, but their overall performance yields the same result. Accordingly, the proposed structure necessitates fewer semiconductor devices (both power switches and diodes) to reach the same gain. Moreover, employing bidirectional switches results in requiring fewer driver circuits. It is worth mentioning

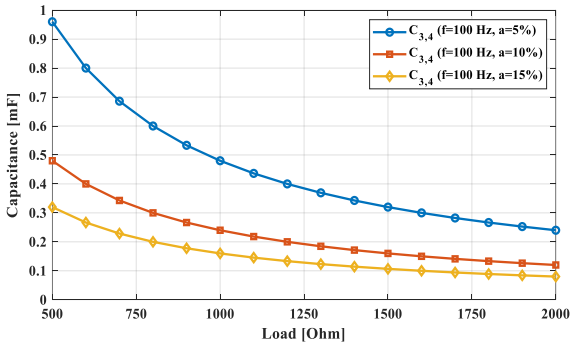

Figure 5. Variation of circuit capacitances

TABLE 3. Comparison of similar structures

Parameter	Proposed	[14]	[18]	[19]	[20]
Voltage Gain	12	12	12	12	12
Number of switches	23	48	23	26	44
Number of series diodes	1	12	5	6	23
Number of driver circuits	18	48	20	26	44
Number of capacitors	6	12	6	6	12

that topologies given by Sakamoto et al. [14] and Redondo [20] used twice the number of capacitors as others. It is notable that despite Sakamoto et al. [14] has a only two simple modes of operation, it requires numerous components. The topologies introduced by Gholamalitabar et al. [18] Alijani et al. [19] and Redondo [20] mainly befit from their fast boosting, and their easily expandable structures. However, they require more semiconductor devices as well as driver circuits. Afterall, the proposed structure outperforms the other similar ones in this context.

3. RESULTS

Considering the precise specifications of the switches, and capacitors based on the test conditions, the circuit was simulated in the MATLAB Simulink environment to verify the correctness of its design. Then, as shown in Figure 6a, a laboratory prototype was implemented to validate the simulation results. Moreover, Figure 6b illusterates the control diagram of the circuit switches where switching signals are provided by the microcontroller. After buffering and isolation, these signals are amplified to be applied to the switches. It is notable that both simulations and experimentations were conducted with the same properties. The parameters of the test system are listed in Table 4.

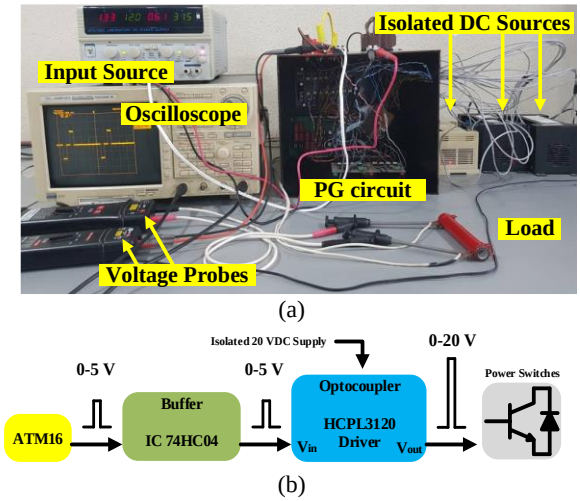

Figure 6. (a) Laboratory test setup, and (b) control diagram of the circuit switches

TABLE 4. Circuit parameters of the proposed structure

Parameters	Value
Input voltage	100 V
Output voltage	1200 V
Output frequency	100 Hz
Power switches	15n120
Load	1 kΩ
Capacitors	C1-C2 =240 µF, 250 V C3-C4 =500 µF, 150 V C5-C6 =120 µF, 450 V
Driver	HCPL3120
Microcontroller	AVR (ATMEGA16A)

Notabaly, the size of the circuit capacitors is determined based on the section 2.2. Then, the nearest commercially available capacitances were selected for the experiments. In such conditions, the pulse generator's output is as Figure 7, with an amplitude 12 times the of the DC input voltage. Each stage of the output voltage lasts one millisecond, resulting in a signal with a frequency of 100 Hz. Therefore, a 1.2 kV pulse is generated from a 100 V input assuring the sufficient behavior of the circuit in boosting a low voltage DC input twelve times to generate the intended output. Furthermore, to better evaluate the speed of the pulse generation process, Figure 7c depicts a rise-time of approximately 5 microseconds. Accordingly, the voltage waveform of half of the capacitors is shown in Figure 8. Since the behavior of the circuit capacitors is similar in pairs, it is sufficient to present only half of them.

As can be seen, the desired pulse is achieved by selecting appropriate capacitors while maintaining their voltage balance. In such conditions, the voltage of the C3, C1, and C5 oscillates around 100, 200, and 400 volts, respectively. Each voltage waveform has a ripple less than 5 percent, confirming their precise design. Since the circuit can operate with various frequencies, Figure 9 provides two sample output voltages with 50 and 1000 Hz frequencies. Moreover, the proposed circuit can generate a combination of wide and narrow pulses, as some applications may require them.

For this purpose, the output voltage should alternate between two specific values at a certain rate to produce such waveforms. For instance, Figure 10 illustrates the circuit's output voltage as a combination of wide (100 Hz) and narrow (12.5 kHz) pulses in which by alternately bypassing capacitors C3 and C4, the pulse amplitude changes between 1 and 1.2 kilovolts. Afterall, the experimental results confirm the aforementioned calculation and simulations, implyng the proper performance of the proposed topology as a pulse generator suitable for applications with a single low voltage input source.

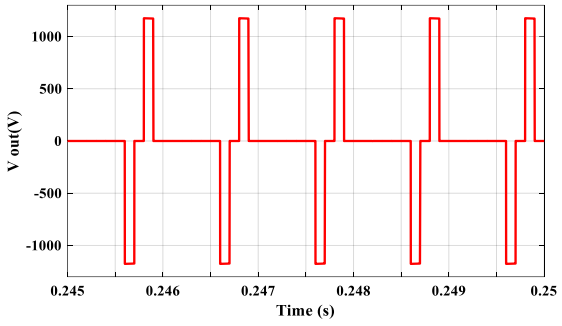

(a)

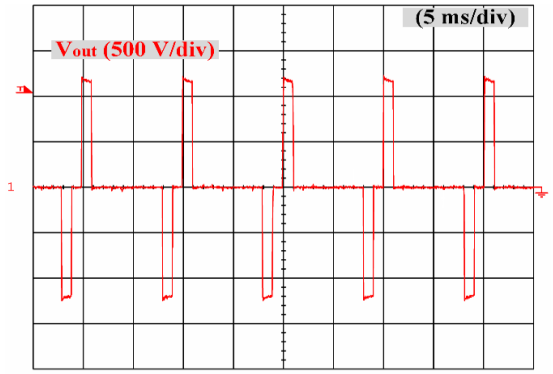

(b)

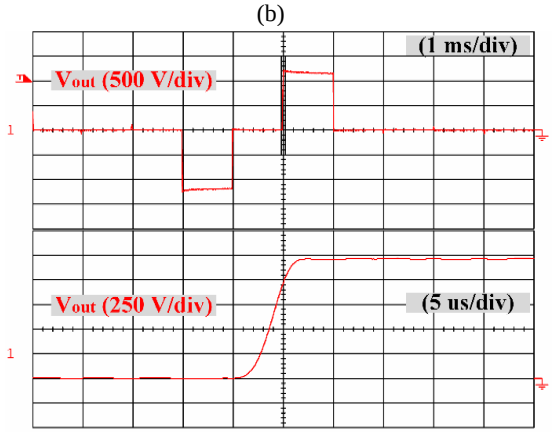

(c)

Figure 7. The output voltage of the proposed pulse generator, (a) simulation, (b) experimental and (c) its rise time

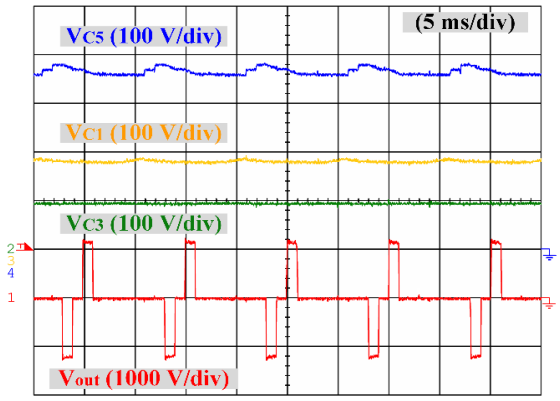

(b)

Figure 8. The output voltage of the proposed pulse generator, (a) simulation and (b) experimental

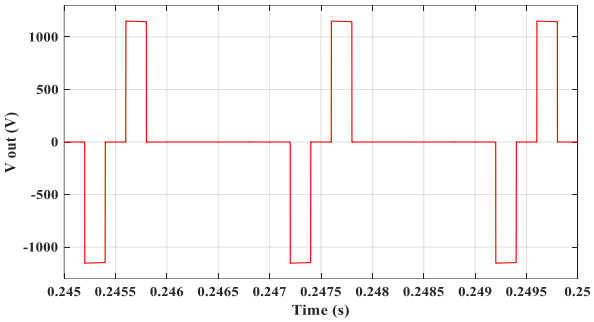

(a)

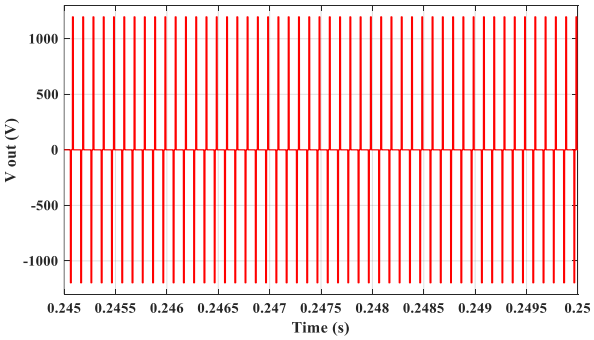

(b)

Figure 9. (a) 50 and (b) 1000 Hz output voltages

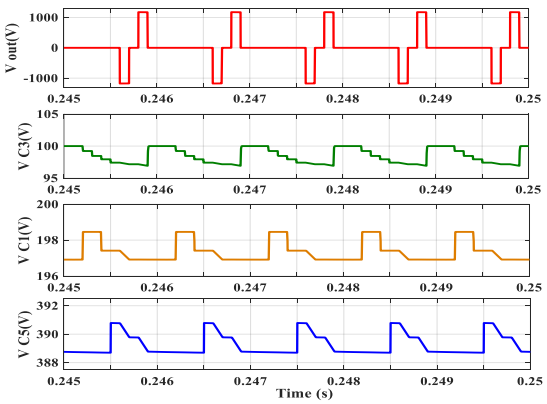

(a)

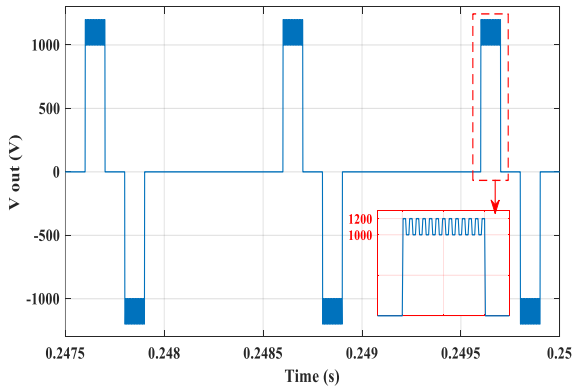

Figure 10. A combination of wide and narrow pulses

4. CONCLUSION

A bipolar pulsed power generator was presented, which can appropriately replace Marx structures in applications with low voltage inputs due to its boosting ability. Circuit topology, operating principles, and different stages of the circuit's operation are presented besides capacitance calculations. Also, the structure was compared to other similar circuits where the results showed that it outperforms them by requiring fewer semiconductor devices to generate the same output pulse. Eventually, simulations were conducted, and by testing a laboratory prototype, a 1.2 kV bipolar voltage pulse was produced from a single DC source with an amplitude of 100 V, whereas it had a 5 µs rise-time. The theoretical bases of the topology, simulation, and experimental results prove the sufficient ability to produce the intended bipolar pulses.

5. REFERENCES

1. Gholamalitabar, H. and Rezanejad, M., "A high gain bipolar pulse generator with low voltage input source", ***International Journal of Engineering, Transactions B: Applications***, Vol. 32, No. 8, (2019), 1126-1133, doi: 10.5829/IJE.2019.32.08B.08.
2. Baek, J.W., Yoo, D.W., Rim, G.-H. and Lai, J.-S., "Solid state marx generator using series-connected IGBTS", ***IEEE Transactions on Plasma Science***, Vol. 33, No. 4, (2005), 1198-1204, doi: 10.1109/MODSYM.2004.1433592.
3. Calico, S., Scott, M. and Clark, M., "Development of a compact marx generator for high-power microwave applications", in Digest of Technical Papers. 11th IEEE International Pulsed Power Conference (Cat. No. 97CH36127), IEEE. Vol. 2, (1997), 1536-1541, doi: 10.1109/PPC.1997.674622.
4. Jambari, H., Azli, N.A. and Piah, M.A.M., "Cascaded h-bridge multilevel inverter based pulsed power supply for liquid food sterilization", in 2010 4th International Power Engineering and Optimization Conference (PEOCO), IEEE. (2010), 154-158, doi: 10.1109/PEOCO.2010.5559161.
5. Schoenbach, K.H., Nuccitelli, R. and Beebe, S.J., "Zap [extreme voltage for fighting diseases]", ***IEEE Spectrum***, Vol. 43, No. 8, (2006), 20-26, doi: 10.1109/MSPEC.2006.1665052.
6. Shohet, J.L., "Plasma-aided manufacturing", ***IEEE Transactions on Plasma Science***, Vol. 19, No. 5, (1991), 725-733, doi: 10.1109/27.108405.
7. Wu, T.-F., Tseng, S., Wu, M.-W. and Chen, Y.-M., "Narrow pulsed voltage generator for liquid food sterilization", in Twenty-First Annual IEEE Applied Power Electronics Conference and Exposition, 2006. APEC'06., IEEE. (2006), doi: 10.1109/APEC.2006.1620715.
8. Yao, C., Dong, S., Zhao, Y., Lv, Y., Liu, H., Gong, L., Ma, J., Wang, H. and Sun, Y., "Bipolar microsecond pulses and insulated needle electrodes for reducing muscle contractions during irreversible electroporation", ***IEEE Transactions on Biomedical Engineering***, Vol. 64, No. 12, (2017), 2924-2937, doi: 10.1109/TBME.2017.2690624.
9. Krishnaswamy, P., Kuthi, A., Vernier, P.T. and Gundersen, M.A., "Compact subnanosecond pulse generator using avalanche transistors for cell electroperturbation studies", ***IEEE Transactions on Dielectrics and Electrical Insulation***, Vol. 14, No. 4, (2007), 873-877, doi: 10.1109/TDEI.2007.4286518.
10. Ding, W., Wang, Y., Fan, C., Gou, Y., Xu, Z. and Yang, L., "A subnanosecond jitter trigger generator utilizing trigatron switch and avalanche transistor circuit", ***IEEE Transactions on Plasma Science***, Vol. 43, No. 4, (2015), 1054-1062, doi: 10.1109/TPS.2015.2402178.
11. Inokuchi, M., Akiyama, M., Sakugawa, T., Akiyama, H. and Ueno, T., "Development of miniature marx generator using bjt", in 2009 IEEE Pulsed Power Conference, IEEE. (2009), 57-60, doi: 10.1109/PPC.2009.5386197.
12. De Angelis, A., Dionigi, M., Giglietti, R. and Carbone, P., "Experimental comparison of low-cost sub-nanosecond pulse generators", ***IEEE Transactions on Instrumentation and Measurement***, Vol. 60, No. 1, (2010), 310-318, doi: 10.1109/TIM.2010.2047591.
13. Tajik, M.R. and Nateghi, A.R., "Design, simulation and performance comparison of pulse power generator based on the avalanche breakdown phenomenon in bipolar junction transistors", in 2020 11th Power Electronics, Drive Systems, and Technologies Conference (PEDSTC), IEEE. (2020), 1-6, doi: 10.1109/PPC.2009.5386197.
14. Sakamoto, T., Nami, A., Akiyama, M. and Akiyama, H., "A repetitive solid state marx-type pulsed power generator using multistage switch-capacitor cells", ***IEEE Transactions on Plasma Science***, Vol. 40, No. 10, (2012), 2316-2321, doi: 10.1109/TPS.2012.2184776.
15. Redondo, L., Zahyka, M. and Kandratsyeu, A., "Solid-state generation of high-frequency burst of bipolar pulses for medical applications", ***IEEE Transactions on Plasma Science***, Vol. 47, No. 8, (2019), 4091-4095, doi: 10.1109/TPS.2019.2923570.
16. Lee, S.-H., Song, S.-H., Jo, H.-B. and Ryoo, H.-J., "Solid-state bipolar pulsed-power modulator based on a half-bridge power cell structure", ***IEEE Transactions on Plasma Science***, Vol. 47, No. 10, (2019), 4466-4472, doi: 10.1109/TPS.2019.2911716.
17. Liu, Y., Fan, R., Zhang, X., Tu, Z. and Zhang, J., "Bipolar high voltage pulse generator without h-bridge based on cascade of positive and negative marx generators", ***IEEE Transactions on Dielectrics and Electrical Insulation***, Vol. 26, No. 2, (2019), 476-483, doi: 10.1109/TDEI.2018.007861.
18. Gholamalitabar, H., Adabi, J. and Rezanejad, M., "A modular step-up high-voltage bipolar pulse generator", ***IEEE Transactions on Plasma Science***, Vol. 47, No. 5, (2019), 2736-2741, doi: 10.1109/TPS.2019.2910022.
19. Alijani, A., Adabi, J. and Rezanejad, M., "A bipolar high-voltage pulsed-power supply based on capacitor-switch voltage multiplier", ***IEEE Transactions on Plasma Science***, Vol. 44, No. 11, (2016), 2880-2885, doi: 10.1109/TPS.2016.2611562.
20. Redondo, L., "New four-switches bipolar solid-state marx generator", in 2013 19th IEEE Pulsed Power Conference (PPC), IEEE. (2013), 1-5, doi: 10.1109/PPC.2013.6627573.

Persian Abstract

چکیده

این مقاله یک مولد توان پالسی را ارائه می‌کند که می‌تواند یک پالس دوقطبی ولتاژ بالا را از یک منبع ورودی نسبتاً کم ولتاژ، بر اساس مفهوم کلید–خازنی، تولید کند. بر اساس در یک الگوی از پیش تعریف شده، مدار ولتاژ ورودی را با ذخیره انرژی در چندین خازن و آزاد کردن آن به بار به طور همزمان افزایش می دهد. شایان ذکر است که این ساختار بدون استفاده از هیچ کلیدی دوسر بار می تواند ترمینال خروجی خود را در حین شارژ کردن خازن ها، اتصال کوتاه کند. این توپولوژی عمدتاً برای کاربردهایی مناسب است که نیاز به پالس ولتاژ بالا دارند و فقط به منابع ورودی ولتاژ پایین دسترسی دارند. محاسبه و به کارگیری دقیق خازن‌ها تضمین می‌کند که مدار می‌تواند پالس‌های خروجی مورد نظر را با افت ولتاژ قابل قبولی تولید کند. در نهایت، MATLAB Simulink برای ارزیابی عملکرد مدار مورد استفاده قرار گرفت و آزمایش‌های تجربی بر روی یک نمونه آزمایشگاهی انجام شد که نتایج آن، عملکرد مناسب مدار را تایید کرد.

AIMS AND SCOPE

The objective of the International Journal of Engineering is to provide a forum for communication of information among the world's scientific and technological community and Iranian scientists and engineers. This journal intends to be of interest and utility to researchers and practitioners in the academic, industrial and governmental sectors. All original research contributions of significant value focused on basics, applications and aspects areas of engineering discipline are welcome.

This journal is published in three quarterly transactions: Transactions A (Basics) deal with the engineering fundamentals, Transactions B (Applications) are concerned with the application of the engineering knowledge in the daily life of the human being and Transactions C (Aspects) - starting from January 2012 - emphasize on the main engineering aspects whose elaboration can yield knowledge and expertise that can equally serve all branches of engineering discipline.

This journal will publish authoritative papers on theoretical and experimental researches and advanced applications embodying the results of extensive field, plant, laboratory or theoretical investigation or new interpretations of existing problems. It may also feature - when appropriate - research notes, technical notes, state-of-the-art survey type papers, short communications, letters to the editor, meeting schedules and conference announcements. The language of publication is English. Each paper should contain an abstract both in English and in Persian. However, for the authors who are not familiar with Persian, the publisher will prepare the latter. The abstracts should not exceed 250 words.

All manuscripts will be peer-reviewed by qualified reviewers. The material should be presented clearly and concisely:

- *Full papers* must be based on completed original works of significant novelty. The papers are not strictly limited in length. However, lengthy contributions may be delayed due to limited space. It is advised to keep papers limited to 7500 words.
- *Research* notes are considered as short items that include theoretical or experimental results of immediate current interest.
- *Technical notes* are also considered as short items of enough technical acceptability with more rapid publication appeal. The length of a research or technical note is recommended not to exceed 2500 words or 4 journal pages (including figures and tables).

Review papers are only considered from highly qualified well-known authors generally assigned by the editorial board or editor in chief. Short communications and letters to the editor should contain a text of about 1000 words and whatever figures and tables that may be required to support the text. They include discussion of full papers and short items and should contribute to the original article by providing confirmation or additional interpretation. Discussion of papers will be referred to author(s) for reply and will concurrently be published with reply of author(s).

INSTRUCTIONS FOR AUTHORS

Submission of a manuscript represents that it has neither been published nor submitted for publication elsewhere and is result of research carried out by author(s). Presentation in a conference and appearance in a symposium proceeding is not considered prior publication.

Authors are required to include a list describing all the symbols and abbreviations in the paper. Use of the international system of measurement units is mandatory.

- On-line submission of manuscripts results in faster publication process and is recommended. Instructions are given in the IJE web sites: www.ije.ir-www.ijeir.info
- Hardcopy submissions must include MS Word and jpg files.
- Manuscripts should be typewritten on one side of A4 paper, double-spaced, with adequate margins.
- References should be numbered in brackets and appear in sequence through the text. List of references should be given at the end of the paper.
- Figure captions are to be indicated under the illustrations. They should sufficiently explain the figures.
- Illustrations should appear in their appropriate places in the text.
- Tables and diagrams should be submitted in a form suitable for reproduction.
- Photographs should be of high quality saved as jpg files.
- Tables, Illustrations, Figures and Diagrams will be normally printed in single column width (8cm). Exceptionally large ones may be printed across two columns (17cm).

PAGE CHARGES AND REPRINTS

The papers are strictly limited in length, maximum 8 journal pages (including figures and tables). For the additional to 8 journal pages, there will be page charges. It is advised to keep papers limited to 3500 words.

Page Charges for Papers More Than 8 Pages (Including Abstract)	
For International Author ***	**$55 / per page**
For Local Author	**100,000 Toman / per page**

AUTHOR CHECKLIST

- Author(s), bio-data including affiliation(s) and mail and e-mail addresses).
- Manuscript including abstracts, key words, illustrations, tables, figures with figure captions and list of references.
- MS Word files of the paper.

International **J**ournal of **E**ngineering, P.O. Box 13145-1659, Tehran, I.R. Iran
Materials and Energy Research Center, 5 Ahuramazda St., Alvand Ave., Argentina Sq., Tehran, Islamic Republic of Iran
www.merc.ac.ir - www.emerc.ac.ir

THOMSON REUTERS

WEB OF SCIENCE

Scopus®

CAS®
A DIVISION OF THE
AMERICAN CHEMICAL SOCIETY

Google
Scholar